ERZİNCAN UNIVERSITY JOURNAL OF SCIENCE AND TECHNOLOGY
ISSN: 1307-9085, e-ISSN: 2149-4584

EDITORIAL BOARD

AIMS AND SCOPE

The aim of the **Erzincan University Journal of Science and Technology** is to publish original research articles and reviews made in the fields of Science, Engineering in order to create a quality academic contribution in these fields.

Research areas covered in the journal:

- Physics, Chemistry, Biology, Mathematics and related areas
- Mechanical, Electrics-Electronics, Civil and related engineering areas
- Health sciences and related areas

Open Access Policy

Erzincan University Journal of Science and Technology is an open access journal which means that all content is freely available without charge to the user or his/her institution. Users are allowed to read, download, copy, distribute, print, search, or link to the full texts of the articles, or use them for any other lawful purpose, without asking prior permission from the publisher or the author. Erzincan University Journal of Science and Technology signed the Budapest Open Access Declaration (https://budapestopenaccessinitiative.org/).

Editor in chief: Doç. Dr. Kemal Volkan ÖZDOKUR
Address: Department of Chemistry, Erzincan Binali Yıldırım University, Erzincan, Türkiye.
E-mail: fbedergierzincan@gmail.com

Publisher: Erzincan Binali Yıldırım University
Address: Erzincan Binali Yıldırım University, Erzincan, Türkiye.

RESEARCH ARTICLES:

e-ISSN: 2149-4584

Erzincan University Journal of Science and Technology

EJSAT 2025, 18 (3) 696-702

Research Article

On the Number of Nonempty Subsets in a Given Set

M. Faysal AKIN [1*], Aziz İLHAN [2*]

[1]Lecturer, Dicle University, Diyarbakır, Turkey
[2]Associate Professor, İnönü University, Malatya, Turkey

Received: 27/05/2024**, Revised:** 30/12/2024**, Accepted:** 13/01/2025**, Published:** 31/12/2025

Abstract

Sets contain some numbers according to their properties and can help us to write some series. At this point, thanks to the equations arising from the mathematical series, the existence of certain proofs can be proved in which generalizations can be expressed. In addition, the proofs can be tools or results in reaching new generalizations. In this direction, the aim of this study is to prove a sum sequence for the calculation of all subsets of a set other than emptiest set in which there are ordered sums of its elements except the empty set. In this direction, a different format of the summation series formed by subtracting the empty set from the number of all subsets that form the ordered sums of a set with n elements different from the empty set is obtained and the equality is proved by inductive proof method. Because of, the obtained general equality is presented as a new sum series. It is predicted that new generalizations can be reached thanks to this equality.

Keywords: Set, sum series, ordered sums, subset.

Bir Kümede Sıralı Toplamların Bulunduğu Tüm Alt Kümelerin Toplam Dizisi Üzerine

Öz

Kümeler özelliklerine göre birtakım sayıları ihtiva etmekte ve bazı serileri yazabilmemize yardımcı olabilmektedir. Bu noktada oluşturulan matematiksel serilerden doğan eşitlikler sayesinde genellemelerin ifade edilebileceği birtakım ispatların varlığı kanıtlanabilmektedir. Ayrıca bu ispatlar yeni genellemelere ulaşmada birer araç veya sonuç olabilmektedir. Bu doğrultuda çalışmanın amacı boş kümeden farklı bir kümede boş küme hariç elemanlarının sıralı toplamlarının bulunduğu tüm alt kümelerinin hesabına yönelik bir toplam dizisinin ispatını yapabilmektir. Bu doğrultuda boş kümeden farklı n elemanlı bir kümenin sıralı toplamlarını oluşturan bütün alt kümelerinin sayısından boş küme çıkartılarak oluşturulan toplam serisinin bir farklı formatı elde edilmiş ve tümevarım ispat yöntemiyle eşitlik ispatlanmıştır. Sonuç olarak elde edilen genel eşitlik yeni bir toplam serisi olarak sunulmuştur. Bu eşitlik sayesinde yeni genellemelere ulaşılabileceği öngörülmektedir.

Anahtar Kelimeler: Küme, toplam serisi, sıralı toplamlar, alt küme.

Corresponding Author: aziz.ilhan@inonu.edu.tr
Cite this Article: Erzincan University Journal of Science and Technology 2025, 18(3)696-702. https://doi.org/10.18185/erzifbed.1490639

1. Introduction and Preliminaries

The concept of the proof in mathematics has been considered extremely important. It has appeared in front of human beings while discussing many mathematical concepts. With the existence of mathematics, the abstract dimension of this science has become more understandable thanks to propositions, theorems and proofs related to these theorems. The first proof recorded in history belongs to the Babylonians. Thales applied the first formal mathematical proof in geometry [1]. This proof is extremely important in revealing the relationship between abstract concepts and concrete concepts. One of the main purposes of different types of the proofs in mathematics is to express the relationships between abstract concepts, to interpret these relationships correctly and to reach new knowledge. At this point, it is possible to obtain new knowledge and advance mathematical knowledge through proofs.

Although the proof condition can be realized in different types, in mathematical theorems involving algebraic expressions and equations, inductive proof is a frequently used type of the proof. As a matter of fact, according to Yıldırım (2011), Euclid's contribution to geometry lies not in presenting original knowledge, but in presenting previously known proofs in a deductive system [2]. In this presentation, from a small number of axioms, postulates and definitions selected as premises, the proofs of all the remaining propositions are given by deductive inference. The propositions proved in this axiomatic system constitute the theorems of the system. It was observed that Euclid, while making proofs, adhered to the requirement of Aristotle, who lived a period before him, that proofs should be made by applying the least number of assumptions [3].

While performing operations on sets, series are used from time to time, and when calculating the sum of subset series, operations can be performed quickly. At this point, number theory comes into play and contributes to mathematics in analyzing certain relationships. One of the important research topics for number theory is to characterize numbers and to evaluate the relations or correlations of numbers with each other. Many problems in number theory can essentially be transformed into the number of subsets of a set with a finite number of elements under certain conditions. Therefore, the result of the problem can be evaluated with different approaches such as reduction, coding, and generating function [4]. In addition, in the proof of the theorem to be constructed in this study, the concept of combination appears as an important element for the solution. Combination: Given $r,\ n \in N$ and $r \leq n$, each of the subsets of a set A with n elements and r elements is called an r′ combination of a set A [5].

One of the important issues in number theory is to characterize numbers and to examine their relationships and relations with each other. In number theory, many problem situations can actually be transformed into the number of subsets of a finite number of elements with certain conditions [6]. As a matter of fact, one of the main objectives of mathematical science is to extend the mathematical structures studied to larger, inclusive mathematical structures and to obtain general mathematical results by working on these extended structures [7]. Although syntactic or sequential proof is based on the formal inference process, it is said that semantic proof production can be fed by intuitive inferences [8]. Therefore, since mathematics is a cumulative science and there is a relational structure between mathematical concepts, it can be

said that it is a necessity to build new knowledge on the previous ones [9]. In this direction, in this study, sum series were handled together with the concept of combination, and a generalization was reached for an equality related to sets by inductive proof.

2. Main Theorems and Proofs

In this section, a different format of the sum series formed by subtracting the empty set from the number of all subsets forming the ordered sums of an n-element set is obtained. In the study, a sum sequence for the calculation of all subsets of a set with ordered sums of its elements except the empty set was proved by inductive proof. In mathematics, induction is a powerful proof technique and has a systematic structure as in other proof techniques [10], [11].

Now we have the following:

Theorem 1: For a series of sums generated by subtracting the empty set from the number of all subsets of a set of *n* elements that form ordered sums. Then we have

$$\sum_{k=1}^{n} 2^{k-1}(\mathrm{n}-\mathrm{k}) = \sum_{k=2}^{n} \binom{n}{k}. \tag{1.1}$$

Proof: Let $A=\{a_1, a_2, \ldots a_n\}$ be a set of *n* elements. Then for the *n-1* elements, each of the ordered binary sums selected from this set, we can write

$a_1+a_2, a_1+a_3, a_1+a_4, \ldots a_1+a_n,$

and for the *n-2* elements, we have

$a_2+a_3, a_2+a_4, a_2+a_5, \ldots a_2+a_n.$

At last, for one element, we get

$a_{n-1}+a_n.$

Thus, we obtain

$$C(n,2) = \frac{n(n-1)}{2}. \tag{1.2}$$

Now, if we write each of the ordered triple sums selected from this set, then for the *n-2* elements, we have

$a_1+a_2+a_3, a_1+a_2+a_4, \ldots a_1+a_2+a_n,$

and for the *n-3* elements, we have

$a_1+a_3+a_4, a_1+a_3+a_5, \ldots a_1+a_3+a_n,$

At last, for one element, we get

$a_1+a_{n-1}+a_n,$

Also with similar way, for the *n-3* elements, we have

$a_2+a_3+a_4,\ a_2+a_3+a_5,\ \ldots\ a_2+a_3+a_n,$

and for the *n-4* elements, we get

$a_2+a_4+a_5,\ a_2+a_4+a_6,\ \ldots\ a_2+a_4+a_n,$

At last, for one element, we get

$a_2+a_{n-1}+a_n.$

Indeed, ın this way the process is executed for the sum of all ternary elements in the last step, for one element, we get

$a_{n-2}+a_{n-1}+a_n.$

Thus, the triple sums are given by

$$C(n,\ 3)=\frac{n(n-1)(n-2)}{3!}. \qquad (1.3)$$

When the process is executed for the sum of all elements, at each step the sum results in a combination expression and at step *n*, for one element, we have

$a_1+a_2+\ldots+a_n.$

Thus, with the n elements sum, we get

$$C(n,\ n)=1. \qquad (1.4)$$

Now, for given all these sums, the number of terms can be expressed by

$$\sum_{k=2}^{n}\binom{n}{k}. \qquad (1.5)$$

But if this sum is considered in terms of each term, then for the number of times we can write

$n-1,\ n-2,\ n-3,\ \ldots\ ,1.$

Thus, we obtain

$1.(n-1)+2.(n-2)+4.(n-3)\ \ldots\ 2^{n-1}[n-(n-1)].$

If we generalize this sum for the grand total, we find

$$\sum_{k=1}^{n} 2^{k-1}(\mathrm{n}-\mathrm{k}). \qquad (1.6)$$

Hence we get the following:

$$\sum_{k=1}^{n} 2^{k-1}(\mathrm{n}-\mathrm{k}) = \sum_{k=2}^{n} \binom{n}{k}. \qquad (1.7)$$

Now let prove equation (1.7) by induction method. As is well known that, the number of all subsets of a set of *n* elements is 2^n. Therefore, we find

$$\sum_{k=1}^{n} \binom{n}{k} = 2^{\mathrm{n}}.$$

Also, one can write

$$\sum_{k=1}^{n} x^k = \frac{1-x^{n+1}}{1-x}.$$

If the derivative of both sides of this equation is taken with respect to *k*, then we have

$$\sum_{k=1}^{n} k.x^{k-1} = \frac{-(n+1).x^n(1-x)+(1-x^{n+1})}{(1-x)^2}$$

For the $x=2$, we obtain

$$\sum_{k=1}^{n} k.2^{k-1} = \frac{(n+1).2^n+(1-2^{n+1})}{(1-2)^2} = n.2^n+2^n+1-2.2^n=(n-1).2^n+1 = \frac{1-2^n}{1-2} = 2^n-1 = \sum_{k=1}^{n} 2^{k-1}$$

Therefore, we have

$$\sum_{k=1}^{n} 2^{k-1}(n-k) = \sum_{k=2}^{n} \binom{n}{k}. \qquad (1.8)$$

Thus from (1.8) we can write

$$\sum_{k=1}^{n} 2^{k-1}(n) - \sum_{k=1}^{n} 2^{k-1}(k) = 2^n-C(n, 0)-C(n, 1)$$

and

$$n.\left(\frac{1-2^n}{1-2}\right) - \left[\frac{(n+1).2^n+(1-2^{n+1})}{1}\right] = 2^n-1-n.$$

Using -1 is in the last equation, we get

$$-n+2^n.n-(n+1).2^n-1+2^{n+1}=2^n-1-n.$$

If the expressions *-1* and *-n* on both sides of the equation are simplified. We get

$$2^n.n-(n+1).2^n+2^{n+1}=2^n.$$

Hence we obtain

$$(2^n.n-2^n.n)-2^n+2.2^n=2^n$$

Hence we get

$$2^n = 2^n$$

Thus, the proof is completed.

3. Conclusion

With the help of numbers and series, certain relationships and generalizations can be reached through consecutive sums performed on a set. When evaluating the relationship between clusters and their subsets, sum series can be utilized from time to time and some inferences can be reached at this point. Therefore, in this study, a different format of the summation series formed by subtracting the empty set from the number of all subsets forming the ordered sums of an *n* element cluster was tried to be determined.

Starting from this point: For the sum series generated by subtracting the empty set from the number of all subsets of set of the *n* elements that form the ordered sums of set of the *n* elements, we get the equation (1.1). Thus if we collect the result, we can give the following:

$$\sum_{k=1}^{n} 2^{k-1}(n) - \sum_{k=1}^{n} 2^{k-1}(k) = \sum_{k=1}^{n} 2^{k-1}(\mathrm{n}-\mathrm{k}) = \sum_{k=2}^{n} \binom{n}{k}$$

Because of the above equation, it is proved by induction that the combinatorial formula obtained for the sum series formed by subtracting the empty set from the number of all subsets forming the ordered sums of a set of *n* elements can actually be expressed by a power series. Thanks to this equality, it is predicted that different proofs in the literature on ordered sums can be carried out and new generalizations can be reached.

Ethics in Publishing

There are no ethical issues regarding the publication of this study

Author Contributions

All authors contributed equally to the study.

References

[1] Baki, A. (2014). Philosophy and history of mathematics (2nd Publication). Baki, A. (Ed.) Pegem Academy, Turkey.

[2] Yıldırım, C. (2011). History of science. (1nd Publication). Yıldırım, C. (Ed.) Remzi Publication, Turkey.

[3] Yıldırım, C. (1996). Mathematical thinking. (1nd Publication). Yıldırım, C. (Ed.) Remzi Publication, Turkey.

[4] Öztürk, F. (1995). Kombinatoric counting problems. (1nd Publication). Öztürk, F. (Ed.) Ankara University Faculty of Science Revolving Fund Enterprise Publications, Turkey.

[5] Bulut, F. (2017). Finding the Nth element of the Fibonacci sequence using Pascal's triangle, Combination and Induction. Al-Jazari Journal of Science and Engineering, 4(3), 429-435.

[6] Atiklik, İ., Çalık, A. C., & İnan, E. (2020). A Different Counting Method for Subsets Generalized via Fibonacci Numbers. Science Harmony, 3(2), 33-44.

[7] Beşer, M. (2011). The Existence of utility functions for partially ordered Hausdorff Spaces. Journal of Social Sciences, 2011(2), 108-111.

[8] Weber, K., & Alcock, L. (2004). Semantic and syntactic proof productions. Educational Studies in Mathematics, 56(2/3), 209-234.

[9] Pala, O., & Narlı, S. (2018). Prospective mathematics teachers' proving approaches and difficulties related to equivalence of ınfinity sets. Turkish Journal of Computer and Mathematics Education, 9(3), 449-475.

[10] Dede, Y. (2013). Proof in mathematics: Importance, types and historical development. Zembat, İ. Ö., Özmantar, M. F. Bingölbali, E. Şandır, H. & Delice A. (Eds.), In mathematical concepts with their definitions and historical development (pp. 15-34). Pegem Academy, Turkey.

[11] Doğan-Dunlap, H., Özdemir-Erdoğan, E., & Kılıç, Ç. (2008). Mathematical induction: Misconceptions and learning difficulties encountered. Özmantar, M. F., Bingölbali, Akkoç, E. H. (Eds.), Mathematical misconceptions and solution suggestions in (pp. 291-327). Pegem Academy, Turkey.

e-ISSN: 2149-4584

Erzincan University Journal of Science and Technology

EJSAT 2025, 18 (3) 703-712

Research Article

A Note on k-Secant Lines of the Klein Cubic Threefold in $PG(4,3)$

Ayşe Bayar [1] Ziya Akça [2*]

[1,2] Eskişehir Osmangazi University, Faculty of Science, Department of Mathematics and Computer Science, 26480 Eskişehir, Türkiye

Received: 26/09/2024, **Revised:** 02/12/2024, **Accepted:** 19/12/2024, **Published:** 31/12/2025

Abstract

In this paper, we developed an algorithm to classify and construct k-secant lines for the Klein cubic threefold $\mathcal{F}$ in the projective space $PG(4,3)$. The algorithm identifies secant lines based on their intersections with $\mathcal{F}$, revealing distinct categories of non-secant and k-secant lines. Additionally, we partitioned the point set of $\mathcal{F}$ into three subsets, uncovering geometric configurations and forming 5-gons related to perspectivity. This analysis provides new insights into the structure of the Klein cubic threefold and its geometric properties.

Keywords: Klein cubic three*f*old, Projective space, Galois field, k-secant lines.

$PG(4,3)$ deki Klein Kübiğin k-kesen Doğruları Üzerine Bir Not

Öz

Bu çalışmada, $PG(4,3)$ projektif uzayındaki Klein kübik $\mathcal{F}$ için k-sekant doğruları belirleyen ve sınıflandıran bir algoritma geliştirdik. Algoritma, $\mathcal{F}$ ile kesişimlerine dayanarak sekant doğrularını belirleyerek, kesen olmayan ve k-kesen doğruların farklı sınıflarını ortaya çıkarmaktadır. Ayrıca, $\mathcal{F}$ nin nokta kümesini üç alt kümeye ayırarak belirli geometrik konfigürasyonları inceledik ve perspektiflikle ilişkili beşgenler (5-gonlar) oluşturduk. Bu analiz, Klein kübik yapısına ve geometrik özelliklerine dair yeni bakış açıları sunmaktadır.

Anahtar Kelimeler: Klein kübik, Projektif uzay, Galois cismi, k-kesen doğrular.

Corresponding Author: zakca@ogu.edu.tr

Cite this Article: Erzincan University Journal of Science and Technology 2025, 18(3)703-712. https://doi.org/10.18185/erzifbed.1556681

1. Introduction

The study of embedded structures in projective spaces has significantly advanced our understanding of geometric relationships and algebraic varieties, offering novel insights into higher-dimensional spaces [1-4, 7]. One important concept in projective geometry is that of *k*-secant lines, which intersect a given surface at precisely *k* distinct points. One of the earliest and most notable examples is the non-singular Klein cubic threefold, initially studied by Felix Klein in 1879 in the 4-dimensional projective space [11]. This surface, denoted by $\mathcal{F}$, is embedded in the 4-dimensional projective space. Its geometric properties, including the classification of its lines, remain a central topic of modern research. Over finite fields, the classification of non-singular cubic surfaces continues to be an active area of investigation. For example, it has been shown that a non-singular cubic surface over the finite field *GF(2)* can contain 15, 9, 5, 3, 2, 1, or 0 lines [9, 10]. Rosati further demonstrated that when the field size q is odd, the number of lines can be one of 27, 15, 9, 7, 5, 3, 2, 1, or 0 [12]. Hirschfeld's foundational work in the 1960s introduced a program to classify cubic surfaces with 27 lines over finite fields [8], and his research on classical configurations such as the double-six has advanced our understanding of these structures [5,9]. This line of research remains important, with algorithms being developed to classify surfaces with 27 lines using the classical theory of double-sixes [6].

The Klein cubic defined by $x^2y + y^2z + z^2v + v^2w + w^2x = 0$ over $\mathbb{C}$ contains neither Eckardt points nor triple lines [13]. But, over $q = 2$, the Klein cubic threefold is a quadric because $x^2 = x$ for each element of $GF(2)$. This quadric has a nucleus, six spreads with five lines, and each point is an Eckardt point [3]. So, we need to investigate these properties over arbitrary fields. For $q = 3$, the aim of the article is to investigate the Klein cubic threefold is structural and geometric properties when extended to a field with three elements. We introduce an algorithm to classify all *k*-secant lines of the Klein cubic threefold $\mathcal{F}$ in $PG(4,3)$. By applying this algorithm, we identify and classify lines based on their intersections with $\mathcal{F}$ at 0, 1, 2, 3, or 4 points. Additionally, we partition the points of $\mathcal{F}$ into three disjoint subsets, each exhibiting unique secant configurations. This analysis of *k*-secant lines and the formation of three distinct 5-gons, based on the points of $\mathcal{F}$ and their perspectivity properties, provided deeper insights into the geometric structure of the Klein cubic threefold.

2. Preliminaries

Let $GF(q)$ denote Galois field of order $q = p^k$, where p is a prime. If any $(n + 1)$-dimensional vector space V, the n-dimensional projective space $PG(4,q)$ over $GF(q)$ is the set of all subspaces of V distinct from the trivial subspaces. The 1-dimensional subspaces are called the points of $PG(n,q)$, the 2-dimensional subspaces are called the (projective) lines and the 3-dimensional ones are called (projective) planes. We note that by going from a vector space to the associated projective space, the dimension decreases by one. Hence, an $(n+1)$-dimensional vector space V gives rise to an n-dimensional projective space $PG(4,q)$. The points in projective space $PG(4,q)$ are defined by equivalence classes of non-zero vectors in the vector

space V. For example, for 4-dimensional vector space, the associated 3-dimensional projective is defined where points are represented by equivalence classes of vectors (v,w,x,y,z) reducing the dimension by one unit.

A point in projective space $PG(n,q)$ is defined by an equivalence class of non-zero vectors in the vector space V. In projective geometry, two non-zero vectors v and w in V are considered equivalent if they differ by a scalar multiple:

$$v \sim w \Leftrightarrow w = \lambda v,\ \lambda \in GF(q)^*.$$

Here, $GF(q)^*$ denotes the set of non-zero elements in $GF(q)$. For example, for $4-$ dimensional vector space, the associated $3-$ dimensional projective is defined where points are represented by equivalence classes of vectors (w,x,y,z), reducing the dimension by one unit.

The $4-$dimensional projective space $PG(4,q)$ over $GF(q)$ contains $q^4+q^3+q^2+q+1$ points. The total number of lines and the number of lines passing through a given point in $PG(4,q)$ are given by the formulas $\frac{(q^5-1).(q^4-1)}{(q^2-1).(q-1)}$ and $\frac{q^4-1}{q-1}$, respectively. Thus, $PG(4,3)$ has 121 points and 1210 lines. In $PG(4,3),$ every line contains 4 points, and 40 lines pass through each point.

We use the combinatorial definition, where a line is considered as a subsets of points in $PG(4,3)$. A line passing through the points $P(a_0,a_1,a_2,a_3,a_4)$ and $Q(b_0,b_1,b_2,b_3,b_4)$ in $PG(4,3),$ where a_i, $b_i \in GF(3),\ i=0,1,2,3,4$, is denoted by:

$$\langle P,Q\rangle = \begin{bmatrix} a_0 & a_1 & a_2 & a_3 & a_4 \\ b_0 & b_1 & b_2 & b_3 & b_4 \end{bmatrix}.$$

Definition 1 The Klein cubic threefold $\mathcal{F}$ is a projective variety given by the equation:

$$\mathcal{F}: \quad x^2y+y^2z+z^2v+v^2w+w^2x=0 \qquad (1)$$

where x,y,z,v and w are the coordinates of a point (v,w,x,y,z) in 4-dimensional projective space. The Klein cubic threefold $\mathcal{F}$ over the field $GF(q)$ can be identified with a set S of the points $PG(4,q)$ that satisfies the equation (1). In particular, for q = 3, the set S consists of 40 point.

3. A Computational Strategy for *k*-Secant Lines of $\mathcal{F}$

In projective space, geometric structures are defined by the relationships a points, lines, and planes, extending beyond the limitations of Euclidean geometry. One intriguing aspect of projective geometry involves the study of *k*-secant lines, which are lines that intersect a given geometric object, such as a curve or surface, at exactly *k* distinct points. The classification and

enumeration of these *k*-secant lines offer deep insights into the underlying geometry of the object. Understanding these relationships is crucial in various fields, including algebraic geometry, where the concept of *k*-secant lines plays a significant role in exploring the configuration and distribution of points within the projective space.

In this section, we focus on classifying the *k*-secant lines that intersect a given cubic threefold $\mathcal{F}$ in $PG(4,3)$. By systematically analyzing these lines, we can uncover patterns and properties that reveal the complexity of the surface's geometry. This classification not only enhances our understanding of the structure of the surface but also contributes to broader applications in algebraic geometry, where the arrangement of *k*-secant lines is instrumental in exploring the deeper aspects of geometric configurations in the projective space. So, we illustrate the algorithm that used to construct *k*-secants of $\mathcal{F}$ in $PG(4,3)$.

Algorithm: Finding all *k*- secants of $\mathcal{F}$

The goal of these algorithms is to identify and classify all *k*-secant lines of the Klein cubic threefold $\mathcal{F}$ in $PG(4,3)$. A *k* -secant line intersects $\mathcal{F}$ at exactly *k* points. The strategy involves constructing lines using points in $PG(4,3)$, tracking their intersections with $\mathcal{F}$, and ensuring each line is unique. This systematic approach helps reveal the geometric structure of $\mathcal{F}$ and its intersection properties.

Step(1): Finding the points and lines of $PG(4,3)$ by the formula defining in equation (1). In this case, we get 121 points and 1210 lines.

Step(2): Finding the points and lines of $\mathcal{F}$ by the formula defining in equation (1). In this case, we get 40 points as shown the set *S*.

Algorithm for Identifying all *k*-secants of $\mathcal{F}$ in projective space $PG(4,3)$.

1. Initialization

Input Sets:

P: A set of points in the projective geometry $PG(4,3)$.

S: A subset of points from *P*.

2. Define Auxiliary Functions

Galois Field Arithmetic:

gf3_add(v_1,v_2). Adds two vectors v_1 and v_2 component-wise under $GF(3)$ arithmetic (i.e., modulo 3).

gf3_mul(scalar, *v*): Multiplies a vector *v* by a scalar under $GF(3)$ arithmetic.

Find Line Function:

find_line (P, P_1, P_2) . Given two points P_1 and P_2, this function computes two more points P_3 and P_4 on the line defined by P_1 and P_2 using the addition and multiplication rules of $GF(3)$. The line $\{P_1, P_2, P_3, P_4\}$ is then returned.

3. Main Function to Find 40 Lines

Step 1: Initialize an empty list lines to store the 40 lines.

Step 2: Initialize a set used points to track the points that have been used, starting with P_1.

Step 3: Create the first line l_1.

Select the first point P_2 from *P* that is not in used points.

Use find line (P, P_1, P_2) to generate the line l_1.

Add l_1 to the lines list and update used points with all points in l_1.

Step 4: Create the next 38 lines (l_2 to l_{39}):

For each line, select the next point P_n from *P* that is not in the set of points used.

Use find line (P, P_1, P_n) to generate the line l_n.

Add l_n to the list of lines and update the set of points used with all points in l_n.

Step 5: Create the final line l_{40}:

Identify the remaining points in *P* that are not in the set of points used.
If there are two or more remaining points, form the line l_{40} using P_1 and the first three remaining points.

Add l_{40} to the list of lines.

4. Iterating Over Subset *S*

Step 6: Initialize an empty set unique lines to store unique lines as frozen sets.

Step 7: Iterate over each point in subset *S*:

For each point P_1 in *S*, call find 40 lines (P, P_1) to generate 40 lines.

For each line, check if there are exactly 0, 1, 2, or 3 points missing in subset *S*.

If such a line is found, convert the line to a frozen set and add it to unique lines if it is not already present.

5. Output

Step 8: Print all unique lines stored in unique lines.

This algorithm methodically identifies and records lines in the projective geometry $PG(4,3)$ that have exactly 0, 1, 2, or 3 missing points from a given subset *S*, ensuring that each line is unique.

Theorem 2 Let $\mathcal{F}$ be the Klein cubic threefold with exactly 40 points. For a given surface $\mathcal{F}$ in the projective space $PG(4,3)$, there are 240 lines that are 0-secant (not intersecting the surface), 480 lines that are 1-secant (intersecting the surface at a single point), 360 lines that are 2-secant (intersecting the surface at exactly two distinct points), 120 lines that are 3-secant (intersecting the surface at exactly three distinct points), and 10 lines that are 4-secant (intersecting the surface at exactly four distinct points).

Proof. Using the algorithm for identifying all k-secants of $\mathcal{F}$ in projective space $PG(4,3)$, we observe the following: There are exactly 10 lines that are 4-secant, meaning they intersect $\mathcal{F}$ at four points, with no missing points from a given subset *S*. There are exactly 120 lines that are 3-secant, intersecting $\mathcal{F}$ at three points, with one missing point from a given subset *S*. Furthermore, there are exactly 360 lines that are 2-secant, intersecting $\mathcal{F}$ at two points, with two missing points from *S*. There are also 480 lines that are 1-secant, intersecting $\mathcal{F}$ at one point, with three missing points from a given subset *S*. Therefore, the number of lines in $PG(4,3)$ that do not intersect $\mathcal{F}$ (0-secant) is found to be 240.

4. Disjoint Subsets and Secant Line Configurations in Klein Cubic Threefold $\mathcal{F}$

To reveal the distinguishing features of $\mathcal{F}$, we write the set *S* of points of $\mathcal{F}$ as the union of three disjoint subsets S_1, S_2 and S_3 such that

$$\begin{aligned} S_1 = \{&(1,0,0,0,0),\ (0,1,0,0,0),(0,0,1,0,0),\ (0,0,0,1,0),\ (0,0,0,0,1),\\ &(0,0,1,0,2),\ (0,1,0,0,1),\ (0,1,0,0,2),\ (0,1,0,1,0),\ (0,1,0,2,0),\\ &(1,0,1,0,0),\ (1,0,2,0,0),\ (1,0,0,1,0),\ (1,0,0,2,0),\ (0,0,1,0,1)\},\end{aligned}$$

$S_2 = \{A_1 = (0,1,1,1,1),\ A_2 = (1,0,1,1,1),\ A_3 = (1,1,0,1,1),\ A_4 = (1,1,1,0,1), A_5 = (1,1,1,1,0)\}$ and $S_3 = S \setminus (S_1 \cup S_2)$. Let the subset E of S_1 be the set of points E_i such that $E_i = (e_1, e_2, e_3, e_4, e_5)$, where $e_j = 1$ for $i = j$, otherwise $e_j = 0$, $i, j \in \{1,2,3,4,5\}$. Also, the points of S_3 that lie on the lines spanned by E_i and A_i, $i = 1,2,...,5$ be C_i such that $C_1 = (1,2,2,2,2)$, $C_2 = (1,2,1,1,1)$, $C_3 = (1,1,2,1,1)$, $C_4 = (1,1,1,2,1)$, and $C_5 = (1,1,1,1,2)$. Let's denote the subset of S_3 consisting of these points by C.

The following theorem gives the *k*-secant line numbers of $\mathcal{F}$ for any point selected in the sets S_1, S_2 and S_3.

Theorem 3 Let $\mathcal{F}$ be the Klein cubic threefold in $PG(4,3)$.

(1) Two of the lines passing through any point of the subset E of S_1 intersect $\mathcal{F}$ at four points; six of these lines intersect $\mathcal{F}$ at three points; twenty-one lines of these lines intersect $\mathcal{F}$ at two points, and eleven of these lines intersect $\mathcal{F}$ at one point.

(2) None of the lines passing through any point A_j, $j = 1,2,...,5$ in the set S_2 intersect $\mathcal{F}$ at four points; twelve lines of these lines intersect $\mathcal{F}$ at three points; fifteen lines of these lines intersect $\mathcal{F}$ at two points, and thirteen lines of these lines intersect with $\mathcal{F}$ at one point.

(3) One of the lines passing through any point in the set S_3 or $S_1 \setminus E$ intersects $\mathcal{F}$ at four points; nine of these lines intersect $\mathcal{F}$ at three points; eighteen of these lines intersect $\mathcal{F}$ at two points, and nine of these lines intersect $\mathcal{F}$ at one point.

Proof. We consider an algorithm for identifying all *k*-secants of $\mathcal{F}$ for each point P_1 in *S*, in projective space $PG(4,3)$. If this algorithm is applied to any point E_i in the set *E* instead of P_1, the *k*-secants of $\mathcal{F}$ passing through each E_i point are found, and the *k*-secant numbers passing through the E_i points, as stated in the theorem, is obtained. Similarly, if this algorithm is applied to any point in the set S_2, or S_3, or $S_1 \setminus \mathrm{E}$ instead of P_1, the number *k*-secants passing through these points, as described in the theorem, is also obtained.

Theorem 4 Consider the sets E, S_2 and C in $\mathcal{F}$. The lines spanned by the pairs of points (E_i, E_{i+1}), (A_i, A_{i+1}), and (C_i, C_{i+1}), where $i = 1,2,...,5$ (mod5), are the 2-secants of the Klein cubic threefold $\mathcal{F}$. Furthermore, if the line spanned by two points E_i and E_j, where *i* and *j* are non-consecutive indices, is 4-secant of $\mathcal{F}$, then the lines spanned by A_i and A_j, or C_i and C_j, for nonconsecutive indices *i* and *j,* are 3-secant of $\mathcal{F}$.

Proof. Let *l* be the line by E_i and E_{i+1}, or A_i and A_{i+1}, or C_i and C_{i+1}, where $i = 1,2,...,5$ (mod5) in $PG(4,3)$. Since the other two points on *l* do not satisfy the equation (1), the line *l* is 2-secant of $\mathcal{F}$. The other two points on the line spanned by E_1 and E_3 are (1, 0, 1, 0) and (1, 0, 2, 0, 0), on the line spanned by E_1 and E_4 are (1, 0, 0, 1, 0) and (1, 0, 0, 2, 0); on the line spanned by E_2 and E_4 are (0, 1, 0, 1, 0) and (0, 1, 0, 2, 0), on the line spanned by E_2 and E_5 are (0, 1, 0, 0, 1) and (0, 1, 0, 0, 2), and on the line spanned by E_3 and E_5 are (0, 0, 1, 0, 1) and (0, 0, 1, 0, 2). Since all these points are in *S*, any line spanned by two points on S_1 with non-consecutive indices forms a 4-secant of $\mathcal{F}$. Similarly, Since there is only one point on the

line spanned by A_i and A_j, or C_i and C_j, where *i* and *j* are non-consecutive indices, this line is 3-secant of $\mathcal{F}$: The proof for S_2 is done similarly.

Theorem 5 In the projective space $PG(4,3)$, in the set $\mathcal{F}$, the sets *E*, S_2, and *C* determine a 5-gon, while the set S_3 forms a spread with five lines.

Proof. Since the sets *E*, S_2, and *C* consist of five points no three of which are collinear, these sets determine a 5-gon. Moreover, since all the points of S_3 lie on the non-intersecting 4-secant lines l_i of $\mathcal{F}$, where $i = 1,2,...,5$ and the lines are given by:

l_1 = {(1, 1, 2, 0, 0), (0, 0, 1, 2, 1), (1, 1, 1, 1, 2), (1, 1, 0, 2, 1)}

l_2 = {(1, 2, 1, 1 1), (1, 2, 2, 2, 0), (1, 2, 0, 0, 2), (0, 0, 1, 1, 2)}

l_3 = {(0, 1, 1, 2, 0), (1, 1, 1, 0, 2), (1, 2, 2, 2, 2), (1, 0, 0, 1, 2)}

l_4 = {(0, 1, 2, 2, 2), (1, 0, 0, 2, 2), (1, 1, 2, 1, 1), (1, 2, 1, 0, 0)}

l_5 = {(1, 0, 2, 1, 1), (1, 2, 0, 0, 1), (1, 1, 1, 2, 1), (0, 1, 2, 1, 0)}

the set S_3 forms a 5-linear spread.

5. Corollary In the context of the theorem, the three distinct 5-gons determined by the points of $\mathcal{F}$ are perspective from a point not contained in $\mathcal{F}$. Moreover, the intersection points of the opposite sides of these 5-gons form a 5-gon that lies outside of $\mathcal{F}$.

Proof. Since the intersection point of the lines connecting the opposite corners of three different 5-gons is (1, 1, 1, 1, 1), this point is the perspectivity center. Additionally, the intersection points of the opposite sides of these pentagons,

$(1, 2, 0, 0, 0), (0, 1, 2, 0, 0), (0, 0, 1, 2, 0), (0, 0, 1, 2, 0), (0, 0, 0, 1, 2)$, and $(1, 0, 0, 0, 2)$

form a 5-gon that lies outside of $\mathcal{F}$.

6. Conclusion

We developed and implemented an algorithm to classify and construct *k*-secant lines for the Klein cubic threefold $\mathcal{F}$ in the projective space $PG(4,3)$. Our algorithm successfully identified and categorized secant lines based on their intersection properties with $\mathcal{F}$. We determined that there are 240 lines that do not intersect $\mathcal{F}$ (0-secant), 480 lines that intersect at a single point (1-secant), 360 lines that intersect at two points (2-secant), 120 lines that intersect at three points (3-secant), and 10 lines that intersect at four points ur points (4-secant).

Additionally, we divided the point set of $\mathcal{F}$ into three distinct subsets, S_1, S_2, and S_3, revealing their specific geometric configurations. This analysis of *k*-secant lines and the formation of three distinct 5-gons, based on the points of $\mathcal{F}$ and their perspectivity properties, provided deeper insights into the geometric structure of the Klein cubic threefold. Our findings contribute to the understanding of projective and algebraic geometry, offering a framework for classifying *k*-secant lines in cubic threefolds. The algorithm developed here can be used as a tool for future studies on higher-dimensional geometric objects in projective spaces.

Ethics in Publishing

There are no ethical issues regarding the publication of this study.

Author Contributions

All authors have investigated and studied no the published version of the manuscript.

Acknowledgments

We would like to thank the referees for the valuable suggestions and comments which improved the revision of the paper.

References

[1] Akça, Z., Bayar, A., Ekmekçi, S., Kaya, R., Thas, J A., Van Maldeghem, H., (2012) Generalized Veronesean embeddings of projective spaces Part II The lax case, Ars Combinatoria, vol. 103, 65-80.

[2] Akça, Z., Bayar, A., Ekmekçi, S., Kaya, R., Van Maldeghem, H., (20120, Bazı geometrilerin sonlu projektif uzaylara gömülmeleri üzerine, Tübitak Proje No: 108T340.

[3] Altıntaş, A., Bayar, A., Ekmekçi, S., Akça, Z.,, (2024) On the Klein cubic threefold in PG(4,2), International J.Math. Combin. Vol.4(2024), 9-19.

[4] Bayar, A., Akça, Z., Ekmekçi, S., (2022) On embedding the projective plane PG(2,4) to the projective space PG(4,4), New Trends in Mathematical Sciences, 10(4), 142-150.

[5] Betten, A., Karaoglu, F., (2019) Cubic surfaces over small finite fields. Designs, Codes and Cryptography, 87 (4): 931-953.

[6] Dickson, L.E., (1915) Projective classification of cubic surfaces modulo 2. Annal sof Mathematics,16: 139-157.

[7] Ekmekçi, S., Bayar, A., Akça, Z., (2022) On the projective planes in projective space PG(4,4), Erciyes Üniversitesi Fen Bilimleri Enstitüsü Fen Bilimleri Dergisi, 38(3), 519–524.

[8] Hirscfeld, JWP., (1967) Classical configurations over finite fields. I. The doublesix and the cubic surface with 27 lines. Rendiconti di Matematica e delle sue Applicazioni, 26 (5): 115-152.

[9] Karaoglu, F., Nonsingular cubic surfaces over F_{2^k} , (2021) Turkish Journal of Mathematics, 45: 2492-2510.

[10] Karaoglu, F., (2022) Smooth cubic surfaces with 15 lines, Applicable Algebra in Engineering, Communication and Computing, 33(16) 823-853.

[11] Klein, F.,. (1879) Uber die Ausásung Gleichungen siebenten und achten Grades. Math. Ann., 15, 251-282.

[12] Rosati, L.A., (1957) L'equazione delle 27 rette della superficie cubica generale in un corpo fiito. Bollettino dell'Unione Matematica Italiana, 12(3): 612-626.

[13] Bockondas, G., Bossoto, B., Eckart points on a cubic threefold, https://arxiv.org/pdf/2309.08124. (13.11.2024).

e-ISSN: 2149-4584

Erzincan University Journal of Science and Technology

EJSAT 2025, 18 (3) 713-725

Research Article

Interval-Valued Fuzzy Sets on Proximal Relator Spaces

Özlem Tekin [1*]

[1] Department of Mathematics, Faculty of Arts and Sciences, Adıyaman University, 02040 Adıyaman, Turkey

Received: 31/10/2024, **Revised:** 30/05/2025, **Accepted:** 02/09/2025, **Published:** 31/12/2025

Abstract

Interval-valued fuzzy sets are a broader form of classical fuzzy sets where membership values are expressed as intervals. In this framework, each element has a real-valued membership degree that falls within the given range of possible values. By helping of this fuzzy relations, it is built the concept of interval-valued fuzzy relations on proximal relator spaces. In the paper, the interval-valued fuzzy proximity axioms are rigorously examined, and corresponding examples are provided to demonstrate their applicability. Also, this paper also considers spatial Lodato and descriptive Lodato proximity relations.

Keywords: Proximity space, fuzzy relation, fuzzy proximity, interval-valued fuzzy sets.

Aralık Değerli Fuzzy Kümeleri Kullanarak Fuzzy Proksimiti Yaklaşımı

Öz

Aralık-değerli fuzzy kümeler, üyelik değerlerinin aralıklar olduğu klasik fuzzy kümelerin bir genellemesidir. Aralık-değerli bulanık kümelerde, muhtemel üyelik derecelerinin üyelik aralığı içinde bir elemanın bir reel değerli üyelik derecesi vardır. Aralık değerli fuzzy bağıntıların yardımıyla, proksimal relator uzayları üzerinde aralık-değerli fuzzy bağıntılar kavramını tanımlıyoruz. Bu çalışmamızda, aralık-değerli fuzzy proksimiti aksiyomları incelenmiş ve bazı örnekler verilmiştir. Ayrıca, uzaysal Lodato ve tanımsal Lodato proksimiti bağıntıları tanımlanmıştır.

Anahtar Kelimeler: Proksimiti uzayı, fuzzy bağıntısı, fuzzy proksimiti, aralık-değerli fuzzy kümeler.

Corresponding Author: oumdu@adiyaman.edu.tr

Cite this Article: Erzincan University Journal of Science and Technology 2025, 18(3)713-725. https://doi.org/10.18185/erzifbed.1576880

1. Introduction

Proximity spaces were defined by Efremovi$\hat{c}$ [7]. The set U, together with the proximity relation that M is near (proximal) N for subsets M and N of any set U, is known as proximity space. Readers can easily access many resources about proximity spaces. Naimpally and Warrack wrote a wonderful book about proximity space and presented it to their readers [14]. Descriptive proximity, a more visual representation of proximity, has been utilized in various applications. A general descriptive proximity is an Efremovi$\hat{c}$ proximity. Peters defined relator space $(U, \mathcal{R}_\delta)$ [19]. To understand easily, he used two relations namely EF-proximity and the Lodato proximity δ_Φ in defining $\mathcal{R}_{\delta_\Phi}$ [17, 18, 20].

$\mathcal{R}$ on U is known as *a relator* on U. $(U, \mathcal{R})$ is called as *a relator space* which is a generalized uniform space lacking all the conditions of uniform space except the reflexivity of the corresponding relations [24]. By using $\mathcal{R}_\delta$ on U, Peters presented a proximal relator space $(U, \mathcal{R}_\delta)$ [20]. For clarity, this space is restricted to three proximity relations only, specifically $(\mathcal{R}_{\tau_{\delta_\Phi}} = \{\delta, \delta_\Phi, \tau_{\delta_\Phi}\})$ [11, 12, 15, 20] .

Fuzzy sets (FS), first introduced by Zadeh, are characterized by a membership function mapping each element to a real value in the range [0,1] [31]. We can see fuzzy set theory various areas such as health science and image processing. However, there may be instabilities in real life, such as hesitation or uncertain decisions get involved and fuzzy set is not available to process some information with fuzziness and uncertainty. Thus, to handle such problems, Atanassov gave an outline of intuitionistic fuzzy sets and their definition (IFS) [1] that can deal with some information with fuzziness and uncertainty in many fields. After fuzzy sets has been caused great achievements and accepted from a mathematical perspective within the scientific domain, researcher proposed a number of theory based on this topic. However, the membership function may contain inaccurate information and might not represent reality precisely in practical applications, such as image processing.

These ideas indicate that in situations where researchers lack precise information about the membership function, constructing fuzzy sets becomes challenging. For this reason, it is proper to represent the membership degree of each element in a fuzzy set using an interval. From these ideas take places the generalization of fuzzy sets known as the framework of interval-valued fuzzy sets, in which the membership degree of each element is represented by a closed subinterval within [0,1].

Interval-valued fuzzy sets were proposed in the seventies. In the same year, Zadeh [32], Grattan-Guiness [9], Jahn [10], and Sambuc [22] each proposed interval-valued fuzzy sets independently, which were subsequently covered in multiple publications. However, the importance of interval-valued fuzzy sets was firmly established by the investigations carried out by Gorzalczany [8] and Türksen [29]. An interval-valued fuzzy set (IVFS) is characterized by a membership function that assigns interval values. Recently, many paper have been published related to IVFS such as approximate reasoning [2], expert systems [4], image processing [3], mobile networks [30], pattern recognition [5], genetic algorithms [13]. Roy and Biswas investigated the subject of interval-valued fuzzy relations. All of these studies demonstrate that the results obtained using IVFSs are superior to those obtained with fuzzy sets. After defining fuzzy proximal relator spaces [15], L-fuzzy proximity [25] and complex fuzzy

proximity [26] is presented by researchers. Thereafter, it is defined spherical fuzzy proximities and Pythagorean fuzzy proximities by using fuzzy relations via relator spaces [27, 28]. Besides, Öztürk carried fuzzy proximities to intuitionistic fuzzy environments [16].

In the context of interval-valued fuzzy sets, each interval reflects the expert's knowledge of well-defined lower and upper bounds for the membership degree of an element in the fuzzy set, despite the exact value within this range remaining unspecified. From a theoretical standpoint, this interpretation is the most appropriate when addressing uncertainty or imprecision in the assessment of membership degrees within fuzzy set theory. When classical fuzzy proximity relations are defined from this perspective, an important advantage emerges: interval-valued fuzzy proximity relations enable the expression of vagueness in specifying a precise membership function. This inherent vagueness, introduced by the applying of interval-valued fuzzy sets, gives rise to outcomes that are less specific but potentially more credible and realistic.

The interval-valued fuzzy proximity relations are an effective tool to determine proximity of different groups that have similar or different by using an interval with uncertainty.

In this paper, we investigate a interval-valued fuzzy spatial proximity relation and a interval-valued fuzzy spatial Lodato proximity relation on the basis of the proposed interval-valued fuzzy proximity relation. The interval-valued fuzzy proximity relations are useful tools to find out the level of connection and difference between three or more sets. Therefore, our main aim in this paper is to create a theoretical infrastructure for subsequent studies.

1. Preliminaries

This section presents a brief overview of the fundamental definitions related to the topic to enhance understanding.

Definition 1 Let U be a nonempty set. A basic proximity δ is a relation on the power set of a nonempty set U, which holds the following axioms for every subset M,N,Q *of* U:

(I_0) $M\ \delta\ N \Longrightarrow M \neq \emptyset, N \neq \emptyset$
(I_1) $M\ \delta\ N$ implies $N\ \delta\ M$.
(I_2) $M \cap N \neq \emptyset$ implies $M\ \delta\ N$.
(I_3) $(M \cup N)\ \delta\ P \Leftrightarrow M\ \delta\ P$ or $N\ \delta\ P$.

Furthermore, if δ holds (I_0)-(I_3) and the following axioms, then it is known to be Lodato proximity:

(I_4) $(M\delta N$ and $n\delta P$ for each $n \in N) \Longrightarrow M\delta P$.

If δ fulfills a basic proximity conditions and (I_6) below, then it is said to be an Efremovič proximity (EF-proximity) on U.

(I_5) If, for any $M, N \subset U$, $M\ \not\delta\ N$, subsets $P, Q \subset U$ *exists,* satisfying $P \cup Q = U$ with $M\ \not\delta\ P$ and $N\ \not\delta\ Q$.

(U, δ) is known as a basic (Lodato, Efremovič) proximity space. The notation $M\ \delta N$ indicates that M is near to N, while $M\ \not\delta\ N$ indicates that M is far from N.

Definition 2 *[21] Let $U \neq \emptyset$.* A descriptive EF-proximity δ_Φ is defined on $\mathcal{P}(U)$, and it fulfills the conditions below for all subsets M, N, Q *of* $\mathcal{P}(U)$*:*

(DP_0) $M \ \delta_\Phi \ N$ implies $M \neq \emptyset, N \neq \emptyset$

(DP_1) $M \ \delta_\Phi \ N$ implies $N \ \delta_\Phi \ M$ (descriptive symmetry).

(DP_2) $M \cap N \neq \emptyset$ implies $M \ \delta_\Phi \ N$.

(DP_3) $(M \cup N) \ \delta_\Phi \ Q \Leftrightarrow M \ \delta_\Phi \ Q$ or $N \ \delta_\Phi \ Q$.

(DP_4) If, for any $M, N \subset U$, $M \ \not\delta_\Phi \ N$, subsets P,Q⊂U exists, satisfying P∪Q=U with $M \ \not\delta_\Phi \ P$ and $N \ \not\delta_\Phi \ Q$. (U, δ_Φ) is a descriptive EF-proximity space.

Definition 3 *[15]* For the relator space $(U, \mathcal{R})$,

$$\mu_{\mathcal{R}}: \mathcal{P}(U) \times \mathcal{P}(U) \longrightarrow [0,1]$$
$$(M, N) \longmapsto \mu_{\mathcal{R}}(M, N)$$

be a fuzzy relation and $M, N \subset U$; then

$$\mathcal{R} = \{((M, N), \mu_{\mathcal{R}}(M, N)) | (M, N) \in \mathcal{P}(U) \times \mathcal{P}(U)\}$$

is known as a fuzzy proximity relation for all $M, N, P \in P(X)$, if it fulfills conditions below:

1) $\mu_{\mathcal{R}}(M, \emptyset) = 0$.

2) $\mu_{\mathcal{R}}(M, N) = \mu_{\mathcal{R}}(N, M)$.

3) $\mu_{\mathcal{R}}(M, N) \neq 0$ implies $M \ \mathcal{R} \ N$.

4) $\mu_{\mathcal{R}}(M, (N \cup Q)) \neq 0$ implies $\mu_{\mathcal{R}}(M, N) \neq 0$ and $M \ \mathcal{R} \ N$ or $\mu_{\mathcal{R}}(M, Q) \neq 0$ and $M \ \mathcal{R} \ Q$.

Definition 4 *[6] Suppose that U be a set that is not empty, $D([0,1])$ denote the collection of each closed subinterval of the interval of* $[0,1]$. $N = [N^L, N^U]: U \to D([0,1])$ *is known as an interval-valued fuzzy set, in U. N^L and N^U are fuzzy sets in U satisfying $N^L(t) \leq N^U(t)$ and $N(t) = [N^L(t), N^U(t)]$ for each $t \in U$. N^L and N^U are the lower and upper points of $D([0,1])$, respectively.*

It is evident that every fuzzy set N in U is also an interval-valued fuzzy set represented as $N = [N, N]$.

2. Main Theorem and Proof

Definition 5 *Suppose that $(U, \mathcal{R})$ be a proximal relator space, $D(I)$ be the set of all closed sub-intervals of the unit interval I, and $\tau_{\mathcal{R}}$ be a fuzzy relation which is given below.*

$$\tau_{\mathcal{R}}: \mathcal{P}(U) \times \mathcal{P}(U) \longrightarrow D(I)$$
$$(M, N) \longmapsto \tau_{\mathcal{R}}(M, N)$$

$\mathcal{R}_\tau$ is named an interval-valued fuzzy proximiy relation, if it holds the following conditions:

$IV1)\ \tau_{\mathcal{R}}(M,\varnothing) = [0,0] = 0.$

$IV2)\ \tau_{\mathcal{R}}(M,N) = \tau_{\mathcal{R}}(N,M).$
$IV3)\ \tau_{\mathcal{R}}(M,N) \neq 0 \Rightarrow M\mathcal{R}_{\tau}N.$
$IV4)\ \tau_{\mathcal{R}}(M,N \cup K) \neq 0 \Rightarrow \tau_{\mathcal{R}}(M,N) \neq 0$ and $M\mathcal{R}_{\tau}N$ or $\tau_{\mathcal{R}}(M,K) \neq 0$ and $M\mathcal{R}_{\tau}K.$

For each $(M,N) \in \mathcal{P}(U) \times \mathcal{P}(U)$, $\tau_{\mathcal{R}}(M,N)$ gives the interval of the link between the sets M and N. In other words, $\tau_{\mathcal{R}}(M,N)$ means in which interval the sets M and N are close to each other. Furthermore, $\tau_{\mathcal{R}}(M,N)$ is known as interval-valued fuzzy proximity measure. Also, the collection of all interval-valued fuzzy proximity relations on $\mathcal{P}(U) \times \mathcal{P}(U)$ is symbolized by $IVFR(\mathcal{P}(U))$.
$\tau_{\mathcal{R}}(M,N) = [\tau_{\mathcal{R}}^{L}(M,N), \tau_{\mathcal{R}}^{U}(M,N)]$, where $\tau_{\mathcal{R}}^{L}(M,N)$ and $\tau_{\mathcal{R}}^{U}(M,N)$ are the lower and upper points for the link between the sets M and N. Interval-valued fuzzy proximity relations are presented with the relational matrix:

$$\mathcal{R}_{\tau} = \begin{bmatrix} \tau_{\mathcal{R}}(M_1,N_1) & \cdots & \tau_{\mathcal{R}}(M_1,N_k) \\ \vdots & \ddots & \vdots \\ \tau_{\mathcal{R}}(M_k,N_1) & \cdots & \tau_{\mathcal{R}}(M_k,N_k) \end{bmatrix} = \begin{bmatrix} [a_1,b_1] & \cdots & [a_1,b_k] \\ \vdots & \ddots & \vdots \\ [a_k,b_1] & \cdots & [a_k,b_k] \end{bmatrix}.$$

Symbol	Interpretation
U	*set that is not empty,*
$\mathcal{R}$ on U	*relator* on U,
$(U,\mathcal{R})$	*proximal relator space,*
$\tau_{\mathcal{R}}$	*fuzzy relation,*
I	*the unit interval,*
$D(I)$	*the set of all closed sub-intervals of the unit interva,*
$\mathcal{P}(U)$	*the power set of* U,
$IVFR(\mathcal{P}(U))$	the set of all interval-valued fuzzy proximity relations

Table 1 : Symbols of Interval-valued fuzzy proximity relations

Definition 6 *Supoose that* $\mathcal{R}_{\tau}$ *be an interval-valued fuzzy proximity relations on* $\mathcal{P}(U)$*. The complement of an interval-valued fuzzy proximity relation* $\mathcal{R}_{\tau}^{C}(M,N)$ *presented as* $\boldsymbol{\tau}_{\mathcal{R}}(M,N)$ *determined by*

$$\boldsymbol{\tau}_{\mathcal{R}}(M,N) = [1 - \tau_{\mathcal{R}}^{U}(M,N), 1 - \tau_{\mathcal{R}}^{L}(M,N)]$$

$$(M,N) \in \mathcal{P}(U) \times \mathcal{P}(U).$$

Definition 7 *Let* $\tau_{\mathcal{R}_1}(M,N), \tau_{\mathcal{R}_2}(M,N) \in D(I)$. *In this case,*

i) $\tau_{\mathcal{R}_1}(M,N) = \tau_{\mathcal{R}_2}(M,N) \Rightarrow \tau^L_{\mathcal{R}_1}(M,N) = \tau^L_{\mathcal{R}_2}(M,N)$ and $\tau^U_{\mathcal{R}_1}(M,N) = \tau^U_{\mathcal{R}_2}(M,N)$.
ii) $\tau_{\mathcal{R}_1}(M,N) \leq \tau_{\mathcal{R}_2}(M,N) \Rightarrow \tau^L_{\mathcal{R}_1}(M,N) \geq \tau^L_{\mathcal{R}_2}(M,N)$ and $\tau^U_{\mathcal{R}_1}(M,N) \leq \tau^U_{\mathcal{R}_2}(M,N)$.

Definition 8 *Suppose that* $U \neq \emptyset$ *and* $\mathcal{R}_\tau$ *be an interval-valued fuzzy proximity relations on* $\mathcal{P}(U)$. $(U,\mathcal{R}_\tau)$ *is known as an interval-valued fuzzy proximal space.*

Definition 9 *Suppose that* $(U,\mathcal{R})$ *be an interval-valued fuzzy proximal space. If* $\mathcal{R}_\tau$ *is an interval-valued fuzzy proximity relations on* $\mathcal{P}(U)$, *in this case* $(U,\mathcal{R},\mathcal{R}_\tau)$ *is called an interval-valued fuzzy proximal relator space.*

Example 1 *Let* $U = \{a,b,c,d,e,f,g,h,i,j,k\}$. *Also,* $M = \{m,n,p,r,s,q\}$, $N = \{o,n,p,r,s,w\}$, $P = \{o,n,p,r,s,q\}$ *and* $Q = \{m,n,p,r,s,y\}$ *are subsets of* U. *Now, we give interval-valued fuzzy proximity relation by using basic proximity.* (U,δ) *represents basic proximity, and* δ *is determined as* $M \ \delta \ N: \Leftrightarrow M \cap N \neq \emptyset$.

Therefore, we easily see $M \ \delta \ N$, $M \ \delta \ P$, $M \ \delta \ Q$, $N \ \delta \ P$, $N \ \delta \ Q$ and $P \ \delta \ Q$ for $M \cap N \neq \emptyset$, $M \cap P \neq \emptyset$, $M \cap Q \neq \emptyset$, $N \cap P \neq \emptyset$, $N \cap Q \neq \emptyset$ and $P \cap Q \neq \emptyset$.

$$\tau_{\mathcal{R}}: \mathcal{P}(U) \times \mathcal{P}(U) \longrightarrow D(I)$$
$$(M,N) \longmapsto \tau_{\mathcal{R}}(M,N)$$

Afterward, it can be seen that $\tau_{\mathcal{R}}$ is shown below.

$$\tau_\delta(M,N) = [0.2,0.5]$$
$$\tau_\delta(M,P) = [0.3,0.7]$$
$$\tau_\delta(M,Q) = [0.11,0.3]$$
$$\tau_\delta(N,P) = [0.13,0.6]$$
$$\tau_\delta(N,Q) = [0.21,0.4]$$
$$\tau_\delta(P,Q) = [0.18,0.5]$$

In this case, we have that

$\tau^U_\delta(M,N) = 0.2$ gives upper bound of the interval $[0.2,0.5]$ and relationship for M and N,

$\tau^L_\delta(M,N) = 0.5$ gives lower bound of the interval $[0.2,0.5]$ and relationship for M and N.

In a similar way, we determine the maximum and minimum strength of the connection for the other sets. Thus,

M and N, $\left(M \ \mathcal{R}_{([0.2,0.5])} N\right)$ are proximal to each other,
M and P, $\left(M \ \mathcal{R}_{([0.3,0.7])} P\right)$ are proximal to each other.

The interval-valued fuzzy proximity can be represented using a relational matrix:

$$\mathcal{R}_\tau = \begin{bmatrix} [1,1] & [0.2,0.5] & [0.7,0.3] & [0.11,0.3] \\ [0.2,0.5] & [1,1] & [0.13,0.6] & [0.21,0.4] \\ [0.3,0.7] & [0.13,0.6] & [1,1] & [0.18,0.5] \\ [0.11,0.3] & [0.21,0.4] & [0.18,0.5] & [1,1] \end{bmatrix}.$$

From here, $\mathcal{R}_\tau$ satisfies the axioms $(IV1)-(IV4)$ and so $\mathcal{R}_\tau$ is an interval-valued fuzzy proximity relation.

In this example, we determine the proximity of the sets $M, N, P \; and \; Q$ by employing an interval to quantify their similarity or difference. Utilizing interval-valued fuzzy proximity relations, we assess the degrees of connection and dissimilarity among $M, N, P \; and \; Q$ For instance, it is observed that the maximum strength of the relation between $P \; and \; Q$ is 0.5, whereas the minimum strength is 0.18.

Example 2 *By using Example 1,* $(U, \mathcal{R}_\tau)$ *is an interval-valued fuzzy proximal space. With the basic proximity* $\mathcal{R} = \{\delta\}$, $(U, \mathcal{R}, \mathcal{R}_\tau)$ *is an interval-valued fuzzy proximal relator space.*

Example 3 *By using Example 1, we can easily find* $\boldsymbol{\tau}_{\mathcal{R}}(M, N) = [1 - \tau_{\mathcal{R}}^{U}(M, N), 1 - \tau_{\mathcal{R}}^{L}(M, N)]$

$$\mathcal{R}_\tau^C = \begin{bmatrix} [0,0] & [0.8,0.5] & [0.3,0.7] & [0.99,0.7] \\ [0.8,0.5] & [0,0] & [0.87,0.4] & [0.79,0.6] \\ [0.3,0.7] & [0.87,0.4] & [0,0] & [0.82,0.5] \\ [0.99,0.7] & [0.79,0.6] & [0.82,0.5] & [0,0] \end{bmatrix}.$$

Therefore, $\mathcal{R}_\tau^C$ satisfies the conditions $(IV1)-(IV4)$ and so $\mathcal{R}_\mathcal{P}^C$is an interval-valued fuzzy proximity relation.

Definition 10 *Suppose that* (U, δ) *be a proximity space and* δ_τ *be an interval-valued fuzzy proximity relation.* δ_τ *is named an interval-valued fuzzy spatial proximity relation if* δ_τ *meets the followings* $(IV\delta1)$-$(IV\delta4)$*:*

$IV\delta1)$ $\tau_\delta(M, \varnothing) = [0,0]$.
$IV\delta2)$ $\tau_\delta(M, N) = \tau_\delta(N, M)$.
$IV\delta3)$ $\tau_\delta(M, N) \neq 0 \Rightarrow M\delta_\tau N$.
$IV\delta4)$ $\tau_\delta(M, N \cup K) \neq 0$ implies $\tau_\delta(M, N) \neq 0$; $M\delta_\tau N$ or $\tau_\delta(M, K) \neq 0$; $M\delta_\tau K$.

Also, (U, δ, δ_τ) is known as an interval-valued fuzzy spatial proximity space.

Definition 11 *Suppose that* δ_τ *be an interval-valued fuzzy proximity relation. If* δ_τ *meets the axioms* $(IV\delta1)$-$(IV\delta4)$ *in Definition 10 and the following axiom* $(IV\delta5)$*, it is known as an interval-valued fuzzy spatial Lodato proximity relation. Furthermore,* (U, δ, δ_τ) *is called an interval-valued fuzzy spatial Lodato proximity space.*

$IV\delta5)$ $\tau_\delta(M, N) \neq 0$ and $\tau_\delta(n, K) \neq 0$ for all $n \in N$ implies $\tau_\delta(M, K) \neq 0$ and $M\delta_\tau K$.

Definition 12 *Suppose that δ_{Φ_τ} be an interval valued fuzzy proximity relation. $(U, \delta_\Phi, \delta_{\Phi_\tau})$ is said to be an interval valued fuzzy descriptive Lodato proximity space, if δ_{Φ_τ} meets the followings*

$IV\delta_\Phi 1)$ $\tau_{\delta_\Phi}(M, \varnothing) = [0,0]$.
$IV\delta_\Phi 2)$ $\tau_{\delta_\Phi}(M, N) = \tau_{\delta_\Phi}(N, M)$.
$IV\delta_\Phi 3)$ $\tau_{\delta_\Phi}(M, N) \neq 0 \Rightarrow M\delta_{\Phi_\tau}N$.
$IV\delta_\Phi 4)$ $\tau_{\delta_\Phi}(M, N \cup K) \neq 0$ implies $\tau_{\delta_\Phi}(M, N) \neq 0$; $M\delta_{\Phi_\tau}N$ or $\tau_{\delta_\Phi}(M, K) \neq 0$; $M\delta_{\Phi_\tau}K$.
$IV\delta_\Phi 5)$ $\tau_{\delta_\Phi}(M, N) \neq 0$ and $\tau_{\delta_\Phi}(k, K) \neq 0$ for all $n \in N$ implies $\tau_{\delta_\Phi}(M, K) \neq 0$ and $M\delta_{\Phi_\tau}K$.

Remark 1 The theory of descriptive nearness is typically employed when handling subsets that share certain common properties, even if they are not spatially proximate. We consider non-abstract points as those with specific locations and measurable attributes. The descriptive theory is especially applicable when emphasizing the distinguishing features of sets of non-abstract points. As an illustration, for a picture element k in a digital image, its gray-level intensity or color can be considered. Nearness or apartness primarily relies on the selected characteristics under comparison. Although the sets are not physically close, they can be regarded as descriptively near according to their features.

As we said before, the uncertainty that comes from using interval-valued fuzzy sets results in outcomes that are not very precise but may be more reliable and realistic. Interval-valued fuzzy proximity relations are a useful method for measuring how close different groups are to each other, even when there is uncertainty, by using value ranges instead of exact numbers. When comparing interval-valued fuzzy descriptive Lodato proximity relations with interval-valued fuzzy spatial Lodato proximity relations, using interval-valued fuzzy proximity relations, one can determine the degree of nearness between distinct groups, even when the relations may not be spatially close but can still be considered descriptively close.

Definition 13 *Suppose that $\mathcal{R}_{\tau_1}$ and $\mathcal{R}_{\tau_2}$ be interval-valued fuzzy proximity relations on $\mathcal{P}(U)$. In this case,*

1) $\mathcal{R}_{\tau_1} \wedge \mathcal{R}_{\tau_2} = \{((M, N), \tau_{\mathcal{R}_1}(M, N) \wedge \tau_{\mathcal{R}_2}(M, N) | (M, N) \in \mathcal{P}(U) \times \mathcal{P}(U)\}$.
Namely, $\bigwedge \tau_{\mathcal{R}_i}(M, N) = [\wedge\tau^L_{\mathcal{R}_i}(M, N),\ \wedge\tau^U_{\mathcal{R}_i}(M, N)]$.
2) $\mathcal{R}_{\tau_1} \vee \mathcal{R}_{\tau_2} = \{((M, N), \tau_{\mathcal{R}_1}(M, N) \vee \tau_{\mathcal{R}_2}(M, N) | (M, N) \in \mathcal{P}(U) \times \mathcal{P}(U)\}$.
Namely, $\bigvee\tau_{\mathcal{R}_i}(M, N) = [\vee\tau^L_{\mathcal{R}_i}(M, N),\ \vee\tau^U_{\mathcal{R}_i}(M, N)]$.

Theorem 1 *Let $\mathcal{R}_{\tau_1}$, $\mathcal{R}_{\tau_2}$ and $\mathcal{R}_{\tau_3}$ be interval-valued fuzzy proximity relations on $\mathcal{P}(U)$. The following properties hold:*

1) $\mathcal{R}_{\tau_1} \wedge (\mathcal{R}_{\tau_2} \vee \mathcal{R}_{\tau_3}) = (\mathcal{R}_{\tau_1} \wedge \mathcal{R}_{\tau_2}) \vee (\mathcal{R}_{\tau_1} \wedge \mathcal{R}_{\tau_3})$.
2) $\mathcal{R}_{\tau_1} \vee (\mathcal{R}_{\tau_2} \wedge \mathcal{R}_{\tau_3}) = (\mathcal{R}_{\tau_1} \vee \mathcal{R}_{\tau_2}) \wedge (\mathcal{R}_{\tau_1} \vee \mathcal{R}_{\tau_3})$.
3) $\mathcal{R}_{\tau_1} \wedge \mathcal{R}_{\tau_2} \leq \mathcal{R}_{\tau_1}$.

4) $\mathcal{R}_{\tau_1} \wedge \mathcal{R}_{\tau_2} \leq \mathcal{R}_{\tau_2}$.

Proof. Let $\mathcal{R}_{\tau_1}$, $\mathcal{R}_{\tau_2}$ and $\mathcal{R}_{\tau_3}$ be interval-valued fuzzy proximity relations.

1) We utilize the fact that the operators ∧ and ∨ satisfy the distributive law when applied to elements of [0,1].

$$\begin{aligned}\tau_{\mathcal{R}_1\wedge(\mathcal{R}_2\vee\mathcal{R}_3)}(M,N) &= \tau_{\mathcal{R}_1}(M,N) \wedge \{\tau_{\mathcal{R}_2}(M,N) \vee \mu_{\mathcal{R}_3}(M,N)\} \\ &= \{\tau_{\mathcal{R}_1}(M,N) \wedge \tau_{\mathcal{R}_2}(M,N)\} \vee \{\tau_{\mathcal{R}_1}(M,N) \wedge \tau_{\mathcal{R}_3}(M,N)\} \\ &= \tau_{\mathcal{R}_1\wedge\mathcal{R}_2}(M,N) \vee \tau_{\mathcal{R}_1\wedge\mathcal{R}_3}(M,N) \\ &= \tau_{(\mathcal{R}_1\wedge\mathcal{R}_2)\vee(\mathcal{R}_1\wedge\mathcal{R}_3)}(M,N).\end{aligned}$$

2) The proof can be carried out in a manner similar to the previous one.

$$\begin{aligned}\tau_{\mathcal{R}_1\vee(\mathcal{R}_2\wedge\mathcal{R}_3)}(M,N) &= \tau_{\mathcal{R}_1}(M,N) \vee \{\tau_{\mathcal{R}_2}(M,N) \wedge \mu_{\mathcal{R}_3}(M,N)\} \\ &= \{\tau_{\mathcal{R}_1}(M,N) \vee \tau_{\mathcal{R}_2}(M,N)\} \wedge \{\tau_{\mathcal{R}_1}(M,N) \vee \tau_{\mathcal{R}_3}(M,N)\} \\ &= \tau_{\mathcal{R}_1\vee\mathcal{R}_2}(M,N) \wedge \tau_{\mathcal{R}_1\vee\mathcal{R}_3}(M,N) \\ &= \tau_{(\mathcal{R}_1\vee\mathcal{R}_2)\wedge(\mathcal{R}_1\vee\mathcal{R}_3)}(M,N).\end{aligned}$$

$3-4)$ $\tau_{\mathcal{R}_1\wedge\mathcal{R}_3}(M,N) = \tau_{\mathcal{R}_1}(M,N) \wedge \tau_{\mathcal{R}_2}(M,N) \leq \tau_{\mathcal{R}_1}(M,N)$ (or $\tau_{\mathcal{R}_2}(M,N)$) the property of the the operator ∧.

Thus, $\mathcal{R}_{\tau_1} \wedge \mathcal{R}_{\tau_2} \leq \mathcal{R}_{\tau_1}(\text{or } \mathcal{R}_{\tau_2})$.

Definition 14 *Let* $\mathcal{R}_{\tau_1} \in IVFR(\mathcal{P}(U) \times \mathcal{P}(V))$ *and* $\mathcal{R}_{\tau_2} \in IVFR(\mathcal{P}(V) \times \mathcal{P}(W))$ *be two interval-valued fuzzy proximity relations:*

$$\mathcal{R}_{\tau_1} = \{\Big((M,N), \tau_{\mathcal{R}_1}(M,N)\Big) | (M,N) \in \mathcal{P}(U) \times \mathcal{P}(V)\}$$

and

$$\mathcal{R}_{\tau_2} = \{\Big((N,K), \tau_{\mathcal{R}_2}(N,K)\Big) | (N,K) \in \mathcal{P}(V) \times \mathcal{P}(W)\}.$$

$\mathcal{R}_{\tau_1} \circ \mathcal{R}_{\tau_2} \in IVFR(\mathcal{P}(U) \times \mathcal{P}(W))$ is determined as

$\mathcal{R}_{\tau_1} \circ \mathcal{R}_{\tau_2} = \{\Big((M,K), \tau_{\mathcal{R}_1\circ\mathcal{R}_2}(M,K)\Big) | (M,K) \in \mathcal{P}(U) \times \mathcal{P}(W)\}$ where

$$\mathcal{R}_{\tau_1} \circ \mathcal{R}_{\tau_2} = [\bigvee_{N\in P(V)} \{{\mathcal{R}_{\tau_1}}^L(M,N) \wedge \mathcal{R}^L_{\tau_2}(N,K)\}, \bigvee_{N\in P(V)} \{{\mathcal{R}_{\tau_1}}^U(M,N) \wedge \mathcal{R}^U_{\tau_2}(N,K)\}].$$

Example 4 *Let* $\mathcal{R}_{\tau_1}$ *and* $\mathcal{R}_{\tau_2}$ *be two interval-valued fuzzy proximity relations on* $\mathcal{P}(U)$.

$$\mathcal{R}_{\tau_1} = \begin{bmatrix}[1,1] & [0.4,0.1] & [0.6,0.8] & [0.2,0.5] \\ [0.4,0.1] & [1,1] & [0.16,0.42] & [0.6,0.17] \\ [0.6,0.8] & [0.16,0.42] & [1,1] & [0.3,0.25] \\ [0.2,0.5] & [0.6,0.17] & [0.3,0.25] & [1,1]\end{bmatrix}$$

and

$$\mathcal{R}_{\tau_2} = \begin{bmatrix}[1,1] & [0.7,0.23] & [0.4,0.42] & [0.11,0.5] \\ [0.7,0.23] & [1,1] & [0.75,0.3] & [0.66,0.15] \\ [0.4,0.42] & [0.75,0.3] & [1,1] & [0.8,0.9] \\ [0.11,0.5] & [0.66,0.15] & [0.8,0.9] & [1,1]\end{bmatrix}.$$

We can be found the max–min composition of them.

$$\mathcal{R}_{\tau_1} \circ \mathcal{R}_{\tau_2} = \begin{bmatrix} [1,1] & [0.7,0.3] & [0.6,0.8] & [0.6,0.8] \\ [0.7,0.42] & [1,1] & [0.75,0.42] & [0.66,0.42] \\ [0.6,0.8] & [0.75,0.42] & [1,1] & [0.8,0.9] \\ [0.6,0.5] & [0.66,0.25] & [0.8,0.9] & [1,1] \end{bmatrix}.$$

Definition 15 *Let $\mathcal{R}_{\tau_1}, \mathcal{R}_{\tau_2}$ present two interval-valued fuzzy proximity relations, and $\tau_{\mathcal{R}_1}, \tau_{\mathcal{R}_2}$ present membership functions of $\mathcal{R}_{\tau_1}, \mathcal{R}_{\tau_2}$. The interval-valued fuzzy proximity intersection of $\tau_{\mathcal{R}_1}$ and $\tau_{\mathcal{R}_2}$ is expressed by $\tau_{\mathcal{R}_1} \otimes \tau_{\mathcal{R}_2}$, and described as below.*

$$\begin{aligned} \left(\tau_{\mathcal{R}_1} \otimes \tau_{\mathcal{R}_2}\right)(M,N) &= \tau_{\mathcal{R}_1}(M,N) \wedge \tau_{\mathcal{R}_2}(M,N) \\ &= [\tau^L_{\mathcal{R}_1}(M,N) \wedge \tau^L_{\mathcal{R}_2}(M,N), \tau^U_{\mathcal{R}_1}(M,N) \wedge \tau^U_{\mathcal{R}_2}(M,N)]. \end{aligned}$$

Example 5 *Let $\mathcal{R}_{\tau_1}$ and $\mathcal{R}_{\tau_2}$ be two interval-valued fuzzy proximity relations on $\mathcal{P}(U)$.*

$$\mathcal{R}_{\tau_1} = \begin{bmatrix} [1,1] & [0.4,0.1] & [0.6,0.8] & [0.2,0.5] \\ [0.4,0.1] & [1,1] & [0.16,0.42] & [0.6,0.17] \\ [0.6,0.8] & [0.16,0.42] & [1,1] & [0.3,0.25] \\ [0.2,0.5] & [0.6,0.17] & [0.3,0.25] & [1,1] \end{bmatrix}$$

and

$$\mathcal{R}_{\tau_2} = \begin{bmatrix} [1,1] & [0.7,0.23] & [0.4,0.42] & [0.11,0.5] \\ [0.7,0.23] & [1,1] & [0.75,0.3] & [0.66,0.15] \\ [0.4,0.42] & [0.75,0.3] & [1,1] & [0.8,0.9] \\ [0.11,0.5] & [0.66,0.15] & [0.8,0.9] & [1,1] \end{bmatrix}.$$

We can be find the intersection of them.

$$\mathcal{R}_{\tau_1 \otimes \tau_2} = \begin{bmatrix} [1,1] & [0.4,0.1] & [0.4,0.42] & [0.11,0.5] \\ [0.4,0.1] & [1,1] & [0.16,0.3] & [0.6,0.15] \\ [0.4,0.42] & [0.16,0.3] & [1,1] & [0.3,0.25] \\ [0.11,0.5] & [0.6,0.15] & [0.3,0.25] & [1,1] \end{bmatrix}.$$

Definition 16 *Let $\mathcal{R}_{\tau_1}, \mathcal{R}_{\tau_2}$ present two interval-valued fuzzy proximity relations, and $\tau_{\mathcal{R}_1}, \tau_{\mathcal{R}_2}$ present membership functions of $\mathcal{R}_{\tau_1}, \mathcal{R}_{\tau_2}$. The interval-valued fuzzy proximity union of $\tau_{\mathcal{R}_1}$ and $\tau_{\mathcal{R}_2}$ is expressed by $\tau_{\mathcal{R}_1} \oplus \tau_{\mathcal{R}_2}$, and described as below.*

$$\begin{aligned} \left(\tau_{\mathcal{R}_1} \oplus \tau_{\mathcal{R}_2}\right)(M,N) &= \tau_{\mathcal{R}_1}(M,N) \vee \tau_{\mathcal{R}_2}(M,N) \\ &= [\tau^L_{\mathcal{R}_1}(M,N) \vee \tau^L_{\mathcal{R}_2}(M,N), \tau^U_{\mathcal{R}_1}(M,N) \vee \tau^U_{\mathcal{R}_2}(M,N)]. \end{aligned}$$

Example 6 *Let $\mathcal{R}_{\tau_1}$ and $\mathcal{R}_{\tau_2}$ be two interval-valued fuzzy proximity relations on $\mathcal{P}(U)$.*

$$\mathcal{R}_{\tau_1} = \begin{bmatrix} [1,1] & [0.4,0.1] & [0.6,0.8] & [0.2,0.5] \\ [0.4,0.1] & [1,1] & [0.16,0.42] & [0.6,0.17] \\ [0.6,0.8] & [0.16,0.42] & [1,1] & [0.3,0.25] \\ [0.2,0.5] & [0.6,0.17] & [0.3,0.25] & [1,1] \end{bmatrix}$$

and

$$\mathcal{R}_{\tau_2} = \begin{bmatrix} [1,1] & [0.7,0.23] & [0.4,0.42] & [0.11,0.5] \\ [0.7,0.23] & [1,1] & [0.75,0.3] & [0.66,0.15] \\ [0.4,0.42] & [0.75,0.3] & [1,1] & [0.8,0.9] \\ [0.11,0.5] & [0.66,0.15] & [0.8,0.9] & [1,1] \end{bmatrix}.$$

We can find the union of them.

$$\mathcal{R}_{\tau_1 \oplus \tau_2} = \begin{bmatrix} [1,1] & [0.7,0.23] & [0.6,0.8] & [0.2,0.5] \\ [0.7,0.23] & [1,1] & [0.75,0.42] & [0.66,0.17] \\ [0.6,0.8] & [0.75,0.42] & [1,1] & [0.8,0.9] \\ [0.2,0.5] & [0.66,0.17] & [0.8,0.9] & [1,1] \end{bmatrix}.$$

4. Conclusion

The interval-valued fuzzy set is an extended concept in which the membership of each element is represented by a closed interval. Clearly, according to this explanation, it entails two functions N^U and N^L. To explore the new approach using proximal spaces for interval-valued fuzzy sets, we introduce the definition of interval-valued fuzzy proximal spaces. After investigating some results concerning interval-valued fuzzy proximity relations, our study has focused on the relationship between Lodato proximity and interval-valued fuzzy proximity. Future work may focus on expanding interval-valued fuzzy sets to encompass other forms, for instance, neutrosophic, bipolar fuzzy sets, characteristically near sets.

Ethics in Publishing

There are no ethical issues regarding the publication of this study.

References

[1] Atanassov K.T., (1986) Intuitionistic fuzzy sets. Fuzzy Sets and Systems 20, 87–96.

[2] Bustince H., (2000) Indicator of inclusion grade for intervalvalued fuzzy sets. Application to approximate reasoning based on interval-valued fuzzy sets., International Journal of Approximate Reasoning, 23(3) 137-209.

[3] Bustince H., Barrenechea, E., Pagola, M., Fernandez, J., (2009) Interval-valued fuzzy sets constructed from matrices: Application to edge detection., Fuzzy Sets and Systems, 60(13), 1819-1840.

[4] Chen S., Wang H., (2009) Evaluating students answer scripts based on interval-valued fuzzy grade sheets., *Expert Systems with Applications*, 36(6), 9839-9846 (2009).

[5] Choi, B., Rhee, F., (2009) Interval type-2 fuzzy membership function generation methods for pattern recognition, Information Sciences, 179(13), 2102-2122.

[6] Concilio A.D., Guadagni C., Peters J.F., Ramanna S., (2018) Descriptive proximities. properties and interplay between classical proximities and overlap, Mat. Comput. Sci. 12: 91–106.

[7] Efremovi̇̂ V.A., (1952) The geometry of proximity. Mat. Sb. N.S. 31(73), 189–200.

[8] Gorzalzany M.B., (1987) A method of inference inapproximate reasoning based on interval-valued fuzzy sets, Fuzzy Sets and Systems 21, 1-17.

[9] Grattan-Guiness I., (1975) Fuzzy membership mapped onto interval and many-valued quantities. Z. Math. Logik. Grundladen Math. 22, 149-160.

[10] Jahn K.U., (1975) Intervall-wertige Mengen, Math.Nach. 68, 115-132.

[11] Lodato M.W., (1964) On topologically induced generalized proximity relations I. Proc. Amer. Math. Soc. 15(3), 417–422.

[12] Lodato M.W., (1966) On topologically induced generalized proximity relations II. Pacific J. Math. 17(1), 131–135.

[13] Martinez, R., Castillo, O., Aguilar, L.T., (2009) Optimization of interval type-2 fuzzy logic controllers for a perturbed autonomous wheeled mobile robot usinggenetic algorithms., Information Sciences, 179(13), 2158- 2174.

[14] Naimpally S.A., Warrack B.D., (1970) Proximity Spaces. Cambridge Tract. 59, England.

[15] Öztürk M.A., İnan E., Tekin Ö., Peters J.F. (2019) Fuzzy proximal relator spaces. Neural Comput. Appl. 31(7), 3201–3210.

[16] Öztürk M.A., (2025) Intuitionistic fuzzy proximal relator spaces, Southeast Asian Bull. Math., (Accepted).

[17] Peters J.F. (2013) Local near sets: pattern discovery in proximity spaces, Mat. Comput. Sci. 7(1), 87–106.

[18] Peters J.F., Naimpally S.A., (2012) Applications of near sets. Notices of the Amer. Math. Soc. 59(4), 536–542.

[19] Peters J.F.,(2013) Near sets: an introduction. Math. Comput. Sci. 7(1), 3–9.

[20] Peters J.F., (2016) Proximal relator spaces. Filomat 30(2), 469–472.

[21] Peters J.F., (2016) Computational Proximity. Excursions in the Topology of Digital Images, Intelligent Systems Reference Library, Springer.

[22] Sambuc R., (1975) Fonctions ϕ-floues. Application laide au diagnostic en pathologie thyroidienne, PhD Thesis, Univ. Marseille, France.

[23] Roy M.K., Biswas R. (1992) I-v fuzzy relations and Sanchez's approach for medical diagnosis, Fuzzy Sets and Systems 47, 35-38.

[24] Szás À., (1987) Basic tools and mild continuties in relator spaces. Acta Math. Hungar. 50(3-4), 177–201.

[25] Tekin Ö., Öztürk M.A., İnan E., (2021) L-Fuzzy relations via proximal spaces. Thai J. Math. 19(2), 557–570, (2021).

[26] Tekin Ö., Öztürk M.A., (2022) Complex fuzzy proximal relator spaces, J. Mult.-Val. Log. Soft Comput. 38(3-4), 355–385.

[27] Tekin Ö., (2023) An approach for spherical fuzzy relations via relator spaces, J Intell Fuzzy Systems, 45(4), 6875–6886.

[28] Tekin Ö., (2024) A novel approximation of Pythagorean fuzzy sets via proximal relator spaces, J. Mult.-Val. Log. Soft Comput. 44(1-2), 71-93.

[29] Turksen I.B., (1986) Interval valued fuzzy sets based on normal forms. Fuzzy Sets and Systems, 20(2), 191-210.

[30] Xia, X. S., Liang, Q. L., (2008) Crosslayer design for mobile ad hoc networks using interval type-2 fuzzy logic systems., International Journal of Uncertainty, Fuzziness and Knowledge-Based Systems, 16(3), 391- 408.

[31] Zadeh L.A., (1965) Fuzzy sets, Inform. and Control 8, 338-353.

[32] Zadeh L.A., (1975) The concept of a linguistic variable and its application to approximate reasoning-I, Inform. Sci. 8, 199-249.

e-ISSN: 2149-4584

Erzincan University Journal of Science and Technology
EJSAT 2025, 18(3), 726–734

Research Article

Physics Informed Neural Network Method for the Numerical Solution of Fractional Diffusion Equations

Mehmet Fatih UÇAR[1*], Burcu Ece ALP[2]

[1*]Department of Mathematics and Computer Science, Istanbul Kultur University, Türkiye
[2]Turkcell Head Office Software Unit Data Analyst Istanbul, Türkiye

Received: 26/10/2024, **Revised:** 13/01/2025, **Accepted:** 23/01/2025, **Published:** 31/12/2025

Abstract

Artificial neural networks are gaining popularity for developing continuous solution functions to address various types of differential equations. In this research, we introduce a physics-informed neural network (PINN) approach for solving fractional diffusion equations with variable coefficients over a finite domain. The PINN framework approximates solutions to fractional PDEs by optimizing a physical loss function that incorporates terms for the residual, boundary conditions, and initial conditions. The fractional PDE is discretized using the Grunwald-Letnikov scheme, and the resulting semi-discrete equation is employed to define the residual term for the PINN. Numerical tests confirm that the proposed PINN method achieves precise solutions within the defined computational space-time domain.

Keywords: 35R11 Fractional partial differential equations, 65N22 Numerical solution of boundary value problems, 68T07 Artificial neural networks and deep learning.

Kesirli Difüzyon Denklemlerinin PINN Metodu ile Sayısal Çözümleri

Öz

Yapay sinir ağları, çeşitli diferansiyel denklemlerin çözümünde sürekli çözüm fonksiyonları oluşturmak için giderek daha fazla kullanılmaktadır. Bu çalışmada, sonlu bir alan üzerinde değişken katsayılı kesirli difüzyon denklemlerini fizik bilgili sinir ağı (PINN) yöntemi ile sayısal çözümlerini ele alacağız. PINN, rezidü, sınır koşulu ve başlangıç koşulundan oluşan fiziksel hata fonksiyonunun değerini en aza indirmek için eğitilerek kesirli PDE'ye yaklaşık çözümler üretir. Kesirli PDE, Grünwald-Letnikov formülü ile ayrıklaştırılır ve elde edilen yarı ayrık denklem, PINN'nin rezidü fonksiyonunu oluşturmak için kullanılır. Ele aldığımız denklemler, mevcut PINN yönteminin dikkate alınan hesaplama uzay-zaman alanı üzerinde doğru çözümler sağladığını göstermektedir.

Anahtar Kelimeler: 35R11 Kesirli türevli kısmi diferansiyel denklemler, 65N22 Sınır değer problemlerinin sayısal çözümleri, 68T07 Yapay sinir ağları ve derin öğrenme.

Corresponding Author: f.ucar@iku.edu.tr
Cite this Article: Erzincan University Journal of Science and Technology 2025, 18(3), 726–734.
https://doi.org/10.18185/erzifbed.1589798

1. Introduction

Neural networks have proven to be highly effective in addressing problems that exhibit nonlinearity. Their ability to tackle nonlinear challenges improves as the number of layers and neurons increases. One application of neural networks involves predicting bankruptcy. Recently, various methods leveraging neural networks have emerged for solving complex nonlinear differential equations. For instance, Mall and Chakraverty [1] proposed an artificial neural network (ANN) approach. Sabir et al. utilized a stochastic numerical algorithm rooted in neural networks to solve boundary value problems [2]. Raissi et al. introduced the Physics-Informed Neural Network (PINN) methodology, which incorporates physics-based constraints [3]. This innovative technique has been applied to both ordinary and partial differential equations. Additionally, Dwivedi et al. devised a distributed learning machine approach to address partial differential equations [4-7].

Fractional calculus has emerged as a significant and dynamic area of research in applied mathematics [8–10]. This field encompasses a broad range of fractional-order operators, including both derivatives and integrals. Recently, a novel definition of the fractional derivative based on a nonsingular kernel was introduced in [11, 12]. Additionally, [13] proposed a new fractional derivative framework utilizing the Mittag-Leffler kernel. Such operators are widely applied to address various challenges in science and engineering. Rostami et al. developed a method to solve high-order fractional differential equations using artificial neural networks (ANN) [14]. Heuristic algorithms have been employed to optimize these complex systems [15]. Alkan et al. investigated different forms of fractional partial differential equations (PDEs) [16–19], while Bektas et al. presented a hybrid approach for solving the fractional NWS equation [20]. Pakdaman et al. combined an ANN with an optimization technique to tackle fractional differential equations [21].

Moreover, the application of ANN to approximate solutions for fractional-order partial differential equations has been extensively studied. A Physics-Informed Neural Network (PINN) approach was extended to fractional problems, introducing an innovative neural network framework [22]. The PINN method has been particularly effective for solving fractional diffusion equations, addressing challenges like prolonged training times and slow convergence that often hinder traditional neural network models. By training the network to minimize a physical loss function composed of residual, boundary, and initial condition terms, the PINN method offers a robust tool for approximating solutions to fractional PDEs.

In this research, the fractional derivative term is approximated using the first-order Grünwald-Letnikov formula, and the resulting semi-discrete equation is utilized to formulate the residual function for the PINN. Numerical results demonstrate that the proposed PINN approach delivers precise solutions within the specified space-time computational domain.

2. Material and Methods

2.1. Fractional Diffusion Equation

We consider the following diffusion equation of order $1 < \beta < 2$

$$\frac{\partial U(x,t)}{\partial t} - d_+(x)\frac{\partial^\beta U(x,t)}{\partial_+ x^\beta} - d_-(x)\frac{\partial^\beta U(x,t)}{\partial_- x^\beta} = f(x,t), \tag{1}$$

$$x_L < x < x_R \qquad 0 < t \leq T,$$
$$U(x_L, t) = 0, \qquad U(x_R, t) = 0, \qquad 0 \leq t \leq T$$
$$U(x, 0) = U_0(x), \qquad x_R \leq x \leq x_L$$

and the Dirichlet boundary condition as

$$U(x_L, t) = 0 \quad \text{and} \quad U(x_R, t) = \xi(t)$$

where the left-sided (-) and the right-sided (+) fractional derivatives $\frac{\partial^\beta U(x,t)}{\partial_- x^\beta}$ and $\frac{\partial^\beta U(x,t)}{\partial_+ x^\beta}$ can be written in the Grünvald-Letkinov form:

$$\frac{\partial^\beta U(x_i, t^m)}{\partial_- x^\beta} = \frac{1}{(\Delta x)^\beta} \sum_{k=0}^{i+1} h_k^{(\beta)} U_{i-k+1}^m + O(h), \tag{2}$$

$$\frac{\partial^\beta U(x_i, t^m)}{\partial_+ x^\beta} = \frac{1}{(\Delta x)^\beta} \sum_{k=0}^{N-i+1} h_k^{(\beta)} U_{i+k-1}^m + O(h). \tag{3}$$

Here, $h_k^{(\beta)} = (-1)^k \binom{\beta}{k} \frac{\Gamma(k-\beta)}{\Gamma(-\beta)\Gamma(k+1)}$ where $\binom{\beta}{k}$ is the fractional binomial coefficient. Furthermore, the coefficients $h_k^{(\beta)}$ can be evaluated in recurrence relation

$$h_0^{(\beta)} = 1, \qquad h_k^{(\beta)} = (1 - \frac{\beta + 1}{k}) h_{k-1}^{(\beta)} \qquad k \geq 1. \tag{4}$$

The case $1 < \beta < 2$, it is beneficial in applications.

2.2. Physics Informed Neural Network(PINN)

(PINNs) are a deep learning framework designed to solve partial differential equations (PDEs) [3]. This approach enables computers to efficiently and accurately compute partial derivatives of functions. The time variable, t, is treated as a specific component of x, while Θ represents the spatial domain. The initial condition can be viewed as a special case of a Dirichlet boundary condition applied to the spatio-temporal domain, making the process relatively straightforward. By training a neural network to minimize a loss function, which incorporates terms for the mismatch of initial and boundary conditions along the space-time boundary as well as the PDE residual at selected interior points, PINNs approximate solutions to PDEs. Furthermore, they allow for direct differentiation of functions.

Let us begin by analyzing a problem expressed as follows:

$$\mathcal{L}U(x,t) = f_{BB}(x,t), \qquad (x,t) \in \Theta \times (0,T], \tag{5}$$
$$U(x,0) = g(x), \qquad x \in \Theta, \tag{6}$$
$$U(x,t) = 0, \qquad x \in \partial\Theta, \tag{7}$$

where the function $g(.)$ represents the initial condition. The proposed approximate solution is defined as

$$\tilde{U}(x,t) = t\rho(x) U_{NN}(x,t;\mu) + g(x), \tag{8}$$

which inherently satisfies the initial and boundary conditions. Here, $L(.)$ denotes either a linear or nonlinear operator.

By defining $z = [x, t]^T$, the PINN method assumes the following approximate function:

$$U_\theta(z) := W^L \sigma^L(W^{L-1}\sigma^{L-1}(...\sigma^1(W^0 z + b^0)) + b^{L-1}) + b^L, \tag{9}$$

where θ represents the set of weight matrices (W) and bias vectors (b). The weight matrices are specified as $W^0 \in R^{m\times 2}$, $W^i \in R^{m\times m}$ $(i = 1, 2, ..., L-1)$ and $W^L \in R^{1\times m}$ where m is the number of neurons and L denotes the total number of layers. The bias vectors are defined as $b^i \in R^{m\times 1}(i = 1, 2, ..., L-1)$ and $b^L \in R$. The activation function $\sigma(.)$ transforms the network into a nonlinear model. The expression in Eq. (9) serves as an approximate function for a multilayer feedforward neural network. This function depends on the parameter set $\theta = W^0, b^0, W^1, b^1, ..., W^L, b^l$, which must be optimized to solve the fractional diffusion equation. The continuous residual function used in this optimization process is expressed as:

$$R_\theta(x, t) := \theta_t u_\theta(x, t) - L[u_\theta](x, t) + q(x, t), \tag{10}$$

which is derived by PINN from Eqs. (2) and (3).

The PINN method minimizes the residual function over the collocation points defined in the region of the fractional differential equation. Simultaneously, the network adjusts the θ parameters to satisfy both boundary and initial conditions. Suppose the collocation points are given as:

$$X_i^r = \{(x_i^r, t_i^r)\}_{i=1}^{N_r} \subset [x_L, x_R]\mathrm{x}[0, T] \tag{11}$$

that is generetad by PINN from Eqs. (2) and (3).

The PINN methodology seeks to minimize the residual function at collocation points within the domain of the fractional differential equation, while simultaneously optimizing the parameter θ to satisfy both boundary and initial conditions. Let the collocation points be defined as follows:

In the standard PINN approach, collocation points are typically chosen randomly. However, in this case, they are taken as uniformly spaced points. This is due to the derivative approximations in equations (2) and (3), which require x_i points with a step size h.

The PINN approach minimizes the following loss functional to solve Eq. (1):

$$\phi_\theta := \phi_\theta^r(X^r) + \phi_\theta^b(X_b^r) + \phi_\theta^s(X_s^r). \tag{12}$$

Here, the functional comprises three distinct loss components corresponding to the residual, initial condition, and boundary conditions. The Nadam optimization algorithm is employed to minimize these loss terms. Specifically, the residual loss function is expressed as:

$$\phi_\theta^r(X^r) = \frac{1}{N_r}\sum_{i=1}^{N_r} |r_\theta(x_i^r, t_i^r)|^2. \tag{13}$$

Meanwhile, the loss functions for initial and boundary conditions are defined as:

$$\phi_\theta^b(X_b^r) = \frac{1}{N_b}\sum_{i=1}^{N_b} |u_\theta(x_i^b, 0) - g(x_i^b)|^2. \tag{14}$$

$$\phi_\theta^s(X_s^r) = \frac{1}{N_s}\sum_{i=1}^{N_s} |u_\theta(x_i^s, t_i^s) - u_b(x_i^s, t_i^s)|^2. \tag{15}$$

The boundary condition function $u_b(x_i^s, t_i^s)$ is given by:

$$U_b(x_i^s, t_i^s) = \begin{cases} 0, & \text{if } x_i^s = x_L, \\ 1, & \text{if } x_i^s = x_R. \end{cases} \tag{16}$$

Thus, solving the optimization problem:

$$\Theta^* = \arg\min_{\phi} \theta(x^R), \tag{17}$$

yields the optimal parameters ϕ^*, which minimize the initial and boundary loss terms.
For this study, the implementation was carried out using the TensorFlow Python library, and the optimal parameters ϕ^* were obtained via the Nadam optimization algorithm.

3. Numerical Example

3.1. Example 1

Let us consider the fractional diffusion equation (1) with

$$d_+(x) = \Gamma(1.2)x^{1.8} \quad \text{and} \quad d_-(x) = \Gamma(1.2)(2-x)^{1.8}.$$

The spatial domain is $[x_R, x_L] = [0, 2]$ and the time interval is $[0, T] = [0, 1]$. The source term and the initial condition are given by

$$f(x,t) = -32e^{-t}[x^2 + (2-x)^2 + 0.125x^2(2-x)^2 - 2.5(x^3 + (2-x)^3) + \frac{25}{22}(x^4 + (2-x)^4)] \tag{18}$$

$$u_0(x) = 4x^2(2-x)^2 \tag{19}$$

respectively. The exact solution to the corresponding fractional diffusion Eq. (1) is given by [18]

$$u(x,t) = 4e^{-t}x^2(2-x)^2. \tag{20}$$

In the numerical experiment, we apply the PINN method with $N = 20$ and $L = 1$ to solve the given equation numerically and absolute errors are presented in Table 1 for different spatial mesh sizes and fixed time step. Also we compare the results with fast forward difference and forward difference results that is obtained in [23].

Table 1: Maximum absolute errors, $\Delta t = 1/128$

n	PINN	FD[23]	FFD[23]
2^6	8.59x10^{-4}	1.74x10^{-2}	1.55x10^{-2}
2^7	2.98x10^{-4}	8.35x10^{-3}	7.02x10^{-3}
2^8	7.25x10^{-5}	4.08x10^{-3}	3.18x10^{-3}

3.2. Example 2

Let us analyze the following other fractional diffusion equation from [24] with

$$d_+(x) = d_-(x) = \frac{\Gamma(2.2)x^{2.8}}{6}. \tag{21}$$

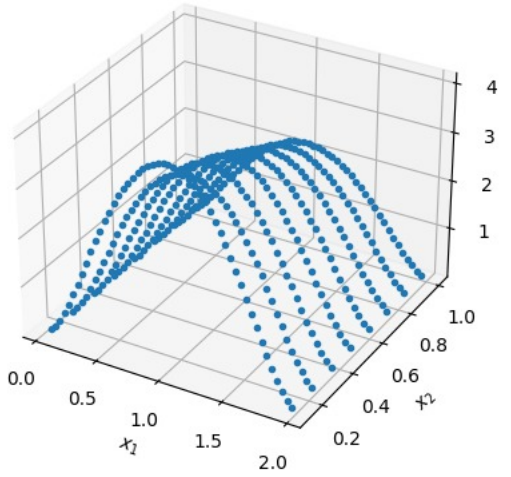

Figure 1: Graph of Ex.1 with $N = 2^7$ and $\Delta t = 1/128$.

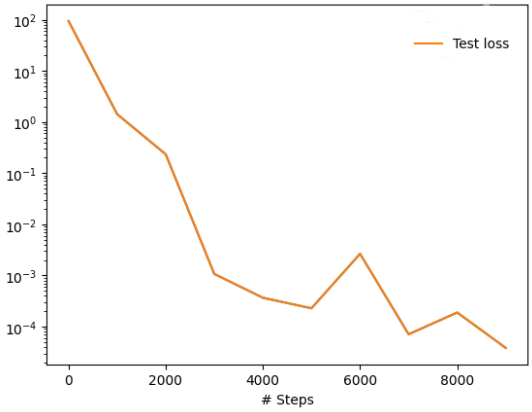

Figure 2: Behaviour of Error for Ex.1.

The spatial domain is $[x_R, x_L] = [0, 1]$ the time interval is $t > 0$. The source function is given by

$$f(x,t) = (1+x)e^{-t}x^3,$$

and the initial condition is given by

$$u(x,0) = x^3, \quad 0 < x < 1.$$

Dirichlet boundary conditions are

$$u(1,t) = 0 \quad \text{and} \quad u(1,t) = e^{-t}, \quad t > 0.$$

The exact solution to the corresponding fractional diffusion equation is given by $u(x,t) = e^{-t}x^3$.
In the numerical experiment, we reapply PINN method with N=5 and N=20 and L=1 to solve the given equation numerically and absolute errors are presented in Table 2 for different spatial mesh sizes and fixed time step. Also we compare the results with non polynomial spline method [24] and local polynomial regression (LPR) method [25].

Table 2: Maximum absolute errors, $\Delta t = 0.01$

n	PINN (N=5, L=1)	PINN (N=20, L=1)	Spline M.[24]	LPR M.[25]
11	0.03687	0.01125	0.1762	0.10446
21	0.01482	0.009588	0.1663	0.10518
61	0.008754	0.005224	0.1307	
121	0.001547	0.0009874	0.0859	

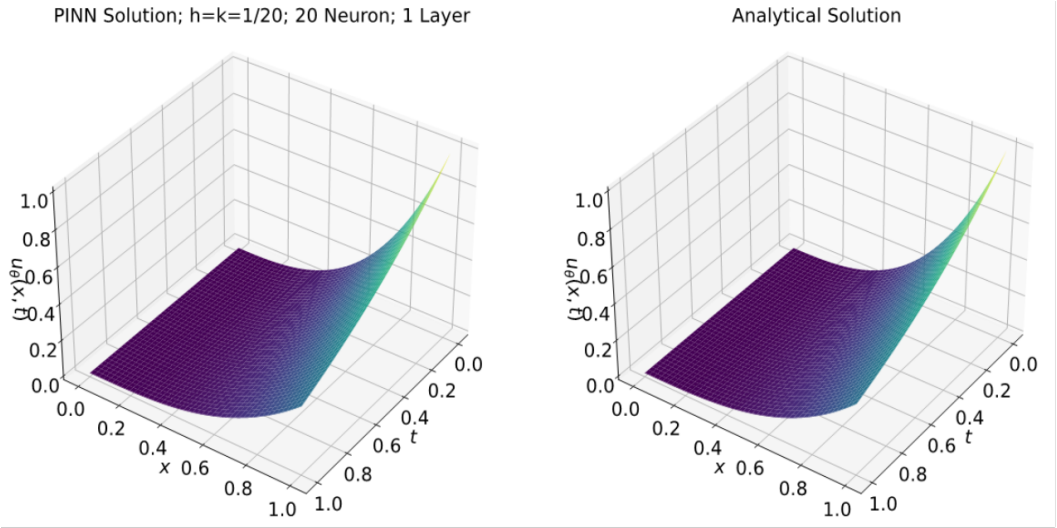

Figure 3: Solution graphs of Ex.2

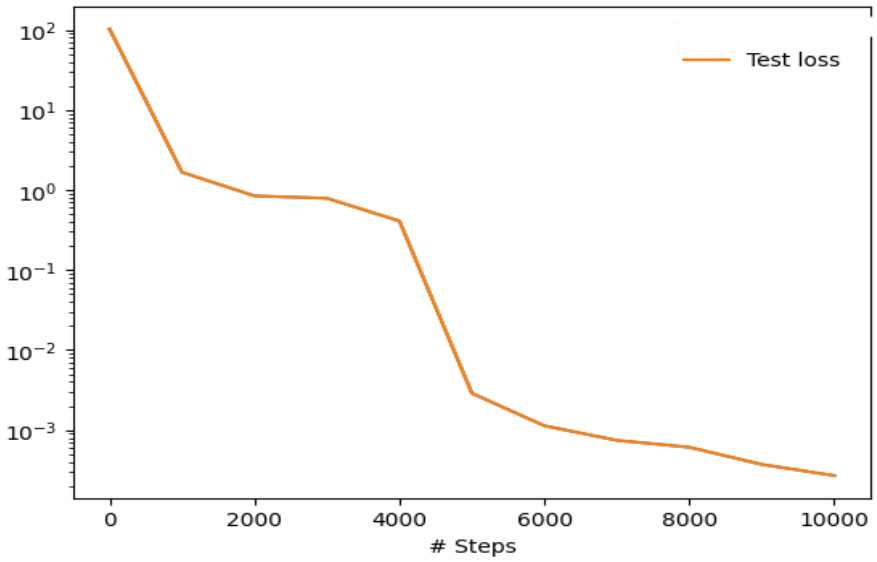

Figure 4: Behaviour of Error for Ex.2

4. Conclusion

This research presents approximate solutions and error analysis for the fractional diffusion equations, achieved through the feed-forward PINN model. Unlike traditional numerical methods, PINNs utilize automatic differentiation to manage differential operators. In contrast to numerical differentiation, automatic differentiation avoids differentiating the data itself. The neural networks designed to solve these problems were implemented using the Nadam optimizer and the Sigmoid activation function within the TensorFlow framework. Based on numerical experiments, it has been concluded that the PINN method offers a promising, convergent alternative. Future research will focus on applying the neural network approach to solve higher-order fractional partial differential equations (PDEs) numerically.

Competing interests:

The authors do not have any competing interests in this research.

Author contributions:

The authors contributed equally to all parts of the article.

Availability of data and materials:

Data sharing is not applicable to this article, as no datasets were generated or analyzed during the current study.

References

[1] Mall S., Chakraverty S.,(2013) Comparison of artificial neural network architecture in solving ordinary differential equations, Adv. Artif. Neural Syst., 2013 , p. 12

[2] Sabir Z., Baleanu D., Shoaib M., Raja M.A.Z., (2021) Design of stochastic numerical solver for the solution of singular three-point second-order boundary value problems, Neural Comput. Appl., 33 (7) , pp. 2427-2443.

[3] Raissi M., Perdikaris P., Karniadakis G.E., (2019) Physics-informed neural networks: A deep learning framework for solving forward and inverse problems involving nonlinear partial differential equations, J. Comput. Phys., 378 , pp. 686-707.

[4] Dwivedi V., Parashar N., Srinivasan B., (2021) Distributed learning machines for solving forward and inverse problems in partial differential equations, Neurocomputing, 420 , pp. 299-316.

[5] Cai S., Wang Z., Wang S., Perdikaris P., Karniadakis G.E., (2021) Physics-informed neural networks for heat transfer problems, J. Heat Transfer, 143 (6) .

[6] Mortari D., (2017) The theory of connections: Connecting points, Mathematics, 5 (4) , p. 57.

[7] Mai T., Mortari D., (2022) Theory of functional connections applied to quadratic and nonlinear programming under equality constraints, J. Comput. Appl. Math., 406 .

[8] Li, X. (2012) Numerical solution of fractional differential equations using cubic B-spline wavelet collocation method, Commun Nonlinear Sci Numer Simulat 17 3934–3946.

[9] Diethelm K., Ford N.J., (2002) Analysis of fractional differential equations, J. Math. Anal. Appl., 265 (2) , pp. 229-248.

[10] Kilbas A.A., Srivastava H.M., Trujillo J.J., (2006) Theory and Applications of Fractional Differential Equations, Vol. 204 Elsevier

[11] Podlubny I., (1998) Fractional Differential Equations: An Introduction to Fractional Derivatives, Fractional Differential Equations, to Methods of their Solution and Some of their Applications Elsevier .

[12] Caputo M., Fabrizio M. A new definition of fractional derivative without singular kernel Prog. Fract. Differ. Appl., 1 (2) , pp. 73-85

[13] Atangana A., Baleanu D., (2015) New fractional derivatives with non-local and non-singular kernel, theory and application to heat transfer model, Therm. Sci., 20 (2) (2016), Article 763769.

[14] Jafarian A., Mokhtarpour M., Baleanu D., (2017) Artificial neural network approach for a class of fractional ordinary differential equation, Neural Comput. Appl., 28 (4) , pp. 765-773.

[15] Sivalingam S.M., Kumar P., Govindaraj V., (2023) The hybrid average subtraction and standard deviation based optimizer, Adv. Eng. Softw., 176 , Article 103387.

[16] Alkan, A. (2022). Improving homotopy analysis method with an optimal parameter for time-fractional Burgers equation. Karamanoğlu Mehmetbey Üniversitesi Mühendislik ve Doğa Bilimleri Dergisi, 4(2), 117-134.

[17] Alkan, A. (2022). Improving Homotopy Analysis Method with An Optimal Parameter for Time-Fractional Burgers Equation. Karamanoğlu Mehmetbey Üniversitesi Mühendislik Ve Doğa Bilimleri Dergisi, 4(2), 117-134. https://doi.org/10.55213/kmujens.1206517

[18] Alkan, A., & Anaç, H. (2024). The novel numerical solutions for time-fractional Fornberg-Whitham equation by using fractional natural transform decomposition method. AIMS Mathematics, 9(9), 25333-25359.

[19] Alkan, A., & Anaç, H. (2024). A new study on the Newell-Whitehead-Segel equation with Caputo-Fabrizio fractional derivative. AIMS Mathematics, 9(10), 27979-27997.

[20] Bektaş, U., & Anaç, H. (2024). A hybrid method to solve a fractional-order Newell–Whitehead–Segel equation. Boundary Value Problems, 2024(1), 38.

[21] Pakdaman M., Ahmadian A., Effati S., Salahshour S., Baleanu D., (2017) Solving differential equations of fractional order using an optimization technique based on training artificial neural network, Appl. Math. Comput., 293 , pp. 81-95.

[22] Pang G., Lu L., Karniadakis G.E., (2019) fPINNs: Fractional physics-informed neural networks, SIAM J. Sci. Comput., 41 (4) , pp. A2603-A2626.

[23] Wang, W., Wang K., Sircar, T. (2019) A direct $0(Nlog^2N)$ finite difference method for fractional diffusion equations, Journal of Computational Physics, 229 8095-8104.

[24] Caglar, S., Ucar, M.F., Caglar, N., Akkoyunlu, C., (2012) Non Polynomial Spline Method for Fractional Diffusion Equation, Journal of Computational Analysis and Applications, 1354 - 1361.

[25] Tadjeran, C., Meerschaert, M. M., (2007) A second-order accurate numerical method for the two-dimensional fractional diffusion equation, Journal of Computational Physics, 220 813–823.

e-ISSN: 2149-4584

Erzincan University Journal of Science and Technology

EJSAT 2025, 18 (3) 735-744

Research Article

On a Conjecture about Profiles of Finite Connected Racks

Selçuk Kayacan[1*]

[1] Bahçeşehir University, Faculty of Engineering and Natural Sciences, Istanbul, Turkey

Received: 26/10/2024, **Revised:** 29/07/2025, **Accepted:** 29/07/2025, **Published:** 31/12/2025

Abstract

A rack is a set equipped with a binary operation for which all left multiplications are automorphisms. A quandle is a rack that satisfies an additional axiom. In a finite connected rack, the cycle type of the permutation induced by left multiplication is independent of the chosen element, and is called the profile of the rack. Hayashi conjectured that, in the profile of a finite connected quandle, the length of any cycle divides the length of the longest cycle. In this paper, we prove Hayashi's conjecture in several specific cases.

Keywords: Finite connected rack, profile of a rack, Hayashi's conjecture.

Sonlu Bağlantılı Rakların Profilleri Hakkında Bir Sanı Üzerine

Öz

Bir rak bir küme ve üzerinde tanımlanmış ikili işlemden oluşup sol çarpımlar kümenin otomorfizmalarıdır. Bir kuandle ise ikili işlemin belli bir aksiyomu sağladığı rak olarak tanımlanır. Sonlu bağlantılı bir rak için bir eleman ile sol çarpımın belirlediği permütasyonun döngü tipi seçilen elemandan bağımsızdır ve bu döngü tipine rakın profili denilir. Hayashi sonlu bağlantılı bir kuandlenin profilinde herhangi bir döngünün uzunluğunun en uzun döngünün uzunluğunu böldüğünü öne sürmüştür. Bu makalede Hayashi'nin sanısını bazı belli durumlar için ispatlıyoruz.

Anahtar Kelimeler: Sonlu bağlantılı rak, rakın profili, Hayashi'nin sanısı.

Corresponding Author: selcuk.kayacan@bau.edu.tr

Cite this Article: Erzincan University Journal of Science and Technology 2025, 18(3)735-744. https://doi.org/10.18185/erzifbed.1591413

1. Introduction

Racks and quandles are algebraic objects that are mostly studied in the context of knot theory. The defining properties of those objects are in a sense compatible with the Reidemeister moves which makes them useful to define knot invariants. For example, in [1] Joyce introduced *knot quandle* and showed that it is a complete invariant for knots. This result was also obtained in [2] by Matveev independently in which the author introduced the notion of distributive groupoid. Also, in [3] Fenn and Rourke proved that the *fundamental rack* is a complete invariant for irreducible framed links in a 3-manifold. There are various notational conventions used to define racks and quandles in literature. In this paper we define racks and quandles in the following way.

A *rack* X is a set together with a binary operation $\triangleright: X \times X \to X$ satisfying the following two axioms:

- (A1) for all $x, y, z \in X$ we have $x \triangleright (y \triangleright z) = (x \triangleright y) \triangleright (x \triangleright z)$
- (A2) for all $x, z \in X$ there is a unique $y \in X$ such that $x \triangleright y = z$

A rack X is a *quandle* if, additionally, it satisfies the following axiom:

- (A3) for all $x \in X$ we have $x \triangleright x = x$

Let G be a group and for any two elements $a, b \in G$ let $a \triangleright b := aba^{-1}$. Then, the group G as well as any conjugacy class of G satisfies those three axioms; hence equipped with the conjugation operation $\triangleright$ each one of them is an example of a quandle. More generally, we call a subset X of G *conjugation rack* if it is a rack with the conjugation operation inherited by the group.

In this paper we only consider finite racks, although some of the statements are also valid for infinite racks. It is customary to identify elements of a finite rack X with integers $1,2, \dots, n$ if X has n elements. By axiom (A2), the map $\phi_x: y \to x \triangleright y$ is a permutation hence is an element of the symmetric group S_n of degree n. A permutation $\sigma \in S_n$ is an automorphism of X if and only if $\sigma(x \triangleright y) = \sigma(x) \triangleright \sigma(y)$ for every $x, y \in X$. By axiom (A1), the map ϕ_x is an automorphism of X.

The set of all automorphisms of X, denoted $\mathsf{Aut}(X)$, form a subgroup of S_n which is called the *automorphism group* of X. The map $\Phi: x \mapsto \phi_x$ defines a rack morphism from X to S_n, where S_n is considered as a quandle with conjugation operation (see Proposition 2). The *inner automorphism group* of X, denoted $\mathsf{Inn}(X)$, is the subgroup of $\mathsf{Aut}(X)$ generated by the elements of $\Phi(X)$. Let σ be an automorphism of X. Since $\sigma\phi_x\sigma^{-1} = \phi_{\sigma(x)}$ for every $x \in X$, we see that $\mathsf{Inn}(X)$ is a normal subgroup of $\mathsf{Aut}(X)$. In general $\mathsf{Inn}(X)$ and $\mathsf{Aut}(X)$ may be different groups.

A rack X is *faithful* if the map $\Phi: X \to \mathsf{Inn}(X)$ is injective. Suppose X is faithful. Obviously, the map Φ is an isomorphism between X and $\Phi(X)$, hence X is a quandle. Moreover, the center of

the inner automorphism group is trivial and the action of $\mathsf{Inn}(X)$ on $\Phi(X)$ by conjugation is faithful (see Proposition 2).

A rack X is *connected* if the action of its inner automorphism group on X itself is transitive. Suppose X is a connected rack. In that case, any two elements of $\Phi(X)$ can be conjugated by an element of $\mathsf{Inn}(X)$. Since in symmetric group conjugate elements have the same cycle type, connectedness of X implies each element of $\Phi(X)$ has the same cycle type. This cycle type $\lambda = (\lambda_0^{a_0}, \lambda_1^{a_1}, \dots, \lambda_t^{a_t})$ is called the *profile* of X. Here λ_s $(0 \leq s \leq t)$ are ordered increasingly. Notice that $x \rhd x = x$ for every $x \in X$ if X is a quandle which means in the profile λ of a quandle X the value of the least element λ_0 must always be 1. The purpose of this paper is to prove some special cases of the following conjecture which was stated by Hayashi originally for quandles (see [4, Conjecture 1.1]).

Conjecture 1. *For a finite connected rack X with profile* $\lambda = (\lambda_0^{a_0}, \lambda_1^{a_1}, \dots, \lambda_t^{a_t})$*, each* λ_s $(0 \leq s \leq t)$ *divides* λ_t.

Let G be a finite group, α be an automorphism of G, and H be a subgroup of G pointwise fixed by α, i.e., $\alpha(h) = h$ for every $h \in H$. One can easily verify that the coset space G/H with the operation $xH \rhd yH := x\alpha(x^{-1}y)H$ satisfies quandle axioms. It is called the *homogeneous quandle* and denoted by (G, H, α). Any finite connected quandle is isomorphic to a homogeneous quandle. Therefore, given the complete list of transitive groups of degree n, it is possible to determine the complete list of non-isomorphic connected quandles of n elements. This method is used by Vendramin to compute all connected quandles having less than 48 elements (see [5]). The list is available in Rig [6], a GAP package designed for computations related to racks and quandles.

We shall prove that Conjecture 1 holds when the inner automorphism group acts on the rack primitively (see Theorem 6). In Table 1 we present permutations of a quandle which is the fourth quandle with 12 elements in Vendramin's list. Here elements of the rack are labeled by the integers $1,2,\dots,12$ and each inner automorphism ϕ_i, for $1 \leq i \leq 12$, is represented as a permutation of the elements of the quandle. The reader may easily verify that the following partition

$$\{1,5,9\},\ \{2,6,10\},\ \{3,7,11\},\ \{4,8,12\}$$

formed by taking the first three numbers in each row of the table is a block system for the action of the inner automorphism group on the rack itself. Thus, the action of the inner automorphism group is not primitive. From the table, it is apparent that the profile of this rack is λ=(1,2,3,6), so Hayashi's conjecture holds in this case as well.

Table 1: Permutations of SmallQuandle(12,4) in Rig

ϕ_1 : (1)(5,9)(2,4,3)(6,12,7,10,8,11)
ϕ_2 : (2)(6,10)(1,3,4)(5,11,8,9,7,12)
ϕ_3 : (3)(7,11)(1,4,2)(5,12,6,9,8,10)
ϕ_4 : (4)(8,12)(1,2,3)(5,10,7,9,6,11)
ϕ_5 : (5)(1,9)(6,8,7)(2,12,3,10,4,11)
ϕ_6 : (6)(2,10)(5,7,8)(1,11,4,9,3,12)
ϕ_7 : (7)(3,11)(5,8,6)(1,12,2,9,4,10)
ϕ_8 : (8)(4,12)(5,6,7)(1,10,3,9,2,11)
ϕ_9 : (9)(1,5)(10,12,11)(2,8,3,6,4,7)
ϕ_{10} : (10)(2,6)(9,11,12)(1,7,4,5,3,8)
ϕ_{11} : (11)(3,7)(9,12,10)(1,8,2,5,4,6)
ϕ_{12} : (12)(4,8)(9,10,11)(1,6,3,5,2,7)

Let A be a finite abelian group and α be an automorphism of A. The corresponding homogeneous quandle $(A, 1, \alpha)$ is called an *affine quandle*. Let $\beta(x) := x - \alpha(x)$ for every $x \in A$. Observe that in $(A, 1, \alpha)$ the quandle operation is defined by

$$x \triangleright y := \alpha(y - x) + x = \alpha(y) + \beta(x) = \beta(x - y) + y$$

and the orbit of y under the action of inner automorphism group is $y + \beta(A)$. Suppose $(A, 1, \alpha)$ is connected. Then β must be a bijection of A. Moreover, the inner automorphism group is isomorphic to a cyclic extension of A, hence is solvable. Now, consider the profile of $(A, 1, \alpha)$. Kajiwara and Nakayama proved in [7] that there must be an element of A whose orbit size under the action of $\langle \phi_x \rangle$ is the order of ϕ_x. Let $\lambda = (\lambda_0^{a_0}, \lambda_1^{a_1}, \dots, \lambda_t^{a_t})$ be the profile of $(A, 1, \alpha)$. Since the least common multiple of the numbers $\lambda_1, \dots, \lambda_t$ divides the order of ϕ_x, Kajiwara and Nakayama's result shows that Hayashi's Conjecture holds for connected affine quandles.

Let C be a conjugacy class of a symmetric group S_d. Hence, the inner automorphism group of C is either isomorphic to A_d or S_d. In particular $\mathsf{Inn}(C)$ is not solvable if $d \geq 5$. Let x be an element of C and let ℓ be the order of x in S_d. To prove Hayashi's Conjecture holds for C, one possible way is to find an element y of C so that $x^k y x^{-k} \neq y$ for $1 \leq k < \ell$. However, this method seems to be not applicable for other classes of groups as we don't have an explicit description of the elements of conjugacy class C.

The aim of this paper is to show that Hayashi's Conjecture holds for some particular classes of racks. The organization of the paper is as follows. In Section 2 we review some of the basic facts on racks and give a group theoretical interpretation of Conjecture 1 (see Proposition 5). In Section 3 we state and prove our main results. To be more precise in Theorem 6 we shall prove that Conjecture 1 holds when the inner automorphism group acts on the rack primitively and in

Theorem 7 we shall show that Conjecture 1 holds for the conjugacy classes in a symmetric group. In either Theorem the proof uses Proposition 5.

2. Prelimineries

The reader may refer to [8] for the basic theory of racks and in particular to Lemma 1.7, Lemma 1.9 and Proposition 3.2 of the same paper for alternative statements and proofs of the following Proposition.

Proposition 2. *Let X be a rack. Then following statements hold.*

(i) The map $\Phi: X \to Inn(X)$ defines a rack morphism between X and $\Phi(X)$ which is an isomorphism if X is faithful.

(ii) If X is faithful, then the action of $Inn(X)$ on X by automorphisms and on $\Phi(X)$ by conjugation are isomorphic and the center of $Inn(X)$ is trivial.

(iii)If X is a conjugation rack and $G := \langle X \rangle$, then the map $\Phi: X \to \Phi(X)$ extends to a map

$$\Phi: G \to Inn(X),$$

(iv) which is a group homomorphism and $Inn(X) \cong G/Z(G)$.

(v) The rack X is connected and faithful if and only if it is isomorphic, as a quandle, to a conjugacy class C of a group G so that $G = \langle C \rangle$ and $Z(G) = 1$.

Proof. (i) Observe that for every $x, y, z \in X$ the equality $\phi_x(y \triangleright z) = \phi_x(y) \triangleright \phi_x(z)$ holds by axiom (A1). In other words $\phi_x \phi_y = \phi_{x \triangleright y} \phi_x$ holds for any two elements $x, y \in X$. However, this means the map Φ takes $x \triangleright y$ into $\phi_x \phi_y \phi_x^{-1} = \phi_x \triangleright \phi_y$ and so Φ is a rack morphism between X and $\Phi(X)$. Further if Φ is injective then X and $\Phi(X)$ would be isomorphic quandles.

(ii) Suppose X is faithful. Pick an automorphism $\sigma \in \mathrm{Inn}(X)$. Since, for any $x \in X$,

$$\Phi(\sigma \cdot x) = \Phi(\sigma(x)) = \phi_{\sigma(x)} = \sigma \phi_x \sigma^{-1} = \sigma \cdot \Phi(x),$$

we see that the map Φ defines an isomorphism between the actions of $\mathrm{Inn}(X)$ on X and on $\Phi(X)$. Now, if σ lies in the center of $\mathrm{Inn}(X)$, then $\phi_{\sigma(x)} = \sigma \phi_x \sigma^{-1} = \phi_x$ for every $x \in X$ implying σ is the identity map on X since the map $\Phi: x \mapsto \phi_x$ is a bijection.

(iii) Consider the map $\Phi: G \to \mathrm{Inn}(X)$ taking an element $g := y_j \dots y_2 y_1$ of G, written as the product of some elements $y_i \in X$ for $1 \leq i \leq j$, to an element ϕ_g of the inner automorphism group $\mathrm{Inn}(X)$, where ϕ_g is defined as the composition

$$\phi_g := \phi_{y_j} \dots \phi_{y_2} \phi_{y_1}.$$

Since, for any element $x \in X$ we have

$$g x g^{-1} = (y_j \triangleright \cdots (y_2 \triangleright (y_1 \triangleright x)) \dots) = \phi_{y_j} \dots \phi_{y_2} \phi_{y_1}(x),$$

the map Φ is well-defined and defines a surjective group homomorphism. Clearly, $g \in \mathsf{Ker}(\Phi)$ if and only if ϕ_g is the identity map which is the case if and only if $gxg^{-1} = x$ for every generator element $x \in X$.

(iv) Suppose X is faithful and connected. Since X is faithful, the rack X is isomorphic to the conjugation rack $\Phi(X)$ and since X is connected, conjugation rack $\Phi(X)$ is a conjugacy class of the inner automorphism group $\mathsf{Inn}(X)$. By the previous part the center of $\mathsf{Inn}(X)$ is trivial.

Conversely, suppose X is isomorphic to a conjugacy class C of a group G so that $G = \langle C \rangle$ and $Z(G) = 1$. By the previous part, the rack C is connected and faithful. Therefore X is faithful and connected as well. ■

Lemma 3 (see [8, Lemma 1.21])**.** *Let X and Y be two racks and let $f: X \to Y$ be a surjective rack homomorphism. Then, for any $y_1, y_2 \in Y$, the cardinalities of the fibers $f^{-1}(y_2)$ and $f^{-1}(y_1 \rhd y_2)$ are equal. In particular, every fiber of Y has the same cardinality if Y is connected.*

Proof. We show that there exist a bijective function $B: X \to X$ such that

$$B(f^{-1}(y_2)) \subseteq f^{-1}(y_1 \rhd y_2) \text{ and } B^{-1}(f^{-1}(y_1 \rhd y_2)) \subseteq f^{-1}(y_2).$$

Let $B(x) := a \rhd x$, where $f(a) = y_1$. Observe that $B^{-1} = \phi_a^{-1} \in \mathsf{Inn}(X)$. Suppose $x \in f^{-1}(y_2)$. Then $f(a \rhd x) = f(a) \rhd f(x) = y_1 \rhd y_2$. That is, $B(x) \in f^{-1}(y_1 \rhd y_2)$. Next, suppose $x \in f^{-1}(y_1 \rhd y_2)$. Then $f(B^{-1}(x)) = f\phi_a^{-1}(x) = \phi_{f(a)}^{-1} f(x) = \phi_{y_1}^{-1}(y_1 \rhd y_2) = y_2$. That is, $B^{-1}(x) \in f^{-1}(y_2)$. ■

Remark. Let X be a finite connected rack and take two elements x, y of X. Let λ_y^x be the orbit size of y and $\bar{\lambda}_y^x$ be the orbit size of ϕ_y under the actions of $\langle \phi_x \rangle$. By Lemma 3, Φ^{-1} yields a partition of X into a disjoint union of fibers of the same size. Observe that for any integer k the element $\phi_x^k(y)$ of X does not lie in the fiber $\Phi^{-1}(\phi_y)$ unless $\phi_x^k \phi_y \phi_x^{-k} = \phi_y$. Therefore $\bar{\lambda}_y^x$ divides λ_y^x.

Let X be a finite connected rack whose profile is $\lambda = (\lambda_0^{a_0}, \lambda_1^{a_1}, \dots, \lambda_t^{a_t})$ and let k be an integer. For a permutation σ of X, the *k-part* of σ is the set of elements of X which appear in a cycle of length k in the permutation σ. And the *λ_s-part* of X is the multiset formed by the λ_s-parts of elements of $\Phi(X)$. For example, if X is the fourth quandle with 12 elements in Vendramin's list, using Table 1, we see that the 2-part of X is

$$\{5,9,6,10,7,11,8,12,1,9,2,10,3,11,4,12,1,5,2,6,3,7,4,8\}.$$

Lemma 4. *Let X be a finite connected rack with profile $\lambda = (\lambda_0^{a_0}, \lambda_1^{a_1}, \dots, \lambda_t^{a_t})$. Then the number of occurrences of each element of X in the λ_s-part of X is same and equal to $a_s\lambda_s/f$ for each λ_s $(0 \le s \le t)$, where f is the cardinality of a fiber of Φ.*

Proof. Let σ be an element of $\mathsf{Inn}(X)$. Conjugating each element of $\Phi(X)$ with σ yields a permutation of $\Phi(X)$. Since $\sigma\phi_x\sigma^{-1} = \phi_{\sigma(x)}$, if $\sigma(u) = v$ for some distinct elements u and v of X then the number of occurrences of u and v in the λ_s-part of X would be the same. The

claim follows from the facts that X is connected and the cardinality of $\Phi(X)$ is $\frac{n}{f}$, where n is the number of elements in X. ■

Next, we shall review Conjecture 1 in group theoretical terms. Let X be a finite connected rack and fix an element $x \in X$. Let $F := \langle \phi_x \rangle$ be the subgroup of $G := \mathsf{Inn}(X)$ generated by ϕ_x and let H be a conjugate of the centralizer of ϕ_x in G. Since the subgroup H of G is the stabilizer of some point in $\Phi(X)$, the action of G on $\Phi(X)$ by conjugation is equivalent to the action of G on the coset space G/H by left multiplication. Let $\lambda = (\lambda_0^{a_0}, \lambda_1^{a_1}, \dots, \lambda_t^{a_t})$ be the profile of $\Phi(X)$. Then, the cycle containing ϕ_y in the permutation ϕ_{ϕ_x} would correspond to the cycle

$$(\phi_y H, \phi_x \phi_y H, \dots, \phi_x^{\lambda_s - 1} \phi_y H).$$

Observe that, the subgroup $\langle \phi_x^{\lambda_s} \rangle$ of F is also a subgroup of $\phi_y H \phi_y^{-1}$.

Proposition 5. *Let X be a finite connected rack and x be an element of X. Let F be the subgroup of $\mathsf{Inn}(X)$ generated by ϕ_x and K be the centralizer of ϕ_x in $\mathsf{Inn}(X)$. Let $\lambda = (\lambda_0^{a_0}, \lambda_1^{a_1}, \dots, \lambda_t^{a_t})$ be the profile of X. The following statements hold:*

(i) If F intersects one of the conjugates of K trivially, then λ_s divides λ_t for each $0 \le s \le t$.

(ii) Conversely, if λ_s divides λ_t for each $0 \le s \le t$ and X is faithful, then F intersects one of the conjugates of K trivially.

Proof. (i) Let k be an integer and $\bar{\lambda} = (\bar{\lambda}_0^{\bar{a}_0}, \bar{\lambda}_1^{\bar{a}_1}, \dots, \bar{\lambda}_{t'}^{\bar{a}_{t'}})$ be the profile of $\Phi(X)$. Let H be a conjugate of K such that the intersection of F with H is trivial. That means

$$(H, \phi_x H, \dots, \phi_x^{k-1} H)$$

is an orbit under the action of F if and only if k equals to the order of ϕ_x. Then, clearly, k equals to $\bar{\lambda}_{t'}$. From the remark following Lemma 3 we see that k divides λ_s for some $0 \le s \le t$ so that the order of ϕ_x is equal to λ_t.

(ii) Since λ_s divides λ_t for each $0 \le s \le t$, we see that the order of ϕ_x is λ_t. By Proposition 2 we know that X and $\Phi(X)$ have the same profiles. Therefore, the order of ϕ_{ϕ_x} is λ_t as well. From this we conclude that there exists an element ϕ_y of $\Phi(X)$ so that $\phi_y K$ lies in an orbit of size λ_t under the action of F, which means the intersection of F with the centralizer of $\phi_{\phi_y(x)}$ is trivial. ■

3. Main Results

Let G be a group acting transitively on a set Ω. A partition of Ω form a block system if the following property is satisfied: for any element g of G an element of the partition is either mapped to itself by g or to another element of the partition. In that case we call the elements of the partition *blocks*. A block system is trivial if either the partition consists of the whole set or it consists of the singletons. We say G acts *primitively* on Ω if the only block systems are the trivial block systems.

Let X be a finite connected rack with profile $\lambda = (\lambda_0^{a_0}, \lambda_1^{a_1}, \dots, \lambda_t^{a_t})$ and k be an integer. For a permutation σ of X, the $\tilde{k}$-*part* of σ is the set of elements of X which appear in a cycle whose length is a divisor of k in the permutation σ. Let x, y be two elements of X. If an automorphism σ of X centralizes ϕ_y, then as a permutation σ preserves λ_s-part of ϕ_y for each λ_s $(0 \leq s \leq t)$. Let K be the $\tilde{k}$-part of ϕ_x and $L := X \backslash K$ be the complement of K in X. If ϕ_x^k centralizes ϕ_y, then ϕ_y centralizes ϕ_x^k as well. However, that means as a permutation ϕ_y preserves the set K as well as the set L. Consider again the fourth quandle with 12 elements in Vendramin's list (see Table 1). Its profile is $\lambda = (1^1, 2^1, 3^1, 6^1)$ so that $\tilde{2}$-part of ϕ_i has 3 elements whereas $\tilde{3}$-part has 4 elements. Now, if ϕ_j centralizes ϕ_i^2 then $\tilde{2}$-parts of ϕ_i and ϕ_j must be the same since the cycle type of ϕ_i^2 is $(1^3, 3^3)$. Moreover, for this example the set of $\tilde{2}$-parts of permutations ϕ_j form a block system for the action of the inner automorphism group. However, we don't know any general method for relating $\tilde{k}$-parts with a block system.

Let H be the stabilizer of an element $x \in \Omega$. Then, the action of G on Ω is primitive if and only if the stabilizer H is a maximal subgroup of G. To see this, observe that if there exists a proper subgroup K of G that contains H strictly, then the cosets of K would be unions of some of the cosets of H in G. However, this determines a non-trivial block system for G/H under the action of G by left multiplication.

Theorem 6. *Let X be a finite connected rack with profile $\lambda = (\lambda_0^{a_0}, \lambda_1^{a_1}, \dots, \lambda_t^{a_t})$. If the inner automorphism group $\mathsf{Inn}(X)$ acts primitively on X, then λ_s divides λ_t for each $0 \leq s \leq t$.*

Proof. By assumption $\mathsf{Inn}(X)$ acts primitively on X. Since the fibers of $\Phi: X \to \Phi(X)$ form a partition of X which is a block system for the action of $\mathsf{Inn}(X)$, the racks X and $\Phi(X)$ are isomorphic and have the same profiles. Moreover, by Proposition 2 the center of $\mathsf{Inn}(X)$ is trivial.

To prove the Theorem suppose contrarily λ_s does not divide λ_t for some $0 \leq s \leq t$. We want to derive a contradiction. Let us fix an element $x \in X$ and let y be an element of X different from x. Let $F := \langle \phi_x \rangle$ and $F' := \langle \phi_y \rangle$. Also, let H be the centralizer of F in $G := \mathsf{Inn}(X)$ and H' be the centralizer of F'. Notice that H' is a conjugate of H. Consider the intersection $I := F \cap H'$. Using Proposition 5(i) contrapositively we see that I is a non-trivial subgroup of G. Now I centralizes both F' and H, so it lies in the center of $\langle F', H \rangle$. Since G acts on X primitively by assumption, we see that H is a maximal subgroup of G. Clearly, we can choose y so that F' is not contained in H. However that means I lies in the center of G which is a contradiction. ■

Recall that in a symmetric group two elements are conjugate if and only if they share the same cycle type. Let C be a conjugacy class in a symmetric group S_d. Recall that a conjugacy class generates a normal subgroup of the group. Therefore, if $d \geq 5$, as a quandle the inner automorphism group $\mathsf{Inn}(C)$ of C is isomorphic to the symmetric group S_d when C is the conjugacy class of an odd permutation and it is isomorphic to the alternating group A_d when C is the conjugacy class of an even permutation different from the identity permutation. Observe that C is faithful when $d \geq 5$ by Proposition 2, since the centers of A_d and S_d are trivial.

Theorem 7. *Let C be a conjugacy class in a symmetric group S_d which is connected as a quandle. If $\lambda = (\lambda_0^{a_0}, \lambda_1^{a_1}, \dots, \lambda_t^{a_t})$ is the profile of C, then λ_s divides λ_t for each $0 \leq s \leq t$.*

Proof. It is clear that the Theorem holds when C is the conjugacy class of a central element. So we assume in the rest of the proof that C is the conjugacy class of a non-central element.

First, we prove the Theorem when the degree of S_d is equal to three or four. If $d = 3$, there are two possibilities. Either C is the conjugacy class of $(1,2)$ or it is the conjugacy class of $(1,2,3)$. In the first case, the inner automorphism group is S_3 and since the center of S_3 is trivial, C is faithful by Proposition 2. The Theorem holds in this case since the order of $(1,2)$ is a prime number. The latter possibility cannot occur as the conjugacy class of $(1,2,3)$ is not connected as a rack.

If $d = 4$, there are four possibilities. The conjugacy class of $(1,2)(3,4)$ generates an abelian subgroup so it is not connected. Also the conjugacy class of $(1,2,3)$ is not connected as a quandle since the action of A_4 on this set is not transitive. But in the remaining two cases the conjugacy class is connected as a quandle. Since the order of an element of the conjugacy class is a prime power in all those last two cases the Theorem holds when the degree of the symmetric group is four.

Next, suppose $d \geq 5$. From the previous explanations we know that C is faithful and the inner automorphism group is isomorphic to either A_d or S_d when $d \geq 5$. Now, fix an element x of C and let $\mu = (\mu_0^{b_0}, \mu_1^{b_1}, \dots, \mu_r^{b_r})$ be the cycle type of x in S_d. Moreover, since the map $\Phi: C \to \mathsf{Inn}(C)$ extends to a group isomorphism, using Proposition 5(i), it is enough to show that $\langle x \rangle$ intersects the centralizer of some element y of C trivially. Suppose $r \geq 1$. Let y be an element of C having the following property: For any $0 \leq s \leq r$ the μ_s-parts of x and y are not coinciding. If the value of $r \geq 1$, the existence of y in S_d or A_d is clear. Let ℓ be the order of x and k be an integer dividing ℓ. Obviously, x^k does not centralize y unless $k = \ell$. Hence the Theorem holds when C is the conjugacy class of an element containing at least two cycles of different lengths in its cycle decomposition. Next, suppose $r = 0$. In that case $d = b_0\mu_0$ and the order of x is μ_0. In turn, the order of ϕ_x is μ_0 as well and we may assume μ_0 is neither 1 nor a prime power since the Theorem holds trivially in those cases. Recall that the centralizer of x in S_d is isomorphic to $C_{\mu_0} \wr S_{b_0}$, where C_{μ_0} is the cyclic group of order μ_0. Moreover, for some conjugate y of x the intersection of $\langle x \rangle$ with the centralizer of y is trivial when $\mu_0 \geq 6$. This completes the proof. ■

The proof of Theorem 7 can be adapted to work when C is the conjugacy class of an alternating group. Notice that a conjugacy class of a simple group is necessarily connected as a quandle. The only complication arises when a conjugacy class of A_d is not a conjugacy class of S_d. Actually this may happen. Let x be an even permutation of S_n whose cycle type is $\mu = (\mu_0^{b_0}, \mu_1^{b_1}, \dots, \mu_r^{b_r})$. The conjugacy class of x in S_n splits into two different conjugacy classes in A_n if μ_s is an odd number and $b_s = 1$ for every $0 \leq s \leq r$. Otherwise, the conjugacy class of x in S_n is same with the conjugacy class of x in A_n. Even in the former case, fixing an element x of C, we can show that there exist an element y of C so that the centralizer of y intersects $\langle x \rangle$ trivially.

Ethics in Publishing

There are no ethical issues regarding the publication of this study.

Acknowledgements

I would like to thank Volkmar Welker for suggesting that I work on Hayashi's Conjecture, David Stanovský for helping improve the statement and proof of Theorem 6, and the anonymous referee whose suggestions greatly improved the exposition. This study was supported by Scientific and Technological Research Council of Turkey (TUBITAK) under the Grant Number 122F490. The author thanks to TUBITAK for their supports.

References

[1] Joyce, D. (1982) *A classifying invariant of knots, the knot quandle*, J. Pure Appl. Algebra **23**, no. 1, 37–65.

[2] Matveev, S. V. (1982) *Distributive groupoids in knot theory*, Mat. Sb. (N.S.), **119(161)**:1(9), 78–88; Sb. Math., **47**:1 (1984), 73–83.

[3] Fenn, R., Rourke, C., (1992) *Racks and links in codimension two*, J. Knot Theory Ramifications **1**, no. 4, 343–406.

[4] Hayashi, C., (2013) *Canonical forms for operation tables of finite connected quandles*, Comm. Algebra **41** 3340–3349.

[5] Vendramin, L., (2012) *On the classification of quandles of low order*, J. Knot Theory Ramifications **21**, no. 9, 1250088.

[6] Vendramin, L., Rig, a GAP package for racks, quandles and Nichols algebras. Available at http://github.com/vendramin/rig/

[7] Kajiwara, T., Nakayama, C., (2016) *A large orbit in a finite affine quandle*, Yokohama Math. J. **62** 25–29.

[8] Andruskiewitsch, N., Graña, M., (2003) *From racks to pointed Hopf algebras*, Adv. Math. **178**, no. 2, 177–243.

e-ISSN: 2149-4584

Erzincan University Journal of Science and Technology

EJSAT 2025, 18 (3) 745-762

Research Article

Antibacterial and Cytotoxic Activity of Silver and Zinc Oxide Nanoparticles Synthesized Using Deep Eutectic Solvent Extraction of the Sea Cucumber-*Holothuria tubulosa*

Hilal TOP HAYTAOGLU[1], Aysegul INAM[2,3], Tulay ONCU ONER[3], Murat ELIBOL[2*]

[1]Biotechnology Program, Graduate School of Natural and Applied Sciences, Ege University, Izmir, Türkiye
[2]Department of Bioengineering, Faculty of Engineering, Ege University, Izmir, Türkiye
[3]Department of Bioengineering, Faculty of Engineering and Natural Sciences, Manisa Celal Bayar University, Manisa, Türkiye

Received: 23/03/2025, **Revised:** 14/07/2025, **Accepted:** 13/08/2025, **Published:** 31/12/2025

Abstract

In this study, we synthesized these nanoparticles (NPs) utilizing a novel approach involving deep eutectic solvent (DES) extraction of the sea cucumber-*Holothuria tubulosa*. Choline chloride-urea (1:2) was used as a DES, facilitating the green synthesis without hazardous chemicals. Spectrophotometric methods were used to determine total phenolic and carbohydrate content of the extract. UV–Vis, DLS and FTIR characterized NPs. The absorption peaks in 400 nm for AgNPs and 378 nm for ZnO-NPs were observed on the UV-Vis. DLS prediction of AgNPs size at 202.2 nm and ZnO-NPs size at 269.9 nm. The cytotoxic activities of the synthesized NPs and DES extract of *H. tubulosa* were evaluated against SH-SY5Y neuroblastoma and BJ normal skin fibroblast cell lines using MTT assay. Cytotoxic effects were observed for all samples in SH-SY5Y cells. However, the IC_{50} value could not be calculated for BJ cells because it was outside the range of the highest concentration tested. Moreover, the antibacterial activities of NPs and DES extract of *H. tubulosa* were investigated against *Escherichia coli* and *Staphylococcus aureus*. The AgNPs exhibited significant inhibitory effects against both tested bacterial strains, demonstrating their antibacterial activity.

Keywords: Deep eutectic solvents, sea cucumber, nanoparticles, antibacterial, cytotoxicity

Deniz Hıyarı-*Holothuria tubulosa*'nın Derin Ötektik Çözücü Ekstraksiyonu Kullanılarak Sentezlenen Gümüş ve Çinko Oksit Nanopartiküllerinin Antibakteriyel ve Sitotoksik Aktivitesi

Öz

Bu çalışmada, deniz hıyarı-*Holothuria tubulosa*'nın derin ötektik çözücü (DES) ekstraksiyonunu içeren yeni bir yaklaşım kullanılarak nanopartiküller (NP'ler) sentezlenmiştir. DES olarak kolin klorür-üre (1:2) kullanılmış ve bu da tehlikeli kimyasallar olmadan yeşil sentezi kolaylaştırmıştır. Ekstraktın toplam fenolik ve karbonhidrat içeriğini belirlemek için spektrofotometrik yöntemler kullanılmıştır. UV-Vis, DLS ve FTIR NP'leri karakterize etmiştir. UV-Vis'te AgNP için 400 nm'de ve ZnO-NP için 378 nm'de absorpsiyon piki gözlenmiştir. DLS, AgNP boyutunu 202.2 nm ve ZnO-NP boyutunu 269.9 nm olarak tespit etmiştir. Sentezlenen NP'lerin ve *H. tubulosa* DES ekstraktının sitotoksik aktiviteleri SH-SY5Y nöroblastoma hücre hattı ve BJ normal deri fibroblast hücre hattı üzerinde MTT testi kullanılarak değerlendirilmiştir. SH-SY5Y hücrelerinde tüm örnekler için sitotoksik etkiler gözlenmiştir. Ancak, BJ hücrelerinde IC_{50} değeri test edilen en yüksek konsantrasyon aralığının dışında kaldığı için hesaplanamamıştır. Ayrıca, NP'lerin ve *H. tubulosa* DES ekstraktının antibakteriyel aktiviteleri *Escherichia coli* ve *Staphylococcus aureus*'a karşı araştırılmıştır. AgNP'ler test edilen her iki bakteri türüne karşı önemli inhibitör etkiler göstererek antibakteriyel aktivitelerini ortaya koymuştur.

Anahtar Kelimeler: derin ötektik çözücüler, deniz hıyarı, nanopartiküller, antibakteriyel, sitotoksisite

Corresponding Author: murat.elibol@ege.edu.tr

Cite this Article: Erzincan University Journal of Science and Technology 2025, 18(3) 745-762. https://doi.org/10.18185/erzifbed.1522211

1. Introduction

Sea cucumbers, also known as Holothurians, are slow-moving marine animals and the most species-rich group of echinoderms. Holothurians are environment-engineers since they help recycle nutrients and stimulate microalgal growth to develop primary productivity. There are more than 1400 species of sea cucumber all around the world, and more than 40 are edible. *Holothuria tubulosa* is a sea cucumber species that is among the most harvested and economically valuable echinoderms found in the Turkish Seas. It is an edible species with a high content of bioactive compounds [1].

Holothurians are of enormous importance because of their high nutritional value in East Asian countries. Although sea cucumbers' nutritional value and chemical composition often vary depending on the growing environment, most species contain a high protein, low-fat content, and no cholesterol [2]. They have attracted significant attention, especially in the pharmaceutical field, due to their high content of secondary metabolites, including triterpene glycosides (saponins), sulfated polysaccharides, sterols, peptides, phenolics, and lectins. Several studies have demonstrated the biological potential of sea cucumbers to exhibit cytotoxic, antiviral, anti-inflammatory, antimicrobial, and antioxidant activities [3].

The most common methodologies for the preparation of active ingredients are extraction, using a mixture of ethanol, methanol, and chloroform as the solvent. However, the usage of these conventional organic solvents has been identified as a significant threat to human health and the ecological environment. Deep eutectic solvents (DESs) represent a novel development in the field of green chemistry, with considerable attention being directed towards their use in a wide range of applications. To date, researchers have investigated the development of innovative DESs with the objective of improving the extraction and separation process [4].

DESs are sustainable solvents derived from mixtures of naturally occurring molecules. Primary metabolites, including organic acids, sugars, amino acids, and choline derivatives, can be utilized in the DES compounds. In this instance, DES is designated as a natural deep eutectic solvent (NADES). The DES combinations utilized in this study belong to the NADES class. DES or NADES is a eutectic mixture that is formed by mixing a hydrogen bonding acceptor (HBA) with a hydrogen bonding donor (HBD). This eutectic mixture has a much lower melting point than the original HBA and HBD. Despite having equivalent properties to ionic liquids, DESs are much cheaper, safer, and biodegradable. Choline chloride (ChCl) is one of the most well-known HBAs for the synthesis of DES [5]. Nevertheless, it is water-soluble and only allows for hydrophilic extraction. In recent years, research on sea cucumbers has been divided into two main categories: the cultivation of sea cucumbers and the exploration of their biological active ingredients. Like many other marine organisms, conventional techniques and organic solvents have been used for the extraction of sea cucumbers. This study is important because it is the first time the extraction of *H. tubulosa* by DES systems has been achieved, and the synthesis of nanoparticles. In addition, a one-step sample preparation method is presented for the preparation of extracts and optimization using DES combinations. The extraction efficiency of the optimal DES-based ultrasound-assisted method is compared with traditional methods to ascertain its efficacy. Also, in the study of *H. tubulosa*, nanoparticle synthesis plays

a pivotal role in exploring the potential biomedical applications of this species. The synthesized nanoparticles are characterized using techniques such as Ultraviolet–Visible spectroscopy (UV–Vis), dynamic light scattering (DLS), and Fourier transform infrared spectroscopy (FTIR). These methods help determine the size, shape, and functional groups of the nanoparticles. The research indicates that silver nanoparticles (AgNPs) and zinc oxide nanoparticles (ZnO-NPs) synthesized using deep eutectic solvent (DES) extraction from *H. tubulosa* have shown significant antibacterial properties and potential cytotoxicity against the cancer cells.

2. Materials and Methods

2.1. Chemicals

Sodium carbonate (Na_2CO_3), phenol and sulphuric acid (>37 %) were obtained from Merck (Darmstadt, Germany). Choline chloride (ChCl) (>98 %), urea (>99 %), Folin-Ciocalteu reagent, gallic acid and glucose were purchased from Sigma (St. Louis, MO, USA). $AgNO_3$ was obtained from Carlo Erba Reagents and $ZnSO_4.7H_2O$ was obtained from AFG Bioscience.

In cytotoxicity assay, DMEM medium (Gibco), FBS (Gibco), 1% penicillin/streptomycin (Gibco), 1% L-glutamine (Gibco), and 1% non-essential amino acid (Gibco), trypsin-EDTA (Gibco), MTT reagent (Sigma), PBS (Gibco), and DMSO (Merck) were used.

In the antibacterial activity test, Mueller Hinton Broth and Agar growth medium (Merck), and antimicrobial susceptibility disk (Oxoid) were used.

2.2. Sample collection and preparation

H. tubulosa is a common species of sea cucumber, particularly prevalent along the Mediterranean and Aegean Sea coasts. The specimens were collected using the bottom trawl fishing technique in Ildir Gulf, situated on the Cesme coast of Izmir, Turkey. The coordinates were 38°39'61.10″ N, 26°46'96.17″ E. Following the morphological identification of the species, the length and weight measurements of the individuals were taken according to the literature. The exact length and weight measurements are also provided in Figure 1. After freezing at -20°C, the Holothurian samples were dried in the sun for three days. Twenty-one grams of dried *H. tubulosa* body walls were cut into small pieces and stored in the dark at a temperature of +4°C until processing.

Figure 1. Preparation of sea cucumber samples

2.3. Deep eutectic solvent synthesis

The DESs were prepared by heating a two-component mixture to 80°C with constant stirring until a homogeneous liquid formed. In this study, the prepared DESs included choline chloride and urea in a 1:2 molar ratio. DES was diluted with water to 52.5% to control viscosity before extraction with sea cucumber.

2.4. Ultrasonication-assisted extraction

An ultrasonic bath system was employed for the ultrasonication-assisted extraction (Jeiotech UC-10), which was equipped with a digital control system for temperature, time, and power (ultrasonic power effective is 380W). Extraction conditions were 40°C, 35 mL/g in 100 minutes. All extractions were conducted at a constant frequency of 37 kHz. Subsequently, the extracts were centrifuged at 5000 × g for 10 minutes, and the supernatants were filtered and subjected to further analysis. The ultrasonic extraction scheme is shown in Figure 2.

Figure 2. Ultrasonic extraction of sea cucumber samples with DES

2.5. Analysis of biometabolites in extracts

Spectrophotometric methods were used to determine the total phenolic and carbohydrate content of the extract.

2.5.1. Total carbohydrates

Total carbohydrates in the extracts were measured by the Dubois method. Glucose was prepared as a standard solution to determine the sugar content of the samples. The first step was to take 0.5 mL of the extract and transfer it to the glass tube. 0.5 mL of each DES was prepared in glass tubes for the blank. 0.5 mL of 5% phenol solution was added to the prepared tubes. Then 2.5 mL of concentrated sulphuric acid was added to the glass tubes, stoppered and vortexed. After 15 minutes in a water bath, the absorbance against the blank was recorded in the spectrophotometer at a wavelength of 490 nm [6].

2.5.2. Total phenolics

The total phenolic content of the extracts was measured using the Folin-Ciocalteu method. The standard used was gallic acid. In a 100 mL erlenmeyer flask, 1 mL of the extracts was first added. Then 22 mL of distilled water and 500 µL of Folin-Ciocalteu reagent were added successively to the extracts. After 3 minutes, 1.5 mL of 3% Na_2CO_3 solution was added. The samples were incubated for a period of 2 hours at room temperature. Absorbance values were read against distilled water at 720 nm using the Optizen Pop UV/Vis spectrophotometer. DES were used instead of the control sample. The absorbance values of the total phenolic content of the sample against the standard curve were used in the equation and the results were expressed in gallic acid equivalents [7, 8].

2.6. Green synthesis of silver and zinc oxide nanoparticles

According to the results of preliminary experiments, 10 mL of extract was added dropwise to 90 ml (1:9) of 2.818 mM $AgNO_3$ solution for the AgNP synthesis. 30 mL of extract was added to 90 ml (1:3) of 4.113 mM $ZnSO_4.7H_2O$ solution for the ZnO-NP synthesis. The solutions were incubated for 2 hours in the dark. Visible color changes confirmed that the solution contained NPs. Due to the secondary metabolites in the sea cucumber, no external chemicals were required to stabilize the NPs produced by this process.

2.7. Characterization of nanoparticles

Ultraviolet–Visible spectroscopy (UV–Vis), dynamic light scattering (DLS) and Fourier transform infrared spectroscopy (FTIR) characterized AgNPs and ZnO-NPs. UV-Vis spectroscopy was used to confirm the formation of NPs. NP optical absorbance was recorded using a UV-Vis spectrophotometer (EasyPlus, Mettler Toledo) at 200-800 nm. The maximum peak absorbance values of NPs were recorded. DLS (Malvern Zetasizer Analyzer) was used to measure the average size of the NPs. The size distribution of the particles in the colloidal suspension was also characterized. The structural characteristics of the NPs were investigated using FTIR spectroscopy (Thermo Scientific, Nicolet, IS20, USA) in the wave number range of 500 cm^{-1} to 4000 cm^{-1}. Surface chemistry and functional group bonding are characterized using this method.

2.8. Biological activities of nanoparticles

2.8.1. Antibacterial analysis

For antibacterial analysis of the extract and nanoparticles, the Kirby-Bauer disk diffusion method was applied. *Staphylococcus aureus* and *Escherichia coli* bacteria were cultured. The turbidity of the bacteria was diluted to correspond to Mc Farland No.1, and then inoculated onto the Mueller Hinton Agar by spreading plate method as 1×10^6 CFU/mL. After inoculation, the samples were impregnated with sterile disks in a volume of 25 µL. The petri dishes were then incubated at 37°C for 24 hours. Then, the zone diameters around the disks were measured according to triple trials [9].

2.8.2. *In vitro* cytotoxicity analysis

The cytotoxic activities of the extract and nanoparticles were evaluated by MTT (3-(4,5-Dimethylthiazol-2-yl)-2,5-Diphenyltetrazolium Bromide) assay. SH-SY5Y human neuroblastoma cell line and healthy BJ normal skin fibroblast cell line were used herein. The cells were cultured in DMEM medium supplemented with 10% FBS (fetal bovine serum), 1% penicillin/streptomycin, 1% L-glutamine, and 1% non-essential amino acid. Cells seeded in T75 flasks were incubated in a 37ºC incubator containing 5% CO_2. ~80 confluent cells were detached from the flask surface using trypsin-EDTA, counted using trypan blue and seeded in 96-well microplates at a concentration of 10^5 cells/ml. After 24 hours of incubation, the medium in 96-well microplates was removed and the cells were treated with different concentrations of extract, silver nanoparticles and zinc oxide nanoparticles. Then, the cells were incubated for 24

hours. At the end of the incubation period, 10 µL of 5 mg/mL MTT/PBS reagent was added to each well and incubated again for 3.5 hours. Afterwards, the culture medium was removed, and formazan crystals were dissolved using 100 µL of DMSO. Absorbance was measured at 570 nm wavelength using a microplate reader. Data were evaluated via the GraphPad Prism program [10].

3. Results and Discussion

3.1. Extraction of biometabolites

The synthesis of nanoparticles is possible with compounds such as phenols, amines, amides, carbohydrates and alkaloids, etc. The reduction of silver ions may be due to phenolic compounds and carbohydrates that may be present in sea cucumbers. For this reason, the total sugars and the total phenolics of the extract were determined by means of spectrophotometric methods. The total sugars and total phenolics were measured as 260 µg/mL and 664 mg GAE/mL, respectively (Table 1). To date, no specific research has been conducted on the metanol extraction of total glucose and the phenolic compounds in *H. tubulosa*. However in Wang, J. and their friends research, sea cucumber (Stichopus japonicus Selenka) gonads chloroform:methanol extraction total sugar was founded 69.1 g/100 g [11].

Table 1. Biometabolites in DES extract

Solvent	Glucose Concentration (µg/ml)	Phenol Concentration (mg/ml)
DES	260,00	664
Methanol	199,32	140

3.2. Characterization of silver nanoparticles

The synthesis of silver nanoparticles (AgNPs) using sea cucumber extract is indicated by a change in solution color from orange to dark brownish black upon the addition of $AgNO_3$ solution, which signifies the formation of the nanoparticles. The analysis conducted using a UV-Vis spectrophotometer corroborates this hypothesis, exhibiting a peak absorption at 400 nm, which is characteristic of AgNPs as shown in Figure 3. This absorption peak can be attributed to the excitation of electrons on the metal surface, which is influenced by the nanoparticles' shape and size.

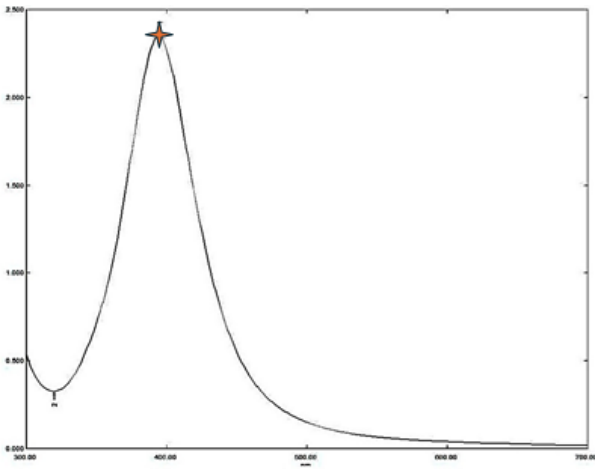

Figure 3. UV-Vis spectrophotometer of AgNPs

The study which is conducted by Srikar et al. (2016) also supports the assertion that AgNPs typically form within the 400-450 nm wavelength range [12].

The objective of the FTIR analysis in this study is to ascertain the interaction between the functional groups extracted and AgNPs. The results of the FTIR analysis of sea cucumber extract nanoparticles (AgNPs) are presented in Figure 4. As can be observed in Figure 4, the spectrum of the sea cucumber extract-AgNPs displays distinct absorption signals at wave numbers 3387 cm^{-1}, 2997 cm^{-1}, and 1649 cm^{-1} [13]. This indicates the interaction of –OH groups, -CH stretching, and C=C aromatic stretching at polyphenolic compounds stemming from the extract. Those functional group's peaks suggest that there has been an interaction between the bioactive compounds in the extract and the silver solution, resulting in the formation of AgNPs.

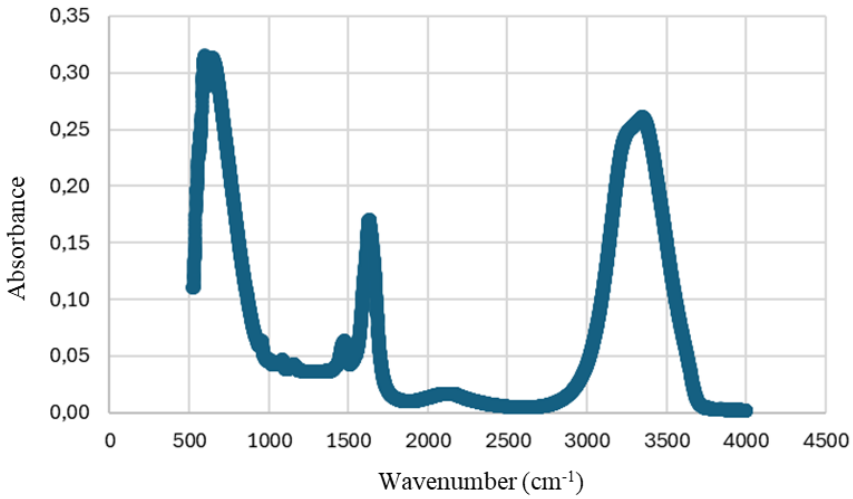

Figure 4. FTIR spectrum of AgNPs

Size distribution and polydispersity index of the nanoparticles (NPs) were analyzed by using the Zetasizer and results are shown in Figure 5. This represents the average size of AgNPs is 202.2 nm, while the polydispersity index (PDI) is 0.246. The PDI which describes the

distribution of particle size was found less than 0.5 for all nanoparticles. When the number of polydispersity index is smaller, the size of the particles is more uniform. Therefore, the polydispersity index affects the particles' characteristics, and it is expected to be less than 0.5 [14]. Previous studies have shown that nanoparticles with sizes less than 300 nm have a good ability to transport the body [15].

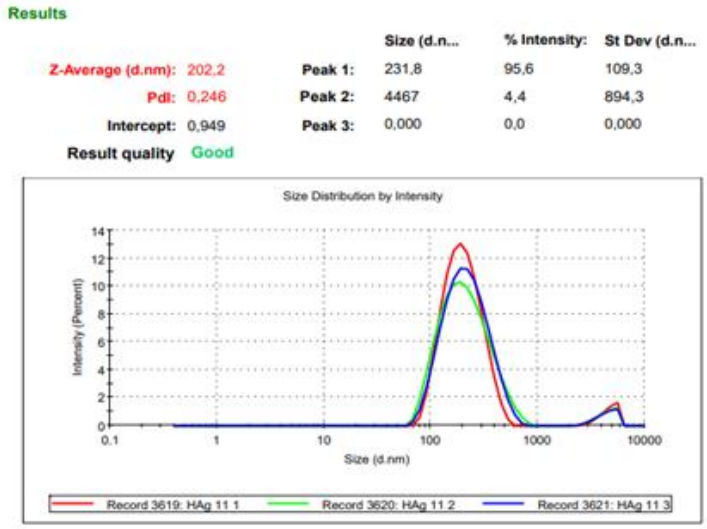

Figure 5. DLS results of AgNPs

3.3. Characterization of zinc nanoparticles

UV-Vis spectroscopy analysis was conducted on a colloidal solution containing ZnO-NPs, with measurements taken within the wavelength range of 200–800 nm. This was done to confirm the reduction of Zn^{2+} to ZnO-NPs. The UV-Vis spectra of the ZnO-NPs sample exhibited a prominent peak at 350-380 nm, which is a characteristic feature of zinc oxide nanoparticles [16,17]. As seen in Figure 6, the specific UV spectrum peak of ZnO-NPs was obtained at 378 nm in our study.

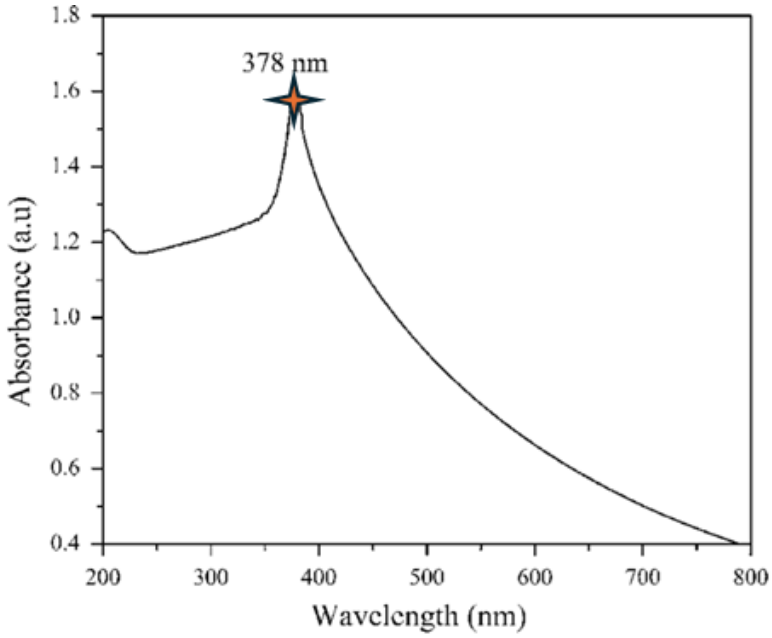

Figure 6. UV-Vis spectrophotometer of ZnO-NPs

As shown in Figure 7, the distinctive absorption band at 590 cm^{-1} (ZnO bond) substantiates the formation of ZnO. The sharp absorption peak at 1610 cm^{-1} is attributed to the amide's carbonyl (C=O) stretching vibration. The band at 1450 cm^{-1} may be attributed to the stretching of C–C groups, while the broad peak at 3450 cm^{-1} corresponds to the vibration of the O–H stretching group in alcohols and phenols. The formation of ZnO was confirmed by the characteristic absorption band at 580 cm^{-1} (ZnO bond) [18,19]. FTIR analysis confirmed the role of sea cucumber DES extract as a reducing and capping agent and the presence of some functional groups.

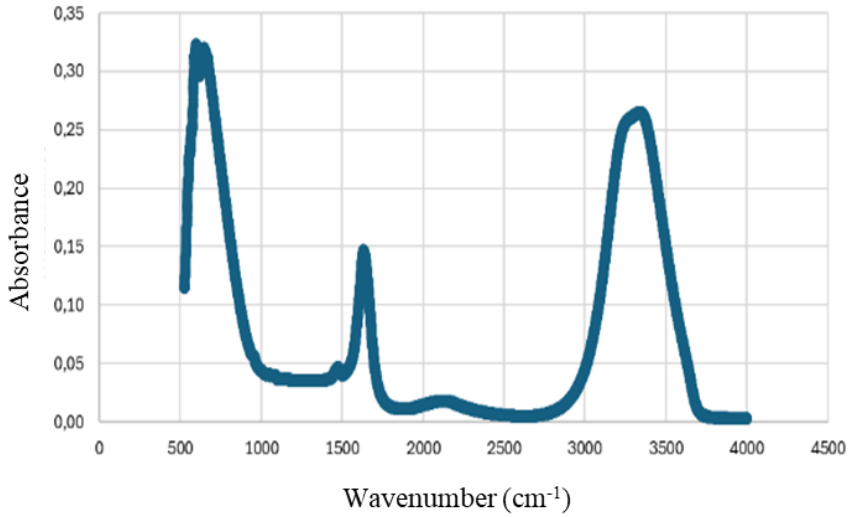

Figure 7. FTIR spectrum of ZnO-NPs

Dynamic Light Scattering (DLS) is an emerging and extensively utilized technique for the calculation of the hydrodynamic diameter of nanoparticle suspensions based on the Brownian

motion of the particles. Jamdagni et al. found that the DLS value was 74.36 nm of ZnO-NP from the flower extract of *Nyctanthes arbor-tristis,* while the PDI value was 0.488. The value in our study was found to be higher compared to the literature; DLS: 269.9 nm, PDI: 0.711 (Figure 8). The polydisperse nature of nanoparticles may explain the variation in nanoparticle size. The degree of "non-uniformity" of a distribution is called polydispersity, so this is an indication of the agglomeration of nanoparticles [20]. These results should be confirmed with the size range of nanoparticles obtained upon synthesis at optimum conditions by using Transmission electron Microscopy (TEM) or Scanning Electron Microscope (SEM) analysis in future research.

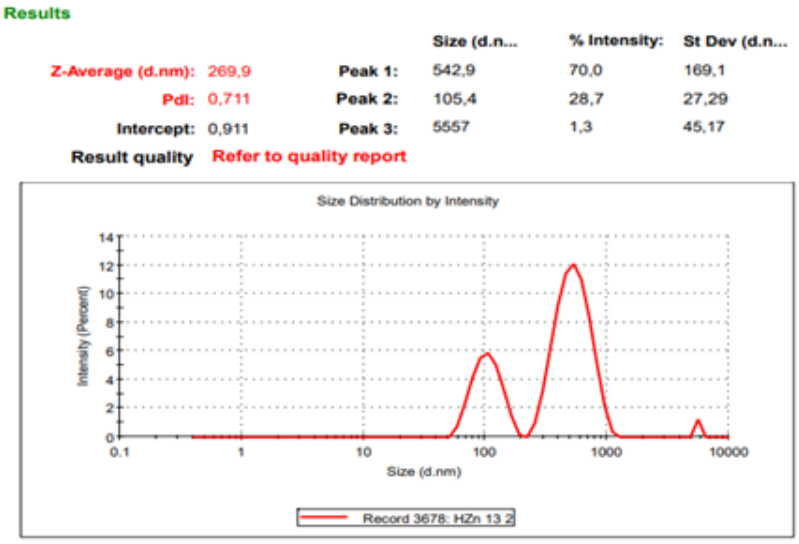

Figure 8. DLS results of ZnO-NPs

3.4. Biological activities of nanoparticles

3.4.1. Antibacterial activity test

Based on an antimicrobial effect analysis, the antibacterial activity of DES extract and synthesized nanoparticles against Gram-positive *S. aureus* and Gram-negative *E. coli* has been investigated according to triple trials. Zones formed around the disks are observed in Figure 9.

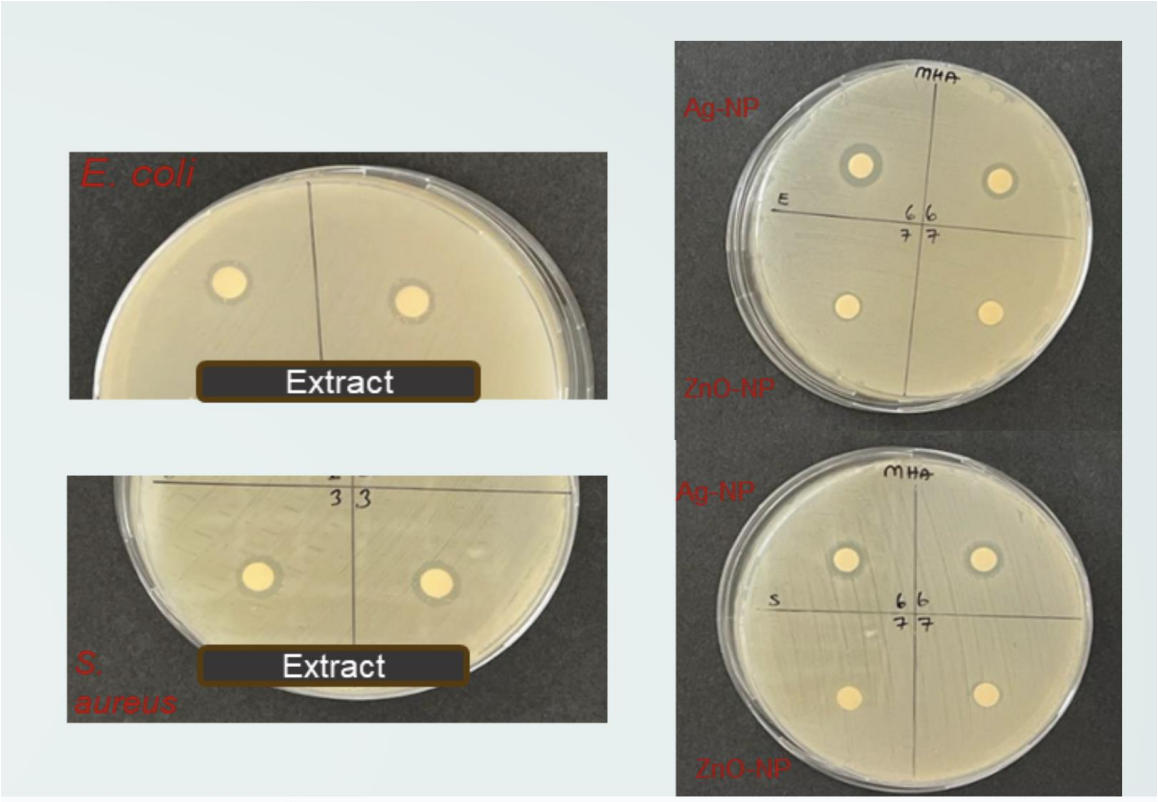

Figure 9. Results of disk diffusion test based on the extract, AgNPs and ZnO-NPs

According to the Kirby-Bauer test, the average inhibition diameters for *E. coli* can be ranked from small to large as ZnO-NPs (7±0.00 mm), extract (8.5±0.50 mm) and AgNPs (11±1.00 mm). On the other hand, the average diameters for *S. aureus* bacterium were measured as ZnO-NPs (7±0.00 mm), extract (10.33±0.57 mm) and AgNPs (11±0.00 mm) from small to large (Table 2). As with silver metal, the antibacterial effect of AgNPs was also detected here. In addition, it is very pleasing that the sea cucumber-DES extract itself also has an antibacterial effect. Similarly, Rosman et al., synthesized AgNPs using the aqueous extract of *Marphysa moribidii* (marine polychaete) and determined significant antibacterial activities against different bacteria [21]. Additionally, Willian et al. studied silver nanoparticles from marine plant as mangrove *Rhizophora stylosa* through green synthesis and found good activity against *E. coli* and *S. aureus* with 4.1-7.2 mm inhibition zones [22]. In contrast to the studies reported to have the remarkable antibacterial effect of zinc nanoparticles, the activity of ZnO-NPs in this concentration was found to be lower in this study. AgNPs are more potent than ZnO-NPs in terms of antibacterial activity, due to their higher rate of ion release capacity and interaction with the bacterial membrane [19]. Among the various physical and chemical factors, nanoparticle size was identified as the parameter that most influences the antimicrobial activity of ZnO-NPs. Generally, smaller particles are more toxic to microorganisms [22]. Therefore, it is important to synthesize AgNPs with the help of sea cucumbers and DES to enhance the antibacterial effect.

Table 2. The inhibition zone diameters of extract, AgNPs and ZnO-NPs

Inhibition zones (mm)	*E.coli -1*	*E.coli-2*	*E.coli-3*	*E. coli average*	*S.aureus-1*	*S.aureus-2*	*S.aureus-3*	*S. aureus average*
Extract	9	8	8.5	8.5±0.50	10	10	11	10.33±0.57
AgNPs	11	12	10	11±1.00	11	11	11	11±0.00
ZnO-NPs	7	7	7	7±0.00	7	7	7	7±0.00

3.4.2. *In vitro* cytotoxicity analysis

To date, different traditional solvents, including chloroform [23], water or methanol [24] were used for extraction from *H. tubulosa*. Herein the effect of DES, a more environmentally friendly solvent, was evaluated. Also, because of their potential for a wide range of biological and medicinal uses, biogenic nanoparticle synthesis made from plants, marine algae, vegetative organs, cells, and extracts has been the subject of numerous research recently [25].

Due to serious complications in the body, cancer remains one of the leading causes of mortality globally. Conventional treatments for cancer, such as chemotherapy, laser therapy, and surgery, which target tumor cells, can also destroy normal healthy cells in addition to having several negative side effects. These days, safe, inexpensive, and environmentally friendly biological sources provide an extensive range of reliable and potent anticancer drugs [25].

In this study, the cytotoxic effects of both DES extract of sea cucumber *H. tubulosa,* and nanoparticles (AgNPs, and ZnO-NPs) produced using DES extract on neuroblastoma cells and BJ normal skin fibroblast cells were tested. For the SH-SY5Y neuroblastoma cell line, the IC_{50} values of DES extract, AgNPs, and ZnO-NPs are 433.8±25.1 µg/mL, 361.8±3.2 µg/mL, and 405.8±5.7 µg/mL, respectively (Figure 10 and 11). According to these results, the cytotoxic effect of AgNPs on SH-SY5Y cells appears to be greater. This is followed by ZnO-NPs and DES extract. On the other hand, IC_{50} values could not be calculated for BJ healthy skin fibroblast cells. Because it was outside the range of the highest concentration tested. In future studies, higher concentrations should be tested in this cell line. Its cytotoxic effects on healthy cells are less than cancer cells. So, when we compare the two different cell lines, both extract and nanoparticles have more cytotoxic activity on the cancer cell line.

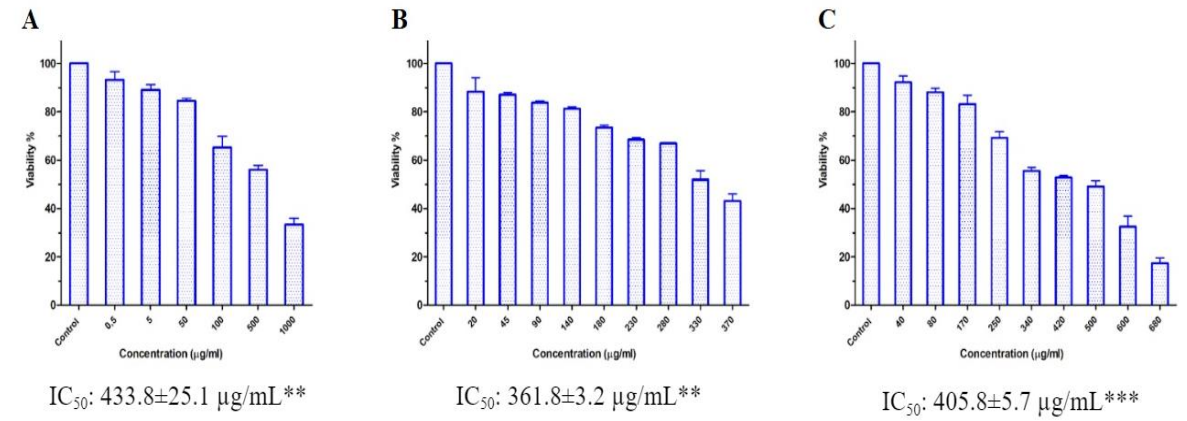

Figure 10. Cell viability values obtained as a result of MTT test in SH-SY5Y neuroblastoma cell line. **A**. DES extract of *H. tubulosa*, **B**. AgNPs, **C.** ZnO-NPs. (**p<0.01, ***p<0.001).

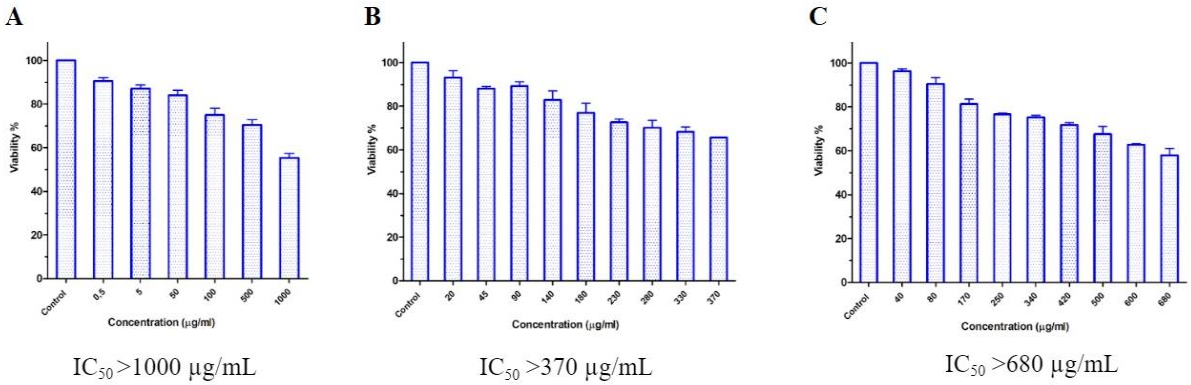

Figure 11. Cell viability values obtained as a result of MTT test in BJ skin fibroblast cell line. **A**. DES extract of *H. tubulosa*, **B**. AgNPs, **C.** ZnO-NPs.

In the study by Alper and Güneş (2020), MTT assays of water and methanol extracts of *H. tubulosa* on cancerous A549 (Human lung adenocarcinoma), HeLa (human cervix adenocarcinoma), PC-3 (human prostate adenocarcinoma), and MCF-7 (human breast adenocarcinoma), and healthy HEK-293 (human embryonic kidney) cell lines. The study determined that the lowest IC_{50} value of the water extract was in A549 cells (IC_{50}=112.8 µg/ml) for a 48-hour incubation period and in HeLa cells (IC_{50}=21.01 µg/ml) for a 72-hour incubation period. The IC_{50} value of the methanol extract was calculated as 83.73 µg/ml for HeLa cells at 48 hours and 63.12 µg/ml for A549 cells at 72 hours [24]. In another study, the cytotoxic activity of chloroform extracts of *H. tubulosa* was studied. Accordingly, IC_{50} values were found to be 709.7, 253.7, 151.6 and 132.2 at 24 hours in A549, HeLa, MCF-7 and PC-3 cell lines, respectively. This value was not determined in the HEK-293 cell line [23]. Production of NPs using extracts from natural substances is emerging as an important area in nanotechnology. The use of natural resources to produce NPs is sustainable, eco-friendly, inexpensive and free of chemical contaminants for biological and medical applications where the purity of NPs is of major concern. Furthermore, NPs synthesized via the green route are more stable and effective in comparison with those produced by physicochemical methods. The results obtained here can

be supported by further experiments. *In vivo* cytotoxic studies of *H. tubulosa* nanoparticles could be applied. Pure compounds can be isolated from *H. tubulosa* using DES instead of toxic solvents.

4. Conclusion

The innovative green synthesis approach using Deep Eutectic Solvent (DES) extraction from *Holothuria tubulosa* has demonstrated significant potential in the biomedical field. Our study successfully synthesized silver nanoparticles (AgNPs) and zinc oxide nanoparticles (ZnO-NPs). The AgNPs exhibited notable antibacterial activity against *Escherichia coli* and *Staphylococcus aureus*, while both AgNPs and ZnO-NPs showed promising cytotoxic effects against the SH-SY5Y neuroblastoma cell line. These findings underscore the potential of sea cucumber-derived nanoparticles as effective agents for cancer therapy and antimicrobial applications, paving the way for further research and development in this exciting domain.

Ethics in Publishing

There are no ethical issues regarding the publication of this study. Ethical approval was not required for the study involving animals in accordance with local legislation and institutional requirements because the species used in the work (*Holothuria tubulosa*) is not included in any taxa listed in Directive 2010/63/EU that regulates the use of live animals for experimental purposes. Therefore, the experiments and animal sampling do not require authorizations.

Author Contributions

Conceptualization and design: Hilal Top Haytaoglu, Aysegul Inam, Tulay Oncu Oner, Murat Elibol; methodology and formal analysis: Hilal Top Haytaoglu, Aysegul Inam, Tulay Oncu Oner, Murat Elibol; validation: Hilal Top Haytaoglu, Aysegul Inam, Tulay Oncu Oner, Murat Elibol; investigation: Hilal Top Haytaoglu, Aysegul Inam, Tulay Oncu Oner, Murat Elibol; Writing – original draft: Hilal Top Haytaoglu, Aysegul Inam, Tulay Oncu Oner, Murat Elibol. The submitted manuscript was accepted and reviewed by all the authors.

Acknowledgment

Hilal Top Haytaoglu would like to thank, Ege University/Faculty of Fisheries for the supply sea cucumber and Res. Assist. Dr. Deniz Günay. Also, H. Top Haytaoglu would also like to thank Council of Higher Education (YÖK) for the 100/2000 doctorate scholarship. Also, this study presented oral in “International Sustainability in Life Congress (SUIC)” on May 20th, 2024, as titled “Antibacterial and cytotoxic activity of silver and zinc oxide nanoparticles synthesized using deep eutectic solvent extraction of the sea cucumber-*Holothuria tubulosa*”.

References

[1] Fagbohun, O. F., Joseph, J. S., Oriyomi, O. V., & Rupasinghe, H. V. (2023). Saponins of North Atlantic Sea Cucumber: Chemistry, health benefits, and future prospectives. Marine Drugs, 21(5), 262.

[2] Maskur, M., Sayuti, M., Widyasari, F., & Setiarto, R. H. B. (2024). Bioactive Compound and Functional Properties of Sea Cucumbers as Nutraceutical Products. Reviews in Agricultural Science, 12, 45-64.

[3] Sanjeewa, K. K., & Herath, K. H. I. N. M. (2023). Bioactive secondary metabolites in sea cucumbers and their potential to use in the functional food industry. Fisheries and Aquatic Sciences, 26(2), 69-86.

[4] Liu, J., Li, X., & Row, K. H. (2022). Development of deep eutectic solvents for sustainable chemistry. Journal of Molecular Liquids, 362, 119654.

[5] Liu, Y., Friesen, J. B., McAlpine, J. B., Lankin, D. C., Chen, S. N., & Pauli, G. F. (2018). Natural deep eutectic solvents: properties, applications, and perspectives. Journal of natural products, 81(3), 679-690.

[6] Dubois, M., Gilles, K. A., Hamilton, J. K., Rebers, P. T., & Smith, F. (1956). Colorimetric method for determination of sugars and related substances. Analytical chemistry, 28(3), 350-356.

[7] Singleton, V. L., Orthofer, R., & Lamuela-Raventós, R. M. (1999). Analysis of total phenols and other oxidation substrates and antioxidants by means of folin-ciocalteu reagent. In Methods in enzymology, 299, 152.

[8] Tüzün, S., Baş, İ., Karakavuk, E., Sanyürek, N. K., & Benzer, F. (2020). Çeşitli pekmez türlerinde farklı yöntemlerle tespit edilen antioksidan aktivitelerin karşılaştırılması. Türk Tarım ve Doğa Bilimleri Dergisi, 7(2), 323-330.

[9] Matuschek, E., Copsey-Mawer, S., Petersson, S., Åhman, J., Morris, T. E., & Kahlmeter, G. (2023). The European committee on antimicrobial susceptibility testing disc diffusion susceptibility testing method for frequently isolated anaerobic bacteria. Clinical Microbiology and Infection, 29(6), 795-e1.

[10] Khanavi, M., Gheidarloo, R., Sadati, N., Ardekani, M. R. S., Nabavi, S. M. B., Tavajohi, S., Ostad, S. N. (2012). Cytotoxicity of fucosterol containing fraction of marine algae against breast and colon carcinoma cell line. Pharmacognosy Magazine, 8(29), 60.

[11] Wang, J., Shi, S., Li, F., Du, X., Kong, B., Wang, H., & Xia, X. (2022). Physicochemical properties and antioxidant activity of polysaccharides obtained from sea cucumber gonads via ultrasound-assisted enzymatic techniques,160, 113307.

[12] Srikar, S. K., Giri, D. D., Pal, D. B., Mishra, P. K., & Upadhyay, S. N. (2016). Green synthesis of silver nanoparticles: a review. Green and Sustainable Chemistry, 6(01), 34.

[13] Thanigaivel, S., Vickram, S., Saranya, V., Ali, H., Alarifi, S., Modigunta, J. K. R., Rohini, K. (2022). Seaweed polysaccharide mediated synthesis of silver nanoparticles and its enhanced disease resistance in Oreochromis mossambicus. Journal of King Saud University-Science, 34(2), 101771.

[14] Nurkhasanah, N., Yuwono, T., Nurani, L. H., Rizki, M. I., & Kraisintu, K. (2015). The development of chitosan nanoparticles from Hibiscus sabdariffa L calyx extract from Indonesia and Thailand, 6(5), 1855-1861.

[15] Sivasankar, M., & Kumar, B. P. (2010). Role of nanoparticles in drug delivery system. International Journal of Research in Pharmaceutical and Biomedical Sciences, 1(2), 41-66.

[16] Mohammadian, M., Es'haghi, Z., & Hooshmand, S. (2018). Green and chemical synthesis of zinc oxide nanoparticles and size evaluation by UV–vis spectroscopy. J Nanomed Res, 7(1), 00175.

[17] Fakhari, S., Jamzad, M., & Kabiri Fard, H. (2019). Green synthesis of zinc oxide nanoparticles: a comparison. Green chemistry letters and reviews, 12(1), 19-24.

[18] Hasaballah, A. I., El-Naggar, H. A., Abd-El Rahman, I. E., Al-Otibi, F., Alahmadi, R. M., Abdelzaher, O. F., ... & Elbahnasawy, M. A. (2023). Surf Redfish-Based ZnO-NPs and Their Biological Activity with Reference to Their Non-Target Toxicity. Marine Drugs, 21(8), 437.

[19] Elbahnasawy, M. A., El-Naggar, H. A., Abd-El Rahman, I. E., Kalaba, M. H., Moghannem, S. A., Al-Otibi, F., ... & Hasaballah, A. I. (2023). Biosynthesized ZnO-NPs Using Sea Cucumber (Holothuria impatiens): Antimicrobial Potential, Insecticidal Activity and In Vivo Toxicity in Nile Tilapia Fish, Oreochromis niloticus. Separations, 10(3), 173.

[20] Jamdagni, P., Khatri, P., & Rana, J. S. (2018). Green synthesis of zinc oxide nanoparticles using flower extract of Nyctanthes arbor-tristis and their antifungal activity. Journal of King Saud University-Science, 30(2), 168-175.

[21] Rosman, N. S. R., Harun, N. A., Idris, I., & Ismail, W. I. W. (2020). Eco-friendly silver nanoparticles (AgNPs) fabricated by green synthesis using the crude extract of marine polychaete, Marphysa moribidii: biosynthesis, characterisation, and antibacterial applications. Heliyon, 6(11).

[22] Willian, N., Syukri, S., Zulhadjri, Z., Pardi, H., & Arief, S. (2021). Marine plant mediated green synthesis of silver nanoparticles using mangrove Rhizophora stylosa: Effect of variable process and their antibacterial activity, F1000Research, 10.

[23] Doğangüneş, M., Türker, A., Güneş, H., & Alper, M. (2021). Cytotoxic and Antioxidant Potential of Chloroform Extract of Holothuria tubulosa Gmelin, 1791. *Russian Journal of*

Marine Biology, *47*(6), 498-507.

[24] Alper, M., & Güneş, M. (2020). Evaluation of cytotoxic, apoptotic effects and phenolic compounds of sea cucumber Holothuria tubulosa (Gmelin, 1791) extracts. *Turkish Journal of Veterinary & Animal Sciences*, *44*(3), 641-655.

[25] Karmous, I., Pandey, A., Haj, K. B., & Chaoui, A. (2020). Efficiency of the green synthesized nanoparticles as new tools in cancer therapy: insights on plant-based bioengineered nanoparticles, biophysical properties, and anticancer roles. Biological trace element research, 196, 330-342.

e-ISSN: 2149-4584

Erzincan University Journal of Science and Technology

EJSAT 2025, 18 (3) 763-780

Research Article

Calculation of Different Intensity Ratios of Samples with Atomic Numbers Between 9≤Z≤83 Using the Dilution Technique

Tuba Akkuş[1], Mehmet Fatih Temiz[2]

[1]Department of Physics, Faculty of Arts and Sciences, Erzincan Binali Yıldırım University, Erzincan, Türkiye, 24100.

[2]Department of Physics, Graduate School of Natural and Applied Sciences, Erzincan Binali Yıldırım University, Erzincan, Türkiye, 24100.

Received: 12/02/2025 **Revised:** 21/06/2025 **Accepted:** 30/06/2025, **Published:** 31/12/2025

Abstract

In this study, the variation of different intensity ratios with the mean atomic number was investigated in the Energy Dispersive X-ray Fluorescence system for qualitative analysis. Fourteen different samples were used in the study. The average atomic numbers of the samples obtained by diluting with cellulose are between 9.74 and 83.00. The samples were excited by photons with 59.54 kiloelectron volt energy from the Americium-241 source and an HpGe detector with 182 electron volt resolution at 5.9 kiloelectron volt was used. The obtained results show that different scattering intensity ratios can be used with high reliability for complex materials in qualitative analysis. In this study, different intensity ratios were plotted as a function of the average atomic number and best fit curves were created. From the obtained fit curves, it was seen that the intensity ratios $I_{L_\alpha}/I_{sc_{(L_\alpha)}}$, $I_{L_\beta}/I_{sc_{(L_\beta)}}$ $I_{K_{\alpha_2}}/I_{sc_{(K_{\alpha_2})}}$ and $I_{K_{\alpha_1}}/I_{sc_{(K_{\alpha_1})}}$ were the best spectral ratio methods that can be used to determine the effective atomic number.

Keywords: EDXRF, intensity ratio, mean atomic number, qualitative analysis.

Seyreltme Tekniği Kullanılarak Atom Numarası 9≤Z≤83 Arasında Olan Numunelerin Farklı Şiddet Oranlarının Hesaplanması

Öz

Bu çalışmada, kalitatif analiz için Enerji Dağılımlı X-ışını Floresan sisteminde farklı şiddet oranlarının ortalama atom numarasına göre değişimi araştırılmıştır. Araştırmada 14 farklı numune kullanıldı. Selüloz ile seyreltilerek elde edilen numunelerin ortalama atom numaraları 9,74 ile 83,00 arasındadır. Numuneler, Americium-241 kaynağından gelen 59,54 kiloelektron volt enerjili fotonlarla uyarıldı ve 5,9 kiloelektron voltta 182 elektron volt çözünürlüğe sahip bir HpGe dedektörü kullanıldı. Elde edilen sonuçlar, kalitatif analizde karmaşık malzemeler için farklı saçılma şiddet oranlarının yüksek güvenilirlikle kullanılabileceğini göstermektedir. Bu çalışmada farklı şiddet oranları, ortalama atom numarasının fonksiyonu olarak çizildi ve en uygun fit eğrileri oluşturuldu. Elde edilen fit eğrilerinden $I_{L_\alpha}/I_{sc_{(L_\alpha)}}$, $I_{L_\beta}/I_{sc_{(L_\beta)}}$ $I_{K_{\alpha_2}}/I_{sc_{(K_{\alpha_2})}}$ ve $I_{K_{\alpha_1}}/I_{sc_{(K_{\alpha_1})}}$ şiddet oranlarının etkin atom numarasının belirlenmesinde kullanılabilecek en iyi spektral oran yöntemleri olduğu görüldü.

Anahtar Kelimeler: EDXRF, şiddet oranı, ortalama atom numarası, kalitatif analiz.

Corresponding Author: takkus@erzincan.edu.tr

Cite this Article: Erzincan University Journal of Science and Technology 2025, 18(3) 763-780. https://doi.org/10.18185/erzifbed.1638042

1. Introduction

Each material has a specific color, texture and appearance. However, these features are insufficient to describe this material. To determine beyond doubt the exact composition of a material, physical and chemical properties generally need to be evaluated. Melting point, color, boiling point, density, electrical conductivity, thermal conductivity, refractive index, and coefficient of expansion are some of the more common physical properties measured to identify an unknown substance. Many of these properties are measurable values that can be compared to known values of elements and compounds. More detailed physical tests deal with measurements based on the internal structure of a material. Depending on the arrangement of particles within a substance, they interact with electromagnetic radiation in different ways. The result of these interactions is an electromagnetic spectrum, which is a pictorial representation of the absorption and emission of electromagnetic radiations of varying energy as they strike and pass through a substance.

Qualitative analysis is a method that examines which elements or compounds a substance consists of and covers a series of analytical chemistry techniques that measure properties that provide non-numerical information about the sample, such as color change, gas release, precipitate formation or dissolution, and whether it has radioactive properties. Quantitative analysis, on the other hand, gives numerical information about the presence rates of the components of a sample, in other words, their relative amounts. There are many areas where qualitative and quantitative analysis is used. In the research of anti-cancer drugs in medicine [1], in the investigation of skin flora from a bacterial perspective [2] ,in the investigation of factors affecting oil production [3], in the analysis of elements in cataracts [4] in determining benign and malignant tumors [5], in researching the contents of ores [6] in determining the structural properties of multi-component bioglasses [7], in investigating selenium species in mushrooms [8], in determining the active ingredients of drugs [9], in detecting fracture patterns of ceramics [10], in thrombin analysis in serum [11], in evaluating air quality [12], in determining the components of hydrocarbon mixtures [13], in the determination of monomers in polyester in food contact materials [14], in the type and quantity analysis of polyphenols in plants [15] ,in the analysis of spectral properties in multicomponent liquid mixtures [16], in measuring the microstructural properties of bones and in determining the degree of mineralization of bones [17], in investigating the dynamics of some diseases [18], in supporting the analytical results of the model applied in biomedical interventions [19], in the determination of clusters in water solutions of alcohols [20], in crystallographic analysis in electroceramics. in evaluating tissues [21], in determining calibration methods in analytical chemistry and in identification analyzes of uncontrolled analytical effects [22], in investigating the nutritional benefits and risks that may occur with the consumption of mussels [23], in sintering analyzes of metals in manufacturing applications [24],in the surface analysis of orthodontic brackets [25] in the analysis of colorants found in candies [26]. There are many studies in the literature about different intensity ratios. Some researchers have studied K x-ray intensity ratios. Kβ/Kα intensity ratios of some copper and zinc alloys were examined at 22.69 keV [27]. Kα/Kβ intensity ratios have been calculated experimentally for elements with atomic numbers in the range of $28 \leq Z \leq 39$. The results obtained were compared with theoretical values [28]. K x-ray intensity ratios of some heavy elements

experimentally calculated using a HPGe detector in the EDXRF system [29]. Kβ/Kα x-ray intensity ratios of Cr, Mn, Fe and Co elements were determined experimentally at 8.735 keV energy [30]. The changes in the Kβ/Kα intensity ratios of MoCu alloys at different concentrations in the external magnetic field were examined [31]. The valence electronic structure of Ni in Ni-B alloy coatings was determined using the Kβ/Kα x-ray intensity ratio [32]. The Kβ/Kα intensity ratios of 3d and 4d transition metals were examined in the external magnetic field [33].

Some researchers have also studied L x-ray intensity ratios. L x-ray intensity ratios of some heavy elements at 20.48 keV were calculated [34]. L x-ray intensity ratios of Hg, Pb and Bi compounds calculated at 59.54 keV [35]. L x-ray intensity ratios of elements with atomic number 74≤Z≤92 calculated at 31.635 keV energy [36]. L x-ray intensity ratios of Dy, Ho, Yb, W, Hg, Tl and Pb elements investigated at 59.54 keV [37]. Different L x-ray intensity ratios have been calculated for Dy, Ho and Er elements and some compounds of these elements [38].Investigated the change of L x-ray intensity ratios with temperature [39].

In this study, total scattering intensity ratios were calculated at four different energies and $(I_{coh} + I_{Comp})/(\mu/\rho)_{L_\alpha}$, $(I_{coh} + I_{Comp})/(\mu/\rho)_{L_\beta}$, $(I_{coh} + I_{Comp})/(\mu/\rho)_{K_{\alpha_2}}$, $(I_{coh} + I_{Comp})/(\mu/\rho)_{K_{\alpha_1}}$, $I_{L_\alpha}/I_{sc_{(L_\alpha)}}$, $I_{L_\beta}/I_{sc_{(L_\beta)}}$, $I_{K_{\alpha_2}}/I_{sc_{(K_{\alpha_2})}}$ and $I_{K_{\alpha_1}}/I_{sc_{(K_{\alpha_1})}}$ intensity ratios were also calculated.

2. Experimental

The schematic of the experimental set-up to be used in this study is shown in Figure 1. The samples were placed in the sample holder located in a chamber called the sample chamber. Thanks to the sample room where the samples were placed, the effects from the air environment were reduced and the best spectrum was tried to be obtained. The 5 Curie (Ci) Americium-241 (Am^{241}) annular source in the sample room was placed in a conical lead collimator. Lead shielding in the sample room was made to prevent harm to the researcher during measurements.

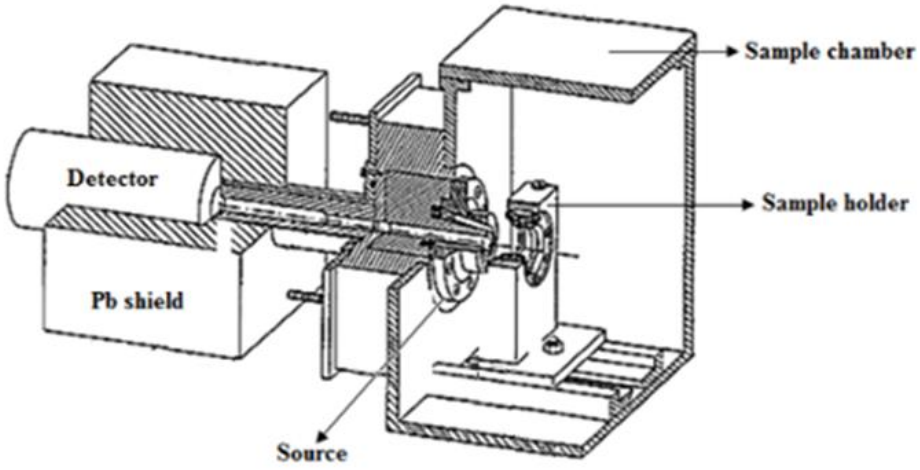

Figure 1. Experimental set up for determination different intensity ratios of samples with atomic numbers. The detector is HPGe detector and the source is Am-241.

An HpGe detector was used to count x-rays. Information about the detector used in this study can be found in Table1.The counting time for each sample is 3600 seconds. In this study, fourteen different samples were prepared using the dilution technique. Samples with different mean atomic numbers were obtained by mixing bismuth (Bi) and cellulose ($C_6H_{10}O_5$) powders. Mean atomic number of cellulose is given by

$$\bar{Z}_c = \frac{\sum_i n_i Z_i}{n} \quad (1)$$

where n is total number of atoms in cellulose, n_i is the number of atoms of the element i., and Z_i is the atomic number of the element i.

Table 1. Some specific features of the detector used in this study.

Configuration	Planar
Resolution at 5.9 keV	182 eV
Crystal diameter	16 mm
Crystal length	10 mm
Beryllium window	0.12 mm
Active area	200 mm^2

The concentrations of bismuth and cellulose in the targets of cellulose are calculated by

$$C_{b(c)}\% = \frac{m_{b(c)}}{m_b + m_c} \times 100 \quad (2)$$

where m_b is the mass of the bismuth and m_c is the mass of the cellulose. The mean atomic number of the prepared samples is calculated by

$$\bar{Z}_s = \bar{Z}_b \times C_b + \bar{Z}_c \times C_c \quad (3)$$

where $\bar{Z}_s$ mean atomic number of the sample, $\bar{Z}_b$ and $\bar{Z}_c$ are the mean atomic numbers of bismuth and cellulose, respectively. Information about the samples used in this study can be found in Table 2.

The total scattering intensity at a given wavelength is expressed as follows [40]

$$I_{sc} = \frac{I_{coh}}{2(\mu/\rho)_{\lambda}} + \frac{I_{Comp}}{2(\mu/\rho)_{\lambda}+(\mu/\rho)_{\lambda-\Delta\lambda}} \quad (4)$$

where I_{coh} and I_{Comp} in equation show the areas under the coherent and Compton peak. $(\mu/\rho)_{\lambda}$mass absorption coefficient of the sample at a specific wavelength (at $K_{\alpha}, K_{\beta}, L_{\alpha}$, L_{β}) and $(\mu/\rho)_{\lambda-\Delta\lambda}$ is the mass absorption coefficient of the sample at the excitation photon energy.

Table 2. Masses, percentage ratios and average atomic numbers of the samples used in this study.

Sample No	m_b (g)	m_c (g)	C_b (%)	C_c (%)	Sample thickness (g/cm^2)	$\overline{Z}_s$
1	0.357	0.000	1.000	0.000	0.255	83.000
2	0.326	0.025	0.929	0.071	0.227	77.371
3	0.300	0.050	0.857	0.143	0.243	71.703
4	0.276	0.075	0.786	0.214	0.230	66.082
5	0.251	0.101	0.713	0.287	0.233	60.377
6	0.225	0.125	0.643	0.357	0.230	54.796
7	0.200	0.151	0.571	0.429	0.224	49.143
8	0.175	0.175	0.500	0.500	0.214	43.551
9	0.150	0.201	0.428	0.572	0.211	37.855
10	0.125	0.225	0.357	0.643	0.195	32.273
11	0.101	0.250	0.287	0.713	0.193	26.718
12	0.075	0.275	0.215	0.785	0.228	21.044
13	0.051	0.301	0.144	0.856	0.204	15.444
14	0.025	0.325	0.072	0.928	0.214	9.743

In addition $(I_{coh} + I_{Comp})/(\mu/\rho)_{L_\alpha}$, $(I_{coh} + I_{Comp})/(\mu/\rho)_{L_\beta}$, $(I_{coh} + I_{Comp})/(\mu/\rho)_{K_{\alpha_2}}$, $(I_{coh} + I_{Comp})/(\mu/\rho)_{K_{\alpha_1}}$, $I_{L_\alpha}/I_{sc_{(L_\alpha)}}$, $I_{L_\beta}/I_{sc_{(L_\beta)}}$, $I_{K_{\alpha_2}}/I_{sc_{(K_{\alpha_2})}}$ ve $I_{K_{\alpha_1}}/I_{sc_{(K_{\alpha_1})}}$ intensity ratios were calculated in this study. The theoretical mass attenuation coefficients were used from the study of Gerward et al. [41].

3. Results and Discussion

The typical spectra of emission (L_α and L_β) , Compton and coherent scattering peaks for samples of some mean atomic numbers are shown in the Fig. 2-4 respectively. When the given spectra are analyzed, the intensities of the characteristic peaks (L_α and L_β) in Figure 2 and the coherent scattering peaks shown in Figure 4 increase with increasing mean atomic number. Since Compton scattering is dominant in samples with low atomic number, it can be seen in Figure 3 that the intensities of Compton scattering peaks decrease with increasing mean atomic number.

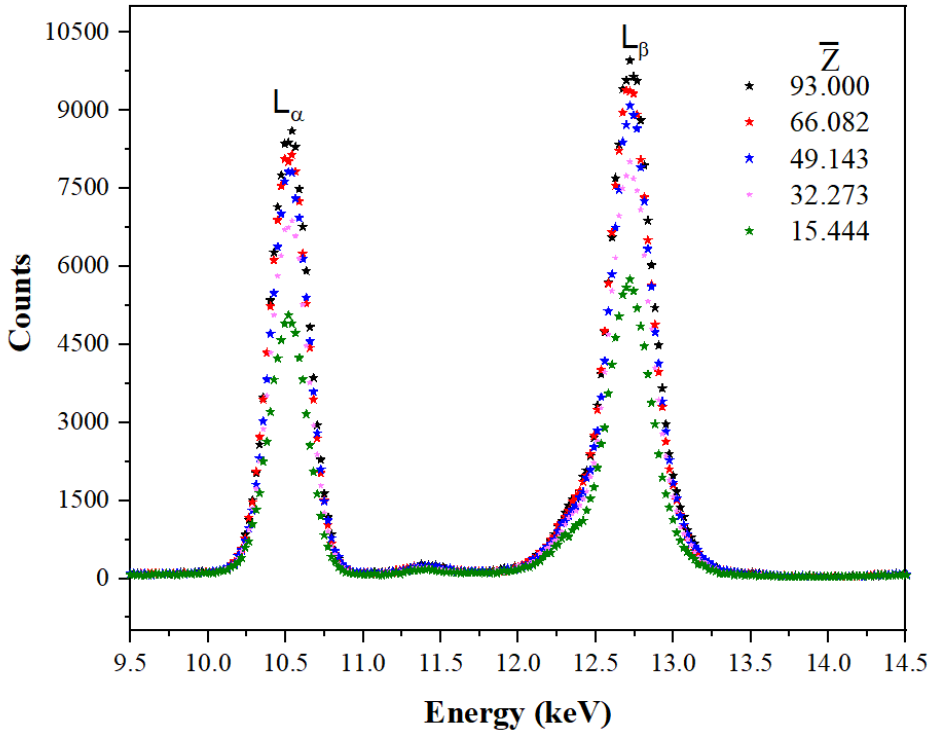

Figure 2. The typical energy dispersive L_α and L_β characteristic x-ray peaks of some samples used in the study with atomic numbers between 9 and 83.

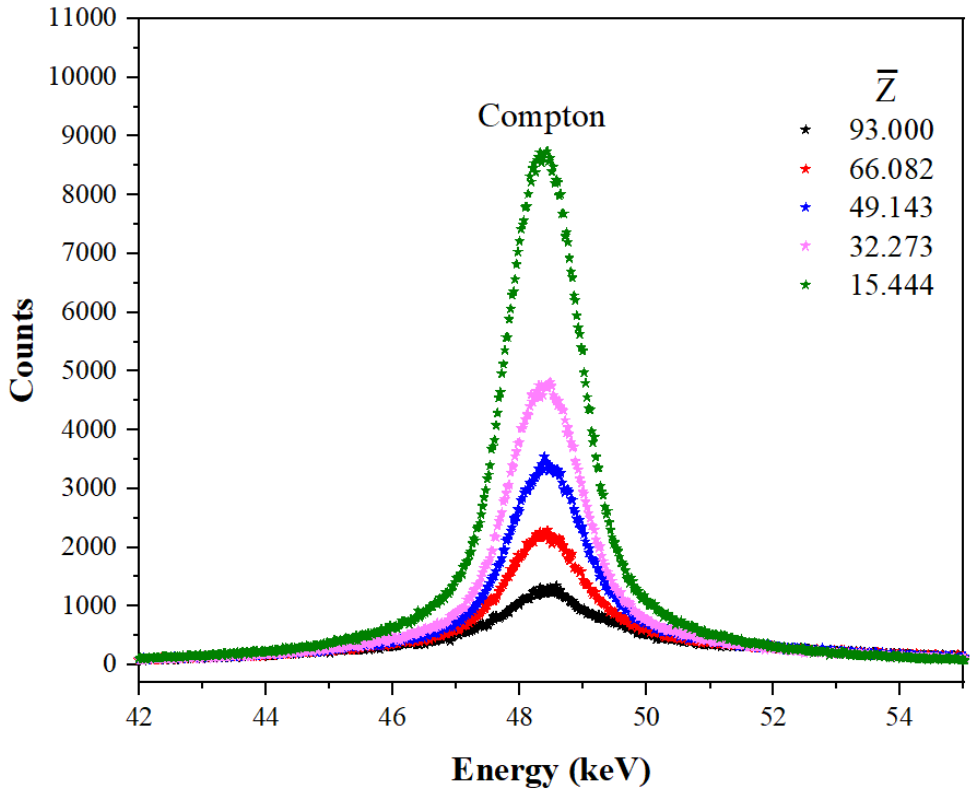

Figure 3. The typical Compton peaks of some samples used in the study with atomic numbers between 9 and 83.

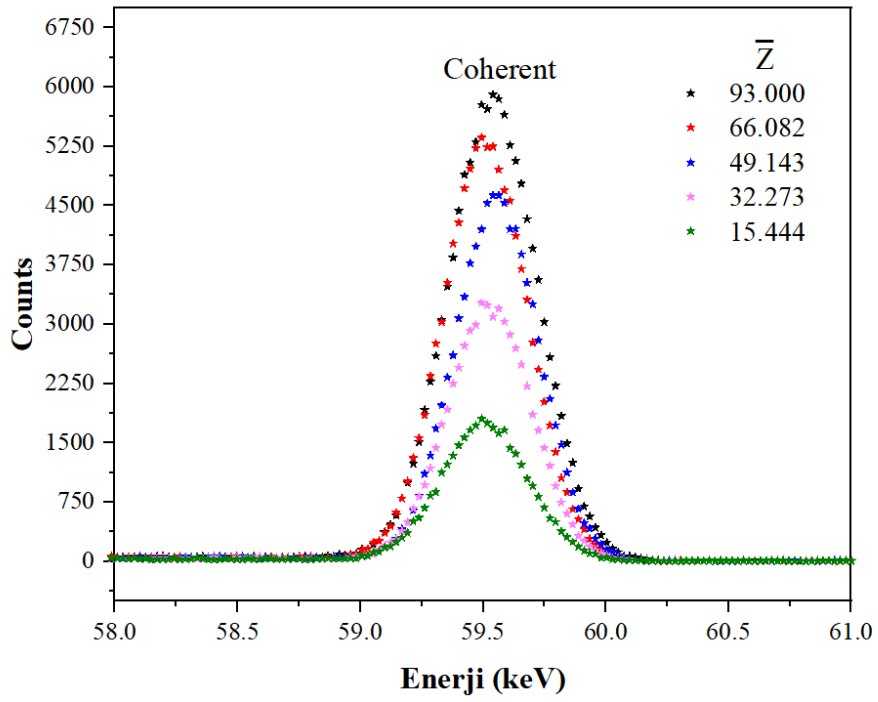

Figure 4. The typical coherent peaks of some samples used in the study with atomic numbers between 9 and 83.

In this study, different intensity ratios of fourteen different samples with average atomic numbers between 9.743 and 83.000 were calculated. The changes in intensity ratios caused by small changes in atomic number have been studied. The total scattering intensity ratios of the obtained samples were calculated at four different energies. These energies are $K_{\alpha_1}, K_{\alpha_2}, L_\alpha, L_\beta$ energies of the bismuth element. The variation of total scattering intensity ratios with mean atomic number is given in Figure 5-8.

In this study the $(\mathrm{I_{coh}} + \mathrm{I_{Comp}})/(\mu/\rho)_{L_\alpha}$, $(\mathrm{I_{coh}} + \mathrm{I_{Comp}})/(\mu/\rho)_{L_\beta}$, $(\mathrm{I_{coh}} + \mathrm{I_{Comp}})/(\mu/\rho)_{K_{\alpha_2}}$, $(\mathrm{I_{coh}} + \mathrm{I_{Comp}})/(\mu/\rho)_{K_{\alpha_1}}$ scattering ratios with mean atomic number is given Figure 9-12. Finally $I_{L_\alpha}/I_{sc_{(L_\alpha)}}$, $I_{L_\beta}/I_{sc_{(L_\beta)}}$, $I_{K_{\alpha_2}}/I_{sc_{(K_{\alpha_2})}}$ ve $I_{K_{\alpha_1}}/I_{sc_{(K_{\alpha_1})}}$ ratios are given Figure 13-16. Correlation coefficients were obtained for each scattering ratio with the Origin program. Correlation coefficient indicates the relationship between variables. The correlation coefficient approaching 1 indicates that the relationship between the variables is gradually increasing. As the correlation coefficient approaches 0, the relationship between the variables will gradually decrease.

As seen in Figure 5-8, the total scattering intensity ratios at $K_{\alpha_1}, K_{\alpha_2}, L_\alpha, L_\beta$ energies are fitted to exponential functions and their correlation coefficient is 0.999.As seen Figure 9-16 the correlation coefficients for $(\mathrm{I_{coh}} + \mathrm{I_{Comp}})/(\mu/\rho)_{L_\alpha}$, $(\mathrm{I_{coh}} + \mathrm{I_{Comp}})/(\mu/\rho)_{L_\beta}$, $(\mathrm{I_{coh}} + \mathrm{I_{Comp}})/(\mu/\rho)_{K_{\alpha_2}}$ and $(\mathrm{I_{coh}} + \mathrm{I_{Comp}})/(\mu/\rho)_{K_{\alpha_1}}$ are 0.972, 0.962, 0.980 and 0.982, respectively. Additionally, the correlation coefficients found for the intensity ratios $I_{L_\alpha}/I_{sc_{(L_\alpha)}}$, $I_{L_\beta}/I_{sc_{(L_\beta)}}$, $I_{K_{\alpha_2}}/I_{sc_{(K_{\alpha_2})}}$ ve $I_{K_{\alpha_1}}/I_{sc_{(K_{\alpha_1})}}$ are 0.988,0.994, 0.995 and 0.996.

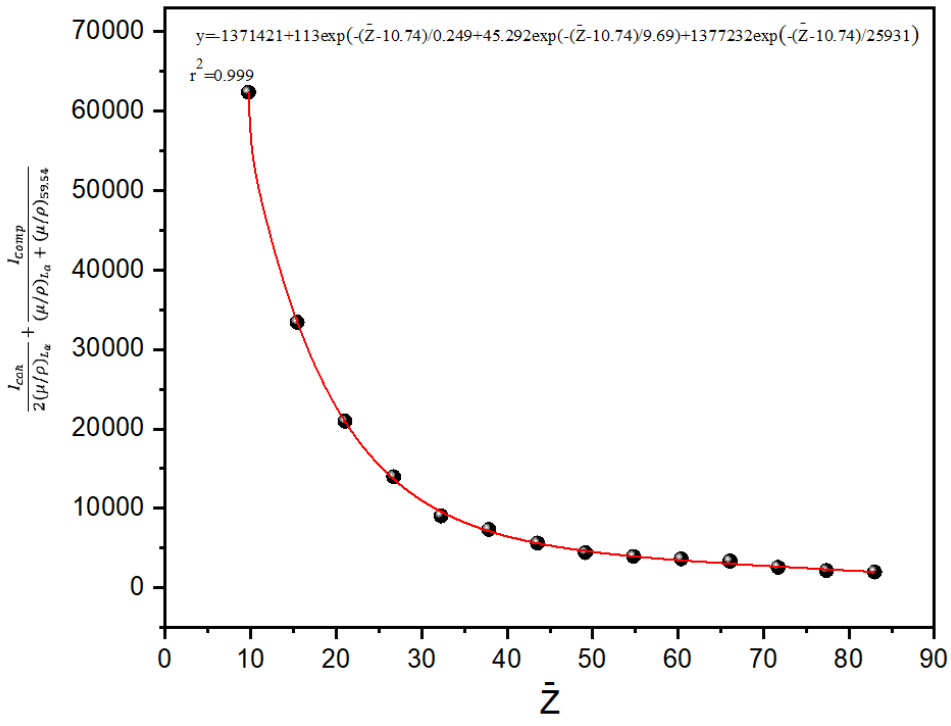

Figure 5. The variation of I_{sc} with mean atomic number at L_α energy.

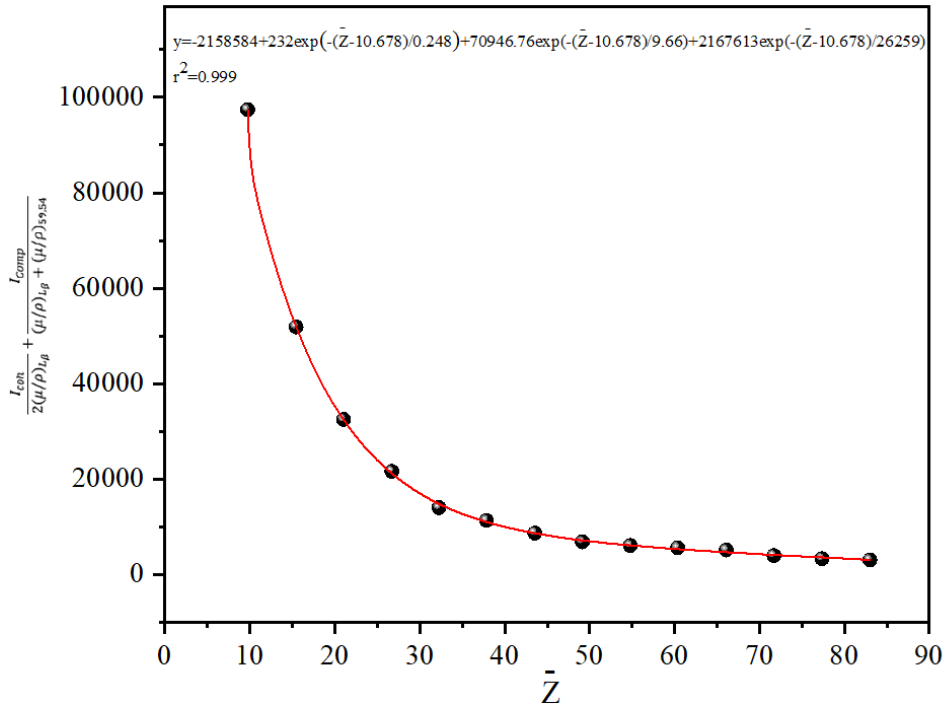

Figure 6. The variation of I_{sc} with mean atomic number at L_β energy

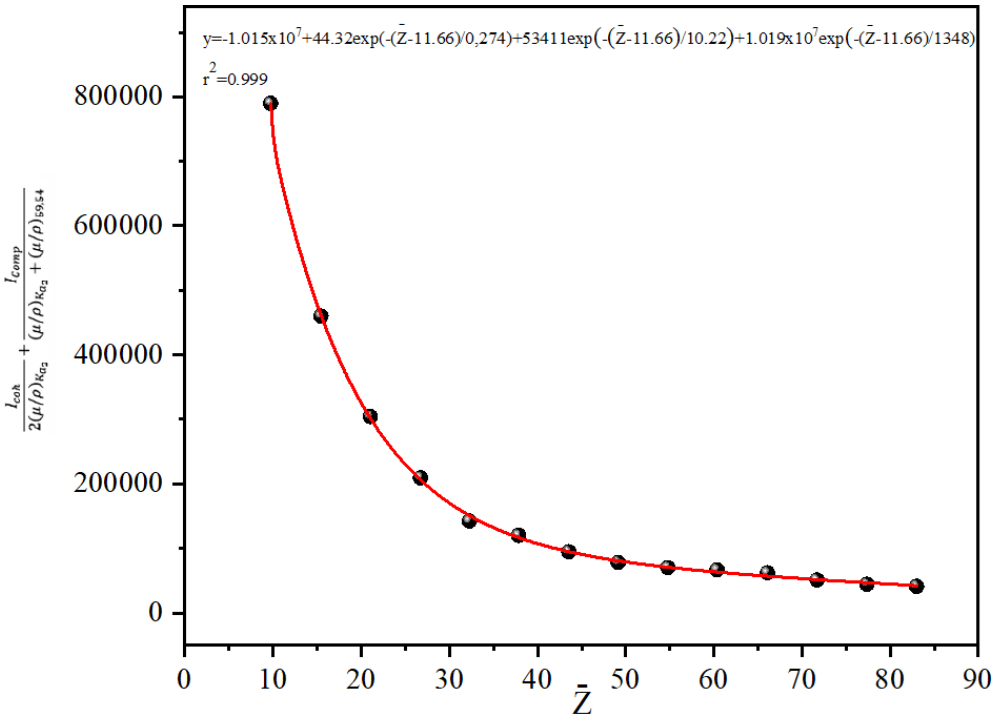

Figure 7. The variation of I_{sc} with mean atomic number at K_{α_2} energy.

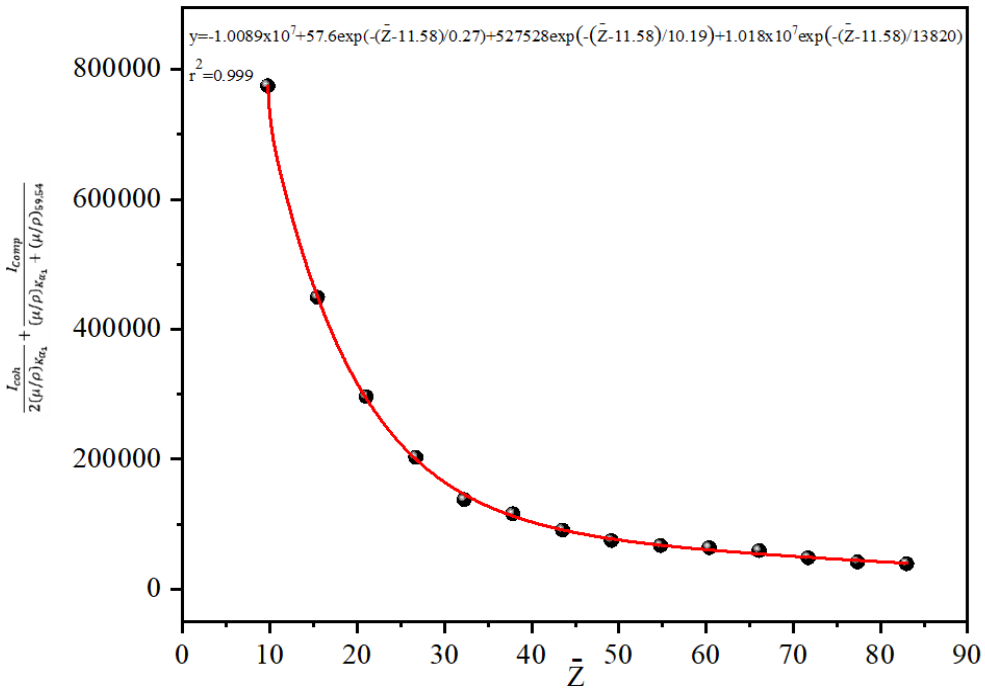

Figure 8. The variation of I_{sc} with mean atomic number at K_{α_1} energy.

In this study the $(\mathrm{I_{coh}} + \mathrm{I_{Comp}})/(\mu/\rho)_{L_\alpha}$, $(\mathrm{I_{coh}} + \mathrm{I_{Comp}})/(\mu/\rho)_{L_\beta}$, $(\mathrm{I_{coh}} + \mathrm{I_{Comp}})/(\mu/\rho)_{K_{\alpha_2}}$, $(\mathrm{I_{coh}} + \mathrm{I_{Comp}})/(\mu/\rho)_{K_{\alpha_1}}$ scattering ratios with mean atomic number is given Figure 9-12.

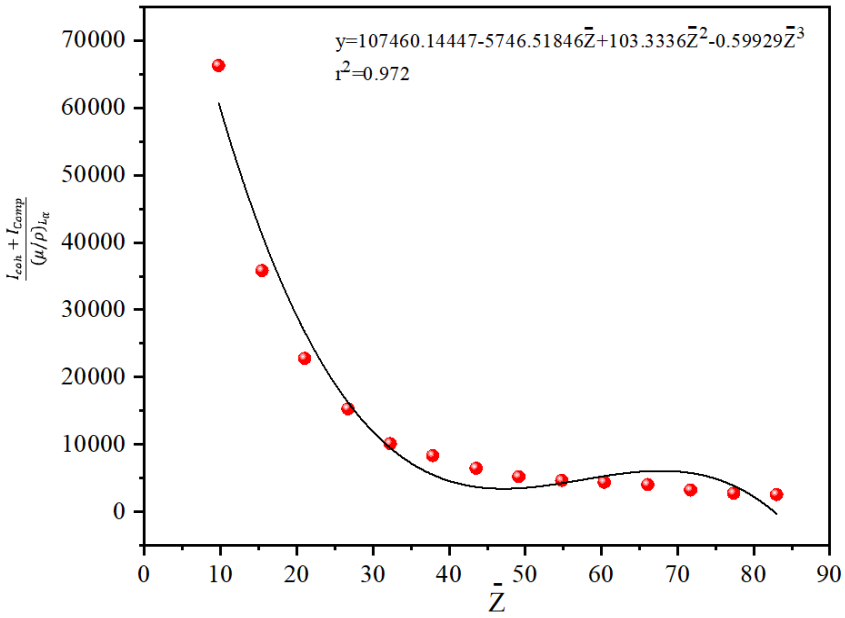

Figure 9. The variation of $I_{coh} + I_{Comp}/(\mu/\rho)_{L_\alpha}$ intensity ratios with mean atomic number. $\mathrm{I_{coh}}$ and $\mathrm{I_{Comp}}$ are elastic and inelastic scattering intensities and $(\mu/\rho)_{L_\alpha}$ shows the mass absorption coefficient at L_α energy.

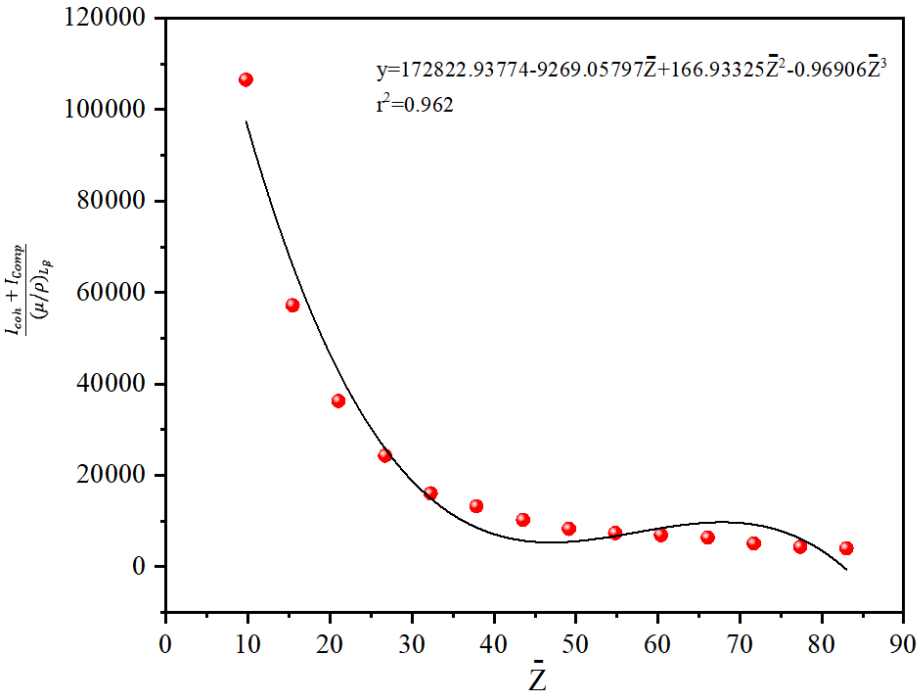

Figure 10. The variation of $I_{coh} + I_{Comp}/\ (\mu/\rho)_{L_\beta}$ intensity ratios with mean atomic number. I_{coh} and I_{Comp} are elastic and inelastic scattering intensities and $(\mu/\rho)_{L_\beta}$ shows the mass absorption coefficient at L_β energy.

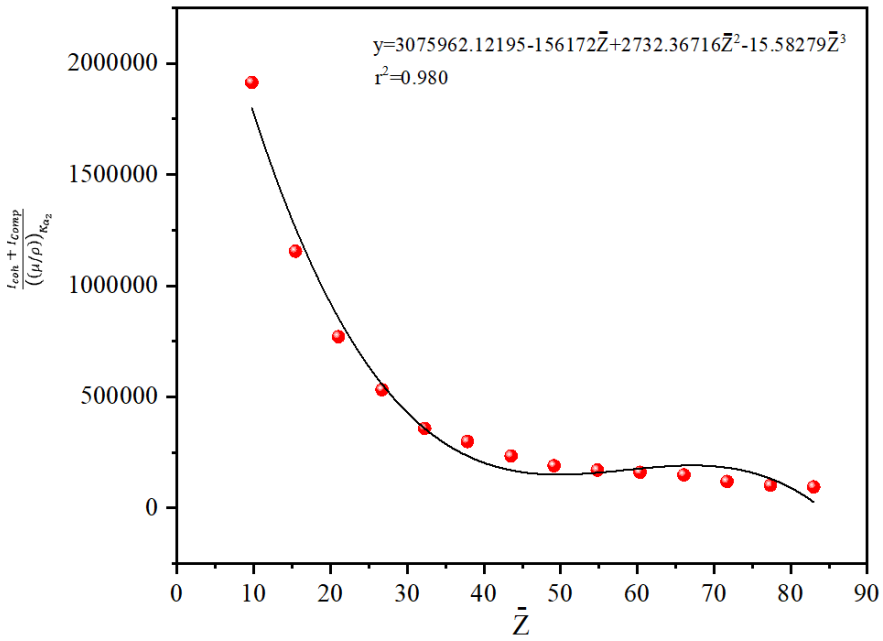

Figure 11. The variation of $I_{coh} + I_{Comp}/\ (\mu/\rho)_{K_{\alpha_2}}$ intensity ratios with mean atomic number. I_{coh} and I_{Comp} are elastic and inelastic scattering intensities and $(\mu/\rho)_{K_{\alpha_2}}$ shows the mass absorption coefficient at K_{α_2} energy.

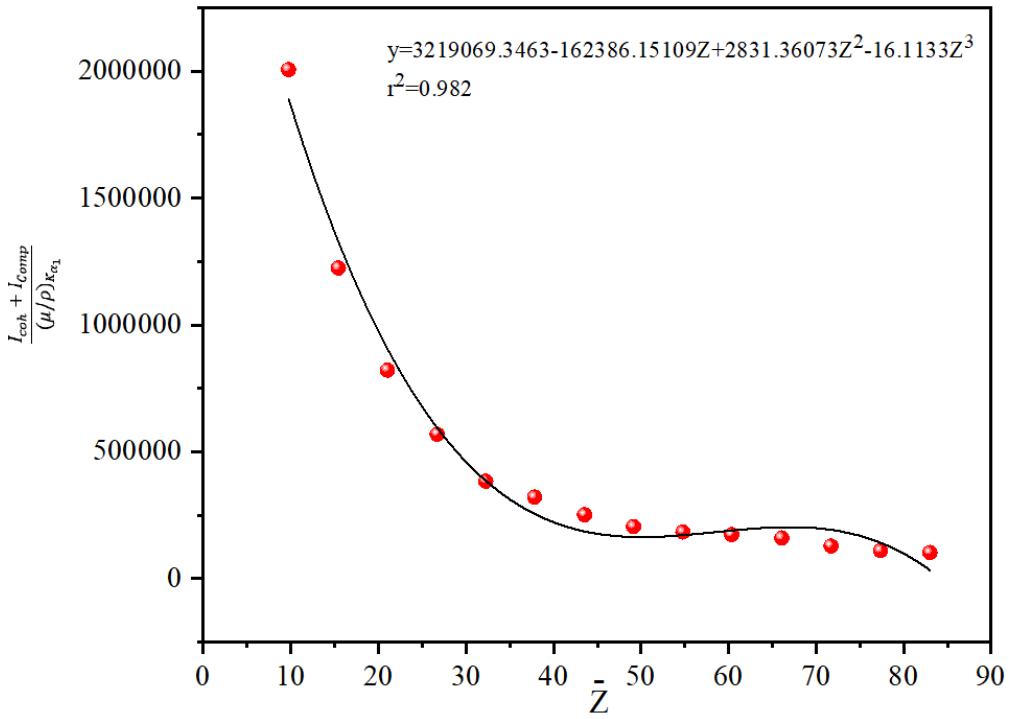

Figure 12. Variation of $I_{coh} + I_{Comp}/\ (\mu/\rho)_{K_{\alpha_1}}$ intensity ratios with mean atomic number. . I_{coh} and I_{Comp} are elastic and inelastic scattering intensities and $(\mu/\rho)_{K_{\alpha_1}}$ shows the mass absorption coefficient at K_{α_1} energy.

Finally $I_{L_\alpha}/I_{sc_{(L_\alpha)}}, I_{L_\beta}/I_{sc_{(L_\beta)}}$, $I_{K_{\alpha_2}}/I_{sc_{(K_{\alpha_2})}}$ ve $I_{K_{\alpha_1}}/I_{sc_{(K_{\alpha_1})}}$ ratios are given Figure 13-16. Correlation coefficients were obtained for each scattering ratio with the Origin program. Correlation coefficient is a coefficient that shows the relationship between variables. The correlation coefficient approaching 1 indicates that the relationship between the variables is gradually increasing. As the correlation coefficient approaches 0, the relationship between the variables will gradually decrease.

As seen in Figure 5-8, the total scattering intensity ratios at $K_{\alpha_1}, K_{\alpha_2}, L_\alpha, L_\beta$ energies are fitted to exponential functions and their correlation coefficient is 0.999.As seen Figure 9-16 the correlation coefficients for $(I_{coh} + I_{Comp})/\ (\mu/\rho)_{L_\alpha}$, $(I_{coh} + I_{Comp})/\ (\mu/\rho)_{L_\beta}$, $(I_{coh} + I_{Comp})/\ (\mu/\rho)_{K_{\alpha_2}}$ and $(I_{coh} + I_{Comp})/\ (\mu/\rho)_{K_{\alpha_1}}$ are 0.972, 0.962, 0.980 and 0.982, respectively. Additionally, the correlation coefficients found for the intensity ratios $I_{L_\alpha}/I_{sc_{(L_\alpha)}}, I_{L_\beta}/I_{sc_{(L_\beta)}}, I_{K_{\alpha_2}}/I_{sc_{(K_{\alpha_2})}}$ ve $I_{K_{\alpha_1}}/I_{sc_{(K_{\alpha_1})}}$ are 0.988,0.994, 0.995 and 0.996.

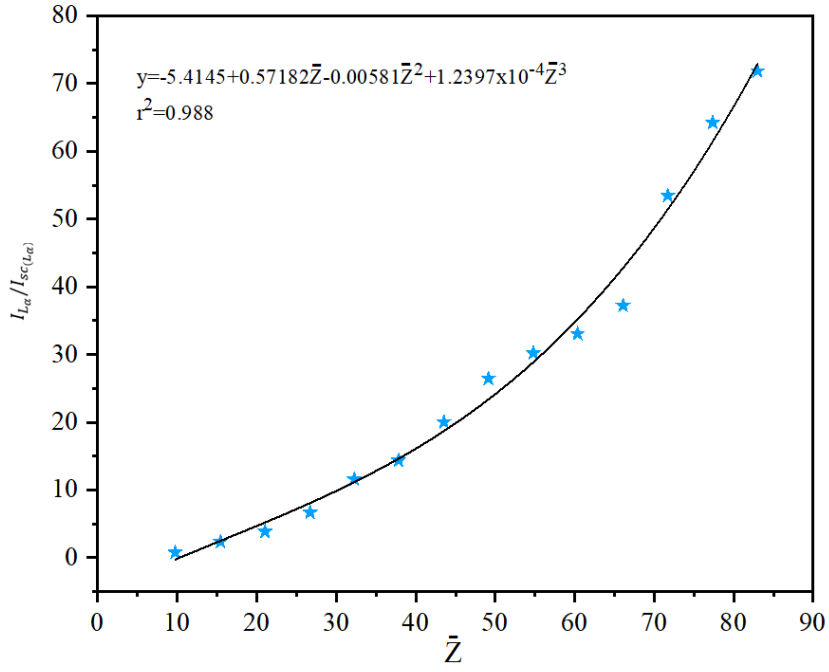

Figure 13. The variation of $I_{L_\alpha}/I_{sc_{(L_\alpha)}}$ intensity ratios with mean atomic number. I_{L_α} is intensity under the L_α peak and $I_{sc_{(L_\alpha)}}$ is the total scattering intensity at L_α energy.

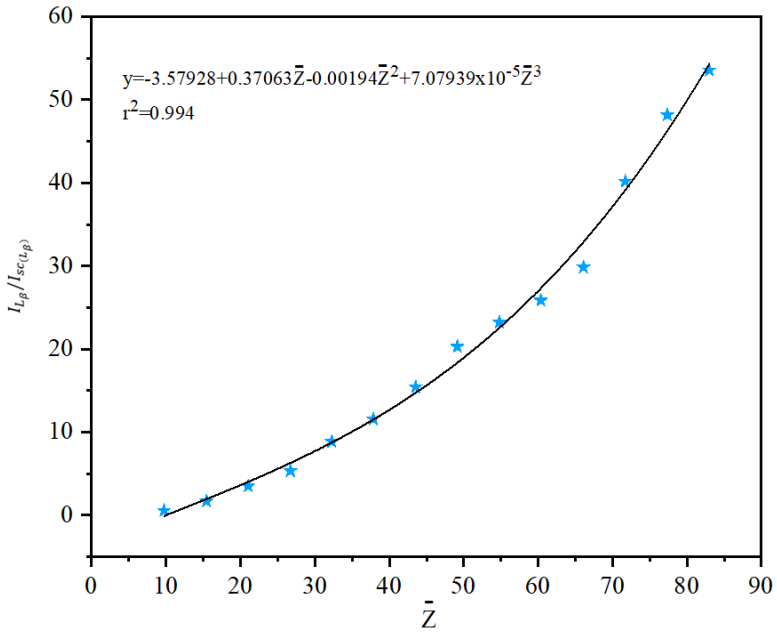

Figure 14. The variation of $I_{L_\beta}/I_{sc_{(L_\beta)}}$ intensity ratios with mean atomic number. I_{L_β} is intensity under the L_β peak and $I_{sc_{(L_\beta)}}$ is the total scattering intensity at L_β energy.

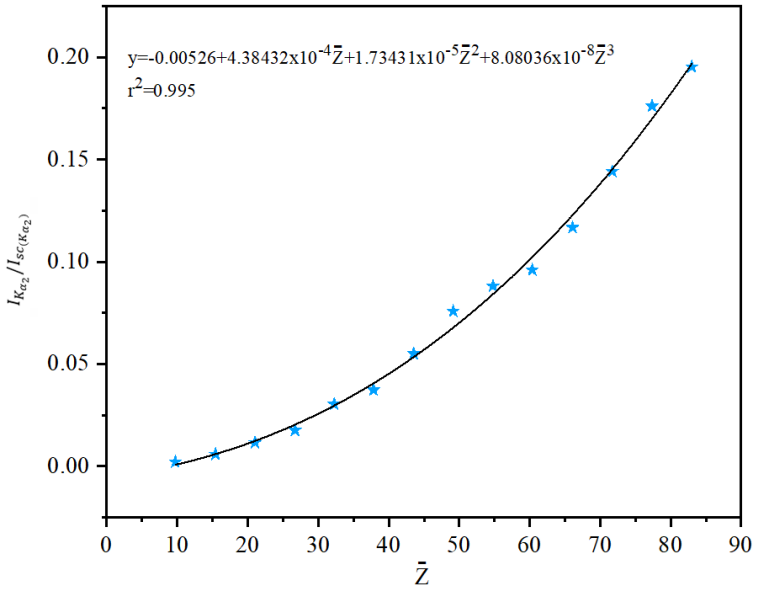

Figure 15. The variation of $I_{K_{\alpha_2}}/I_{sc_{(K_{\alpha_2})}}$ intensity ratios with mean atomic number. $I_{K_{\alpha_2}}$ is intensity under the $I_{K_{\alpha_2}}$ peak and $I_{sc_{(K_{\alpha_2})}}$ is the total scattering intensity at K_{α_2} energy.

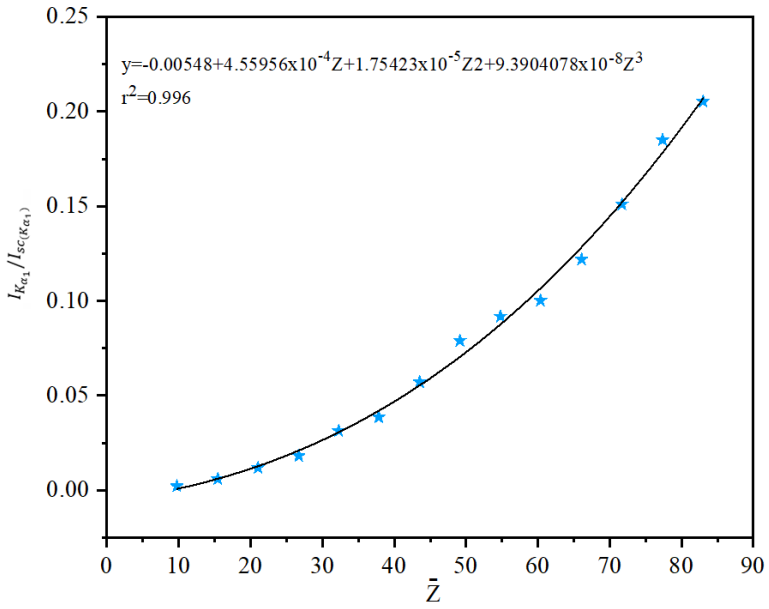

Figure 16. The variation of $I_{K_{\alpha_1}}/I_{sc_{(K_{\alpha_1})}}$ intensity ratios with mean atomic number. $I_{K_{\alpha_1}}$ is intensity under the $I_{K_{\alpha_1}}$ peak and $I_{sc_{(K_{\alpha_1})}}$ is the total scattering intensity at K_{α_1} energy.

4. Conclusions

In this study, different intensity ratios of fourteen samples with atomic numbers between 9.74 and 83.00 were calculated using the dilution technique. The changes of different intensity ratios with the mean atomic number are shown in graphs and correlation coefficients are calculated. As seen from Figure5-16 correlation coefficients are greater than 0.960. When the results are examined carefully, it shows that different intensity ratios can be used safely in the analysis of complex materials. It is also clear that qualitative analysis of complex materials can be performed using the dilution technique without the need for expensive standard samples.

Correlation coefficients provide information about the best intensity ratios that can be used to find the effective/equivalent atomic number of a complex material. As can be seen from the obtained fit curves, $I_{L_\alpha}/I_{sc_{(L_\alpha)}}$, $I_{L_\beta}/I_{sc_{(L_\beta)}}$ $I_{K_{\alpha_2}}/I_{sc_{(K_{\alpha_2})}}$ and $I_{K_{\alpha_1}}/I_{sc_{(K_{\alpha_1})}}$ intensity ratios are the best spectral ratio methods that can be used to determine the effective atomic number. Such studies will also help develop databases such as WinXCom and ANSI, which are used to find the effective atomic number theoretically and semiempirically.

Ethics in Publishing

There are no ethical issues regarding the publication of this study.

Author Contributions

Tuba AKKUŞ: Conceptualization, Methodology, Data, curation, Writing – original draft preparation.

Mehmet Fatih TEMİZ: Collecting data, evaluating the results, writing article.

References

[1] Hassib, Sonia T. Qualitative and quantitative analysis of uracil anticancer drugs. *Talanta* **1981**, 28(9), 685-687.

[2]Greil, J. D;Joly, B; Chanal, M; Cluzel, R. Qualitative and quantitative analysis of skin flora on hands after" hygienic type handwashing with a liquid soap and with a detergent bactericidal solution. Pathologie Biologie **1984**, 32(5).

[3]Svoboda, K. P; Hay, R. K; Waterman, P. G. Growing summer savory (Satureja hortensis) in Scotland: Quantitative and qualitative analysis of the volatile oil and factors influencing oil production. Journal of the Science of Food and Agriculture **1990**, 53(2), 193-202.

[4]Ekinci, N; Astam, N; Sahin, Y. Qualitative and quantitative analysis of the cataract using EDXRF. Journal of Quantitative Spectroscopy and Radiative Transfer, 2002, 72(6), 783-787.

[5]Jelesijevic, T; Jovanović, M; Knežević, M; Aleksić-Kovačević, S. Quantitative and qualitative analysis of Ag-NOR in benign and malignant canine mammary gland tumors, Acta Veterinaria-Beograd 2003, 53(5-6), 353-360.

[6]Ekinci, N; Gürol, A; Polat, R; Budak, G; Karabulut, A. The qualitative and quantitative analysis of Sarıkamış ore by energy dispersive X-ray fluorescence. Journal of Radioanalytical and Nuclear Chemistry **2003**, 258 (1), 163-165.

[7] Linati, L; Lusvardi, G; Malavasi, G; Menabue, L; Menziani, M. C; Mustarelli, P; Segre, U. Qualitative and Quantitative Structure− Property Relationships Analysis of Multicomponent Potential Bioglasses. The Journal of Physical Chemistry B **2005**, 109(11), 4989-4998.

[8]Huerta, V. D; Sánchez, M. L. F; Sanz-Medel, A. Qualitative and quantitative speciation analysis of water soluble selenium in three edible wild mushrooms species by liquid chromatography using post-column isotope dilution ICP–MS. Analytica Chimica Acta **2005**, 538(1-2), 99-105.

[9]Gunasekaran, S; Devi, T. R; Sakthivel, P. S. Qualitative and quantitative analysis on fibrates-A spectroscopic study. Asian Journal of Chemistry 2008, 20(6), 4249.

[10]Oilo, M; Tvinnereim, H. M; Gjerdet, N. R. Qualitative and quantitative fracture analyses of high-strength ceramics. European Journal of Oral Sciences **2009**,117(2), 187-193.

[11] Ge, J; Liu, Z; Zhi, Z; Zhao, X. S. Qualitative and quantitative thrombin analysis in serum using aptamers and gold nanoparticles through progressive dilution. Analytical Biochemistry **2011**, 413(1), 75-77.

[12] Qin, Y; Liu, J; Wang, G; Zhang, Y. Evaluation of indoor air quality based on qualitative, quantitative and olfactory analysis. Chinese Science Bulletin, 2013,58(9), 986-991.

[13]Vesnin, V. L. Qualitative Analysis of Liquid Hydrocarbon Mixtures by Absorption Spectra of Their Vapors. Journal of Applied Spectroscopy 2016, 83(5), 840-844.

[14]Brenz, F; Linke, S; Simat, T. (2017). Qualitative and quantitative analysis of monomers in polyesters for food contact materials. Food Additives & Contaminants: Part A **2017** 34(2), 307-319.

[15]Tzima, K; Brunton, N. P; Rai, D. K. Qualitative and quantitative analysis of polyphenols in Lamiaceae plants-A review. Plants **2018**, 7(2), 25.

[16]Tang, Y;Si, G; Sun, W; Li, B; Li, D; Hu, X. Analysis of temperature adaptability of qualitative analysis model for liquid multicomponent mixtures. Optik **2019**,198, 163221.

[17]Obata, Y; Bale, H. A; Barnard, H. S; Parkinson, D. Y; Alliston, T; Acevedo, C. Quantitative and qualitative bone imaging: A review of synchrotron radiation microtomography analysis in bone research. Journal of the mechanical behavior of biomedical materials 2010, 110, 103887.

[18]Faniran, T. S; Nkamba, L. N; Manga, T. T. Qualitative and Quantitative Analyses of COVID-19 Dynamics Axioms **2021**, 10(3), 210.

[19]Pedro, S. A; Rwezaura, H; Mandipezar, A; Tchuenche, J. M. Qualitative Analysis of an influenza model with biomedical interventions. Chaos, Solitons & Fractals **2019**, 146, 110852.

[20] Chechko, V. E. Qualitative analysis of the clustering in water solutions of alcohols III. Ukrayins' kij Fyizichnij Zhurnal (Kyiv) 2021, 66(10), 865-872.

[21] Fancher, C. M. Diffraction Methods for Qualitative and Quantitative Texture Analysis of Ferroelectric Ceramics Materials **2021**, 14(19), 5633.

[22]Koscielniak, P. Calibration methods in qualitative analysis. TrAC Trends in Analytical Chemistry **2022**, 150, 116587.

[23]Mititelu, M; Neacșu, S. M; Oprea, ; Dumitrescu, D. E;Nedelescu, M;Drăgănescu, D; Ghica, M. Black Sea Mussels Qualitative and Quantitative Chemical Analysis: Nutritional Benefits and Possible Risks through Consumption. Nutrients **2022**, 14(5), 964.

[24]Ott, J;Burghardt, A; Britz, D; Majauskaite, S; Mücklich, F. Qualitative and Quantitative Microstructural Analysis of Copper for Sintering Process Optimization in Additive Manufacturing Application. Practical Metallography **2021**, 58(1), 32-47.

[25] Doomen, R. A; Nedeljkovic, I; Kuitert, R. B; Kleverlaan, C. J;Aydin, B. Corrosion of orthodontic brackets: qualitative and quantitative surface analysis. The Angle Orthodontist **2022**, 92(5),661-668.

[26]He, S. H; Jiang, H. Qualitative and quantitative analysis of some co-existing colorants in some hard candies. Journal of Food Composition and Analysis **2022**, 109, 104475.

[27]Porikli, S.Chemical shift and intensity ratio values of dyspersium, holmium and erbium L X-ray emission lines . Radiation Physics and Chemistry **2012**,81(2),113-117.

[28]Yılmaz, R. Kb/Ka X-ray intensity ratios for some elements in the atomic number range 28≤Z≤39 at 16.896 keV Journal of Radiation Research and Applied Sciences **2017**, 10, 172-177.

[29] Sakar, E;Gurol, A; Bastug A. Experimental K X-ray intensity ratios of some heavy elements. Radiation Physics and Chemistry **2017**,131, 105-107.

[30]Yılmaz, R. Kβ/Kα X-Ray Intensity Ratios for Cr, Mn, Fe, and Co Excited by 8.735 keV Energy. Acta Physıca Polonıca A **2018**, 133, 5.

[31]Ugurlu, M.; Alım,B; Demir,L. The relationship between the external magnetic field and K X-ray intensity ratios of immiscible MoxAg1-x alloys, Radiation Physics and Chemistry **2019**, 165, 108396.

[32] Cengiz, E; Köksal, O; Apaydın, G; Karahan, İ; Ünal, E. Determination of valence electronic structure of Ni in Ni-B alloy coatings using Kβ-to-Kα X-ray intensity ratios. Applied Radiation and Isotopes, **2019**, 144, 24-28.

[33]Ugurlu, M; Demir,L. Relative K X-ray intensity ratios of the first and second transition elements in the magnetic field. Journal of Molecular Structure **2020**,1203, 127458

[34]Ismail, A. M; Malhi, N. B. L-shell x-ray relative intensities of some heavy elements excited by 20.48 keV x-rays. X-Ray Spectrometry **2000**, 29(4), 317-319

[35]Tırasoglu, E; Çevik, U; Ertugral, B; Apaydın, G;Ertugrul, M; Kobya, A. I. Chemical effects on Lα, Lβ, Lγ, Ll, and Lη X-ray production cross-sections and Li/Lα X-ray intensity ratios of Hg, Pb and Bi compound at 59.54 keV. The European Physical Journal D **2003**,26, 231-236

[36] Turgut, U; Ertuğrul, M. L X-ray intensity ratios for elements in the range $74 \leq Z \leq 92$ at 31.635 keV", Nuclear Instruments and Methods in Physics Research Section B **2004**, 222(3-4), 432-436.

[37]Yalçın, P; Porikli S; Kurucu, Y; Şahin, Y. Measurement of relative L X-ray intensity ratio following radioactive decay and photoionization. Physics Latters B **2008**, 663,3, 186-190.

[38] Porikli, S; Demir, D; Kurucu, Y.Variation of Kβ/ Kα X-ray intensity ratio and lineshape with the effects of external magnetic field and chemical combination. European Physical Journal D **2008**, 47,3, 315-323.

[39] Cinan, E; Ertuğrul, M; Aygün, B; Sayyed, M. I; Kurucu, Y; Özdemir, Y. Determination of the effect of temperature on relative L X-ray intensity ratio of gadolinium, dysprosium and erbium. Radiation Physics and Chemistry **2021**. 183, 109389.

[40] Bertin, E.P. Principles and practice of X-ray spectrometric analysis, second ed. Plenum Press, New York, 1975.

[41]Gerward, L; Guilbert, N; Jensen, K. B; Levring, H. X-ray absorption in matter Reengineering XCOM. Radiation Physics and Chemistry 2001, 60, 23–24.

e-ISSN: 2149-4584

Erzincan University Journal of Science and Technology

EJSAT 2025, 18 (3) 781-788

Research Article

The Effects of Garlic Extracts on Prostate Cancer

Furkan KUZNEK[1], Recep İLHAN[2], Gökçe YILDIRIM BUHARALIOĞLU[3], Ahmet EMİR[1*]

[1]Department of Pharmacognosy, Faculty of Pharmacy, Ege University, İzmir, Turkey
[2]Department of Biochemistry, Faculty of Pharmacy, Ege University, Izmir, Turkey
[3]Department of Pharmacology, Faculty of Pharmacy, Ege University, İzmir, Turkey

Received: 18/02/2025, **Revised:** 24/03/2025, **Accepted:** 24/03/2025, **Published:** 31/12/2025

Abstract

In the current study, garlic samples obtained from various provinces of Turkey, including Kastamonu, Balikesir, Edirne, and Aksaray, were analyzed for their chemical composition and biological activity. The organosulfur content of the prepared extracts was assessed using GC-MS. A total of seven compounds were identified across all samples, with 3-Vinyl-4H-1,2-dithiin and 2-Vinyl-4H-1,3-dithiin recognised as the predominant compounds. Additionally, the effects of these extracts at concentration of 25, 50, 75, 100, 150 and 200 µg/ml on benign prostatic hyperplasia (BPH), as well as on the LNCaP, DU145, and PC3 cell lines, were evaluated using MTT assays. Cytotoxic activity was detected in all samples examined. The most pronounced activity was recorded against the LNCaP cell lines, exhibiting varying IC_{50} values ranging from 23.91 to 48.84 µg/ml.

Keywords: Garlic, Organosulfur compounds, Prostate cancer

Sarımsak Ekstrelerinin Prostat Kanseri Üzerindeki Etkileri

Öz

Mevcut çalışmada, Kastamonu, Balıkesir, Edirne ve Aksaray olmak üzere Türkiye'nin çeşitli illerinden temin edilen sarımsak örnekleri kimyasal bileşimleri ve biyolojik aktiviteleri açısından analiz edildi. Hazırlanan ekstraktların organosülfür içeriği GC-MS kullanılarak değerlendirildi. Tüm örneklerde toplam yedi bileşik tanımlandı ve 3-Vinil-4H-1,2-ditiin ve 2-Vinil-4H-1,3-ditiin baskın bileşikler olarak tanındı. Ek olarak, bu ekstraktların iyi huylu prostat hiperplazisi (BPH) üzerindeki etkileri ve LNCaP, DU145 ve PC3 hücre hatları üzerindeki etkileri MTT analizleri kullanılarak değerlendirildi. İncelenen tüm örneklerde sitotoksik aktivite tespit edildi. En belirgin aktivite, 23,91 ila 48,84 µg/ml arasında değişen IC_{50} değerleri gösteren LNCaP hücre hatlarına karşı kaydedildi.

Anahtar Kelimeler: Sarımsak, Organosülfür bileşikleri, Prostat kanseri

Corresponding Author: ahmet.emir@ege.edu.tr

Cite this Article: Erzincan University Journal of Science and Technology 2025, 18(3) 781-788. https://doi.org/10.18185/erzifbed.1641990

1. Introduction

The genus *Allium* L. comprises approximately 900 species and is recognized as a taxonomically complex and highly variable group, primarily distributed throughout the northern hemisphere. Historically, *Allium* was classified within the Liliaceae family; however, recent molecular studies conducted by the Angiosperm Phylogeny Group (APG) have led to a reevaluation of its taxonomic standing. Consequently, *Allium* has been reclassified into the Amaryllidaceae family, within the subfamily Allioideae and the tribe Allieae [1]. *Allium sativum*, commonly known as garlic, is the most widely cultivated and consumed vegetable in this genus. Apart from its culinary use, garlic exhibits a wide range of biological activities. This species significantly influences the cardiovascular system through its hypotensive, hypolipidemic, antiplatelet, and hypocholesterolemic effects. Additionally, it demonstrates anticarcinogenic properties by regulating cell proliferation, apoptosis, and immune responses [2].

The biological effects of garlic are primarily attributed to various chemical compounds present within the bulb, with a significant portion of research focusing on specific organosulfur constituents. Members of the *Allium* genus typically contain S-Alk(en)yl cysteine sulfoxides, which are non-protein sulfur-containing amino acids. These compounds are characterised by the absence of odor and function as precursors to the volatile and distinctive aromatic constituents of *Allium* plants [3].

(+)-S-allyl-L-cysteine sulfoxide (ACSO), commonly referred to as alliin, was the first stable precursor compound associated with garlic to be identified. It serves as the primary organosulfur component responsible for the release of most odorous volatiles when garlic is crushed or cut [4]. In addition to alliin, three other principal sulfoxide compounds have been identified in *Allium* species: (+)-S-methyl-L-cysteine sulfoxide (methiin, or MCSO), (+)-S-propyl-L-cysteine sulfoxide (propiin, or PCSO), and (+)-S-trans-1-propenyl-L-cysteine sulfoxide (isoalliin, or TPCSO) [5]. Allinase, a lyase enzyme, is released upon crushing, chopping, or grinding garlic. This enzyme catalyzes the breakdown of alliin, yielding pyruvate, ammonia, and sulfenic acids. Sulfenic acid, an unstable compound, undergoes self-condensation, ultimately forming allicin. Allicin, in turn, is highly reactive and decomposes into dithiins, polysulfides, and ajoenes through a process known as allylization [6].

Prostate cancer is one of the most prevalent cancers worlwide and ranks as the most frequent cancer among men in the United States, being the second leading cause of cancer-related fatalities in the country. The beneficial effects of garlic and its organosulfur compounds on prostate cancer have been substantiated through epidemiological studies, clinical trials, and experimental research [7]. In the current study, garlic samples were obtained from various regions, including Kastamonu, Balıkesir, Edirne, and Aksaray. The extracts derived from these samples were analyzed for their content of allicin-derived compounds. Furthermore, the effects of these extracts on benign prostatic hyperplasia (BPH), as well as on the LNCaP, DU145 and PC3 cell lines, were assessed.

2. Material and Methods

2.1. Plant Material

Garlic samples were provided from local producers (Kastamonu, Balıkesir, Edirne ve Aksaray) in June 2023.

2.2. Chemicals and Reagents

Hydrocarbon mixtures (C_7-C_{30} n-alkanes), diethyl ether, MTT (M5665) were purchased from Sigma Aldrich. RPMI 1640 (21875-034) and DMEM/F-12 (31330-038) were provided from Thermo. DMSO was purchased from VWR. were purchased from Sigma Aldrich.

2.3. Sample Preparation

Garlic samples (10 g) were crushed and left for thirty minutes to allow for the formation of organosulfur compounds through the reaction catalyzed by allinase. The samples were then transferred into falcon tube, and 30 ml of ether was added. The extraction process was conducted three times with constant stirring using a rotator. Subsequently, the samples were centrifuged for 30 minutes to isolate the supernatants. The liquid portion was then evaporated using a rotary evaporator under reduced pressure, and the resulting extracts were preserved at 4°C until further analysis.

2.4. GC-MS Analysis

The evaluation of the samples was conducted using GC-MS (Agilent 5977A Series) that had an HP-5MS Ultra Inert (Agilent) capillary column (60 m x 0.250 m x 0.25 μm). Information about the experimental procedure was provided in the previous study [8].

2.5. Cell Culture

BPH (Primary Prostate Epithelial Cell line), DU145 (Prostate Epithelial Cells cell line), PC3 (prostatic adenocarcinoma cell line) and LNCaP (human prostate adenocarcinoma cell line) were sourced from ATCC and stored in liquid nitrogen in our stock. For cytotoxicity assays, the cells were cultured in 100 mm dishes and passaged until reaching 70% confluence. The cultures were maintained in a humidified incubator at 37°C with 5% carbon dioxide.

2.6. Cytotoxicity assays (MTT)

To determine the IC_{50} values of extracts prepared in DMSO at concentrations of 25, 50, 75, 100, 150 and 200 μg/ml, cells were initially plated in 96-well culture plates, and cell viability assays were conducted after a 24-hour incubation period. Following a 48-hour exposure to the extracts, an MTT assay was carried out. A 0.5 mg/mL MTT reagent was added to the wells of the 96-well plate and incubated for 4 hours. After incubation, the medium was discarded, and 200 μL of DMSO was added to dissolve the formazan crystals. Absorbance was measured using a microplate reader at 570-690 nm, with blank wells (no cells) serving to account for any background absorbance. The IC_{50} values were calculated by comparing extract treated cells

versus control group, which is treated just equal volume of DMSO in which extract is applied, through regression analysis using GraphPad Prism version 10.16.

Results and Discussion

Ether extracts of garlic samples obtained from different localities in Türkiye were prepared and these extracts were evaluated in terms of chemical profile and biological activity. The following codes were assigned to extracts: GK for Kastamonu, GE for Edirne, GA for Aksaray, and GB for Balıkesir. The chemical profiles of the samples were analyzed using GC/MS, and the Total Ion Chromatograms (TIC) are illustrated in Figures 1 through 4.

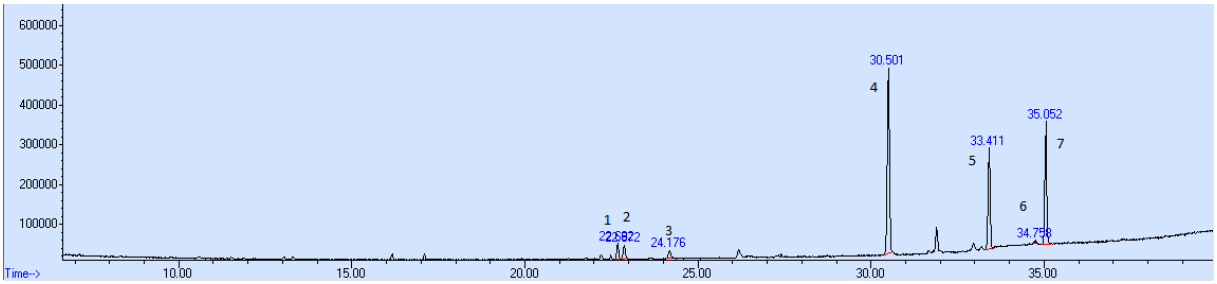

Figure 1. TIC of GK

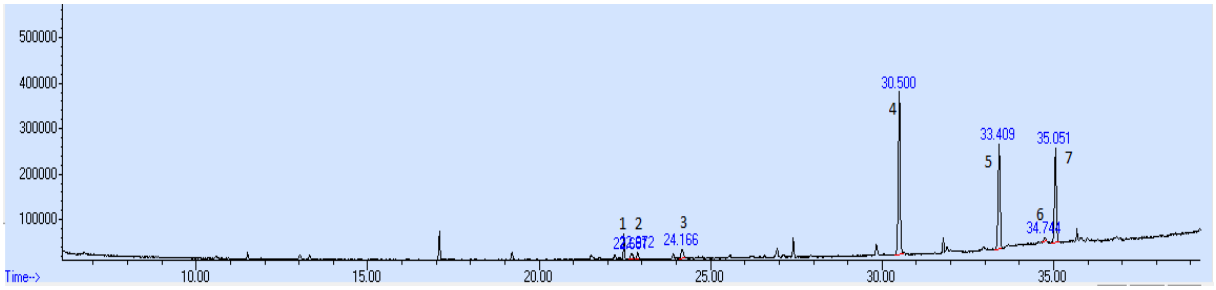

Figure 2. TIC of GE

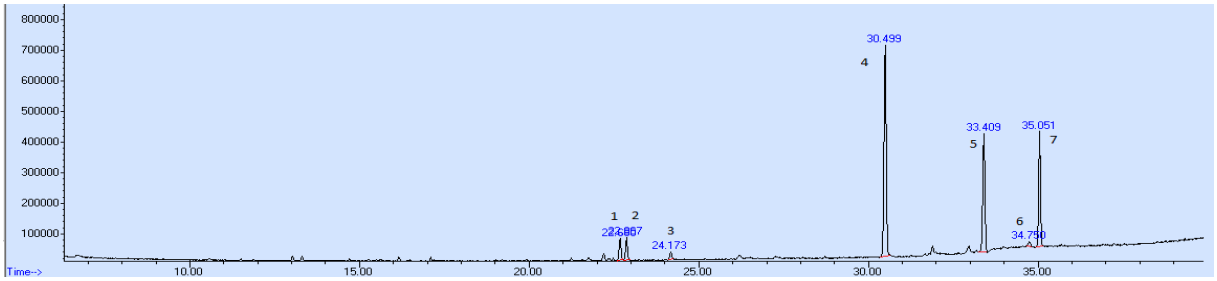

Figure 3. TIC of GA

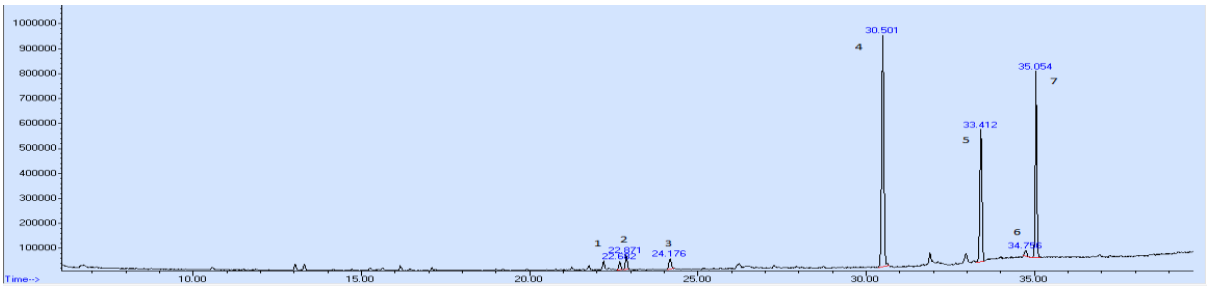

Figure 4. TIC of GB

The identification of individual organosulphur compounds in the samples was performed by comparing their RI values and mass spectra with those documented in the NIST 14 and Wiley libraries. In total, seven organosulfur compounds were identified in the analysed samples (Table 1).

Table 1. Organosulfur Compound Composition of Garlic Extracts from Different Regions of Türkiye.

No	RI[a]	RI[b]	Compound	GK(%)	GE(%)	GA(%)	GB(%)
1	1076	1077	Diallyl disulfide	3.28	1.76	3.93	1.31
2	1097	1097	Allyl(Z)-1-Propenyl disulfide	2.90	1.65	4.34	2.43
3	1141	1143	Allyl methyl trisulfide	2.51	2.42	1.91	1.87
4	1175	1175	3-Vinyl-4H-1,2-dithiin	37.38	37.63	39.82	38.70
5	1217	1217	2-Vinyl-4H-1,3-dithiine	23.53	24.97	24.44	24.43
6	1289	1289	Diallyl trisulfide	1.42	1.99	1.31	1.37
7	1517	1517	Butylhydroxytoluene	20.63	19.59	19.44	22.86
			Total %	91.65	90.01	95.19	92.97

[a]Retention index calculated on HP-5MS column using the homologous series; [b]Literature retention index found in NIST Chemical WebBook.

Among these, 3-Vinyl-4H-1,2-dithiin and 2-Vinyl-4H-1,3-dithiin were identified as the predominant compounds. Previous studies have reported these compounds as dominant in extraction methods, particularly when parameters such as temperature and pH were varied. The specific extraction conditions employed during the process influence the formation of different alliin-derived compounds [9-11]. In contrast, a study conducted on garlic samples collected from various regions of Türkiye, including Kastamonu and Aksaray, employed the Headspace-Gas Chromatography-Mass Spectrometry method to analyze volatile components, revealing diallyl disulphide as the predominant compound present in all samples [12].

The effects of the extracts on benign prostatic hyperplasia (BPH), as well as their cytotoxicity against LNCaP, DU145, and PC3 cell lines, were evaluated. The results are presented in Table 2.

Table 2. The Cytotoxic Activities Against BPH, LNCaP, DU145, and PC3 Cell Lines of Garlic Extracts from Different Regions of Türkiye (IC_{50} μg/mL).

Sample	BPH	LNCaP	DU145	PC3
GK	125.9	34.42	63.05	64.32
GE	77.91	25.28	35.99	37.99
GA	145.5	23.91	72.45	64.06
GB	140.3	48.84	93.70	76.91

The biological activities of extracts with comparable organosulfur content exhibited similar patterns, demonstrating varying degrees of efficacy across all tested cell lines. The most

pronounced cytotoxic activity was observed against the LNCaP cell lines in all samples. Moreover, the reduced cytotoxic in BPH cell lines, relative to other tested cell lines, indicates the potential selectivity of these extracts for targeting prostate cancer. The cytotoxic activity observed in all samples may be attributed to the presence of 3-Vinyl-4H-1,2-dithiin and 2-Vinyl-4H-1,3-dithiin, the principal constituents of the extracts. However, to date, no studies have specifically investigated the cytotoxic activity of these compounds against these particular cell lines. In contrast, the cytotoxic properties of minor components, such as diallyl disulfide and diallyl trisulfide, have been well documented in prostate cancer research. These compounds exert their effects through various mechanisms. In a comparative study, PC-3 prostate cancer cells were compared to noncancerous PNT1A cells, which displayed a greater resistance to cell death induced by diallyl trisulfide. The study reported that phosphorylation of p66Shc at serine 36 and the activation of extracellular signal-regulated kinase 1/2 were significantly lower in PNT1A cells compared to PC-3 cells [13]. Also Kim et al., 2007 reported that the treatment with diallyl trisulfide activates a mitochondria mediated apoptosis pathway in LNCaP, LNCaP-C81 and LNCaP-C4-2 cell lines regardless of their androgen responsiveness. In contrast, normal prostate epithelial cell line (PrEC) displayed markedly greater resistance to apoptosis induced by diallyl trisulfide [14]. The other minor compound diallyl disulfide has been shown to inhibit the proliferation of prostate cancer cells by inducing apoptosis [15]. Further research has demonstrated that diallyl disulfide induces cell cycle arrest at the G2/M transition in PC-3 cells by downregulating CDK1 expression. These findings indicate that diallyl disulfide suppresses the proliferation of prostate cancer cells through cell cycle regulation [16].

3. Conclusion

In conclusion, the current study presented the organosulfur contents and cytotoxic activities of garlic samples provided from different localities of Türkiye against BPH, LNCaP, DU145, and PC3 cell lines. The organosulfur content across all samples exhibited similarity, with 3-Vinyl-4H-1,2-dithiin and 2-Vinyl-4H-1,3-dithiin identified as the predominant compounds. This observation suggests that the employed extraction method was effective for these major compounds, regardless of the sample variations. Furthermore, the cytotoxic activities of the samples demonstrated high levels. The observed reduction in cytotoxic activity within the BPH cell lines, when compared to other cell lines, underscores the potential efficacy of the samples in targeting prostate cancer. Therefore, the findings of this study indicate that the effects of 3-Vinyl-4H-1,2-dithiin and 2-Vinyl-4H-1,3-dithiin compounds on prostate cancer require additional investigation using both in vitro and in vivo methods.

Ethics in Publishing

There are no ethical issues regarding the publication of this study.

Author Contributions

Furkan Kuznek: Preparation of garlic extracts, Recep İlhan-Gökçe Yıldırım Buharalıoğlu: Cytotoxic activity experiments (equal), Ahmet Emir: Analysing the samples, design and coordinating the study, writing the manuscript.

Acknowledgements

This work was supported by Ege University Scientific Research Projects Coordination Unit. Project Number: 29638.

References

[1] Emir, A., Emir C., (2020) Chemical profiles and biological properties of methanol extracts of *Allium pallens* L. from different localities in Turkey, Archives of Biological Sciences, 72(2), 193-201.

[2] Das, S., (2002) Garlic-A natural source of cancer preventive compounds, Asian Pacific Journal of Cancer Prevention, 3, 305-311.

[3] Rose, P., Whiteman, M., Moore, P.K., Zhu, Y.Z., (2005) Bioactive S-alk(en)yl cysteine sulfoxide metabolites in the genus *Allium*: the chemistry of potential therapeutic agents, Natural Product Reports, 22, 351-368.

[4] Stoll, A., Seebeck, E., (1947) Über Alliin, die genuine muttersubstanz des knoblauchöls, Experentia, 3, 114-115.

[5] Virtanen, A.L., Matikkala, E.J., (1959) The Isolation of S-Methylcysteine-sulphoxide and S-n-Propylcysteine-sulfoxide from Onion (*Allium cepa)* and the antibiotic activity of crushed onion. Acta Chemica Scandinavica, 13(9), 1898-1900.

[6] Trio, P.Z., You, S., He, X., He, J., Sakao, K., Hou, D., (2014) Chemopreventive functions and molecular mechanisms of garlic organosulfur compounds, Food & Function, 5(5), 833-844.

[7] Devrim, E., Durak, İ., (2007) Is garlic a promising food for benign prostatichyperplasia and prostate cancer?, Molecular Nutrition & Food Research, 51(11), 1319-1323.

[8] Emir, C., Emir A., (2022) Chemical analysis and enzyme inhibitory activities of essential oil obtained from *Allium proponticum* subsp. *proponticum*, an endemic species, Journal of Research in Pharmacy, 26(3), 574-580.

[9] Zheng, P., Sheng, X., Ding, Y., Hu, Y., (2006) Study of organosulfur compounds in fresh garlic by gas chromatography/mass spectrometry incorporated with temperature-programmable cold on-column injection, Chinese Journal of Chromatography, 24(4), 351-353.

[10] Yu, T.H., Wu, C.M., Liou, Y.C., (1989) Effects of pH Adjustment and subsequent heat treatment on the formation of volatile compounds of garlic, Journal of Food Science, 54(3), 632-635.

[11] Cadwallader, K., Potts, D., Brisske-BeVier, L., Mirarefi, S., (2011) Contribution of volatile sulfur compounds to the characteristic aroma of roasted garlic, ACS Symposium Series, 1068, 137-151.

[12] Akan, S., (2022) Morphological characterisation and volatile analysis of Turkish garlic genotypes, Turkish Journal of Agriculture and Forestry, 46(4), 424–440.

[13] Borkowska, A., Knap, N., Antosiewicz, J., (2013) Diallyl trisulfide is more cytotoxic to prostate cancer cells PC-3 than to noncancerous epithelial cell line PNT1A: A possible role of p66Shc signaling axis, Nutrition and Cancer, 65(5), 711-717.

[14] Kim, Y.A., Xiao, D., Xiao, H., Powolny, A.A., Lew, K.L., Reilly, M.L., Zeng, Y., Wang, Z., Singh, S.V., (2007) Mitochondria-mediated apoptosis by diallyl trisulfide in human prostate cancer cells is associated with generation of reactive oxygen species and regulated by Bax/Bak. Molecular Cancer Therapeutics, 6(5), 1599-1609.

[15] Arunkumar, A., Vijayababu, M.R., Kanagaraj, P., Balasubramanian, K., Aruldhas, M.M., Arunakaran, J., (2005) Growth suppressing effect of garlic compound diallyl disulfide on prostate cancer cell line (PC-3) in vitro. Biological and Pharmaceutical Bulletin 28(4), 740-743.

[16] Arunkumar, A., Vijayababu, M.R., Srinivasan, N., Aruldhas, M.M., Arunakaran, J., (2006) Garlic compound, fiallyl disulfide induces cell cycle arrest in prostate cancer cell line PC-3. Molecular and Cellular Biochemistry, 288(1–2), 107-113.

e-ISSN: 2149-4584

Erzincan University Journal of Science and Technology

EJSAT 2025, 18 (3) 789-798

Research Article

Biological Activities of Two *Stacys* Species: *Stachys thirkei* K. Koch and *Stachys macrantha* (K. Kock) Stearn

Gökçe YILDIRIM BUHARALIOĞLU[1], Recep İLHAN[2], Hasan YILDIRIM[3], Ceren EMİR[4*]

[1]Department of Pharmacology, Faculty of Pharmacy, Ege University, Izmir, Türkiye
[2]Deparment of Biochemistry, Faculty of Pharmacy, Ege University, Izmir, Türkiye
[3] Department of Biology, Faculty of Science, Ege University, İzmir, Türkiye
[4] Department of Pharmacognosy, Faculty of Pharmacy, Ege University, Izmir, Türkiye

Received: 10/03/2025, **Revised:** 02/05/2025, **Accepted:** 07/05/2025, **Published:** 31/12/2025

Abstract

The study aimed to investigate the antioxidant activities of methanol extracts from aerial parts of *Stachys thirkei* and *Stachys macrantha* growing in Eastern Anatolia using the DPPH (1,1- Diphenyl-2-picrylhydrazyl) and ABTS (2,2'-azino-bis(3-ethyl-benzothiazoline-6- sulphonic acid)) methods, as well as their cytotoxic effects on BPH, DU-145, PC-3, and LNCaP cell lines by MTT (3-(4,5-dimethylthiazol-2-yl)-2,5-diphenyltetrazolium bromide) assay. Radical scavenging activities were determined spectrophotometrically, revealing that both species exhibited high antioxidant capacity; however, *S. thirkei* demonstrated relatively higher activity. In the preliminary investigation of potential treatments for prostate cancer, neither species affected the viability of the BPH, DU-145, or PC-3 cell lines. Only the *S. thirkei* extract exhibited a cytotoxic effect on LNCaP cell lines, with an IC_{50} value of 19.25 µg/mL.

Keywords: *Stachys thirkei*, *Stachys macrantha*, antioxidant activity, cytotoxicity

İki *Stacys* Türü Üzerinde Fitokimyasal Çalışmalar: *Stachys thirkei* K. Koch ve *Stachys macrantha* (K. Kock) Stearn

Öz

Çalışmanın amacı, Doğu Anadolu'da yetişen *Stachys thirkei* ve *Stachys macrantha* bitkilerinin toprak üstü kısımlarının metanol ekstrelerinin antioksidan aktivitelerini DPPH (1,1- Difenil-2-pikrilhidrazil) ve ABTS (2,2'-azino-bis(3-etill-benzotiyazolin-6- sülfonik asit)) yöntemleri kullanarak, BPH, DU-145, PC-3 ve LNCaP hücre hatları üzerindeki sitotoksik etkilerini de MTT (3-(4,5-dimetiltiyazol-2-il)-2,5-difeniltetrazolyum bromit) analizi ile araştırmaktır. Radikal süpürücü aktiviteler spektrofotometrik olarak belirlenmiş ve her iki türün de yüksek antioksidan kapasiteye sahip olduğu ortaya çıkmıştır; ancak *S. thirkei* örneği nispeten daha yüksek aktivite göstermiştir. Prostat kanseri için potansiyel tedavilerin ön araştırmasında, iki tür de BPH, DU-145 veya PC-3 hücre hatlarının canlılığını etkilememiştir. Sadece *S. thirkei* ekstresinin LNCaP hücre hatları üzerinde IC_{50}: 19,25 µg/mL değeriyle sitotoksisik etkiye sahip olduğu görülmüştür.

Anahtar Kelimeler: *Stachys thirkei*, *Stachys macrantha*, antioksidan aktivite, sitotoksisite

Corresponding Author: ceren.acir@ege.edu.tr

Cite this Article: Erzincan University Journal of Science and Technology 2025, 18(3) 789-798. https://doi.org/10.18185/erzifbed.1654740

1. Introduction

The genus *Stachys* L. is part of the tribe Lamioideae and the subfamily Stachydeae Dumort, which is the second largest subfamily within the Lamiaceae family. Globally, there are 362 species and 435 taxa within this genus [1], with Türkiye hosting 96 species and 123 taxa. Notably, 67 of these taxa are endemic to Türkiye giving the country an impressive endemism rate of 54% [2]. As such, Türkiye is recognized as one of the most significant gene centers for this genus. *Stachys* species are traditionally utilized as herbal tea and this usage has been known for treating extensive disorders comprising common colds, asthma, stomach diseases, and skin inflammations [3]. Regarding the ethnopharmacological usage of *Stachys*, several researchs have been conducted about their biological effects such as anti-inflammatory activity, cytotoxic, antioxidant, analgesic, and antibacterial [4-7]. The physiological and pharmacological activities described in the literature are closely associated with the rich diversity of secondary metabolite groups found in *Stachys*, which include volatile oils, phenolic acids, flavonoids, lignans, iridoids, diterpenes, and triterpenes [8-11]. Among the phytochemical studies, limited reports have been about *Stachys thirkei* K. Koch and *Stachys macrantha* (K. Kock) Stearn. The antimutagenic effect of ethanolic extracts of *S. thirkei* was tested using the AMES assay [12]. Other research pointed that antioxidant and antimicrobial activities of different extracts of *S. thirkei* [13]. The chemical composition of *S. thirkei* was investigated by high performance liquid chromatography (HPLC) and acteoside, lavandulifolioside, isoscutellarein and chlorogenic acid were detected [14]. As for *S. macrantha*, macranthoside, harpagide, allobetonicoside, ajugol, 8-*O*-acetyl-harpagide, ajugoside and reptoside were isolated from iridoids, lavandulifolioside, verbascoside, leucosceptoside A and martynoside were isolated from phenylpropanoids [15]. In another study, the main iridoids of *S. macrantha* growing in Hungary, harpagoside, harpagide and acetylharpagide, were determined by thin layer chromatography (TLC)-densitometric method. [16]. Moreover, volatile compounds of *S. macrantha* from Türkiye were analyzed by solid phase microextraction (SPME) method coupled with gas chromatography-flame ionization detector (GC-FID) and gas chromatography- mass spectrometry (GC-MS), *α*-pinene, *p*-cymene and carvacrol were the main components [17].

According to data obtained from Cancer Fact&Figures by the American Cancer Society, prostate cancer (PCa) is placed on top of the estimated new cases list of cancer statistics with a rate of 29 %. Strikingly, it is the second leading cause of cancer (after lung cancer with 20 %) with 11 % based on a list of estimated deaths amongst men. Patients with localized PCa have high recovery rates after treatment with prostatectomy and radiotherapy. Androgen deprivation therapy (ADT) is still considered the gold standard therapy for the treatment of locally advanced and metastatic PCa [18]. For patients with metastatic PCa, ADT treatment initially works well but for most patients, treatment resistance occurs inevitably due to the progression of the disease to the more aggressive and lethal stage which is known as castration-resistant PCa [19]. Although overall survival of patients has been improved by the development of new therapeutic options, metastatic castration-resistant PCa is still not curable and unfortunately, patients die within 2-3 years [18, 20-22]. Therefore, it is crucial to develop new therapeutic strategies for

the treatment of the disease and to preserve the patient's quality of life. Interest in phytotherapeutics has increased recently due to their safety and fewer side effects, even though many chemotherapeutic drugs used today are derived from plants. While the cytotoxic effects of *Stachys* species are recognized, particularly owing to their diterpenes and phenolics, research on prostate cancer using PC-3 cell lines has focused solely on the species *S. parviflora* [23] and *S. obtusicrena* [24]. In addition, studies conducted on Iranian *Stachys* species, *S. byzantina*, *S. inflata*, *S.setifera*, *S.persica*, *S.laxa*, *S. trinervis*, *S. subaphylla*, and *S. turcomanica*, evaluated their extracts for cytotoxic effects on various cell lines, including HT-29 (colon carcinoma), CaCo-2 (colorectal adenocarcinoma), T-47D (breast ductal carcinoma), and NIH-3T3 (Swiss Mouse embriyo fibroblast), with the exception of prostate cancer cell lines. The chloroform extract of *S. setifera* demonstrated pronounced cytotoxicity across all tested cell lines [25]. Conversely, the chloroform and ethyl acetate fractions of *S. laxa* and *S. turcomanica* exhibited notable cytotoxic effects specifically on HT-29 and T-47D cell lines [26]. Additionally, the HepG2 (hepatocellular carcinoma) cell line was also investigated, and the hydroalcoholic extract of *S. pilifera* [27] and the dichloromethane extract of *S. circinata* [28] were found to be significantly cytotoxic against this cell line. Polyphenols, found commonly in the *Stachys* genus, play a unique dual role as both antioxidants and pro-oxidants. Their antioxidant properties help reduce the imbalance caused by oxidative stress, while their pro-oxidant effects can induce cytotoxicity in cancer cells. Furthermore, polyphenols can inhibit several neoplastic processes, including cell proliferation, invasion, metastasis, and angiogenesis [29,30]. For that reason, we aimed to search antioxidant and cytotoxic effects of *S. thirkei* and *S. macrantha* from Eastern Anatolia. This is the first report of these two *Stachys* species on BPH (primary prostate epithelial cells), DU145 (prostate epithelial cells), PC3 (prostate adenocarcinoma cells), and LNCaP (human prostate adenocarcinoma cells) cell lines.

2. Materials and Methods

2.1. Chemicals and Reagents

DPPH (1,1- Diphenyl-2-picrylhydrazyl), ABTS (2,2'-azino-bis(3-ethyl-benzothiazoline-6-sulphonic acid)), trolox, methanol, potassium persulfate, and MTT (3-(4,5-dimethylthiazol-2-yl)-2,5-diphenyltetrazolium bromide were purchased from Sigma Aldrich (USA).

2.2. Plant Materials and Extraction

S. thirkei was collected from Pötürge, Malatya on 13.07.2024, and *S. macrantha* was collected from Çıldır, Ardahan on 21.07.2024. Both of them were identified by Prof. Dr. Hasan Yıldırım. Voucher specimens (No: H.Yıldırım 10984, H.Yıldırım 11020, respectively) have been deposited in the Herbarium of the EGE University. The methanol extracts were prepared from the aerial parts of *Stachys* species. Five grams of air-dried, powdered plant material were macerated in 100 mL of methanol three times. The solvent was then removed under reduced pressure using a rotary evaporator (Büchi, Switzerland). The extraction yields were assessed 2.708 for *S. thirkei* and 13.82 for *S. macrantha*, relatively (%, w/w).

2.3. Antioxidant Activity

2.3.1. 1,1- Diphenyl-2-picrylhydrazyl (DPPH) Assay

According to the Blois method [31], methanol extract concentrations ranging from 1 to 1000 ppm were used. After incubating the sample and DPPH solution in the dark for 30 minutes, the absorbance change was measured at 517 nm. Trolox served as the positive control. The IC_{50} values of the extracts were then calculated with three parallels. A UV-visible spectrophotometer (Optima SP-3000 Nano, Japan) was utilized to obtain the absorbance readings.

2.3.2. 2,2'-Azino-bis(3-ethyl-benzothiazoline-6- sulphonic acid) (ABTS) Assay

The blue-green ABTS+· radical was generated by mixing an ABTS solution (7 mM) with a potassium persulfate solution (2.45 mM) and incubating the mixture at room temperature for 16 hours [32]. After the incubation, the ABTS+· solution was diluted with ethanol, and methanol extract was added to this mixture. The combined solution was then incubated at 25°C for 2 hours, after which the absorbance was measured at 734 nm. Trolox was used as the positive control.

2.4. Cell Culture

BPH (Primary Prostate Epithelial Cell line), DU145 (Prostate Epithelial Cells cell line), PC3 (prostatic adenocarcinom cell line), and LNCaP (human prostate adenocarcinoma cell line) were obtained from ATCC and are preserved in liquid nitrogen in our inventory. For cytotoxicity assays, the cells were grown in 100 mm dishes and subcultured until they reached approximately 70 % confluence. The cultures were kept in a humidified incubator at 37°C with 5 % carbon dioxide.

2.5. Cytotoxicity Activity

To assess the IC_{50} values extracts were prepared in DMSO at concentrations of 10, 25, 50, 100, 200 and 400 µg/ml. Cells were first seeded in 96-well culture plates, and cell viability was measured after 24 hours of incubation. After a 48-hour exposure to the extracts, an MTT assay was performed. A 0.5 mg/mL MTT solution was introduced into the wells of the 96-well plate and incubated for 4 hours. Following the incubation, the medium was removed, and 200 µL of DMSO was added to dissolve the formazone crystals. Absorbance was recorded using a microplate reader (Varioskan, Thermo Fisher Scientific, USA) at wavelengths between 570-690 nm, with blank wells (without cells) used to correct for any background absorbance. The IC_{50} values were calculated using regression analysis in GraphPad Prism version 10. The MTT results presented here were obtained from five replicate wells for each condition

2.6. Statistical Analysis

The IC_{50} results were presented as means ± standard errors. ANOVA (One-way analysis ofvariance) followed by Tukey's test was applied to determine differences among. Analyses with *p* values less than 0.05 were considered statistically significant.

3. Results and Discussion

The antioxidant activity results of methanol extracts were given in Table 1. In both DPPH and ABTS analyses, the IC_{50} values of *S. thirkei* are lower than those of *S. macrantha*, indicating that the antioxidant capacity of *S. thirkei* extract surpasses that of *S. macrantha* extract. In the literature, a study, along with *S. thirkei* from Düzce, presented DPPH and ABTS activities for hydrolyzable and extractable phenolics of plant extract. The phenolics' DPPH activity values ranged from 39.97±0.88 to 172.16±9.78 µmol Trolox/g, while ABTS results were calculated between 78.52±1.99 to 198.87±1.25 µmol Trolox/g [33]. In another study, the DPPH activity was investigated in three different, chloroform, n-hexane, and methanol extracts, of the *S. thirkei* plant collected from Tekirdağ, and methanol extract was found to be most active with a value of 0.039118±0.005585 mg ascorbic acid/mg extract [13]. As for *S. macrantha*, researchers collected samples from Gümüşhane, and among the diverse samples, the methanol extract showed potent activity with 23.62±0.1 mg trolox/ g extract for DPPH; 49.99±1.6 mg trolox/ g extract for ABTS [34]. The findings from this study were inconsistent with the results obtained from the abovementioned *Stachys* species due to differences in collection location and timing. Numerous studies have shown that geographical variations can lead to changes in the composition of phytochemicals.

Table 1. Antioxidant activities of methanol extracts of *S. thirkei* and *S. macrantha*

Methanol extracts	DPPH (IC_{50} mg/mL)	ABTS (IC_{50} mg/mL)
S. thirkei	0.675 ± 0.48^{a}	0.893 ± 0.68^{a}
S. macrantha	1.052 ± 0.92^{a}	1.570 ± 0.57^{a}
Trolox*	0.035 ± 0.07^{b}	0.028 ± 0.03^{b}

Superscripts indicate significant differences in the studied extracts ($P<0.05$), * positive control for antioxidant tests.

This study investigated the cytotoxic effects of two *Stachys* species on four cancer cell lines: BPH, DU-145, PC-3, and LNCaP for prostate cancer. The methanol extracts from *S. thirkei* and *S*. macrantha showed no activity against the BPH, DU-145, and PC-3 cell lines. However, S. *thirkei* exhibited cytotoxic effects on the LNCaP cell line, with an IC_{50} value of 19.25 µg/mL across varying concentrations in Figure 1. This situation may correlate with not only the stronger antioxidant activity of *S. thirkei* but also with its iridoid and phenylpropanoid contents. It has been reported that acteoside, verbascoside common phenylpropanoid glycoside, has inhibitory effect on prostate specific antigen level [35]. Previously, Serbetci et al. reported that

verbascoside was found to major compound in *S. thirkei* by HPLC-ESI/MS [14]. Additionally, different species *S. parviflora* has been studied for isolation of tanshinones and their cytotoxicity on MCF-7 and PC-3 cells. The results pointed that 1-hydroxy-tanshinone IIA induced DNA fragmentation in PC-3 cells [23]. Also, the endemic *S. obtusicrena* from Iran was analyzed for its antitumor activity in PC-3 cells. The methanol extract of this plant reduced cell viability by 98.3 ± 21.0 % at a concentration of 100 µg/mL [24].

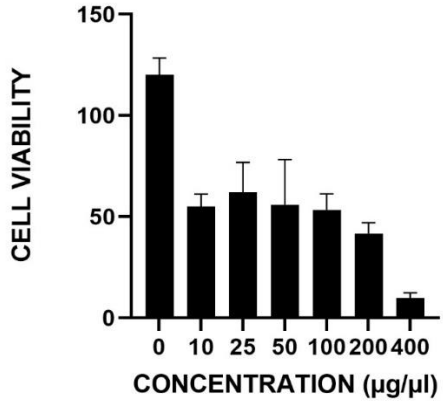

Figure 1. Cell viability of LNCaP against *S. thirkei* extract

4. Conclusion

In the current study, the antioxidant activities of two *Stachys* species growing in Eastern Anatolia were investigated. Both methanol extracts of species exhibited antioxidant activity, with *S. thirkei* showing relatively stronger effects and several studies have reported that oxidative stress are related to prostate cancer strictly. Furthermore, cytotoxic activity experiments conducted on prostate cancer cells revealed that the *S. thirkei* species collected from Malatya had cytotoxic effects on the LNCaP cell line. Consequently, this research data contributes to the limited number of researches on these two species and prostate cancer treatment at the same time, however further isolation and mechanisms of biological activity investigations are needed.

Ethics in Publishing

There are no ethical issues regarding the publication of this study.

Author Contributions

Gökçe YILDIRIM BUHARALIOĞLU-Recep İLHAN: Cytotoxicity assay, Hasan YILDIRIM: Plant collection and identification, Ceren EMİR: analyzing experiments, writing and editing manuscript.

Acknowledgements

This study was not supported by any project.

References

[1] POWO (2022). Onward (continuously updated). Stachys L. Plants of the World Online. Facilitated by the Royal Botanic Gardens, Kew. Available from: https://powo.science.kew.org/taxon/ urn: lsid:ipni.org:names:325931-2 [29.03.2022].

[2] Güner, Ö., Özdöl, T., Yıldırım, H. (2023) A New Rupicolous Species from West of Türkiye: *Stachys cuhacioglui* (Lamiaceae), Türler ve Habitatlar, 4(2): 98–109.

[3] Tomou, E. M., Barda, C., Skaltsa, H. (2020) Genus *Stachys*: A review of traditional uses, phytochemistry and bioactivity, Medicine, 7:63-136.

[4] Háznagy-Radnai, E., Rethy, B., Czigle, S., Zupko, I., Weber, E., Martinek, T., Falkay, G.Y., Máthé, I. (2008) Cytotoxic activities of *Stachys* species, Fitoterapia, 79: 595-597.

[5] Tundis, R., Peruzzi, L., Menichini, F. (2014) Phytochemical and biological studies of *Stachys* species in relation to chemotaxonomy: A review, Phytochemistry, 102: 7-39.

[6] Khanavi, M., Sharifzadeh, M., Hadjiakhoondi, A., Shafiee, A. (2005) Phytochemical investigation and anti-inflammatory activity of aerial parts of *Stachys byzantina* C. Koch., Journal of Ethnopharmacology, 97: 463-468.

[7] Sadeghi, H., Mansourian, M., Kokhdan, E. P., Salehpour, Z., Sadati, I., Abbaszadeh-Goudarzi, K., Asfaram, A., Doustimotlagh, A. H. (2020) Antioxidant and protective effect of *Stachys pilifera* Benth against nephrotoxicity induced by cisplatin in rats, Journal of Food Biochemistry, 44: e13190.

[8] Marin, P., Grayer, R., Grujic-Jovanovic, S., Kite, G., Veitch, N. (2004) Glycosides of tricetin methyl esters as chemosystematic markers in *Stachys* subgenus *Betonica*, Phytochemistry, 65: 1247-1253.

[9] Karioti, A., Bolognesi, L., Vincieri, F. F., Bilia, A. R. (2010) Analysis of the constituents of aqueous preparations of *Stachys recta* by HPLC-DAD and HPLC-ESI-MS, Journal of Pharmaceutical and Biomedical Analysis, 53: 15-23.

[10] Meremeti, A., Karioti, A., Skaltsa, H., Heilmann, J., Sticher, O. (2004) Secondary metabolites from *Stachys ionica,* Biochemical Systematical Ecology, 32: 139-151.

[11] Piozzi, F., Bruno, M. (2011) Diterpenoids from roots and aerial parts of the genus *Stachys*, Records of Natural Products, 5: 1-11.

[12] Rasgele, P. G., Dulger, G. (2021) Chemical Compositions and Antimutagenic Effects of Ethanolic Extracts of *Stachys thirkei* and *Stachys annua* subsp. *annua* using the Ames Assay, Pharmaceutical Chemistry Journal, 54(12): 1255-1262.

[13] Toplan-Gulsoy, G., Taskin, T., Kara, E. M., Genç, G. E. (2021) Antioxidant and antimicrobial activities of various extracts from *Stachys cretica* subsp. *bulgarica* Rech.f., *Stachys byzantina* K. Koch and *Stachys thirkei* K. Koch., Istanbul Journal of Pharmacy, 51(3): 341-347.

[14] Serbetci, T., Karioti, A., Akalın, E., Bilia, A. R. (2012) HPLC-DAD/ESI/MS analyses of aqueous preparations from *Stachys thirkei* K. Koch and quantification of major phenolic components, Planta Medica, 78(11): 1222.

[15] Calıs, I., Basaran, A. A., Saracoglu, I., Sticher, O. (1992) Iridoids and phenylpropanoid glycosides from *Stachys macrantha*, Phytochemistry, 31(1): 167-169.

[16] Háznagy-Radnai, E., Czigle, S., Janicsák, G., Máthé, I. (2006) Iridoids of *Stachys* species growing in Hungary, Journal of Planar Chromatography-Modern TLC, 19(109): 187-190.

[17] Renda, G., Bektas, N. Y., Korkmaz, B., Çelik, G., Sevgi, S., Yayli, N. (2017) Volatile constituents of three *Stachys* L. species from Turkey, Marmara Pharmaceutical Journal, 21(2): 278-285.

[18] Luef, B., Handle, F., Kharaishvili, G., Hager, M., Rainer, J., Janetschek, G., Hruby, S., Englberger, C., Bouchal, J., Santer, F. R., Culig, Z. (2016) The AR/NCOA1 axis regulates prostate cancer migration by involvement of PRKD1, Endocrine-Related Cancer, 23(6): 495–508.

[19] Kulasegaran, T., Oliveira, N. (2024) Metastatic Castration-Resistant Prostate Cancer: Advances in Treatment and Symptom Management, Current Treatment Options in Oncology, *25*, 914–931.

[20] Davey, R. A., Grossmann, M. (2016) Androgen Receptor Structure, Function and Biology: From Bench to Bedside, The Clinical Biochemist Reviews, 37(1): 3-15.

[21] Shafi, A. A., Yen, A. E., Weigel, N. L. (2013) Androgen receptors in hormone-dependent and castration-resistant prostate cancer, Pharmacology & Therapeutics, 140(3): 223–238.

[22] Sheahan, A. V., Ellis, L. (2018) Epigenetic reprogramming: A key mechanism driving therapeutic resistance, Urologic Oncology: Seminars and Original Investigations, 36(8): 375–379.

[23] Shakeri, A., Hafezian, T., Kúsz, N., Hohmann, J., Boozari, M., Mottaghipisheh, J., Emami, SA., Tayarani-Najaran, Z., Asili, J. (2022) Cytotoxicity, apoptosis inducing

activity and Western blot analysis of tanshinone derivatives from *Stachys parviflora* on prostate and breast cancer cells, Molecular Biology Reports, 49(9): 8251-8258.

[24] Emami, S. A., Kheshami, S., Ramazani, E., Akaberi, M., Iranshahy, M., Kazemi, S. M., Tayarani-Najaran, Z. (2019) Cytotoxic Activity of Thirteen Endemic and Rare Plants from Chaharmahal and Bakhtiari Province in Iran, Iranian Journal of Pharmaceutical Research, 18(4): 1912-1920.

[25] Ostad, S. N., Vazirian, M., Manayi, A., Hadjiakhoondi, A., Khanavi, M. (2014) Comparison of cytotoxic activity of some Iranian *Stachys* spp. extracts on different cancer cell lines, Research Journal of Pharmacognosy, 1(2): 23-28.

[26] Khanavi, M., Manayi, A., Lotfi, M., Abbasi, R., Majdzadeh, M., Ostad, S. N. (2012) Investigation of Cytotoxic Activity in Four *Stachys* species from Iran, Iranian Journal of Pharmaceutical Research, 11(2): 589-593.

[27] Barmoudeh, Z., Ardakani, M. T., Doustimotlagh, A. H., Bardania, H. (2022) Evaluation of the Antioxidant and Anticancer Activities of Hydroalcoholic Extracts of *Thymus daenensis* Čelak and *Stachys pilifera* Benth, Journal of Toxicology, 924265.

[28] Slimani, W., Maioli, M., Cruciani, S., Zerizer, S., Santaniello, S., Kabouche, Z., Coradduzza, D., Chessa, M., Fancello, S., Migheli, R., Serra, P. A., & D'hallewin, G. (2023) Antioxidant, Anti-Inflammatory and Anti-Proliferative Properties of *Stachys circinata* on HepG2 and MCF7 Cells, Plants, 12(12), 2272.

[29] Jassbi, A. R., Miri, R., Asadollahi, M., Javanmardi, N., Firuzi, O. (2013) Cytotoxic, antioxidant and antimicrobial effects of nine species of woundwort (*Stachys*) plants, Pharmaceutical Biology, 52(1), 62–67.

[30] Lachowicz-Wiśniewska, S., Pratap-Singh, A., Kapusta, I., Kruszyńska, A., Rapak, A., Ochmian, I., Cebulak, T., Żukiewicz-Sobczak, W., & Rubiński, P. (2022) Flowers and Leaves Extracts of *Stachys palustris* L. Exhibit Stronger Anti-Proliferative, Antioxidant, Anti-Diabetic, and Anti-Obesity Potencies than Stems and Roots Due to More Phenolic Compounds as Revealed by UPLC-PDA-ESI-TQD-MS/MS, Pharmaceuticals, 15(7), 785.

[31] Blois, M. S. (1958) Antioxidant determinations by the use of a stable free radical, Nature, 181, 1199-1200.

[32] Re, R., Pellegrini, N., Proteggente, A., Pannala, A., Yang, M., Rice-Ewans, C. (1999) Antioxidant activity applying an improved ABTS radical cation decolorization assay, Free Radical Biology&Medicine, 26(9): 1231-1237.

[33] Aydın, E., Goc-Rasgele, P., Dulger, G. (2022) First Report on Bio-accessibility, Anti-oxidant Activity and Total Phenolic Compounds From *Stachys thirkei* C. Koch Using A

Simulated In Vitro Digestion System, Journal of Advanced Research in Natural and Applied Sciences, 8(2): 188-200.

[34] Özcan, K., Acet, T. (2022) *Stachys macrantha* (K.Koch) Stearn'ın Biyolojik Aktivitesinin Belirlenmesi, Bitlis Eren University Journal of Science, 11(1): 156-163.

[35] Marcoccia, D., Georgiev, M. I., Alipieva, K. I., Lorenzetti, S. (2014) Inhibition of the DHT-induced PSA secretion by *Verbascum xanthophoeniceum* and *Serenoa repens* extracts in human LNCaP prostate epithelial cells, Journal of Ethnopharmacology, 155(1): 616-625.

e-ISSN: 2149-4584

Erzincan University Journal of Science and Technology

EJSAT 2025, 18 (3) 799-816

Research Article

Investigation of Thermal Degradation Kinetics of Polylactide-Perlite Composites

Sıla Gümüştaş*, Nazlı Gül Aksoy Bodu

Ege University, Faculty of Science, Chemistry Department, Bornova/Izmir, 35100, Türkiye

Received: 11/03/2025, **Revised:** 04/06/2025, **Accepted:** 18/09/2025, **Published:** 31/12/2025

Abstract

In this study, the thermal degradation behavior and kinetics of biodegradable and biocompatible polylactide were investigated by preparing composites with low-cost perlite at various ratios under an inert atmosphere. Polylactide (PLA) was characterized with FTIR, ^{1}H-NMR, ^{13}C-NMR, GPC and TGA after being synthesized with ring-opening polymerization in the presence of tin octoate. The number average molecular weight (Mn) of the synthesized polymer was determined to be 20,091 g/mol. PLA/perlite composites were prepared with the method of solvent casting, by mixing the synthesized PLA in ratios of 10%, 20% and 40% with perlite. The structure of the composites was characterized by FTIR, while their thermal properties were analyzed using TGA. The PLA/perlite (60/40) composite exhibited an increase in degradation temperature of approximately 35 °C compared to pure PLA. The thermal degradation kinetics of the polymeric and composite material was investigated at different heating rates (5-10-15 and 20 °C/min) with thermogravimetric analysis using the Flynn-Wall-Ozawa, Tang and Kissinger methods. The thermal degradation activation energies were determined as 114.59 kJ/mol, 112.06 kJ/mol and 124.12 kJ/mol respectively. These results highlight the potential of PLA/perlite composites as cost-effective and thermally stable alternatives for sustainable material applications.

Keywords: Polylactide, perlite, biodegradable polymers composite, thermal degradation kinetics

Polilaktit-Perlit Kompozitlerinin Termal Bozunma Kinetiğinin İncelenmesi

Öz

Bu çalışmada; biyobozunur ve biyouyumlu olan polilaktitin, düşük maliyetli perlit ile farklı oranlarda kompozitleri hazırlanarak inert atmosferde termal bozunma davranışı ve kinetiği incelendi. Polilaktit, (PLA), kalay oktoat varlığında halka açılma polimerizasyonuyla sentezlenerek; FTIR, ^{1}H-NMR, ^{13}C-NMR, GPC ve TGA ile karakterize edildi. Polimerin sayı ortalama moleküler ağırlığı (Mn) 20091 g/mol olarak bulundu. Sentezlenen PLA, %10, %20 ve %40 oranlarında perlit ile karıştırılarak çözgen uçurma yöntemiyle PLA/perlit kompozitleri hazırlandı. Kompozitlerin yapısı FTIR ile karakterize edilirken termal özellikleri TGA ile incelendi. PLA/perlit (60/40) kompoziti, saf PLA'ya kıyasla yaklaşık 35 °C daha yüksek bir bozunma sıcaklığı göstermiştir. Polimer ve kompozit malzemenin termal bozunma kinetiği farklı ısıtma hızlarında (5-10-15 ve 20 °C/dk) termogravimetrik analiz ile Flynn-Wall-Ozawa, Tang ve Kissinger metotları ile incelendi. Termal bozunma aktivasyon enerjileri sırasıyla 114,59 kJ/mol, 112,06 kJ/mol ve 124,12 kJ/mol olarak bulundu. Bu sonuçlar, PLA/perlit kompozitlerinin sürdürülebilir malzeme uygulamaları için ekonomik ve termal olarak kararlı alternatifler olma potansiyelini vurgulamaktadır.

Anahtar Kelimeler: Polilaktit, perlit, biyobozunur polimer kompoziti, termal bozunma kinetiği

Corresponding Author: sila.gumustas@ege.edu.tr

Cite this Article: Erzincan University Journal of Science and Technology 2025, 18(3) 799-816. https://doi.org/10.18185/erzifbed.1655686

1. Introduction

In the modern era, the demand for bio-based polymers has increased significantly with the impact of adopting the cyclical economic model, environmental issues and rising energy prices [1, 2]. These polymers offer environment-friendly solutions which may serve as a substitute for the oil-based alternatives and they have a widespread area of usage in numerous industries such as textile, food, cosmetics, construction and medicine [3]. Especially polylactide (PLA) comes to the forefront among the bio-based polymers thanks to its availability of being extracted from reliable sources, its biocompatible structure and its biodegradable thermoplastic features [4]. Previous studies indicate that PLA has a broad spectrum of usage, including medicine carriage systems, packaging materials, fibers and other applications. These studies also indicate that each newly examined property contributes to environmental protection goals [5]. However, there are still studies required for improving some features of PLA such as mechanical endurance, thermal stability, gas barrier feature, solvent resistance and flame retardant performance [6].

In order to increase the performance of polymers, either chemical or physical methods can be applied. The chemical methods comprise the modification of the polymer structure with functional groups and these methods may provide significant enhancements in the performance of the polymer. However, these kinds of modifications are strongly dependent on the synthesis step and they might require complex procedures [7, 8]. On the other hand, in physical methods, the addition of inorganic particulates to the polymer by using various techniques may improve the stability and other functional features of the materials [9]. In this context, the composite materials obtained by adding the natural backfill materials to the biodegradable polymers are remarkable in terms of their application fields, thanks to their environment-friendly and cost-friendly nature. The performance of polymer composites containing minerals are affected by numerous characteristic factors such as the size, shape and addition amount of the particulates [10-14.]. Perlite, which is a natural clay, is used in many fields such as insulation products, paints, cement and plaster coatings, pharmaceuticals, dental materials, cleaning agents, soil and water filtration applications. Also, it has been utilized as an alternative inorganic filling agent in polymeric composite studies [15-21]. In one of their studies Tian and Tagaya prepared PLA/perlite and PLA/montmorillonite (MMT) composites with the methods of melt extrusion and solvent casting, and investigated the effects of organic/inorganic ratio and types of inorganic compounds on the characterization of the materials [6]. Together with the mathematical models applied, the analysis of the thermal degradation kinetics of a material may provide detailed information about the kinetic parameters and mechanisms related to the process, and it may enable the development of applications regarding the relevant product [22, 23]. Thermogravimetric analysis (TGA) is a widely used and reliable technique for investigating thermal degradation kinetics [24, 25]. While there are isothermal or non-isothermal techniques which can be used in the calculation of the activation energy, the methods without isoconversional models, especially the Flynn-Wall-Ozawa (FWO) method has become one of the most recognized and preferred methods, since it provides high accuracy and reliability in the thermal degradation analysis of solid materials. This method is being used frequently by many researchers [25-28].

Polylactide has a more sensitive thermal characteristic above the melting heat, especially during the process. This situation can cause a limitation on the number of application fields for PLA and various challenges encountered during the production process. Therefore, the new studies that are carried out for the purpose of extending the application fields of PLA and decreasing the production costs of it by increasing the thermal stability of PLA are quite remarkable. So far there is no record of a study in the literature which addresses the thermal degradation kinetics of PLA/perlite composites. Therefore, among various inorganic fillers, perlite was chosen due to its natural abundance, low cost, lightweight structure, and its potential to improve thermal properties without significantly affecting the biodegradability of PLA. In this paper, polylactide was synthesized and characterized by FTIR, ^{1}H-NMR, GPC and TGA analysis. Polymer composites were prepared at different PLA/perlite ratios by solvent casting method. Then the optimum polymer/perlite ratio was determined according to the increase in thermal character. The thermal degradation kinetics studies of PLA/Perlite composite were investigated employing Flynn-Wall-Ozawa, Tang and Kissinger process.

2. Material and Methods

2.1 Materials

All reactions and manipulations were carried out using conventional schlenck tube techniques. The L-lactide (98%) with m.p. 93 °C was obtained from Alfa Aesar. It was purified by recrystallization three times from dry ethyl acetate, dried under vacuum and kept under argon. It was stored at 4 °C. Tin 2-ethylhexanoate (95%) was purchased from Sigma-Aldrich, and was used without further purification. Commercial grade dichloromethane, chloroform and toluene (Sigma-Aldrich) were used without any purification. Perlite was obtained from Genper Expanded Perlite Industry Business Co. (Turkey). Before use, it was dried in a vacuum oven and ground then the particles passed through a 63-micron sieve were used.

2.2 Characterization techniques

FTIR spectra were taken with a PerkinElmer Spectrum Two FT-IR Spectrometer with ATR attachment. ^{1}H-NMR (400 MHz) and ^{13}C NMR (100 MHz) spectra were recorded in $CDCl_3$ containing TMS as an internal standard, using a Varian AS-400 spectrometer. Chemical shifts are reported in ppm. J values were given in Hz. Thermal analysis of polymer and composites were carried out using PerkinElmer Pyris 1 TG/DTA in the temperature range of 25-600 °C at the different rate (5-10-15-20 °C/min) under nitrogen flow (100mL/min). Molecular weight (M_n and M_w) of synthesized polymers were determined by gel permeation chromatography (GPC) on a Hewlett-Packard (HP) HPLC system with a differential refractometer detector. THF served as the eluent at a flow rate of 1.0 mL/min. The molecular weights and polydispersities were reported versus monodisperse polystyrene standard.

2.3 Polymerization of L-lactide (LLA)

Purified L-lactide was added in a schlenk tube. It was dried for half an hour under high vacuum (5 mmHg) at room temperature. Then, the tin (II) ethylhexanoate was added into schlenk

keeping with the monomer to initiator ratio at 100. Polymerizations were carried out under 130 °C and 8 h under in inert atmosphere [31]. At the end of the reaction time, the schlenk was immersed quickly in liquid nitrogen to stop the polymerization. The obtained products were dissolved in dichloromethane and precipitated in large amount of methanol. The precipitated polymers were dried at room temperature in vacuum oven for 24 hours. The polymers were characterized by using FTIR, ^{1}H NMR, ^{13}C NMR, GPC and TG methods.

2.4 Preparation of PLA/perlite composites

Polymer composites were prepared using solvent casting method, with a polymer/additive ratio of as 90/10, 80/20, 60/40 (w/w). Firstly, the predetermined amount of PLA was solved in chloroform for about an hour. Then, the determined amount of perlite additive was added to the polymer solution. Then, the mixture was stirred for about 24 hours in a closed beaker with the aid of a magnetic stirrer, and then the solvent was evaporated for one day at room temperature. The product was dried in a vacuum oven at 45 °C for 24 hours.

2.5 Thermal degradation kinetic methods

Dynamic thermogravimetric methods are widely employed in the investigation of polymer degradation processes and play an important role in elucidating the underlying mechanisms [32-34].

The rate of solid-state, non-isothermal decomposition reactions is commonly expressed using an Arrhenius-type equation, which correlates the decomposition rate with the activation energy and temperature through an exponential function, as presented in Equation (1). This equation is the fundamental expressions of analytical methods to calculate kinetic parameters on the basis of TG data.

$$\frac{d\alpha}{dT} = \left(\frac{A}{\beta}\right) exp\left(\frac{-E}{RT}\right) f(\alpha) \quad (1)$$

where A is the pre-exponential factor (min^{-1}), assumed to be independent of temperature, E is the activation energy (kJ/mol), T is the absolute temperature (K), and R is the gas constant (8.314 J mol^{-1} K^{-1}).

By rearranging Equation 1 and integrating both sides of the equation, the following equation (2) is obtained:

$$g(\alpha) = \left(\frac{A}{\beta}\right) \int_{T_0}^{T} exp\left(\frac{-E}{RT}\right) dT = \left(\frac{AE}{\beta R}\right) p(u) \quad (2)$$

$$p(u) = \int_{\infty}^{u} -\left(\frac{e^{-u}}{u^2}\right) du \text{ and } u = \frac{E}{RT}$$

There are several methods based on the basic rate equation to understand the thermal degradation kinetics process from TGA and DTG data. In this study, the thermal degradation activation energy (E) value of the PLA/perlite composite was calculated using the Flynn-Wall-Ozawa, Kissinger and Tang integral methods, which are integral isoconversion methods.

2.5.1 Flynn-Wall-Ozawa Process

This method, which is isoconversional, is used to determine the activation energy, which is a function of the degree of conversion, without knowing the reaction mechanism. The temperatures corresponding to the constant values obtained from the thermograms taken at different heating rates are measured and the calculation is made using the equation (1) [35, 36] below:

$$log\beta = log\left[\frac{AE}{g(\alpha)R}\right] - 2.315 - \frac{0.457E}{RT} \quad (1)$$

The logarithmic expression can also be written by converting it to the natural logarithm:

$$ln\beta = ln\frac{AE}{g(\alpha)R} - 5.331 - 1.052\left(\frac{E}{RT}\right)$$

where T is the absolute temperature, β is the heating rate, E is the activation energy, A is the pre-exponential factor (min^{-1}), α is the conversion degree and R is the universal gas constant (8.314 J/K mol). Plotting ln (β) against 1/T should give straight lines and its slope is directly proportional to the activation energy (-E/R).

2.5.2 Kissenger process

The Kissinger method, which is another non-isothermal kinetic method independent of the reaction mechanism, was used to calculate the activation energy. The activation energy for the Kissinger method can be determined by the following equation (2) [37]:

$$ln\left(\frac{\beta}{T_{max}^2}\right) = \left\{ln\frac{AR}{E} + ln[n(1-\alpha_{max})^{n-1}]\right\} - \frac{E}{RT_{max}} \quad (2)$$

Here, β represents the heating rate; T_{max} is the temperature at the maximum degradation point in the DTG thermogram; α_{max} denotes the maximum conversion rate; and n is the reaction order. The activation energy (Ea) is calculated from the slope of the plot of $\ln(\beta/T^2_{max})$ versus 1/T.

2.5.3 Tang Method

Tang proposed a modified form of Equation (2) to enhance the accuracy of the integral temperature approach. This approach, known as the Tang method, can be expressed as follows [38]:

$$ln\left(\frac{\beta}{T^{1.894661}}\right) = ln\left(\frac{AE}{Rg(\alpha)}\right) + 3.635041 - 1.894661\ lnE - \frac{1.001450E}{RT} \quad (3)$$

A graph is plotted between $\ln(\beta/T^{1.894661})$ and 1/T, and the activation energy (E) is determined from the slope of the graph as (-1.001450E/R).

3. Results and Discussion

3.1 Characterization of the PLA and PLA/perlite composite

Polylactide was synthesized by coordination-insertion ring opening polymerization reaction of L-lactide with tin(II) 2-ethylhexanoate in bulk medium at 130 °C, 8 h and monomer/initiator ratio was 100. The general polymerization reaction scheme was given in Scheme 1.

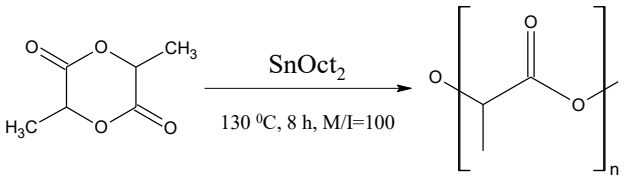

Scheme 1. The general polymerization scheme for PLA initiated by $SnOct_2$

The FTIR spectrum of PLA can be seen at Figure 3.1. The peaks at 2998 cm^{-1} and 2950 cm^{-1} are belong to the C–H stretching vibration in polymer. The characteristic band at 1752 cm^{-1} corresponds to the C=O bond stretching. The absorption peaks at 1183 cm^{-1} and 1081 cm^{-1} are associated with the C–C and C–O–C stretching vibrations, respectively. In the ^{1}H-NMR (400 MHz, $CDCl_3$) spectrum, the peaks at δ 1.57 ppm (d, 3H, J = 6.8 Hz) and 5.17 ppm (q, 1H, J = 6.8-7.2-14.0 Hz) correspond to the –C**H**$_3$ and C**H**–groups, respectively (Figure 3.1-b). The ^{13}C NMR spectrum of the polymer is also shown in Figure 3.1(c). ^{13}C-NMR (100 MHz, $CDCl_3$) signals at 169.55 ppm, 68.98 ppm and 16.61 ppm assigned to the O**C**OCH–, –CO**C**HCH$_3$ and –CH**C**H$_3$– groups, respectively. The number average molecular weight (Mn) of synthesized polymer was found as 20,091 g/mol (PDI=2.13) by GPC. The thermal character of the polymer was investigated by thermogravimetric analysis (TGA), and the thermogram recorded at a heating rate of 10 °C/min under a nitrogen atmosphere is presented at Figure 3.1(d). The degradation of PLA occurs in a single step, with the degradation temperature range and the maximum degradation temperature determined to be 170–275 °C and approximately 250 °C, respectively. The 4% residue observed at 600 °C is likely due to the metal compound used in the initiator.

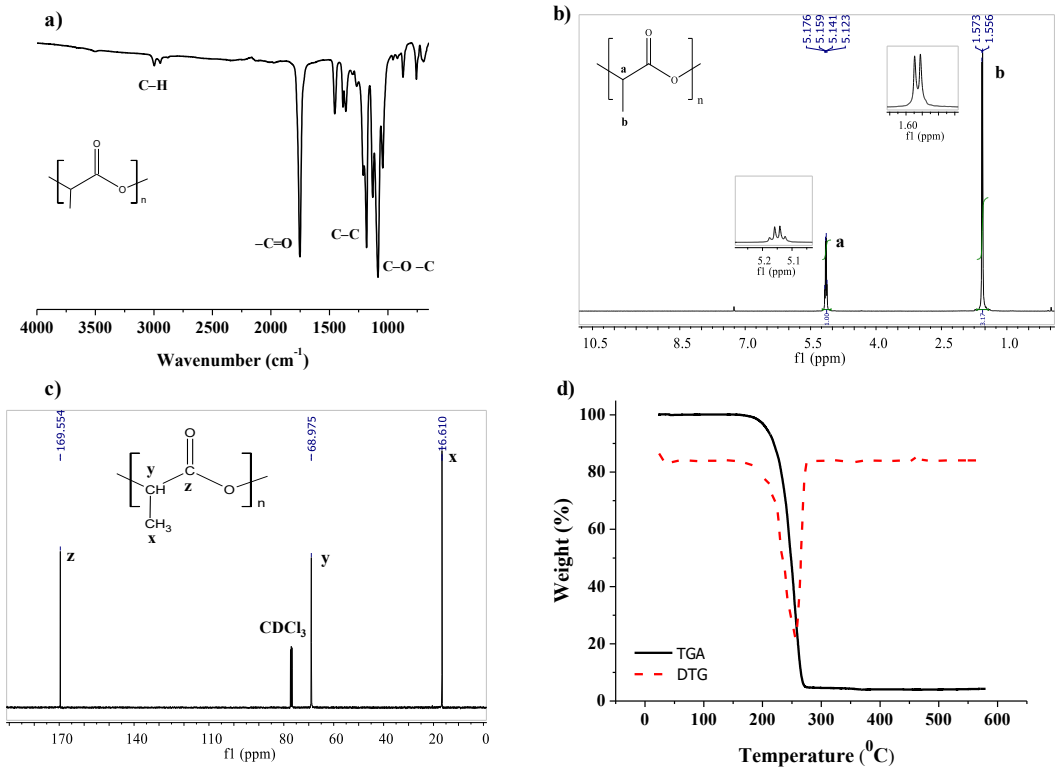

Figure 3.1 FTIR (a), ^{1}H-NMR (b) and ^{13}C-NMR (c) spectrum, TGA and DTG curve (d) of polylactide.

In the FTIR spectrum of perlite (Figure 3.2), a characteristic broad Si–O–M (M=Si or Al) band was observed at 1015 cm^{-1}. The peak at 788 cm^{-1} was assigned to the symmetric stretching vibration of the Si–O bond [39, 40]. The TGA analysis of perlite, performed under a nitrogen atmosphere at a heating rate of 10 °C/min, is shown in Figure 3.2 (b). It was determined that the degradation of perlite occurred slowly, and the remaining weight was 96% at 600 °C.

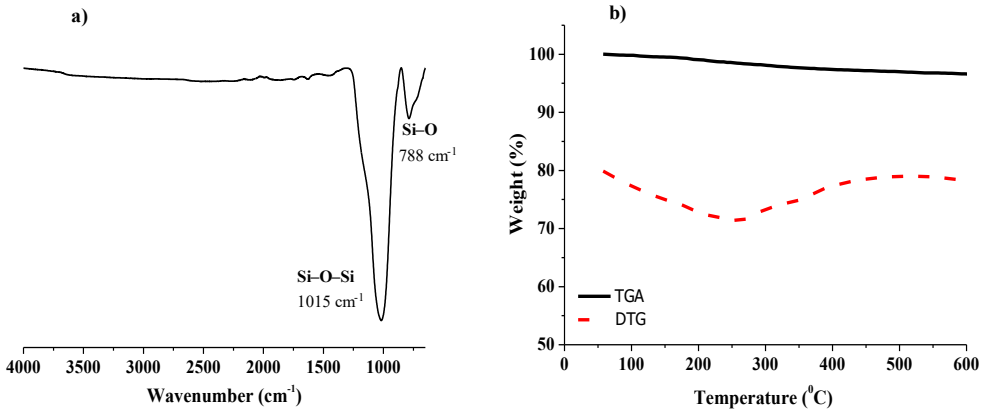

Figure 3.2 FTIR spectrum (a) and TG and DTG curve (b) of perlite.

The FTIR spectra of Perlite/PLA composites with 10%, 20%, and 40% perlite content are presented comparatively in Figure 3.3(a). The characteristic C–H and C=O stretching vibration peaks of the polymer are observed at approximately 2900 cm^{-1} and 1750 cm^{-1}, respectively. The broad band between 1100 cm^{-1} and 950 cm^{-1} arises from the overlap of the C–O–C bond present in the polymer structure and the Si–O–Si bond in perlite. This observation confirms the successful formation of the composite.

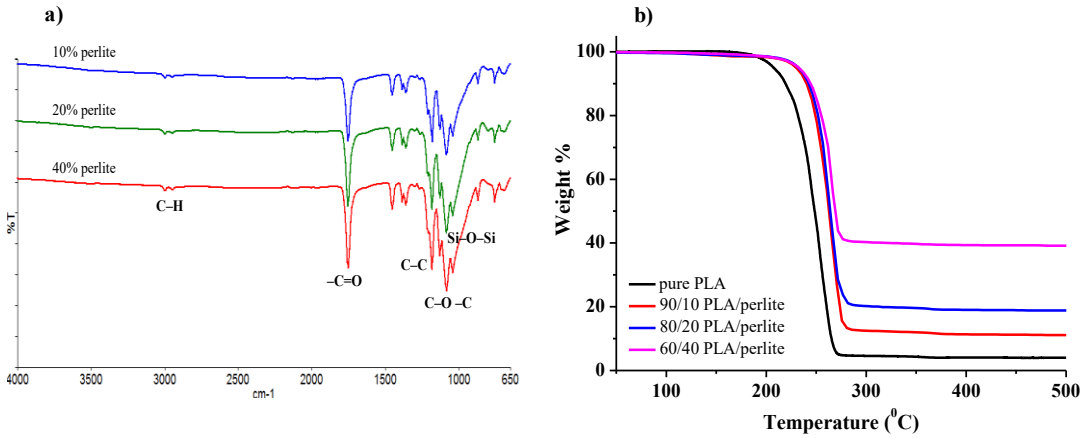

Figure 3.3 FTIR spectra (a) and TGA thermograms (b) of pure PLA and PLA/Perlite composites prepared in different ratios.

The thermogravimetric analysis results related to pure PLA and PLA composites with varying perlite ratios are given at Figure 3.3 (b), obtained under a nitrogen atmosphere at a heating rate of 10 °C/min. Degradation takes place in single step for both pure polymer and for the composites that have been prepared. The different mass amounts of composites left over from the degradation are proportionate with the perlite they contain. And this situation indicates that the additive is homogeneously spread into the polymer. It was determined from the thermograph that the pure PLA starts degrading at ~205 °C and the perlite/PLA composites in ratios of 10%, 20% and 40% degrade at ~233 °C, 237 °C and 239 °C respectively. It is considered that the onset degradation temperature of perlite/PLA composite being 35 °C higher compared to pure polymer shall yield a significant outcome in terms of increasing thermal stability and decreasing the costs for the application fields. Besides, since there are not significant differences between the degradation temperatures of the perlite/PLA composites in ratios of 10%, 20% and 40% according the analysis results, and since it will be more advantageous in application fields in terms of costs, the ratio of 40%, which comprises the highest level of additive, is preferred in the studies of thermal degradation kinetics.

3.2 Thermal Degradation Kinetics of PLA and PLA/Perlite Composite

In order to investigate the thermal degradation kinetics of pure PLA and PLA/perlite (60/40), using the thermogravimetric analysis method (TGA), the thermographs of the samples were obtained in a nitrogen atmosphere from 25 °C' to 600 °C', with heating rates of 5, 10, 15 and 20 °C/min. The TGA and DTG curves obtained at different heating rates for polymer and composite are given at Figure 3.4. After examining the termographs, it was clarified that the change in the heating rates does not create any difference in the thermal degradation characteristic of polymer and composite. However, it was observed that the onset degradation temperatures of both PLA and PLA/perlite composite increases and that the apex of DTG curves ascend to higher temperature levels with increasing heating rates (β). This increase can be attributed to the reduced time for heat transfer at higher heating rates, as the sample reaches the target temperature more rapidly, which may result in incomplete thermal equilibrium. Therefore, it can be noted that heating rate has a significant effect on the thermal degradation kinetics of the sample [29].

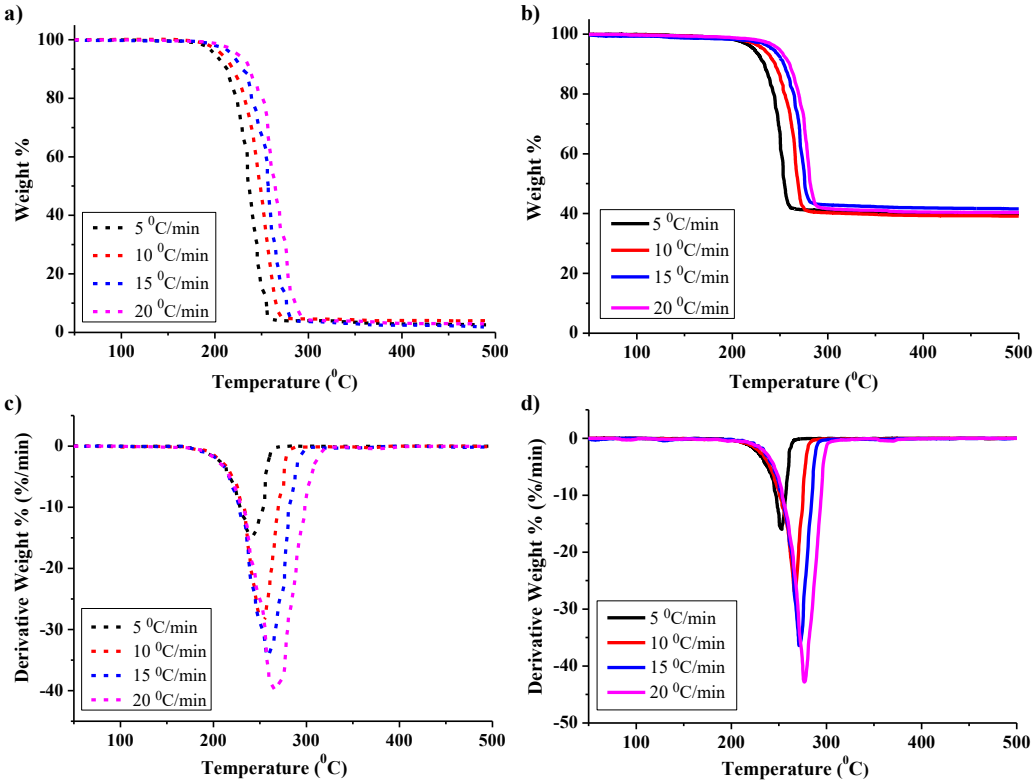

Figure 3.4 TGA and DTG curves of PLA (a and c) and PLA/Perlite (60/40) composite (b and d) at different heating rates.

Firstly, iso-conversional Flynn–Wall–Ozawa (FWO) method was applied for calculating the thermal degradation activation energies (E) of PLA and PLA/perlite. The TGA characteristic heat values obtained for 0.05 and 0.10 conversion values at different heating rates (β) are given at Table 3.1. Graphs were drawn between log β values corresponding to the 1/T value which is calculated at different conversion values pertaining to different heating rates (β), and they are given at Figure 3.5 (a and b) for polymer and composite. It is apparent that PLA and its composite have a similar inclination at different heating rates. However, the values of the slopes and overall form of the curves indicate that these two materials have different thermal stabilities. This situation proves that adding perlite to the PLA matrix affects the degradation behavior of the polymer. The conversion values for PLA are (α) 0.05, 0.10, 0.15, 0.20, 0.25, 0.30, 0.35, 0.40, 0.45, 0.50, 0.55, 0.60, 0.65, 0.70, 0.75 and 0.80; And the transformation values for PLA/perlite are (α) 0.05, 0.10, 0.15, 0.20, 0.25, 0.30, 0.35, 0.40, 0.45, 0.50 and 0.55.

Table 3.1 Characteristic temperatures of the thermal degradation of PLA and PLA/Perlite (60/40) composite

β (°C/min)	**T_i** (°C)		**T_{max}** (°C)		**T_d (α=0.05)** (°C)		**T_d (α=0.10)** (°C)	
	PLA	**PLA/perlite**	**PLA**	**PLA/perlite**	**PLA**	**PLA/perlite**	**PLA**	**PLA/perlite**
5	193.4	215.6	240.7	252.3	200.8	223.0	213.5	233.5
10	202.6	225.7	252.6	266.3	213.0	233.2	225.0	244.9
15	213.5	237.6	258.1	271.7	217.8	242.7	229.2	253.9
20	218.5	242.6	267.5	277.0	224.1	248.7	237.2	260.1

T_i: Initial temperature of the TG; **T_{max}:** Peak temperature of the DTG; **T_d**: Degradation temperature for a specific degradation percentage

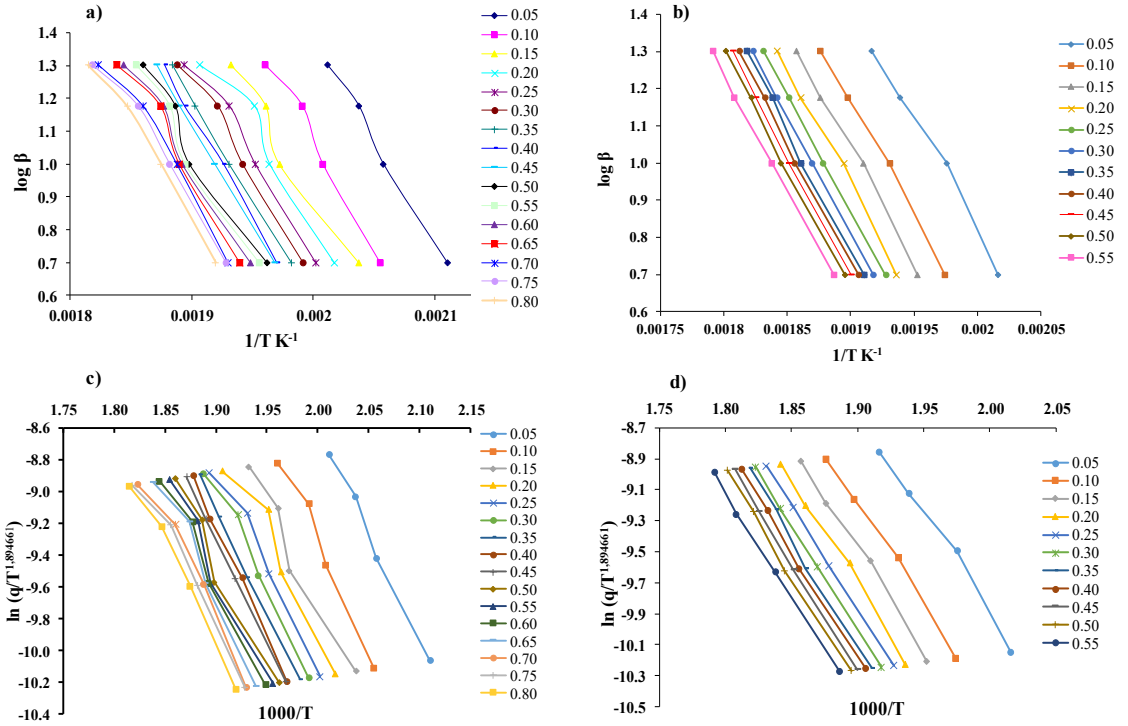

Figure 3.5 Curves of PLA and PLA/Perlite (60/40) composite at different conversion values, respectively for the Flynn-Wall-Ozawa (a and b) and Tang (c and d) methods.

Based on the FWO method, using Equation 1, the inclination values (-0.457E/R) were calculated from the graphs drawn between log β - 1/T corresponding to different conversion values, and the activation energy (E) was determined specifically for each conversion value.

$$log\beta = log\left[\frac{AE}{g(\alpha)R}\right] - 2.315 - \frac{0.457E}{RT} \quad (1)$$

Based on the activation energy values obtained from the inclination values corresponding to different conversion values, the average activation energies of PLA and PLA/perlite composite were determined as 108.39 kJ/mol and 114.59 kJ/mol respectively (Table 3.2). For PLA, the value which is closest to the average activation energy value (108.39 kJ/mol) was obtained at conversion value 30%, and for PLA/Perlite composite, this value was obtained at conversion value 20%. The higher thermal degradation activation energy of PLA/perlite composite compared to pure PLA indicates that the additive is effective towards the slow-paced progression of the process of polymer's degradation mechanism.

The Tang method, which is one of the isoconversional methods, demonstrates a similar approach to Flynn-Wall-Ozawa (FWO) and Kissinger-Akahira-Sunose (KAS) methods when calculating the activation energy in kinetic analysis, however, it differs drastically from them when it comes to mathematical expressions. By using Equation 3, the activation energy (Ea) and logarithmic prefactor (InA) values were also calculated using Tang model. The Figure 3.5 (c and d) shows respectively for PLA and PLA/perlite composite the graphs of 1000/T

corresponding to ln [q/$T^{1.894661}$] at 5-10 °C/min heating rates within the total conversion range of 5-80%. Based on the data obtained from these graphs, the activation energy value (Ea) obtained for PLA ranges between 97.78 and 116.36 kJ/mol depending on the conversion values, while this value ranges between 105.74 and 116.72 kJ/mol for PLA/perlite composite (Table 3.2). The average activation energy values for PLA and PLA/perlite composite were calculated as 105.75 kJ/mol and 112.06 kJ/mol respectively, based on Tang method. In general, the results obtained with Tang method are coherent with the results obtained with FWO method and they indicate that the perlite additive increases the activation energy.

Table 3.2 Activation energies calculated using the Flynn-Wall-Ozawa and Tang methods at different conversion values.

	Flynn-Wall-Ozawa method				**Tang method**			
α (%)	**Ea (kJ/mol)**		**R^2**		**Ea (kJ/mol)**		**R^2**	
	PLA	**PLA/perlite**	**PLA**	**PLA/perlite**	**PLA**	**PLA/perlite**	**PLA**	**PLA/perlite**
0.05	112.55	108.24	0.9931	0.9897	110.64	105.74	0.9921	0.9881
0.10	118.19	110.69	0.9821	0.9962	116.36	108.14	0.9796	0.9956
0.15	104.66	113.18	0.9673	0.9960	102.07	110.67	0.9624	0.9954
0.20	101.24	114.52	0.9502	0.9952	98.37	112.01	0.9421	0.9945
0.25	103.21	113.88	0.9786	0.9997	100.38	111.30	0.9749	0.9997
0.30	108.36	114.74	0.9843	0.9998	105.76	112.17	0.9817	0.9998
0.35	110.71	119.09	0.9992	0.9970	108.20	116.72	0.9991	0.9966
0.40	116.85	117.06	0.9976	0.9981	114.61	114.56	0.9972	0.9979
0.45	111.63	117.70	0.9997	0.9993	109.11	115.20	0.9997	0.9992
0.50	107.51	117.58	0.9688	0.9978	104.75	115.05	0.9639	0.9975
0.55	109.11	113.85	0.9738	0.9988	106.41	111.09	0.9698	0.9987
0.60	107.60		0.9802		104.78		0.9770	
0.65	111.80		0.9728		109.16		0.9685	
0.70	103.68		0.9737		100.56		0.9690	
0.75	101.04		0.9773		97.78		0.9731	
0.80	106.10		0.9868		103.07		0.9844	
Average:	**108.39**	**114.59**			**105.75**	**112.06**		

The activation energy values of PLA and PLA/perlite composites were also calculated using the Kissinger method, which is another kinetic method independent from the reaction mechanism. The relevant equation on which the method is based, is given below at (Equation 2).

$$ln\left(\frac{\beta}{T_{max}^2}\right) = \left\{ln\frac{AR}{E} + ln[n(1-\alpha_{max})^{n-1}]\right\} - \frac{E}{RT_{max}} \quad (2)$$

The temperature levels at which (T_{max}) the degradation occurs in the fastest form at different heating speeds (β) were determined from the DTG curves of the samples of pure polymer and composite, and they are presented at Table 3.3 and Table 3.4. A graph was drawn between ln (β/T^2max) values obtained at different heating rates and $1000/T_{max}$ using Equation 2, and the activation energy values were calculated using the slope values (m= -E/R) obtained from this graph. The graphs generated for PLA and PLA/perlite composite are shown at Figure 3.6 (a and b, respectively. The activation energies calculated with this method were determined as 101.06 kJ/mol for PLA and 124.12 kJ/mol for PLA/perlite composite.

Table 3.3 Maximum degradation temperatures (T_{max}) of PLA at different heating rates

β (°C/min)	**T_{max}** (°C)	**T_{max}** (K)	**T^2_{max}**	**ln (β/T^2_{max})**	**$1000/T_{max}$**
5	240.70	513.70	263888	-10.87	1.95
10	253.56	526.56	277265	-10.23	1.90
15	261.10	534.10	285263	-9.85	1.87
20	270.58	543.58	295479	-9.60	1.84

Table 3.4 Maximum degradation temperatures (T_{max}) of PLA/Perlite (60/40) composite at different heating rates

β (°C/min)	**T_{max}** (°C)	**T_{max}** (K)	**T^2_{max}**	**ln (β/T^2_{max})**	**$1000/T_{max}$**
5	251.86	524.86	275478	-10.92	1.91
10	266.27	539.27	290812	-10.28	1.85
15	271.31	544.31	296273	-9.89	1.84
20	276.98	549.98	302478	-9.62	1.82

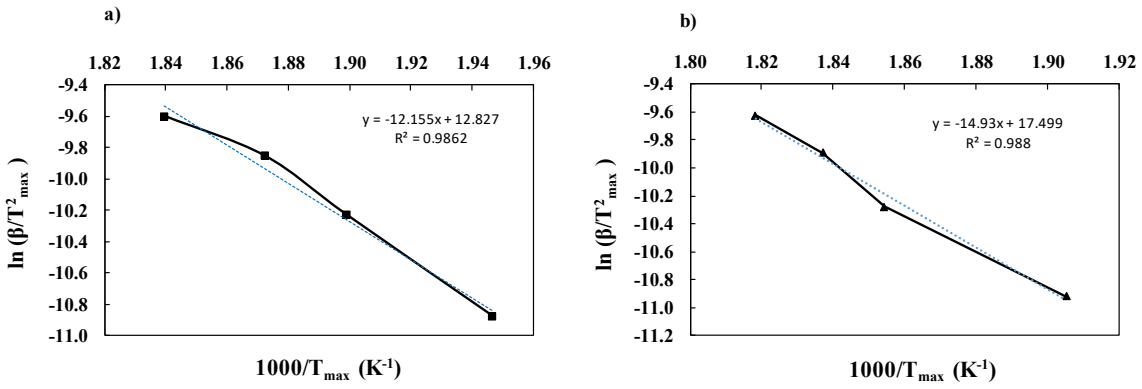

Figure 3.6 Kissinger curves of PLA (**a**) and PLA/Perlite (60/40) composite (**b**) plotted between ln (β/T^2_{max}) and $1000/T_{max}$

4. Conclusion

For the purpose of increasing the basic thermal stability of the biodegradable and biocompatible Polylactide, PLA/perlite composites with the perlite additive in different ratios (10%, 20%, 40%) were prepared by using the method of solvent casting. It was determined that a 40% addition of perlite increases the degradation temperature of neat PLA by 35 °C. However, TGA thermograms showed that increasing the perlite content did not significantly alter the overall thermal stability of the polymer. Using the Flynn-Wall-Ozawa, Tang and Kissinger methods, the thermal degradation activation energies for PLA were calculated as 108.39 kJ/mol, 105.75 and 101.06 kJ/mol respectively, and for PLA/perlite composite (60/40) they were calculated as 114.59 kJ/mol, 112.06 and 124.12 kJ/mol respectively. The determination of a higher value of degradation activation energy for PLA/perlite compared to pure PLA after calculation with the applied methods, indicates that perlite has a complicating effect on the process of the degradative reaction of polymer. In other words, it has been revealed that the perlite, which is used as an additive, causes the decrease of the PLA's rate constant (k). The observed increase in the thermal stability of PLA with the addition of perlite suggests that this composite material could serve as a promising alternative for applications such as packaging and biodegradable agricultural films. In future studies, the use of surface-modified perlite or hybrid filler systems may be explored to further enhance both the thermal and mechanical properties.

Ethics in Publishing

There are no ethical issues regarding the publication of this study.

Author Contributions

S.G. designed the study. S.G. and N.A.B. conducted the experiments. S.G. evaluated the analysis results and performed the calculations. S.G. wrote the manuscript. All authors have read and approved the published version of the manuscript.

Acknowledgements

The authors also would like to thank TUBITAK (Program for the University Students at undergraduate level Program Number TUBITAK 2209-A).

References

[1] Lv, S., Zhang, Y., Tan, H., (2019) Thermal and thermo-oxidative degradation kinetics and characteristics of poly (lactic acid) and its composites, Waste Management, 87, 335–344. https://doi.org/10.1016/j.wasman.2019.02.027.

[2] Zhang, J.-F., Sun, X., (2005) Biodegradable polymers for industrial applications, Smith, R. (ed), 10-Poly(lactic acid)-based bioplastics,Woodhead Publishing, Cambridge, 251–288. https://doi.org/10.1533/9781845690762.2.251.

[3] Unal, B., Yalcinkaya, E. E., Gumustas, S., Sonmez, B., Ozkan, M., Balcan, M., Demirkol, D. O., Timur, S., (2017) Polyglycolide-montmorillonite as a novel nanocomposite platform for biosensing applications, New Journal of Chemistry, 41, 9371–9379. https://doi.org/10.1039/c7nj01751k.

[4] Balcan, S., Balcan, M., Çetinkaya, B., (2013) Poly(l-lactide) initiated by silver N-heterocyclic carbene complexes: synthesis, characterization and properties, Polymer Bulletin, 70, 3475–3485. https://doi.org/10.1007/s00289-013-1034-9.

[5] Martin, O., Avérous, L., (2001) Poly(lactic acid): plasticization and properties of biodegradable multiphase systems, Polymer, 42 (14), 6209–6219. https://doi.org/10.1016/S0032-3861(01)00086-6.

[6] Tian, H., Tagaya, H., (2007) Preparation, characterization and mechanical properties of the polylactide/perlite and the polylactide/montmorillonite composites, J Mater Sci 42, 3244–3250. https://doi.org/10.1007/s10853-006-0230-5.

[7] Chung, S. J., Kwon, K. Y., Lee, S. W., Jin, J. I., Lee, C. H., Lee, C. E., Park, Y., (1998). Highly efficient light-emitting diodes based on an organic-soluble poly(p-phenylenevinylene) derivative carrying the electron-transporting PBD moiety, Advanced Materials, 10 (14), 1112-1116. https://doi.org/10.1002/(SICI)1521-4095(199810)10:14<1112::AID-ADMA1112>3.0.CO;2-P.

[8] Li, A.-K., Yang S. S., Jean W.-Y., Hsu C.-S., Hsieh B. R., (2000) Poly(2,3-diphenylphenylene vinylene) Derivatives Having Liquid Crystalline Side Groups, Chem Mater, 12 (9), 2741-2744. https://doi.org/10.1021/cm000295f.

[9] Neugebauer, H., Brabec, C., Hummelen, J.C., Sariciftci, N.S., (2000) Stability and photodegradation mechanisms of conjugated polymer/fullerene plastic solar cells, Solar Energy Materials and Solar Cells, 61 (1), 35-42. https://doi.org/10.1016/S0927-0248(99)00094-X.

[10] Theberge, J. E. (1982) Mineral reinforced thermoplastic composites, Journal of Elastomers & Plastics, 14 (2), 100-108. https://doi.org/10.1177/009524438201400202.

[11] Liang, J.-Z., (2013) Reinforcement and quantitative description of inorganic particulate-filled polymer composites, Composites Part B: Engineering, 51, 224-232. https://doi.org/10.1016/j.compositesb.2013.03.019.

[12] Rothon, R. N. (Ed.). (2003). Particulate-filled polymer composites, 53-81, iSmithers Rapra Publishing, UK.

[13] Yang, K., Yang, Q., Li, G., Sun, Y., Feng, D., (2006) Morphology and mechanical properties of polypropylene/calcium carbonate nanocomposites, Materials Letters, 60 (6), 805-809. https://doi.org/10.1016/j.matlet.2005.10.020.

[14] Dike A.S., (2020) Preparation and characterization of calcite loaded poly (lactic acid) composite materials, Erzincan University Journal of Science and Technology, 13 (1), 162-170. https://doi.org/10.18185/erzifbed.638547.

[15] Alghadi, A. M., Tirkes, S., Tayfun, U., (2020) Mechanical, thermo-mechanical and morphological characterization of ABS based composites loaded with perlite mineral, Mater. Res. Express, 7, 01530. https://doi.org/10.1088/2053-1591/ab551b.

[16] Atagür, M., Sarikanat, M., Uysalman, T., Polat, O., Yakar Elbeyli I., Seki, Y., Sever, K., (2018) Mechanical, thermal, and viscoelastic investigations on expanded perlite–filled high-density polyethylene composite, Journal of Elastomers & Plastics, 50 (8), 747–761, https://doi.org/10.1177/0095244318765045.

[17] de Oliveira, A.G., Jandorno, J.C., da Rocha, E.B.D., de Sousa, A.M.F., da Silva, A.L.N., (2019) Evaluation of expanded perlite behavior in PS/Perlite composites, Applied Clay Science, 181, 105223. https://doi.org/10.1016/j.clay.2019.105223.

[18] Aval ST, Davachi SM, Sahraeian R, Dadmohammadi Y, Heidari BS, Seyfi J, Hejazi I, Mosleh I, Abbaspourrad A (2020) Nanoperlite effect on thermal, rheological, surface and cellular properties of poly lactic acid/nanoperlite nanocomposites for multipurpose applications, Polymer Testing 91, 106779. https://doi.org/10.1016/j.polymertesting.2020.106779.

[19] Rashad, A.M., (2016) A synopsis about perlite as building material – A best practice guide for Civil Engineer, Construction and Building Materials, 121, 338–353. https://doi.org/10.1016/j.conbuildmat.2016.06.001.

[20] Sayadi, A., Neitzert, T. R., Clifton G. C., (2018) Influence of poly-lactic acid on the properties of perlite concrete, Construction and Building Materials, 189, 660–675. https://doi.org/10.1016/j.conbuildmat.2018.09.029.

[21] Eğri, Ö., (2019) Use of microperlite in direct polymerization of lactic acid, International Journal of Polymer Analysis and Characterization, 24 (2), 142–149. https://doi.org/10.1080/1023666X.2018.1562412.

[22] Mothé, C.G., de Miranda, I.C., (2013) Study of kinetic parameters of thermal decomposition of bagasse and sugarcane straw using Friedman and Ozawa–Flynn–Wall isoconversional methods, J Therm Anal Calorim, 113, 497–505. https://doi.org/10.1007/s10973-013-3163-7.

[23] Lv, X., Fang, J., Xie, J., Yang, X., Wang, J., (2018) Thermal stability of phosphorus-containing epoxy resins by thermogravimetric analysis, Polymers and Polymer Composites, 26 (7), 400-407. https://doi.org/10.1177/0967391118808701.

[24] Barneto, A. G., Carmona, J. A., Alfonso, J. E. M., Serrano, R. S., (2010) Simulation of the thermogravimetry analysis of three non-wood pulps, Bioresource Technology, 101 (9), 3220–3229. https://doi.org/10.1016/j.biortech.2009.12.034.

[25] Peng, X., Ma, X., Lin, Y., Guo, Z., Hu, S., Ning, X., Cao, Y., Zhang, Y., (2015) Co-pyrolysis between microalgae and textile dyeing sludge by TG–FTIR: Kinetics and products, Energy Conversion and Management, 100, 391–402. https://doi.org/10.1016/j.enconman.2015.05.025.

[26] Dhyani, V., Kumar, J., Bhaskar, T., (2017) Thermal decomposition kinetics of sorghum straw via thermogravimetric analysis, Bioresource Technology, 245, 1122–1129. https://doi.org/10.1016/j.biortech.2017.08.189.

[27] Kaur, R., Gera, P., Jha, M. K., Bhaskar, T., (2018) Pyrolysis kinetics and thermodynamic parameters of castor (Ricinus communis) residue using thermogravimetric analysis, Bioresource Technology, 250, 422–428. https://doi.org/10.1016/j.biortech.2017.11.077.

[28] Mishra, R. K., Mohanty, K., (2018) Pyrolysis kinetics and thermal behavior of waste sawdust biomass using thermogravimetric analysis, Bioresource Technology, 251, 63–74. https://doi.org/10.1016/j.biortech.2017.12.029.

[29] Carrasco, F., Pérez-Maqueda, L. A., Sánchez-Jiménez, P. E., Perejón, A., Santana, O. O., Maspoch, M.L., (2013) Enhanced general analytical equation for the kinetics of the thermal degradation of poly(lactic acid) driven by random scission, Polymer Testing, 32 (5), 937–945. https://doi.org/10.1016/j.polymertesting.2013.04.013.

[30] Blanco, I., (2014) End-life prediction of commercial PLA used for food packaging through short term TGA experiments: Real chance or low reliability?, Chinese Journal of Polymer Science, 32 (6), 681–689. https://doi.org/10.1007/s10118-014-1453-6.

[31] Schwach, G., Coudane, J., Engel, R., Vert, M., (1997) More about the polymerization of lactides in the presence of stannous octoate, Journal of Polymer Science Part A: Polymer Chemistry, 35 (16), 3431–3440, https://doi.org/10.1002/(SICI)1099-0518(19971130)35:16<3431::AID-POLA10>3.0.CO;2-G.

[32] Vyazovkin, S., Burnham, A. K., Criado, J. M., Pérez-Maqueda, L. A., Popescu, C., Sbirrazzuoli, N., (2011) ICTAC Kinetics Committee recommendations for performing kinetic computations on thermal analysis data, Thermochimica Acta, 520 (1-2), 1-19, https://doi.org/10.1016/j.tca.2011.03.034.

[33] Vyazovkin, S., Isoconversional Kinetics Of Thermally Stimulated Processes, Springer, Cham, 2015, https://doi.org/10.1007/978-3-319-14175-6.

[34] Vyazovkin, S., Sbirrazzuoli, N., (2006) Isoconversional kinetic analysis of thermally stimulated processes in polymers, Macromolecular Rapid Communications, 27 (18), 1515–1532. https://doi.org/10.1002/marc.200600404.

[35] Flynn, J. H., Wall, L. A., (1966) A quick, direct method for the determination of activation energy from thermogravimetric data, Journal of Polymer Science Part B: Polymer Letters, 4, 323–328. http://dx.doi.org/10.1002/pol.1966.110040504.

[36] Ozawa, T., (1986) Applicability of Friedman plot, Journal of Thermal Analysis, 31, 547-551. https://doi.org/10.1007/BF01914230.

[37] Kissinger, H.E., (1957) Reaction kinetics in differential thermal analysis, Analytical Chemistry, 29, 1702-1706. http://dx.doi.org/10.1021/ac60131a045.

[38] Tang, W., Liu, Y.; Zhang, C. H.; Wang, C., (2003) Thermochim Acta, 40, 839.

[39] Zujovic, Z., Wheelwright, W. V., Kilmartin, P. A., Hanna, J. V., Cooney R. P., (2018) Structural investigations of perlite and expanded perlite using ^{1}H, ^{27}Al and ^{29}Si solid-state NMR, Ceramics International, 44 (3) 2952–2958. https://doi.org/10.1016/j.ceramint.2017.11.047.

[40] Kabra, S. P., Katara, S., Rani, A., (2013) Characterization and study of Turkish perlite, International Journal of Innovative Research in Science, Engineering and Technology, 2, 4319–4326. https://api.semanticscholar.org/CorpusID:59405544.

e-ISSN: 2149-4584

Erzincan University Journal of Science and Technology

EJSAT 2025, 18 (3) 817-827

Research Article

Composite Metal Oxide Modified–Graphene Oxide Electrode for Gallic Acid Determination

Çağrı Ceylan KOÇAK[1*]

[1] Bergama Vocational School, Dokuz Eylul University, Izmir, Turkey.

Received: 21/05/2025, **Revised:** 17/09/2025, **Accepted:** 20/09/2025, **Published:** 31/12/2025

Abstract

The development of selective and sensitive electrochemical sensors for the determination of phenolic compounds remains an important issue due to the limited stability and sensitivity of electrode materials. In this study, composite metal oxide modified graphene oxides were prepared on the surface of a glassy carbon electrode. For this aim, a graphene oxide-modified/glassy carbon electrode (GO/GCE) was initially prepared using the drop-dry technique. Subsequently, tellurium oxide- zinc oxide nanoparticles (TeOx-ZnOx) were modified onto the GO/GCE surface using an electrochemical method (TeOx-ZnOx/GO/GCE). The prepared modified surface was compared with other electrodes using electrochemical impedance spectroscopy and cyclic voltammetry. The electrochemical behavior of gallic acid was investigated with the TeOx-ZnOx/GO/GCE in a pH 2.3 Britton-Robinson buffer. Under optimized conditions, the sensor exhibited a linear range of 0.5 µmol L^{-1} -1000 µmol L^{-1} for gallic acid detection using the amperometry technique, with a limit of detection (LOD) of 0.2 µmol L^{-1}. Real sample analysis was successfully performed with tea samples. In conclusion, the proposed composite modified electrode provides a stable surface for accurate and sensitive analysis of gallic acid determination. As a result, the prepared TeOx–ZnOx composite structure contributes to the literature by providing a stable and sensitive platform as a new electrode surface for the determination of gallic acid.

Keywords: Gallic acid, graphene oxide, tellurium oxide, zinc oxide, modified electrode

Gallik Asit Tayinine Yönelik Kompozit Metal Oksit ile Modifiye Edilmiş Grafen Oksit Elektrot

Öz

Fenolik bileşiklerin tayini için seçimli ve duyarlı elektrokimyasal sensörlerin geliştirilmesi, elektrot malzemelerinin sınırlı kararlılığı ve hassasiyeti nedeniyle önemli bir konu olmaya devam etmektedir. Bu çalışmada kompozit metal oksit modifiye grafen oksitler camımsı karbon elektrot yüzeyinde hazırlanmıştır. Bu amaçla, öncelikle drop-dry tekniğiyle grafen oksit modifiye/camımsı karbon elektrot (GO/GCE) hazırlanmıştır. Ardından GO/GCE yüzeyine elektrokimyasal yöntemle tellür oksit-çinko oksit nanoparçacıklar (TeOx-ZnOx) modifiye edilmiştir (TeOx-ZnOx/GO/GCE). Hazırlanan modifiye yüzey elektrokimyasal impedans spektroskopisi tekniği ve döngüsel voltammetri kullanılarak diğer elektrotlar ile karşılaştırılmıştır. TeOx-ZnOx/GO/GCE ile gallik asidin elektrokimyasal davranışı pH 2.3 Britton-Robinson tamponu içerisinde incelenmiştir. Optimize edilmiş koşullar altında, sensörün gallik asidi tespit etmek için amperometri tekniği ile elde edilen lineer ölçüm aralığı 0.5 µmol L^{-1} - 1000 µmol L^{-1} olup, LOD (tayin sınırı) 0.2 µmol L^{-1} olarak belirlenmiştir. Gerçek örnek analizi çay örneğinde başarıyla çalışılmıştır. Sonuç olarak, önerilen kompozit modifiye elektrodun, gallic acid tayinine yönelik kararlı bir yüzey olarak doğru ve duyarlı bir analize imkan sağladığı görülmektedir. Sonuç olarak, hazırlanan novel TeOx–ZnOx kompozit yapısı, gallic acid tayini için yeni bir elektrot yüzeyi olarak kararlı ve duyarlı bir platform sunarak literatüre katkı sunmuştur.

Anahtar Kelimeler: Gallik Asit, grafen oksit, tellür oksit, çinko oksit, modifiye elektrot

Corresponding Author: ceylan.kocak@deu.edu.tr

Cite this Article: Erzincan University Journal of Science and Technology 2025, 18(3) 817-827. https://doi.org/10.18185/erzifbed.1703916

1. Introduction

Gallic acid is a phenolic compound naturally found in various plants. Known primarily for its antioxidant properties, it also exhibits antimicrobial, anti-inflammatory, and potential anticancer activities [1–3]. Thanks to these beneficial properties, it is widely used in the pharmaceutical, food and cosmetic industries [4–6]. Accurate determination of the amount of gallic acid in various samples is of great importance for both monitoring product quality and evaluating health-related effects [7].

Various analytical techniques such as spectrophotometry, high-performance liquid chromatography (HPLC) [8,9], capillary electrophoresis [10], and electrochemical techniques [11,12] have been employed for the determination of gallic acid. However, many of these methods have certain drawbacks, including the need for expensive instrumentation, complex sample preparation procedures, and time-consuming processes. Due to these limitations, electroanalytical methods—particularly voltammetric techniques—have gained increasing attention in recent years for the analysis of phenolic compounds such as gallic acid [13,14]. Electrochemical sensors are of particular interest owing to their high sensitivity, rapid detection capabilities, and versatility in surface modification with different materials [15,16].

Graphene oxide (GO) is one of the frequently preferred materials as electrode material in sensor applications. These structures obtained by oxidation of graphite are a nanomaterial that attracts attention thanks to its large surface area and functional surface groups. The fact that it can be easily modified with many materials makes it preferred for a wide variety of applications [17,18]. Metal oxides are compounds with a wide range of electronic and structural diversity [19]. In recent years, composite metal oxide structures formed by combining different metal oxides have attracted increasing interest in electrochemical applications. Such composites offer higher surface activity, improved conductivity and enhanced electrocatalytic performance by combining the individual properties of the components. In particular, combinations of semiconducting metal oxides such as tellurium oxide, manganese oxide, zinc oxide, nickel oxide and cobalt oxide accelerate charge transfer on the electrode surface and significantly increase the sensitivity of sensors [20–23]. Thus, it becomes possible to develop both low cost and high performance electrochemical sensors.

Although various metal oxides have been used in many different applications, TeOx has been studied to a limited extent despite its redox-active properties that facilitate electron transfer. ZnOx, on the other hand, is a widely used material due to its high stability and catalytic activity. Combining these two oxides is expected to produce a synergistic effect, leading to increased conductivity, improved electrocatalytic response, and a more stable electrode surface. No studies have been reported in the literature on the use of a TeOx–ZnOx composite structure integrated with graphene oxide for gallic acid determination. This represents the originality of the study. In this study, a new electrode developed by combining composite metal oxides with graphene oxide structure is presented. It was prepared by modification of graphene oxide on the glassy carbon electrode surface followed by electrochemical deposition of TeOx-ZnOx nanoparticles. The electrochemical performance of the prepared electrode surface on the determination of gallic acid was evaluated. The results obtained from CV and amperometry

studies under optimum conditions show that the developed electrode surface is a practical and effective alternative for gallic acid analysis.

2. Material and Methods

Gallic acid, tellurium dioxide (TeO_2), zinc sulfate ($ZnSO_4$), and graphene were purchased from Sigma-Aldrich. Britton-Robinson (B-R) buffer solutions in the pH range of 2.0–6 was prepared using a mixture of acetic acid, phosphoric acid, and boric acid, and the desired pH was adjusted with 0.2 M NaOH. All solutions were prepared with ultrapure deionized water.

Electrochemical measurements were carried out using an Autolab PGSTAT 101 voltammetric device in a standard three-electrode system (modified glassy carbon electrode (GCE) as the working electrode, a platinum wire as the counter electrode, and an Ag/AgCl (sat. KCl) electrode as the reference). Cyclic voltammetry (CV) and amperometry were used for analytical studies under optimized conditions in 0.1 M B-R buffer solution (pH 2.3). Electrochemical impedance spectroscopy (EIS) was employed to characterize the modified electrode surfaces.

Fabrication of the TeOx-ZnOx/GO Modified Electrode

Initially, the bare GCE was polished with alumina slurry, rinsed with distilled water, and sonicated in ethanol and water sequentially. To prepare the GO-modified electrode, a homogeneous dispersion of GO (10 µL) was drop-cast onto the clean GCE surface and dried at room temperature. The composite metallic oxide layer was subsequently deposited by electrochemical codeposition. For this, the GO-modified electrode was immersed in a solution containing 3.0 mM TeO_2 and 1.0 mM $ZnSO_4$ dissolved in 0.1 M HCl, and CV was applied in the potential range of –1.3 V to +1.0 V for 10 cycles at 100 mV s^{-1}. The obtained TeOx-ZnOx/GO/GCE was rinsed and dried before use.

Real Sample Preparation

A black tea sample was purchased from a local market. The preparation procedure was followed according to our previous publication [24], ensuring consistency with earlier studies. Each real tea sample analysis was performed in triplicate to ensure reproducibility. 2 g of dried tea leaves were infused in 50 mL of hot distilled water for 15 minutes. After cooling to room temperature, the solution was filtered to obtain a clear extract. An appropriate volume of the filtrate was diluted with supporting electrolyte and used directly for voltammetric measurements. Known concentrations of standard gallic acid solution were added to the tea sample for recovery studies.

3. Results and Discussion

Fig. 1A shows the cyclic voltammetry (CV) curves used to compare the electrochemical behavior of bare GCE, GO/GCE, TeOx-ZnOx/GCE, and TeOx-ZnOx/GO/GCE electrodes in 0.1 M B-R buffer solution (pH 2.3) containing 0.1 mmol L^{-1} gallic acid. The bare GCE showed a weak and broad oxidation peak, indicating sluggish electron transfer and limited surface activity. Upon modification with GOs, a clear enhancement in peak current was observed, which is mainly attributed to the large surface area of GO. When the GCE was modified with TeOx-ZnOx nanoparticles, a current increase was detected. This can be explained by the redox behavior of TeOx, which plays a key role in promoting electron exchange at the electrode surface. ZnOx likely contributes to a more stable structure and additional active sites. The most significant enhancement in electrochemical response was obtained at the TeOx-ZnOx/GO/GCE electrode. The remarkable increase in oxidation peak current indicates a synergistic effect among TeOx, ZnOx, and GO. While GO provides a large and conductive surface, TeOx improves electron transfer kinetics, and ZnOx offers structural support and catalytic contribution. The combination of these materials results in a composite surface with enhanced electron transfer capability and improved interaction with gallic acid molecules. These findings indicate that the proposed TeOx-ZnOx/GO/GCE electrode offers a promising surface for the electrochemical determination of gallic acid.

Moreover, the interfacial properties of all electrodes were studied via EIS measurements were carried out in a solution containing 5.0 mmol L^{-1} $[Fe(CN)_6]^{3-/4-}$ and 0.1 M KCl. The Nyquist plots (Fig. 1B) clearly reveal that the charge transfer resistance (Rct) values vary significantly among the different electrode surfaces. Bare GCE exhibited the largest semicircle diameter, corresponding to the highest Rct (698 Ω), indicating poor electron transfer kinetics. Modification with GOs significantly reduced Rct (387 Ω), reflecting the improved conductivity and enhanced charge transport pathways offered by the graphene network. The TeOx-ZnOx/GCE electrode also showed a smaller semicircle than bare GCE, due to the redox-active behavior of TeOx and the catalytic contribution of ZnOx. The TeOx-ZnOx/GO/GCE electrode exhibited the smallest semicircle among all, indicating the lowest Rct (72 Ω) and the increased charge transfer characteristics. This confirms the synergistic effect between the conductive GOs and the electrocatalytically active TeOx-ZnOx nanoparticles. The combined structure promotes efficient electron transfer at the electrode–electrolyte interface, which agrees with the CV results and supports the good performance of the composite electrode for gallic acid detection.

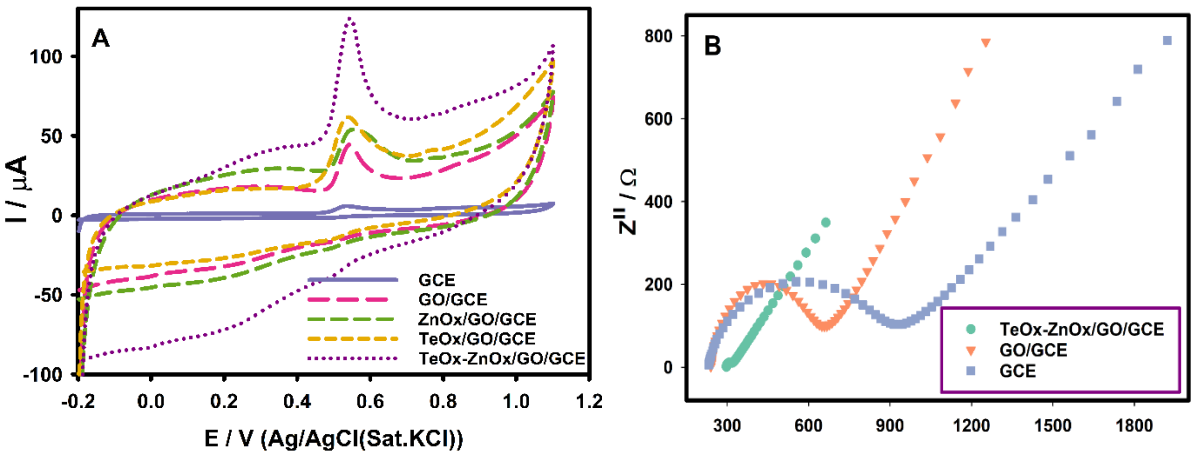

Figure 1. A) CVs of GCE, GO/GCE, TeOx/GO/GCE, ZnOx/GO/GCE, TeOx-ZnOx/GO/GCE electrodes recorded in 0.1 mmol L^{-1} gallic acid in pH 2.3 B-R buffer solution. **B)** Nyquist plots of the modified electrodes in a solution containing 5 mmol L^{-1} $[Fe(CN)_6]^{3-/4-}$ and 0.1 M KCl.

The electrochemical behavior of gallic acid at the TeOx-ZnOx/GO/GCE electrode was further investigated by cyclic voltammetry at varying scan rates between 5 and 200 mV s^{-1} (Figure 2). As the scan rate increased, an enhancement in the anodic peak current was observed. In addition, the anodic peak potential showed a slight positive shift with increasing scan rate, which is characteristic of a quasi-reversible electron transfer. The inset of Figure 2 demonstrates a good linear relationship between the anodic peak current (Ipa) and the square root of scan rate ($\nu^{1/2}$), indicating that the oxidation of gallic acid occurs through a diffusion-controlled process on the modified electrode surface. The corresponding linear regression was obtained as Ipa= 6.974 $\nu^{1/2}$ -4.51169 (R^2 = 0.9992).

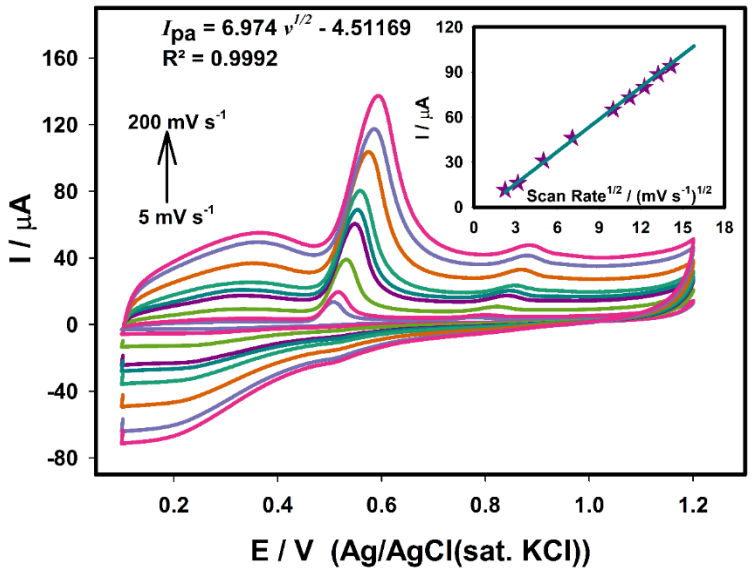

Figure 2. CVs of gallic acid (10 µM in pH 2.3 B-R buffer) at the TeOx-ZnOx/GO/GCE electrode recorded at different scan rates (5–200 mV s^{-1}). (Inset: The linear relationship between the anodic peak current and the square root of scan rate).

Fig. 3 shows the amperogram of gallic acid (GA) added at increasing concentrations in pH 2.3 BR buffer solution. Increasing peak currents have been observed at the TeOx-ZnOx/GO/GCE electrode with rising GA concentrations. As can be seen from the calibration curve in the inset, a linear relationship has been obtained within the concentration range of 0.5 µmol L^{-1} to 1000 µmol L^{-1}, described by the equations as; Ip (µA)=20032·C_{GA} (mol L^{-1}) + 9.9447 (R^2 = 0.9928), and Ip (µA)=108731·C_{GA} (mol L^{-1}) – 0.1004 (R^2 = 0.9987) with the detection limit has been calculated as 0.2 µmol L^{-1}. These results demonstrate the success of the proposed electrode for GA determination.

The analytical performance of the proposed TeOx–ZnOx/GO/GCE electrode has been compared with previously reported gallic acid sensors. The obtained LOD and wide linear range are comparable to those of carbon paste electrodes modified with carbon nanotubes (LOD: 0.3 µmol L^{-1}, range: 0.5–15 µmol L^{-1} [25]), and gelatin-functionalised reduced graphene oxide (LOD: 0.47 µmol L^{-1}, range: 1–110 µmol L^{-1} [26]), and superior to several previously reported electrodes. Although some advanced nanocomposite-based electrodes, such as Poly(L-Methionine)/Carbon Nanotube Glassy Carbon Electrode (LOD: 3.1 nmol L^{-1} [24]) or ZrO_2/Co_3O_4/ reduced graphene oxide nanocomposite (LOD: 1.56 nmol L^{-1} [27]), exhibit lower detection limits, their linear ranges are relatively narrow. In contrast, the TeOx–ZnOx/GO/GCE electrode offers a balanced performance with both a low detection limit and a broad linear range.

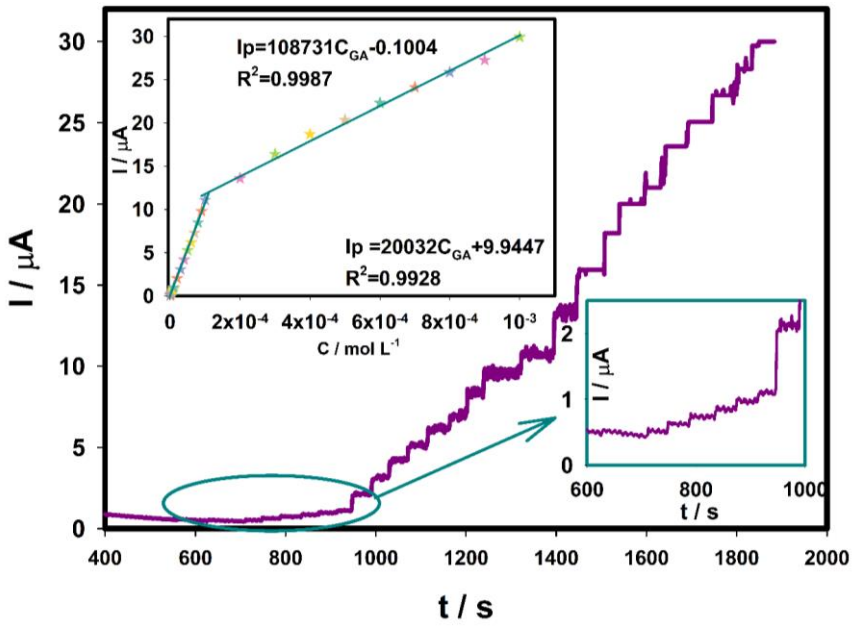

Figure 3. Amperometric measurement results of gallic acid at TeOx-ZnOx/GO/GCE electrode with increasing concentrations (0.5–1000 µmol L^{-1}) in pH 2.3 B-R buffer solution. (Inset: The related calibration curve).

Stability is an extremely important parameter, especially for electrochemical sensors that require long-term and repetitive use. As shown in Figure 4, the stability of the TeOx-ZnOx/GO/GCE electrode was investigated over a period of 7 days by recording the GA oxidation peak current values. During this time, the electrode retained 96.6% of its initial peak current, demonstrating high stability with no significant signal loss. These results indicate that the developed electrode has excellent operational stability and confirm its potential as a promising candidate for sensor applications. Moreover, five independently prepared TeOx–ZnOx/GO/GCE electrodes were tested under same experimental conditions. The relative standard deviation values were calculated as 3.9% for intra-day (n = 5) and 4.3% for inter-day (n = 5) measurements, confirming good repeatability and reproducibility of the electrode response.

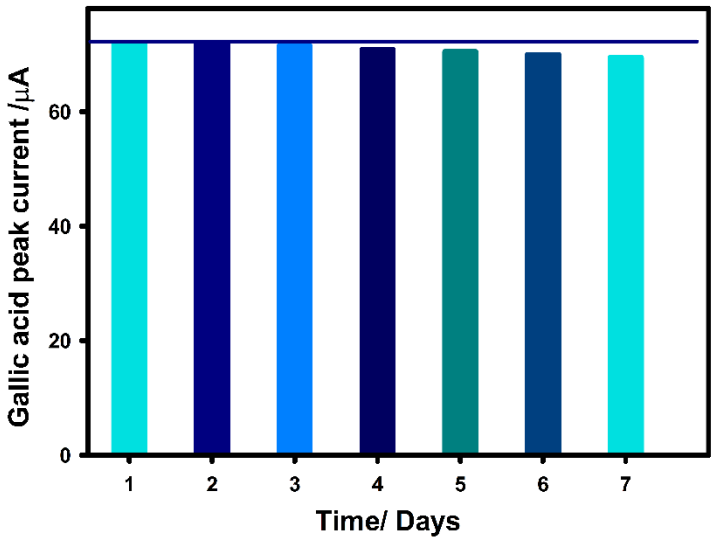

Figure 4. Bar graph for the stability of the TeOx-ZnOx/GO/GCE electrode over 7 days.

The determination of gallic acid in black tea was successfully carried out method and results were represented in Table 1. The recovery percentages obtained for the spiked samples clearly show the accuracy of the method. Each recovery experiment was performed in triplicate (n = 3), and the mean values are presented. For added concentrations of 10, 20, and 30 µmol L^{-1}, the recoveries were 104.6%, 101.2%, and 98.4%, respectively. These results confirm that the method is reliable. In addition, the low RSD (%) values indicate good repeatability of the measurements. Overall, the developed TeOx-ZnOx/GO/GCE electrode appears to be an applicable surface for gallic acid detection in real samples.

Table 1. Gallic acid determination in tea samples using the TeOx-ZnOx/GO/GCE electrode (n = 3).

Sample	Added (μmol L^{-1})	Found (μmol L^{-1})	Recovery (%)	RSD (%)
Black Tea	0	20.7	-	3.4
	10	32.12	104.6	3.2
	20	41.2	101.2	2.6
	30	49.9	98.4	2.4

4. Conclusion

In this study, a composite metal oxide modified–graphene oxide electrode (TeOx-ZnOx/GO/GCE) was successfully developed for the electrochemical determination of gallic acid. The combination of tellurium oxide and zinc oxide enhanced the electrocatalytic activity. TeOx facilitates charge transfer processes due to its semiconducting nature and favorable surface characteristic. ZnOx contributes to the structural stability of the electrode and provides additional active sites. GO supports the formation of active regions on the electrode surface through its large surface area and functional surface groups. As a result, the developed sensor exhibited high sensitivity, a low detection limit, and good stability. Its successful performance in real sample analysis using tea further demonstrated its practical applicability. Overall, the TeOx-ZnOx/GO modified electrode highlights the potential of composite metal oxide–graphene structures in the development of effective electrochemical sensors. Since the performance of the electrode has been evaluated only for gallic acid in tea matrices, this indicates a limitation in scope. Future studies focusing on different phenolic compounds and more complex real samples could further confirm the robustness of the sensor, keeping the platform promising for practical industrial applications

Ethics in Publishing

There are no ethical issues regarding the publication of this study

Author Contributions

The author was responsible for the investigation, conception, design, data collection, analysis, and interpretation of the research, as well as writing and editing the manuscript.

References

[1] Keyvani-Ghamsari, S.; Rahimi, M.; Khorsandi, K. An Update on the Potential Mechanism of Gallic Acid as an Antibacterial and Anticancer Agent. *Food Science and Nutrition*, **2023**, *11*, 5856–5872.

[2] Holghoomi, R.; Kiani, M.H.; Rahdar, A.; Hashemi, S.M.; Romanholo Ferreira, L.F.; Fathi-karkan, S. Nanoparticle-Delivered Gallic Acid: A New Frontier in Cancer Therapy. *Journal of Drug Delivery Science and Technology*, **2024**, *101*.

[3] Bai, J.; Zhang, Y.; Tang, C.; Hou, Y.; Ai, X.; Chen, X.; Zhang, Y.; Wang, X.; Meng, X. Gallic Acid: Pharmacological Activities and Molecular Mechanisms Involved in Inflammation-Related Diseases. *Biomedicine and Pharmacotherapy*, **2021**, *133*.

[4] Zhang, K. qiang; Lin, L. liang; Xu, H. jun. Research on Antioxidant Performance of Diglucosyl Gallic Acid and Its Application in Emulsion Cosmetics. *Int J Cosmet Sci*, **2022**, *44*, 177–188.

[5] Hadidi, M.; Liñán-Atero, R.; Tarahi, M.; Christodoulou, M.C.; Aghababaei, F. The Potential Health Benefits of Gallic Acid: Therapeutic and Food Applications. *Antioxidants*, **2024**, *13*.

[6] Falahi, S.; Falahi, S.; Zarejousheghani, M.; Ehrlich, H.; Joseph, Y.; Rahimi, P. Electrochemical Sensing of Gallic Acid in Beverages Using a 3D Bio-Nanocomposite Based on Carbon Nanotubes/Spongin-Atacamite. *Biosensors (Basel)*, **2023**, *13*.

[7] Zhao, H.; Zhao, M.; Han, J.; Li, Z.; Tang, J.; Wang, Z.; Wang, G.; Komarneni, S. Room-Temperature Fabrication of Zeolitic Imidazolate Framework-8 Nanoparticles Combined with Graphitized and Carbonylated Carbon Nanotubes Networks for the Ultrasensitive Gallic Acid Electrochemical Detection. *Food Chem*, **2025**, *465*.

[8] Jakabová, S.; Árvay, J.; Šnirc, M.; Lakatošová, J.; Ondejčíková, A.; Golian, J. HPLC-DAD Method for Simultaneous Determination of Gallic Acid, Catechins, and Methylxanthines and Its Application in Quantitative Analysis and Origin Identification of Green Tea. *Heliyon*, **2024**, *10*.

[9] Gültekin-Özgüven, M.; Davarci, F.; Pasli, A.A.; Demir, N.; Özçelik, B. Determination of Phenolic Compounds by Ultra High Liquid Chromatography-Tandem Mass Spectrometry: Applications in Nuts. *LWT*, **2015**, *64*, 42–49.

[10] Yue, M.E.; Jiang, T.F.; Shi, Y.P. Determination of Gallic Acid and Salidroside in Rhodiola and Its Preparation by Capillary Electrophoresis. In *Journal of Analytical Chemistry*; **2006**; Vol. 61, pp. 365–368.

[11] Di Giulio, T.; Ramírez-Morales, M.A.; Mastronardi, V.; Mele, G.; Brescia, R.; Pompa, P.P.; Malitesta, C.; De Benedetto, G.E.; Moglianetti, M.; Malvindi, M.A.; Mazzotta, E.

Electrochemical Determination of Gallic Acid in Tea Samples Using Pyramidal Pt Nanoparticles. *Adv Electron Mater*, **2024**.

[12] Koçak, Ç.C.; Karabiberoğlu, Ş.U.; Dursun, Z. Highly Sensitive Determination of Gallic Acid on Poly (L-Methionine)-Carbon Nanotube Composite Electrode. *Journal of Electroanalytical Chemistry*, **2019**, *853*.

[13] Sarıbaş, P.; Yıldız, C.; Eskiköy Bayraktepe, D.; Pekin Turan, M.; Yazan, Z. Gold Nanoparticles Decorated Kaolinite Mineral Modified Screen-Printed Electrode: Use for Simple, Sensitive Determination of Gallic Acid in Food Samples. *Food Chem*, **2024**, *453*.

[14] Achache, M.; El-Haddar, S.; El Haddaoui, H.; Idrissi, G.E.; Draoui, K.; Bouchta, D.; Choukairi, M. An Electrochemical Sensor Based on a Carbon Paste Electrode Modified with Lanthanum Nanocomposites for Gallic Acid Determination in Fruit Juice Samples. *Mater Chem Phys*, **2025**, *332*.

[15] Aslışen, B.; Koçak, S. Preparation of Mixed-Valent Manganese-Vanadium Oxide and Au Nanoparticle Modified Graphene Oxide Nanosheets Electrodes for the Simultaneous Determination of Hydrazine and Nitrite. *Journal of Electroanalytical Chemistry*, **2022**, *904*.

[16] Aslışen, B.; Koçak, Ç.C.; Koçak, S. Electrochemical Determination of Sesamol in Foods by Square Wave Voltammetry at a Boron-Doped Diamond Electrode. *Anal Lett*, **2020**, *53*, 343–354.

[17] Baruah, A.; Newar, R.; Das, S.; Kalita, N.; Nath, M.; Ghosh, P.; Chinnam, S.; Sarma, H.; Narayan, M. Biomedical Applications of Graphene-Based Nanomaterials: Recent Progress, Challenges, and Prospects in Highly Sensitive Biosensors. *Discover Nano*, **2024**, *19*.

[18] Mushahary, N.; Sarkar, A.; Basumatary, F.; Brahma, S.; Das, B.; Basumatary, S. Recent Developments on Graphene Oxide and Its Composite Materials: From Fundamentals to Applications in Biodiesel Synthesis, Adsorption, Photocatalysis, Supercapacitors, Sensors and Antimicrobial Activity. *Results in Surfaces and Interfaces*, **2024**, *15*.

[19] Ayan, E.M.; Karabiberoğlu, Ş.U.; Dursun, Z. A Practical Electrochemical Sensor for Atenolol Detection Based on a Graphene Oxide Composite Film Doped with Zinc Oxide Nanoparticles. *ChemistrySelect*, **2020**, *5*, 8846–8852.

[20] Ozdokur, K.V.; Demir, B.; Atman, E.; Tatli, A.Y.; Yilmaz, B.; Demirkol, D.O.; Kocak, S.; Timur, S.; Ertas, F.N. A Novel Ethanol Biosensor on Pulsed Deposited MnOx-MoOx Electrode Decorated with Pt Nanoparticles. *Sens Actuators B Chem*, **2016**, *237*, 291–297.

[21] Davaslıoğlu, İ.Ç.; Volkan Özdokur, K.; Koçak, S.; Çırak, Ç.; Çağlar, B.; Çırak, B.B.; Nil Ertaş, F. WO3 Decorated TiO2 Nanotube Array Electrode: Preparation, Characterization and Superior Photoelectrochemical Performance for Rhodamine B Dye Degradation. *J Mol Struct*, **2021**, *1241*.

[22] Tan, P.; Niu, C.; Lin, Z.; Lin, J.Y.; Long, L.; Zhang, Y.; Wilk, G.; Wang, H.; Ye, P.D. Wafer-Scale Atomic Layer-Deposited TeOx/Te Heterostructure P-Type Thin-Film Transistors. *Nano Lett*, **2024**.

[23] Liu, A.; Kim, Y.S.; Kim, M.G.; Reo, Y.; Zou, T.; Choi, T.; Bai, S.; Zhu, H.; Noh, Y.Y. Selenium-Alloyed Tellurium Oxide for Amorphous p-Channel Transistors. *Nature*, **2024**, *629*, 798–802.

[24] Koçak, Ç.C.; Karabiberoğlu, Ş.U.; Dursun, Z. Highly Sensitive Determination of Gallic Acid on Poly (L-Methionine)-Carbon Nanotube Composite Electrode. *Journal of Electroanalytical Chemistry*, **2019**, *853*.

[25] Souza, L.P.; Calegari, F.; Zarbin, A.J.G.; Marcolino-Júnior, L.H.; Bergamini, M.F. Voltammetric Determination of the Antioxidant Capacity in Wine Samples Using a Carbon Nanotube Modified Electrode. In *Journal of Agricultural and Food Chemistry*; **2011**; Vol. 59, pp. 7620–7625.

[26] Chekin, F.; Bagheri, S.; Bee, S.; Hamid, A. *Glassy Carbon Electrodes Modified with Gelatin Functionalized Reduced Graphene Oxide Nanosheet for Determination of Gallic Acid*; **2015**; Vol. 38.

[27] Puangjan, A.; Chaiyasith, S. An Efficient ZrO2/Co3O4/Reduced Graphene Oxide Nanocomposite Electrochemical Sensor for Simultaneous Determination of Gallic Acid, Caffeic Acid and Protocatechuic Acid Natural Antioxidants. *Electrochim Acta*, **2016**, *211*, 273–288.

e-ISSN: 2149-4584

Erzincan University Journal of Science and Technology

EJSAT 2025, 18 (3) 828-841

Research Article

Evaluation of The Quality Characteristics of Dried Erzincan Tulum Cheese by Hot Air Circulation Dryer at Different Temperatures

Bekir BATMAZ[1], Mustafa Fatih ERTUGAY[2*]

[1]Çankaya District Directorate of Agriculture and Forestry, Ankara, Turkey
[2] Faculty of Engineering-Architecture, Department of Food Engineering, Erzincan Binali Yıldırım University, Erzincan, Turkey

Received: 02/06/2025, **Revised:** 22/07/2025, **Accepted:** 18/09/2025, **Published:** 31/12/2025

Abstract

Erzincan Tulum Cheese, a geographically indicated product made from high-fat sheep's milk, is among the most recognized varieties of tulum cheese in Türkiye. This study aimed to explore a novel application area for Erzincan Tulum Cheese by transforming it into a powdered form through drying. The drying process was employed not only to extend the product's shelf life but also to introduce a new traditional dried cheese format to consumers. Drying was conducted using a hot air circulation oven at three different temperatures of 40, 50 and 60°C until the final moisture content reached approximately 10%. The resulting cheese powders were analyzed for their physical, chemical, and microbiological properties. Among the tested conditions, drying at 50°C for 210 minutes yielded the most favorable quality attributes. Based on the findings, this innovative form of Erzincan Tulum Cheese shows potential as a flavoring agent in various food applications, including soups, pizzas, pasta dishes, chips, sauces, and ready-to-eat meals.

Keywords: Erzincan Tulum Cheese, cheese drying, hot air circulation drying, powdered cheese

Farklı Sıcaklıklarda Sıcak Hava Sirkülasyonlu Kurutucu ile Kurutulan Erzincan Tulum Peynirinin Kalite Özelliklerinin Değerlendirilmesi

Öz

Erzincan Tulum Peyniri, yüksek yağ oranına sahip koyun sütünden üretilen ve coğrafi işaret ile korunan bir peynirdir. Türkiye'nin en çok bilinen tulum peynirlerinden biridir. Bu çalışmanın amacı, Erzincan tulum peynirine yeni bir kullanım alanı sağlamaktır. Bu amaçla, kurutma işlemi sadece peynirin raf ömrünü uzatmak için değil, aynı zamanda tüketiciler için toz formda geleneksel kurutulmuş peynir olarak yeni bir ürün geliştirmek için de kullanılmıştır. Erzincan tulum peyniri, son üründeki nem içeriği yaklaşık %10'a ulaşana kadar 40, 50 ve 60°C'lik sıcaklıklarda sıcak hava sirkülasyonlu kurutma fırınında kurutulmuştur. Peynir tozlarının fiziksel, kimyasal ve mikrobiyolojik özellikleri incelenmiştir. 50 °C'de 210 dakika boyunca yapılan kurutmanın en yüksek kaliteyi sağladığı belirlenmiştir. Bu yeni tip Erzincan Tulum Peynirinin çorbalarda, pizzalarda, makarnalarda, cipslerde, soslarda ve yemeklerde baharat olarak kullanılabileceği sonucuna varılmıştır.

Anahtar Kelimeler: Erzincan tulum peyniri, peynir kurutma, sıcak hava sirkülasyonlu kurutma, toz peynir

Corresponding Author: mfertugay@erzincan.edu.tr

Cite this Article: Erzincan University Journal of Science and Technology 2025, 18(3) 828-841. https://doi.org/10.18185/erzifbed.1709912

1. Introduction

Cheese is one of the most widely consumed dairy products globally and plays a significant role in human nutrition. Across different regions of the world, a diverse range of production methods have evolved. While cheese was originally developed as a means of preserving the nutritional components of milk, it has since become a key dietary item valued for both its nutritional profile and sensory characteristics [1]. Among dairy products, cheese stands out for its variety, attracting considerable attention from consumers. It is also a rich source of essential nutrients, including fats, proteins, vitamins, calcium, magnesium, and potassium.

There are approximately 4,000 recognized cheese varieties worldwide, with around 130 of them originating from Türkiye. Among these, white cheese and kashar cheese are the most widely produced in the country, followed by various regional types such as tulum cheese, herb cheese, pot cheese, lor cheese, and cube cheese [2]. According to data from the Turkish Statistical Institute (TÜİK), white cheese constitutes 60% of Türkiye's total cheese production, while kashar cheese accounts for 15%. Another 15% consists of tulum and Mihaliç cheeses, and the remaining 10% comprises various locally produced cheeses [3]. Tulum cheese is produced in several regions and often takes on regional names, including Erzincan Tulum (Şavak) Cheese, Divle Tulum Cheese (Karaman), Çimi Tulum Cheese (Antalya), Isparta Tulum Cheese, Selçuklu Tulum Cheese (Konya), and İzmir Tulum Cheese, which is typically stored in brine [4]. Erzincan Tulum Cheese is distinguished by its white to creamy color, high fat content, buttery aroma, and semi-hard, crumbly texture. It is traditionally made from sheep's milk and was the first tulum cheese in Türkiye to receive geographical indication status, granted by the Turkish Patent and Trademark Office in 2000 [5].

Milk and dairy products are highly perishable due to their rich microbial load and elevated water activity. To mitigate spoilage and extend shelf life, various food processing technologies are applied, with drying being among the most prevalent. The food industry employs a wide array of drying methods, including freeze drying, hot-air drying, fluidized bed drying, spray drying, and microwave-assisted drying. In addition, advanced techniques such as osmotic dehydration and hybrid drying—which integrate multiple drying technologies—are increasingly utilized to optimize processing efficiency and improve product quality. Among these, tray drying is commonly used for dehydrating cheese under controlled conditions, offering notable advantages such as operational simplicity and cost-effectiveness [6].

The development of dehydrated cheese products dates back to World War II, when the U.S. Army utilized cheese powder in industrially produced, cheese-based rations due to its superior stability at elevated storage temperatures compared to natural cheese, which required refrigeration [7,8]. Since that time, dehydrated cheese has evolved into a widely used dairy ingredient, valued both as a flavor enhancer and a nutritional supplement in a variety of food formulations [9].

Cheese can be subjected to drying processes to reduce its moisture content, thereby extending shelf life, improving transportability, and creating value-added derivative products suitable for diverse food applications [10]. Owing to their prolonged shelf stability, ease of use, and reduced

transportation and storage costs—particularly the lack of need for refrigeration—cheese powders have become widely utilized additives across the food industry [11,12,13]. Beyond their practicality, cheese powders serve as highly versatile ingredients: they impart intense cheese flavor in snack formulations, function as binding agents in coated nut products, and act as thickeners in instant mixes, ready-to-eat meals, sauces, and dips. In bakery applications, cheese powder may also contribute to leavening and enhance the texture, consistency, and shelf stability of seasoning blends [14,15,16]. The scope of cheese powder applications continues to expand due to these functional advantages. Granulated and dried cheese powders offer key benefits such as enhanced microbiological safety, extended shelf life, and immediate usability. Furthermore, their suitability as seasonings or topping ingredients broadens their potential for incorporation into a wide range of food products.

In this study, preliminary trials were carried out to determine the optimal drying temperature and duration for Erzincan Tulum Cheese. The samples were dried using a hot air circulation tray dryer until a final moisture content of approximately 10% was achieved. The impact of varying drying temperatures and times on the quality characteristics of the cheese was systematically investigated. Upon completion of the drying process, the physical, chemical, and microbiological properties of the resulting cheese powders were analyzed. The temperature condition that produced the most favorable effects on the final product was identified, with the overarching goal of introducing a novel form of Erzincan Tulum Cheese suitable for broader food applications.

2. Materials and Methods

2.1. Materials

Erzincan Tulum Cheese used in the study was sourced from a local producer and stored at −18°C in airtight, sealed jars until further analysis. All chemicals used in the experimental procedures were of analytical grade and were obtained from Sigma-Aldrich. Based on preliminary trials, a final moisture content of approximately 10% was reached after 270, 210, and 180 minutes of drying at temperatures of 40, 50, and 60°C, respectively.

2.2. Methods

2.2.1. Hot air circulation drying process

To establish the appropriate drying conditions for use in a hot air circulation drying oven, Erzincan Tulum cheese samples were subjected to drying at various temperatures and durations (Table 1). In preliminary experiments, the optimum sample amount and thickness, temperature and time were determined to achieve a target moisture content (10%). Prior to drying, the samples were crumbled and spread on sieves to achieve an approximate thickness of 0.5 cm. The moisture content of cheese samples was measured in every 30 minutes during drying. Based on these trials, further drying process was carried out in a hot air circulation dryer at temperatures of 40, 50 and 60°C for durations of 270, 210, and 180 minutes, respectively. The

dried samples were then granulated using a blender to create a uniform structure and stored in the refrigerator (+4°C) until further analysis.

Table 1. The change in moisture content (%) of Erzincan Tulum cheese samples during drying

Time (min)	40°C	50°C	60°C
Control	40,85	40,67	40,78
30	38,15	35,88	37,30
60	36,64	30,40	29,80
90	30,40	26,10	22,30
120	27,16	19,69	16,22
150	21,80	14,72	13,81
180	16,51	12,44	10,93
210	15,30	10,26	9,52
240	11,04	9,79	8,93
270	10,01	9,57	7,67

2.2.2. Chemical and physical analyses

Dry matter, protein, and titratable acid were determined according to standard methods of the Association of Official Analytical Chemists (AOAC) [17], fat, salt and ash contents of cheese powders according to the methods defined by Kurt et al. (2007) [18]. Powdered cheese sample (10 g) was mixed with 15 mL of distilled water until a homogeneous mixture was obtained, the pH values of the mixture were measured using a digital pH meter (Hanna HI 2002-02 edge, Hanna Inc., Romania) [19].

The water activity (a_w) of the samples was measured at 25°C using a water activity meter (Testo 650, Testo Inc., NJ, USA). The color parameters L^* (lightness), a^* (redness), and b^* (yellowness) were measured using a Chroma Meter CR-400 (Konica Minolta Business Technologies, Inc., Tokyo, Japan). The chroma (C) value, color change (ΔE) and the Browning Index (BI) were calculated using the L^*, a^*, and b^* values according to the following equations [20,21].

$$C = \sqrt{a^2 + b^2} \quad (1)$$

$$BI = \frac{100 \times \left(\frac{a+1{,}75 \times L}{5{,}647 \times L + a - 3{,}012 \times b}\right) - 0{,}31}{0{,}17} \quad (2)$$

$$\Delta E = \sqrt{(\Delta L)^2 + (\Delta a)^2 + (\Delta b)^2} \quad (3)$$

2.2.3. Microbiological analyses

The microbiological analyses of cheese powder were conducted before and after drying. 10 g of sample was suspended in 90 mL of sterile ¼ Ringer solution (Merck, Darmstadt, Germany) and homogenized for 5 minutes using a magnetic stirrer (Heidolph MR Hei-Tec, Schwabach, Germany). Serial 10-fold dilutions were prepared using 9 mL of sterile Ringer solution for each

dilution step. The pour plate technique and aerobic incubation were used to determine the total mesophilic aerobic bacteria (TMAB) and yeast and mold counts. TMAB was enumerated on Plate Count Agar (PCA; Merck) following incubation at 37°C for 2-3 days, while yeast and mold counts were determined on Potato Dextrose Agar (PDA; Merck) after incubation at 25°C for 5-7 days. The results were expressed as the logarithm of the mean colony-forming units per gram of cheese (log cfu g^{-1}).

2.2.4. Statistical analysis

The statistical analysis of the data obtained was analyzed using SPSS statistical package programme at 95% confidence interval. One-way analysis of variance (ANOVA) was used for comparison. In cases where the difference between samples was significant, Duncan Multiple Comparison test was used to determine the difference between means. The significance of differences between treatments was evaluated at a significance level of $p<0.05$.

3. Results and Discussion

Cheese samples were dried at 40, 50, and 60°C temperatures in a hot air circulation dryer. Initial moisture content of the control cheese was approximately 40%. The final moisture contents of the powdered cheese samples dried at 40, 50 and 60°C were 10.01, 9.57, and 7.67%, respectively. During the drying process, samples dried at 50°C exhibited lower agglomeration and more stable drying behavior, whereas those dried at 60°C showed the highest degree of agglomeration along with increased fat loss observed (Figure 1). Research on spray drying conditions in cheese powder production has shown that increasing outlet air temperatures can cause a significant reduction in free fat content, indicating higher fat loss at elevated temperatures [22].

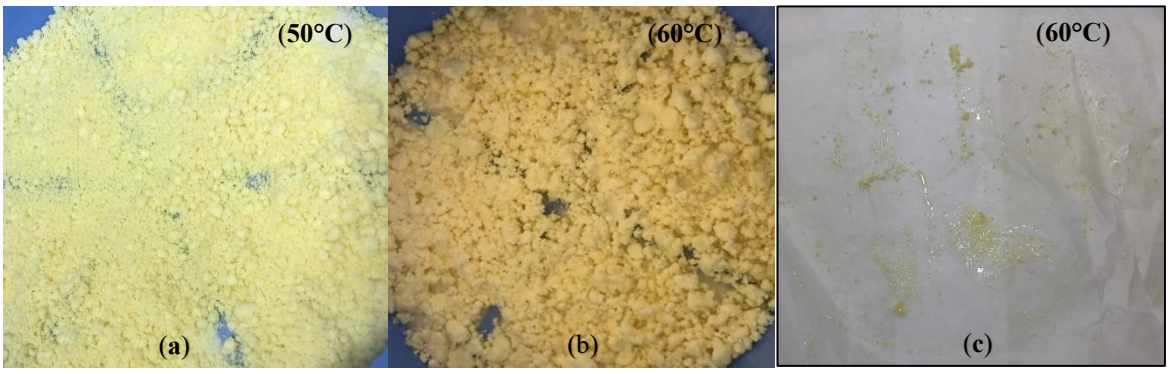

Figure 1. Agglomeration (a, b) and fat leakage (c) during drying.

The variations in cheese samples moisture content with drying time is presented in Figure 2. The drying temperature is an important parameter for the moisture content of the cheese. The moisture content decreased with the increase in drying time. The drying time required to reach the target moisture content (10%) was 270 minutes at 40°C, which decreased to 210 minutes at 50°C and further to 170 minutes at 60°C. It is well established that increasing the drying air temperature enhances both diffusion and mass transfer rates, thereby accelerating moisture removal and significantly reducing the overall drying time [23].

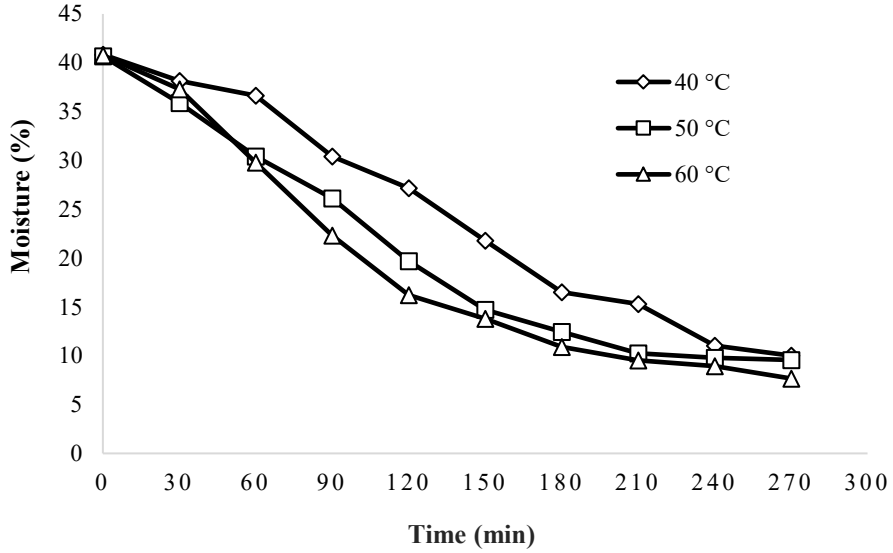

Figure 2. Drying curves of cheese at different drying conditions.

3.1. Physical and chemical characteristics

Drying is a complex operation involving simultaneous physical, chemical, and biochemical transformations that occur during the removal of moisture from a product [24]. The process can significantly influence the compositional and functional properties of food, with outcomes varying based on the drying technique employed, the intensity of thermal exposure, and the specific processing parameters applied [25]. The physical and chemical properties of both the control sample and the powdered forms of Erzincan Tulum Cheese are presented in Table 2.

Table 2. Physical and chemical characteristics of Erzincan Tulum Cheese and powdered cheese samples.

	Control	**Powdered cheese**		
		40°C	**50°C**	**60°C**
Dry matter (%)	60,40±0,55^{a}	92,80±0,14^{b}	92,60±0,34^{b}	93,01±0,02^{b}
Fat (%)	30,50±0,14^{a}	23,90±0,42^{b}	26,45±0,21^{c}	25,70±0,17^{d}
Protein (%)	20,89±0,09^{a}	35,26±2,67^{b}	35,07±0,2^{b}	32,61±0,11^{c}
Ash (%)	3,76±0,056^{a}	5,60±0,39^{b}	5,70±0,02^{c}	5,90±0,25^{d}
Salt (%)	2,10±0,14^{a}	3,26±0,014^{b}	3,20±0,015^{b}	3,24±0,014^{b}
pH	5,56±0,28^{a}	4,80±0,28^{b}	4,73±0,14^{bc}	4,69±0,00^{c}
Acidity (Lactic acid %)	1,56±0,014^{a}	2,20±0,00^{c}	2,10±0,070^{bc}	2,00±0,071^{b}
Water activity (a_{w})	0,944±0,02^{a}	0,563±0,03^{b}	0,558±0,03^{b}	0,551±0,01^{b}

Means within a row with different superscripts are significantly different ($p<0.05$).

As presented in Table 2, a substantial increase in dry matter content was observed following the drying process, rising from 60.40% in the control sample to over 92% in all dried cheese samples. This increase is attributed to the substantial moisture evaporation during drying. Although the dry matter values showed slight variations across the temperature range of 40°C to 60°C, the trend suggests an eventual equilibrium point where further moisture loss becomes

negligible [26]. A notable reduction in fat content was observed in the dried samples compared to the control. This decrease is likely due to lipid migration or leakage during the drying process, particularly at higher temperatures [27]. When exposed to heat, cheese melts and fat is readily released from the protein matrix, contributing to this loss [28]. While the absolute protein content remains unaffected by the drying process, the reduction in moisture results in a higher relative protein concentration on a dry matter basis in the dried cheese compared to the fresh sample. Therefore, the process does not diminish the total amount of protein but increases its proportion relative to overall weight due to the reduced water content [29,30]. The ash content, which reflects the total mineral composition, also increased with rising drying temperatures. This effect is primarily due to the concentration resulting from moisture loss, as minerals remain stable under thermal treatment. Consequently, the increase in ash content represents relative accumulation rather than an absolute gain—similar to the behavior of salt during drying. Furthermore, a gradual decline in pH was observed with increasing drying temperatures, accompanied by a corresponding rise in titratable acidity.

Moisture content indicates the total water present in a food system, while water activity (a_w) reflects the availability of free water responsible for biochemical reactions. It serves as a critical indicator for predicting the shelf life of the resulting powder product [31]. The water activity (a_w) values of the powdered cheese samples were measured as 0.563, 0.558, and 0.551 at 40, 50, and 60°C, respectively, whereas the a_w of the control sample was 0.944. A significant ($p < 0.05$) reduction in a_w was observed with increasing drying temperatures from 40°C to 60°C. It was stated that at higher drying temperatures, the rate of heat transfer increases, providing greater driving force for moisture evaporation and accelerating the moisture loss. This results in the dried cheese foam with reduced a_w [32]. Given the high nutritional value of dairy products, the a_w value of 0.944 observed in the control sample represents a highly favorable environment for the growth of pathogenic microorganisms since it exceeds the critical threshold of 0.91 required for bacterial proliferation. The results presented in Table 2 reveals that the a_w values of the granulated Erzincan Tulum cheese samples dried at 40, 50, and 60°C are all below $a_w = 0.61$—the critical limit for microbial activity—indicating that the dried products fall within a microbiologically safe range. Although the a_w values of the granulated powder samples were found to be very similar, the effect of drying temperature on a_w was statistically significant ($p < 0.05$).

3.2. Color

Color is a critical quality attribute of powders, significantly affecting their sensory appeal, perceived quality, and market value. It is influenced by various factors, including drying temperature and duration, enzymatic and non-enzymatic browning reactions, moisture content, and surface water levels [33,34]. The changes in the color of the cheese samples dried at different temperatures and the control sample were given in Figure 3. As can be seen from the Figure 3, the color changes in the cheese samples became more pronounced as the temperature increased.

Figure 3. The color changing of control and dried cheese samples.

*L**, *a**, *b**, *C**, *BI* and *⊿E* were significantly influenced ($p < 0.05$) by the drying temperature (Table 3). Compared to control, the powdered cheese samples exhibited dark color resulting in lower lightness (*L**) value, as well as higher redness (*a**) and yellowness (*b**) value. This can be attributed to the pigment degradation associated with Maillard reaction [35,36]. The similar results were obtained in other studies [37,38].

Table 3. Color properties of Erzincan Tulum Cheese and powdered cheese samples.

	Control	Powdered cheese		
		40°C	50°C	60°C
L	93,76±0,80^{a}	75,37±0,67^{b}	68,88±1,65^{c}	73,75±0,41^{d}
a	-4,36±0,03^{b}	-4,40±0,08^{a}	-4,37±0,01^{b}	-4,48±0,09^{a}
b	17,40±0,65^{a}	21,27±0,32^{b}	21,41±0,19^{b}	24,70±0,08^{c}
C	17,94 ±0,63^{a}	21,72±0,33^{b}	21,85±0,18^{b}	25,10±0,09^{c}
BI	198,84±0,71^{a}	195,98±0,47^{b}	213,55±0,72^{c}	217,16±0,20^{d}
⊿E	-	19,28±1,32^{b}	25,18±2,30^{c}	21,27±0,99^{d}

Means within a row with different superscripts are significantly different ($p<0.05$).

The chroma (*C**) value, which reflects the saturation, purity, or intensity of visual color, increased in all powdered cheese samples compared to the control ($p < 0.05$). At the same time, *BI* also increased with increasing drying temperature. The Maillard reaction is considered one of the key factors influencing the browning index during the food drying process [39]. The total color difference (*⊿E*) between the control and powdered cheese samples ranged from 19.28 (40°C) to 25.18 (50°C). It was stated that the perceivable color differences can be analytically classified as very distinct (*⊿E* > 3), distinct (1.5 < *⊿E* < 3), and small (*⊿E* < 1.5) [40]. Thus, indicates perceptible to very distinct color changes compared to the control.

3.3. Microbiological analyses

TMAB and yeast-moulds were significantly influenced ($p<0.05$) by the drying temperature (Table 4). The microbial composition of cheese can be attributed to three principal sources: the indigenous microbiota of the raw milk, the starter cultures intentionally added during manufacturing, and contamination occurred during processing. Contamination by yeasts and molds often results from post-processing recontamination of the final product. Cheese can become contaminated through exposure to these microorganisms, which may be present on various surfaces and environments within the production facility, including air, equipment, water, and brine [41].

Table 4. Microbiological analysis results of Erzincan Tulum cheese samples (log cfu g^{-1})

Sample	TMAB	Yeast-Moulds
Control	7,62±0,035[a]	5,17±0,063[a]
40°C	6,83±0,049[b]	3,84±0,021[b]
50°C	6,32±0,042[c]	3,36±0,098[c]
60°C	3,36±0,077[d]	2,57±0,042[d]

Means within a row with different superscripts are significantly different ($p<0.05$).

According to the Turkish Codex Regulation on Microbiological Criteria [42], there are no specified limits for TMAB and yeast–moulds counts in cheese. It can be seen that initial counts of TMAB and yeast-moulds were 7.62 and 5.17 log cfu g^{-1}, respectively. In this study, TMAB and yeast-moulds counts exhibited a significant decline with increasing drying temperatures reaching 3.36 and 2.57 log cfu g^{-1} at 60 °C, respectively. Reduction in TMAB count followed same trend as yeast-moulds, at higher drying temperature the inactivation effect was higher. The bactericidal effect of increased temperature is well documented, as higher thermal conditions lead to substantial microbial inactivation [43,44,45]. Drying at this temperature appears to be particularly effective in enhancing microbial safety and may represent a critical threshold for processing. Overall, drying at 60 °C yielded the lowest microbial loads for both TMAB and yeast–moulds, indicating its potential as the optimal temperature for ensuring microbiological safety in powdered cheese production. Nevertheless, this microbial advantage must be weighed against potential compromises in quality attributes such as color, flavor, and functional properties at elevated drying temperatures.

4. Conclusion

The powdering of food products offers notable advantages in terms of storage efficiency, logistical convenience, and extended shelf life. Moreover, this technique, when applied to various types of cheese, enables the development of novel applications. The resulting cheese powders are commonly utilized in products such as chips, soups, sauces, crackers, ready meals, and other food items. It is anticipated that granulating Erzincan Tulum cheese will broaden its range of applications, as its intense flavor allows for effective use in small quantities.

This study demonstrated that hot air circulation drying is an effective method for transforming traditionally produced Erzincan Tulum cheese into a powdered form with extended shelf life

and potential for broader culinary applications. Among the tested temperatures, drying at 50 °C for 210 minutes was found to be the most suitable condition, offering a favorable balance between physicochemical quality and microbial safety. While drying at 60 °C resulted in the lowest microbial counts, it also caused negative effect on appearance of powdered cheese.

The drying process significantly reduced moisture content and water activity, placing the powdered cheese in a microbiologically safe range. Additionally, drying led to concentration of protein and minerals due to moisture removal, although a reduction in fat content was observed, particularly at higher temperatures. Color analysis indicated that increasing temperature intensified browning and color changes, likely due to Maillard reactions, potentially affecting consumer perception.

Overall, granulated Erzincan Tulum cheese produced at 50 °C drying temperature holds promise as a functional and flavorful ingredient for incorporation into various food products such as soups, sauces, ready meals, and snacks. The findings highlight the potential for developing novel dairy-based powdered products using traditional cheeses, contributing both to value-added utilization and to regional product innovation.

Acknowledgments

This manuscript is derived from the author's master's thesis titled 'Drying and determination of some quality parameters of Erzincan tulum cheese' submitted to Erzincan Binali Yıldırım University under the supervision of Prof. Dr. Mustafa Fatih Ertugay.

Ethics in Publishing

This study does not involve any ethical concerns related to its publication.

Author Contributions

All authors made equal contributions to the preparation and writing of this manuscript.

References

[1] Hastaoğlu, E., Erdoğan, M., & Işkın, M. (2021). Gastronomi turizmi kapsamında Türkiye peynir çeşitliliği haritası. *Atatürk Üniversitesi Sosyal Bilimler Enstitüsü Dergisi, 25*(3), 1084–1113. https://doi.org/10.53487/ataunisosbil.958028

[2] Kamber, U. (2015). Traditional Turkey cheeses and their classification. *Van Veterinary Journal, 26*(3), 161–171. https://doi.org/10.29185/vanvetj.251045

[3] Hayaloğlu, A. A. (2008). Türkiye'nin peynirleri-Genel bir perspektif. *Türkiye 10. Gıda Kongresi*, 21-23 Mayıs, Erzurum.

[4] Çakmakçı, S., & Çakır, Y. (2012). Erzincan Tulum (Şavak) peyniri ve benzeri peynirlerimiz. *3. Geleneksel Gıdalar Sempozyumu*, 10-12 Mayıs, Konya, Türkiye.

[5] Çakır, Y., & Çakmakçı, S. (2020). Comparison of some quality properties of Erzincan tulum cheeses produced from raw and pasteurized Akkaraman sheep milk. *Turkish Journal of Agricultural and Natural Sciences, 7*(4), 972–982. https://doi.org/10.30910/turkjans.761327

[6] Ergene, G., & Arslan, S. (2019). Chemical and sensory characteristics of dried çökelek cheeses at different temperatures. *Journal of Food Processing and Preservation, 43*(6), e13985. https://doi.org/10.1111/jfpp.13985

[7] Fox, P. F., Guinee, T. P., Cogan, T. M., & McSweeney, P. L. H. (2017). Cheese as an ingredient. In *Fundamentals of Cheese Science* (2nd ed., pp. 629–679). Springer. https://doi.org/10.1007/978-1-4899-7681-9_18

[8] Guinee, T. P., & Kilcawley, K. N. (2017). Ingredient cheese and cheese-based ingredients. In P. F. Fox, P. L. H. McSweeney, T. M. Cogan, & T. P. Guinee (Eds.), *Cheese* (pp. 715–755). Elsevier. https://doi.org/10.1016/B978-0-08-100596-5.00661-2

[9] Deshwal, G. K., Akshit, F. N. U., Altay, I., & Huppertz, T. (2024). A review on the production and characteristics of cheese powders. *Foods, 13*(14), 2204. https://doi.org/10.3390/foods13142204

[10] Köprüalan, Ö., Elmas, F., Bodruk, A., Arıkaya, Ş., Koç, M., & Koca, N. (2020). Drying kinetics of reduced fat white cheese dried by different methods. *Gıda*, 45(6), 1201–1214. https://doi.org/10.15237/gida.GD20107

[11] Varming, C., Beck, T. K., Petersen, M. A., & Ardö, Y. (2011). Impact of processing steps on the composition of volatile compounds in cheese powders. *International Journal of Dairy Technology, 64*(2), 197–206. https://doi.org/10.1111/j.1471-0307.2010.00650.x

[12] Ceylan Şahin, C., Erbay, Z., & Koca, N. (2018). The physical, microstructural, chemical and sensorial properties of spray dried full-fat white cheese powders stored in different multilayer packages. *Journal of Food Engineering*, 229, 57–64. https://doi.org/10.1016/j.jfoodeng.2017.11.022

[13] Felix Da Silva, D., Ahrné, L., Larsen, F. H., Hougaard, A. B., & Ipsen, R. (2018). Physical and functional properties of cheese powders affected by sweet whey powder addition before or after spray drying. *Powder Technology, 323*, 139–148. https://doi.org/10.1016/j.powtec.2017.10.014

[14] Ma, X., Wang, J., Lu, X., & Qiao, C. A. (2013). Two-stage process for the production of a novel cheese flavor powder. *Journal of Food Process Engineering, 36*, 591–597. https://doi.org/10.1111/j.1745-4530.2011.00677.x

[15] Urgu, M., Ünlütürk, S., & Koca, N. (2018). Effects of fat reduction on the stability, microstructure, rheological and color characteristics of white-brined cheese emulsion with different emulsifying salt amounts. *Korean Journal for Food Science of Animal Resources, 38*(5), 866–877. https://doi.org/10.5851/kosfa.2018.e8

[16] Urgu, M., Türk, A., Ünlütürk, S., Kaymak-Ertekin, F., & Koca, N. (2019). Milk fat substitution by microparticulated protein in reduced-fat cheese emulsion: The effects on stability, microstructure, rheological and sensory properties. *Food Science and Animal Resources, 39*(1), 23–34. https://doi.org/10.5851/kosfa.2018.e60

[17] AOAC (1990). In K. Helrich (Ed.), Official Methods of Analysis (15th ed.). Arlington, VA, USA: Association of Official Analytical Chemists, Inc.

[18] Kurt, A., Cakmakci, S., & Caglar, A., (2007). Süt ve Mamülleri Muayene Analiz Metotları Rehberi. Atatürk Üniversitesi Ziraat Fakültesi Yayınları No: 257, 398 p, Erzurum, Turkey (In Turkish).

[19] Savello, P. A., Ernstrom, C. A., & Kalab, M. (1989). Microstructure and meltability of model process cheese made with rennet and acid casein. *Journal of Dairy Science, 72*(1), 1–11. https://doi.org/10.3168/jds.S0022-0302(89)79073-1

[20] Askari, G. R., Emam-Djomeh, Z., & Mousavi, S. M. (2008). Investigation of the effects of microwave treatment on the optical properties of apple slices during drying. *Drying Technology, 26*(10), 1362–1368. https://doi.org/10.1080/07373930802463342

[21] Erbay, Z., & Koca, N. (2015). Effects of whey or maltodextrin addition during production on physical quality of white cheese powder during storage. *Journal of Dairy Science, 98*(12), 8391–8404. https://doi.org/10.3168/jds.2015-9765

[22] Koca, N., Erbay, Z., & Kaymak-Ertekin, F. (2015). Effects of spray-drying conditions on the chemical, physical, and sensory properties of cheese powder. *Journal of Dairy Science, 98*(5), 2934–2943. https://doi.org/10.3168/jds.2014-9111

[23] Tülek, Y., & Demiray, E. (2014). Effect of hot air drying and different pretreatments on color and drying characteristics of persimmons. *Journal of Agricultural Sciences, 20*(1), 27–37.

[24] Erbay, Z., Koca, N., Kaymak-Ertekin, F., & Ucuncu, M. (2015). Optimization of spray drying process in cheese powder production. *Food and Bioproducts Processing, 93*, 156–165. https://doi.org/10.1016/j.fbp.2013.12.008

[25] Guiné, R. (2018). The drying of foods and its effect on the physical, chemical, sensorial and nutritional properties. *International Journal of Food Engineering, 4*(2), 93–100. https://doi.org/10.18178/ijfe.4.2.93-100

[26] Tarapata, J., Szymańska, E., van der Meulen, L., Miltenburg, J., & Huppertz, T. (2025). Moisture loss from cheese during baking: Influence of cheese type, cheese mass, and temperature. *Foods, 14*(2), 165. https://doi.org/10.3390/foods14020165

[27] Hwang, I. S., Lee, K. B., Shin, Y. K., Baik, M. Y., & Kim, B. Y. (2015). Effect of drying and storage on the rheological characteristics of mozzarella cheese. *Food Science and Biotechnology, 24*(6), 2041–2044. https://doi.org/10.1007/s10068-015-0271-0

[28] Center for Dairy Research. (2000). The melt and stretch of cheese. Dairy Pipeline, 12(1).

[29] Schuck, P. (2014). Effects of drying on milk proteins. In *Milk Proteins* (pp. 319–342). Elsevier. https://doi.org/10.1016/B978-0-12-374039-7.00009-X

[30] Domínguez-Niño, A., Cantú-Lozano, D., Ragazzo-Sanchez, J. A., Andrade-González, I., & Luna-Solano, G. (2018). Energy requirements and production cost of the spray drying process of cheese whey. *Drying Technology, 36*(5), 597–608. https://doi.org/10.1080/07373937.2018.1425143

[31] Izadi, Z., Mohebbi, M., Shahidi, F., Varidi, M., & Salahi, M. R. (2020). Cheese powder production and characterization: A foam-mat drying approach. *Food and Bioproducts Processing, 123*, 225–237. https://doi.org/10.1016/j.fbp.2020.02.004

[32] Salahi, M. R., Mohebbi, M., & Taghizadeh, M. (2017). Development of cantaloupe (Cucumis melo) pulp powder using foam-mat drying method: Effects of drying conditions on microstructural of mat and physicochemical properties of powder. *Drying Technology, 35*(15), 1897–1908. https://doi.org/10.1080/07373937.2017.1291518

[33] Viuda-Martos, M., Ruiz-Navajas, Y., Martín-Sánchez, A., Sánchez-Zapata, E., Fernández-López, J., Sendra, E., Sayas-Barberá, E., Navarro, C., & Pérez-Álvarez, J. A. (2012). Chemical, physico-chemical and functional properties of pomegranate (Punica granatum L.) bagasses powder co-product. *Journal of Food Engineering, 110*(2), 220–224. https://doi.org/10.1016/j.jfoodeng.2011.05.029

[34] Dehghannya, J., Pourahmad, M., Ghanbarzadeh, B., & Ghaffari, H. (2018). Influence of foam thickness on production of lime juice powder during foam mat drying: Experimental and numerical investigation. *Powder Technology, 328*, 470–484. https://doi.org/10.1016/j.powtec.2018.01.015

[35] Montoya-Ballesteros, L. C., González-León, A., García-Alvarado, M. A., & Rodríguez-Jimenes, G. C. (2014). Bioactive compounds during drying of chili peppers. *Drying Technology, 32*(12), 1486–1499. https://doi.org/10.1080/07373937.2014.902381

[36] Bi, Y. X., Zielinska, S., Ni, J. B., Li, X. X., Xue, X. F., Tian, W. L., Peng, W. J., & Fang, X. M. (2022). Effects of hot-air drying temperature on drying characteristics and color deterioration of rape bee pollen. *Food Chemistry, 16*, 100464. https://doi.org/10.1016/j.foodchem.2022.100464

[37] Michalska, A., Honke, J., Łysiak, G., & Andlauer, W. (2016). Effect of drying parameters on the formation of early and intermediate stage products of the Maillard reaction in different

plum (Prunus domestica L.) cultivars. *LWT - Food Science and Technology, 65*, 932–938. https://doi.org/10.1016/j.lwt.2015.09.029

[38] Wongwiwat, P., & Wattanachant, S. (2016). Color characteristics and Maillard reactions of chicken meat jerky with different sweeteners during storage. *Walailak Journal of Science and Technology (WJST)*, *13*(3), 141–155. https://doi.org/10.14456/WJST.2016.15

[39] Aktağ, I. G., & Gökmen, V. (2021). Investigations on the formation of α-dicarbonyl compounds and 5-hydroxymethylfurfural in fruit products during storage: New insights into the role of Maillard reaction. *Food Chemistry, 363*, 130280. https://doi.org/10.1016/j.foodchem.2021.130280

[40] Adekunte, J. A., Ragain, J. C., & Johnston, W. M. (2010). Minimum color differences for discriminating mismatch between composite and tooth color. *Journal of Prosthetic Dentistry, 103*(5), 325–331. https://doi.org/10.1016/S0022-3913(10)60069-2

[41] Kongo, M., & Malcata, F. X. (2016). Cheese: Chemistry and microbiology. In *Encyclopedia of Food and Health* (pp. 735–740). Elsevier. https://doi.org/10.1016/B978-0-12-384947-2.00135-5

[42] TGK (Türk Gıda Kodeksi). Mikrobiyolojik 2011. Kriterler Yönetmeliği, Resmi Gazete Tarihi: 29.12.2011, Sayı: 28157.

[43] Sung, N., & Collins, M. T. (2000). Effect of three factors in cheese production (pH, salt, and heat) on *Mycobacterium avium* subsp. *paratuberculosis* viability. *Applied and Environmental Microbiology, 66*(4), 1334–1339. https://doi.org/10.1128/AEM.66.4.1334-1339.2000

[44] Ghandi, A., Powell, I., Chen, X. D., & Adhikari, B. (2012). Drying kinetics and survival studies of dairy fermentation bacteria in convective air drying environment using single droplet drying. *Journal of Food Engineering, 110*(3), 405–417. https://doi.org/10.1016/j.jfoodeng.2011.12.031

[45] Possas, A., Bonilla-Luque, O. M., & Valero, A. (2021). From cheese-making to consumption: Exploring the microbial safety of cheeses through predictive microbiology models. *Foods*, *10*(2), 355. https://doi.org/10.3390/foods10020355

e-ISSN: 2149-4584

Erzincan University Journal of Science and Technology

EJSAT 2025, 18 (3) 842-857

Research Article

Lepton Flavor Violating Tau Decays in The Constrained MSSM-Seesaw Model

Vael HAJAHMAD *, Mahmoud ALBARI, Ali Ercan EKİNCİ

Erzincan Binali Yildirim University, Faculty of Arts and Sciences, Physics Department, Erzincan

Received: 20/06/2025, **Revised:** 23/07/2025, **Accepted:** 29/07/2025, **Published:** 31/12/2025

Abstract

The flavor violation of leptons may occur in specific particle interactions, a phenomenon referred to as lepton flavor violation (LFV). Within the standard model of particle physics (SM), lepton flavors are predicted to be strictly conserved. Thus, any observed violations could provide significant insights into physics beyond the standard model (BSM). This research focuses on examining LFV in tau decays within the framework of supersymmetric models (SUSY), specifically the constrained minimal supersymmetric standard model (CMSSM) which is extended by the seesaw type-I mechanism. By including right-handed neutrino fields and the seesaw mechanism, the CMSSM model offers explanations for phenomena including neutrino masses. The primary objective is to conduct a phenomenological analysis of LFV in tau decays for the following channels: $\tau^- \longrightarrow e^-e^+e^-, \tau^- \longrightarrow \mu^-\mu^+\mu^-, \tau^- \longrightarrow e^-\mu^+\mu^-, \tau^- \longrightarrow \mu^-e^+e^-, \tau^- \longrightarrow e^+\mu^-\mu^-, \tau^- \longrightarrow \mu^+e^-e^-$. We meticulously calibrated the parameters using the constraints from the current experimental bounds on neutrino and supersymmetric particle masses. We calculate the branching ratios of the LFV of tau decays, the numerical results are found to be in the order of 10^{-9}**.** The prediction of the branching ratios is found to be several orders of magnitude below the current experimental bounds.

Keywords: Lepton flavor violation, Supersymmetry, Seesaw Mechanism

Kısıtlı MSSM-Seesaw Modelinde Lepton Lezzet İhlalli Tau Bozunmaları

Öz

Leptonların lezzet ihlali, belirli parçacık etkileşimlerinde ortaya çıkabilir ve bu olaya lepton lezzet ihlali (LFV) denir. Parçacık fiziğinin standart modelinde (SM), lepton lezzetlerinin kesinlikle korunacağı öngörülmektedir. Bu nedenle, gözlemlenen herhangi bir ihlal, standart modelin ötesindeki fizik hakkında önemli bilgiler sağlayabilir (BSM). Bu araştırma, süpersimetrik modeller (SUSY) çerçevesinde, özellikle de seesaw tip-I mekanizması ile genişletilmiş kısıtlı minimal süpersimetrik standart model (CMSSM) içinde tau bozunumlarında LFV'yi incelemeye odaklanmaktadır. CMSSM modeli, sağ el nötrino alanlarını entegre eder ve seesaw mekanizması, nötrino kütleleri dahil olmak üzere çeşitli fenomenleri açıklamaktadır. Temel amaç, aşağıdaki kanallarda tau bozunumlarında LFV'nin fenomenolojik analizini yapmaktır: $\tau^- \longrightarrow e^-e^+e^-, \tau^- \longrightarrow \mu^-\mu^+\mu^-, \tau^- \longrightarrow e^-\mu^+\mu^-, \tau^- \longrightarrow \mu^-e^+e^-, \tau^- \longrightarrow e^+\mu^-\mu^-, \tau^- \longrightarrow \mu^+e^-e^-$. Nötrino ve süpersimetrik parçacık kütlelerine ilişkin mevcut deneysel sınırlamalardan elde edilen kısıtlamaları kullanarak parametreleri titizlikle kalibre ettik. Tau bozunumlarının LFV'sinin dallanma oranlarını hesapladık ve sayısal sonuçların10^{-9}. Dallanma oranlarının tahmini, mevcut deneysel sınırların birkaç mertebe altında bulunmuştur.

Anahtar Kelimeler: Lepton lezzet ihlali, Seesaw Mekanizma, Süpersimetri

Corresponding Author: whahmad@erzincan.edu.tr

Cite this Article: Erzincan University Journal of Science and Technology 2025, 18(3) 842-857. https://doi.org/10.18185/erzifbed.1723439

Introduction

The Standard Model (SM) of particle physics has been remarkably successful in describing the known elementary particles and their interactions. However, it fails to provide a mechanism for neutrino mass generation, a deficiency highlighted by the experimental confirmation of neutrino oscillations. This phenomenon implies the violation of lepton flavor in the neutral lepton sector and strongly motivates the search for physics beyond the Standard Model (BSM). One of the most well-studied frameworks that address some of the shortcomings of the SM is the Minimal Supersymmetric Standard Model (MSSM), which introduces a supersymmetric partner for each SM particle. MSSM offers attractive theoretical advantages, such as the stabilization of the Higgs mass hierarchy and the unification of gauge couplings at high energy scales. Nevertheless, it does not accommodate neutrino masses by itself. To resolve this, the MSSM can be extended by a Type-I seesaw model, in which three heavy right-handed neutrinos are introduced. This allows for the generation of small Majorana masses for left-handed neutrinos via high-scale interactions. When the universality of soft SUSY-breaking parameters is assumed at a high-energy scale, the model becomes the Constrained MSSM (CMSSM), reducing the number of free parameters and improving predictability. In such a setup, the inclusion of the seesaw mechanism induces charged lepton flavor violation via radiative corrections involving the neutrino Yukawa couplings. Among the various (LFV) observables, rare tau decays are of particular interest, especially the purely leptonic three-body decay modes, which include: $\tau^- \rightarrow e^- e^+ e^-$, $\tau^- \rightarrow \mu^- \mu^+ \mu^-$, $\tau^- \rightarrow e^- \mu^+ \mu^-$, $\tau^- \rightarrow \mu^- e^+ e^-$, $\tau^- \rightarrow e^+ \mu^- \mu^-$, $\tau^- \rightarrow \mu^+ e^- e^-$.This work presents a comprehensive phenomenological analysis of these six LFV tau decay channels within the CMSSM extended by the Type-I seesaw mechanism. The study investigates how the corresponding branching ratios are affected by key supersymmetric parameters such as the universal scalar mass m_0, gaugino mass $M_{1/2}$, trilinear coupling A_0, ratio of Higgs vacuum expectation values tanβ, and the sign of the Higgsino mass parameter μ. By exploring the parameter space, we aim to uncover distinctive features of LFV in the SUSY-seesaw framework and evaluate the model's testability in current or future experiments.

Literature Review and Experimental Constraints

Several theoretical works have established the relevance of lepton flavor violating (LFV) tau decays in the context of supersymmetric seesaw models. In particular Antusch et al. [1] and Ilakovac et al. [2] have performed direct computations of three-lepton tau decay modes such as $\tau^- \rightarrow \mu^- \mu^+ \mu^-$, $\tau^- \rightarrow e^- e^+ e^-$, $\tau^- \rightarrow e^- \mu^+ \mu^-$, $\tau^- \rightarrow \mu^- e^+ e^-$ in both Type-I and inverse seesaw models. These studies demonstrated the dependence of branching ratios on the seesaw scale, the structure of the neutrino Yukawa couplings, and SUSY-breaking parameters. Additionally, Abada et al. [3] emphasized the role of non-dipole operators, showing that decay ratios can differentiate among new physics operators. Wang et al. [4] contributed with a detailed RG-evolution formalism for Type-I seesaw models, which we incorporate in our analysis to evolve parameters from high-energy input to the electroweak scale. Building upon these foundations, our work investigates all six LFV tau decay channels under the constrained MSSM seesaw framework [5]. The present bounds and future sensitivities for these decay modes are taken

directly from the original publications of the BaBar and Belle collaborations, as summarized in the table below.

Table 1. Current Limits and Future Projections for Rare Tau LFV Decays.

LFV Process	BR Present Bound	Future Sensitivity
$\tau^- \rightarrow e^- e^+ e^-$	2.7×10^{-8} [6]	$\sim 1.0 \times 10^{-9}$ [7]
$\tau^- \rightarrow \mu^- \mu^+ \mu^-$	2.1×10^{-8} [6]	$\sim 1.0 \times 10^{-9}$ [7]
$\tau^- \rightarrow e^- \mu^+ \mu^-$	2.7×10^{-8} [6]	$\sim 1.0 \times 10^{-9}$ [7]
$\tau^- \rightarrow \mu^- e^+ e^-$	1.8×10^{-8} [6]	$\sim 1.0 \times 10^{-9}$ [7]
$\tau^- \rightarrow e^+ \mu^- \mu^-$	1.7×10^{-8} [6]	$\sim 1.0 \times 10^{-9}$ [7]
$\tau^- \rightarrow \mu^+ e^- e^-$	1.5×10^{-8} [6]	$\sim 1.0 \times 10^{-9}$ [7]

CMSSM Models and the Seesaw Mechanism

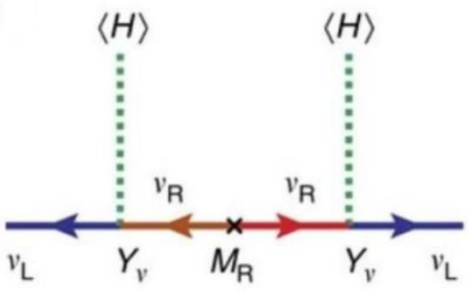

Figure 1. Canonical Seesaw Model Type-I.

The seesaw mechanism is one of the most compelling theoretical frameworks to explain the smallness of neutrino masses compared to other fermions in the Standard Model [8]. In the Type-I seesaw model, heavy right-handed neutrinos (ν_R) are introduced, which are singlets under the Standard Model gauge group and can carry large Majorana masses (M_R) [9]. These right-handed neutrinos interact with left-handed neutrinos (ν_L) via Yukawa couplings ($Y\nu$) and the vacuum expectation value of the Higgs field.

$$M\nu = -\langle H \rangle^2 \, Y\nu \, M_R^{-1} \, Y^T\nu$$

This equation, widely used in neutrino mass generation studies, demonstrates that the light neutrino mass Mν is suppressed by the large mass scale M_R of the right-handed neutrinos. The larger the M_R, the smaller the resulting mass of the left-handed neutrino, which is the core idea of the seesaw effect [9]. The accompanying Feynman diagram, shown in Figure 1, illustrates this process: a left-handed neutrino (ν_L) couples to a heavy right-handed neutrino (ν_R) via Yukawa interaction and Higgs exchange, then returns to Feynman diagram, showing ν_L propagating to itself via an intermediate heavy ν_R exchange through Higgs interactions ($\langle H \rangle$), resulting in an effective light neutrino mass as shown in Figure 1.

Main Characteristics and SUSY-Breaking Mechanism in the CMSSM

The super partners of the known Standard Model particles make up the MSSM's minimum particle content, which is preserved by the CMSSM. These super partners are introduced to preserve the symmetry of fermions and bosons [10, 11]**.** Supersymmetry breaks at high energies, often at the scale of the Grand Unified Theory (GUT), according to the CMSSM [10]. The breaking of supersymmetry results in the introduction of soft SUSY-breaking components into the Lagrange, such as mass terms, trilinear couplings, and bilinear Higgs terms.

$$-L_{soft,\ lepton} = \sum_{i=gen} \quad m_{\tilde{L}i}^2 \tilde{L}_i^\dagger \tilde{L}_i + m_{\tilde{l}_{Ri}}^2 \tilde{l}_{Ri}^\dagger \tilde{l}_{Ri} + m_{\tilde{\nu}_{Ri}}^2 \tilde{\nu}_{Ri}^\dagger \tilde{\nu}_{Ri}$$
$$+ \sum_{i,j=gen} \quad A_{ij}^l y_{ij}^l \, \tilde{l}_{Ri} H_d \tilde{L}_j + A_{ij}^\nu y_{ij}^\nu \, \tilde{\nu}_{Ri} H_u \tilde{L}_j + h.c.$$

The terms $m_{\tilde{L}i}^2$, $m_{\tilde{l}_{Ri}}^2$ and $m_{\tilde{\nu}_{Ri}}^2$ correspond to the squared mass terms of the supersymmetric partners of the left-handed leptons, right-handed charged leptons, and right-handed neutrinos, respectively. The indices i and j denote the generation number, referring to the first, second, or third family of leptons. The quantities $T_{ij}^l = A_{ij}^l y_{ij}^l$, $T_{ij}^\nu = A_{ij}^\nu y_{ij}^\nu$: A_{ij}^l and A_{ij}^ν represent the trilinear coupling terms for the charged leptons and neutrinos, respectively. Here, A_{ij}^l and A_{ij}^ν are the trilinear scalar coupling coefficients, while y_{ij}^l and y_{ij}^ν are the respective Yukawa couplings. The abbreviation h.c. stands for Hermitian conjugate, indicating that the Hermitian conjugate of the preceding term should also be included to ensure the Lagrangian is Hermitian [13].

Similarly, the lagrangian can be constructed to describe the interactions and behaviors of both the Higgs and gaugino fields [12]. At the grand unified theory (GUT) scale, $A_l = A_d = A_u = A_\nu = A_0$ represents the common scalar trilinear coupling in the constrained MSSM (CMSSM). In the CMSSM, $m_{1/2}$ denotes the universal gaugino mass $M_1 = M_2 = M_3 = m_{1/2}$. m_0 denotes the square of the symmetry-breaking masses of both supersymmetric fermions and Higgs doublets combining to a common value: $m_{\tilde{l}_R}^2 = m_{\tilde{L}}^2 = m_{\tilde{\nu}}^2 = m_0^2\ I\ \&\ m_{\tilde{H}_u}^2 = m_{\tilde{H}_d}^2 = m_0^2$. sign(μ) denotes the sign of the MSSM's supersymmetric Higgs mass parameter. tan (β) reflects the ratio of the vacuum expectation values of the two Higgs fields in the framework of the Minimal Supersymmetric Standard Model (MSSM) [15]. Msusy is the predicted scale at which supersymmetry will be achieved, which is commonly regarded as the average mass of the

supersymmetric particles (Msusy =1000GeV) [16]. The ratio of the Higgs vacuum expectation values, tanβ, is defined at the electroweak scale, while sign(μ) simply indicates the sign of the Higgsino mass parameter and is not associated with a particular energy scale.

Renormalization Group Equations (RGEs) and Lepton Flavor Violation

Renormalization group equations (RGEs) are a set of mathematical expressions that elucidate the way couplings and parameters in a given theory evolve as the energy scale at which the theory is probed,changes and varies. The equations of reorganization incorporate the quantum aspects of particle interactions and contribute to facilitating the understanding of how the characteristics of a specific theory change as we transition from high-energy scale to low-energy scale. The significance of RGEs in the context of Supersymmetry and Lepton Flavor Violation (LFV) [17]. Supersymmetric theories, such as CMSSM models, employ RGEs to explore the evolution of supersymmetry-breaking parameters and couplings with respect to changes in energy scale. The RGEs enable the examination of the behavior of supersymmetric models at various energy scales by accounting for the impacts of particle interactions and renormalization [12]. In the supersymmetric Seesaw Type-I model, two key parameters govern the radiative effects transmitted via RGEs: the neutrino Yukawa coupling matrix ($\boldsymbol{y_\nu}$) and the right-handed neutrino mass matrix M_R [18]. These parameters play a crucial role in generating LFV through the running of soft mass parameters. Specifically, the mass matrix of the left-handed sleptons acquires an additional RGE-induced contribution that leads to flavor-violating off-diagonal entries. This contribution is given by:

$$\Delta m_{\tilde{L}}^2 = -\frac{1}{8\,\pi^2} m_0^2 \left\{ 3 + \frac{A_0^2}{m_0^2} \right\} Y_\nu^\dagger Y_\nu \; log \; \left(\frac{M_{GUT}}{M_R} \right)$$

This equation demonstrates how the presence of the Yukawa coupling matrix (Y_ν) leads to non-universality in the slepton soft masses, a necessary condition for observable LFV processes in the left-handed slepton sector [19]. In contrast, the mass matrix of the right-handed sleptons does not receive any analogous contribution under the leading-log approximation, and remains flavor-diagonal in this framework:

$$\Delta m_{\tilde{e}}^2 = 0$$

Furthermore, the trilinear coupling terms associated with the charged leptons also undergo RGE evolution, acquiring corrections that are proportional to both the charged lepton Yukawa couplings and the neutrino Yukawa structure. This correction is expressed as:

$$\Delta T_l^2 = \frac{-3}{8\,\pi^2} A_0 Y_l Y_\nu^\dagger Y_\nu \; log \; \left(\frac{M_{GUT}}{M_R} \right)$$

These trilinear contributions are typically suppressed by the smallness of the charged lepton masses, particularly in the case of linear triplet coupling terms [15, 25].

Finally, in the constrained MSSM scenario, the trilinear scalar coupling A_0 is often expressed in terms of a dimensionless constant a_0 using the relation:

$$\frac{A_0}{m_0} = const = a_0 \Longrightarrow A_0 = a_0\, m_0$$

This parametrization reduces the number of free inputs in phenomenological analyses and facilitates numerical studies of LFV observables.

Analysis and Results

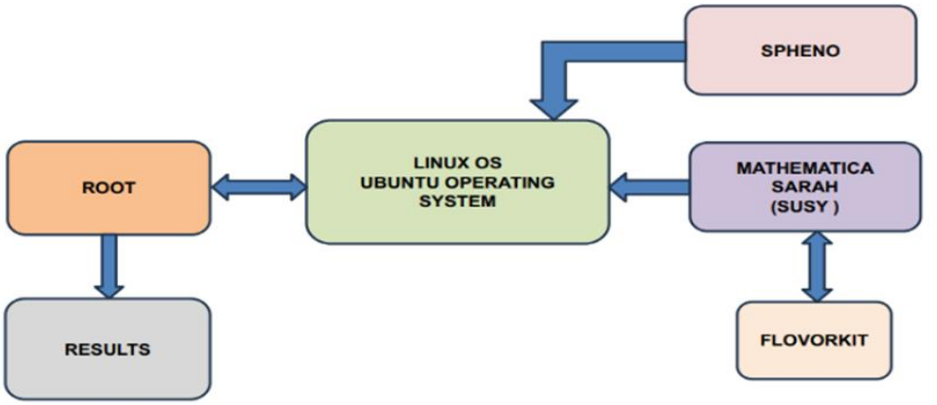

Figure 2. Workflow for SUSY Model Analysis using SPheno, SARAH, and ROOT.

In this section, the numerical results are implemented using the SARAH, SPheno and FlavorKit packages [26–29]. SARAH package is a Mathematica package for building and analyzing SUSY and non-SUSY models. It creates source code for Spheno tool. SPheno stands for S(upersymmetric) Pheno(menology). The SPheno code is written in Fortran-90 and it calculates the SUSY spectrum using low energy data and a user supplied high scale model as input like MSSM, type-I seesaw (type-II and type-III seesaw), NMSSM and other models. Furthermore, the FlavorKit package which is included in SARAH can compute a wide range of flavor observables like LFV in Z boson, Higgs and lepton decays [30-32].

Analysis of the Decay Width Γ ($\ell\alpha \to 3\ell\beta$) in Lepton Flavor Physics

$$\Gamma(\ell\alpha \to 3\ell\beta) = \frac{m_{l_\alpha}^5}{512\pi^3}\left[e^4(|K_2^L|^2 + |K_2^R|^2)\left(\frac{16}{3} log\ \frac{m_{l_\alpha}}{m_{l_\beta}} - \frac{22}{3}\right)\right.$$

$$+\frac{1}{24}(|A_{LL}^S|^2 + |A_{RR}^S|^2) + \frac{1}{12}(|A_{LR}^S|^2 + |A_{RL}^S|^2)$$

$$\left.+\frac{2}{3}\left(\left|\widehat{A_{LL}^V}\right|^2 + \left|\widehat{A_{RR}^V}\right|^2\right) + \frac{1}{3}\left(\left|\widehat{A_{LR}^V}\right|^2 + \left|\widehat{A_{RL}^V}\right|^2\right) + 6(|A_{LL}^T|^2 + |A_{RT}^T|^2)\right]$$

$$+\frac{e^2}{3}(K_2^L A_{RL}^{S*} + K_2^R A_{LR}^{S*} + \text{c.c.}) - \frac{2e^2}{3}\left(K_2^L \widehat{A_{RL}^{V*}} + K_2^R \widehat{A_{LR}^{V*}} + \text{c.c.}\right)$$
$$-\frac{4e^2}{3}\left(K_2^L \widehat{A_{RR}^{V*}} + K_2^R \widehat{A_{LL}^{V*}} + \text{c.c.}\right)$$

$$-\frac{1}{12}(A_{LL}^S A_{LL}^{T*} + A_{RR}^S A_{RR}^{T*} + \text{c.c.}) - \frac{1}{6}\left(A_{LR}^S \widehat{A_{LR}^{V*}} + A_{RL}^S \widehat{A_{RL}^{V*}} + \text{c.c.}\right)]$$

The following definition is used in the analysis: $\widehat{A_{XY}^V} = A_{XY}^V + e^2 K_1^X \quad (X, Y = L, R)$ [16].

The equation describes the decay width Γ (ℓα→3ℓβ), which represents the probability of a lepton ℓα decaying into three other leptons ℓβ. This process is relevant in the context of flavor physics, particularly in Beyond Standard Model (BSM) theories that include additional interactions.

Parameter Explanation:

- Γ(ℓα→3ℓβ): Decay width for the process where a leptonℓα decays into three leptons ℓβ.
- mℓα: Mass of the decaying lepton.
- $\boldsymbol{K_2^L, K_2^R}$: Wilson coefficients that describe the coupling of the interaction to the left-handed L or right-handed R component of the lepton.
- $\boldsymbol{A_{LL}^S, A_{RR}^S, A_{LR}^S, A_{RL}^S}$: These terms represent scalar couplings between the involved leptons.
- $\boldsymbol{\widehat{A_{LL}^V}, \widehat{A_{RR}^V}, \widehat{A_{LR}^V}, \widehat{A_{RL}^V}}$: These terms describe vector interactions, where $\boldsymbol{\widehat{A_{XY}^V}}$ s a combination of the original vector coupling $\boldsymbol{\widehat{A_{XY}^V}}$ and a term involving $\boldsymbol{K_1^X}$.
- $\boldsymbol{A_{LL}^T, A_{RT}^T}$: Tensor couplings, responsible for higher-order interactions.

Input Parameters for Numerical Analysis

The equation describes the decay rate for the transition of a lepton into three leptons of another flavor. Parameters like A_0, m_0, $m_{1/2}$, tan(β), sign(μ) influence the Wilson coefficients and therefore the couplings that mediate these decays. The processes in question are infrequent within the framework of the Standard Model and have yet to be detected through empirical observation. The final parameters in our study are: A_0, m_0, $m_{1/2}$, tan(β), sign(μ), y_ν, M_R. In the numerical analysis, models with large mixing in the neutrino Yukawa matrix y_ν are realized using the parametrization: $y_\nu = D_u U_{PMNS}^\dagger$, where y_ν is the Yukawa neutrino coupling matrix, Du is the diagonal Yukawa coupling matrix for top quarks, and UPMNS is the leptonic mixing matrix [19]. For our numerical results, we choose $m_{\nu 1} \approx$ O (10^{-3} eV). Accordingly, the heavy right-handed neutrino masses M_R are fixed as: (MR1, MR2, MR3) = (4.0×10^9 GeV, 4.0×10^9

GeV, 5.9×10¹⁴ GeV) [15]. The free parameters in the analysis are A_0, $m_{1/2}$, m_0, tan(β), while the sign of μ is taken as either positive or negative.

Analyzing the variation of BR ($\tau^- \rightarrow e^+ \mu^- \mu^-$) as a function of m_0

Figure 3 illustrates the upper limit of the branching ratio BR ($\tau^- \rightarrow e^+ \mu^- \mu^-$) as a function of m_0, for fixed values of A_0 = 300 GeV and tan(β) = 40, while varying $m_{1/2}$ in the range [160 – 460] GeV. The SUSY scale is set to M_{SUSY} = 1000 GeV. The x-axis represents m_0, and the y-axis shows the logarithmic value of the branching ratio. A shaded yellow region indicates the sensitivity range of the FCC experiment. From this figure, it is observed that the branching ratio decreases with increasing m_0 for all values of $m_{1/2}$. The highest BR values are obtained at low m_0, particularly for $m_{1/2}$ = 160 GeV. These values lie within the FCC sensitivity region up to approximately $m_0 \approx$ 600–660 GeV.

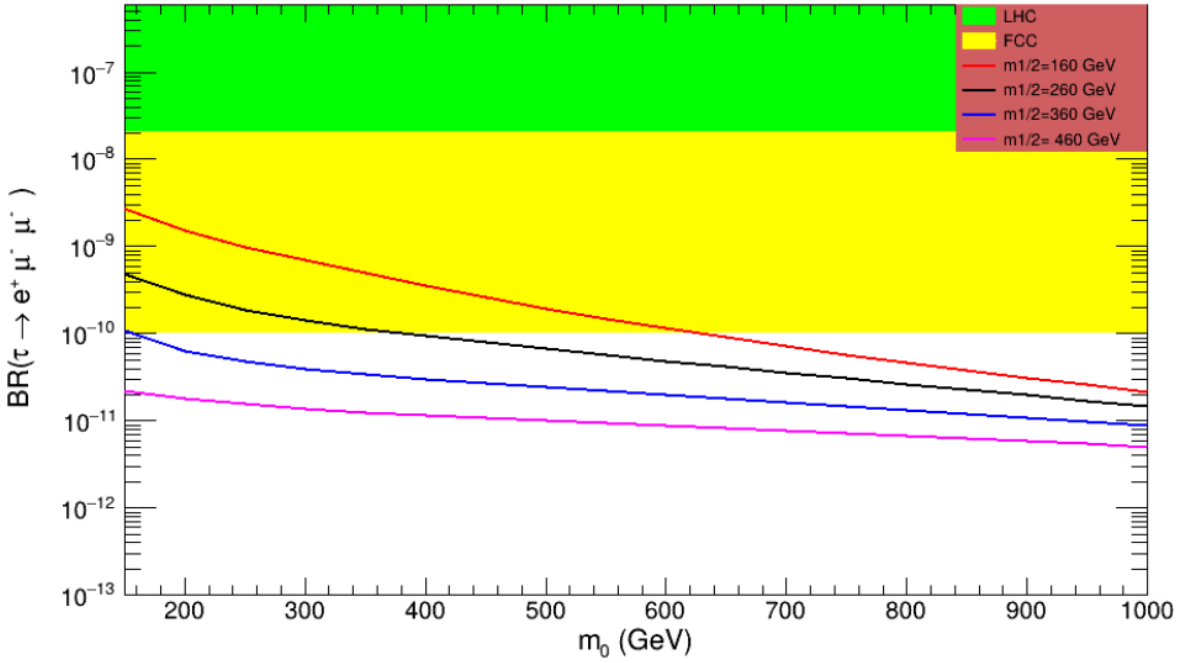

Figure 3. The upper limit of BR ($\tau^- \rightarrow e^+ \mu^- \mu^-$) as function of m_0, m_0 = [150-1000] GeV, A_0= 300 GeV, $m_{1/2}$ = [160 – 460] GeV, tan(β) = 40 and M_{SUSY} =1000 GeV.

Analyzing the variation of BR ($\tau^- \rightarrow e^- \mu^+ \mu^-$) as a function of m_0

Figure 4 presents the behavior of the branching ratio BR ($\tau^- \rightarrow e^- \mu^+ \mu^-$) as a function of the soft SUSY-breaking mass parameter m_0, under the conditions A_0 = 300 GeV and tan(β) = 40. The parameter $m_{1/2}$ varies within the range 160 to 460 GeV, while the SUSY scale is fixed at M_{SUSY} = 1000 GeV. The horizontal axis corresponds to m_0 in GeV, and the vertical axis shows the branching ratio on a logarithmic scale. Experimental sensitivity regions are highlighted: the yellow band corresponds to FCC reach, and the green region indicates the LHC exclusion limit.

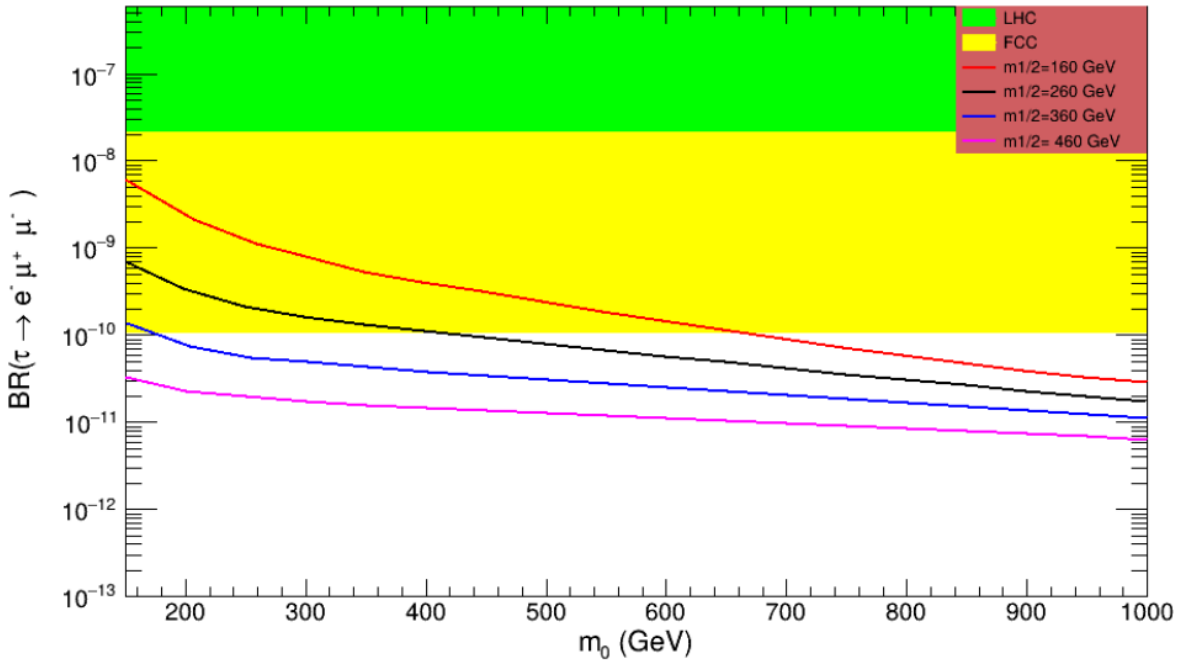

Figure 4. The upper limit of BR ($\tau^- \rightarrow e^- \mu^+ \mu^-$) as function of m_0, m_0 = [150-1000] GeV, A_0= 300 GeV, $m_{1/2}$ = [160 – 460] GeV, tan(β) = 40 and M_{SUSY} =1000 GeV.

As depicted in the figure, the branching ratio steadily declines with increasing m_0 across all values of $m_{1/2}$. The largest values of BR are obtained when $m_{1/2}$ is set to 160 GeV and m_0 is small, placing the curve well within the FCC sensitivity band up to approximately $m_0 \approx$ 600–660 GeV. This trend reinforces the conclusion that scenarios with lighter soft-breaking parameters are more likely to be observable.

Analyzing the variation of BR ($\tau^- \rightarrow \mu^+ e^- e^-$) as function of m_0

Figure 5 displays the upper limit of the branching ratio BR ($\tau^- \rightarrow \mu^+ e^- e^-$) as a function of m_0 in the range from 150 to 1000 GeV. This evaluation is conducted under the condition A_0 = 300 GeV as well as tan(β) = 40 and with four different values of $m_{1/2}$: 160 GeV (red), 260 GeV (black), 360 GeV (blue), and 460 GeV (magenta), while is M_{SUSY} = 1000 GeV. The plot highlights how the decay rate changes in response to variations in m_0 and $m_{1/2}$.

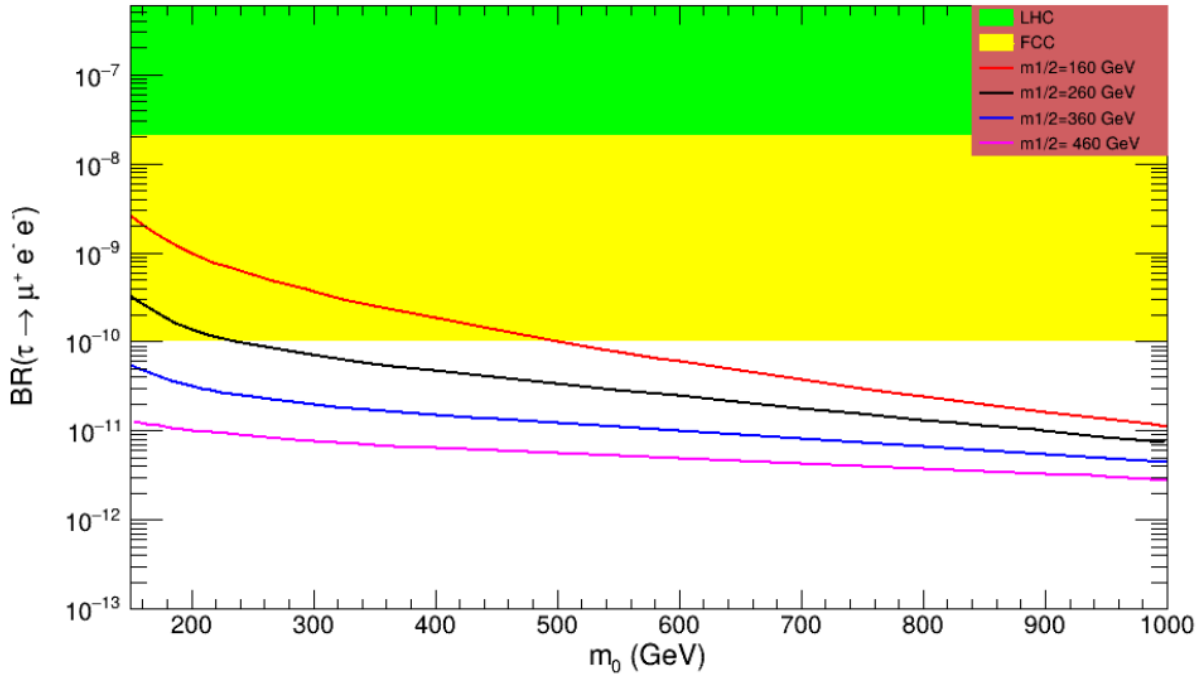

Figure 5. The upper limit of BR ($\tau^- \longrightarrow \mu^+ e^- e^-$) as a function of m_0, m_0 = [150-1000] GeV, A_0= 300 GeV, $m_{1/2}$ = [160 – 460] GeV, tan(β) = 40 and M_{SUSY} =1000 GeV.

As the value of m_0 increases, the branching ratio decreases consistently across all $m_{1/2}$ settings. This downward trend reflects the suppressive effect of larger soft-breaking mass parameters on the decay $\tau^- \longrightarrow \mu^+ e^- e^-$. Among the tested values, the most prominent decay rates are found at the lowest m_0 and smallest $m_{1/2}$, placing them within or near the sensitivity range of current and next-generation collider experiments. The dependency on m_0 and $m_{1/2}$ underscores how sensitive this process is to the supersymmetric mass configuration, while the fixed value of A_0 influences the overall scale of the branching ratio curves. Such results strengthen the case for improving experimental reach, particularly in regions of low m_0, where detection is more feasible.

Analyzing the variation of BR ($\tau^- \longrightarrow \mu^- e^+ e^-$) as function of m_0

Figure 6 presents the variation of the branching ratio (BR) for the lepton flavor-violating decay $\tau^- \longrightarrow \mu^- e^+ e^-$ as a function of the soft SUSY-breaking scalar mass parameter m_0, within the interval 150 to 1000 GeV. The analysis is carried out under the fixed conditions A_0 = 300 GeV and M_{SUSY} = 1000 GeV, while the gaugino mass parameter $m_{1/2}$ varies among the values 160 GeV, 260 GeV, 360 GeV, and 460 GeV. The colored curves in the plot correspond to these values respectively, with red representing 160 GeV, black for 260 GeV, blue for 360 GeV, and magenta for 460 GeV. As shown, the branching ratio exhibits a clear inverse correlation with m_0; as m_0 increases, BR decreases monotonically across all values of $m_{1/2}$. The highest values of BR are observed at low m_0 and low $m_{1/2}$, particularly around m_0 = 150 GeV and $m_{1/2}$ = 160 GeV.

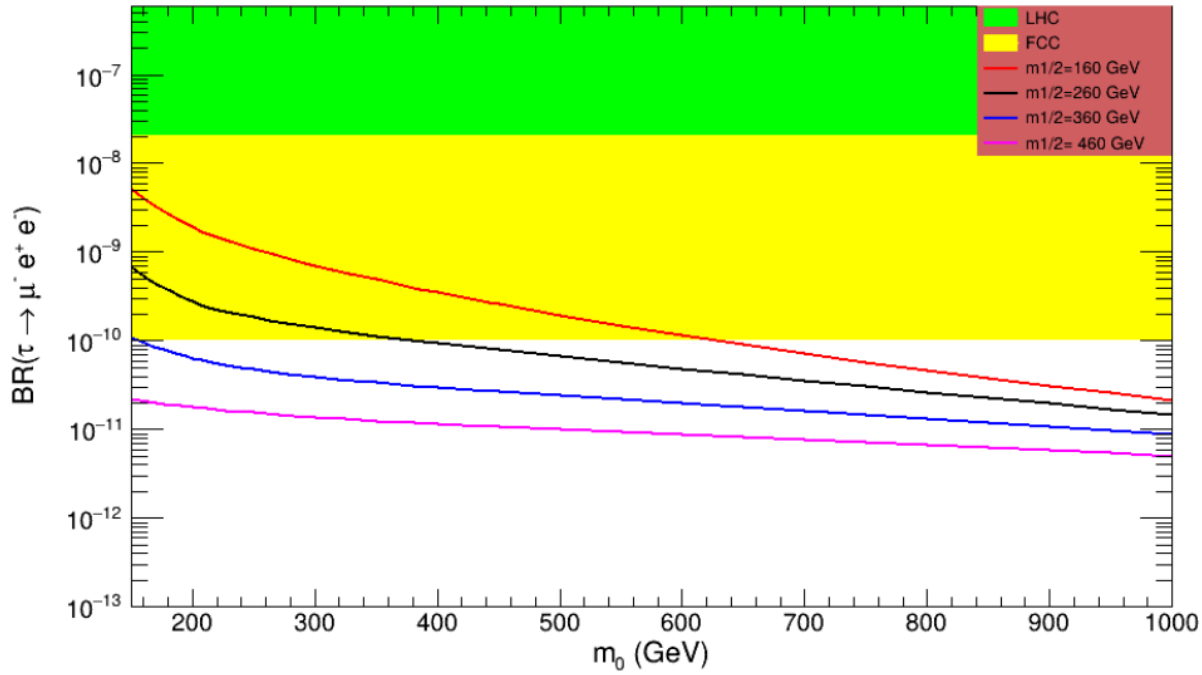

Figure 6. The upper limit of BR ($\tau^- \longrightarrow \mu^+ e^- e^+$) as a function of m_0, m_0 = [150-1000] GeV, A_0= 300 GeV, $m_{1/2}$ = [160 – 460] GeV, tan(β) = 40 and M_{SUSY} =1000 GeV.

These values place the prediction well within the projected sensitivity range of the Future Circular Collider (FCC), which is represented in yellow on the plot, while the current LHC exclusion region is indicated in green. The results highlight that scenarios with lighter soft-breaking parameters enhance the detectability of $\tau^- \longrightarrow \mu^- e^+ e^-$ decays, reinforcing the significance of future high-precision experiments in probing such rare processes.

Analyzing the variation of BR ($\tau \rightarrow 3\mu$) as a function of m_0

Figure 7 illustrates the behavior of the branching ratio (BR) for the lepton flavor-violating decay $\tau \longrightarrow 3\mu$ as a function of the soft SUSY-breaking scalar mass parameter m_0, in the range from 150 to 1000 GeV. The analysis is conducted with fixed values A_0 = 300 GeV, M_{SUSY} = 1000 GeV, and various values of $m_{1/2}$: 160, 260, 360, and 460 GeV, represented respectively by blue, black, magenta, and brown curves. The plot reveals that the branching ratio decreases progressively as m_0 increases, consistent across all values of $m_{1/2}$. The maximum branching ratio is observed for the lowest tested point: m_0 = 150 GeV and $m_{1/2}$ = 160 GeV, as shown by the blue curve. Importantly, these values place the BR well within Future Circular Collider (FCC), which is represented in yellow on the plot, while the current exclusion region of the Large Hadron Collider (LHC) is indicated in green.

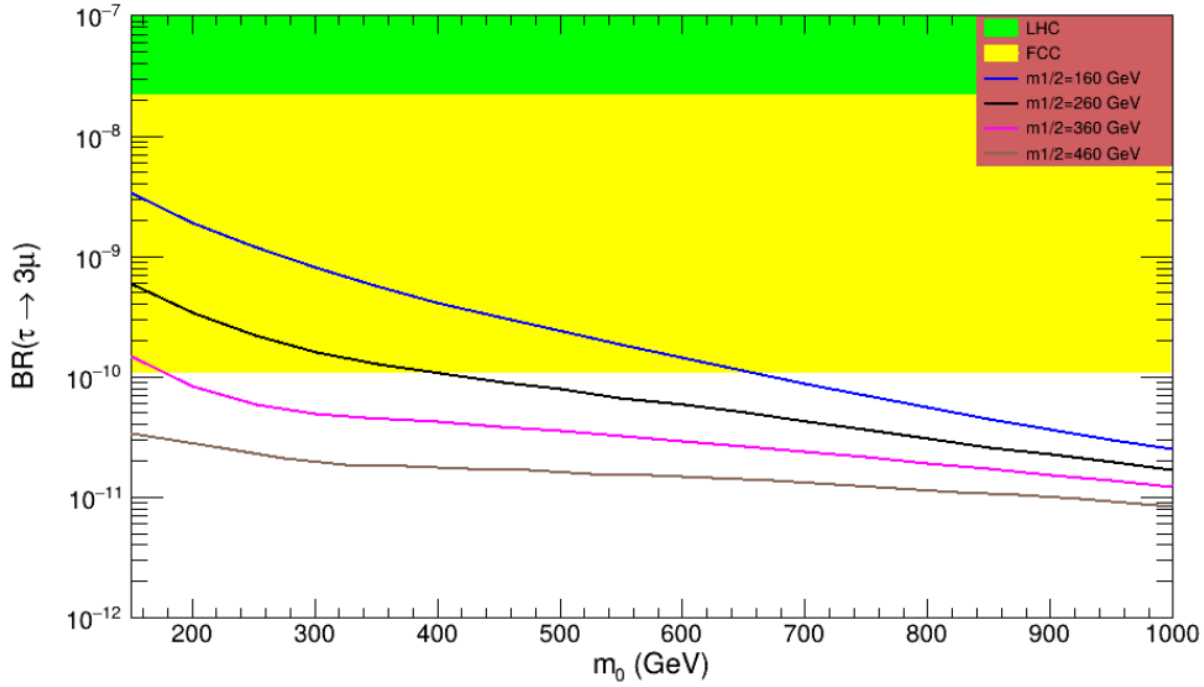

Figure 7. The upper Limit of BR ($\tau \longrightarrow 3\mu$), as function of m_0, m_0 = [150-1000] GeV, A_0= 300 GeV, $m_{1/2}$ = [160 – 460] GeV, tan(β) = 40 and M_{SUSY} =1000 GeV.

This trend highlights the importance of low-mass SUSY scenarios in enhancing the detectability of rare $\tau \longrightarrow 3\mu$ decays and motivates further investigation using current and next-generation high-precision experiments.

Analyzing the variation of BR ($\tau \rightarrow 3e$) as a function of m_0

Figure 8 illustrates the behavior of the branching ratio (BR) for the lepton flavor-violating decay $\tau \longrightarrow 3e$ as a function of the soft SUSY-breaking scalar mass parameter m_0, with a fixed trilinear coupling A_0 = 300 GeV, and SUSY scale M_{SUSY} = 1000 GeV. The gaugino mass parameter $m_{1/2}$ is varied across four values: 160 GeV, 260 GeV, 360 GeV, and 460 GeV, represented respectively by blue, black, magenta, and brown curves. As shown in the plot, the branching ratio decreases consistently with increasing m_0 for all values of $m_{1/2}$, indicating a strong inverse relationship.

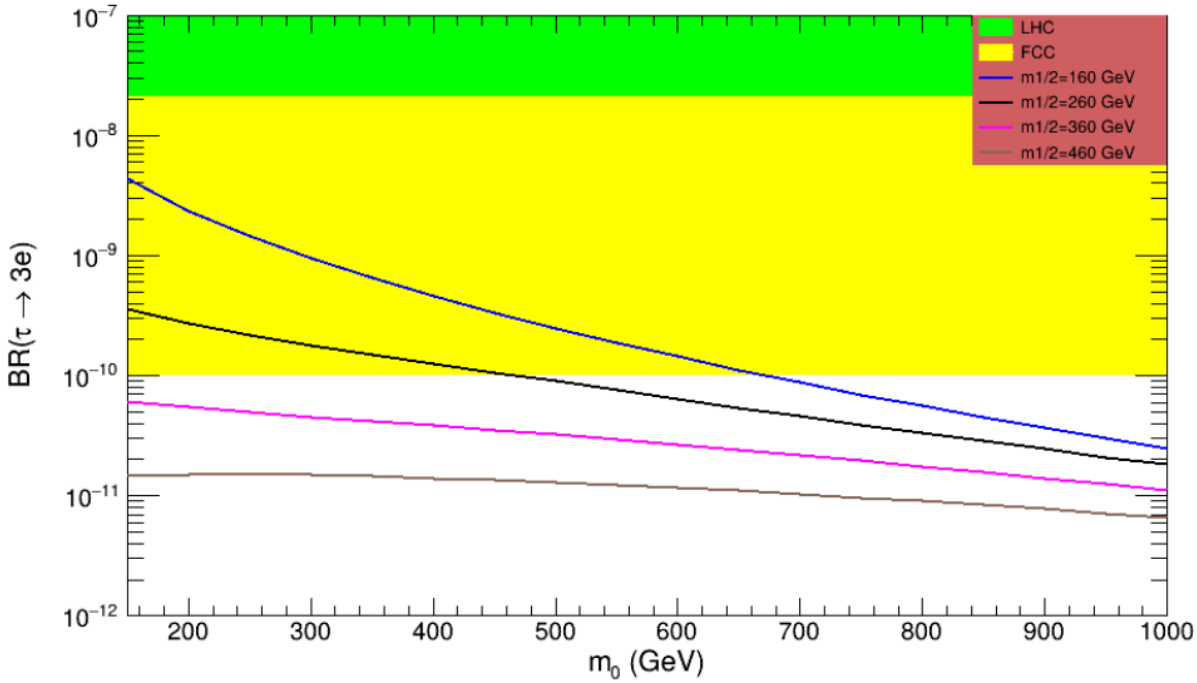

Figure 8. The upper limit of BR (τ⟶3e), as function of m_0, m_0 = [150-1000] GeV, A_0 = 300 GeV, $m_{1/2}$ = [160 – 460] GeV, tan(β) = 40 and M_{SUSY} =1000 GeV.

The highest BR is observed when $m_{1/2}$ = 160 GeV and m_0 = 150 GeV, shown by the blue curve.

Comparative Discussion and General Remarks

A comparative analysis of the six LFV tau decay channels: $\tau^- \rightarrow e^- e^+ e^-$, $\tau^- \rightarrow \mu^- \mu^+ \mu^-$, $\tau^- \rightarrow e^- \mu^+ \mu^-$, $\tau^- \rightarrow \mu^- e^+ e^-$, $\tau^- \rightarrow e^+ \mu^- \mu^-$, and $\tau^- \rightarrow \mu^+ e^- e^-$ reveals remarkably similar behavior across all modes with respect to the SUSY-breaking parameters. Each channel shows a decreasing trend in branching ratio as the soft mass parameters m_0 and $m_{1/2}$ increase.

Table 2. Summary of LFV Tau Decay Channels

Decay Channel	BR (Predicted)	Future Sensitivity	BR Present Bound
$\tau^- \rightarrow e^- e^+ e^-$	3.2×10^{-9}	$\leq 1 \times 10^{-9}$[6]	2.7×10^{-8} [7]
$\tau^- \rightarrow \mu^- \mu^+ \mu^-$	2.1×10^{-9}	$\leq 1 \times 10^{-9}$[6]	2.1×10^{-8} [7]
$\tau^- \rightarrow e^- \mu^+ \mu^-$	4.6×10^{-9}	$\leq 1 \times 10^{-9}$[6]	2.7×10^{-8} [7]
$\tau^- \rightarrow \mu^- e^+ e^-$	4.5×10^{-9}	$\leq 1 \times 10^{-9}$[6]	1.8×10^{-8} [7]
$\tau^- \rightarrow e^+ \mu^- \mu^-$	2.8×10^{-9}	$\leq 1 \times 10^{-9}$[6]	1.7×10^{-8} [7]
$\tau^- \rightarrow \mu^+ e^- e^-$	2.2×10^{-9}	$\leq 1 \times 10^{-9}$[6]	1.5×10^{-8} [7]

While some differences in sensitivity profiles exist, all predicted branching ratios lie around the order of 10^{-9} and are predominantly influenced by combinations of m_0, $m_{1/2}$. Importantly, many of these channels fall within the projected sensitivity of future experiments such as the Future Circular Collider (FCC), particularly in regions with m_0 = 150 GeV and $m_{1/2}$ = 160 GeV. These findings, summarized in Table 2, underscore the relevance of LFV tau decays in probing supersymmetric scenarios beyond the Standard Model. Moreover, when comparing the predicted branching ratios with current experimental limits, it becomes evident that most channels are already quite close to the current experimental bounds. This proximity reinforces the experimental feasibility of detecting such processes in upcoming facilities and positions these decay modes as promising targets for constraining or validating SUSY parameter spaces.

Conclusion and Outlook

In this work, we have conducted a comprehensive investigation of six lepton flavor violating (LFV) decay modes of the tau lepton: $\tau^- \to e^- e^+ e^-$, $\tau^- \to \mu^- \mu^+ \mu^-$, $\tau^- \to e^- \mu^+ \mu^-$, $\tau^- \to \mu^- e^+ e^-$, $\tau^- \to e^+ \mu^- \mu^-$, and $\tau^- \to \mu^+ e^- e^-$, within the framework of the constrained MSSM-seesaw (CMSSM + Type-I) model. In our numerical analysis, we fixed the trilinear coupling at A_0 = 300 GeV and scanned the scalar soft-breaking mass m_0 over the range [150–1000] GeV, and the gaugino mass parameter $m_{1/2}$ over the range [160–460] GeV. These parameter settings were selected to cover a wide region of phenomenologically viable SUSY scenarios. Through this detailed scan, we find that all channels show a similar sensitivity to these parameters. The predicted branching ratios are typically of the order of 10^{-9}. Notably, several channels fall within the sensitivity range of future experiments such as the Future Circular Collider (FCC), especially when m_0 = 150 GeV and $m_{1/2}$ = 160 GeV. These results indicate that LFV tau decays can offer valuable insight into supersymmetric models beyond the Standard Model.

Future Work

Our findings highlight significant advancements in the detection and measurement of rare tau decay processes. Compared to existing experimental limits, our results show considerable improvements, with several instances surpassing these benchmarks. Future projections suggest that upcoming experiments could achieve even higher sensitivities. These measurements are crucial for testing the Standard Model of particle physics and exploring new physics. Rare tau decays offer a sensitive probe for detecting new particles or interactions beyond the Standard Model. Enhanced sensitivity in these measurements could lead to groundbreaking discoveries in particle physics. Our study demonstrates substantial progress in understanding rare tau decay processes. Advanced future experiments with higher sensitivity will not only deepen our comprehension but also pave the way for uncovering new physics beyond the Standard Model.

Ethics in Publishing

There are no ethical issues regarding the publication of this study

ACKNOWLEDGMENTS

The authors thank the administration of scientific research at Erzincan Binali Yildirim University/Türkiye.

References

1. **Antusch S, Arganda E, Herrero MJ, Teixeira AM.** "LFV in tau and muon decays within SUSY seesaw." *arXiv:hep-ph/0610439*. Published online 2006.

2. **Ilakovac A, Pilaftsis A.** "Flavour-violating charged lepton decays in seesaw-type models." *Nucl Phys B.* 1995;437(3):491–526. *arXiv:hep-ph/9403398*.

3. **Abada A, Alonso R, De Romeri V, Vicente A.** "Enhancing lepton flavour violation in the supersymmetric inverse seesaw beyond the dipole contribution." *JHEP.* 2014;2014(4):1–36. *arXiv:1401.4266*.

4. **Wang W, Zhang Z, Wang Z.** "RG evolution and lepton flavor violation in Type-I see-saw." *Eur Phys J C.* 2015;75(12):597. *arXiv:1509.05388*.

5. **Hisano J, Moroi T, Tobe K, Yamaguchi M.** Lepton-flavor violation via right-handed neutrino Yukawa couplings in supersymmetric standard model. *Phys Rev D.* 1996;53(5):2442–2459.

6. **Hayasaka K, Inami K, Miyazaki Y.** Search for lepton flavor violating Tau decays into three leptons with 719 million produced $Tau^{+}Tau^{-}$ pairs. Phys Lett B. 2010; 687:139–143.

7. **Aushev T, Bartel W, Bondar A, Brodzicka J, Browder TE, Chang P, et al.** Physics at super B factory. arXiv [Preprint]. arXiv:1002.5012.

8. **Arganda E, Herrero MJ.** "Lepton flavour violation in constrained MSSM-seesaw models". arXiv08100160. Published online 2008.

9. **J. Masias, N. Cerna-Velazco, J. Jones-Perez, and W. Porod**. "Resolving a challenging supersymmetric low-scale seesaw scenario at the ILC", Phys. Rev. D 103, 115028 (2021)

10. **Hirsch M,Joaquim F,Vicente A**. **"**Constrained SUSY seesaws with a 125 GeV Higgs", Journal of High Energy Physics (2012) 2012(11), 10.1007/JHEP11(2012)105.

11**. I.J.R. Aitchison and A.J.G. Hey.** "Gauge Theories in Particle Physics", Volume 2 (Taylor & Francis, 2013)

12**. Jones, J.** L. "Gauge coupling unification in MSSM + 5 flavors". Physical Review D, 79(7), 075009 (2008).

13. **Goto T, Okada Y, Shindou T, Tanaka M, Watanabe R.** "Lepton flavor violation in the supersymmetric seesaw model after the LHC 8 TeV run". Phys Rev D. 2015;91(3):33007.

14. **Srednicki, Mark.** "Quantum field theory. Cambridge University Press, 2007", Chapter 22

15**. Girrbach J, Mertens S, Nierste U,** Wiesenfeldt S. "Lepton flavour violation in the MSSM". J High Energy Phys. 2010;2010(5):1-48.

16**. Berezinsky, V., and Kachelriess, M.** "Monte Carlo simulation for jet fragmentation in SUSY-QCD." CERN-TH 2000-232, IFIC/00-49. arXiv preprint hep-ph/0009053, 2000.

17. **Wang, Y., Zhang, D., & Zhou, S. (2023).** "Complete one-loop renormalization-group equations in the seesaw effective field theories". arXiv preprint arXiv:2302.08140

18**. J. F. Kamenik and M. Nemevšek.** "Lepton flavor violation in type I+ III seesaw," J. High Energy Phys., vol. 2009, no. 11, p. 23, 2009

19. **V. Brdar, A. J. Helmboldt, S. Iwamoto, and K. Schmitz.** "Type I seesaw mechanism as the common origin of neutrino mass, baryon asymmetry, and the electroweak scale," Phys. Rev. D, vol. 100, no. 7, p. 75029, 2019.

20**. G. Cvetič, C. Dib, C. S. Kim, and J. D. Kim**. Phys. Rev. D 66, 034008 – Published 13 August 2002; Erratum Phys. Rev. D 68, 059901 (2003)

21. **A. Abada, D. Das, A. Vicente, and C. Weiland.** "Enhancing lepton flavour violation in the supersymmetric inverse seesaw beyond the dipole contribution," J. High Energy Phys., vol. 2012, no. 9, pp. 1–34, 2012.

22**. K. Hayasaka, et al.** "Search for Lepton Flavor Violating τ Decays into Three Leptons with 719 million Produced τ+τ- Pairs", Phys. Lett. B687 (2010) 139.

23. **E. Arganda and M. J. Herrero**, Phys.Rev. D73 (2006), 055003, [hep-ph/0510405]

24. **Goodsell, M.D., Nickel, K. & Staub, F.**, "Two-loop Higgs mass calculations in supersymmetric models beyond the MSSM with SARAH and SPheno", Eur. Phys. J. C 75, 32 (2015).

25. **Bernigaud, J., Forster, A.K., Herrmann, B.**, et al, "Data-driven analysis of a SUSY GUT of flavour", J. High Energ. Phys. 2022, 156 (2022).

26. **Staub, F.,** Computer.Physics.Commun. **181**, 1077–1086 (2010) https://doi.org/10.1016/j.cpc.2010.01.011 arXiv:0909.2863 [hep-ph]

27. **Staub, F.,** Computer.Physics.Commun. **185**, 1773–1790 (2014) https://doi.org/10.1016/j.cpc.2014.02.018 arXiv:1309.7223 [hep-ph]

28. **Goodsell, M.D., Nickel, K., Staub, F.,** Eur. Phys. J. C **75** (2015) https://doi.org/10.1140/epjc/s10052-014-3247-y arXiv:1411.0675 [hep-ph]

29. **Bernigaud, J., Forster, A.K., Herrmann, B., King, S.F., Porod, W., Rowley, S.J.,** J. High Energ. Phys. **2022** (2022) https://doi.org/10.1007/JHEP05(2022)156 arXiv:2111.10199 [hep-ph]

30. **Porod, W., Staub, F., Vicente, A.,** Eur. Phys. J. C **74** (2014) https://doi.org/10.1140/epjc/s10052-014-2992-2 arXiv:1405.1434 [hep-ph]

31. **Bi, X.-J., Dei, Y.-B., Qi, X.-Y.,** Phys. Rev. D **63**, 096008 (2001) https://doi.org/10.1103/PhysRevD.63.096008, arXiv:hep-ph/0010270 [hep-ph]

32. **Navas, S.,** (Particle Data Group), Phys. Rev. D **110**, 030001 (2024) https://doi.org/10.1103/PhysRevD.110.030001

e-ISSN: 2149-4584

Erzincan University Journal of Science and Technology

EJSAT 2025, 18 (3) 858-875

Research Article

The Distribution of Prosthetic Treatments Type, Number, Year Applied and Patients Age and Gender for Patients Applying to the Prosthodontics Department Between 2014-2020

Funda Bayındır[1], Fatih Oktay[2,3*], Muhammed Kürüm[2]

[1]Atatürk University, Faculty of Dentistry, 25100, Erzurum, Turkey
[2]Erzincan Binali Yıldırım University, Oral and Dental Health Education and Research Hospital, 24100, Erzincan, Turkey
[3]Ataturk University, Institute of Health Sciences, 25100, Erzurum, Turkey

Received: 16/10/2024, **Revised:** 16/11/2024, **Accepted:** 30/11/2024, **Published:** 31/12/2025

Abstract

This study contains the distribution of prosthetic treatments' type, number and the year applied as well as their patients' sex and age given to patients who applied to the Ataturk University Faculty of Dentistry Prosthodontic Clinic between the years 2014 and 2020. Out of 202128 treatments administered to patients between the ages of 12 and 98, 104537 treatments were administered to women whilst 97951 treatments were administered to men. Between the ages 0 and 19, 303 treatments were administered to women whilst 119 were administered to men, for ages 20-34, 11541 to women and 8497 to men, for ages 35-49, 38413 to women, 30058 to men, for ages 50-64, 39346 to women, 40217 to men and for 65 years and above, 14934 to women, 18700 to men respectively. Most of the treatments were given to patients between the age of 50 and 64 with a total of 79563 treatments. Most applied treatments were the veener ceramic restorations. The study is based off of the treatment count of major prosthetic treatments and has been conducted accordingly.

The data for the major prosthetic treatments have been initially divided into the following categories: tooth supported fixed dental prostheses, removable partial dentures, total prosthetics, implant supported fixed dentures, implant supported removable dentures and immediate dentures.

Keywords: Denture types, patient distribution, prosthetic treatment

2014-2020 Yılları Arasında Protetik Diş Tedavisi Anabilim Dalına Başvuran Hastalara Uygulanan Tedavilerin Yaşa, Cinsiyete ve Yıllara Göre Dağılımının İncelenmesi

Özet

Bu çalışma; 2014-2020 yılları arasında yedi yıl boyunca Atatürk Üniversitesi Diş Hekimliği Fakültesi Protetik Diş Tedavisi kliniğine başvuran hastalara uygulanan protetik tedavi şekillerini, protetik işlem sayılarını, yıllara, cinsiyete ve yaşa göre dağılımını içermektedir. Kliniğimize başvuran hastaların yaşları; 12-98 arasında olup, toplam 202128 işlemden 104537 işlem kadın, 97591 işlem erkektir. Yaş grupları olarak 0-19 yaş aralığında 303 işlem kadın 119 işlem erkek, 20-34 yaş aralığında11541 işlem kadın 8497 işlem erkek, 35-49 yaş aralığında 38413 işlem kadın 30058 işlem erkek, 50-64 yaş aralığı 39.346 işlem kadın 40217 işlem erkek ve 65 yaş ve üzeri 14934 işlem kadın 18700 işlem erkek hastalar olmuştur. Başvuranlar arasında hastalara en fazla 79563'le 50-64 yaş aralığı, en çok uygulanan protez tipi ise veneer seramik kuron protezler olmuştur. Çalışmada uygulanan majör protetik tedavilerin işlem sayıları esas olarak incelemeye tabi tutulmuştur. Uygulanan majör protetik tedaviler ile ilgili veriler öncelikle; diş destekli sabit protezler, hareketli bölümlü protezler, tam protezler, implant destekli sabit protezler, implant destekli hareketli protez ve immediate protez uygulamaları olarak gruplara ayrılmıştır.

Anahtar Kelimeler: Dental protez tipleri, hasta dağılımı, protetik tedavi

Corresponding Author: oktayfatih@hotmail.com

Cite this Article: Erzincan University Journal of Science and Technology 2025, 18(3)858-875. https://doi.org/10.18185/erzifbed.1568418

1. Introductıon

Prosthodontics is a dental specialty concerned with the diagnosis, treatment planning, and rehabilitation of patients suffering from partial or complete edentulism by utilizing biocompatible materials. This field focuses on restoring oral function, comfort, appearance, and health. It is one of the fundamental branches of dentistry. Tooth loss or tissue loss resulting from dental issues can lead to problems in aesthetics, speech, mastication, and nutrition, extending to social and emotional difficulties, thereby directly affecting the patient's quality of life negatively [1]. It is a health issue that negatively impacts the quality of life, ranging from problems related to aesthetics, speech, chewing, and nutrition, to challenges in social relationships and emotional distress [2, 3].

In developed countries, the prevalence and extent of tooth loss have significantly decreased in recent years [4-7]. The incidence of edentulism has decreased by approximately 4-10% per decade [6, 7]. With the improvement of living conditions through the advancement of technology and science, the elderly population has shown a growing trend both globally and in our country. The increasing elderly population, which will continue to rise dramatically in the coming years, remains the primary reason for the high prevalence of edentulism [6]. As a result, prosthetic care is common in many European countries, especially among the elderly [8]. Furthermore, correlations between national welfare, irregular-to-regular dental visits, rural residency, age, gender, education, and the prevalence of edentulism and prosthetic care have also been demonstrated [6, 9].

The primary goal of prosthetic treatment is to replace missing teeth in partially or completely edentulous patients, restore function and aesthetics, and preserve the health of the remaining oral tissues. Prosthetic treatment combines various clinical and laboratory procedures that lead to the placement of either fixed (crowns and bridges) or removable (partial and complete) prostheses [10]. In principle, treatment with various types of removable prostheses is generally less successful compared to fixed prostheses. Therefore, removable prosthesis treatment is indicated only when fixed prosthesis treatment on teeth or dental implants is excluded due to clinical or financial factors [11, 12]. In recent years, it has been proven that removable prostheses supported by dental implants are a highly successful form of prosthetic treatment for edentulous patients, and their use is steadily increasing. However, due to increased complexity and higher costs, they are significantly less common than conventional prosthetic treatments without dental implants [13, 14].

Modern medicine aims to continuously improve the quality of human life, striving to maintain the highest level of comfort for individuals in both general health and oral health, especially as life expectancy increases. Oral and dental health problems are among the most common public health issues worldwide. A large portion of individuals are affected by these problems throughout their lives [15, 16].

Tooth loss significantly affects an individual’s aesthetics, function, and phonation. In modern dentistry, dental-supported fixed prostheses, removable prostheses, and implant-supported

fixed or removable prostheses are utilized to rehabilitate tooth deficiencies, taking into account the needs and expectations of the patient [14, 17, 18].

In Turkey, the population aged 65 and over, considered the elderly population, was 6,192,962 in 2014, and increased by 16% over the following five years, reaching 7,186,204 in 2018. The proportion of the elderly population within the total population rose from 8% in 2014 to 8.8% in 2018. The population aged 65 and over, considered as the elderly population, was 7,186,204 in 2018. Over the past five years, it increased by 21.4%, reaching 8,722,806 in 2023. The proportion of the elderly population within the total population rose from 8.8% in 2018 to 10.2% in 2023. In 2023, 44.5% of the elderly population consisted of men, while 55.5% were women. According to population projections, the proportion of the elderly population is expected to reach 12.9% in 2030, 16.3% in 2040, 22.6% in 2060, and 25.6% in 2080 [19].

Problems with the overall appearance of teeth are one of the most significant factors impacting individuals' social lives. Teeth that are aesthetically pleasing and harmoniously aligned when smiling positively affect a person's life and are one of the most evident signs of personal care. A pleasant smile significantly enhances communication and self-confidence, contributing to greater success and happiness in both professional and personal life. Teeth are considered an inseparable part of beauty. Missing teeth not only cause functional and structural problems but also affect individuals' psychology and social interactions [20].

It is important to understand the causes and patterns of tooth loss in the population for the planning of dental health services. Findings indicating changes in the level of edentulism within the population and the reasons for tooth loss serve as a guide in the appropriate preparation of national oral health service planning [21].

In the study, the distribution of major prosthetic treatment modalities applied to patients who presented to our clinic between 2014 and 2020 was analyzed over a seven-year period, categorized by year, gender, and age. The aim was to determine the types of treatments administered to patients and the proportions in which these treatments were provided.

2. Material and Method

The study was approved by the Ethics Committee of the Dean's Office of the Faculty of Dentistry of Ataturk University (Decision No. 2022-99). In the study, the ages of patients who applied to the Department of Prosthetic Dentistry at the faculty between 2014 and 2020 ranged from 12 to 98 years. A total of 22,348 patients visited the clinic, and 202,128 prosthetic procedures were performed, with 104,537 procedures carried out on female patients and 97,591 on male patients. Among the patients, the distribution by age groups is as follows:

- In the 0-19 age range, there were 303 procedures for females and 119 for males.
- In the 20-34 age range, 11,541 procedures were performed on females and 8,497 on males.
- In the 35-49 age range, there were 38,413 procedures for females and 30,058 for males.

- In the 50-64 age range, 39,346 procedures were performed on females and 40,217 on males.
- For patients aged 65 and above, there were 14,934 procedures for females and 18,700 for males.

The data obtained from the evaluation of protocol records of patients who presented between 2014 and 2020 were analyzed to assess the distribution of treatments performed by year, categorized by age and gender.

The data related to the major prosthetic treatments performed were initially categorized into fixed prostheses, removable partial dentures, complete dentures, implant-supported fixed prostheses, implant-supported removable prostheses, and immediate denture applications. Fixed prostheses included metal-ceramic restorations, full ceramic restorations, acrylic veneer restorations, precision-retained crowns, single-piece cast crown restorations, laminate veneer composite restorations, Maryland adhesive restorations, and zirconia restorations. Removable partial dentures were classified into acrylic and metal types, while complete dentures were also categorized as acrylic and metal. Additionally, implant-supported fixed prostheses, implant-supported removable prostheses, and immediate denture applications were evaluated as separate groups.

Descriptive statistics were performed for all variables. The normality of the variables was assessed using the Kolmogorov-Smirnov test. For variables that exhibited a normal distribution, descriptive analyses were conducted using the mean and standard deviation, while median and minimum-maximum values were used for variables that did not show a normal distribution. When making intergroup comparisons by year, the One-Way ANOVA test was applied for data that demonstrated normal distribution, whereas the Kruskal-Wallis test was utilized for data that did not. The Chi-Square test was employed for the evaluation of categorical data. A statistical significance level of $p < 0.05$ was accepted.

Statistical analyses were performed using SPSS 22.0 (Statistical Package for Social Sciences for Windows version 22.0; IBM Corp. Released 2013. IBM SPSS Statistics for Windows, Version 22.0. IBM Corp. Armonk, NY, USA).

3. Results and Discussion

The distribution of patients who presented to the clinic between 2014 and 2020 by gender and age, the proportions of the prostheses performed, and the total amounts of treatment administered to female and male patients across the years were evaluated using graphs. Among the procedures conducted, the most frequently performed treatments in terms of both workload and procedural intensity were dental-supported fixed crowns and bridges, implant-supported crowns and bridges, complete dentures, removable partial dentures, implant-supported removable prostheses, and immediate dentures. A total of 81,037 procedures were included in the study.

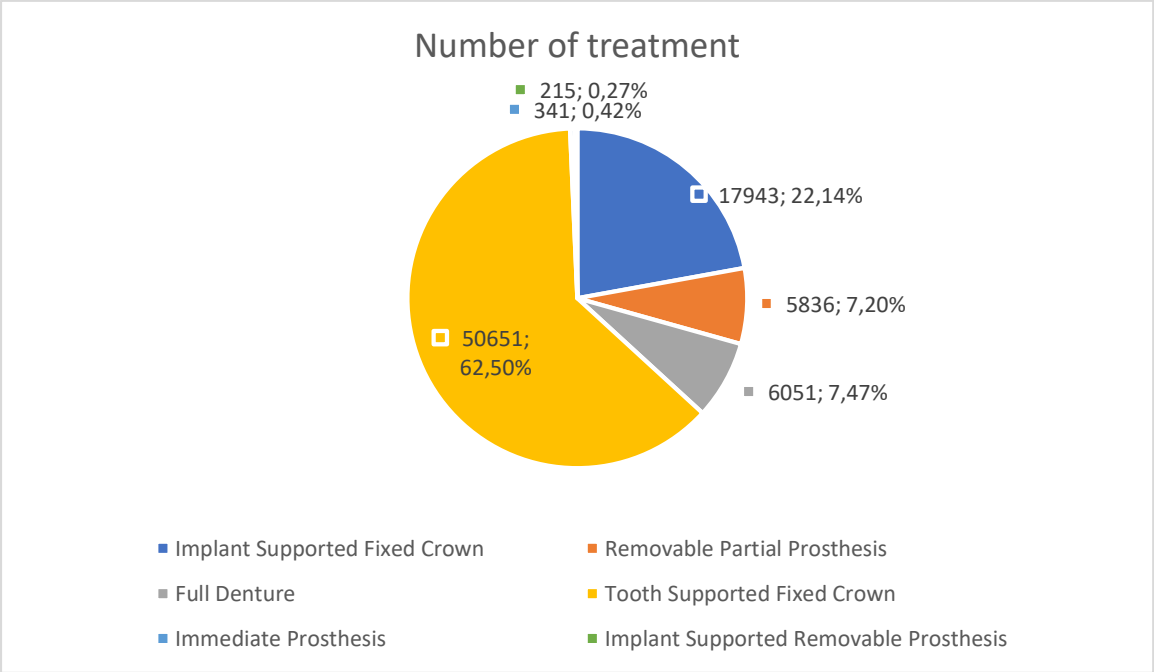

Figure 1. Distribution of major prosthetic treatments applied to patients.

In Figure 1, the distribution of major prosthetic treatments applied to patients is presented. Among the major prosthetic treatments administered to the patients, the highest proportion is 50,651 (62.50%) for dental-supported fixed crown and bridge prostheses, followed by 17,943 (22.14%) for implant-supported fixed crown and bridge prostheses, 6,051 (7.47%) for complete dentures, 5,836 (7.20%) for removable partial dentures, 341 (0.42%) for immediate dentures, and 215 (0.27%) for implant-supported removable prostheses.

In patients who received tooth-supported fixed crown and bridge prostheses, the overall average age is 46.86, with an average age of 47.59 for male patients and 46.20 for female patients. In patients who received implant-supported fixed crown and bridge prostheses, the overall average age is 47.41, with an average age of 49.38 for male patients and 45.38 for female patients. For patients who received complete dentures, the overall average age is 65.48, with an average age of 65.53 for male patients and 65.42 for female patients. In patients who received removable partial dentures, the overall average age is 58.05, with an average age of 58.71 for male patients and 57.47 for female patients. In patients who received implant-supported removable prostheses, the overall average age is 63.81, with an average age of 65.52 for male patients and 62.47 for female patients. For patients who received immediate dentures, the overall average age is 53.87, with an average age of 53.92 for male patients and 53.82 for female patients.

As seen in Figure 1, the number of procedures performed for implant and tooth-supported fixed prostheses was 68,594 (84.64%), while the number of removable prostheses was 12,443 (15.36%).

Table 1. Age distribution of patients who underwent major prosthetic procedures in the clinic.

	Min.	Max.	Average Age	Average Man	Average Woman
Tooth-Supported Fixed Crown	14	92	46,86	47,59	46,20
Implant Supported Fixed Crown	17	92	47,41	49,38	45,38
Full Denture	20	97	65,48	65,53	65,42
Removable Partial Prosthesis	22	98	58,05	57,47	58,71
Implant Supported Removable Prosthesis	26	89	63,81	65,52	62,47
Immediate Prosthesis	20	91	53,87	53,92	53,82

When comparing the number of major treatment procedures performed on all patients included in the study by gender, a statistically significant difference was found between women and men ($p < 0.001$) (Figure 2).

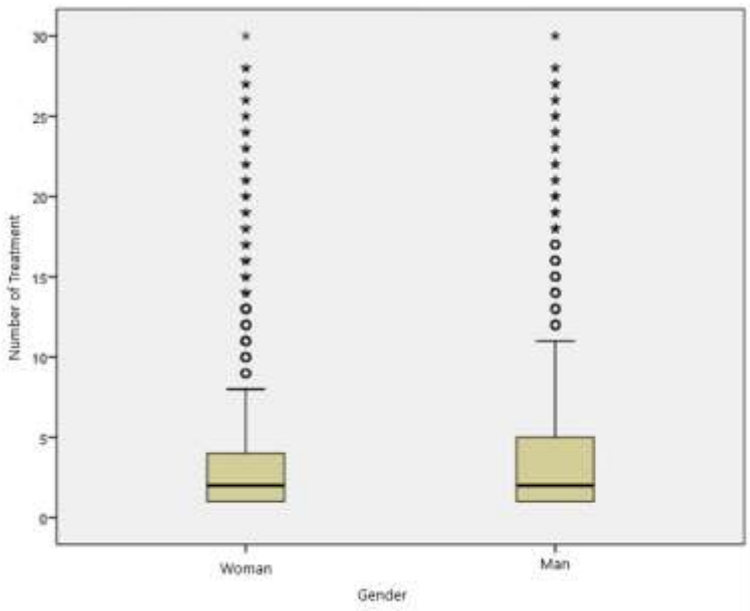

Figure 2. Comparison of the number of procedures performed between female and male patients.

A statistically significant difference was found when comparing the number of procedures performed on patients by year ($p < 0.001$) (Figure 3).

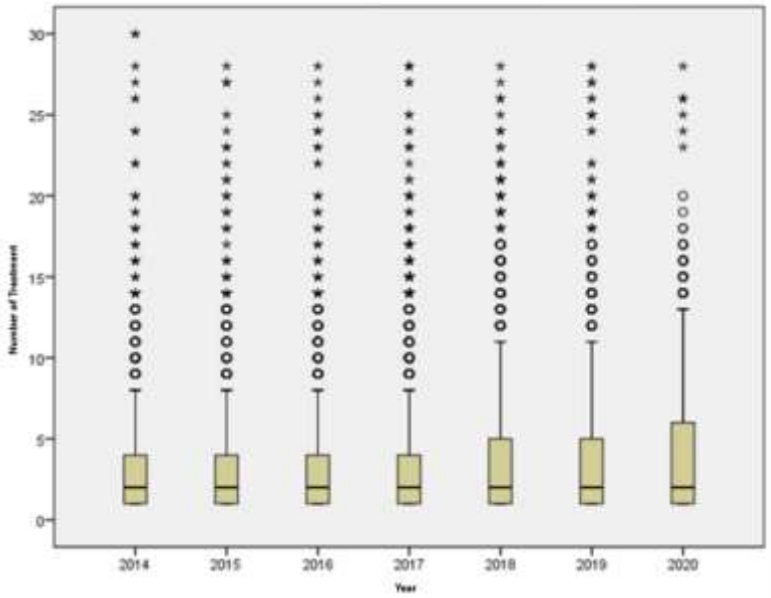

Figure 3. Comparison of the number of procedures performed by year.

When comparing the genders of the patients included in the study by year, no significant difference was found between the groups (p = 0.966).

Table 2. Comparison of patients' demographic data and the number of procedures performed by year.

	2014	**2015**	**2016**	**2017**	**2018**	**2019**	**2020**	**P**
Patient	2277	2848	2713	4202	4256	4394	1657	
Average Age ± S.S	52.9±14.5	52.7±15	51.6±15.3	52.4±14.7	51.4±14.2	51.5±13.9	49.9±13.3	<0.001
Gender (M/W)	1170/1107	1467/1381	1407/1306	2132/2070	2197/2059	2256/2138	839/818	0.966
Treatment Medyan (min-max)	2(1-30)	2(1-28)	2(1-28)	2(1-28)	2(1-28)	2(1-28)	2(1-28)	<0.001

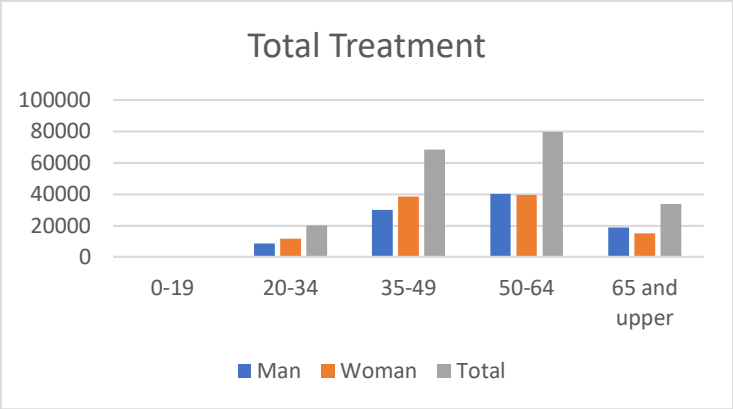

Figure 4. Distribution of the total number of prosthetic procedures performed between 2014 and 2020 by gender, age range, and overall total.

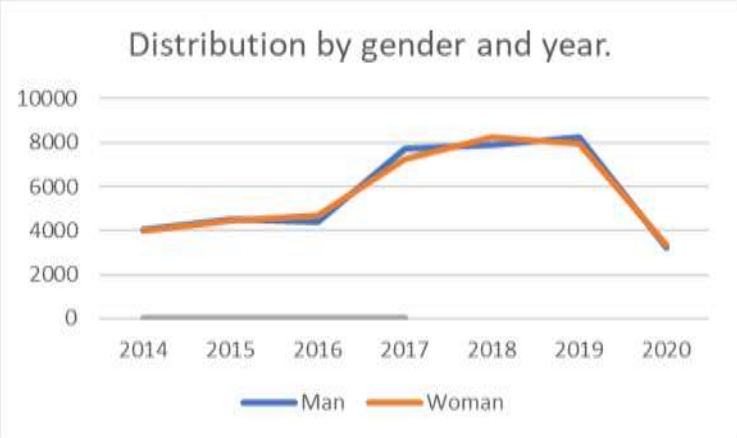

Figure 5. Distribution of total prosthetic procedures by gender and year.

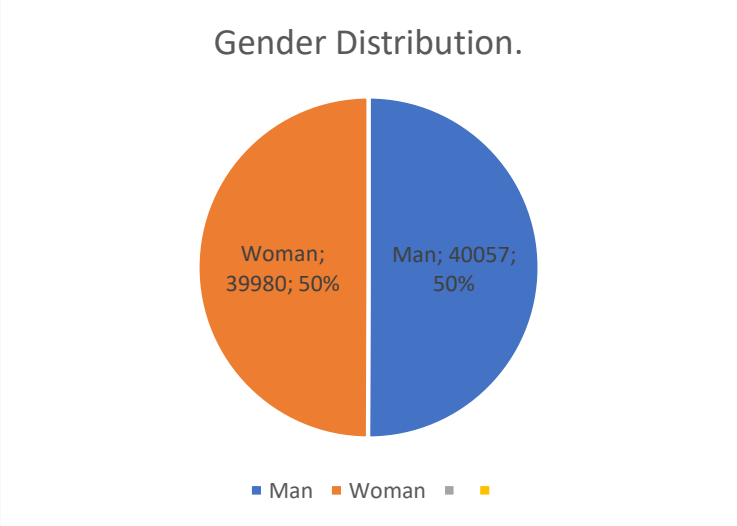

Figure 6. Distribution of the number of procedures performed on patients receiving major prosthetic treatment in the clinic by gender.

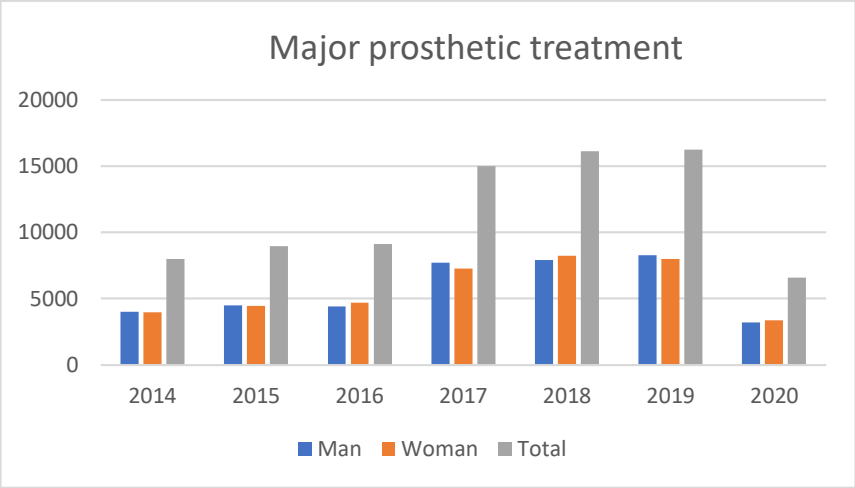

Figure 7. Distribution of the number of major prosthetic treatment procedures performed between 2014 and 2020 by gender and overall total.

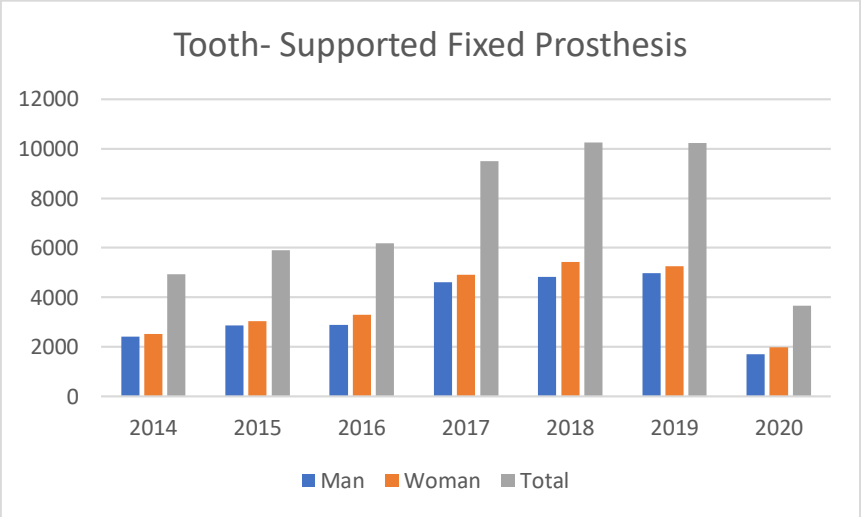

Figure 8. Distribution of the number of dental-supported fixed crown and bridge prosthesis procedures performed between 2014 and 2020 by year, gender, and overall total.

The distributions of dental-supported fixed crown and bridge prosthesis applications by year are shown in the graph.

Between 2014 and 2016, a similar number of procedures were performed, followed by an increase in 2017, 2018, and 2019, with a noticeable decrease in 2020 compared to all previous years. In the procedures performed between 2014 and 2020, the number of procedures for female patients was relatively higher each year. The highest number of dental-supported fixed crown and bridge prosthesis procedures was performed in 2018 and 2019.

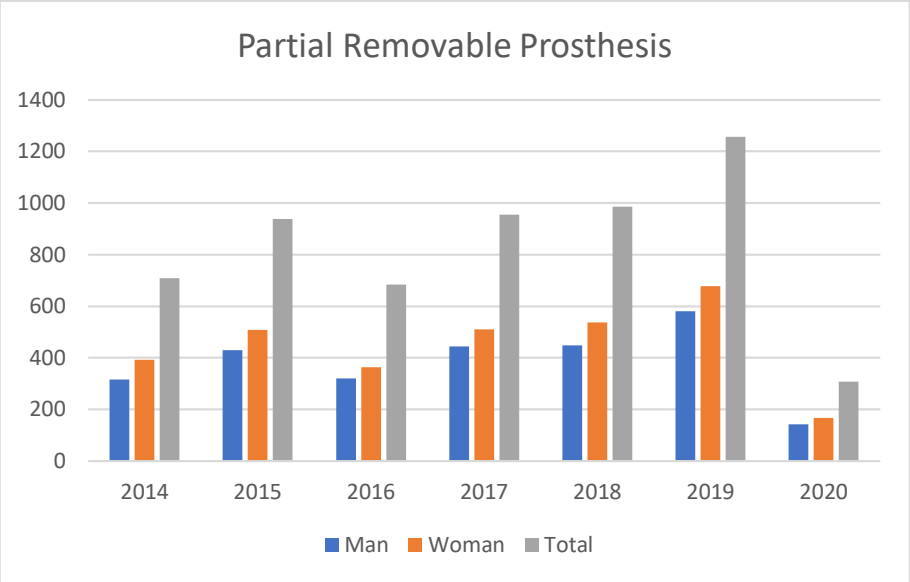

Figure 9. Distribution of removable partial denture applications between 2014 and 2020 by year, gender, and overall total.

The distributions of removable partial denture applications by year are shown in the graph.

Between 2014 and 2016, a similar number of procedures were performed, followed by an increase in 2015, 2017, 2018, and 2019, a slight decrease in 2016, and a noticeable decline in 2020 compared to all previous years. In the procedures performed between 2014 and 2020, the number of procedures for female patients was relatively higher each year.

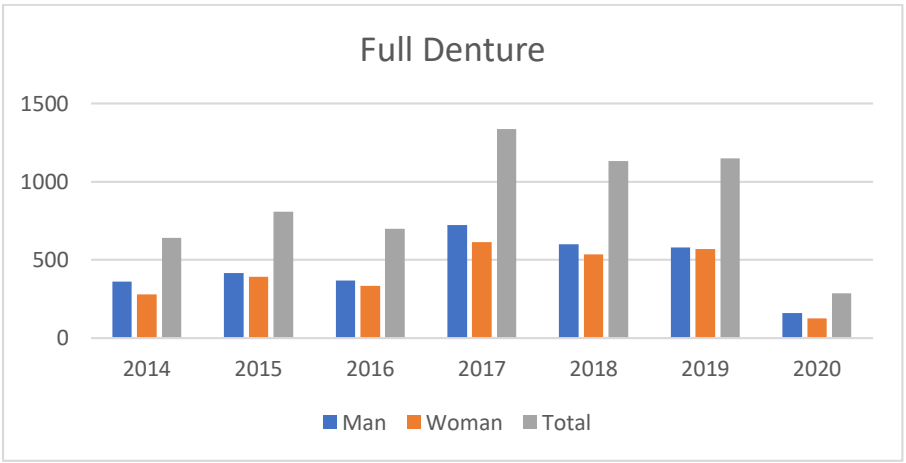

Figure 10. Distribution of complete denture applications between 2014 and 2020 by year, gender, and overall total.

The distributions of complete denture applications by year are shown in the graph.

Between 2014 and 2016, a similar number of procedures were performed, followed by an increase in 2017, 2018, and 2019, with a noticeable decline in 2020 compared to all previous years. In the procedures performed between 2014 and 2020, the number of procedures for male

patients was relatively higher each year. The highest as 1337 number of complete denture procedures was performed in 2017.

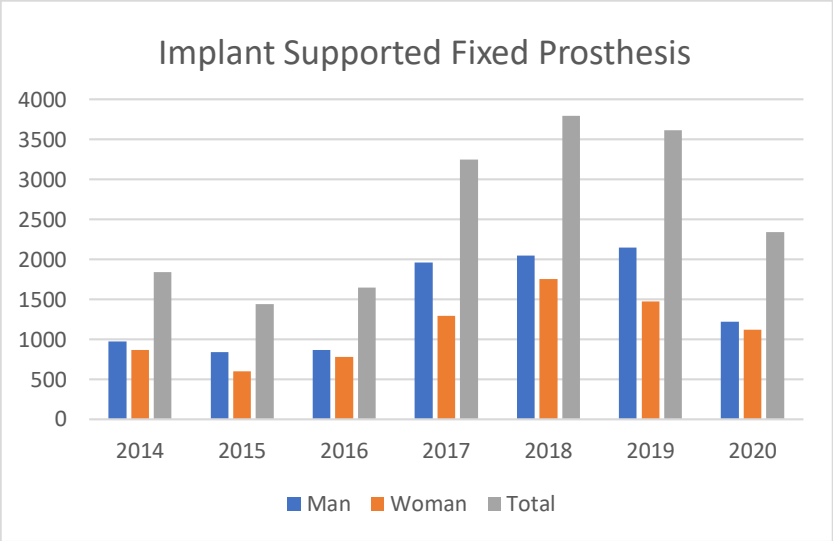

Figure 11. Distribution of implant-supported fixed crown and bridge prosthesis applications between 2014 and 2020 by year, gender, and overall total.

The distributions of implant-supported fixed crown and bridge prosthesis applications by year are shown in the graph.

Between 2014 and 2016, a similar number of procedures were performed, with a subsequent increase in 2017, 2018, and 2019, followed by a noticeable decline in 2020. In all years from

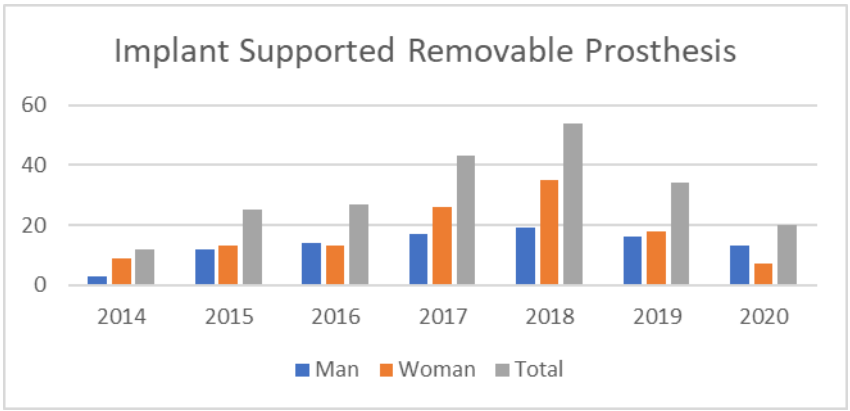

Figure 12. Distribution of implant-supported removable prosthesis applications between 2014 and 2020 by year, gender, and overall total.

The distributions of implant-supported removable prosthesis applications by year are shown in the graph.

2014 to 2020, the number of procedures performed on male patients was higher than that of female patients. Specifically, in 2014, there were 971 procedures for males and 870 for females; in 2015, 844 for males and 600 for females; in 2016, 869 for males and 780 for females; in

2017, 1,959 for males and 1,292 for females; in 2018, 2,048 for males and 1,752 for females; in 2019, 2,145 for males and 1,474 for females; and in 2020, 1,220 for males and 1,122 for females.

From 2014 to 2018, there was a consistent increase in the number of procedures, followed by a decrease from 2019 to 2020. The number of procedures varied by gender, with the highest as 54 number of procedures performed in 2018 for implant-supported removable prostheses.

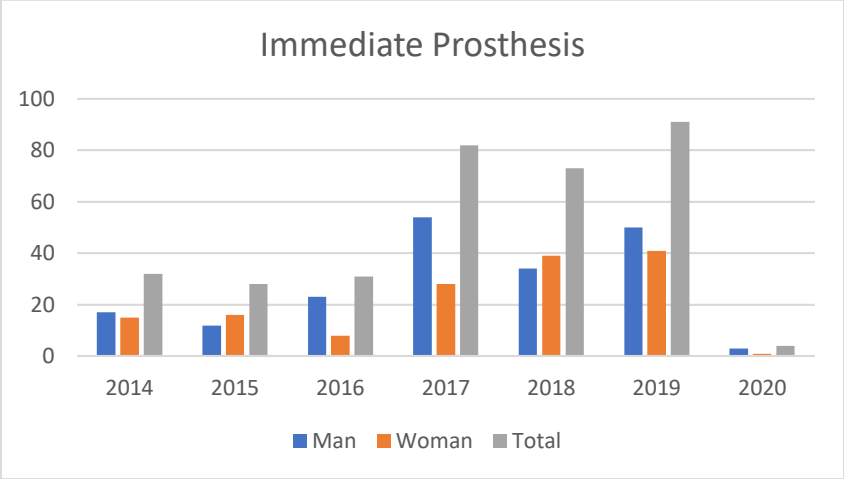

Figure 13. Distribution of immediate prosthesis applications between 2014 and 2020 by year, gender, and overall total.

In the study, we examined the distribution of procedures performed on patients receiving treatment at the Prosthetic Dentistry Clinic of Atatürk University Faculty of Dentistry according to age, gender, and year, as well as the types of prosthetic procedures performed.

Data on prosthetic care in different countries, environments, and patient groups can be particularly relevant for everyone involved in health service planning and organization, as well as in health education[14, 22].

Oral and dental health are determinants of overall health status and are directly related to quality of life[23].

Bayındır et Al. [29] examined the distribution of prosthesis types applied to 19,410 patients at the Department of Prosthetic Dentistry of Atatürk University Faculty of Dentistry between 1988 and 2000. The most commonly used types of prostheses were reported as total prostheses at 19.59%, crowns at 15.63%, and bridge prostheses at 15.10%. The rate of removable partial dentures was reported as 12.61%. In the study, crowns and bridge prostheses were categorized into two types: implant-supported and tooth-supported fixed crowns and bridges. In the findings, the proportions were as follows: tooth-supported fixed prosthesis patients at 62.50%, implant-supported fixed crowns and bridge prostheses at 22.14%, total prostheses at 7.47%, removable partial dentures at 7.20%, immediate prostheses at 0.42%, and implant-supported removable prostheses at 0.27%. From this perspective, it can be concluded that, similar to the findings of Bayındır and colleagues [29], crown and bridge prostheses were the most frequently

performed types of prostheses in the study. However, the number of procedures for removable partial dentures and total prostheses has decreased compared to the proportions reported by Bayındır et al. [29] for the years 1988-2000. This decrease is attributed to the fact that implant-supported prostheses have become an alternative to removable partial and total dentures. In the same study, the average age of patients using total prostheses was found to be 50.02 years for males and 53.34 years for females, whereas in the study, the average age of patients using total prostheses was 65.53 years for males and 65.42 years for females. Similarly, in the earlier study, the average age of patients using removable partial dentures was 43.78 years for males and 39.28 years for females, while in the study, the average age of patients using removable partial dentures was 57.47 years for males and 58.71 years for females.

The results of a study made by Akın et al. [30] on 615 patients at the Department of Prosthetic Dentistry of Cumhuriyet University Faculty of Dentistry indicate that the distribution of patients for prosthetic treatments was as follows: 43.40% received fixed prostheses, while 56.6% received removable prostheses (with 32.9% being partial dentures, 16.1% total dentures, and 7.6% consisting of unilateral total and opposing partial denture cases). In the study, these proportions, in terms of the number of procedures, were as follows: 62.5% for tooth-supported fixed prosthesis patients, 22.14% for implant-supported fixed crowns, 7.47% for total prostheses, 7.20% for removable partial dentures, 0.42% for immediate prostheses, and 0.27% for implant-supported removable prostheses. The findings of Akın and colleagues [30] show a partial similarity to the study in terms of ranking. However, the ages of the patients presenting to the clinic ranged from 12 to 98 years. Out of a total of 202,128 procedures, 104,537 were performed on female patients, while 97,591 were performed on male patients.

In their study, Aydemir and Ceylan [31] reported that among patients receiving prosthetics, 53% had fixed prostheses, 17.07% had partial prostheses, and 29.26% had total prostheses. They also argued that, unlike age, gender did not significantly affect the type and necessity of prosthetic treatment. In the study, however, when examining the number of procedures performed, it was found that 84.64% of patients received fixed prostheses, while 15.36% received removable prostheses. A statistical comparison of the major treatment procedures performed on all patients included in the study revealed a significant difference between women and men ($P<0.001$).

In the study by Bulucu et al. [32], which examined the distribution of prosthesis types used by a total of 203 patients who visited Ondokuz Mayıs University Faculty of Dentistry, it was found that, consistent with the findings, patients had the highest need for fixed prostheses and the least need for total prostheses.

In the study conducted by Lin et al. [33] on 1,515 individuals in Southern China, it was reported that 35.7% of individuals were treated with fixed prostheses, 16.5% with removable partial dentures, and 10.2% with complete dentures. These proportions show similarities in ranking with the results of the study.

In the end of 2019, a new strain of coronavirus (2019-nCoV) emerged in Wuhan, China, causing the spread of the COVID-19 pandemic worldwide. The virus began to spread in China in

January 2020 and has since spread to many other countries. On 11 March 2020, the World Health Organization (WHO) declared a global pandemic after 118,319 coronavirus cases and 4,292 deaths were reported worldwide [34]. This situation revealed that the ventilation infrastructure of university dental hospitals was not adequately prepared for an airborne outbreak, and the generation of aerosols during dental treatments has made these settings among the highest-risk areas for droplet-transmitted infections [35, 36]. As a result, patients deferred non-urgent prosthetic dental treatments during this period. The impact of the COVID-19 pandemic, which affected both the world and our country in 2020, on interventional procedures has been clearly documented in data. Notably, fixed crown and bridge restorations, which are associated with high aerosol production, saw a marked decline. The number of fixed crown and bridge procedures decreased from 10,220 in 2019 to 3,659 in 2020. The most significant reduction was observed in fixed dental crown and bridge restorations, followed by implant-supported fixed crowns. Other procedures experienced comparatively smaller declines.

4. Conclusion and Recommendations

In the research, the aim was to examine the distribution of major prosthetic procedures performed on patients treated at the Prosthetic Dentistry Clinic of Atatürk University Faculty of Dentistry. The results of the data analysis can be summarized as follows:

1. When examining the distribution of procedures performed on patients between 2014 and 2020, it was observed that the most frequently applied prosthetic procedure was fixed dental crowns and bridge prostheses (including metal-supported ceramic restorations, all-ceramic restorations, acrylic veneer restorations, precision attachment crowns, single-piece cast crown restorations, laminate veneer composite restorations, Maryland adhesive restorations, and zirconium dioxide restorations) with a total of 50,651 (62.50%). The other fixed prosthetic restorations were implant-supported fixed crowns and bridge prostheses, totaling 17,943 (22.14%). The total number of fixed restorations was 68,594 (84.64%).

2. Among removable prostheses, the most frequently applied type was complete dentures at 6,051 (7.47%), followed by removable partial dentures at 5,836 (7.20%), immediate dentures at 341 (0.42%), and implant-supported removable dentures at 215 (0.27%).

3. It was seen that the most frequently performed procedure among other prosthetic treatments was crown removal at 26,516, the second most was temporary crowns at 10,717, and the third was repair procedures, followed by night guards, occlusal wear, and various other prosthetic procedures.

4. In the cases of complete dentures and implant-supported fixed crown bridge procedures, a higher number of procedures were performed on male patients compared to female patients.

However, it was observed that fixed crown bridge prostheses and removable partial dentures were applied in larger numbers to female patients.

5. The effect of the COVID-19 pandemic, which has impacted the entire world and the country in 2020, was clearly observed in the graphs depicting its impact on interventional procedures. Notably, there was a significant decline in fixed crown bridge restorations, which are associated with high aerosol production.

6. When the distribution of patient numbers over the years was examined, an increase in the number of patients was observed between 2016 and 2017, followed by a decrease in 2020. The number of fixed crown and bridge procedures decreased from 10,220 in 2019 to 3,659 in 2020. Similarly, the number of implant-supported fixed crown and bridge procedures dropped from 3,619 in 2019 to 2,342 in 2020. The most significant decline was seen in fixed dental crown bridge restorations, followed by implant-supported fixed crowns. The decline in other procedures was relatively less.

Ethics in Publishing

This study was approved by the Ethics Committee of the Faculty of Dentistry, Atatürk University (Decision No: 99, Date: December 29, 2022).

Author Contributions:

Bayındır F.: Study design, supervision of the research process, evaluation of results, and critical revision of the manuscript.
Oktay F.: Data collection, statistical analysis, interpretation of the results, and manuscript writing.
Kürüm M.: Data organization, review of clinical records, and verification of the results.
All authors have read and approved the final version of the manuscript.

Acknowledgement

We would like to thank the Ethics Committee of the Dean's Office of the Faculty of Dentistry of Ataturk University (Decision No. 2022-99). This study was presented at Turkish Society of prostodontics and implantology 7. International Spring Symposium, held from 21 to 22 October 2022 in İstanbul, Turkey.

References

[1] Academy of Prosthodontics. (1999). “The glossary of prosthodontic terms”. Mosby.

[2] Bozdemir, E., Yilmaz., H. & Orhan, H. (2010). Dişsiz Yaşlı Hastalarda Panoramik Radyografi Bulguları. *Süleyman Demirel Üniversitesi Sağlık Bilimleri Enstitüsü Dergisi*, 1(2), 82-87.

[3] Haikola, B., Oikarinen, K., Söderholm, A. L., Remes-Lyly, T. & Sipilä, K. (2008). Prevalence of edentulousness and related factors among elderly Finns. *Journal of oral rehabilitation*, 35(11), 827-835.

[4] Šket, T., Kukec, A., Kosem, R. & Artnik, B. (2017). The history of public health use of fluorides in caries prevention. *Zdravstveno varstvo*, 56(2), 140-146.

[5] Douglass, C. W., Jette, A. M., Fox, C. H., Tennstedt, S. L., Joshi, A., Feldman, H. A., McGuire, S. M. & McKinlay, J. B. (1993). Oral health status of the elderly in New England. *Journal of gerontology*, 48(2), M39-M46.

[6] Li, K.Y., Wong, M.C.M. & Lam, K.F. (2011). Age, period, and cohort analysis of regular dental care behavior and edentulism: A marginal approach. *BMC Oral Health*, 11(9), 1-14.

[7] Sanders, A. E., Slade, G. D., Carter, K. D. & Stewart, J. F. (2004). Trends in prevalence of complete tooth loss among Australians, 1979-2002. *Australian and New Zealand Journal of Public Health*, 28(6), 549-554.

[8] Wanyonyi, K.L., Radford, D.R. & Gallagher, J.E. (2017). Dental treatment in a state-funded primary dental care facility: contextual and individual predictors of treatment need?. *PloS One*, 12(1), 0169004.

[9] Hugo, F. N., Hilgert, J. B., de Sousa, M.daL., da Silva, D. D. & Pucca Jr., G. A (2007). Correlates of partial tooth loss and edentulism in the Brazilian elderly. *Community dentistry and oral epidemiology*, 35(3), 224-232.

[10] Academy of Prosthodontics (1999) The glossary of prosthodontic terms. Mosby.

[11] Pjetursson, B. E., Brägger, U., Lang, N. P. & Zwahlen, M. (2007) Comparison of survival and complication rates of tooth-supported fixed dental prostheses (FDPs) and implant-supported FDPs and single crowns (SCs). *Clinical Oral İmplants Research*, 3, 97-113.

[12] Vermeulen, A. H., Keltjens, H. M., van't Hof, M. A. & Kayser, A. F. (1996) Ten-year evaluation of removable partial dentures: survival rates based on retreatment, not wearing and replacement. *The Journal of Prosthetic Dentistry*, 76(3), 267-272.

[13] Yamazaki, T., Martiniuk, A. L., Irie, K., Sokejima, S. & Lee, C. M. (2016) Does a mandibular overdenture improve nutrient intake and markers of nutritional status better than conventional complete denture? A systematic review and meta-analysis. *BMJ Open*, 6(8), e011799.

[14] Müller, F. (2014) Interventions for edentate elders--what is the evidence? *Gerodontology*, 31(l), 44-51.

[15] Akın, H., Tugut, F., Güney, Ü., Akar, T. & Özdemir, A. (2011) Yaş, cinsiyet, eğitim durumu ve gelir düzeyinin, diş kaybı ve protetik tedaviler üzerindeki etkilerinin değerlendirilmesi. *Cumhuriyet Dental Journal*, 14(3), 204-210.

[16] Kara, D. M. C. & Zihni, D. M. (2004) Erzurum bölgesindeki hastaların ağız ve periodontal sağlık konusundaki bilgi düzeyleri. *Atatürk Üniversitesi Diş Hekimliği Fakültesi Dergisi*, 2004(3).

[17] Douglass, C. W., Shih, A. & Ostry, L. (2002) Will there be a need for complete dentures in the United States in 2020? *The Journal of Prosthetic Dentistry*, 87(1), 5-8.

[18] Müller, F., Naharro, M. & Carlsson, G.E. (2007) What are the prevalence and incidence of tooth loss in the adult and elderly population in Europe? *Clinical Oral Implants Research*, 18, 2-14.

[19] İstatistiklerle yaşlılar. Türkiye İstatistik Kurumu, Haber Bülteni. 2023.

[20] Kisely, S. (2016) No mental health without oral health. *Canadian Journal of Psychiatry*, 61(5), 277-82.

[21] Görgün, D., Özperk, D. & Yazıcıoğlu, P. (1995) Kalıcı dişlerde çekim nedenlerinin değerlendirilmesi. *Atatürk Üniversitesi Diş Hekimliği Fakültesi Dergisi*, 1995(2).

[22] Mather, H., Thomason, M. & Ellis, J. (2018) Are UK graduates equipped with the skill set required to meet the demands of the UK's edentulous population? *British Dental Journal*, 225(1), 15-18.

[23] Çam, F. & Kumru, S. (2020) Ağız ve diş sağlığında hasta algısı ve kamu ağız ve diş sağlığı hizmetlerinin hasta bakış açısı ile değerlendirilmesi. *Sağlık ve Toplum*, 30(2), 123-139.

[24] Özkan, Y., Özcan, M., Kulak, Y., Kazazoglu, E. & Arikan, A. (2011) General health, dental status and perceived dental treatment needs of an elderly population in Istanbul. *Gerodontology*, 28(1), 28-36.

[25] Hämäläinen, P., Meurman, J. H., Keskinen, M. & Heikkinen, E. (2004) Changes in dental status over 10 years in 80-year-old people: a prospective cohort study. *Community Dentistry and Oral Epidemiology*, 32(5), 374-384.

[26] Pajukoski, H., Meurman, J. H., Snellman-Gröhn, S. & Sulkava, R. (1999) Oral health in hospitalized and nonhospitalized community-dwelling elderly patients. *Oral Surgery, Oral Medicine, Oral Pathology, Oral Radiology, and Endodontics*, 88(4), 437-443.

[27] Ünlüer, Ş., Gökalp, S. & Doğan, B.G. (2007) Oral health status of the elderly in a residential home in Turkey. *Gerodontology*, 24(1), 22-29.

[28] Marcus, P. A., Joshi, A., Jones, J. A. & Morgano, S. M. (1996) Complete edentulism and denture use for elders in New England. *The Journal of Prosthetic Dentistry*, 76(3), 260-266.

[29] Bayındır, F. & Baydaş, S. (2001) 1988-2000 yılları arasında protetik diş tedavisi anabilim dalına başvuran hastalara uygulanan tedavilerin yaşa ve cinsiyete göre dağılımının incelenmesi. *Atatürk Üniversitesi Diş Hekimliği Fakültesi Dergisi*, 2001(2).

[30] Akın, H., Tugut, F., Güney, Ü., Akar, T. & Özdemir, A. (2011) Yaş, cinsiyet, eğitim durumu ve gelir düzeyinin, diş kaybı ve protetik tedaviler üzerindeki etkilerinin değerlendirilmesi. *Cumhuriyet Dental Journal*, 14(3), 204-210.

[31] Aydemir, H. & Ceylan, G.K. (1999) Orta karadeniz bölgesinde yaşayan bireylerin ağız-diş sağlığı düzeyi. *Atatürk Üniversitesi Diş Hekimliği Fakültesi Dergisi*, 1999(1).

[32] Bulucu, B., Saraç, Ş. & Saraç, D. (2001) 18 yaş ve üzeri bireylerin dmf-t indeksi ve protetik tedavi açısından değerlendirilmesi. *Ondokuz Mayıs Üniversitesi Diş Hekimliği Fakültesi Dergisi*, 2(5).

[33] Lin, H. C., Corbet, E.F., Lo, E.C. & Zhang, H.G. (2001) Tooth loss, occluding pairs, and prosthetic status of Chinese adults. *Journal of Dental Research*, 80(5), 1491-1495.

[34] World Health Organization [Internet]. Prevention, identification and management of health worker infection in the context of COVID-19- 2 February 2022. Available from: https://www.who.int/publications/i/item/10665-336265

[35] Sakallı, O.A., Sakallı, S., Akbaşak, A.Ö. & Erkut, S. (2022). Yeni tip koronavirüs (covid-19) salgınının diş hekimlerinin tedavi kliniği düzeni üzerine etkisi. *ADO Klinik Bilimler Dergisi*, 11(2), 140-149.

[36] Ge, Z.Y., Yang, L.M., Xia, J.J., Fu, X.H. & Zhang, Y.Z. Possible aerosol transmission of COVID-19 and special precautions in dentistry. *Journal of Zhejiang University Science B*, 21, 361-368.

e-ISSN: 2149-4584

Erzincan University Journal of Science and Technology

EJSAT 2025, 18 (3) 876-891

Research Article

Design and Evaluation of a Cost-Effective Battery Management System for CERYAN Using Nuvoton

Seda Kul[1*], A. Ozgur Polat[1,2], Sevval Yorulmaz[2], S. Alperen Celtek[3]

[1]Karamanoglu Mehmetbey University, Engineering Faculty, Electrical and Electronics Engineering Karaman, Türkiye

[2] Solvaytech Engineering, Adana, Türkiye

[3]Karamanoglu Mehmetbey University, Engineering Faculty, Energy Systems Engineering Karaman, Türkiye

Received: 17/11/2024, **Revised:** 05/06/2025, **Accepted:** 29/07/2025, **Published:** 31/12/2025

Abstract

The development of Electric Vehicles (EVs) has accelerated advances in battery technology. A Battery Management System (BMS) is essential to use batteries in EVs safely and efficiently. The basic functions of a BMS include measurement, monitoring, and balancing. In the rapidly growing field of micromobility, achieving cost-effective balancing requires high-accuracy measurements. In this study, a BMS design was made with a Nuvoton NUC131 microcontroller for CERYAN, an L6e light electric vehicle, and was evaluated in terms of measurement, performance, and cost. As a result, the unit cost of the Nuvoton microcontroller is approximately 30% lower than that of STM32Fx, one of the most commonly used microcontrollers; therefore, the designed BMS prototype achieves a 27% cost reduction. In addition, the ADC measurement error is approximately 0.7 mV, which allows accurate measurement of cell voltages and efficient balancing.

Keywords: Battery management system, electric vehicle, microcontroller, Nuvoton, BMS

Nuvoton Kullanılarak CERYAN İçin Maliyet Etkin Bir BMS'nin Tasarımı ve Değerlendirilmesi

Öz

Elektrikli araçların (EA) gelişimi, pil teknolojisindeki ilerlemeleri hızlandırmıştır. Pil Yönetim Sistemi (PYS), pillerin EA'larda güvenli ve verimli kullanımı için olmazsa olmazdır. Bir PYS'nin temel işlevleri ölçüm, izleme ve dengeleme işlemlerini kapsar. Hızla büyüyen mikromobilite alanında, maliyet etkin dengeleme sağlamak yüksek doğruluklu ölçümler gerektirir. Bu çalışmada, L6e sınıfı hafif elektrikli araç olan CERYAN için Nuvoton NUC131 mikrodenetleyicisi kullanılarak bir PYS tasarımı gerçekleştirilmiş ve ölçüm, performans ve maliyet açısından değerlendirilmiştir. Sonuç olarak, Nuvoton mikrodenetleyicisinin birim maliyeti, en yaygın kullanılan mikrodenetleyicilerden biri olan STM32Fx'e kıyasla yaklaşık %30 daha düşük olduğundan, tasarlanan PYS prototipinin birim maliyeti %27 daha düşüktür. Ayrıca, ADC ölçüm hatası yaklaşık 0,7 mV olup, bu değer hücre voltajlarının doğru ölçümüne ve verimli dengelemeye olanak sağlamaktadır.

Anahtar Kelimeler: Pil yönetim sistemi, elektrikli araç, mikrodenetleyici, Nuvoton, BMS

Corresponding Author: sedakul@kmu.edu.tr

Cite this Article: Erzincan University Journal of Science and Technology 2025, 18(3)876-891. https://doi.org/10.18185/erzifbed.1586782

1. Introduction

Sustainable and environmentally friendly alternatives are becoming increasingly important in the rapidly evolving transportation sector. The most significant advances in these alternatives involve the development and design of electric vehicles (EVs). EVs are integral to the automotive economy and excel in sustainability due to their zero emissions, which aligns with essential goals in green energy transformation. On the other hand, storage systems should be considered in electric vehicle design, considering the entire life cycle of the EV [1].

Storage systems incorporate various battery types and capacities. Lithium-based batteries are the most widely used power source in EV technology due to their high energy density and long cycle life [2]. Battery Management System (BMS) monitors battery parameters for safe, reliable, and optimum operation of batteries, determines standard management intervals according to voltage levels, and determines the current operating conditions of the battery pack according to temperature readings [3].

The effective and safe operation of EVs depends on continuous BMS monitoring to ensure battery pack longevity and range [4], [5]. BMS maintenance involves temperature monitoring, cell balancing, State of Charge (SoC) management [6], [7], and optimization of battery life and performance during charge/discharge cycles. Battery Management Systems (BMS) are crucial for ensuring efficient and safe EV battery operation. Their primary responsibilities include accurate estimation of battery status parameters—State of Charge (SoC), State of Health (SoH), and State of Temperature (SoT)—which are essential for evaluating current battery conditions and predicting remaining driving range [8–10]. Given battery capacity variability, these estimations are vital for extending battery life and optimizing performance.

In addition to SoC, the accurate estimation of the State of Health (SoH) is also essential in predicting the long-term performance, safety, and reliability of batteries in electric vehicles. SoH provides insight into battery degradation patterns and capacity fade over time, which directly affect the vehicle's range and operational safety. Without reliable SoH estimation, it becomes difficult to detect early signs of aging or internal damage, potentially leading to unexpected battery failures in critical EV applications. Therefore, incorporating SoH monitoring into BMS design is a crucial step toward ensuring the overall robustness and lifecycle management of electric vehicle batteries [8–10].

In addition, the BMS manages cell balancing and controls the charge/discharge operations of the battery pack to maintain uniformity among cells and prevent overcharging or deep discharging [8], [11]. Thermal management is another critical function, enabling the BMS to regulate the battery's temperature to prevent overheating and degradation, particularly under high-load or extreme environmental conditions [12], [13]. Furthermore, the system is responsible fo Furthermore, the system is responsible for detecting and diagnosing faults, allowing early identification of potential failures and enhancing operational safety [14], [15]. Finally, the BMS facilitates communication with the user and other vehicle systems through interfaces designed for data exchange and system monitoring [15].

In [16], issues such as the state of charge and the health status of existing BMSs that directly affect the battery's performance are discussed, and solutions are presented. In [17], the hardware concepts of BMS are discussed and evaluated in terms of EVs and other applications. The direct estimation method [18] used to calculate SOC has been widely preferred because it is easy to implement. The open-circuit Voltage (OCV) estimation method is one of them. Xing and colleagues [19] collected data by measuring open circuit voltage and created a lookup table for SOC estimation. Internal resistance [20] calculated using battery voltage and current values is another parameter other than OCV used in SOC estimation.

The BMS system uses microcontrollers to perform all the specified functions of the system controls. Therefore, the selection of battery status and life estimation methods, cost, and system performance are considered to be the most optimum design and design parameters [21]. Designers prioritize making products that are environmentally friendly, energy-efficient, and zero-energy [22], in addition to producing high-performance electric vehicles. In the literature, the most widely used microcontrollers in such BMS applications are the STM32Fx series microcontrollers of STMicroelectronics [23], [24]. Considering the time loss that may occur due to computational costs and the chip crisis, Nuvoton company was preferred due to its better price and performance and easy availability. Nuvoton has also been used in the BMS design of electric garbage compaction trucks [25].

Based on a comprehensive literature review and analysis of advantages and disadvantages, this study presents a cost-effective BMS design utilizing the Nuvoton microcontroller with passive balancing methodology. The SOC estimate was made using the ampere counting method.

In general, the contributions of this study to the literature can be summarized as follows:

Cost-effectiveness: The system is designed using microcontrollers and carefully selected components that offer an optimal balance between cost and performance, making it highly affordable for practical applications.

Modularity: The design supports integration into modular battery packs, allowing flexibility in adapting to various battery configurations.

Compact structure: Its space-efficient design enables easy integration, especially in systems with limited physical space.

Stackable architecture: Thanks to its compact and modular nature, combined with isolated SPI communication, the system supports stackable implementation, enabling scalability in larger battery systems.

Isolated communication: The use of isolated SPI interfaces ensures safe and reliable data exchange between modules, enhancing the system's robustness and safety.

The rest of the paper is organized as follows: Section 2 introduces the battery management system and experimental setup and modeling of the BMS system. Section 3 presents the results of the studies, and the conclusion part is given in Section 4.

2. Material and Methods

2.1. Battery Management Systems for EVs

Batteries are electrical energy storage systems that constitute one of the most critical EV components, capable of storing significant energy amounts over extended periods, with implications for both cost and design considerations. It is divided into primary and secondary batteries, which can be charged and non-chargeable. Secondary batteries, known as rechargeable batteries, are preferred, especially for EVs. EV batteries generally consist of Li-ion batteries [26]. The batteries used in EVs and their comparative features are detailed in [27].

These battery structures consist of cells, and any cell deterioration directly affects battery life and performance. Therefore, battery systems need to be monitored correctly and have a monitoring system. A battery management system (BMS) is required for this.

BMS is a management scheme that monitors the operating system and performance of the battery pack in the energy storage system, controls its separation from the system when necessary, and optimizes it. There are some requirements for managing and integrating batteries into the battery management system. The optimum levels of these requirements directly affect battery efficiency and life [28]. It is designed to control the most efficient operation of blocks with different functions required for energy management and security in EV applications. In addition, it controls many parameters, including State of Charge (SoC) estimation, overcurrent protection, cell balancing, and thermal monitoring of battery cells, to ensure the safe operation of Li-ion batteries, which are among the preferred ones [26]. Figure 1 shows the battery management system for EVs with the corresponding functional module.

Figure 1. Battery management system for EVs

Off-the-shelf Application Specific Integrated Circuits (ASICs) are used for basic monitoring and measurement functionality. For small personal electronic devices with one battery cell, simple fuel gauge ICs provide voltage monitoring, temperature measurement, current measurement, and SOC estimation. For higher-power applications with multiple cells, ICs provide monitoring and balancing tools for multiple cells simultaneously. Advanced functions such as SOC estimation and power estimation algorithms are implemented in a centralized

module known as BMS-Master. Current measurements can be done using two sensor technologies: galvanically or isolated and hall sensors [29].

Battery cells can show voltage level differences due to production, working conditions, and environmental factors. Over time, these differences can cause some batteries in the pack to charge or discharge quickly and thus cause capacity loss and rapid aging of these battery cells. This situation within the pack is referred to as an imbalance between batteries. If an imbalance occurs, it leads to inaccurate calculations in SOC estimation. Cell voltages are monitored to prevent imbalance, and cells with high voltage differences are identified. The resulting cell imbalance is compensated with one of the cell balancing methods—cell balancing methods, which are divided into active and passive [30], [31].

The main function of the BMS includes battery condition estimation [32]. A robust estimation of SOC [33] is crucial to provide the customer with an accurate indication of the remaining range. Battery SOC is defined as the ratio of the coulomb charge currently stored in the cell to the total charge capacity of the cell. SOC cannot be measured directly, as it depends on many dynamic parameters used in sensors. Prediction algorithms are used to estimate the SOC. Estimation algorithms include measurement-based, adaptive filter, observer-based, and data-driven-based algorithms. Measurement-based estimation algorithms include Coulomb-Counting[34], Open Circuit Voltage [35], [36], and electrochemical impedance stereoscopy methods that calculate SOC by measuring physical quantities directly related to SOC. The Coulomb-Counting way, which is the most widely used method, estimates SOC by integrating the battery current. The OCV method estimates SOC based on the battery's open circuit voltage obtained after a long resting period. Adaptive filter and observer methods estimate SOC as a function of cell current, voltage, and temperature.

2.2. Experimental Setup and Modeling of the System

This study designed the battery pack according to the voltage and capacity requirements for the L6e class light electric vehicle called CERYAN, developed by Solvaytech Engineering Company in Türkiye. Cylindrical 18650 Li-ion cells were preferred. The selected battery cell has a nominal voltage of 3.7 V, a maximum voltage of 4.2 V, and a capacity of 3500 mAh. It was configured with 12 series and 19 parallel cell connections, resulting in a nominal voltage of 48 V and a total capacity of 66.5 Ah. The charge temperature range is 0/50°C, the discharge temperature range is -30°C/+60°C and the maximum discharge current is 10 A. Figure 2 shows battery parameter testing within the vehicle's Digital Twin model range calculation module, developed in MATLAB/Simulink. The number of parallel cells was determined based on the battery capacity required to achieve the desired range.

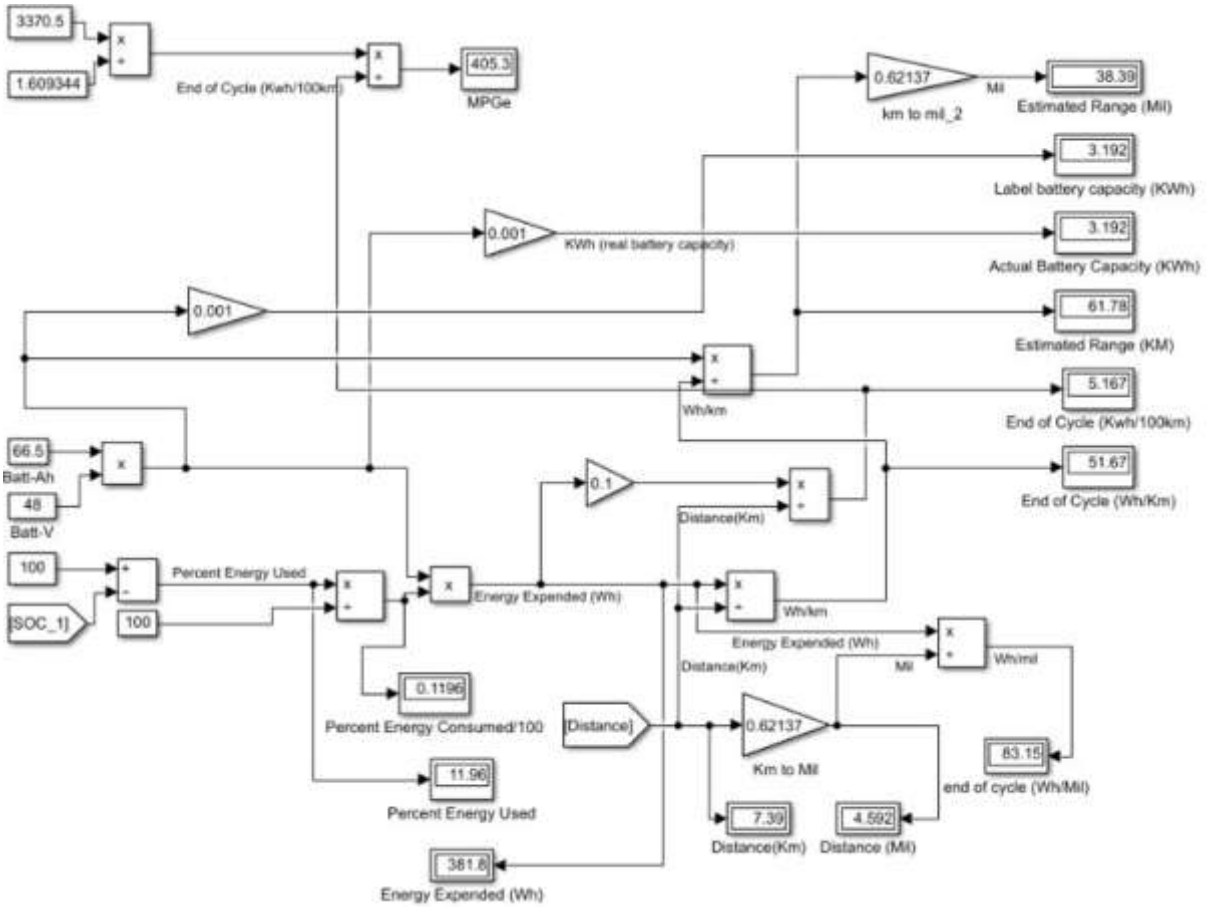

Figure 2. CERYAN Range Calculation based on the Battery capacity

Ensuring that the batteries operate within a safe range requires controlling them within specific limits. The safe operating range for the Li-ion batteries used in the CERYAN electric vehicle is specified in the manufacturer's information document as a voltage range of 2.5 V - 4.2 V and a temperature range of -30°C to +60°C. The BMS designed within this project's scope calculates the remaining energy based on the batteries' current, temperature, and voltage conditions, providing control and monitoring to ensure that the batteries operate within a safe range. Due to the chip crisis, sourcing off-the-shelf Application-Specific Integrated Circuits (ASICs) became difficult; therefore, monitoring and measurement circuit control was implemented using microcontrollers in master-slave topology. This study used the NUC131 microcontroller from Nuvoton as both the slave and master controller for BMS operations. The slave microcontrollers manage cell measurements and the balancing process, while the master microcontroller monitors the battery pack current and temperature. The master microcontroller receives cell voltage information from the slave microcontrollers via isolated SPI communication and, based on the collected data, activates the protection algorithm when necessary. The master also estimates the battery status using prediction algorithms and communicates it to the Electronic Control Unit (ECU) via CAN-Bus communication. Multiple slaves were used due to multiple battery packs in the CERYAN micro electric vehicle, providing the advantage of a stackable design, as shown in Figure 3. The BMS block diagram is provided in Figure 4, where the microcontrollers are represented as a single block.

a **b**

Figure 3. a) Block Diagram of BMS b) 3D CAD Design of Multiple Battery Pack

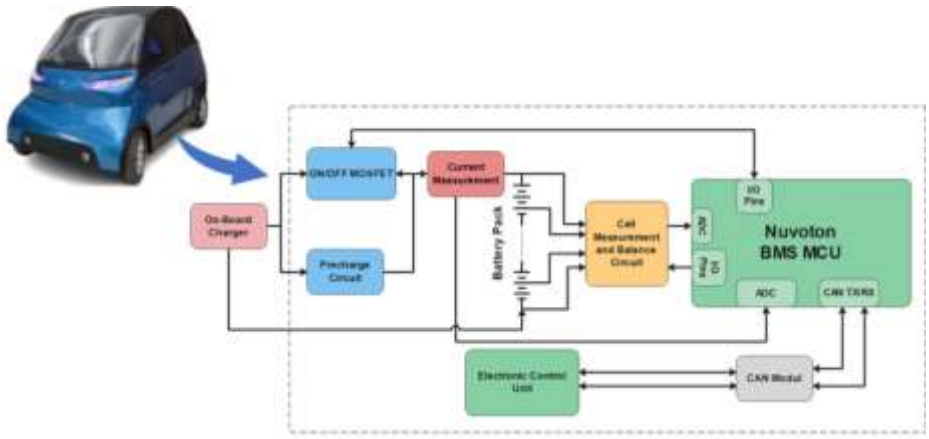

Figure 4. Block Diagram of BMS of CERYAN

Changing the differential Op-Amp gain with resistors reduced the cell voltages to suit the MCU ADC input voltage range. However, one advantage of the Nuvoton NUC131 microcontroller is that the ADC input voltage can be a maximum of 5.5 V. Thus since the battery cell voltage range is already between 2.5 V and 4.2 V, voltages can be measured directly without the need to halve the gain in the differential Op-Amp method. This has resulted in fewer components being used in the design and reduced PCB dimensions, thus reducing the cost. Cell voltage measurements are then performed by connecting the Op-Amp outputs to the ADC inputs.

The Hall effect current sensor measures the current drawing from/flowing into the battery pack. Temperature measurement is obtained using the DS18B20 temperature sensor. DS18B20 sensor is a digital temperature sensor that measures between -55 $°C$ / +125 $°C$ with 9–12-bit resolution. The sensor, which communicates using the One-Wire communication protocol, is a device communications bus system that can connect multiple temperature sensors to a single I/O pin.

The minimum and maximum voltage values set for batteries operating within certain limits are 2,7 V and 4,1 V, respectively. Current limits were determined by applying the World Motorcycle Test Cycle (WMTC) to the battery pack specified in the Digital Twin model. In this cycle, as seen in Figure 5, a maximum instantaneous current of 254 A is drawn from the battery. Considering the batteries' thermal management, the microcontroller's current limit was

determined as 200 A, as it would be more suitable for the efficiency of the battery pack. For the temperature, a maximum of 60 degrees during discharge and a maximum of 45 degrees during charge is chosen.

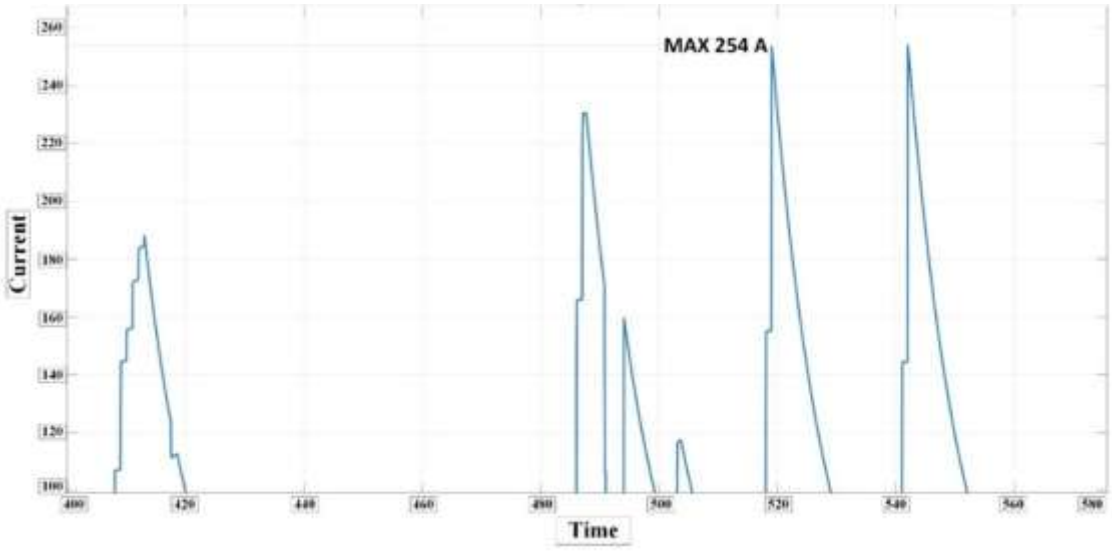

Figure 5. WMTC Cycle test on the battery pack

The microcontroller evaluates the values obtained from the measurement circuits. If it is detected that the limit values have been exceeded, the protection circuit is activated. One of the limit values is set as the upper voltage limit. During charging, when the battery pack reaches the upper limit value of 49.2 V, the protection circuit terminates the charging process. Another limit value is the lower voltage limit. During discharge, when a voltage of 32.4 V is measured, the BMS issues an over-discharge warning on the display and gradually stops the discharge process at the voltage level specified by the manufacturer. The current limit, another critical threshold, is monitored by the Hall effect sensor. If the sensor detects current values exceeding the set limit, the system disconnects the relay between the load/charger and the battery pack.

Over time, due to production and usage conditions, voltage differences may develop between the cells in the battery pack, limiting the batteries' long-term usability. The previously mentioned passive cell balancing method is employed to correct cell imbalance.

Using the passive balancing method, the BMS prevents further charging of cells that reach the voltage limit of 4.1 V during charging and waits for the other cells to reach the 4.1 V level. In the balancing process, a certain current is passed through the bleeder resistors connected to each series cell in a switching manner, generating heat. This process dissipates energy in the fully charged cells and brings them to the same level as the others. The passive balancing operation is controlled by the microcontroller in the system, as seen in Fig. 6. The microcontroller averages the incoming cell data. The average value is subtracted from each cell voltage, and if the resulting value exceeds 50 mV, the microcontroller sends a signal to the MOSFETs used as switching elements. This allows current to pass through the resistors via the MOSFET, dissipating the excess charge in the cell. This process is continuously repeated during charging.

High-power Surface Mount Device (SMD) resistors are used as bleeder resistors, with their values determined based on the balancing current.

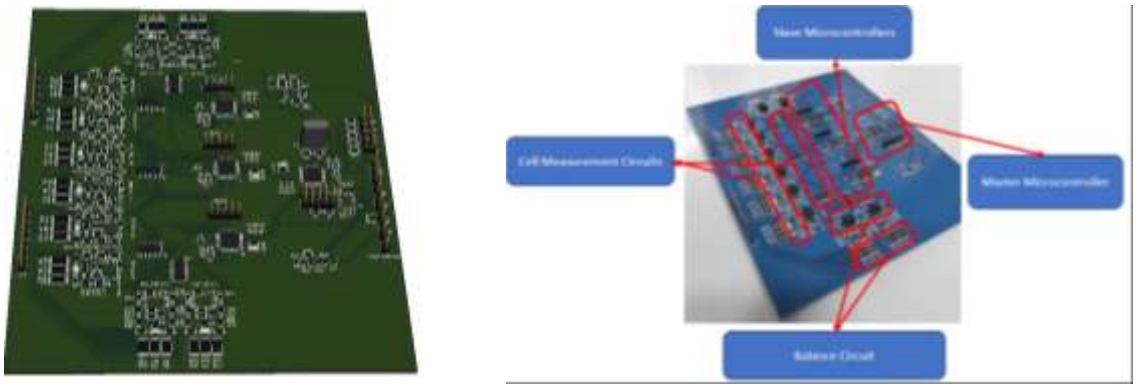

a b

Figure 6. A) BMS Board 3D View and b) PCB view with parts

3. Results And Discussion

In this study, a cost-effective Battery Management System (BMS) was designed for use in L6e class light electric vehicles. The primary reason for selecting the Nuvoton M0 series microcontroller is its specific design for high-temperature and harsh operating conditions. The microcontroller's features, including 17 ADC channels, 6 PWM channels, and four timers, have proven effective in ensuring the precise monitoring and control functions required by the BMS, as seen in Fig. 7. Additionally, its support for various communication protocols such as UART, SPI, I2C, and CAN-Bus enhances system flexibility. It enables the design of multi-battery pack systems. Furthermore, another significant advantage is including the CAN-Bus protocol, which is essential for communication in automotive electronics.

Results demonstrate that the Nuvoton microcontroller offers high performance with a unit cost approximately 80% lower than the STM32Fx series. This cost advantage, combined with production continuity during periods of battery-integrated circuit market unavailability, demonstrates Nuvoton's viability as a commercially attractive alternative, particularly for cost-sensitive light electric vehicle applications. The growing popularity and accessibility of Nuvoton microcontrollers may further promote the adoption of this technology in future applications.

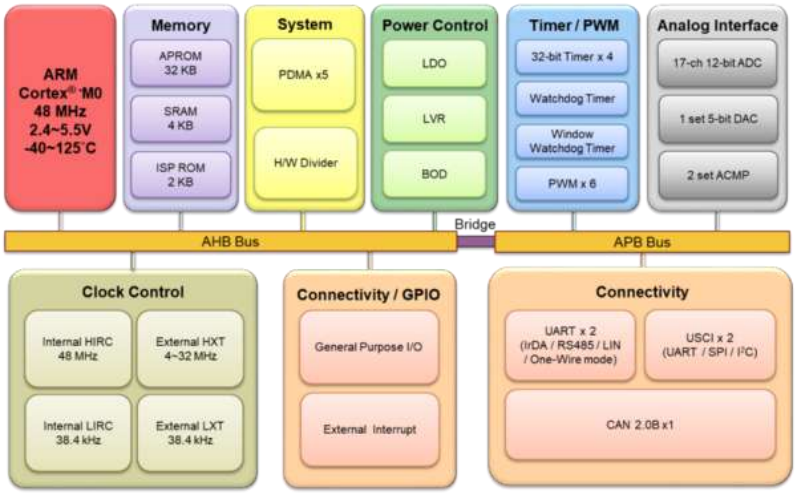

Figure 7. Nuvoton NUC131 Microcontroller Block Diagram

The battery pack was formed according to the specifications of the CERYAN EV. As seen in Table 1, it is calculated that for CERYAN with a 48 V 3 kW motor, battery cells with a nominal voltage of 3.7 V and a rated capacity of 3500 mAh should be used in 12 series and 19 parallel using the digital twin model for a range of 60 km.

Table 1. Specifications of CERYAN and BMS

Parameter	*CERYAN*	*Battery*
Voltage	48V	3,6 V – 3500 mAh
Power	3kW	12Series 48 V
Range	60km	19 Parallel 66,5 Ah

For BMS and microcontroller testing, battery cell voltages were initially recorded. After the connection between the BMS and the battery pack, the microcontroller ADC measurement accuracy was checked from the microcontroller interface. The differential Op-Amp output in the measurement circuit and the MCU ADC measurement results were compared with the noted voltage values. As a result of the comparison, it was observed that the voltages were measured with an average error of ±0.7mV in the microcontroller. This result satisfies the minimum error requirement for the BMS's measurement and SOC estimation functions.

During charging, the BMS passive balancing algorithm was activated in the battery pack. According to the algorithm, after the cell voltages are measured, they are averaged, and the difference between the average and each cell voltage is calculated. If the resulting value exceeds 50 mV, a signal is sent to the bleeding resistor switch to stabilize that cell. As shown in Figure 8, cells with significant initial voltage differences achieved balance by the end of the charging process.

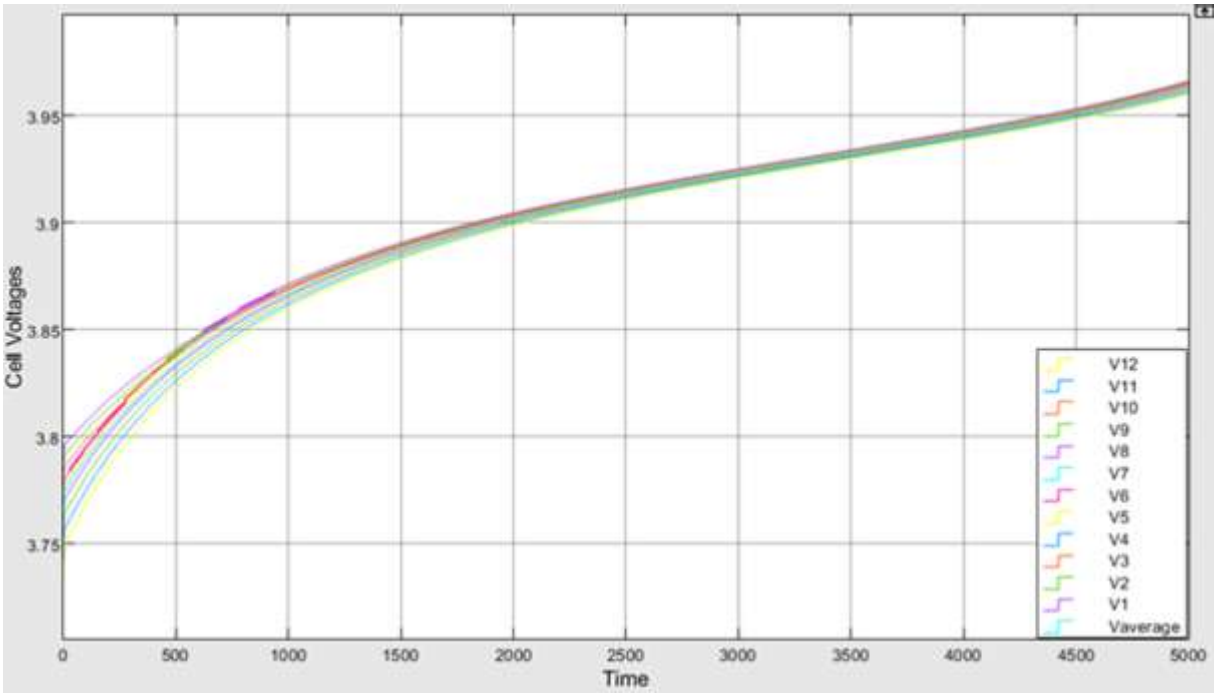

Figure 8. Balance Algorithm Results

Table 2 shows that both microcontrollers are suitable for automotive applications; however, the NUC131 is more specifically designed for certain automotive environments, such as BMS and motor control, while the STM32F042 provides a more general-purpose automotive solution with the added feature of USB connectivity.

The NUC131 may offer a more appropriate solution for specific automotive applications like BMS and motor drivers. In contrast, the STM32F042, with its USB connectivity, offers a broader range of features and support, making it more versatile across various applications.

Table 2. Comparison of STM32F0xx and Nuvoton NUC131

	STM32F0xx	*Nuvoton NUC131*
Core	ARM Cortex-M0	ARM Cortex-M0
Clock Speed	Up to 48 MHz	Up to 50 MHz
Flash Memory	32 KB	32 KB to 128 KB
RAM	6 KB	4 KB to 16 KB
Operating Voltage	2.0V to 3.6V	2.5V to 5.5V
ADC	12-bit ADC with up to 10 channels	12-bit ADC with 17 channels
Timers	Up to 5 (16-bit)	Multiple 16-bit
Communication Interfaces	USART, SPI, I2C, CAN	UART, SPI, I2C, CAN
Price	★	★★

This study eradicates microcontroller-based measurement errors due to the Nuvoton microcontroller's low ADC measurement errors. As a result of the experiment, it was observed

that measurements were taken with an error of 0.7 mV. In addition, the microcontroller software interface is straightforward to use with NuLink on-board debugger and programmer. Another advantage of the microcontroller is the broad ADC input voltage range. Since the ADC input voltage range of other microcontrollers is usually a maximum of 3.6 V, the ADC output is perceived as maximum for cell voltages of 3.6 V and above. When using a differential Op-Amp, the circuit should be designed so that the Op-Amp gain is 0.5 V/V. This can be solved by using an extra resistor in the design. The extra resistor increases the cost. At the same time, it increases the design cost, and the PCB manufacturing cost as it causes the PCB dimensions to become more prominent. Table 3 shows the cost analyses of the STM32Fx microcontroller, frequently used in the literature, and the Nuvoton microcontroller used in the Solvaytech BMS design. As seen in the table, the unit cost of the Nuvoton microcontroller is approximately 30% cheaper than the STM32Fx microcontroller. The unit cost of the BMS designed with a Nuvoton microcontroller is 27% cheaper, as shown in the table.

Table 3. Cost Analysis of BMS with Two Different Microcontrollers

	MicroController Price			*Active and Passive Components*			*BMS Unit Price*		
	Quantity			*Quantity*			*Quantity*		
	1	10	1000	1	10	1000	1	10	1000
12S19P BMS (STM Controller)	$2,78	$1,75	$1,51	$ 35,25	$28,50	$20,81	$38,03	$30,25	$ 22,32
12S19P BMS (Nuvoton Controller)	$2,01	$1,75	$1,33	$ 27,50	$23,25	$16,25	$29,51	$25,00	$17,58

4. Conclusions

With the development of Electric Vehicles (EVs), the advancement of battery technology has also accelerated. A Battery Management System (BMS) is essential for using batteries safely and efficiently in EVs. The basic functions of a BMS include measurement, monitoring, and balancing. In the rapidly growing field of micromobility, achieving cost-effective balancing requires high-accuracy measurements. This can be achieved by using high-quality ASICs or microcontrollers for measurement. In this study, ASICs could not be used due to accessibility issues, so the measurement circuit was designed using the differential Op-Amp method. The measurements were performed with a Nuvoton M0 series microcontroller. The measurement, performance, and cost values of the BMS prepared with the Nuvoton NUC131 microcontroller were discussed. Since the unit cost of the Nuvoton microcontroller is approximately 30% lower than that of STM32Fx (one of the most commonly used microcontrollers), the designed BMS

prototype unit cost is 27% lower. The Nuvoton M0 series microcontroller provides a cost advantage in design due to its wide ADC input voltage range. In addition, the ADC measurement error is approximately 0.7 mV, allowing for accurate measurement of cell voltages and efficient balancing. Future work will use this microcontroller to estimate the remaining healthy life of batteries using artificial neural networks. However, given potential uncertainties in long-term availability and supply chain stability of the Nuvoton NUC131 microcontroller, future work will explore alternative microcontrollers with similar cost-performance characteristics to ensure BMS scalability and commercial viability. In this context, cross-platform compatibility and firmware portability will be prioritized to enable seamless transitions between different microcontroller families in case of supply disruptions.

Although the proposed passive balancing method offers a cost-effective solution, it inherently results in heat dissipation during the balancing process. This heat can negatively impact battery performance and accelerate aging, particularly under high-current discharge conditions. To address these thermal concerns, future studies will focus on optimizing the balancing algorithm to reduce unnecessary energy loss and improve thermal efficiency. Additionally, alternative strategies such as semi-passive or active balancing methods will be evaluated to achieve a better balance between cost, efficiency, and thermal safety.

Ethics in Publishing

There are no ethical issues regarding the publication of this study.

Author Contributions

S.K; Designing the study, evaluating the results, writing

A.O.P; Prototip desing, evaluating the result, collecting data

S.Y; Prototip desing, writing, evaluating the result

S.A.C; writing, evaluating the result

Acknowledgments

Funding: This research was supported by the KOSGEB R&D Innovation Project (Project Number: sCAPE2018)

References

[1] Patil, S. D., Dharan, S. R., MR, D. & SR, B. S. (2023). Battery Management System (BMS80) to Improve Battery Life in Electric Vehicles. Computational Learning & Intelligence Computational Learning & Intelligence, 2(2), Accessed: Nov. 13, 2024. [Online]. Available: https://milestoneresearch.in/JOURNALS/index.php/IJCLI/article/view/82

[2] Bhuvaneswari, S., Mohan, A. & Sundaram, A. (2024). Improved BMS: A Smart Electric Vehicle Design based on an Intelligent Battery Management System. 2024 International Conference on Inventive Computation Technologies (ICICT), *IEEE*, 1999-2006.

[3] Liu, Q. & Chen, G. (2023). Design of Electric Vehicle Battery Management System. 2023 International Conference on Power, Grid and Energy Storage, Journal of Physics: Conference Series, *IOP Publishing*, 2614, 012001.

[4] Pradhan, S. K. & Chakraborty, B. (2022). Battery management strategies: An essential review for battery state of health monitoring techniques. *Journal of Energy Storage*, 51, 104427.

[5] Raghavan, A., Kiesel, P., Sommer, L. W., Schwartz, J., Lochbaum, A., Hegyi, A., Schuh, A., Arakaki, K., Saha, B., Ganguli, A., Kim, K. H., Kim, C., Hah, H. J., Kim, S., Hwang, G.-O., Chung, G.-C., Choi, B. & Alamgir, M. (2017). Embedded fiber-optic sensing for accurate internal monitoring of cell state in advanced battery management systems part 1: Cell embedding method and performance. *Journal of Power Sources*, 341, 466-473A.

[6] Lin, Q., Wang, J., Xiong, R., Shen, W. & He, H. (2019). Towards a smarter battery management system: A critical review on optimal charging methods of lithium ion batteries. Energy, *Elsevier*, 183(C), 220-234.

[7] Raoofi, T. & Yildiz, M. (2023). Comprehensive review of battery state estimation strategies using machine learning for battery Management Systems of Aircraft Propulsion Batteries. *Journal of Energy Storage*, 59, 106486.

[8] How, D. N. T., Hannan, M. A., Lipu, M. S. H., Sahari, K. S. M., Ker, P. J. & Muttaqi, K. M. (2020). State-of-Charge Estimation of Li-Ion Battery in Electric Vehicles: A Deep Neural Network Approach. *IEEE Transactions on Industry Applications*, 56(5), 5565-5574.

[9] Gabbar, H. A., Othman, A. M. & Abdussami, M. R. (2021). Review of Battery Management Systems (BMS) Development and Industrial Standards. *Technologies*, 9(2), 28.

[10] Hannan, M. A., Hoque, M. M., Mohamed, A. & Ayob, A. (2017). Review of energy storage systems for electric vehicle applications: Issues and challenges. *Renewable and Sustainable Energy Reviews*, 69, 771-789.

[11] Ouyang, Q., Han, W., Zou, C., Xu, G. & Wang, Z. (2020). Cell Balancing Control for Lithium-Ion Battery Packs: A Hierarchical Optimal Approach. *IEEE Transactions on Industrial Informatics*, 16(8), 5065-5075.

[12] Zhang, J., Zhang, L., Sun, F. & Wang, Z. (2018). An Overview on Thermal Safety Issues of Lithium-ion Batteries for Electric Vehicle Application. *IEEE Access*, 6, 23848-23863.

[13] Yu, C. & Chau, K. T. (2009). Thermoelectric automotive waste heat energy recovery using maximum power point tracking. *Energy Conversion and Management*, 50 (6), 1506-1512.

[14] Li, D., Zhang, Z., Liu, P., Wang Z. & Zhang, L. (2021). Battery Fault Diagnosis for Electric Vehicles Based on Voltage Abnormality by Combining the Long Short-Term Memory Neural Network and the Equivalent Circuit Model. *IEEE Transactions on Power Electronics*, 36(2), 1303-1315.

[15] Song, Y., Peng, Y. & Liu, D. (2021). Model-Based Health Diagnosis for Lithium-Ion Battery Pack in Space Applications. *IEEE Transactions on Industrial Electronics*, 68(12), 12375-12384.

[16] Xing, Y., Ma, E. W. M., Tsui, K. L. & Pecht, M. (2011). Battery Management Systems in Electric and Hybrid Vehicles. *Energies*, 4(11), 1840-1857.

[17] Lelie, M., Braun, T., Knips, M., Nordmann, H., Ringbeck, F., Zappen, H. & Sauer, D. U. (2018). Battery Management System Hardware Concepts: An Overview. *Applied Sciences*, 8(4), 534.

[18] Wang, Y., Tian, J., Sun, Z., Wang, L., Xu, R., Li, M. & Chen, Z. (2020). A comprehensive review of battery modeling and state estimation approaches for advanced battery management systems. *Renewable and Sustainable Energy Reviews*, 131, 110015.

[19] Xing, Y., He, W., Pecht, M. & Tsui, K. L. (2014). State of charge estimation of lithium-ion batteries using the open-circuit voltage at various ambient temperatures. *Applied Energy*, 113, 106-115.

[20] Laadjal, K. & Cardoso, A. J. M. (2021). Estimation of Lithium-Ion Batteries State-Condition in Electric Vehicle Applications: Issues and State of the Art. *Electronics*, 10(13), 1588.

[21] Moulik, B., Dubey, A. K. & Ali A. M. (2023). A Battery Modeling Technique Based on Fusion of Hybrid and Adaptive Algorithms for Real-Time Applications in Pure EVs. *IEEE Transactions on Intelligent Transportation Systems*, 24(3), 2760-2771.

[22] Polat, A. O., Celtek, S. A., Kul, S., Balci, S., Rawat, N., Oubelaid, A. & Bajaj, M. (2024). Zero Energy Vehicle Concept: L6e Electric Vehicle Design for Sustainable Urban Transportation. *E3S Web of Conferences (ICPGRES-2024)*, 564, 02001.

[23] Inan, R., Güçkiran, M., Altinişik, Y. E., Tek, S. E. & Potuk, M. (2023). Real-time implementation of battery management system designed with improved passive balancing technique for electric vehicles. *Journal of the Faculty of Engineering and Architecture of Gazi University*, 38(3), 1757-1768.

[24] Saleh, Y. B. & Kürüm, H. (2021). Design of Energy Management System Base on lithium-ion Battery. *European Journal of Science and Technology*, 28, 1144-1151.

[25] Wu, T.-H. & Chen, P.-Y. (2024). Battery Management System for Electric Garbage Compactor Trucks. *IEEE Access*, 12, 88596–88607.

[26] Waseem, M., Ahmad, M., Parveen, A. & Suhaib, M. (2023). Battery technologies and functionality of battery management system for EVs: Current status, key challenges, and future prospectives. *Journal of Power Sources*, 580, 233349.

[27] Thangavel, S., Mohanraj, D., Girijaprasanna, T., Raju, S., Dhanamjayulu, C. & Muyeen, S. M. (2023). A Comprehensive Review on Electric Vehicle: Battery Management System, Charging Station, Traction Motors. *IEEE Access*, 11, 20994-21019.

[28] Krishna, T. N. V., Kumar, V. S. V. P. D., Srinivasa Rao, S. & Chang, L. (2024). "Powering the Future: Advanced Battery Management Systems (BMS) for Electric Vehicles. *Energies*, 17(14), 3360.

[29] Kumar, R. R., Bharatiraja, C., Udhayakumar, K., Devakirubakaran, S., Sekar, K. S. & Mihet-Popa, L. (2023). Advances in Batteries, Battery Modeling, Battery Management System, Battery Thermal Management, SOC, SOH, and Charge/Discharge Characteristics in EV Applications. *IEEE Access*, 11, 105761-105809.

[30] Omariba, Z. B., Zhang, L. & Sun, D. (2019). Review of Battery Cell Balancing Methodologies for Optimizing Battery Pack Performance in Electric Vehicles. *IEEE Access*, 7, 129335-129352.

[31] Manas, M., Yadav, R. & Dubey, R. K. (2023). Designing a battery Management system for electric vehicles: A congregated approach. *Journal of Energy Storage*, 74 (A).

[32] Hannan, M. A., Hoque, M. M., Hussain, A., Yusof, Y. & Ker, P. J. (2018). State-of-the-Art and Energy Management System of Lithium-Ion Batteries in Electric Vehicle Applications: Issues and Recommendations. *IEEE Access*, 19362-19378.

[33] Marques, T. M. B., dos Santos, J. L. F., Castanho, D. S., Ferreira, M. B., Stevan, S. L., Jr., Illa Font, C. H., Antonini Alves, T., Piekarski, C. M., Siqueira, H. V. & Corrêa, F. C. (2023). An Overview of Methods and Technologies for Estimating Battery State of Charge in Electric Vehicles. *Energies*, 16(13), 5050.

[34] He, L. & Guo, D. (2019). An Improved Coulomb Counting Approach Based on Numerical Iteration for SOC Estimation with Real-Time Error Correction Ability. *IEEE Access*, 7, 74274-74282.

[35] Emami, A., Akbarizadeh, G. & Mahmoudi, A. (2024). A Novel Approach for Real-Time Estimation of State of Charge in Li-Ion Battery Through Hybrid Methodology. *IEEE Access*, 12, 148979-148989.

[36] Kadem, O. & Kim, J. (2023). Real-Time State of Charge-Open Circuit Voltage Curve Construction for Battery State of Charge Estimation. *IEEE Transactions on Vehicular Technology*, 72 (7), 8613- 8622.

e-ISSN: 2149-4584

Erzincan University Journal of Science and Technology

EJSAT 2025, 18 (3) 892-916

Research Article

Multi-frame Fusion Methods Based on Cepstral Coefficients for Drone Classification

Nida Kumbasar[1,3], Rabiye Kılıç[2,3*], Emin Argun Oral[3], Ibrahim Yucel Ozbek[3,4]

[1] Informatics and Information Security Research Center (BİLGEM), TUBİTAK, 41470, Kocaeli, Turkey
[2] Department of Computer Engineering, Ataturk University, 25240, Erzurum, Turkey
[3] Department of Electrical Electronics Engineering, Ataturk University, 25240, Erzurum, Turkey
[4] Department of Artificial Intelligence and Data Engineering, 25240, Erzurum, Turkey

Received: 20/11/2024, **Revised:** 07/02/2025, **Accepted:** 18/02/2025, **Published:** 31/12/2025

Abstract

The increasing popularity of drones in recent years has resulted in privacy and security vulnerabilities. Today, drones can be easily purchased and used, leading to concerns about intrusion into private areas. Detecting the presence of drones and identifying their operation mode is of great importance. Various detection techniques, including video, sound, thermal imaging, and Radio Frequency (RF) signals, are employed for drone detection and classification. In this study, RF signals are utilized for classifying drones using DroneRF dataset, which is a publicly available open-source dataset. It consists of four main classes for drone types, namely AR, Bebop, Phantom drones and back ground for no drone existence. The dataset is further divide into ten sub-classes representing different operating modes of each drone. Operating mode classification is crucial for security reasons since they represent drones' specific activity. To achieve high performance in drone classification, we propose the multi-frame majority voting method using cepstral coefficients. Drone signals are divided into multiple frames (2, 4, and 8), and each frame is analyzed using Mel Frequency Cepstral Coefficients (MFCC) and Linear Frequency Cepstral Coefficients (LFCC) attributes. Each frame is classified by Support Vector Machine (SVM), and majority voting is applied to the predictions from the frames. Results show 100% accuracy for drone classification (4-Class) and 99.11% accuracy for defining operating modes (10-Class). The proposed method outperforms existing methods in drone classification using the DroneRF dataset.

Keywords: Drone classification, RF signal, MFCC, LFCC, SVM

Kepstral Katsayılara Dayalı Çoklu Çerçeve Füzyon Yaklaşımıyla Drone Sınıflandırması

Öz

Son yıllarda dronların artan popüleritesi gizlilik ve güvenlik açıklarına yol açmıştır. Günümüzde dronlar kolayca satın alınıp kullanılabilmekte ve bu da özel alanlara izinsiz girilmesi konusunda endişelere yol açmaktadır. Dronların varlığını tespit etmek ve çalışma modlarını belirlemek büyük önem taşımaktadır. Dron tespiti ve sınıflandırması için video, ses, termal görüntüleme ve Radyo Frekansı (RF) sinyalleri dahil olmak üzere çeşitli tespit teknikleri kullanılmaktadır. Bu çalışmada, DroneRF veri kümesi kullanılarak dronların sınıflandırılması için RF sinyalleri kullanılmıştır. Bu veri kümesi, kamuya açık açık kaynaklı bir veri kümesidir. AR, Bebop, Phantom dronları ve dron olmayan arka plan olmak üzere dron tipleri için dört ana sınıftan oluşmaktadır. Veri kümesi ayrıca her bir dronun farklı çalışma modlarını temsil eden on alt sınıfa ayrılmıştır. Çalışma modu sınıflandırması, dronların belirli aktivitesini temsil ettikleri için güvenlik açısından önemlidir. Dron sınıflandırmasında yüksek performans elde etmek için, kepstral katsayıları kullanarak çok çerçeveli çoğunluk oylama yöntemini öneriyoruz. İHA sinyalleri birden fazla çerçeveye (2, 4 ve 8) bölünür ve her çerçeve Mel Frekans Kepstral Katsayıları (MFCC) ve Doğrusal Frekans Kepstral Katsayıları (LFCC) nitelikleri kullanılarak analiz edilir. Her çerçeve Destek Vektör Makinesi (SVM) tarafından sınıflandırılır ve çerçevelerden gelen tahminlere çoğunluk oyu uygulanır. Sonuçlar, İHA sınıflandırması için %100 doğruluk (4-Sınıf) ve çalışma modlarını tanımlamak için %99,11 doğruluk (10-Sınıf) gösterir. Önerilen yöntem, DroneRF veri setini kullanarak İHA sınıflandırmasında mevcut yöntemlerden daha iyi performans gösterir.

Anahtar Kelimeler: Drone sınıflandırması, RF sinyali, MFCC, LFCC, SVM

Corresponding Author: rabiyekilic@atauni.edu.tr

Cite this Article: Erzincan University Journal of Science and Technology 2025, 18(3)892-916. https://doi.org/10.18185/erzifbed.1587701

1. Introduction

Significant technological advances in the drone industry have led to an increasing number of such devices used in different applications [1, 2]. Drones are increasingly being equipped with the latest technologies and sensors, such as Global Positioning System (GPS), Laser Imaging Detection and Ranging (LIDAR), radar, and vision sensors. Today, with the development of drone technology, drones are used for various purposes such as cinematography, agriculture, photography, and entertainment [3]. Drones, despite their advantageous functions, also serve illegal purposes and pose a threat to public safety [4-5]. The increasing use of Unmanned Aerial Vehicle (UAVs) creates both security and privacy vulnerabilities. It is known that UAVs are used for malicious purposes such as cybercrime, terrorism, and drug trafficking [6]. For this reason, detecting foreign drones is extremely important today. Automatically detecting and identifying a drone is a difficult process. Radar sensing [7], vision sensing [8], acoustic sensing [9], and Radio Frequency, (RF) fingerprint-based sensing [10] are some of the most widely used technologies to detect and classify drones. The methods used in the literature for drone detection and classification are briefly summarized as follows. Radar detection uses an active sensor in detection systems to determine the range, angle, or speed of the drone. A radar system consists of a transmitter, a receiver, and a processor. Traditional radar systems will fail to detect a mini drone due to the small radar cross-sectional area. To overcome this problem, researchers use a multi-static radar or a Frequency Modulated Continuous Wave (FMCW) radar [10, 11]. To distinguish drones from birds, rotor blade rotation and clear micro-Doppler signatures are used in radar rotation analysis [12, 13]. Video/image detection includes both visual and thermal sensing. In the studies [15, 16, 17], researchers perform drone detection by analyzing color, shape, and edge information. The detection method is reliable but requires a line of sight between the drone and the camera, and performance is highly dependent on daylight conditions and weather conditions such as dust, rain, fog, and cloud. The similarity of a bird to a drone complicates the task for a video detector. In the study in [18], a 2-Dimensional (2D) scale was classified as a drone or bird with a neural network using the invariant Generic Fourier Descriptor (GFD) features with rotation and translation. In addition, drone model classification was done by proposing a Convolutional Neural Network (CNN) that describes drone models in real-life videos [19]. In addition to these studies, recently Ahmad et al. [44] proposed an architecture consisting of two main modules on RGB drone images. The first one is a Visual Geometry Group based convolutional neural network (VGG-CNN) framework for detection, and the second one is a mask region based double convolutional neural network (MR-DCNN) framework for identification of drone type, payload and flight characteristics. Some studies in the literature [20, 21, 22] have utilized acoustic detection to detect drone presence. In this approach, the sounds produced by flying drones with the help of microphones are used. Acoustic sensing generally works well in a quiet or less noisy environment, but performance suffers when the environment is noisy, such as in urban or industrial areas. In another study, Mel-Frequency Cepstral Coefficients (MFCCs) derived from sound signatures are then fed to CNN, which predicts the presence of a drone [23]. In another study, a new frequency feature extraction method based on the Prony's algorithm was utilized for drone detection and classification with acoustic signals [47]. This study by Najafi et al. the performance of the

method was compared with traditional audio features such as MFCCs, Gamma Tone Cepstral Coefficients (GTCCs) and Fast Fourier Transform (FFT). As an alternate approach, drone-emitted RF signals have been recently used for drone detection. A large dataset, namely DroneRF, has been created from different drones for that purpose [24]. Al-Sa'd et al. [10] used Deep Neural Networks (DNN) to detect the presence, type, and flight mode of a drone. The performance of each DNN is verified by 10-fold cross-validation and evaluated using a variety of metrics. Al-Emadi et al. [25] proposed a new RF-based drone detection solution using the CNN method. Medaiyese et al. [26], a machine learning model was developed using the XGBoost algorithm to detect and identify the presence of a drone and its type. Evaluated using 10-fold cross-validation the XGBoost model. Allahham et al. [27] propose a deep learning-based approach for drone detection, type identification, and state identification using a multi-channel 1-Dimensional (1D) CNN. Swinney et al. [28] plot the spectrogram, histogram, raw IQ, and Power Spectral Density (PSD) as well as graphical representations of RF signals. Features are extracted using a pre-trained ResNet50 CNN in the ImageNet data. Finally, drone RF signals are classified with the machine learning model Logistic Regression (LR) as a classifier. Ensemble learning was performed with the dataset K-Nearest Neighbor (KNN) and XGBoost preprocessed with FFT drone modes, and classification was done with the hierarchical learning method by Nemer et al. [29]. Kılıç et al. [30] extracted features from PSD, MFCC, and Linear Frequency Cepstral Coefficients (LFCC) improved filter banks and parameters, and classification was with the Support Vector Machine (SVM). Hybrid Model with Feature Fusion Network (HMFFNet) model structure is proposed by Kumbasar et al. [31]. In that study, the RF signals were converted into images using spectrogram, persistence spectrum, and percentile spectrum; the next features were obtained by using VGG19. Obtained features were classified by SVM. Huynh et al. [32] created a CNN structure called RF-UAVNet. In other study RF signals are adapted according to the signal properties; sampling structure based on the compressively sensed theory and data preprocessing method is performed by Mo et al. [33]. Next, the neural network structure is designed to detect and classify RF fingerprints. In another study [34], the loads carried by drones are estimated up to 200 m using five different drones. They constructed features using GMM-UBM supervector normalization with MFCC and classified their self-produced dataset signals with a SVM classifier. AlKhonaini et al. [43] trained the reinforcement learning algorithm with an entropy regularization term hierarchically (with 2,4,10 classes respectively) with multiple policies. They also comprehensively evaluated the performance during training and testing using several metrics, including loss, average return per episode, time, and energy consumption, in addition to accuracy. Zahid et al. [45] combined automatic and manual feature extraction techniques for drone signal classification with RF signals, integrated wavelet-based noise removal into the framework, and proposed a compound ensemble learning (CEL)-based neural network. Haque et al. [46] proposed an explainable AI-based approach for drone recognition and identification with RF signals using SHapley Additive Explanations (SHAP) and Local Interpretable Model-agnostic Explanations (LIME) approaches. Table 1 presents a comparative analysis of drone detection methods using RF signals.

In this study, a particular focus is placed on the detection of drones using RF signals, employing advanced methods like majority voting, utilized to improve accuracy performance by combining the results of multiple tests, and cepstral coefficients such as MFCC and LFCC. These methods offer promising results by enabling more accurate identification and classification of drones in various environmental conditions.

The main motivation of the proposed work is the classification of drones using drone RF signals. For this purpose, RF signals are split into multiple frames (2, 4, and 8). RF signals are divided into multi-frames, and experimental studies are carried out for each frame. MFCC and LFCC features are obtained. Estimation of each frame using SVM, drone types, and drone modes are classified with majority voting.

- There are studies in the literature as a single frame. In this study, a single frame was defined as the baseline. Performance was measured from frames divided into multi frames.
- Unlike the multi-segment numbers (100, 1000, etc.) used in the literature, the RF signals were divided into a small number of segments (2, 4, and 8) in this study.
- The drone RF signal was estimated by voting the prediction obtained from each frame by majority voting.
- The results obtained with MFCC and LFCC were compared in terms of drone classification performances.

Table 1. Comparative analysis of drone detection methods using RF signals

Study	Dataset Used	Techniques Applied	Evaluation Method	Number of Class	Accuracy (%)
Al-Sa'd et al. [10]	DroneRF	Deep Neural Networks (DNN)	10-fold cross-validation	2-4-10	99.7-84.5-46.8
Al-Emadi et al. [25]	DroneRF	Convolutional Neural Network (CNN)	10-fold ross-validation	2-4-10	99.8-85.8-59.20
Medaiyese et al. [26]	DroneRF	XGBoost	10-fold cross-validation	2-4-10	99.96-90.73-70.09
Allahham et al. [27]	DroneRF	Multi-channel 1D CNN	Not specified	2-4-10	100-94.6-87.4
Swinney et al. [28]	DroneRF	ResNet50, Logistic Regression (LR)	5-fold cross-validation	10	91
Nemer et al. [29]	Custom RF Dataset	Ensemble Learning (KNN, XGBoost, FFT)	Hierarchical Learning Method	2-10	99.5-99.2

Study	Dataset Used	Techniques Applied	Evaluation Method	Number of Class	Accuracy (%)
Kılıç et al. [30]	DroneRF	SVM with PSD, MFCC, LFCC features	10-fold ross-validation	2-4-10	100-98.67-95.15
Kumbasar et al. [31]	DroneRF	VGG19-SVM Hybrid model	10-fold ross-validation	2-4-10	100-99.55-97.75
AlKhonaini et al. [43]	DroneRF	Reinforcement Learning with Hierarchical Training	Cross-entropy loss, Multiple Metrics	2-4-4	99.7
Zahid et al. [45]	RF Drone Signals	Compound Ensemble Learning (CEL)	Machine Learning Evaluation	15	99.0
Najafi et al. [47]	Acoustic Signals	Prony's Algorithm for Frequency Feature Extraction	Comparison with MFCCs, GTCCs, FFTs	4	93.6

The remainder of the paper is organized as follows: Section 2 presents the materials and methods used in this study. Section 3 details the experimental setup, while Section 4 provides the experimental results and numerical analysis. Section 5 compares the proposed method with existing approaches from the literature, and Section 6 concludes the study.

2. Material and Methods

This section describes the materials and methods used for drone detection and classification using RF signals. We focus on the multi-frame classification method proposed in this study, which differs from the single-frame method used in prior research. The dataset used in the proposed method, DroneRF, and the multi-frame classification approach are explained in detail. The process begins with the division of RF signals into multiple frames. For each frame, feature extraction techniques are applied to obtain low-band and high-band features. These extracted features are then classified using Support Vector Machine (SVM). To enhance the accuracy of the classification, majority voting is employed, where predictions from each frame are combined to determine the final classification result.

DroneRF Database

In this study, the open-source DroneRF dataset is used [10, 24]. The dataset consists of 227 recorded segments collected from 3 different drones (Bebop, AR, and Phantom drones) and

background. The dataset is in comma separated values (csv) files. It includes RF signals when there is no drone and RF signals when there is a drone in different modes. It consists of 4 different modes, such as off, on and connected, hovering, flying, and video recording, as listed below.

- Mode 1: On and connected to the controller
- Mode 2: No physical intervention
- Mode 3: Drone flying without video recording
- Mode 4: Flying with video recording

Baseline Method (Single Frame)

In the literature, there are studies [30, 31] carried out without dividing drone RF signals into multiple frames, or when the RF signals are split into multiple frames, each frame is estimated. The success rate is presented on a frame-by-frame basis, not for the entire signal.

In this study, unlike the literature, the RF signals divided into multi-frames are estimated for each frame, and the final class of the entire signal is determined by majority voting. Fig. 1 shows the comparison chart of the single frame used in the literature and the proposed method (multi frame). The multi-frame method used in the study is explained in detail in the following sections.

Fig. 1 illustrates a comparative analysis between the baseline single-frame method and the proposed multi-frame approach for drone detection and classification. The baseline method processes low-band and high-band RF signals as a single frame, extracting features (F_L, F_H) and feeding them into a single SVM model (M) to produce a prediction (P). In contrast, the proposed multi-frame method incorporates multiple frames and extracts features (F_L^1, F_L^2,..., F_L^m and F_H^1, F_H^2,..., F_H^m) from each frame. These extracted features are then independently processed using multiple SVM models (M_1, M_2,..., M_m), generating individual predictions (P_1, P_2,..., P_m). A final classification result (P_F) is obtained through a voting mechanism, which aggregates the predictions of such multiple frames. This methodology enhances classification accuracy by leveraging temporal information and mitigating potential misclassifications associated with single-frame analysis.

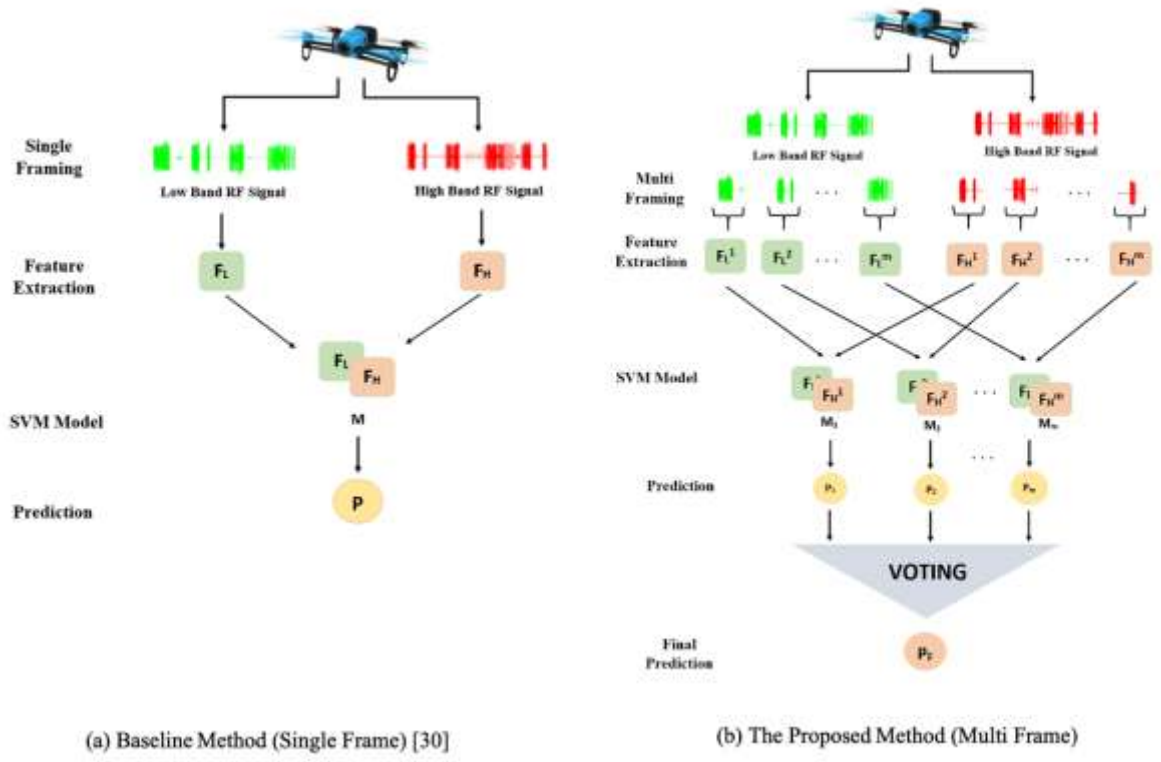

Fig. 1. Comparison of drone detection methods. (a) The baseline method uses single-frame feature extraction and SVM Classification [30]. (b) The proposed multi-frame method enhances accuracy through feature extraction across multiple frames and majority voting.

The Proposed Method (Multi-Frame)

In this study, multi-frame is suggested as the proposed method. RF signals are received and processed by receivers when there is no drone and when there is a drone. Bebop, AR, and Phantom drones used in receiving RF signals operate in different bandwidth ranges. It is assumed that they use WiFi operating at 2.4 GHz while creating this dataset. Two NI USRP-2943R RF receivers were used. The first receiver captures the lower half (low) of the frequency band, and the second receiver records the upper half (high). Thus, there are 454 RF signal files in total. Recordings are taken as 10.25 seconds in total. In 5.25 seconds of this received signal, the RF drone is in communication. Bebop, AR, and Phantom drones were used while receiving RF signals. The drone RF dataset has more than 40 GB of data.

Drone RF signals are divided into 2, 4, and 8 frames to be used in experimental studies. The same process is applied to both the low and high bands of a drone signal. Fig. 2 depicts the decomposition of the drone's RF signal into low-band and high-band components, which are further divided into 2-frame, 4-frame, and 8-frame segments. This multi-frame approach enhances temporal feature extraction, improving the accuracy and robustness of drone detection compared to single-frame methods.

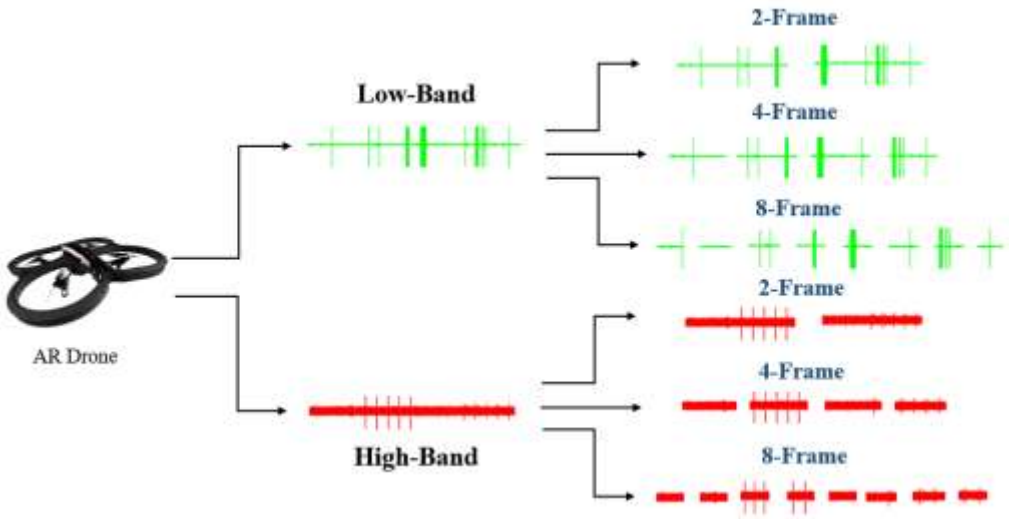

Fig. 2. Drone RF signal separated into its frames.

Feature Extraction with Cepstral Coefficients

Cepstral coefficients are commonly used to extract features from time-varying signals. By switching to the frequency space, signal processing is provided [35, 36].

Step 1 Framing: It can be seen that time-varying signals do not change much in short time intervals. For this reason, signals are processed by framing them at certain lengths.

Step 2 Windowing: The framing process causes discontinuity in the signal. In order to prevent these discontinuities, windowing is done. Hamming windowing, which is widely used, was used in this study. Hamming windowing is given in Eq. 1.

$$w(n) = 0.54 - 0.46\cos(2\pi n/N - 1) \quad (1)$$
$$N - 1 \geq n \geq 0$$

where $w(n)$ represents the value of the Hamming window for n, frame time-index, N is the total length of the window, typically the length of the segment of the signal that is being analyzed.

Step 3 FFT: The transition from the time domain to the frequency domain of the windows consisting of (N) samples is realized with the FFT. The (x_n) signals in the time domain are converted to the frequency space expressed by (X_k) in Eq.2 with the following formula.

$$X_k = \sum_{n=0}^{N-1}(x_n)e^{-j2\pi kn/N}, \quad \text{k}= 0, 1, \dots, N-1 \quad (2)$$

Step 4 Filter Banks: Cepstral coefficient scales obtained with Mel and linear filters are used as features in drone detection and classification. LFCC, fixed-width filters, defined in the frequency domain, are utilized, while those with varying width according to Mel-scale are used

in the MFCC process. Three parameters define such filter banks. These are the total number of filters F, minimum frequency (f_{min}), and maximum frequency (f_{max}) in the filtering band. These parameters are defined in [37].

The widths of Mel frequency filters are determined according to the sensitivity in the frequency space. Corresponding filter bank examples are shown in Fig. 3. In a mel-scale filter bank, narrow triangular filters are used at low frequencies and wider filters are used at high frequencies. Thus, the signal in the frequency space is converted into a mel-scale power spectrum. In linear-scale filter bank filters of equal width are used at each frequency value.

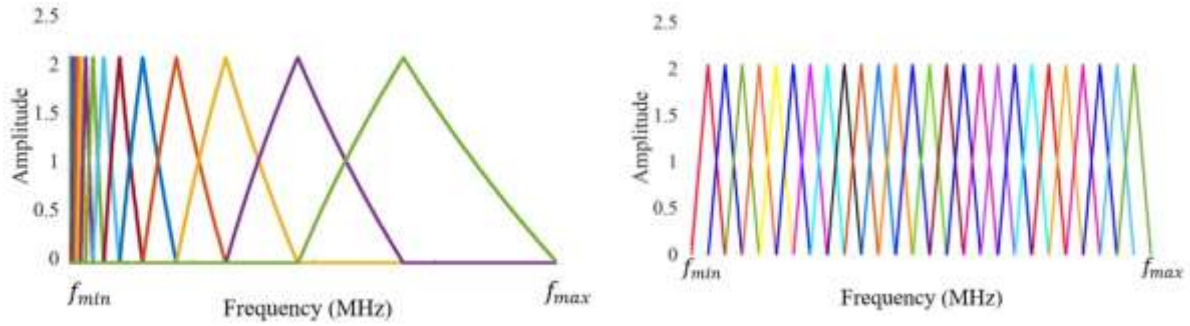

(a) (b)

Fig. 3. Filter banks used in cepstral coefficients; (a) Mel-scale filter bank, (b)Linear-scale filter bank.

Step 5 Cepstrum Coefficients: The last step is to obtain the cepstrum coefficients. It reveals the differences and similarities with the cepstral coefficients. There are cepstrum coefficients with Discrete Cos Transform (DCT). First of all, $H_m(k)$ Mel frequency filter bank, is multiplied by $X_n(k)$, the input signal, as shown in Eq. 3.

$$S_n^m = \sum_{k=0}^{N-1} X_n(k).H_m(k) \tag{3}$$

$$log(S_n^m) = log\big(X_n(k).H_m(k)\big) = log\big(X_n(k)\big) + log\big(H_m(k)\big) \tag{4}$$

$$\text{cepstrum(k)} = \frac{1}{2\pi}\int_{-\pi}^{\pi} log(S_n^m).e^{jwk}dw \tag{5}$$

Eq.4 applies a logarithmic transformation to the power spectrum of the signal. This is usually utilized to make the dynamic range of the signal more manageable and to better analyze the signal at different frequencies. Eq. 5 uses the inverse Fourier transform to extract the cepstrum coefficients from the logarithmic spectrum. This transforms the frequency components of the signal into a representation in the time domain.

Support vector machine (SVM) Classifier

SVM (Support Vector Machine) classification is one of the widely used methods [38]. It provides drawing the most appropriate line to separate the elements of each class shown on the

plane. These lines are also called decision boundaries or hyperplanes. Support vector machines are basically divided into linear and non-linear. Linear support vector machines are often used to distinguish between the two classes. There are support vectors representing each class. Usually these class labels are used as $(-1, +1)$. A straight line is drawn to center the boundary planes. This line is called hyper plane [39,40]. It is decided which class the incoming data belongs to, depending on whether (y) is (-1) or $(+1)$.

Nonlinear SVMs do not have a hyperplane. Data that is not separated linearly is based on the principle of classification by mapping in high [41]. It is the tradeoff parameter used to increase the distance of the support vectors used in the equation from the hyperplane and to reduce the classification error. The optimization problem can be solved by the Lagrangian multiplier method. Another space conversion process is performed using kernel tricks known as the kernel plane [42]. The most commonly used kernel methods are polynomial kernel and Radial Basis Function (RBF) kernel. Thus, each kernel function corresponds to a new feature space. In this study, classification process was carried out by experiments with SVM parameters linear, polynomial, and RBF kernel parameters.

Majority Voting Based Multi-Frames

Within the scope of this study, drone detection and classification, majority voting is done based on multi-frames. First, the low- and high-band signals received from the drone are divided into multiple frames (m frames), and attributes are obtained for each frame. Then, the features obtained from the low-high band were combined and used to create the model with SVM. Each frame of the RF signal is estimated. And finally, the RF signal's class is estimated by voting by majority voting for each frame.

3. Results and Discussion

3.1. Results

In this section, performance metrics of experimental studies, experimental setup, preparation of train and test data, and SVM parameters are explained.

Performance Metrics

The classification performance of the proposed study is evaluated in terms of Accuracy, Precision, Recall and F1 score metrics as defined in Eqs. 6-9.

$$Accuracy = \frac{TP+TN}{TP+TN+FP+FN} \quad (6)$$

$$Precision = \frac{TP}{TP+FP} \quad (7)$$

$$Recall = \frac{TP}{TP+FN} \quad (8)$$

$$F1\ score = 2\frac{Precision.Recall}{Precision+Recall} \quad (9)$$

In these equations, TP (True Positive) and FN (False Negative) represent data of a particular class that is predicted as the correct class or other classes, correspondingly. TN (True Negative) and FP (False Positive), on the other hand, represent data from other classes that is predicted as other-class and particular class, respectively.

Experimental Setup

All experiments for the proposed drone detection and classification system are performed on a 10-core i9-7900X central processing unit (CPU) with 128GB of RAM and the Ubuntu 18.04.4 LTS Linux operating system platform. Preprocessing of the DroneRF dataset and proposed algorithms are developed using MATLABR2019b software backed by three GeForce RTX 2080Ti graphics processing units (GPUs).

Train and Test Data Preparation

It is one of the commonly used methods for separating the dataset into train and test. The dataset is randomly divided into k parts. When k is taken as 10, the dataset is divided into 10 parts. With the dataset, it is possible to train 10 times with different parts and test 10 times on different parts. This method ensures the accuracy of the prepared model.

SVM Parameters

The SVM model is created after the extracted features are grouped as train and test with cross-validation. Different kernel functions, such as linear, polynomial, and Gaussian functions, are tested as kernel functions, and the Gauss function that performed the highest accuracy is determined as the kernel function. Experimental studies are performed for various values of kernel scale (v) and penalty parameter (C) in the range from 2^{-15} to 2^{15} with the power increments. In this study, the one-vs-one method is preferred for SVM because it offered better results than one-vs-all.

Performance Analysis

In this section, the experimental results of the proposed multi-frame late fusion methods are described. LFCC and MFCC are represented as features of RF signals. First, the methods used to develop MFCC and LFCC features and their results are presented. Experimental studies are repeated for 2, 4, and 8 frames, and the results are shown. Finally, the proposed method is compared with the literature.

Adjusted Features for MFCC and LFCC

This section shows the improvement of the proposed method by adjusting the LFCC and MFCC feature parameters and adding new features. For that, to better clarify the obtained results, abbreviations used in the reported results are given in Table 2.

Table 2. Abbreviations used in the tables.

D	Default
O	Zero-Order Coefficient
E	Log Energy (in time domain)
NC	Number of cepstral Coefficient

Single-Frame Classification Results

Drone signals are classified as a single frame by Kılıç et al. [30]. The features of each signal were extracted using MFCC and LFCC, and the success rates obtained as a result of 2, 4, and 10 class classification with SVM are shown in Table 3.

The bottom row of the Tables (3-4-5-6) presents the parameter combinations for which the relevant result was obtained. The plus sign (+) indicates to be used together.

Table 3. Single-frame based accuracy rates with MFCC and LFCC features [30]

	Accuracy (%)		
	2-Class	**4-Class**	**10-Class**
MFCC	100	98.67	90.33
LFCC	100	98.67	95.29
Parameters:	D, NC=12	D+O+E, NC=12	D+E, NC=13

When Table 3 is examined, without dividing drone signal frames; 100% success rate has been achieved in the classification of drone with or without (2-Class). A success rate of 98.67% is achieved in drone types (4-Class) and 95.29% in classification between drone modes (10-Class) by using LFCC.

The Proposed Multi-Frame Classification Results

In this section, since 100% accuracy was achieved 2-class (drone detection) single frame [30], experimental studies are carried out for 4 and 10 classes. Each drone signal is divided into 2, 4, and 8 multi-frame, and the features obtained from each frame are classified by SVM, and the success rates obtained by using majority voting are shown in Table 4.

Table 4. Multi-frame based accuracy rates with MFCC and LFCC features

	Accuracy (%)			
Number of Frames	**MFCC**		**LFCC**	
	4-Class	10-Class	4-Class	10-Class

2	98.23	89.43	98.23	94.86
4	**99.55**	93.90	**100**	**97.09**
8	**99.55**	**94.79**	99.89	95.27
Parameters:	D+O+E, NC=12	D+E, NC=13	D+O+E, NC=12	D+E, NC=13

From the comparison of MFCC and LFCC results presented in Table 4, the accuracy rate of the multi-frame based classification depends on the number of frames. The best results of 100% and 97.09% are obtained for 4 frames in 4-Class problem and for 4 frames in 10-Class problem in LFCC, respectively.

Figs. 4 and 5 present the classification percent accuracy comparisons between the single-frame method and the proposed multi-frame approach for 4-class and 10-class classification tasks, respectively. In Figure 4, the multi-frame approach significantly improves accuracy compared to the single-frame method, with the 4-frame configuration achieving 100% accuracy with LFCC features and 99.55% with MFCC features. The 8-frame configuration also maintains high accuracy (99.89% for LFCC and 99.55% for MFCC), demonstrating the effectiveness of incorporating temporal information. Similarly, Figure 5 shows that the multi-frame approach enhances accuracy in the 10-class classification task, with the 4-frame configuration achieving the highest accuracy (97.09%) using MFCC features, followed by the 8-frame method (95.27% for MFCC and 94.79% for LFCC). However, the 2-frame configuration exhibits a slight decrease in accuracy compared to the single-frame method in LFCC-based classification, indicating that a higher number of frames is more beneficial. These results confirm that multi-frame processing significantly improves classification accuracy, particularly when an optimal number of frames is utilized, making it more effective than the traditional single-frame approach.

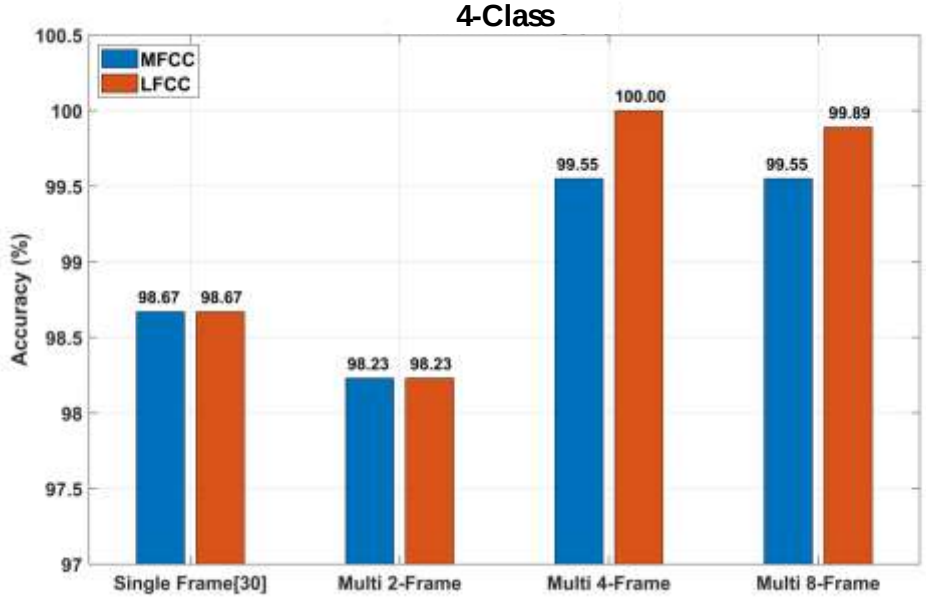

Fig. 4. Comparison of single frame [30] and multi-frame results for 4-Class

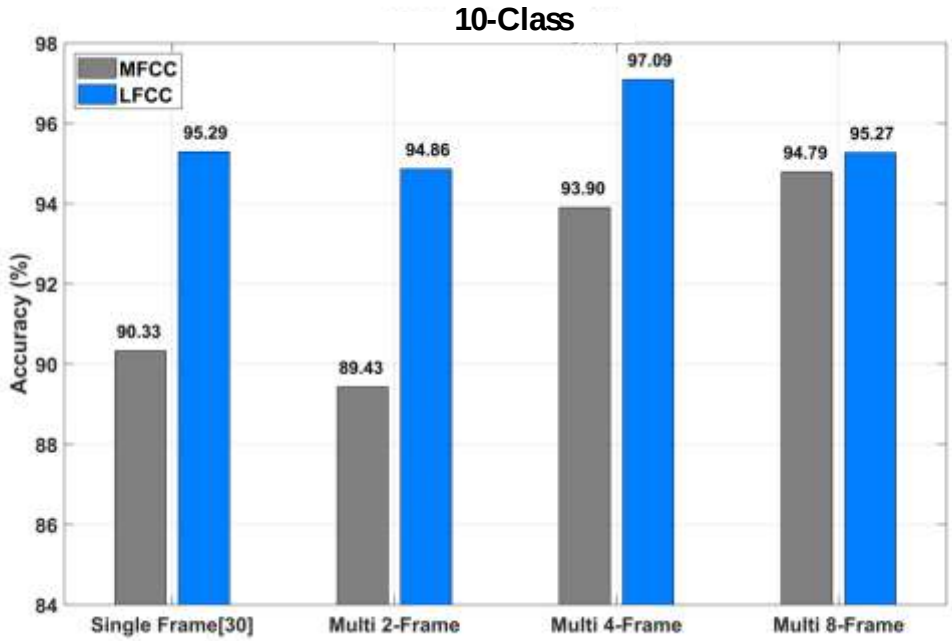

Fig. 5. Comparison of single frame [30] and multi-frame results for 10-Class

The Effect of Overlap-Rate on Success Rate

In this section, the effect of overlap on the success rate is analyzed. Classification is done with no overlap (0%), 50%, and 75% overlap. In Table 5, the success rate obtained with MFCC is presented by overlapping.

Table 5. Overlapped multi-frame accuracy rates with MFCC

	Accuracy (%)					
	4-Class			**10-Class**		
	Overlap rate			**Overlap rate**		
Number of frames	**0%**	**50%**	**75%**	**0%**	**50%**	**75%**
2	98.23	100	99.55	89.43	95.15	96.91
4	99.55	100	99.55	93.90	97.35	98.67
8	99.55	100	100	94.79	98.80	99.11
Parameters:	D+O+E, NC=12			D+E, NC=13		

From the evaluation of Table 5, the 4-Class problem yields a 100% accuracy rate with the use of a 50% overlap ratio, while that of the 10-Class problem increases to 99.11% with a 75% overlap ratio, all with MFCC features.

It is clear that the accuracy rate of MFCC and LFCC feature-based classification is improved to 100% in the 4-Class problem with multi-frame.

On the other hand, the accuracy rate dependency on overlap ratio is only investigated for the 10-Class problem using LFCC features since full accuracy is obtainable without overlapping frames in the 4-Class problem. It is determined that the accuracy rate increases from 97.09% to 97.35% with an overlapping ratio of 75% as shown in Table 6.

Table 6. Overlapped multi-frame accuracy rates with LFCC for 10-Class

	Accuracy (%)		
Number of	**Overlap rate**		
Frames	**0%**	**50%**	**75%**
2	94.86	93.39	93.39
4	97.09	96.18	97.35
8	95.27	96.47	97.35
Parameters:	D+E, NF=13		

In the 10-Class problem, the accuracy rate changes from 94.79% to 99.11% with frame overlapping for MFCC-based features, yielding a 4.55% increase. That of LFCC, on the other hand, shows a 0.31% increase for the 97.35% best accuracy rate. Fig. 6 presents a comparative analysis of classification accuracy for the 10-class task using single-frame, multi-frame, and multi-frame with overlap approaches. The results indicate that the multi-frame approach outperforms the single-frame method, with accuracy increasing from 90.33% (MFCC) and 95.29% (LFCC) to 94.79% (LFCC) and 97.09% (MFCC), respectively. Furthermore,

introducing frame overlap approach improves the accuracy with 99.11% (MFCC) and 97.35% (LFCC). These results demonstrate that multi-frame processing significantly improves classification performance, while incorporating overlap further refines feature extraction, leading to higher accuracy in drone detection and classification tasks.

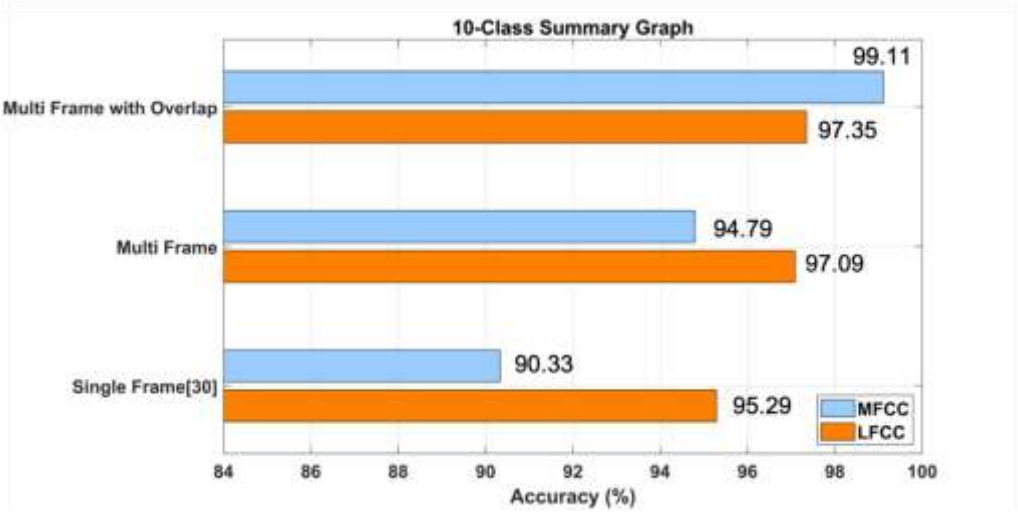

Fig. 6. The effect of multi-frame on accuracy rate for 10-Class.

By using the DroneRF dataset, a 100% success rate is achieved in the classification of 2 and 4 class drone RF signals and 99.11% in the classification with 10-Class. Only the drone operation mode (10-Class) confusion matrix is shown in Fig. 7, since 100% success was finally achieved in drone detection (2-Class) and drone classification (4-Class) problems.

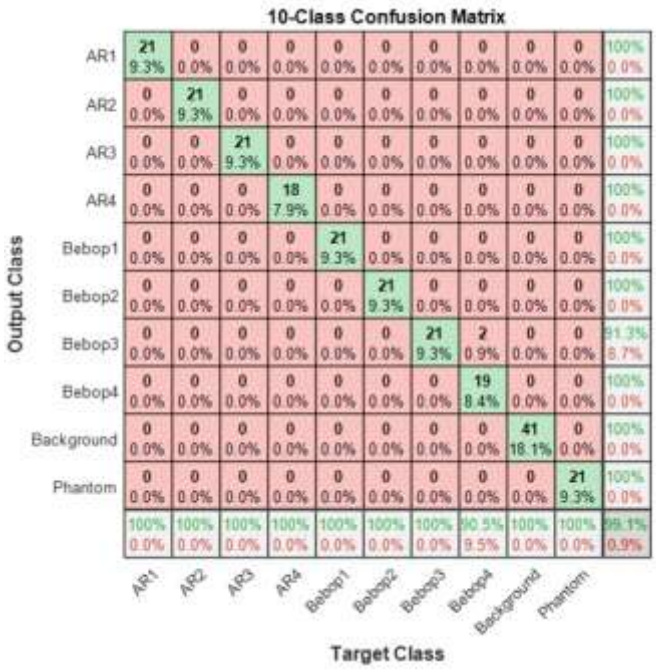

Fig. 7. Operation mode recognition (10-Class) confusion matrix.

The Accuracy, F1 Score, Recall and Precision values of the proposed method are obtained as in Table 7.

Table 7. Accuracy, F1 score, Recall and Precision values of the proposed method.

		MFCC	**LFCC**
Accuracy (%)	2 Class	100	100
	4 Class	100	100
	10 Class	99.11	97.35
F1 score (%)	2 Class	100	100
	4 Class	100	100
	10 Class	99.06	97.11
Recall (%)	2 Class	100	100
	4 Class	100	100
	10 Class	99.07	97.06
Precision (%)	2 Class	100	100
	4 Class	100	100
	10 Class	99.09	97.34

3.2. Discussion

In this section, the proposed method is compared with the studies in the literature using the DroneRF dataset and is shown in Table 8.

Al-Sa'd et al. [10] used three DNNs through signals divided into 100 segments, using 10-fold cross-validation. They performed the power spectrum as the feature set, which is obtained from the combined magnitude DFT of low- and high-band signals. Al-Emadi et al. [25] proposed a method using a CNN architecture that consists of five 1D convolutional layers, utilizing 10-fold cross-validation. While they slightly improved the accuracy results of Al-Sa'd et al. [10] for 2, 4, and 10-Class problems. Medaiyese et al. [26] proposed three machine learning models utilizing the XGBoost algorithm and evaluated these models using 10-fold cross validation. Their major contribution to accuracy is compared to Al-Emadi et al. [25] in the 10-Class problem. Allahham et al. [27] channelized the RF Drone signals' full spectrum into multiple channels and considered each one as a separate input of multi-channel 1D CNN. It is used with RF signals divided into approximately 370 segments. Swinney et al. [28] RF signals as spectrogram, histogram, raw IQ constellation, and PSD graphical representations. The features are extracted using ResNet50 and classify by LR utilizing 5-fold cross-validation as10-Class drone signals. Kılıç et al. [30] extract features with PSD, MFCC, and LFCC and classify them with SVM. In that study, RF signals are handled as 1 segment, and 10-fold cross-validation is

used in classification. By Kumbasar et al. [31], RF signals are represented by images using spectrogram, persistence spectrum, and percentile spectrum with HMFFNet model structure classified by SVM and the features obtained using VGG19. In that study, DroneRF data was discussed into 1, 10, and 100 segments, and 10-fold cross-validation was carried out in their studies. Huynh et al. [32] with the CNN architecture they call RF-UAVNet 10-fold cross validation performed in the study, which is done by dividing the approximate signals into 1000 segments.

With the proposed MFCC and LFCC feature multi-frame majority voting method, 100% accuracy has been achieved in the 4-Class classification. An accuracy rate of 99.11% is achieved in 10-Class classification. Experimental studies are carried out according to 2, 4, and 8 segments. 10-fold cross validation is used to calculate the accuracy rate.

Table 8. Comparison of studies using the DroneRF dataset

	Accuracy (%)			**F1 score (%)**		
Literature	**2-Class**	**4-Class**	**10-Class**	**2-Class**	**4-Class**	**10-Class**
Al-Sa'd et al.[10]	99.70	84.50	46.80	99.50	78.80	43.00
Al-Emadi et al.[25]	99.80	85.80	59.20	99.70	84.68	55.10
Medaiyese et al.[26]	99.96	90.73	70.09		N/A	
Allahham et al.[27]	100	94.60	87.40	100	91	77.00
Swinney et al.[28]	N/A		91.00	N/A		91.20
Kılıç et al.[30]	100	98.67	95.15	100	98.70	94.72
Kumbasar et al.[31]	100	99.55	97.75	100	99.69	97.57
Huynh et al.[32]	99.85	98.55	95.33	99.75	98.48	95.06
The Proposed Study (Multi Frame Majority Voting)						
MFCC	N/A	**100**	**99.11**	N/A	**100**	**99.06**
LFCC	N/A	**100**	97.35	N/A	**100**	97.11

Analysis of time dependent signal requires the use of an optimum frame-length to better extract features as there exists a trade of between the temporal and frequency resolution, known as Heisenberg Uncertainty Principle [48], and this frame-length, in general, depends on the specific data. Hence, in the proposed study, all experimental studies were performed for different frame-lengths to gather best results to suit DroneRF data. For that purpose, different frame lengths were examined by splitting the data into 2, 4 and 8 frames, and the corresponding results yielded that the best performance was acquired for the length obtained with 4-frame splitting. Another parameter in the feature extraction process is the filtering characteristic to select different frequency content of the signal. For that, MFCC and LFCC approaches were

utilized, and LFCC based feature set performed better compared to MFCC based feature set. This is probably due to the fact that Mel-frequency filtering is optimized for human hearing system as varying band-widths are utilized in MFCC [49]. On the other hand, it is observed that the linear band-width approach of LFCC, which equally partitions the frequency range, yielded better result compared to MFCC, and hence, the use of LFCC approach is better suited for drone rf signals. A final discussion should be addressed regarding the effect of framing approach on the computational complexity of the proposed method. This is important as the overlapping is also utilized in the study, and this operation results in the increased amount of data to process yielding slightly increased processing time at a gain of increased accuracy performance. The results demonstrate that the proposed multi-frame approach improves drone detection accuracy compared to single-frame methods. However, the study has certain limitations. The computational complexity increases due to the multi-frame processing and majority voting mechanism, which extends the inference time compared to single-frame classification. Additionally, the approach relies on the quality of RF signals, making it sensitive to environmental variations and potential external interference. Moreover, the study primarily focuses on specific drone models and RF signal characteristics, and further validation with a broader dataset is necessary to improve generalizability. Addressing these limitations in future work will enhance the efficiency and robustness of the proposed approach.

4. Conclusion

In this study, the problem of detection and classification of different types of drones is investigated. In the proposed approach, the multi-frame majority voting method is used. In the study using drone RF signals, 2, 4, and 8 frames are separated, and each frame min is extracted with MFCC and LFCC and classified by SVM. Then the estimation of each signal frame is voted, and the RF signal is estimated. In the study, a success rate of 100% and 99.11% was achieved in the classification of drone types and drone modes, respectively. The results obtained were compared with studies using the same dataset in the literature. It is seen that the proposed method gives better results than classifications with drone types in the current literature.

The proposed approach holds great potential for real-world applications, including security monitoring, airport surveillance, and restricted area monitoring, where real-time detection and classification of drones are crucial. The ability to detect drones using RF signals makes it particularly useful in environments with limited visibility or challenging conditions such as fog or darkness, where optical detection methods may fail.

In future studies, it is planned to develop the dataset by taking RF signals from different drone models and to work on the problem of drone detection and classification.

Ethics in Publishing

There are no ethical issues regarding the publication of this study.

Author Contributions

Kumbasar N.: Conceptualization, Methodology, Software, Validation, Editing original draft.
Kılıç R.: Conceptualization, Literature search, Data collection, Writing original draft.
Oral E.A.: Analysis, Supervision.
Ozbek I.Y.: Interpretation, Project administration All authors have read and agreed to the published version of the manuscript.

References

[1] Zeng, Y., Zhang, R. & Lim, T. J. (2016). Wireless communications with unmanned aerial vehicles: Opportunities and challenges. *IEEE Communications Magazine*, 54(5), 36-42.

[2] Akter, R., Doan, V.-S., Lee, J.-M. & Kim, D.-S. (2021). CNN-SSDI: Convolution neural network inspired surveillance system for UAVs detection and identification. *Computer Networks*, 201, 108519.

[3] Hassanalian, M. & Abdelkefi, A. (2017). Classifications, applications, and design challenges of drones: A review. *Progress in Aerospace Sciences*, 91, 99-131.

[4] Taha, B. & Shoufan, A. (2019). Machine learning-based drone detection and classification: State-of-the-art in research. *IEEE Access*, 7, 138669-138682.

[5] Ritchie, M., Fioranelli, F. & Borrion, H. (2017). Micro UAV crime prevention: Can we help Princess Leia? In Crime prevention in the 21st century (pp. 359-376). Springer.

[6] Harkins, G. (2020). Illicit drone flights surge along us-mexico border as smugglers hunt for soft spots. accessed.

[7] Mehta, V., Dadboud, F., Bolic, M. & Mantegh, I. (2023). A Deep Learning Approach for Drone Detection and Classification Using Radar and Camera Sensor Fusion. *IEEE Sensors Applications Symposium (SAS)*, 01-06.

[8] Rozantsev, A., Lepetit, V. & Fua, P. (2016). Detecting flying objects using a single moving camera. *IEEE Transactions on Pattern Analysis and Machine Intelligence*, 39(5), 879-892.

[9] Busset, J., Perrodin, F., Wellig, P., Ott, B., Heutschi, K., Rühl, T. & Nussbaumer, T. (2015). Detection and tracking of drones using advanced acoustic cameras. *Unmanned/Unattended Sensors and Sensor Networks XI; and Advanced Free-Space Optical Communication Techniques and Applications*, 9647, 53-60.

[10] Al-Sa'd, M. F., Al-Ali, A., Mohamed, A., Khattab, T. & Erbad, A. (2019). RF-based drone detection and identification using deep learning approaches: An initiative towards a large open source drone database. *Future Generation Computer Systems*, 100, 86-97.

[11] Fioranelli, F., Ritchie, M., Griffiths, H. & Borrion, H. (2015). Classification of loaded/unloaded micro-drones using multistatic radar. *Electronics Letters*, 51(22), 1813-1815.

[12] Drozdowicz, J., Wielgo, M., Samczynski, P., Kulpa, K., Krzonkalla, J., Mordzonek, M., Bryl, M. & Jakielaszek, Z. (2016). 35 GHz FMCW drone detection system. *2016 17th International Radar Symposium (IRS)*, 1-4.

[13] Fuhrmann, L., Biallawons, O., Klare, J., Panhuber, R., Klenke, R. & Ender, J. (2017). Micro-Doppler analysis and classification of UAVs at Ka band. *2017 18th International Radar Symposium (IRS)*, 1-9.

[14] Ritchie, M., Fioranelli, F., Griffiths, H. & Torvik., B. (2016). Monostatic and bistatic radar measurements of birds and micro-drone. *2016 IEEE Radar Conference (RadarConf)*, 1-5.

[15] Zhang, Z., Cao, Y., Ding, M., Zhuang, L. & Yao, W. (2016). An intruder detection algorithm for vision based sense and avoid system. *2016 International Conference on Unmanned Aircraft Systems (ICUAS)*, 550-556.

[16] Ganti, S. R. & Kim, Y. (2016). Implementation of detection and tracking mechanism for small UAS. *2016 International Conference on Unmanned Aircraft Systems (ICUAS)*, 1254-1260.

[17] Stolkin, R., Rees, D., Talha, M. & Florescu, I. (2012). Bayesian fusion of thermal and visible spectra camera data for region based tracking with rapid background adaptation. *2012 IEEE International Conference on Multisensor Fusion and Integration for Intelligent Systems (MFI)*, 192-199.

[18] Unlu, E., Zenou, E. & Riviere, N. (2018). Using shape descriptors for UAV detection. *Electronic Imaging*, 2018(9), 121-128.

[19] Wisniewski, M., Rana, Z. A. & Petrunin, I. (2022). Drone Model Classification Using Convolutional Neural Network Trained on Synthetic Data. *Journal of Imaging*, 8(8), 218.

[20] Kim, J., Park, C., Ahn, J., Ko, Y., Park, J. & Gallagher, J. C. (2017). Real-time UAV sound detection and analysis system. *2017 IEEE Sensors Applications Symposium (SAS)*, 1-5.

[21] Siriphun, N., Kashihara, S., Fall, D. & Khurat, A. (2018). Distinguishing drone types based on acoustic wave by IoT device. *2018 22nd International Computer Science and Engineering Conference (ICSEC)*, 1-4.

[22] Anwar, M. Z., Kaleem, Z. & Jamalipour, A. (2019). Machine learning inspired sound-based amateur drone detection for public safety applications. *IEEE Transactions on Vehicular Technology*, 68(3), 2526-2534.

[23] Alaparthy, V., Mandal, S. & Cummings, M. L. (2021). A comparison of machine learning and human performance in the real-time acoustic detection of drones. *IEEE Aerospace*.

[24] Allahham, M. H. D. S., Al-Sa'd, M. F., Al-Ali, A., Mohamed, A., Khattab, T. & Erbad, A. (2019). DroneRF dataset: A dataset of drones for RF-based detection, classification and identification. *Data in Brief*, 26, 104313.

[25] Al-Emadi, S. & Al-Senaid, F. (2020). Drone detection approach based on radio-frequency using convolutional neural network. *2020 IEEE International Conference on Informatics, IoT, and Enabling Technologies (ICIoT)*, 29-34.

[26] Medaiyese, O. O., Syed, A. & Lauf, A. P. (2021). Machine learning framework for RF-based drone detection and identification system. *2021 2nd International Conference On Smart Cities, Automation and Intelligent Computing Systems (ICON-SONICS)*, 58-64.

[27] Allahham, M. S., Khattab, T. & Mohamed, A. (2020). Deep learning for rf-based drone detection and identification: A multi-channel 1-d convolutional neural networks approach. *2020 IEEE International Conference on Informatics, IoT, and Enabling Technologies (ICIoT)*, 112-117.

[28] Swinney, C. J. & Woods, J. C. (2021). Unmanned aerial vehicle operating mode classification using deep residual learning feature extraction. *Aerospace*, 8(3), 79.

[29] Nemer, I., Sheltami, T., Ahmad, I., Yasar, A. U.-H. & Abdeen, M. A. R. (2021). RF-based UAV detection and identification using hierarchical learning approach. *Sensors*, 21(6), 1947.

[30] Kılıç, R., Kumbasar, N., Oral, E. A. & Ozbek, I. Y. (2022). Drone classification using RF signal based spectral features. *Engineering Science and Technology, an International Journal*, 28, 101028.

[31] Kumbasar, N., Kılıç, R., Oral, E. A. & Ozbek, I. Y. (2022). Comparison of spectrogram, persistence spectrum and percentile spectrum based image representation performances in drone detection and classification using novel HMFFNet: Hybrid Model with Feature Fusion Network. *Expert Systems with Applications*, 206, 117654.

[32] Huynh-The, T., Pham, Q.-V., Nguyen, T.-V., Da Costa, D. B. & Kim, D.-S. (2022). RF-UAVNet: High-Performance Convolutional Network for RF-Based Drone Surveillance Systems. *IEEE Access*, 10, 49696-49707.

[33] Mo, Y., Huang, J. & Qian, G. (2022). Deep Learning Approach to UAV Detection and Classification by Using Compressively Sensed RF Signal. *Sensors*, 22(8), 3072.

[34] Nguyen, P., Kakaraparthi, V., Bui, N., Umamahesh, N., Pham, N., Truong, H., Guddeti, Y., Bharadia, D., Han, R., Frew, E., Massey, D. & Vu, T. (2020). DroneScale: drone load estimation via remote passive RF sensing. *Proceedings of the 18th Conference on Embedded Networked Sensor Systems*, 326-339.

[35] Paul S, B. S., Glittas, A. X. & Gopalakrishnan, L. (2021). A low latency modular-level deeply integrated MFCC feature extraction architecture for speech recognition. *Integration*, 76, 69-75.

[36] Kumaran, U., Radha Rammohan, S., Nagarajan, S. M. & Prathik, A. (2021). Fusion of mel and gammatone frequency cepstral coefficients for speech emotion recognition using deep C-RNN. *International Journal of Speech Technology*, 24(2), 303-314.

[37] Nagarajan, S., Nettimi, S. S. S., Kumar, L. S., Nath, M. K. & Kanhe, A. (2020). Speech emotion recognition using cepstral features extracted with novel triangular filter banks based on bark and ERB frequency scales. *Digital Signal Processing*, 104, 102763.

[38] Burges, C. J. C. (1998). A tutorial on support vector machines for pattern recognition. *Data Mining and Knowledge Discovery*, 2(2), 121-167.

[39] Oral, E. A., Çodur, M. M. & Ozbek, I. Y. (2017). Sleep stage classification based on filter bank optimization. *2017 25th Signal Processing and Communications Applications Conference (SIU)*, 1-4.

[40] Alsarhan, A., Alauthman, M., Alshdaifat, E., Al-Ghuwairi, A.-R. & Al-Dubai, A. (2021). Machine Learning-driven optimization for SVM-based intrusion detection system in vehicular ad hoc networks. *Journal of Ambient Intelligence and Humanized Computing*, 1-10.

[41] Gani, E. & Manzie, C. (2004). Intelligent computing methods for indicated torque reconstruction. *Proceedings of the 2004 Intelligent Sensors, Sensor Networks and Information Processing Conference*, 259–264.

[42] Achirul Nanda, M., Boro Seminar, K., Nandika, D. & Maddu, A. (2018). A comparison study of kernel functions in the support vector machine and its application for termite detection. *Information*, 9(1), 5.

[43] AlKhonaini, A., Sheltami, T., Mahmoud, A. & Imam, M. (2024). UAV Detection Using Reinforcement Learning. *Sensors*, 24(6), 1870.

[44] Ahmad, I., Narmeen, R., Alawad, M. A., Alkhrijah, Y. & Ho, P. H. (2024). Integrating Visual Geometry and Mask Region CNN for Enhanced UAV Detection and Identification. In 2024 IEEE 100th Vehicular Technology Conference (VTC2024-Fall) (pp. 1-6). *IEEE*.

[45] Zahid, M. U., Nisar, M. D., Fazil, A., Ryu, J. & Shah, M. H. (2024). Composite Ensemble Learning Framework for Passive Drone Radio Frequency Fingerprinting in Sixth-Generation Networks. *Sensors*, 24(17), 5618.

[46] Haque, E., Hasan, K., Ahmed, I., Alam, M. S. & Islam, T. (2024). Towards an Interpretable AI Framework for Advanced Classification of Unmanned Aerial Vehicles (UAVs). In 2024

IEEE 21st Consumer Communications & Networking Conference (CCNC) (pp. 644-645). *IEEE*.

[47] Najafi, J., Mirzakuchaki, S. & Shamaghdari, S. (2025). Autonomous Drone Detection and Classification Using Computer Vision and Prony Algorithm-Based Frequency Feature Extraction. *Journal of Intelligent and Robotic Systems*, 111(1), 1-21.

[48] Dias, N. C., de Gosson, M. & Prata, J. N. (2024). A metaplectic perspective of uncertainty principles in the Linear Canonical Transform domain. *Journal of Functional Analysis*, 287(4), 110494.

[49] Kinoshita, Y., Osanai, T. & Clermont, F. (2022). Sub-band cepstral distance as an alternative to formants: Quantitative evidence from a forensic comparison experiment. *Journal of Phonetics*, 94, 101177.

e-ISSN: 2149-4584

Erzincan University Journal of Science and Technology

EJSAT 2025, 18 (3) 917-932

Research Article

Effect of Azelaic Acid Priming on Some Germination and Seedling Parameter in Barley (*Hordeum vulgare* L.) Seeds under Salt Stress

Aslı Güleç[1*], Nurcan Yavuz[2], Aras Türkoğlu[3]

[1]Department of Agricultural Structures and Irrigation, Institute of Science, Selcuk University, Konya, Türkiye
[2]Department of Agricultural Structures and Irrigation, Faculty of Agriculture, Selcuk University, Konya, Türkiye
[3]Department of Field Crops, Faculty of Agriculture, Necmettin Erbakan University, Konya, Türkiye

Received: 24/12/2024, **Revised:** 27/05/2025, **Accepted:** 10/07/2025, **Published:** 31/12/2025

Abstract

This study was conducted to evaluate the effects of azelaic acid (AzA) priming on germination and some seedling parameters for seeds of barley (*Hordeum vulgare* L.) under salt stress conditions. In current research, four different salinity levels (0, 25 mM, 50 mM, 100 mM NaCl) and 2 different doses of AzA (0 mM, 0.5 mM) with 3 replicates were examined according to a complete randomized design. The variety of Larende barley was used as seed material. Analysis of variance showed that the effect of AzA priming on shoot length, root fresh weight and shoot fresh weight of barley was significant ($p \leq 0.01$), while the effect on other parameters was found insignificant ($p \geq 0.05$). NaCl levels significantly affected all parameters ($p \leq 0.01$). In the AzA × NaCl interaction, root fresh weight, shoot fresh weight, salt tolerance index and relative water content were affected significantly ($p \leq 0.01$). In examine the effects of salinity levels on barley plant, especially on germination parameters, the values obtained from 0, 25 and 50 mM applications were in the same significance group. According to this result, when evaluated in terms of germination, it was concluded that water having 50 mM or less salt content can be used in barley cultivation. It is thought that it would be appropriate to try AzA at different doses and different salt levels in order to understand the effects of AzA treatment more clearly.

Keywords: Barley, Germination, Azelaic acid, NaCl, Pre-treatment.

Azelaik Asit Ön Uygulamasının Tuz Stresi Altındaki Arpa (Hordeum vulgare L.) Tohumlarında Bazı Çimlenme ve Fide Parametreleri Üzerine Etkisi

Öz

Bu çalışma, azelaik asit (AzA) ön uygulamasının tuz stresi koşullarındaki arpa *(Hordeum vulgare* L.) tohumlarının çimlenme ve bazı fide parametreleri üzerindeki etkilerini değerlendirmek amacıyla yürütülmüştür. Araştırma, tesadüf parselleri deneme desenine göre, dört farklı tuzluluk düzeyinde (0, 25 mM, 50 mM, 100 mM NaCl) ve iki farklı dozda AzA (0 mM, 0.5 mM) uygulaması, üç tekerrürlü olarak yürütülmüştür. Tohum materyali olarak arpa çeşidi Larende kullanılmıştır. Çalışmada çimlenme ve bazı fide gelişim parametreleri (çimlenme oranı, ortalama çimlenme zamanı, çimlenme gücü indeksi, kök uzunluğu, sürgün uzunluğu, kök yaş ağırlığı, sürgün yaş ağırlığı, tuz tolerans indeksi, su kullanım etkinliği, bağıl su içeriği) saptanmıştır. Varyans analiz sonuçlarına göre arpada AzA ön uygulaması; sürgün uzunluğu, kök yaş ağırlığı ve sürgün yaş ağırlığı üzerine önemli düzeyde ($p \leq 0.01$) etki etmiş olup, diğer parametreler üzerine etkisi önemsiz bulunmuştur ($p \geq 0.05$). NaCl seviyeleri tüm parametreleri önemli düzeyde etkilemiştir ($p \leq 0.01$). AzA × NaCl interaksiyonunda ise kök yaş ağırlığı, sürgün yaş ağırlığı, tuz tolerans indeksi ve bağıl su içeriği önemli düzeyde etkilenmiştir ($p \leq 0.01$). Arpa bitkisinde tuzluluk seviyelerinin özellikle çimlenme parametreleri üzerindeki etkilerine bakıldığında, 0, 25 ve 50 mM uygulamalarından elde edilen değerler aynı önemlilik grubunda yer almıştır. Bu sonuca göre çimlenme açısından değerlendirildiğinde arpa yetiştiriciliğinde 50 mM ve daha az tuz içeren suların kullanılabileceği sonucuna varılmıştır. AzA uygulamasının etkilerinin daha net anlaşılabilmesi için farklı dozlarda ve farklı tuz seviyelerinde denenmesinin uygun olacağı düşünülmektedir.

Anahtar Kelimeler: Arpa, Çimlenme, Azelaik asit, NaCl, Ön uygulama.

Abstract of this paper were presented as an oral presentation at the VI[th] International Turkish World Science and Engineering Congress (TURK-COSE 2024).

Corresponding Author: asliturkgulec@gmail.com

Cite this Article: Erzincan University Journal of Science and Technology 2025, 18(3)917-932. https://doi.org/10.18185/erzifbed.1606529

1. Introduction

Barley (*Hordeum vulgare* L.) is a member of the Poaceae family and one of the first field crops to be cultivated [1]. This crop, one of the most cultivated cereals in the world, ranks fourth following by wheat, maize and paddy [2] and is an important source of animal feed, rich in fibre and bioactive compounds and highly nutritious, as well as an important component of the malt industry [3]. Compared to other cereals, barley has advantages such as earliness, drought tolerance and adaptability to different soils [4, 5].

Plants can be exposed to various stresses known as biotic and abiotic. Stress factors significantly affect plant development processes, cause oxidative damage and lead to significant agricultural production losses. Drought and salinity are the most common abiotic stress factors[6]. Due to water shortage problem low quality water in arid and semi-arid regions has to be used intensively in agricultural production. For this reason, the problem of salinisation and alkalisation in agricultural lands is increasing dramatically. This situation increases the osmotic pressure in the rhizosphere zone and prevents the plant's water uptake through the roots or causes ion toxicity [7, 8]. Therefore, it is very important to understand the response mechanisms of plants to be able to evaluate stress tolerances and crop resilience in different crops. One of the primary physiological responses to salinity stress is a reduction in photosynthetic activity(performance). Salinity stress causes stomatal closure in exposed plants and reduces the amount of photosynthesis by limiting CO_2 uptake [9]. In genarally, salt stress is characterised by disruption in the homeostasis of Na^+ and Cl^- ions starting with specific ion toxicity, resulting in stomatal closure and increased ROS production in chloroplasts, and causes inhibition of plant growth [10, 11]. Therefore, amelioration of stress tolerance through various strategies is critical for plant survival and productivity.

Germination and early seedling phases of plants are the most sensitive cycles to stress factors. For this reason, adaptation possibilities during germination and different techniques to increase the tolerance of seeds to salinity have been investigated for many years. One of the most frequently used techniques is seed or seedling priming. Seed priming is based on pre-exposure of seeds to chemicals or stress factors (salinity, drought, etc.). This increases the plant's resistance to subsequent stresses and its ability to rapidly detect secondary signals [12]. Many effective compounds are used to increase the practicability of this technique and are the subject of research.

Azelaic acid (AzA), a compound whose effect on plants has been tested under normal conditions or biotic stress (pathogen) conditions, has been used in medicine, cosmetics and pharmacological fields since it was first discovered [13, 14]. In a study, it was reported that azelaic acid compounds, exist in the biochemical cycle of plants, can survive biotic stress conditions [15]. Recently, this molecule, which is known to accumulate in the root system,[16] has attracted attention as a preparatory molecule in the systemic acquired resistance (SAR) mechanism of plants. In addition, azelaic acid, one of the structures that constitute the signal transduction components of the induced systemic resistance (ISR) mechanism, is reported to provide a faster and stronger accumulation of salicylic acid (SA) in response to infection or oxidation [17]. However, studies on its effects against abiotic stress factors are quite limited. In

a study, it was reported that overexpression of AZI (Azelaic Acid Induced) gene in Arabidopsis plants is sensitive to drought stress, notwithstanding increases cold and salt tolerance via abscisic acid (ABA) [18]. Haghighi and Sheibanirad [19]; applied 0, 8, 10 and 24 mg/L azelaic acid exogenously to tomato plants under 0, 100, 150 and 200 mM salinity conditions. They reported that especially 8 mg/L AzA dose can maintain the gas exchange capacity at optimum level, induce osmotic balance and reduce the effects of salinity at salinity levels up to 100 mM.

In the investigation of tolerance mechanisms with different seed preparation methods, the effect of salicylic acid (SA), jasmonic acid (JA) and similar signalling molecules have been investigated, but it has been stated that AzA is also involved in tolerance mechanisms [20] Although barley is one of the plants with high salt tolerance, it is a plant that is severely affected by salt stress during germination and early seedling periods [21, 22]. The aim of this study was to determine the agronomic responses of barley to different doses of salt (NaCl) with azelaic acid priming during germination and early seedling stage.

2. Material and Methods

In this study, two different doses of AzA (0 mM, 0.5 mM) and four different salt (NaCl) levels (0; control, 25, 50, 50 and 100 mM) were applied to seeds of the barley Larende cultivar. Barley seeds were kept in different concentrations of AzA solutions at 4 ◦C for 12 hours. Those seeds were then dried at +25 ◦C for 5 hours. The seeds primed with pure water and AzA were sown in pots of 9 cm in diameter and 14 cm in height, using a mixture of sand and topsoil (1:2), with 15 seeds per pot. The pots were designed according to a completely randomised experimental design with three replications. Samples of the soil mixture placed in the pots were analysed such as field capacity and permenant wilting point in the laboratory. Irrigation water was applied at 2-day irrigation intervals according to the weighting method to fill the moisture deficit to the field capacity. During irrigation applications, special care was taken to avoid direct contact of irrigation water with plant leaves. For 10 days, the germinated seeds in the pots were counted daily at the same time and the data were recorded. A seedling was considered to have emerged when a hypocotyl appeared on the soil surface [23]. At the end of this period, the seedlings were harvested and physiological measurements were made using a metric ruler and a precision scale.

In order to determine the effect of the treatments on germination parameters, germination rate (GR) was calculated by Equation 1, germination vigour index (GVI) was calculated by Equation 2 in accordance of Türkoğlu, et al. [23] and mean germination time (MGR) was calculated by Equation 3 suggested by Süheri, et al. [24].

GR (%) = (Total number of germinated seeds/total number of seeds) x 100 (Eq.1).

GVI= (mean shoot length + mean root length) × total germination rate (Eq.2).

$MGT = \Sigma(fx)/\Sigma f$ *(Eq. 3).*

Where *f* is the number of germinating seeds on the counting day and *x* is the number of days of counting.

To determine the effect on early seedling performance; root fresh weight (RFW), shoot fresh weight (SFW) values were measured and salt tolerance index (STI) was calculated using Equation 4 according to Kusvuran, et al. [25], water use efficiency (WUE) was calculated using Equation 5 according to Liu, et al. [26] and relative water content (RWC) was calculated using Equation 6 according to Yavuz, et al. [27];

STI (%) = (Total fresh weight at salt concentration/total fresh weight in control) x 100 (Eq. 4)

WUE = Dry biomass / water consumption in the experiment (Eq. 5)

$$RWC\ (\%) = [(FW-DW) / (TW-DW)] \times 100 \quad (Eq.\ 6)$$

In this equation, FW stands for fresh weight, DW for dry weight and TW for turgor weight.

The effects of AzA priming and NaCl doses on the parameters examined in the experiment were subjected to analysis of variance according to 2 × 4 factorial and a completely randomised trial design with 3 replications (SPSS 27 software, SPSS Inc., IBM). The differences between the mean s of these parameters were determined by Duncan test at 5% significance level.

3. Results and Discussion

3.1. Results

Barley seeds germinated in about 2 days and their development was observed for 10 days (Figure 1). AzA applied to the seed did not contribute positively to the germination parameters under salt stress conditions, while it exhibited ameliorative effects on some seedling parameters. The mean values and significance groups of germination parameters obtained from the treatments are given in Table 1.

The applied NaCl levels had a significant effect ($p \leq 0.01$) on germination rate (GR), while the effect of AzA and AzA × NaCl interaction was found insignificant ($p \geq 0.05$) (Table 1). Considering the mean s of NaCl levels, the highest germination rate (GR) was obtained from 0, 25 and 50 mM NaCl stress treatments as 96%, 94% and 93%, respectively, and the lowest GR was obtained from 100 mM NaCl application as 74% due to the increase in stress (Table 1).

Mean germination time (MGT) is defined as the time taken for a seed to germinate. The effect of salt stresses on MGT was significant ($P \leq 0.01$) (Table 1). The effects of AzA and AzA x NaCl stresses interactions on MGT were found insignificant ($p \geq 0.05$) (Table 1).

Figure 1. Some agronomic differences in barley seedlings primed with water (0 mM) and azelaic acid (0.5 mM) before sowing.

In terms of salinity, the mean germination time was 4.60 days in the control (0 mM NaCl), followed by 25 mM NaCl application with 4.70 days, and the latest MGT value was realised in 100 mM NaCl application with 5.77 days. As the salt content increased, germination time was delayed as expected. When AzA treatments were analysed based on mean s, the lowest mean germination time was obtained from 0.5 mM AzA treatment (5.04 days) compared to the control treatment (5.15 days) (Table 1). AzA and salt stress interactions were not separated into significance groups and the lowest MGT was obtained as 4.42 days from the group with 0.5 AzA priming and no salt stress (0.5-0) with 8% difference compared to the control group (0-0).

Germination vigour index (GVI) is an important parameter to determine rapid and uniform emergence and seedling formation under various conditions [29]. NaCl stresses had a statistically significant ($P \leq 0.01$) effect on GVI values, whereas the interactions of AzA and AzA x NaCl stresses were insignificant ($p \geq 0.05$) as seen in Table 1. When the mean s were analysed in terms of NaCl stresses, the highest GVI was found in the control group with 2449.58, while 100 mM NaCl treatment ranked last with 1332.69 (Table 1). Although AzA x NaCl interaction values were statistically insignificant, the highest GVI value was obtained as 2490.44 in 0.5 mM AzA priming and 25 mM salt level (Table 1).

Root and shoot length are important indicators in determining the level of stress tolerance. The effect of NaCl treatments on root length (RL) was significant ($P<0.01$), while the effect of AzA and AzA x NaCl stresses interaction was insignificant (Table 1).

In terms of salinity, the highest root length (RL) values were obtained from 0 mM NaCl (14.95 cm), 25 mM NaCl (14.45 cm) and 50 mM NaCl (14.01 cm) treatments and the lowest value was obtained from 100 mM NaCl (10.91) treatment. According to the mean s of AzA treatments; the highest root length was obtained from 0.5 mM AzA treatment with 14.06 cm and the lowest value was obtained from 0 mM AzA treatment with 13.09 cm.

Table 1. Germination parameters of barley against salinity stresses and azelaic acid priming.

Treatments	GR (%)	MGT (Day)	GVI	RL (cm)	SL (cm)
AzA (mM)					
0	92	5.15	2100.76	13.09	9.54^{B}
0.5	87	5.04	2160.10	14.06	10.33^{A}
NaCl (mM)					
0	96^{A}	4.60^{B}	2449.58^{A}	14.95^{A}	11.35^{A}
25	94^{A}	4.70^{B}	2392.39^{A}	14.45^{A}	10.80^{AB}
50	93^{A}	5.29^{AB}	2347.06^{A}	14.01^{A}	10.49^{B}
100	74^{B}	5.77^{A}	1332.69^{B}	10.91^{B}	7.11^{C}
Aza × NaCl					
0 mM × 0 mM	98	4.79	2467.72	14.28	10.98
0 mM × 25 mM	93	4.52	2294.33	13.88	10.56
0 mM × 50 mM	96	5.55	2285.67	13.57	10.28
0 mM × 100 mM	80	5.73	1355.33	10.65	6.34
0.5 mM × 0 mM	89	4.42	2431.44	15.63	11.73
0.5 mM × 25 mm	96	4.89	2490.44	15.01	11.03
0.5 mM × 50 mM	96	5.02	2408.44	14.45	10.70
0.5 mM × 100 mM	69	5.82	1310.06	11.17	7.88
Sources of Variation					
F value (AzA)	$3,6^{ns}$	$0,3^{ns}$	$0,3^{ns}$	$3,3^{ns}$	$11,7^{**}$
F value (NaCl)	$18,1^{**}$	$6,2^{**}$	$27,2^{**}$	$11,7^{**}$	$68,6^{**}$
F value (AzA × NaCl)	$1,9^{ns}$	$0,9^{ns}$	$0,3^{ns}$	$0,1^{ns}$	$1,2^{ns}$

**. P<0.01; *. P<0.05; ns: not significant. Uppercase and lowercase letters indicate Duncan groups for Azelaic acid and salinity (NaCl) stress respectively. GR, germination rate; MGT, mean germination time; GVI, germination vigor index; RL, root lenght; SL, shoot lenght.

According to these data, 0.5 mM AzA treatment increased root length more by comparison to the control (Table 1). While no significant difference was observed in the AzA x NaCl interaction, the highest root length of 15.63 cm was obtained from 0.5 mM AzA x 0 mM NaCl treatment. This value represents 9% longer root length compared to the control group (0-0) (Table 1).

The effect of AzA priming and NaCl treatments on shoot length (SL) was highly significant (P<0.01) and the effect of AzA x NaCl stresses interaction was insignificant ($p \geq 0.05$) (Table 1). In examined the AzA means, 8% more shoot length was obtained from the group treated with 0.5 mM AzA priming (10.33 cm) compared to the untreated group (9.54 cm). According to this assessment, AzA application positively affected the shoot length parameter. According to the means of NaCl treatments, the highest shoot length was obtained from 0 mM NaCl (11.35 cm) and the lowest value was obtained from 100 mM NaCl (7.11 cm) due to the increase in salt stress (Table 1). When the interaction values between AzA and salt stress were examined, the highest shoot length was observed as 11.73 cm in 0.5 mM AzA - 0 mM NaCl treatment with a 6% difference compared to the control (0-0) (Table 1).

The effects of AzA, NaCl stress treatments and AzA x NaCl stress interactions on root fresh weight (RFW) were statistically significant (P<0.01) (Table 2). According to AzA means; the highest RFW was obtained from 0.5 mM AzA priming treatment with 0.190 g and the lowest value was obtained from 0 mM AzA treatment with 0.140 g.

According to the means of salinity doses, the highest root fresh weight was 0.212 g at 50 mM NaCl dose, followed by 0 mM NaCl (0.188 g) and 25 mM NaCl (0.181 g), respectively. The lowest root fresh weight was obtained from 100 mM NaCl (0.079 g) stress treatment (Table 2). When the mean s of AzA x NaCl interactions in Figure 1 prepared according to Table 2 data are analysed, the highest root fresh weight was obtained from 0.5 mM AzA priming and 0 mM NaCl interaction with 0.246 g, followed by 0.5 mM AzA priming and 25 mM NaCl interaction with 0.235 g. The lowest root fresh weight values were obtained from the 100 mM NaCl stress levels of 0 and 0.5 mM AzA priming treatments with 0.080 g and 0.077 g, respectively (Fig.1).

The effect of AzA, NaCl stress applications and AzA x NaCl interaction on salt tolerance index (STI) was statistically significant (P<0.01) (Table 2). According to the means of AzA priming treatments; the highest STI value was obtained from 0.5 mM AzA priming (125.9) with 43% difference and the lowest STI value was obtained from 0 mM AzA priming groups (72.1). According to the means of salinity stresses, the highest salt tolerance index value was 131.7 in 50 mM NaCl stress conditions and the lowest value was 57.7 in 100 mM NaCl stress treatments (Table 2). When the means of AzA × NaCl interaction were analysed, the highest salt tolerance index values were 156.56 and 156.18 in 0 mM and 25 mM NaCl stress conditions with 0.5 mM AzA priming, and the lowest STI values were 51.1 and 64.26 in 100 mM salt level of both priming treatments (Fig. 3).

Table 2. Early seedling performance parameters of barley against salinity stresses and azelaic acid priming.

Treatments	RFW (g)	SFW (g)	STI (%)	WUE (g/L)	RWC (%)
AzA (mM)					
0	0.14^{B}	0.15^{B}	72.11^{B}	0.114^{B}	86.33
0.5	0.19^{A}	0.18^{A}	125.91^{A}	0.132^{A}	84.37
NaCl (mM)					
0	0.19^{A}	0.189^{AB}	78.28^{B}	0.145^{A}	88.57^{A}
25	0.18^{A}	0.195^{A}	128.40^{A}	0.139^{A}	88.71^{A}
50	0.21^{A}	0.175^{B}	131.68^{A}	0.125^{A}	84.11^{B}
100	0.08^{B}	0.091^{C}	57.68^{B}	0.081^{B}	80.01^{C}
Azelaic acid × NaCl					
0 mM × 0 mM	0.130^{b}	0.167^{b}	0.00^{d}	0.13	94.70^{a}
0 mM × 25 mM	0.126^{b}	0.176^{b}	100.61^{b}	0.13	85.62^{b}
0 mM × 50 mM	0.225^{a}	0.177^{b}	136.72^{a}	0.12	84.26^{bc}
0 mM × 100 mM	0.080^{b}	0.074^{d}	51.10^{c}	0.07	80.75^{bc}
0.5 mM × 0 mM	0.246^{a}	0.211^{a}	156.56^{a}	0.16	82.44^{bc}
0.5 mM × 25 mm	0.235^{a}	0.213^{a}	156.18^{a}	0.15	91.81^{a}
0.5 mM × 50 mM	0.198^{a}	0.172^{b}	126.63^{ab}	0.13	83.95^{bc}
0.5 mM × 100 mM	0.077^{b}	0.108^{c}	64.26^{c}	0.09	79.26^{c}
Sources of Variation					
F value (AzA)	$9,9^{**}$	$20,6^{**}$	$44,1^{**}$	$6,4^{*}$	$2,9^{ns}$
F value (NaCl)	$13,4^{**}$	$63,6^{**}$	$20,7^{**}$	$16,4^{**}$	$12,9^{**}$
F value (AzA × NaCl)	$5,2^{**}$	$3,3^{*}$	$20,7^{**}$	$0,09^{ns}$	$10,9^{**}$

**. P<0.01; *. P<0.05; ns: not significant. Uppercase and lowercase letters indicate Duncan groups for Azelaic acid and salinity (NaCl) stress respectively. RFW, root fresh weight; SFW, shoot fresh weight; STI, salt tolerance index; WUE, water use efficient; RWC, relative water content.

The effect of AzA, NaCl stress applications and AzA x NaCl interaction on salt tolerance index (STI) was statistically significant (P<0.01) (Table 2). According to the means of AzA priming treatments; the highest STI value was obtained from 0.5 mM AzA priming (125.9) with 43% difference and the lowest STI value was obtained from 0 mM AzA priming groups (72.1). According to the means of salinity stresses, the highest salt tolerance index value was 131.7 in 50 mM NaCl stress conditions and the lowest value was 57.7 in 100 mM NaCl stress treatments (Table 2). When the means of AzA × NaCl interaction were analysed, the highest salt tolerance index values were 156.56 and 156.18 in 0 mM and 25 mM NaCl stress conditions with 0.5 mM AzA priming, and the lowest STI values were 51.1 and 64.26 in 100 mM salt level of both priming treatments (Fig. 3).

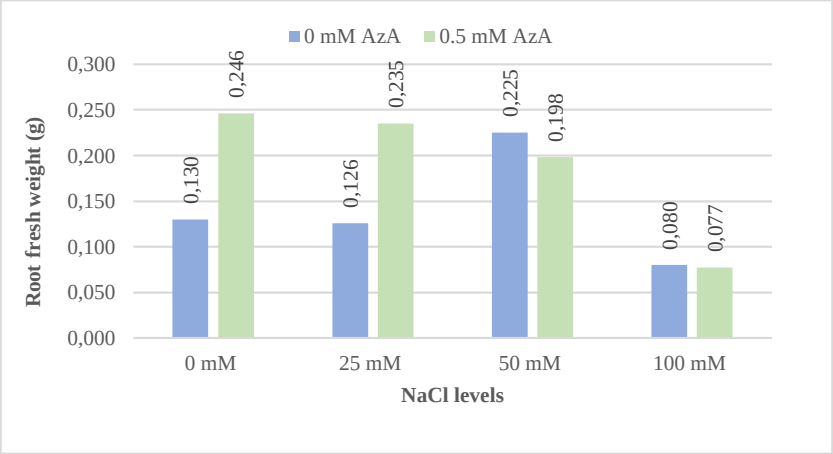

Figure 2. Changes in the root fresh weight of barley against salinity stresses and Azelaic acid priming.

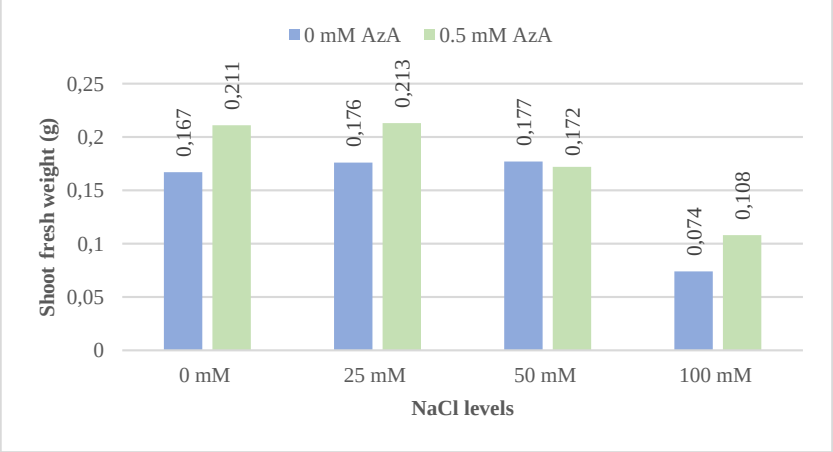

Figure 3. Changes in the shoot fresh weight of barley against salinity stresses and Azelaic acid priming

Water use efficiency (WUE) values were significantly affected by AzA priming and salt stress applications (P<0.01). The effect of AzA x NaCl interaction on WUE values was statistically insignificant (Table 2). According to AzA means; the highest WUE value was obtained as 0.132

g/L from 0.5 mM azelaic acid priming groups with a difference of about 14% and the lowest WUE value was obtained as 0.114 g/L from 0 mM AzA (pure water) priming groups. According to salinity (NaCl) means, the highest WUE value (0.145 g/L was obtained from 0 mM NaCl dose and the lowest value (0.082 g/L) was obtained from 100 mM NaCl dose (Table 2). The highest WUE values were obtained from 0.5 mM AzA x 0 mM NaCl (0.157 g/L) and 0.5 mM AzA x 25 mM NaCl (0.147 g/L) interactions with 15% and 10% difference, respectively, although there was no statistically significant difference (Table 2).

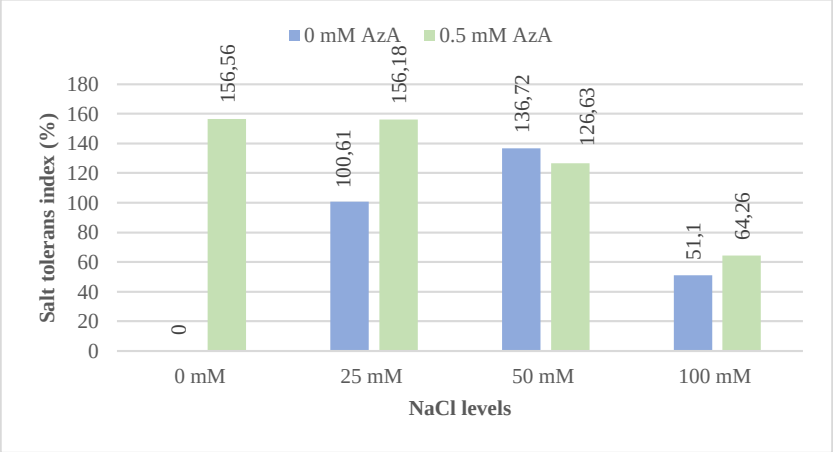

Figure 4. Changes in the salt tolerance index of barley against salinity stresses and Azelaic acid priming.

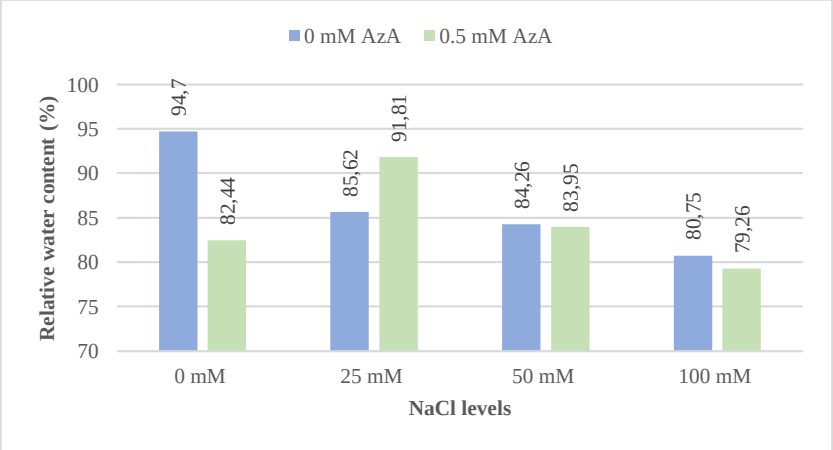

Figure 5. Changes in the relative water content of barley against salinity stresses and Azelaic acid priming.

The effect of NaCl stress applications and AzA x NaCl interactions on relative water content (RWC) was significant ($P<0.01$), while the effect of AzA treatment was statistically insignificant (Table 2). According to salt stress means, the highest RWC value was 88.7% in 25 mM NaCl applications and the lowest value was 80.0% in 100 mM NaCl applications (Table

2). When the means of AzA x NaCl interaction were analysed, the highest RWC value was obtained as 94.7% from the control group, followed by 0.5 mM AzA x 25 mM NaCl interaction with 91.8% (Fig. 4).

3.2. Discussion

Stress conditions in germination and early seedling processes of cultivated plants limit the potential yield as well as quality [28].

Germination rate was in the same group with the control (0 mM NaCl) at NaCl doses up to 50 mM. On the contrary, the highest decrease in germination rate occurred at 100 mM NaCl dose. In many studies, it was reported that the increase in salt levels caused a decrease in germination rates [29-31]. The longest mean germination time was obtained in 100 mM NaCl application and germination took 20.4% longer than the control (0 mM NaCl) application. In similar studies, it was reported that germination time increased with increasing salt doses [5, 32].

Germination vigour index is one of the traits most affected by increasing stress conditions as a component of germination rate, root length and shoot length parameters [33]. According to the results, germination strength index values decreased by 2 to 46% compared to the non-salt (NaCl) group due to the increase in salt stress. The decrease in germination strength with increasing NaCl levels has been reported in studies on different plants [30, 34, 35]. Although there was no statistically significant difference in terms of the azelaic acid treatment agent used and its interaction with NaCl, it was observed that the germination vigour was higher in seeds primed with azelaic acid, especially when the same salinity groups at 25 mM and 50 mM NaCl levels were compared. It has been reported that priming applications may have different effects on the germination strength index depending on the genotype and stress factors. [36-38].

Root and shoot length are the most important parameters for salt stress. The root is in direct contact with the soil and absorbs soil water, while the shoot transmits the water to the rest of the plant [39]. Thus, the responses of root and shoot length values to salt stress are very important. In our study, it was observed that root length values decreased as NaCl dose increased. In different studies supporting our results, it has been reported that root development was decreased in relation to the optimum water intake and the dose of salt factor during the germination period [40, 41]. There is no significant effect on root lengths in terms of interactions with AzA and NaCl, but when the interactions of salinity groups with AzA priming and pure water priming were compared, it was observed that root lengths were 9% (0 mM NaCl), 8% (25 mM NaCl), 6% (50 mM NaCl) and 5% (100 mM NaCl) higher in seeds primed with 0.5 mM azelaic acid. Altuner, et al. [42] and Başaran and Doğrusöz [43] reported that osmopriming treatment applied to seeds increased root length. However, depending on the type and intended use of the osmopriming agent, growth and development inhibition may be caused by increases in dose [44]. According to the results obtained from in this study, AzA had a significant effect on shoot length and increased it by 8%. It can be said that 0.5 mM AzA priming application encouraged shoot development. Haghighi and Sheibanirad [19] reported that azelaic acid improved growth under salinity conditions. In contrast, decreases in shoot length values were observed with increasing salinity stress.

According to the results obtained from the barley plant, root fresh weights did not response a significant difference at salinity levels up to 50 mM, and a root fresh weight reduction of approximately 58% was observed at 100 mM NaCl dose compared to the control. On the other hand, it was observed that azelaic acid application had a positive effect in 0 and 25 mM NaCl conditions and increased root fresh weights by 47% and 44%, respectively, compared to the control (0 mM AzA × 0 mM NaCl) group. In different studies, it has been reported that salinity problems in the growing environment of the plant are effective on root fresh weight and increases in salt dose cause root fresh weights to decrease [45, 46].

According to the current study results, no significant difference was observed in the water use efficiency values of salt treatments up to 50 mM, while the lowest WUE value was observed at 100 mM NaCl dose. In a lot of studies, a steady increase in water use efficiency was observed under salt stress due to a reduction in transpiration due to a decrease in photosynthetic activity. This regulation contributes to the survival and development of the stressed plant under stress conditions by enabling it to optimise water use within its tolerance limits. [47-49]. Boussora, et al. [50] reported that salt stress had a significant effect on water use efficiency in their study on the tolerance of barley to salt stress. Contrary to this, in this study, it was observed that 0.5 mM AzA treatment of barley seeds increased the WUE values by about 14% compared to the control (0 mM AzA) group.

Relative water content is a measure of plant water status, reflecting the balance between water supply and water loss. In this study, decreases in RWC compared to the control were observed due to increasing salt stress conditions. As stated in previous studies, decreases in relative water content occur under salt stress conditions [51, 52]. Alsamadany, et al. [53] reported that there was a general tendency of decrease in RWC values compared to the control under salt stress conditions in their study with barley. On the other hand, 0.5 mM AzA treatment to seed resulted in 7% higher RWC under low (25 mM NaCl) salt stress conditions compared to the same salinity group without azelaic acid treatment.

4. Conclusion

In this research, although azelaic acid treatment of barley seeds did not have a significant effect on germination parameters against increasing salt doses, it was concluded that it positively supported the germination vigour index under low salinity conditions. However, it was determined that azelaic acid alleviated the negative effect of increasing salt doses especially in some seedling parameters. Germination and development processes were adversely affected due to the disruption of water uptake at high salt concentration. When the data are evaluated in terms of germination; it is predicted that water containing salt with values of 50 mM and below can be used in barley production. However, it was observed that azelaic acid reduced the negative effects of salt up to a certain point and contributed positively in terms of biomass. It is considered that this study may contribute to the utilisation of marginal land and water resources in agriculture. Accordingly, in order to better understand the osmoregulatory effect of azelaic acid that increases biomass values, different doses and priming durations under different salt stress conditions should be investigated by comprehensively.

Ethics in Publishing

There are no ethical issues regarding the publication of this study.

Author Contributions

Güleç A.: Writing, Materials, Investigation, Formal analysis.
Yavuz N.: Writing – review & editing, Methodology, Formal analysis, Validation.
Türkoğlu A.: Methodology, Formal analysis, Validation.

References

[1] Aliniaeifard, S., Hajilou, J. & Tabatabaei, S. J. (2016). Photosynthetic and growth responses of olive to proline and salicylic acid under salinity condition. *Notulae Botanicae Horti Agrobotanici Cluj-Napoca*, 44(2), 579-585.

[2] Alsamadany, H., Abdulbaki, A. S. & Alzahrani, Y. (2024). Unravelling drought and salinity stress responses in barley genotypes: physiological, biochemical, and molecular insights. *Frontiers in plant science*, 15, 1417021.

[3] Altuner, F., Erol, O., Tunctürk, R. & Baran, İ. (2020). Effect of salt (NaCl) stress on germination properties of quinoa (Chenopodium quinoa Willd.) seeds subjected to gibberellic acid (GA3) pre-treatment. *Kahramanmaraş Sütçü İmam University Journal of Agriculture and Nature*, 23(2), 350-357.

[4] Altuner, F., Oral, E. & Baran, İ. (2022). Bazı Arpa (*Hordeum vulgare* L.) Çeşitlerinde tuz (NaCl) stresinin çimlenme özellikleri üzerine etkilerinin belirlenmesi. *Tekirdağ Ziraat Fakültesi Dergisi*, 19(1), 39-50.

[5] Atkinson, N. J., Lilley, C. J. & Urwin, P. E. (2013). Identification of genes involved in the response of Arabidopsis to simultaneous biotic and abiotic stresses. *Plant physiology*, 162(4), 2028-2041.

[6] Badea, A. & Wijekoon, C. (2021). Benefits of Barley Grain in Animal and Human Diets. Chapter in a book: Cereal Grains. *IntechOpen*, 2021.

[7] Baig, Z., Khan, N., Sahar, S., Sattar, S. & Zehra, R. (2021). Effects of seed priming with ascorbic acid to mitigate salinity stress on three wheat (Triticum aestivum L.) cultivars. *Acta Ecologica Sinica*, 41(5), 491-498.

[8] Başaran, U. & Doğrusöz, M. Ç. (2022). Effect of Organic Compound-Based Priming and Seed Coating on Seedling Development and Characteristics of Alfalfa (Medicago sativa L.). *ISPEC Journal of Agricultural Sciences*, 6(4), 667-679.

[9] Bayat, E., Koşunkartay, H. & Kodaz, S. (2022). The Effect of Salinity Stress on Germination Parameters of Kırık Bread Wheat Variety (Triticum aestivum L.). *European Journal of Science and Technology*, 41, 246-251.

[10] Benlioğlu, B. & Özkan, U. (2015). Bazı arpa çeşitlerinin (*Hordeum vulgare* L.) çimlenme dönemlerinde farklı dozlardaki tuz stresine tepkilerinin belirlenmesi. *Tarla Bitkileri Merkez Araştırma Enstitüsü Dergisi*, 24(2), 109-114.

[11] Blattner, F. R. (2018). Taxonomy of the genus Hordeum and barley (Hordeum vulgare). *The barley genome*, 11-23.

[12] Borges, A. A., Jiménez-Arias, D., Expósito-Rodríguez, M., Sandalio, L. M. & Pérez, J. A. (2014). Priming crops against biotic and abiotic stresses: MSB as a tool for studying mechanisms. *Frontiers Media SA*, 5, 642.

[13] Boussora, F., Triki, T., Bennani, L., Bagues, M., Ben Ali, S., Ferchichi, A., Ngaz, K. & Guasmi, F. (2024). Mineral accumulation, relative water content and gas exchange are the main physiological regulating mechanisms to cope with salt stress in barley. *Scientific Reports*, 14(1), 14931.

[14] Cecchini, N. M., Roychoudhry, S., Speed, D. J., Steffes, K., Tambe, A., Zodrow, K., Konstantinoff, K., Jung, H. W., Engle, N. L. & Tschaplinski, T. J. (2019). Underground azelaic acid–conferred resistance to Pseudomonas syringae in Arabidopsis. *Molecular Plant-Microbe Interactions*, 32(1), 86-94.

[15] Chauhan, A., Rajput, N., Kumar, D., Kumar, A. & Chaudhry, A. (2016). Effect of different salt concentration on seed germination and seedling growth of different varieties of oat (Avena sativa L.). *International Journal of Information Research and Review*, 3(7), 2627-2632.

[16] Choudhary, S., Wani, K. I., Naeem, M., Khan, M. M. A. & Aftab, T. (2023). Cellular responses, osmotic adjustments, and role of osmolytes in providing salt stress resilience in higher plants: polyamines and nitric oxide crosstalk. *Journal of plant growth regulation*, 42(2), 539-553.

[17] Çifci, E. A., Kurt, P. Ö. & Yağdı, K. (2013). Effects of different salt concentrations on germination of triticale varieties. *Journal of Agricultural Faculty of Uludag University*, 27(2), 1-12.

[18] Daneshmand, F., Arvin, M. J. & Kalantari, K. M. (2010). Physiological responses to NaCl stress in three wild species of potato in vitro. *Acta Physiologiae Plantarum*, 32, 91-101.

[19] Demiroğlu Topçu, G., Dumanoğlu, Z. & Özkan, Ş. (2018). The effects of different seed size and salinity on germination and some early growth parameters of annual ryegrass (Lolium multiflorum L.) cultivars. *2nd International Vocational Science Symposium*, 26-28.

[20] Dinler, B. S. & Cetinkaya, H. (2024). An overview on Azelaic Acid: Biosynthesis, signalling and the action under stress conditions in plants. *Journal of Plant Stress Physiology*, 10, 8-12.

[21] Doğan, R. & Çarpıcı, E. B. (2016). Farklı tuz konsantrasyonlarının bazı tritikale hatlarının çimlenmesi üzerine etkileri. *KSÜ Doğa Bilimleri Dergisi*, 19(2), 130-135.

[22] Ghoohestani, A., Gheisary, H., Zahedi, S. M. & Dolatkhahi, A. (2012). Effect of seed priming of tomato with salicylic acid, ascorbic acid and hydrogen peroxideon germination and plantlet growth in saline conditions. *International journal of Agronomy and Plant Production*, 3(S), 700-704.

[23] Ghorbani, S., Etminan, A., Rashidi, V., Pour-Aboughadareh, A. & Shooshtari, L. (2023). Delineation of physiological and transcriptional responses of different barley genotypes to salt stress. *Cereal Research Communications*, 51(2), 367-377.

[24] Güleç, A., Yavuz, N. & Yavuz, D. (2025). Effect of Azelaic Acid Pre-Application to Maize (Zea mays L.) Seeds on Germination and Early Seedling Period under Salinity Stress Conditions. *International Journal of Advanced Natural Sciences and Engineering Researches*, 9, 296-303.

[25] Güngör, H., Çıkılı, Y. & Dumlupınar, Z. (2017). Effects of salt stress on germination and seedling development of some commercial and local oat genotypes. *KSÜ Journal of Natural Sciences*, 20, 263-267.

[26] Haghighi, M. & Sheibanirad, A. (2018). Evaluating of Azealic Acid on Tomato Vegetative and Photosynthetic Parameters under Salinity Stress. *Journal of Horticultural Science*, 32(2), 287-300.

[27] Haliloğlu, K., Türkoğlu, A. & Aydin, M. (2022). Determination of imazamox herbicide dose in in vivo selection in wheat (Triticum aestivum L.). *Eregli journal of Agricultural Science*.

[28] Hozayn, M. & Ahmed, A. A. (2019). Effect of magneto-priming by tryptophan and ascorbic acid on germination attributes of barley (Hordeum vulgare, L.) under salinity stress. *EurAsian Journal of BioSciences*, 13(1), 245-251.

[29] Hussain, S., Khaliq, A., Matloob, A., Wahid, M. A. & Afzal, I. (2013). Germination and growth response of three wheat cultivars to NaCl salinity. *Soil Environment*, 32(1), 36-43.

[30] Işık, M. İ., Güleç, A., Türkoğlu, A. & Armağan, M. (2024). Exploring the Impact of Gypsophila perfoliata L. Root Extract on Germination and Seedling Growth Parameters of Sweet Sorghum and Hungarian Vetch. *Erzincan University Journal of Science and Technology*, 17(2), 327-337.

[31] Jadidi, O., Etminan, A., Azizi-Nezhad, R., Ebrahimi, A. & Pour-Aboughadareh, A. (2022). Physiological and molecular responses of barley genotypes to salinity stress. *Genes*, 13(11), 2040.

[32] Jung, H. W., Tschaplinski, T. J., Wang, L., Glazebrook, J. & Greenberg, J. T. (2009). Priming in systemic plant immunity. *Science*, 324(5923), 89-91.

[33] Kalaji, H. M., Bosa, K., Kościelniak, J. & Żuk-Gołaszewska, K. (2011). Effects of salt stress on photosystem II efficiency and CO2 assimilation of two Syrian barley landraces. *Environmental and Experimental Botany*, 73, 64-72.

[34] Karaman, R. (2023). Reaction of Chickpea Genotypes to Salinity-Inhibiting Applications at Different Salt Stress Levels. *Gesunde Pflanzen*, 75(5), 1823-1831.

[35] Kiremit, M. S., Hacıkamiloğlu, M. S., Arslan, H. & Orhan, K. (2017). Farklı sulama suyu tuzluluk seviyelerinin keten (Linum usitatissimum L.)'in çimlenme ve erken fide gelişimi üzerine etkisi. *Anadolu Tarım Bilimleri Dergisi*, 32(3), 350-357.

[36] Kusvuran, A., Nazli, R. & Kusvuran, S. (2015). The effects of salinity on seed germination in perennial ryegrass (Lolium perenne L.) varieties. *Türk Tarım ve Doğa Bilimleri Dergisi*, 2(1), 78-84.

[37] Leonetti, P., Hanafy, M. S., Tayade, R., Ramakrishnan, M., Sonah, H. & Jacobsen, H.-J. (2023). Leveraging genomics, phenomics, and plant biotechnology approaches for improving abiotic and biotic stress tolerance in cereals and legumes. *Frontiers Media SA*, 14, 1307390.

[38] Liu, J., Li, H., Yuan, Z., Feng, J., Chen, S., Sun, G., Wei, Z. & Hu, T. (2024). Effects of microbial fertilizer and irrigation amount on growth, physiology and water use efficiency of tomato in greenhouse. *Scientia Horticulturae*, 323, 112553.

[39] Mian, A., Oomen, R. J., Isayenkov, S., Sentenac, H., Maathuis, F. J. & Véry, A. A. (2011). Over-expression of an Na+-and K+-permeable HKT transporter in barley improves salt tolerance. *The Plant Journal*, 68(3), 468-479.

[40] Mukhtarova, L. S., Mukhitova, F. K., Gogolev, Y. V. & Grechkin, A. N. (2011). Hydroperoxide lyase cascade in pea seedlings: Non-volatile oxylipins and their age and stress dependent alterations. *Phytochemistry*, 72(4-5), 356-364.

[41] Öner, F. & Kırlı, A. (2018). Effects of salt stress on germination and seedling growth of different bread wheat (Triticum aestivum L.) cultivars. *Akademik Ziraat Dergisi*, 7(2), 191-196.

[42] Özkorkmaz, F., Yılmaz, N. & Öner, F. (2020). Researching germination properties of bean (Phaseolus vulgaris L.) under polyethylene glycol osmotic stress and saline conditions. *Akademik Ziraat Dergisi*, 9(2), 251-258.

[43] Parihar, P., Singh, S., Singh, R., Singh, V. P. & Prasad, S. M. (2015). Effect of salinity stress on plants and its tolerance strategies: a review. *Environmental science and pollution research*, 22, 4056-4075.

[44] Qayyum, A., Al Ayoubi, S., Sher, A., Bibi, Y., Ahmad, S., Shen, Z. & Jenks, M. A. (2021). Improvement in drought tolerance in bread wheat is related to an improvement in osmolyte production, antioxidant enzyme activities, and gaseous exchange. *Saudi journal of biological sciences*, 28(9), 5238-5249.

[45] Sharipova, G., Ivanov, R., Veselov, D., Akhiyarova, G., Seldimirova, O., Galin, I., Fricke, W., Vysotskaya, L. & Kudoyarova, G. (2022). Effect of salinity on stomatal conductance, leaf hydraulic conductance, HvPIP2 aquaporin, and abscisic acid abundance in barley leaf cells. *International Journal of Molecular Sciences*, 23(22), 14282.

[46] Sirat, A. & Sezer, İ. (2013). Investigation of yield, yield components and some quality traits of some two-row barley (*Hordeum vulgare* conv. distichon) varieties in Samsun ecological conditions. *Yüzüncü Yıl Üniversitesi Tarım Bilimleri Dergisi.*

[47] Süheri, S., Yaylalı, İ. K., Yavuz, D. & Yavuz, N. (2019). The effect of sodium chloride salinity on coated and uncoated alfalfa seeds germination. *Harran Tarım ve Gıda Bilimleri Dergisi*, 23(1), 31-38.

[48] Topçu, G. D. & Özkan, Ş. S. (2017). Determination of the Effect of Concentrations on Germination Characteristics of Some Barley (*Hordeum vulgare* L.) Varieties. *ÇOMÜ Ziraat Fakültesi Dergisi*, 5(2), 37-43.

[49] Türkoğlu, A., Tosun, M., Haliloğlu, K. & Karagöz, H. (2022). Effects of early drought stress on germination and seedling growth parameters of Kırik bread wheat (Triticum aestivum L.). *Ereğli Journal of Agricultural Sciences*, 2, 75-80.

[50] Vy, T. H., Nguyen, N. C., Xuan, H. T. L. & Thao, N. P. (2018). Role of GmNAC019 transcription factor in salinity and drought tolerance of transgenic Arabidopsis thaliana. *Journal of Biotechnology*, 16(4), 611-619.

[51] Yavuz, D., Kılıç, E., Seymen, M., Dal, Y., Kayak, N., Kal, Ü. & Yavuz, N. (2022). The effect of irrigation water salinity on the morph-physiological and biochemical properties of spinach under deficit irrigation conditions. *Scientia Horticulturae*, 304, 111272.

[52] Yavuz, D., Başтаş, K. K., Seymen, M., Yavuz, N., Kurtar, E. S., Süheri, S., Türkmen, Ö., Gür, A. & Kıymacı, G. (2023). Role of ACC deaminase-producing rhizobacteria in alleviation of water stress in watermelon. *Scientia Horticulturae*, 321, 112288.

[53] Yu, K., Soares, J. M., Mandal, M. K., Wang, C., Chanda, B., Gifford, A. N., Fowler, J. S., Navarre, D., Kachroo, A. & Kachroo, P. (2013). A feedback regulatory loop between G3P and lipid transfer proteins DIR1 and AZI1 mediates azelaic-acid-induced systemic immunity. *Cell Reports*, 3(4), 1266-1278.

e-ISSN: 2149-4584

Erzincan University Journal of Science and Technology

EJSAT 2025, 18 (3) 933-950

Research Article

Development of a MOF Based Potentiometric Sensor for Determination of Rhodamine B

Nurcan Kaya[1], Gulsah Saydan Kanberoglu[1*]

[1] Department of Chemistry, Faculty of Science, Van Yuzuncu Yil University, Turkey

Received: 29/11/2024, **Revised:** 02/06/2025, **Accepted:** 14/07/2025, **Published:** 31/12/2025

Abstract

Rhodamine B (RB) is a basic, red, and cationic dye belonging to the class of xanthene dyes. Rhodamine B is harmful to human and animal health when ingested or is in contact with the skin. It causes irritation to the skin, eyes, and respiratory tract. Experimental studies have shown that Rhodamine B exhibits carcinogenicity, reproductive and developmental toxicity, neurotoxicity, and chronic toxicity in humans and animals. In this study, a Rhodamine B-selective potentiometric sensor was developed by using MIL-53 (Al) (Material Institute Lavoisier) as the ionophore in the prepared membrane composition. The sensor, prepared with a membrane composition of 6% MIL-53 (Al), 26% PVC (Polyvinyl chloride), and 68% DOS (bis(2-ethylhexyl) sebacate), exhibited the best potentiometric performance. The Rhodamine B-selective sensor exhibited a linear response in the concentration range of 1.0×10^{-6} M to 1.0×10^{-2} M with a slope of 58.0 mV/decade and a detection limit of (LOD) 5.0×10^{-7} M in Rhodamine B solutions adjusted to pH 4.50. The response time of the Rhodamine B-selective sensor was less than 5 seconds and was unaffected by hydronium ions in the pH range of 4.49 to 8.08. Analytical application of the sensor was successfully carried out in Van Lake, wastewater, and tap water.

Keywords: Determination of Rhodamine B, metal organic framework, **p**otentiometric sensor

Rodamin B Tayini için MOF Temelli Potansiyometrik Sensör Geliştirilmesi

Öz

Rodamin B (RB), ksanten boyaları sınıfına ait bazik, kırmızı ve katyonik bir boyar maddedir. Rodamin B, ağızdan alındığında veya deri ile teması halinde insan ve hayvan sağlığı için zararlıdır. Ciltte, gözlerde ve solunum yollarında tahrişe neden olur. Deneysel çalışmalar, rodamin B'nin insanlarda ve hayvanlarda kanserojenlik, üreme ve gelişimsel toksisite, nörotoksisite ve kronik toksisite sergilediğini göstermiştir. Bu çalışmada, hazırlanan membran bileşiminde iyonofor olarak MIL-53 (Al) (Material Institute Lavoisier) kullanılarak Rodamin B-seçici potansiyometrik sensör geliştirildi. %6 MIL-53 (Al), %26 PVC (Polivinil klorür), %68 DOS (Bis(2-etilhekzil) sebakat) membran bileşimi ile hazırlanan sensör en iyi potansiyometrik performans özelliği sergiledi. Rodamin B-seçici sensör, 1.0×10^{-6} M-1.0×10^{-2} M konsantrasyon aralığında pH 4.50'e ayarlanan Rodamin B çözeltilerinde 58.0 mV/onkat'lık eğim ve 5.0×10^{-7} M tayin limiti (LOD) ile doğrusal bir cevap sergiledi. Rodamin B-seçici sensörün cevap zamanı 5 saniyeden düşük olduğu ve pH 4.49-8.08 aralığında hidronyum iyonlarından etkilenmediği belirlendi. Sensörün analitik uygulaması Van Gölü, atık su ve çeşme suyunda başarıyla gerçekleştirildi.

Anahtar Kelimeler: Metal organik kafes yapısı, potansiyometrik sensör, Rodamin B tayini

Corresponding Author: gskanberoglu@yyu.edu.tr

Cite this Article: Erzincan University Journal of Science and Technology 2025, 18(3) 933-950. https://doi.org/10.18185/erzifbed.1593344

1. Introduction

The structure of Rhodamine B contains a carboxylic acid functional group on the benzene ring and an N,N-diethylamino group attached to the xanthene moiety [1]. Figure 1 shows the molecular structure of Rhodamine B. Rhodamine B is a synthetic xanthene dye with a wide range of applications. It is extensively used in the textile industry for dyeing cotton, wool, and synthetic fibers, and is also employed in the production of furniture and cosmetic products. Beyond industrial applications, Rhodamine B serves as a fluorescent tracer in analytical and photochemical techniques, biological assays, and microbiological studies. Its strong fluorescent properties make it especially valuable in hydrogeological applications, where it is used to trace and monitor water flow in both natural and engineered water systems. As a result, it is found in the wastewater of many industrial, chemical, biomedical and photochemical laboratories [2]. Rhodamine B is used illegally to impart natural color to food products. Contamination levels in products such as pepper powder, pepper oil, and pepper paste were found to range from 0.021 to 50 μg/g [3]. Rhodamine B causes acute poisoning, liver dysfunction, cardiovascular disease, cancer, premature birth, nausea, irritation of the skin, eyes and respiratory tract when ingested by humans. Experimentally, Rhodamine B has been shown to have carcinogenicity, reproductive and developmental toxicity, neurotoxicity, and chronic toxicity to humans and animals [4, 5]. Therefore, the determination of Rhodamine B is of great importance.

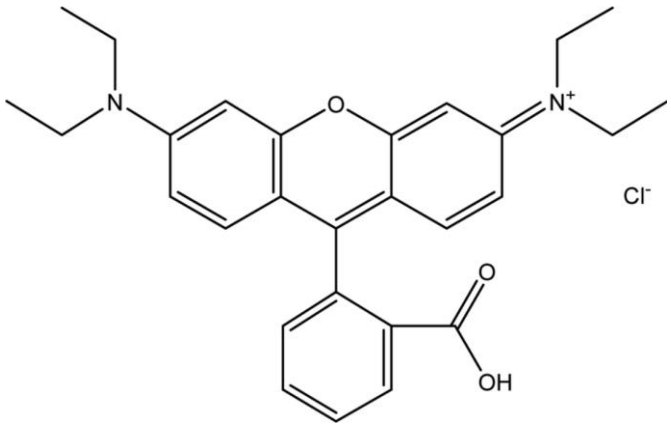

Figure 1. Chemical structure of Rhodamine B

Determination of Rhodamine B was carried out by Electrokinetic capillary chromatography [6], amperometry [7], high-pressure liquid fluorescence chromatography [8], reversed-phase high-performance liquid chromatography coupled with mass spectrometry [9], high-performance liquid chromatography combined with a fluorescence detector (FLD) [3], fluorimetry [10], extraction methods [11-13], voltammetry [14], surface-enhanced Raman spectroscopy [15], and ELISA [16]. However, these methods have disadvantages such as long analysis times, the need for preliminary separation steps (e.g., solid-phase extraction) and the use of expensive equipment. Therefore, it is important to develop a method for the determination of Rhodamine B that is cost-effective, simple, sensitive, and rapid.

Potentiometry is a powerful and versatile analytical method as it provides high sensitivity, accuracy, and precision as well as a wide linear range with low-cost instrumentation. It has several advantages, such as simplicity, low cost, speed, reliability, and not requiring expert technicians to perform the procedure. Since potentiometric methods do not require the application of an external potential, they are considered the simplest among all electroanalytical

techniques in terms of signal transmission [17]. Potentiometric ion selective electrodes are used in the determination of anionic and cationic species in many fields such as medicine, drug analysis, industrial and agricultural fields [18]. Studies on ion-selective electrodes began in the late 1960s and interest in ion-selective electrodes still continues to grow [19]. Ion-selective electrodes are the chemical sensors with the longest history and probably the most frequent routine application. Ion-selective electrodes are considered to be one of the most effective methods for the direct analysis of ionic species and indirect determination of non-ionic components in complex samples [20]. The field of clinical chemistry is the most important application area of ion-selective electrodes. The use of ion-selective electrodes in the analysis of samples containing multiple ionic species (such as water and soil) provides advantageous measurement data [21]. Ion-selective electrodes have many advantages such as short response time, excellent selectivity and affordability. ISEs offer many advantages, including short response times, excellent selectivity, and cost-effectiveness. Recently, metal-organic framework (MOF)-based materials have attracted considerable attention for enhancing the performance of ISEs due to their superior conductivity and specific ion-binding capabilities.

Metal–organic frameworks (MOFs) are porous materials constructed from metal ions or metal clusters coordinated to organic linkers. They possess exceptionally high surface areas. Due to the presence of organic linkers, MOFs are compatible with various polymers. This characteristic renders them superior to zeolites, and they can also be synthesized with tunable pore sizes [22–25]. MOFs have found applications in diverse fields such as gas adsorption, purification and storage, drug delivery, sensing, and catalysis [26]. Although MOFs have recently been widely employed in electrochemical sensor applications, their use in potentiometric sensors remains limited [27].

Among various metal-organic frameworks (MOFs), MIL-53 (Al) stands out as a promising candidate due to its tunable pore structure and excellent stability, making it a valuable material for enhancing the performance of ion-selective electrodes. The MIL-53(Al) structure consists of rod-like metallic secondary building units, in which aluminum (III) ions are connected via μ^2-OH bridging groups [28]. Much research has been done on MIL-53 compounds because they exhibit a high degree of reversible flexibility within their lattice structure. However, what makes this particular class of MOFs interesting for further investigation is their high thermal stability up to 500°C [29]. For instance, MIL-53(Al) has been used as an ionophore in sensors designed for the determination of pharmaceutical compounds such as imipramine hydrochloride [27] and maprotiline hydrochloride [30]. A potentiometric sensor based on ion pair was developed for the determination of Rhodamine B [31]. However, no potentiometric sensor based on MOF has been developed for the determination of Rhodamine B. In this study, for the first time, a MOF-based potentiometric PVC membrane ion-selective sensor was fabricated for the determination of Rhodamine B, thereby introducing a novel MOF-based approach for dye detection.

2. Material and Methods

2.1. Chemicals and Apparatus

Rhodamine B (ISOLAB, Germany) was obtained from the company. Tetrahydrofuran (THF), high-molecular-weight-poly (vinyl chloride) (PVC), MIL-53 (Al), nitrophenyloctylether (NPOE), bis(2-ethyl)hexyl sebacate (DOS) and dibutylphthalate (DBP) were sourced from Sigma-Aldrich (Germany). The epoxy (TP3100) and hardener (Desmodur RFE) employed in the preparation of the solid-contact were acquired from Denlaks (Turkey) and Bayer (Germany) companies, respectively. All chemicals employed in solution preparation throughout this study were analytical grade and procured from Sigma-Aldrich (Germany). For the potentiometric application, wastewater, Van Lake water and tap water samples taken from Van were used. All solutions were prepared with 18.3 MΩ deionized pure water. A Gamry (USA) brand saturated Ag/AgCl electrode served as the reference electrode throughout the potential measurements. All potentiometric measurements were conducted using a custom-made computer-controlled potentiometric measurement system.

2.2 Preparing the Sensors

The sensors were first coated with solid contact. Solid contact was prepared by adding THF to 35% (w/w) epoxy, 15% (w/w) hardener and 50% (w/w) graphite to obtain a suitable homogenized mixture. Then, the open end of a copper wire was dipped into this mixture and the wire was coated with solid contact. It was then left to dry in the dark at room temperature for 24 hours. Then, the membranes were prepared and the surface of the solid contacts were covered with the membrane. The composition of the membranes consists of PVC, different types of plasticizers, MIL-53 (Al) and sometimes KTpClPB (potassium tetrakis(4-chlorophenyl)borate). Membranes were prepared by dissolving 100 mg of total membrane mass in 1 mL of THF. It was dried at room temperature in the dark for 24 hours. Prepared sensors were conditioned in 1.0×10^{-2} M Rhodamine B solutions for 12 hours.

3. Results and Disscussion

3.1. Determination of Optimum Membrane Composition

The potentiometric properties of a PVC membrane ion-selective sensor are highly dependent on the membrane composition. Twelve different sensors were obtained with different types and ratios of ionophore, plasticizer, ionizer and PVC. The sensor with the best performance was determined. The membrane compositions tested for the development of the Rhodamine B-selective sensor and their potentiometric performance properties are given in Table 1 and Table 2, respectively.

Table 1. The studied membrane compositions for the membrane optimization study

	Membrane Composition (%w/w)					
	Polymer	**Plasticizer**			**Ionophore**	**Ionic Additive**
Sensor No	**PVC**	**NPOE**	**DBF**	**DOS**	**MIL-53**	**KTpCIPB**
A-1	26.0	67.0	-	-	6.0	1.0
A-2	26.0	68.0	-	-	6.0	-
A-3	26.0	-	67.0	-	6.0	1.0
A-4	26.0	-	68.0	-	6.0	-
A-5	26.0	-	-	67.0	6.0	1.0
A-6	**26.0**	**-**	**-**	**68.0**	**6.0**	**-**
A-7	32.0	64.0		-	3.0	1.0
A-8	32.0	65.0	-	-	3.0	-
A-9	32.0	-	64.0	-	3.0	1.0
A-10	32.0	-	65.0	-	3.0	-
A-11	32.0	-	-	64.0	3.0	1.0
A-12	32.0	-	-	65.0	3.0	-

Table 2. Potentiometric performance characteristics of electrodes made from different membrane compositions for Rhodamine B solutions prepared in deionized water

Sensor No	Slope, mV/decade	Detection Limit, M	Linear Range, M	R^2
A-1	60.0	1.0×10^{-7}	1.0×10^{-6}-1.0×10^{-2}	0.9898
A-2	47.4	1.0×10^{-6}	1.0×10^{-6}-1.0×10^{-2}	0.9934
A-3	62.5	5.0×10^{-7}	1.0×10^{-6}-1.0×10^{-2}	0.9936
A-4	55.0	1.0×10^{-7}	1.0×10^{-6}-1.0×10^{-2}	0.9883
A-5	62.8	5.0×10^{-7}	1.0×10^{-6}-1.0×10^{-2}	0.9923
A-6	**52.2**	**1.0×10^{-7}**	**1.0×10^{-7}-1.0×10^{-2}**	**0.9902**
A-7	66.1	1.0×10^{-6}	1.0×10^{-6}-1.0×10^{-2}	0.9928
A-8	52.3	1.0×10^{-6}	1.0×10^{-6}-1.0×10^{-2}	0.9701
A-9	67.3	1.0×10^{-6}	1.0×10^{-6}-1.0×10^{-2}	0.9935
A-10	52.4	1.0×10^{-6}	1.0×10^{-6}-1.0×10^{-2}	0.9875
A-11	64.0	1.0×10^{-6}	$1.0x10^{-6}$-1.0×10^{-2}	0.9914
A-12	55.9	1.0×10^{-6}	$1.0x10^{-6}$-1.0×10^{-2}	0.9936

3.2. Determination of Detection Limit, Linear Working Range, and Slope

Measurements taken in a series of Rhodamine B standard solutions (1.0×10^{-2} M-1.0×10^{-7} M) prepared in deionized water were used to create the calibration chart. The resulting calibration graph was used for slope, linear working range and R^2 calculations. The detection limit of the Rhodamine B-selective sensor was determined according to IUPAC [32]. For this purpose, potential measurements of low and high concentrations of Rhodamine B were made at 25±1°C. The potential-time graph obtained for Rhodamine B solutions at different concentrations with the Rhodamine B-selective sensor is shown in Figure 2 and its calibration graph is shown in Figure 3. The sensor shows a linear response in Rhodamine B solutions prepared in deionized water over the concentration range of 1.0×10^{-7} M to 1.0×10^{-2} M with a slope of 52.2 mV/decade and a detection limit of 1.0×10^{-7} M.

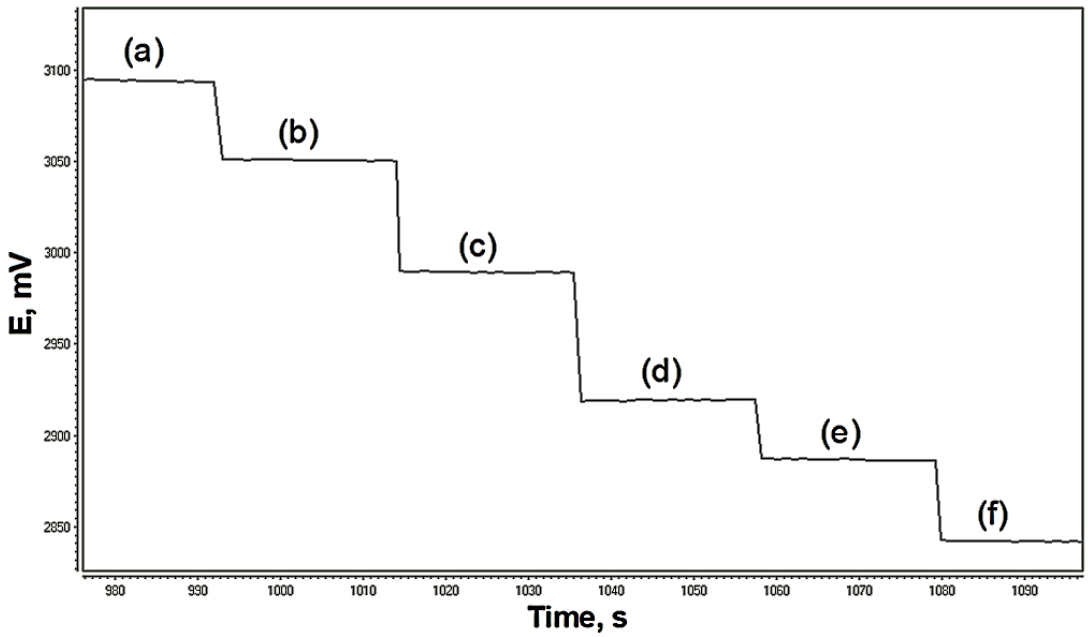

Figure 2. Potentiometric responses of the Rhodamine B-selective sensor in Rhodamine B solutions prepared in deionized water in the concentration range of 1.0×10^{-2} M-1.0×10^{-7} M. (a) 1.0×10^{-2} M (b) 1.0×10^{-3} M (c) 1.0×10^{-4} M (d) 1.0×10^{-5} M (e) 1.0×10^{-6} M (f) 1.0×10^{-7} M

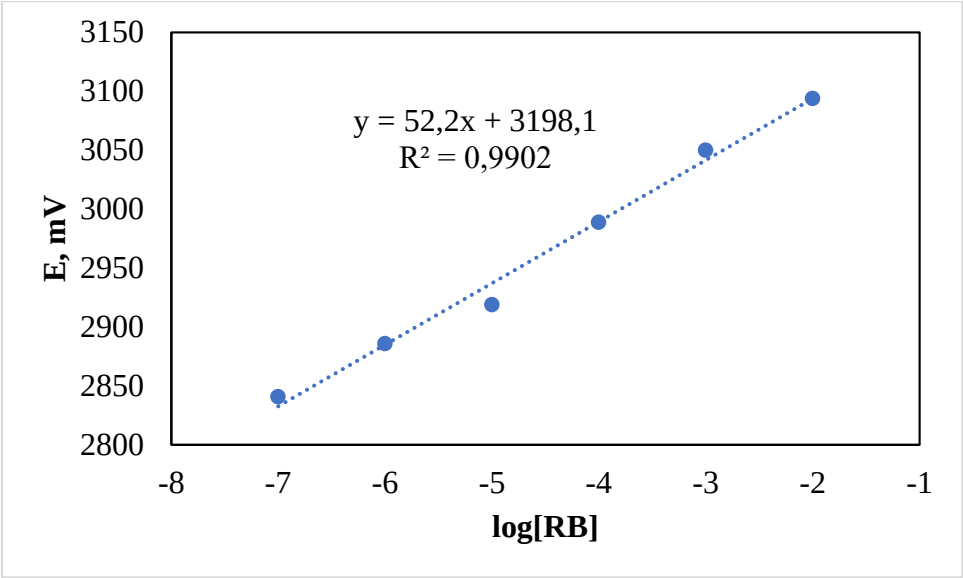

Figure 3. Calibration graph obtained for Rhodamine B standard solutions prepared in deionized water using sensor number A-6

The potentiometric responses of the Rhodamine B-selective sensor number A-6, adjusted to pH 4.50 using HCl and NaOH for 1.0×10^{-2} M-1.0×10^{-6} M Rhodamine B solutions, are shown in Figure 4. The calibration graph obtained is also given in Figure 5. The detection limit of the Rhodamine B-selective sensor was determined according to IUPAC [32]. For this purpose, Rhodamine B potential measurements were made at 25±1°C. Sensor number A-6 showed linearity in the concentration range of 1.0×10^{-2}-1.0×10^{-6} M with a concentration change of 58.0 mV/decade, and the detection limit of the proposed Rhodamine B-selective sensor was calculated as 5.0×10^{-7} M.

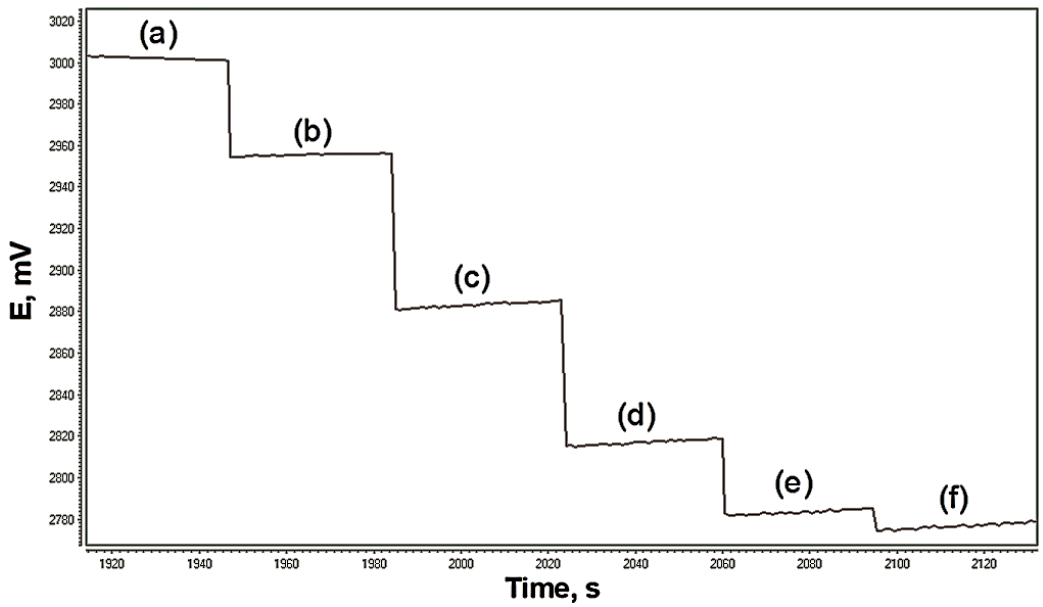

Figure 4. Potentiometric responses of the Rhodamine B-selective sensor to Rhodamine B solutions in the concentration range of 1.0×10^{-2} M-1.0×10^{-7} M adjusted to pH 4.50. (a) 1.0×10^{-2} M (b) 1.0×10^{-3} M (c) 1.0×10^{-4} M (d) 1.0×10^{-5} M (e) 1.0×10^{-6} M (f) 1.0×10^{-7} M

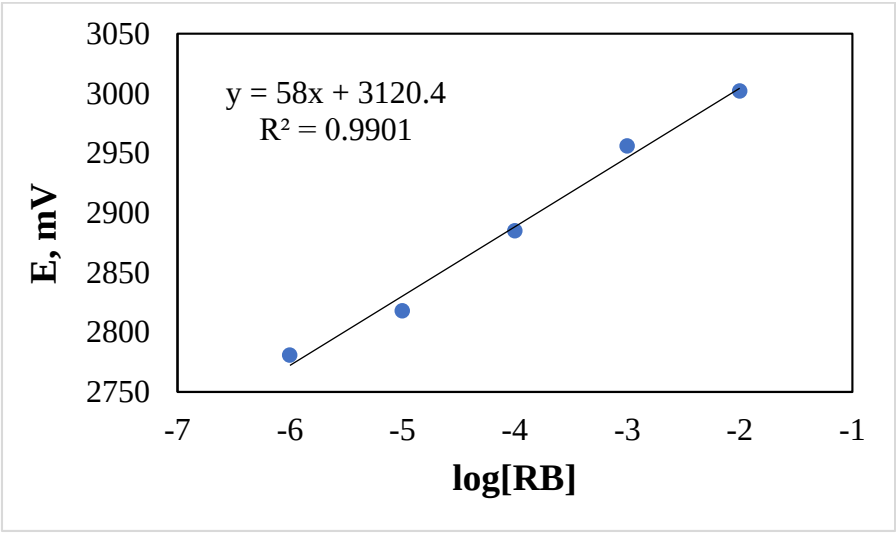

Figure 5. Calibration graph obtained from standard Rhodamine B solutions in the concentration range of 1.0×10^{-2} M-1.0×10^{-6} M adjusted to pH 4.50 using the Rhodamine B-selective sensor

3.3. Determination of Repeatability of Rhodamine B-Selective Sensor

In order to determine the repeatability of the Rhodamine B selective sensor, consecutive measurements were carried out in 1.0×10^{-3}, 1.0×10^{-4} and 1.0×10^{-5} M Rhodamine B solutions with pH adjusted to 4.50. The potential-time graph showing the repeatability of the Rhodamine B-selective sensor is given in Figure 6. The means and standard deviations for 1.0×10^{-3} M, 1.0×10^{-4} M and 1.0×10^{-5} M Rhodamine B solutions (pH=4.50) were calculated as 2959.6±2.3 mV, 2896±0.4 mV and 2831.8±1.1 mV, respectively. The potential values measured with the

Rhodamine B-selective sensor in 1.0×10^{-3}, 1.0×10^{-4} and 1.0×10^{-5} M Rhodamine B solutions (pH=4.50) are given in Table 3.

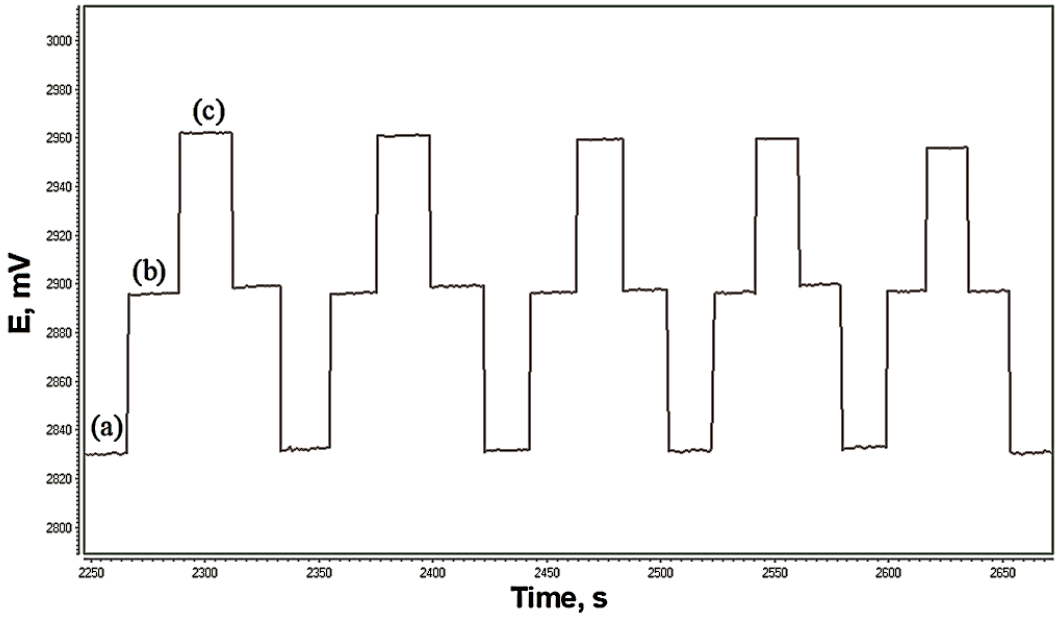

Figure 6. Repeatability of Rhodamine B-selective sensor in (a) 1.0×10^{-5} M, (b) 1.0×10^{-4} M and (c) 1.0×10^{-3} M Rhodamine B solutions (pH=4.50)

Table 3. Potential values measured with Rhodamine B-selective sensor in 1.0×10^{-3} M, 1.0×10^{-4} M and 1.0×10^{-5} M Rhodamine B solutions (pH=4.50)

Concentration (M)	1	2	3	4	5	$\bar{x}\pm s$
1.0×10^{-3}	2962	2961	2959	2960	2956	2959.6±2.3
1.0×10^{-4}	2896	2896	2895	2896	2896	2896.0±0.4
1.0×10^{-5}	2832	2832	2832	2833	2830	2831.8±1.1

3.4. Determination of Response Time of Rhodamine B-Selective Sensor

In order to determine the response time of the sensor, the calibration solutions were continuously mixed at a constant speed. The measurements were taken with the sensor from low concentration to high concentration and from high concentration to low concentration. The average of the 95% of the time at which the potentials became stable was determined as the response time of the sensor. The time required for the sensor to reach equilibrium in 1.0×10^{-4} M and 1.0×10^{-3} M Rhodamine B solutions (pH=4.50) is shown in Figure 7. The average response time of the sensor was determined to be less than 5 seconds.

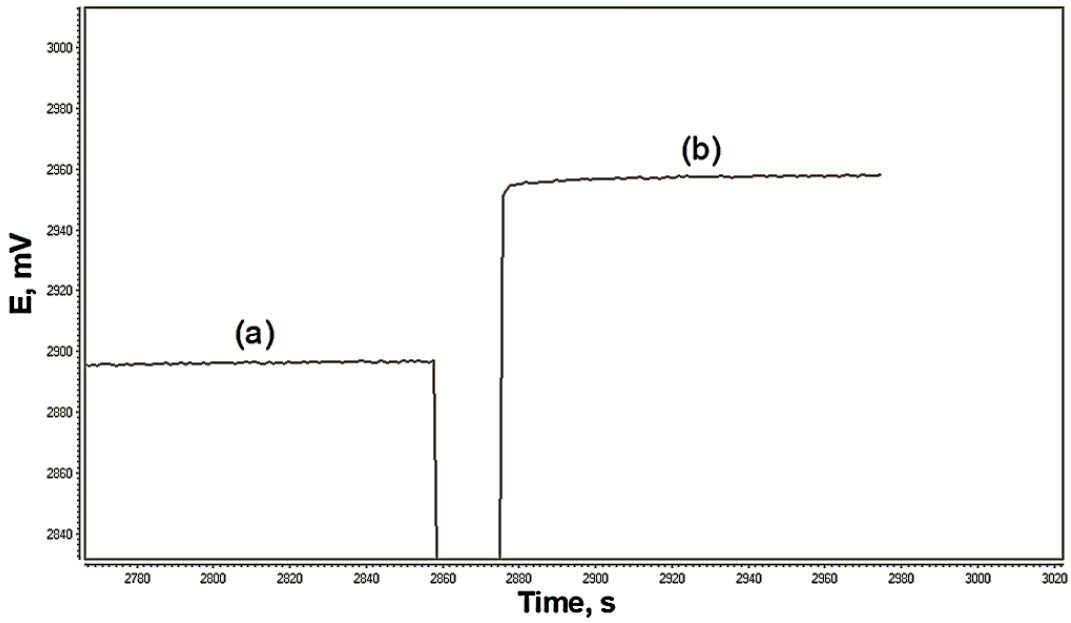

Figure 7. Response time of Rhodamine B-selective sensor in (a) 1.0×10^{-4} M and (b) 1.0×10^{-3} M Rhodamine B solutions

3.5. Determination of pH Working Range of Rhodamine B-selective Sensor

To determine the pH working range of the Rhodamine B-selective sensor, 25 mL of 1.0×10^{-3} M Rhodamine B solutions were prepared. The prepared Rhodamine B solutions were mixed at a certain speed and at this time, the Rhodamine B-selective sensor numbered A-6, the reference electrode and also the pH meter were immersed in the solutions. The pH value of the solution was changed by adding HCl and NaOH to the Rhodamine B solution little by little. The pH value and corresponding potential values were recorded each time an acid and base were added to the Rhodamine B solution. The potential value corresponding to the pH values was plotted on the graph. The pH study graph is given in Figure 8. Since there was no significant change in the potential in the pH range of 4.49-8.08, it is clear that the potential of the sensor was not affected by hydronium ions in this pH range. The pH working range of the Rhodamine B-selective sensor was determined as 4.49-8.08. Below a pH of 4.49, the observed increase in measured potential can be attributed to the interference effect of hydronium ions present in the measurement media at elevated concentrations. Conversely, it was observed that above pH 8.08, the sensor potentials began to decline rapidly. This decline is rationalized by the gradual reduction in the amount of protonated rhodamine B at higher pH levels, aligning with anticipated behavior.

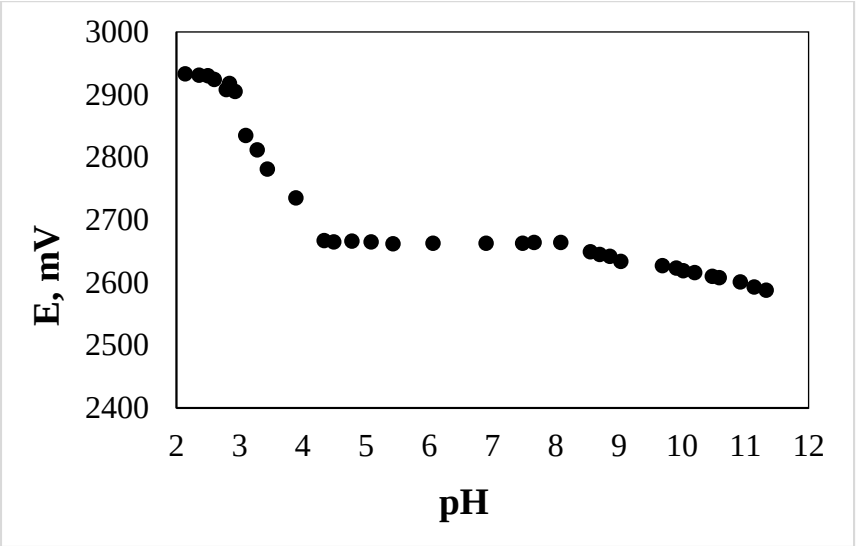

Figure 8. pH working range of Rhodamine B-selective sensor

3.6. Determination of Selectivity of Rhodamine B-Selective Sensor

To determine the effects of some alkali metals, heavy metals, and alkaline earth metals on the response of the Rhodamine B-selective sensor, selectivity coefficients against these species were calculated using the separate solution method (E_A=E_B). Potentiometric measurements of commonly occurring ions were taken in the concentration range of 1.0×10^{-6} M-1.0×10^{-2} M. The potential value obtained at a concentration of 1.0×10^{-2} M of the interfering ion was written in the calibration graph obtained for Rhodamine B and the selectivity coefficient was calculated according to the separate solution method. The graph showing the selectivity of the Rhodamine B-selective sensor is given in Figure 9. The selectivity coefficients of the Rhodamine B-selective sensor calculated according to the separate solution method are given in Table 4. When the selectivity coefficient values in Table 4 are examined, it can be said that the developed PVC membrane Rhodamine B-selective sensor exhibits a highly selective potentiometric response. The most interfering ions on the potential response of the sensor were NH_4^+ and K^+. Even in the presence of these ions, the developed PVC membrane rhodamine B-selective sensor exhibited a selective response of more than approximately 1000 times for the target analyte.

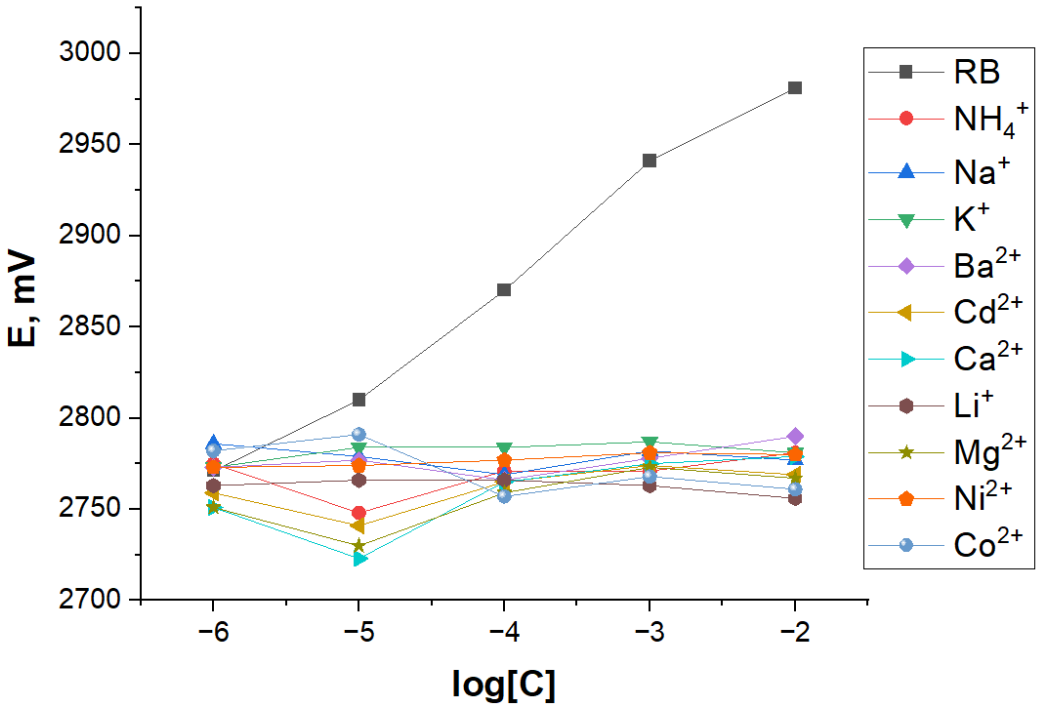

Figure 9. Graph showing the selectivity of the Rhodamine B-selective sensor

Table 4. The calculated selectivity coefficients of Rhodamine B selective sensor for studied interferents

Interferents	$K_{RB/Interferent}$	$-\log K_{RB/Interferent}$
NH_4^+	2.04×10^{-4}	3.69
K^+	2.04×10^{-4}	3.69
Na^+	1.69×10^{-4}	3.77
Li^+	7.07×10^{-5}	4.15
Ba^{2+}	2.95×10^{-5}	4.53
Ni^{2+}	1.94×10^{-5}	4.71
Ca^{2+}	1.86×10^{-5}	4.73
Cd^{2+}	1.23×10^{-5}	4.91
Mg^{+2}	1.12×10^{-5}	4.95
Co^{2+}	8.71×10^{-6}	5.06

3.7. Determination of Life-Time

In order to determine the life-time of the Rhodamine B selective sensor, measurements were taken every day in the concentration range of 1.0×10^{-2} M-1.0×10^{-6} M in standard Rhodamine B solutions adjusted to pH 4.50 using the Rhodamine B selective sensor. The obtained slope values were plotted against time. Before each calibration run, the Rhodamine B selective sensor was conditioned in 1.0×10^{-2} M Rhodamine B solution for half an hour. The sensors were kept in the dark when not in use. The plot illustrating the slopes of the proposed electrode over time Figure 10 shows that there is no significant change in the slope of the sensor over a period of 23 days. We can say that the recommended sensor can be used for 23 days without any sensitivity problems. Consequently, the life-time of the Rhodamine B-selective sensor is 23 days.

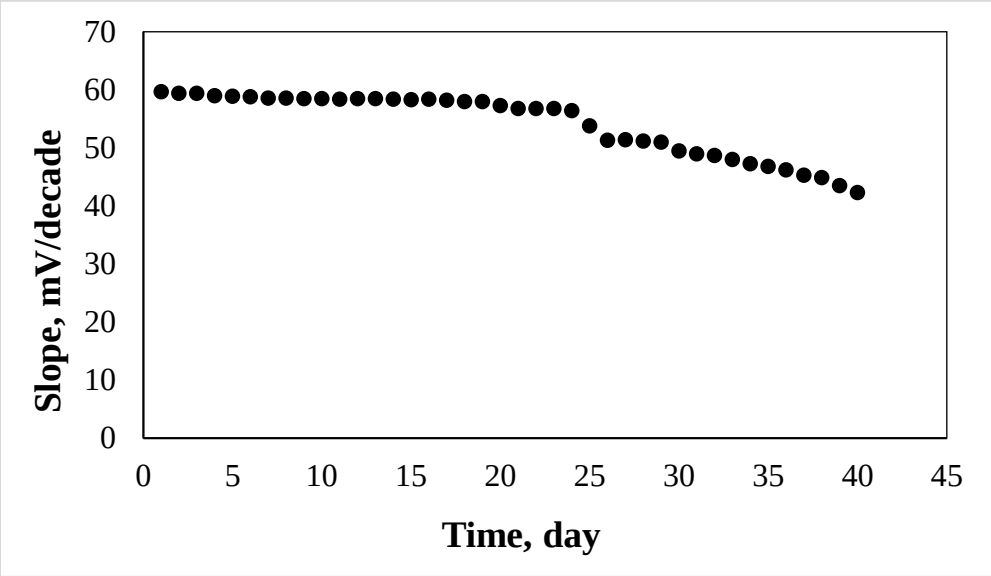

Figure 10. Graph showing the life-time of the Rhodamine B-selective sensor

3.8. Analytical Application of Rhodamine B-Selective Sensor

Analytical application of the sensor was carried out by adding Rhodamine B to Van Lake water, wastewater, and tap water samples and directly determining the Rhodamine B content in the samples. Samples S1 (tap water, 1.0×10^{-3} M), S2 (tap water, 1.0×10^{-4} M), S3 (wastewater, 1.0×10^{-3} M), S4 (Van Lake water, 1.0×10^{-3} M), S5 (Van Lake water, 1.0×10^{-4} M) were prepared. The pH of all samples and 1.0×10^{-2} M-1.0×10^{-6} M Rhodamine B solutions were adjusted to 4.50 (with 1.0 M HCl and 1.0 M NaOH). Calibration graph was obtained using Rhodamine B-selective sensor in 1.0×10^{-2} M-1.0×10^{-6} M Rhodamine B solutions with pH adjusted to 4.50. The potentiometric responses obtained for the measurement of samples S1, S2, S3, S4 and S5 are shown in Figure 11, Figure 12 and Figure 13, respectively. The corresponding sample contents were calculated using the potential values recorded from the sample solutions and the relevant calibration equation. The statistical analysis results obtained are given in Table 5.

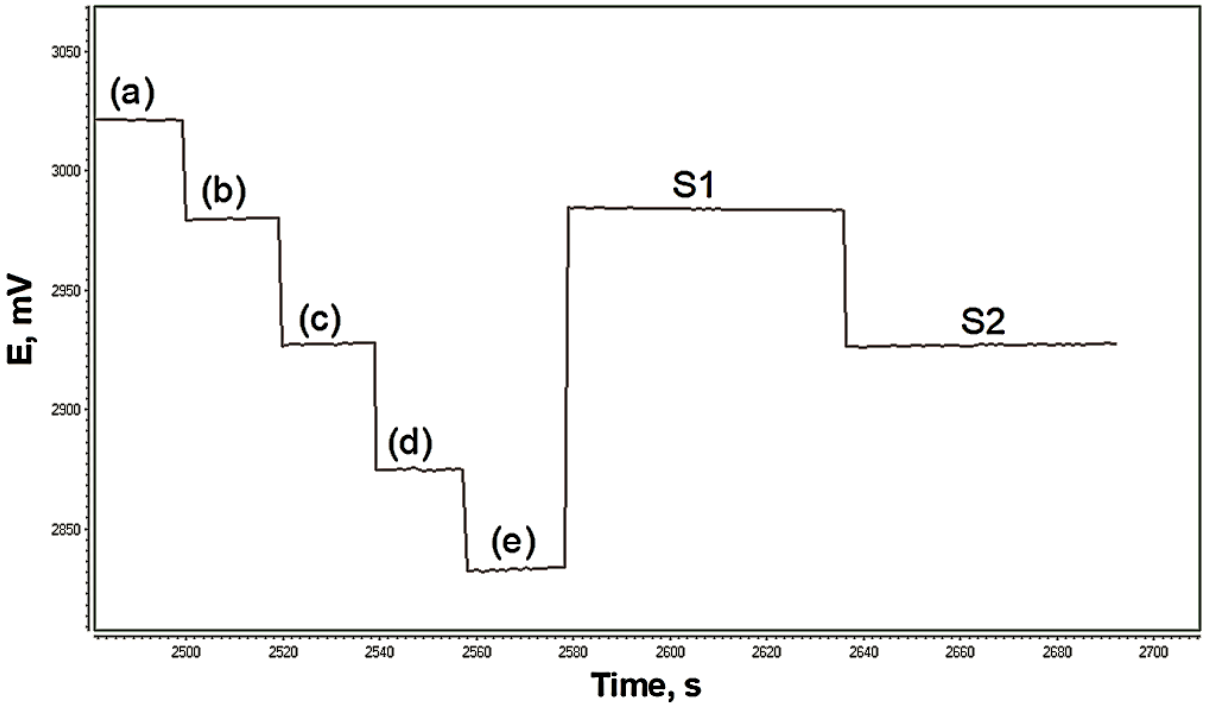

Figure 11. Response of Rhodamine B-selective sensor to Rhodamine B solutions in the concentration range of 1.0×10^{-2} M-1.0×10^{-6} M (pH 4.50), S1 and S2 tap water samples. (a) 1.0×10^{-2} M (b) 1.0×10^{-3} M (c) 1.0×10^{-4} M (d) 1.0×10^{-5} M (e) 1.0×10^{-6} M

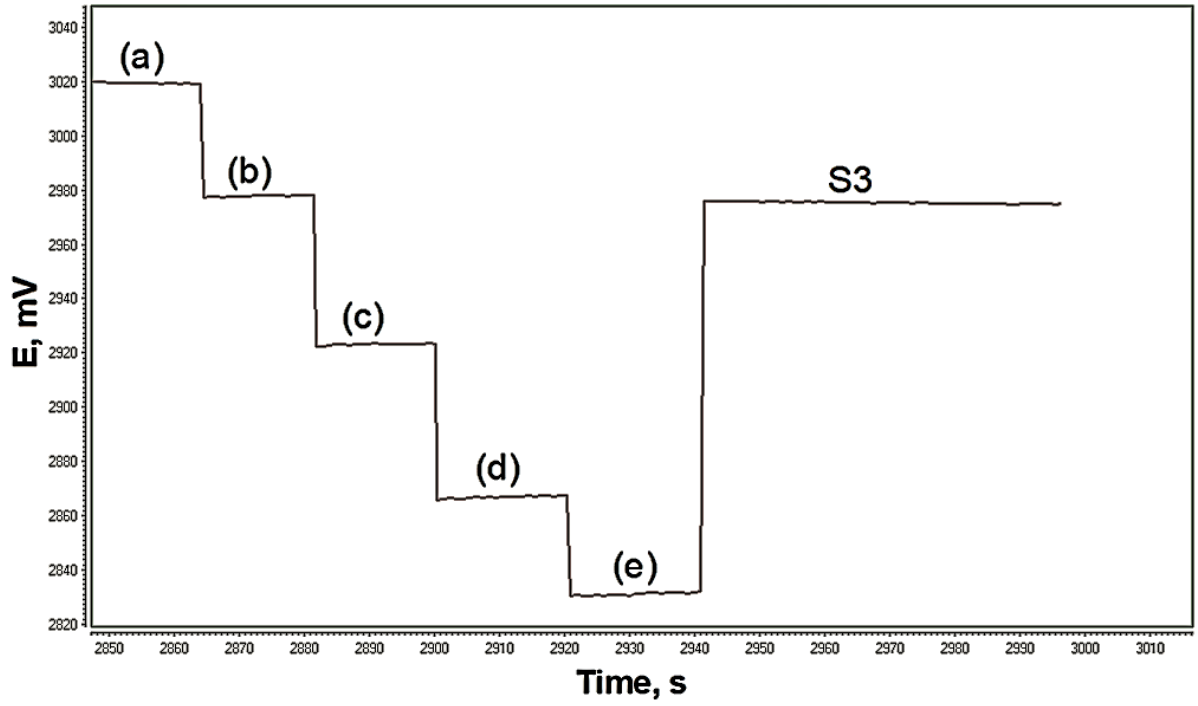

Figure 12. Response of Rhodamine B-selective sensor to Rhodamine B solutions in the concentration range of 1.0×10^{-2} M-1.0×10^{-6} M (pH 4.50) and S3 sample prepared in wastewater. (a) 1.0×10^{-2} M (b) 1.0×10^{-3} M (c) 1.0×10^{-4} M (d) 1.0×10^{-5} M (e) 1.0×10^{-6} M

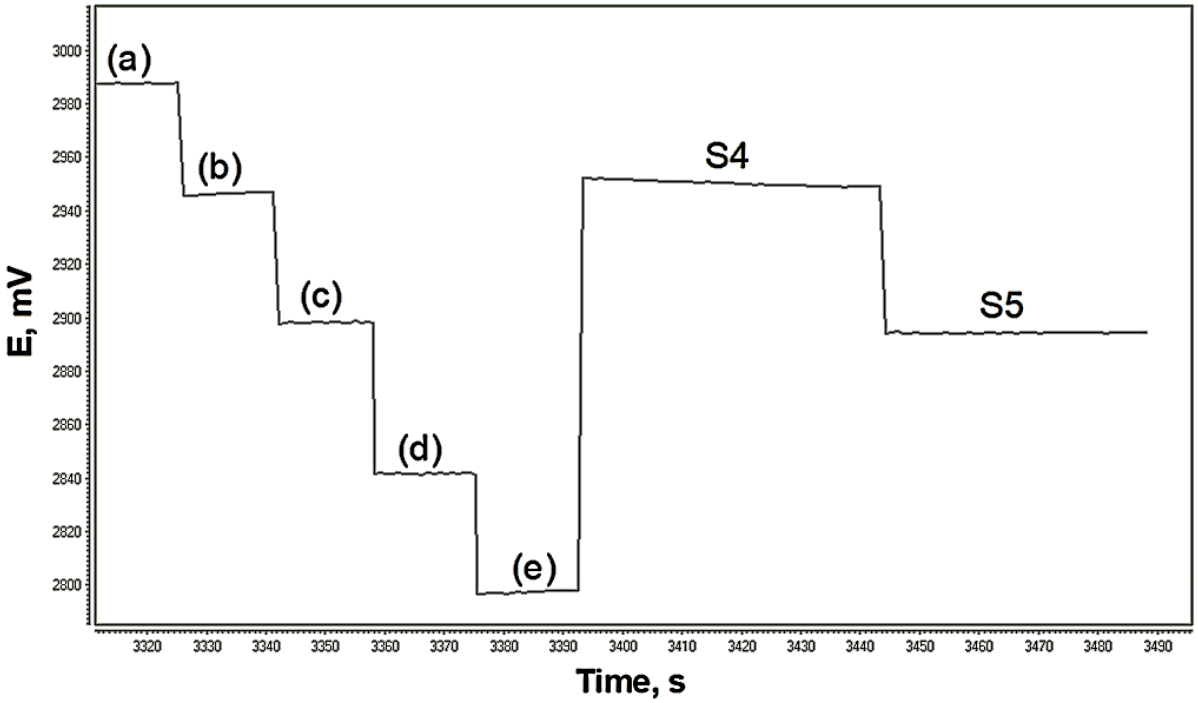

Figure 13. Response of Rhodamine B-selective sensor to Rhodamine B solutions in the concentration range of 1.0×10^{-2} M-1.0×10^{-6} M (pH 4.50), S4 and S5 Van Lake water samples. (a) 1.0×10^{-2} M (b) 1.0×10^{-3} M (c) 1.0×10^{-4} M (d) 1.0×10^{-5} M (e) 1.0×10^{-6} M

Table 5. Statistical evaluation of sample analyses with Rhodamine B-selective sensor using potentiometric analysis results

	Added (mg/mL)	Found (mg/mL)	Recovery (%)	Er (%)
S1 (Tap water)	4.79×10^{-1}	4.69×10^{-1}	97.91	2.09
S2 (Tap water)	4.79×10^{-2}	4.78×10^{-2}	99.79	0.21
S3 (Wastewater)	4.79×10^{-1}	4.65×10^{-1}	97.08	2.92
S4 (Van Lake water)	4.79×10^{-1}	4.83×10^{-1}	100.84	0.83
S5 (Van Lake water)	4.79×10^{-2}	4.77×10^{-2}	99.58	0.41

4. Conclusion

MIL-53 (Al), a metal organic framework, was used as the ionophore in the membrane composition of the Rhodamine B-selective sensor. When compared in terms of potentiometric performance properties, the optimum membrane composition was determined as 6% MIL-53

(Al), 26% PVC, 68% DOS. The response time of the sensor was determined to be less than 5 seconds. The sensor has a life-time of 23 days. The pH range in which the Rhodamine B-selective sensor was not affected by hydronium ions was determined to be 4.49-8.08. The developed Rhodamine B-selective sensor was successfully applied in the studies to determine the 1.0×10^{-3} M and 1.0×10^{-4} M Rhodamine B content in tap water, Van Lake water, and wastewater. The developed sensor has many advantages such as practical, wide linear working range, short response time, economical, sensitivity, low detection limit and high selectivity. In the literature, only one potentiometric sensor has been encountered so far for the determination of Rhodamine B [31]. It is given in comparison with the sensor we developed in Table 6. In this study, the potentiometric sensor we developed for the determination of Rhodamine B is easier to prepare and has a shorter response time.

Table 6. Comparison of the developed sensor with various reported Rhodamine B-selective sensors

Linear Range, M	Response Time, s	Life-time, day	pH Working Range	Detection Limit, M	Reference No
1.0×10^{-6}- 1.0×10^{-3}	8	28	3.00–7.00	5.0×10^{-7}	[31]
1.0×10^{-6}-1.0×10^{-2}	<5	23	4.49-8.08	5.0×10^{-7}	This study

Ethics in Publishing

There are no ethical issues regarding the publication of this study

Author Contributions

The authors contributed equally to the work.

Acknowledgements

We would like to thank Van Yuzuncu Yil University, Scientific Research Projects Coordination Office (Project No = FYL-2023-10450) for their financial support. We thank to Assoc. Prof. Dr. Mustafa Tekpınar for his help to edit the language of the text.

References

[1] Arıbuğa, H., 2022. Demir (III) iyonuna hassas, tiyofen ile modifiye edilmiş rodamin tabanlı yeni tip sensörün sentezi, karakterizasyonu ve uygulamaları. Yüksek lisans tezi, İstanbul Teknik Üniversitesi, Türkiye.

[2] Ünsal, Y. E. 2016. Sudan blue II, rodamin B ve kurkumin boyar maddelerinin ayrılması, zenginleştirilmesi ve spektrofotometrik tayini. Doktora tezi, Gaziosmanpaşa Üniversitesi, Türkiye.

[3] Qi, P., Lin, Z., Li, J., Wang, C., Meng, W., Hong, H., Zhang, X., 2014. Development of a rapid, simple and sensitive HPLC-FLD method for determination of Rhodamine B in chili-containing products, Food Chemistry, 164, 98-103.

[4] Jain, R., Mathur, M., Sikarwar, S., Mittal, A., 2007. Removal of the hazardous dye Rhodamine B through photocatalytic and adsorption treatments. Journal of Environmental Management, 85(4), 956-964.

[5] Sulistina, D. R., Martini, S., 2020. The effect of Rhodamine B on the cerebellum and brainstem tissue of Rattus norvegicus. Journal of Public Health Research, 9(2), 101-104.

[6] Desiderio, C., Marra, C., Fanali, S. 1998. Quantitative analysis of synthetic dyes in lipstick by micellar electrokinetic capillary chromatography. Electrophoresis, 19(8-9), 1478-1483.

[7] Wang, W., Leng, J., Yu, Y., Lu, L., Bai, L., Qiu, X., 2014. An electropolymerized rhodamine B sensing film-based electrochemical sensor for nitrite with high sensitivity and selectivity, International Journal of Electrochemical Science, 9(2), 921-930.

[8] Chiang, T. L., Wang, Y. C., Ding, W. H., 2012. Trace determination of Rhodamine B and rhodamine 6G dyes in aqueous samples by solid-phase extraction and high-performance liquid chromatography coupled with fluorescence detection, Journal of the Chinese Chemical Society, 59(4), 515-519.

[9] Botek, P., PouStka, J., Hajslova, J., 2007. Determination of banned dyes in spices by liquid chromatography-mass spectrometry, Czech Journal of Food Science, 25(1), 17-24.

[10] Alesso, M., Bondioli, G., Talío, M. C., Luconi, M. O., Fernández, L. P., 2012. Micelles mediated separation fluorimetric methodology for Rhodamine B determination in condiments, snacks and candies, Food Chemistry, 134(1), 513-517.

[11] Su, X., Li, X., Li, J., Liu, M., Lei, F., Tan, X., Luo, W., 2015. Synthesis and characterization of core–shell magnetic molecularly imprinted polymers for solid-phase extraction and determination of Rhodamine B in food, Food Chemistry, 171, 292-297.

[12] Soylak, M., Unsal, Y. E., Yilmaz, E., Tuzen, M., 2011. Determination of rhodamine B in soft drink, wastewater and lipstick samples after solid phase extraction, Food and Chemical Toxicology, 49(8), 1796-1799.

[13] Xiao, N., Deng, J., Huang, K., Ju, S., Hu, C., Liang, J., 2014. Application of derivative and derivative ratio spectrophotometry to simultaneous trace determination of Rhodamine B and rhodamine 6G after dispersive liquid–liquid microextraction, Spectrochimica Acta Part A: Molecular and Biomolecular Spectroscopy, 128, 312-318.

[14] Zhu, X., Wu, G., Wang, C., Zhang, D., Yuan, X., 2018. A miniature and low-cost electrochemical system for sensitive determination of Rhodamine B, Measurement, 120, 206-212.

[15] Lin, S., Lin, X., Lou, X. T., Yang, F., Lin, D. Y., Lu, Z. W., 2015. Rapid and sensitive SERS method for determination of Rhodamine B in chili powder with paper-based substrates, Analytical Methods, 7(12), 5289-5294.

[16] Oplatowska, M., Elliott, C. T., 2011. Development and validation of rapid disequilibrium enzyme-linked immunosorbent assays for the detection of Methyl Yellow and Rhodamine B dyes in foods. Analyst, 136(11), 2403-2410.

[17] Mohammed, Q. A. M., 2022. Potansiyometrik ifosfamid-seçici sensör geliştirilmesi ve analitik uygulamaları. Yüksek lisans tezi, Erzincan Binali Yıldırım Üniversitesi, Türkiye.

[18] Özbek, O., Işıldak, Ö., Yiğit, K. M., Çetin, A., 2020. Atık Su Analizlerinde Potansiyometrik Sensörlerin Kullanımı, Turkish Journal of Science and Health, 1(2), 70-78.

[19] Pretsch, E., 2007. The new wave of ion-selective electrodes, TrAC Trends in Analytical Chemistry, 26(1), 46–51.

[20] Ayanoğlu, M. N., 2014. Perklorat ve salisilat anyonlarına duyarlı iyon-seçici elektrotlar hazırlanması. Yüksek lisans tezi, Ankara Üniversitesi, Türkiye.

[21] Asan, A., 2019. İyon-seçici elektrotlar kullanılarak çevre numunelerindeki sularda sertlik tayini, ALKÜ Fen Bilimleri Dergisi, 1(1), 8-19.

[22] Sumida, K., Rogow, D. L., Mason, J. A., McDonald, T. M., Bloch, E. D., Herm, Z. R., Long, J. R., 2012. Carbon dioxide capture in metal–organic frameworks, Chemical Reviews, 112(2), 724-781.

[23] Stock, N., Biswas, S., 2012. Synthesis of metal-organic frameworks (MOFs): routes to various MOF topologies, morphologies, and composites, Chemical Reviews, 112(2), 933-969.

[24] Furukawa, H., Cordova, K. E., O'Keeffe, M., Yaghi, O. M., 2013. The chemistry and applications of metal-organic frameworks, Science, 341(6149), 1230444.

[25] Tu, T. N., Nguyen, M. V., Nguyen, H. L., Yuliarto, B., Cordova, K. E., Demir, S., 2018. Designing bipyridine-functionalized zirconium metal–organic frameworks as a platform for clean energy and other emerging applications, Coordination Chemistry Reviews, 364, 33-50.

[26] Shojaei, F., Zohdi, S. H., Atashi, H., Mirzaei, A. A., 2023. Feasibility study on the use of MIL-53 (Al) as a support for iron catalysts in the CO hydrogenation reaction, Journal of Particle Science and Technology, 9(1), 43-49.

[27] Subasi, Y., Kanberoglu, G. S., Coldur, F., Cubuk, O., Zahmakiran, M., 2022. Development of MOF-based PVC membrane potentiometric sensor for determination of imipramine hydrochloride, Chemical Papers, 76(8), 5105-5117.

[28] Geçgel, C. (2020). Fonksiyonelleştirilmiş metal organik kafes yapıların sentezi, karakterizasyonu ve katalitik etkileri. Doktora tezi, Mersin Üniversitesi, Türkiye.

[29] Johansson, J. O. (2019). Single crystal to single crystal transformations of MIL-53 Metal Organic Frameworks. Master's Thesis, The University of Manchester, England.

[30] Tekce, S., Subasi, Y., Coldur, F., Kanberoglu, G. S., Zahmakiran, M., 2022. Development of a PVC Membrane Potentiometric Sensor with Low Detection Limit and Wide Linear Range for the Determination of Maprotiline in Pharmaceutical Formulations, Chemistry Select, 7(2), 1-8.

[31] Khaled, E., El-Ries, M. A., Zidane, F. I., Ibrahim, S. A., Abd-Elmonem, M. S., 2010. A simple potentiometric sensor for rhodamine B. Sensing in electroanalysis, 5, 127-140.

[32] Buck, R. P., Lindner, E., 1994. Recommendations for nomenclature of ionselective electrodes (IUPAC Recommendations 1994). Pure and Applied Chemistry, 66(12), 2527-2536.

e-ISSN: 2149-4584

Erzincan University Journal of Science and Technology

EJSAT 2025, 18 (3) 951-962

Research Article

Effects of Plant Growth Promoting Rhizobacteria (PGPR) Applications on Biochemical Activity and Enzyme Activity in Strawberries

Mehmet YAMAN[1], Ahmet SÜMBÜL[2*], Ahmet SAY[3]

[1]Erciyes University, Faculty of Agriculture, Department of Horticulture, Kayseri-TÜRKİYE
[2]Sivas Cumhuriyet University, Suşehri Timur Karabal Vocational School, Department of Plant and Animal Production, Sivas-TÜRKİYE
[3]Erciyes University, Faculty of Agriculture, Department of Agricultural Biotechnology, Kayseri-TÜRKİYE

Received: 24/12/2024, **Revised:** 24/01/2025, **Accepted:** 28/01/2025, **Published:** 31/12/2025

Abstract

Plant growth promoting rhizobacteria (PGPR), which have environmentally friendly properties, are important for their use as biofertilizers and biocontrol agents. The aim of this study was to determine the effects of single and combined applications of PGPR bacteria on maloninaldehyde (MDA), proline, superoxide dismutase (SOD), peroxidase (POD) and catalase (CAT) activities of leaves in Albion and Monterey strawberry cultivars. *Bacillus subtilis* OSU-142 (*B. subtilis* OSU-142), *Bacillus megaterium* M3 (*B. megaterium* M3) and *Paenibacillus polymyx* (*P. polymyx*) were used as PGPR in the study. The effect of rhizobacteria varied according to strawberry cultivars. Rhizobacteria applications showed positive effects on MDA, SOD and POD. However, rhizobacteria treatments did not have a significant effect on proline, while they showed a varying effect on CAT according to the cultivars. In this study, significant results were obtained on the effects of strawberry and rhizobacteria application on biochemical activity and enzymatic activity. The results of this study may provide important clues for future studies on similar subjects.

Keywords: Strawberry, enzyme activity, antioxidant enzyme, rhizobacteria, PGPR

Bitki Büyümesini Teşvik Eden Rizobakteri (PGPR) Uygulamalarının Çileklerde Biyokimyasal Aktivite ve Enzim Aktivitesi Üzerine Etkileri

Öz

Çevre dostu özelliğe sahip olan bitki büyümesini teşvik eden rizobakteriler (PGPR), biyogübre ve biyokontrol ajanı olarak kullanımıyla önem arz etmektedir. Bu çalışmanın amacı, Albion ve Monterey çilek çeşitlerinde PGPR bakterilerinin tekli ve kombine uygulamalarının yaprakların maloninaldehit (MDA), prolin, süperoksit dismutaz (SOD), peroksidaz (POD) ve katalaz (CAT) aktiviteleri üzerine etkilerini belirlemektir. Çalışmada *Bacillus subtilis* OSU-142 (*B. subtilis* OSU-142), *Bacillus megaterium* M3 (*B. megaterium* M3) ve *Paenibacillus polymyx* (*P. polymyx*) PGPR olarak kullanılmıştır. Rizobakterilerin etkisi çeşitlere göre değişiklik göstemiştir. Rizobakteri uygulamaları MDA, SOD ve POD üzerinde olumlu etki göstermiştir. Ancak rizobakteri uygulamalarının prolin üzerinde önemli derecede bir etkisi görülmez iken CAT üzerinde ise çeşitlere göre değişen etki göstermiştir. Bu çalışmada, çilekte rizobakteri uygulamasının biyokimyasal ve enzimatik aktivite üzerindeki etkileri konusunda çok önemli sonuçlar elde edilmiştir. Bu çalışmanın sonuçları gelecekte bu konuda yapılacak çalışmalar için önemli ipuçları sağlayabilir.

Anahtar Kelimeler: Çilek, enzim aktivitesi, antioksidan enzim, rizobakteri, PGPR

Corresponding Author: asumbul3188@gmail.com

Cite this Article: Erzincan University Journal of Science and Technology 2025, 18(3) 951-962. https://doi.org/10.18185/erzifbed.1606768

1. Introduction

Türkiye is among the important countries in the world in terms of fruit growing due to its different climate and soil conditions. Many of the fruit species grown in Türkiye are of commercial importance. One of these fruit species is strawberry (*Fragaria x ananassa* Duch). Strawberry, which is one of the temperate climate fruit species, is grown almost everywhere in the world within wide ecological boundaries from Ecuador to Siberia thanks to its high adaptability. Strawberry is an important berry fruit that is consumed with pleasure by people and has a great market advantage as fresh and industrial [1].

Strawberries are one of the most important sources of bioactive substances that are important for healthy nutrition, such as vitamins, minerals, sugars, anthocyanins, phenols, flavonoids and antioxidants. Thanks to its high biochemical content and antioxidant potential, strawberries provide a direct effect against diseases such as cardiovascular and cardiometabolic diseases [2]. Strawberry fruits are an important fruit due to their antioxidant, anti-inflammatory, antihyperlipidemic and blood pressure lowering effects [3].

With the understanding of the importance of strawberries in human nutrition, the demand for strawberry fruits is increasing day by day. In response to the increasing demand for strawberries, the use of chemical fertilizers and chemical pesticides is becoming widespread to increase yield and quality. Indiscriminate use of chemical fertilizers causes air, water and soil pollution and is dangerous for human health. Indiscriminate use of chemical fertilizers causes air, water and soil pollution and is dangerous for human health. Alternative production systems that are more environmentally friendly and conducive to soil health are urgently needed [4]. Plant growth-promoting microorganisms are generally classified as biofertilisers, which increase nutrient levels in the plant; phyto-stimulants, which promote plant growth by producing plant hormones; root cleaners, which break down resistant toxic pollutants; and biopesticides, which control disease by producing antibiotic and antifungal metabolites. The application of environmentally friendly and soil-friendly biofertilisers and biocontrol agents in agriculture has increased in recent years [5].

Soil microorganisms improve nutrient uptake by plants and have great potential when used as biofertilizers. Free-living microorganisms used as biological control agents or biofertilizers are known as PGPR [6]. PGPR are free-living organisms in the soil and are very beneficial in plant production. These rhizobacteria generally belong to the species Pseudomonas spp., Azospirillum spp., Burkholderia spp., Bacillus spp., Enterobacter spp., Rhizobium spp., Erwinia spp., Serratia spp., Alcaligenes spp., Arthrobacter spp., Acinetobacter spp. and Flavobacterium spp. [7]. Rhizobacteria have many benefits on plant growth and productivity. Rhizobacteria increase plant growth by increasing nutrients in plants. They especially increase nitrogen fixation [8] and phosphorus solubility [9]. In recent years, the use of rhizobacteria in sustainable agriculture has increased to increase soil fertility, improve agricultural products and reduce the negative effects of chemical fertilizers on the environment [10]. In addition, rhizobacteria increase the resistance of plants against biotic and abiotic stress conditions such as water stress [11], high temperature [12], low temperature [13], salinity [14], lime [15], heavy metal [16] and biotic factors [17].

Plants are exposed to abiotic (frost, salinity, high temperature, drought, etc.) and biotic (pathogens, competition between organisms) stress factors. Abiotic and biotic stress factors reduce the biosynthetic capacity of plants and cause plant death as the effect of stress increase [18]. When plants are exposed to stress, they try to protect themselves from the negative effects of stress by activating various metabolic, physiological and biochemical mechanisms [19, 20]. Plant cells produce oxygen radicals and their derivatives, reactive oxygen species (ROS), during various processes associated with abiotic stress. ROS production, one of the most important consequences of abiotic stress, disrupts the balance between both enzymatic and non-enzymatic antioxidant defence systems and causes oxidative stress in plants [19]. ROS are highly reactive and damage biomolecules such as lipids, proteins and nucleic acids [21]. Plants have developed an effective antioxidant system to protect against the effects of oxidative stress [22].

The aim of this study was to investigate the effects of single and combined applications of PGPR bacteria (*B. subtilis* OSU-142, *B. megaterium* M3, *P. polymyx*) on MDA, proline, SOD, POD and CAT activities in the leaves of Albion and Monterey strawberry cultivars.

2. Material and Methods

Plant Material

Albion and Monterey strawberry cultivars (*Fragaria x ananassa* Duch), which constitute the study material, were selected from the open growing area in Develi district of Kayseri province in 2023. The study was carried out in three replications and ten plants were used for each replication. The leaf samples were transported to the laboratory in cold chain and stored at -80 °C until analysis.

Methods

In the study, *B. megaterium* M3, *B. subtilis* OSU-142, *P. polymyxa* species were used as bacteria. All bacterial strains were obtained from Dr. Metin Turan (Istanbul Yeditepe University, Faculty of Engineering and Architecture, Department of Genetics and Bioengineering culture collection). Bacteria were grown on nutrient agar by line plate inoculation method and kept at 27 °C for 48 h. At the end of this period, a single colony was taken from the cultures that completed growth and transferred to bottles containing 250 ml nutrient broth. Bacteria were grown aerobically in flasks on a rotating shaker (150 rpm) for 48 h at 27 °C. Then, bacterial suspensions were diluted in sterile distilled water to a final concentration of 108 CFU mL^{-1}. The bacterial suspensions obtained were applied to soil as 10 mL for each bacterial species in Albion and Monterey varieties. Bacterial species *B. megaterium* M3, *B. subtilis* OSU-142 and *P. polymyxa* PGPR were applied as single applications. Also, a mixture of equal amounts of these three bacterial species was applied as a mixed application. Bacterial applications were applied to the root areas of the plants from the soil. This study was carried out as four bacterial treatments and one control group application.

Lipid peroxidation (MDA) analysis: 0.5 g of fresh leaf sample was homogenized with 10 mL of 0.1% trichloroacetic acid (TCA) solution and then centrifuged at 10000 rpm for 10 min. 1 ml of the obtained supernatant was transferred to the tubes and 4 mL of 20% TCA and 0.5% thiobarbituric acid (TBA) were added to the tubes. The obtained mixture was kept in a water

bath at 95℃ for 30 minutes and then the samples were quickly cooled in ice. The cooled samples were centrifuged at 10000 rpm for 10 minutes. The absorbance of the supernatant formed in the tubes after centrifugation was read at 532 and 600 nm wavelengths on a spectrophotometer. Lipid peroxidation was calculated as nmol/g Maloninaldehyde (MDA) with the formula MDA= (A532- A600) x Extract volume (ml) / (155mM/cm x Sample amount (mg)) (Stresty and Rao, 1999).

Proline analysis: Proline analysis was determined by modifying the method specified by [23]. For the analysis, 0.5 g of leaf sample was pulverized in liquid nitrogen. The pulverized samples were taken into tubes and then mixed with 3 ml of 3% sulfosalicic acid solution. The mixture obtained was centrifuged at 15000 rpm for 10 minutes at room temperature. After transferring 2 ml of the supernatant to each tube, two parallels were performed for each tube. 2 ml of glacial acetic acid and 2 ml of acetic acid with phosphoric acid and ninhydrin solution were added to the tubes. The tubes were boiled for one hour and then subjected to a rapid cooling process in ice water. 4 ml of toluene was added to the cooled tubes and vortexed for 30 seconds. Then it was kept for 5 min and the absorbance of the pink phase formed at the top was read at 520 nm wavelength in a spectrophotometer. Proline contents were determined using the equation of the standard graph.

Preparation of extracts for measurement of SOD, POD and CAT analysis activities: 0.5 g of fresh leaf samples were homogenized in 5 ml of 50 mM phosphoric buffer (pH: 7.0). Homogenates were centrifuged at 15000 rpm for 15 min at 4℃. Obtained supernatants were stored at -80℃ for determination of enzyme activities [24].

SOD, POD & CAT analysis: Frozen samples were pulverized using liquid nitrogen. 1 mM ethylenediaminetetraacetic acid (EDTA) was extracted with cold 0.1 mM phosphate buffer (pH 7.8) containing 1 mM phenylmethanesulfonylfluoride (PMSF) and 0.5% polyvinylpyrrolidone (PVP). Spectrophotometry was used to determine CAT, POD and SOD enzymatic activities in apoplastic fractions of samples. CAT activity was measured by monitoring the decrease in absorbance at 240 nm in a solution of 50 mM phosphate buffer (pH 7.5) containing 20 mM H_2O_2. One unit of CAT activity is defined as the amount of enzyme using 1 μmol of H_2O_2 per minute. POD activity was evaluated by observing the increase in absorbance at 470 nm. The reaction mixture for POD activity measurement consisted of 50 mM phosphate buffer (pH: 5.5) containing 1 mM guaiacol and 0.5 mM H_2O_2. One unit of POD activity was defined as the amount of enzyme causing an absorbance increase of 0.01 per minute. SOD activity in apoplastic fractions was estimated by recording the decrease in optical density of the nitro-blue tetrazolium dye by the enzyme. Absorbance values were determined at 560 nm wavelength. One unit of enzyme activity was defined as the amount of enzyme required to reduce the absorbance reading by 50% compared to tubes without enzyme. Antioxidant enzyme activity results were expressed as enzyme units (EU) per gram of leaf fresh weight (fw).

Data Analysis

In order to determine the differences between the parameters examined in the study, the data were subjected to analysis of variance (ANOVA). Differences between means were compared

with Tukey's multiple comparison test. Heatmap and principal component analysis of the data were performed using the JMP PRO 17 statistical package program.

3. Results and Disscussion

The effects of bacterial applications on biochemical (MDA and proline) and antioxidant enzyme activities (SOD, POD and CAT) in the leaves of Albion and Monterey strawberry cultivars are given in Table 1. Biochemical and antioxidant enzyme activities of leaves differed according to strawberry cultivars. The effect of bacterial applications on the examined parameters was found to be statistically significant ($p<0.05$).

In the control application, the MDA content of the leaves was determined as 14.49 nmol/g in the Albion variety, while it was determined as 8.41 nmol/g in the Monterey variety. The effect of bacterial applications varied according to varieties. The highest MDA content was detected in *P. polymyxa* bacterial application in both varieties. The highest MDA content was determined as 19.27 nmol/g in the Albion variety. The lowest MDA content was observed in *B. megaterium* M3 (6.65 nmol/g) treatment in Albion variety and in *B. subtilis* OSU-142 (13.98 nmol/g) treatment in Monterey variety. The lowest MDA content was observed in application of *B. megaterium* M3 (6.65 nmol/g) in Albion variety and in application of *B. subtilis* OSU-142 (13.98 nmol/g) in Monterey variety. MDA, which is an important marker for determining the degree of membrane damage due to oxidative stress in plants under abiotic stresses is a product of lipid peroxidation accumulated in plant tissues under stress conditions [25]. High MDA concentration in plant tissues is associated with oxidative damage of plant cell membranes [26]. High MDA content in plants indicates that the plant is sensitive to stress, while low MDA content in plants indicates that the plant is resistant to stress [27]. Decreasing MDA content due to increased antioxidant enzyme activities in plant tissues helps the plant survive under stress conditions [28, 29]. Rhizobacteria applications were reported to reduce MDA content in rice by [30], in wheat by [31], in strawberry by [32] and [15]. In general, the effect of bacterial applications on MDA content varied according to strawberry varieties. In the Albion variety, bacterial applications (except for the *P. polymyxa* bacterial application) showed lower values than control application, while in the Monterey variety, the control application showed lower values than bacterial applications.

The proline contents of the leaves were similar in both varieties in the control application. The effect of bacterial applications varied according to varieties. *B. megaterium* M3 (0.11 mg/g) application in Albion variety and *P. polymyxa* (0.11 mg/g) application in Monterey variety showed the highest proline content. Other bacterial applications generally showed similar results to the control application in varieties. Plants provide tolerance to stress factors with the help of osmotic regulators [33]. Plants minimize damage to cells by accumulating osmolytes in cells and thus aim to adapt to stress. Osmotic regulation mechanisms protect plants from stress by osmotic adjustments through detoxifying reactive oxygen species (ROS), stabilizing membranes, and natural structures of enzymes and proteins [34]. Proline, one of the important osmolytes for plants, provides protection of the cell against ROS accumulation in the cell and regulates the redox homeostasis of the cell [35]. The cellular level of proline varies between species and depends on the severity and duration of the stress situation [36]. Some studies

reported that rhizobacteria applications increased proline content [37, 38] and some studies reported that rhizobacteria applications decreased proline content [31, 39]. It has also been reported that rhizobacteria application decreases proline concentration and increases defence enzymes against stress [40]. As a result, our study findings are consistent with the literature.

SOD activity of leaves was determined between 117.01 EU/g plant (Albion) and 148.10 EU/g plant (Monterey) in control applications. In Albion variety, *P. polymyxa* (162.73 EU/g plant) and *B. megaterium* M3 (159.87 EU/g plant) bacteria applications showed the highest values, while in Monterey variety, *B. megaterium* M3 (187.77 EU/g plant) and *P. polymyxa* (186.53 EU/g plant) bacteria applications showed the highest values. Mix application showed the lowest SOD activity values in both varieties. The lowest SOD activity was determined as 98.28 EU/g plant in Albion variety and 104.91 EU/g plant in Monterey variety. In general, SOD activity showed lower values in Albion variety. POD activity of leaves was determined between 242.00 EU/g plant (Monterey) and 2266.67 EU/g plant (Albion) in control applications. In general, POD activity in bacterial applications showed higher values in Albion cultivar compared to Monterey cultivar. The highest POD activity was detected in Mix bacteria application (7071.10 EU/g plant) in Albion variety, while it was detected in *P. polymyxa* bacteria application (2033.33 EU/g plant) in Monterey variety. In the Albion variety, lower POD activity was detected in the *P polymyxa* and B subtilis OSU-142 bacterial applications compared to the control, while in the Monterey variety, lower POD activity was detected in the control application compared to the bacterial applications. In control applications, the CAT activity of leaves was found to be highest in the Albion variety (5806.00 EU/g plant) and lowest in the Monterey variety (2966.00 EU/g plant). The effects of bacterial applications on CAT activity differed according to the varieties. In Albion variety, the highest CAT activity was determined in *B. megaterium* M3 treatment (5402.00 EU/g plant) and the lowest CAT activity was determined in *P. polymyxa* treatment (1598.00 EU/g plant), while in Monterey variety, the highest CAT activity was determined in *P. polymyxa* treatment (6190.00 EU/g plant) and the lowest CAT activity was determined in *B. subtilis* OSU-142 treatment (140.00 EU/g plant). Plants exposed to stress can overcome oxidative stress by activating antioxidant defense systems [41, 42]. Antioxidant enzymes such as SOD, POD and CAT protect plants against oxidative stress (Khan et al. 2019a). Although some researchers reported that rhizobacteria applications increased antioxidant enzyme activities [15, 28, 31, 32, 43], some researchers reported that rhizobacteria applications decreased antioxidant enzyme activities [30]. The degree of increase in antioxidant enzyme activity and antioxidant content under stress varies significantly among many plant species and even between two varieties of the same species. The degree of response of plants depends on the plant species, growth, metabolic status, intensity and duration of stress [18, 44]. According to our study results, antioxidant enzymes varied according to varieties and rhizobacteria applications. In general, rhizobacteria applications showed positive effects on SOD and POD activities, but showed varying effects on CAT activities. This situation can be explained by the fact that high SOD activity can inactivate CAT activity [45].

Table 1. Effects of rhizobacteria applications on leaf biochemical and antioxidant enzyme activities

		MDA (nmol/g)	Prolin (mg/g)	SOD (EU/g plant)	POD (EU/g plant)	CAT (EU/g plant)
Albion	Control	14.49±0.10 b	0.09±0.00 b	117.01±1.49 c	2266.67±41.63 c	5806.00±223.72 a
	P. polymyxa	19.27±0.13 a	0.09±0.00 b	162.73±1.17 a	1486.67±30.55 e	1598.00±90.27 e
	B. subtilis OSU-142	9.33±0.16 c	0.07±0.00 c	151.35±3.41 b	1826.67±30.55 d	4662.00±89.60 c
	B. megaterium M3	6.65±0.17 d	0.11±0.00 a	159.87±0.81 a	4333.33±128.58 b	5402.00±12.00 b
	Mix	9.31±0.21 c	0.07±0.00 c	98.28±1.00 d	7071.10±3.81 a	3188.00±104.84 d
Monterey	Control	8.41±0.10 c	0.08±0.00 b	148.10±0.20 c	242.00±3.46 e	2966.00±96.99 bc
	P. polymyxa	16.43±0.04 a	0.15±0.00 a	186.63±5.14 a	2033.33±80.83 a	6190.00±90.27 a
	B. subtilis OSU-142	13.98±0.15 b	0.07±0.00 c	156.88±0.85 b	473.33±64.29 d	140.00±17.32 d
	B. megaterium M3	14.30±0.39 b	0.07±0.00 c	187.77±0.49 a	1493.33±80.83 b	3054.00±41.57 b
	Mix	14.39±0.23 b	0.07±0.00 c	104.91±0.63 d	693.33±11.55 c	2626.00±289.14 c

The heatmap analysis and principal component analysis graphs of the parameters examined in the study are presented in Figure 1. Heatmap and principal component analysis graphs were made to reveal the effectiveness of bacterial applications according to the examined parameters. In the heatmap analysis, the color intensity changing from blue to red indicates that the values of the bacteria related to the examined parameters have increased. According to the hetmap analysis, rhizobacteria applications were divided into two groups. *P. polymyxa* was grouped separately from other rhizobacteria applications. *P. polymyxa* showed high values on MDA, proline, SOD, while it showed partially high values on CAT. *B. megaterium* M3 rhizobacteria showed high effect on SOD and CAT activitiy, control application showed high effect on CAT activity and Mix application showed high effect on POD activity. In general, the effect of B. subtilis OSU-142 rhizobacteria on the examined parameters was not high.

The principal component analysis plot shows positive correlation between narrow-angle features and negative correlation between wide-angle features [46]. According to the principal component analysis graph, it can be said that POD activity and other parameters show a negative correlation among the examined parameters.

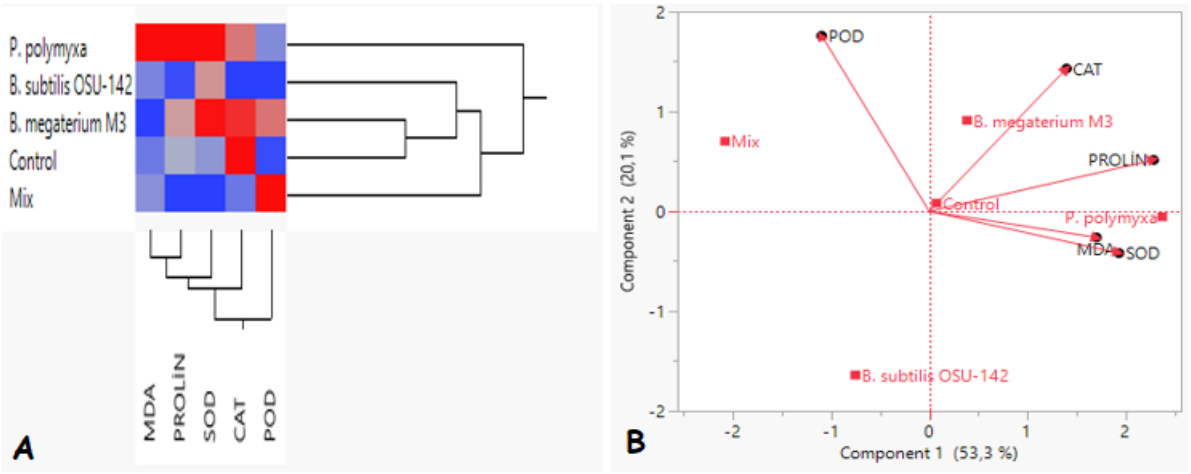

Figure 1. Heatmap and PCA analysis graph of the investigated parameters of bacteria applications (A: Heatmap analysis, B: PCA analysis graph of two components)

4. Conclusion

The effects of rhizobacteria applications in the study vary according to the varieties. However, rhizobacteria applications showed different levels of positive effects on MDA, proline and

antioxidant enzymes (SOD, POD and CAT). As a result of the study, it was concluded that plant growth-promoting rhizobacteria applications can be used as biofertilizers and biocontrol agents in strawberries. In order to fully reveal the effects of using rhizobacteria on strawberries, different bacterial species and mixtures need to be tested on different varieties. The information obtained as a result of the study will shed light on future studies on similar subjects.

Ethics in Publishing

There are no ethical issues regarding the publication of this study

Author Contributions

All authors contributed to the design of the study, collection of data, evaluation of the results, and writing of the article.

References

[1] Amil-Ruiz, F., Blanco-Portales, R., Munoz-Blanco, J., Caballero, J.L., (2011) The strawberry plant defense mechanism: A molecular review, Plant and cell physiology, 52(11), 1873-1903.

[2] Koraqi, H., Petkoska, A. T., Khalid, W., Sehrish, A., Ambreen, S., Lorenzo, J. M., (2023) Optimization of the extraction conditions of antioxidant phenolic compounds from strawberry fruits (*Fragaria x ananassa* Duch.) using response surface methodology. Food Analytical Methods, 16(6), 1030-1042.

[3] Basu, A., Nguyen, A., Betts, N.M. Lyons, T.J. 2014. Strawberry as a functional food: an evidence-based review. Critical Reviews in Food Science and Nutrition, 54, 790-806

[4] Ali, S., Moon, Y. S., Hamayun, M., Khan, M. A., Bibi, K., & Lee, I. J. (2022). Pragmatic role of microbial plant biostimulants in abiotic stress relief in crop plants. Journal of Plant Interactions, 17(1), 705-718.

[5] Arikan, S., Ipek, M., Pirlak, L., (2016). Effect of some plant growth promoting rhizobacteria (PGPR) on growth, leaf water content and membrane permeability of two citrus rootstock under salt stress condition. In Proceedings of the VII International Scientific Agriculture Symposium, Jahorina, Bosnia and Herzegovina, 6–9 October 2016; 845–850.

[6] Verma, P. P., Shelake, R. M., Das, S., Sharma, P., Kim, J. Y., (2019). Plant growth-promoting rhizobacteria (PGPR) and fungi (PGPF): potential biological control agents of diseases and pests. Microbial Interventions in Agriculture and Environment: Volume 1: Research Trends, Priorities and Prospects, 281-311.

[7] Adeyemi, N. O., Atayese, M. O., Olubode, A. A., Akan, M. E., (2020). Effect of commercial arbuscular mycorrhizal fungi inoculant on growth and yield of soybean under controlled and natural field conditions. Journal of Plant Nutrition, 43(4), 487-499.

[8] Fukami, J., de la Osa, C., Ollero, F. J., Megías, M., Hungria, M., (2017). Co-inoculation of maize with *Azospirillum brasilense* and *Rhizobium tropici* as a strategy to mitigate salinity stress. Functional Plant Biology, 45(3), 328-339.

[9] Soumare, A., Boubekri, K., Lyamlouli, K., Hafidi, M., Ouhdouch, Y., Kouisni, L., (2020). From isolation of phosphate solubilizing microbes to their formulation and use as biofertilizers: status and needs. Frontiers in bioengineering and biotechnology, 7, 425.

[10] Yaman, M., Yildiz, E., Sumbul, A., Ercisli, S., Sonmez, O., Gunes, A., Say, A., Kece, Y.M., Unsal, H. T. (2023). The Effect of PGPR Applications on Bioactive Content and Fruit Characteristics of Different Apple Scion–Rootstock Combinations. Erwerbs-Obstbau, 65(5), 1267-1273.

[11] Paliwoda, D., Mikiciuk, G., Mikiciuk, M., Kisiel, A., Sas-Paszt, L., Miller, T., (2022). Effects of rhizosphere bacteria on strawberry plants (*Fragaria× ananassa* Duch.) under water deficit. International Journal of Molecular Sciences, 23(18), 10449.

[12] Meena, H., Ahmed, M. A., Prakash, P., (2015). Amelioration of heat stress in wheat, *Triticum aestivum* by PGPR (*Pseudomonas aeruginosa* strain 2CpS1). Biosci Biotechno Res, 8(2), 171-174.

[13] Zubair, M., Hanif, A., Farzand, A., Sheikh, T. M. M., Khan, A. R., Suleman, M., Gao, X. (2019). Genetic screening and expression analysis of psychrophilic Bacillus spp. reveal their potential to alleviate cold stress and modulate phytohormones in wheat. Microorganisms, 7(9), 337.

[14] Sangiorgio, D., Cellini, A., Spinelli, F., Donati, I., (2023). Promoting strawberry (*Fragaria× ananassa*) stress resistance, growth, and yield using native bacterial biostimulants. Agronomy, 13(2), 529.

[15] Arıkan, Ş., İpek, M., Eşitken, A., Pırlak, L., Dönmez, M. F., Turan, M., (2020). Plant growth promoting rhizobacteria mitigate deleterious combined effects of salinity and lime in soil in strawberry plants. Journal of Plant Nutrition, 43(13), 2028-2039.

[16] Kang, S. M., Asaf, S., Khan, A. L., Lubna, Khan, A., Mun, B. G., Lee, I. J., (2020). Complete genome sequence of *Pseudomonas psychrotolerans* CS51, a plant growth-promoting bacterium, under heavy metal stress conditions. Microorganisms, 8(3), 382.

[17] Lee, B. D., Dutta, S., Ryu, H., Yoo, S. J., Suh, D. S., Park, K., (2015). Induction of systemic resistance in Panax ginseng against *Phytophthora cactorum* by native *Bacillus amyloliquefaciens* HK34. Journal of Ginseng Research, 39(3), 213-220.

[18] Kalefetoğlu, T., Ekmekci, Y., (2005). The effects of drought on plant sand tolerance mechanisms. Gazi University Journal of Science, 18(4), 723-740.

[19] Hasanuzzaman, M., Bhuyan, M. H. M. B., Zulfiqar, F., Raza, A., Mohsin, S.M., Mahmud, J.A., Fotopoulos, V., (2020). Reactive Oxygen Species and Antioxidant Defense in Plants under Abiotic Stress: Revisiting the Crucial Role of a Universal Defense Regulator. Antioxidants, 9(8), 681.

[20] Giordano, M., Petropoulos, S.A., Rouphael, Y., (2021). Response and defence mechanisms of vegetable crops against drought, heat and salinity stress. Agriculture 11(5):463.

[21] Apel, K., Hirt, H., (2004). Reactive oxygen species: metabolism, oxidative stress, and signal transduction. Annu. Rev. Plant Biol., 55(1), 373-399.

[22] Ahmad, P., Kumar, A., Ashraf, M., Akram, N. A., (2012). Salt-induced changes in photosynthetic activity and oxidative defense system of three cultivars of mustard (*Brassica juncea* L.). African Journal of Biotechnology, 11(11), 2694.

[23] Karabal, E., Yücel, M., Öktem, H.A., (2003). Antioxidant responses of tolerant and sensitive barley cultivars to boron toxicity. Plant Sci 164:925–933

[24] Wang, S., Liang, D., Li, C., Hao, Y., Ma, F., Shu, H., (2012). Influence of drought stress on the cellular ultrastructure and antioxidant system in leaves of drought-tolerant and drought-sensitive apple rootstocks. Plant Physiology and Biochemistry, 51: 81-89.

[25] Kar, M., Öztürk, N., (2020). The evulation of stress related gene expression level and relationship to cellular H_2O_2 in chickpea (*Cicer arietinum* L.) under copper stress. Bursa Uludağ Üniversitesi Ziraat Fakültesi Dergisi, 34(2), 303-315.

[26] Assaha, D. V. M., Liu Li Yun, L. L., Mekawy, A. M. M., Ueda, A., Nagaoka, T., Saneoka, H., (2015). Effect of salt stress on Na accumulation, antioxidant enzyme activities and activity of cell wall peroxidase of huckleberry (*Solanum scabrum*) and eggplant (*Solanum melongena*).

[27] Koca, H., Bor, M., Özdemir, F., & Türkan, İ. (2007). The effect of salt stress on lipid peroxidation, antioxidative enzymes and proline content of sesame cultivars. Environmental and experimental Botany, 60(3), 344-351.

[28] Karagöz, H., Çakmakçi, R., Hosseinpour, A., Kodaz, S., (2018). Alleviation of water stress and promotion of the growth of sugar beet (*Beta vulgaris* L.) plants by multi-traits rhizobacteria. Applied Ecology and Environmental Res. 16(5):6801-6813.

[29] Yassin, M., El Sabagh, A., Mekawy, A. M. M., Islam, M. S., Hossain, A., Barutcular, C., Saneoka, H., (2019). Comparative performance of two bread wheat (*Triticum aestivum* L.) genotypes under salinity stress. Applied Ecology & Environmental Research, 17(2).

[30] Jha, Y., Subramanian, R. B., (2014). PGPR regulate caspase-like activity, programmed cell death, and antioxidant enzyme activity in paddy under salinity. Physiology and Molecular Biology of Plants, 20, 201-207.

[31] Khan, N., Bano, A., Babar, M. A. (2019). The stimulatory effects of plant growth promoting rhizobacteria and plant growth regulators on wheat physiology grown in sandy soil. Archives of microbiology, 201(6), 769-785.

[32] Erdogan, U., Çakmakçi, R., Varmazyarı, A., Turan, M., Erdogan, Y., Kıtır, N., (2016). Role of inoculation with multi-trait rhizobacteria on strawberries under water deficit stress. Zemdirbyste-Agriculture, 103(1), 67-76.

[33] Ahmed, C. B., Rouina, B. B., Boukhris, M., (2008). Changes in water relations, photosynthetic activity and proline accumulation in one-year-old olive trees (*Olea europaea* L. cv. Chemlali) in response to NaCl salinity. Acta Physiologiae Plantarum, 30, 553-560.

[34] Farooq, M., Wahid, A., Kobayashi, N., Fujita, D., Basra, S., (2009). Plant drought stress: effects, mechanisms and management. In: Lichtfouse E, Navarrete M, Debaeke P, Souchère V, Alberola C (eds) Sustainable agriculture. Springer, Berlin, pp 153–188

[35] Sharma, S., Villamor, J.G., Verslues, P.E., (2011). Essential role of tissue specific proline synthesis and catabolism in growth and redox balance at low water potential. Plant Physiol 157(1):292–304.

[36] Delauney, A.J., Verma, D.P.S., (1993). Cloning of ornithine δ-aminotransferase cDNA from *Vigna aconitifolia* by trans-complementation in Escherichia coli and regulation of proline biosynthe sis. Plant J 4:215–223

[37] Matysik, J., Alia, Bhalu, B., Mohanty, P., (2002). Molecular mechanisms of quenching of reactive oxygen species by proline under stress in plants. Current Science, 525-532.

[38] Nawaz, S., Bano, A., (2020). Effects of PGPR (*Pseudomonas* sp.) and Ag-nanoparticles on enzymatic activity and physiology of cucumber. Recent patents on food, nutrition & agriculture, 11(2), 124-136.

[39] Khan, N., Bano, A., Rahman, M.A., Guo, J., Kang, Z., Babar, M.A., (2019). Comparative physiological and metabolic analysis reveals a complex mechanism involved in drought tolerance in chickpea (*Cicer arietinum* L.) induced by PGPR and PGRs. Sci Rep 9(1):2097

[40] Singh, R.P., Jha, P.N., (2017). The PGPR *Stenotrophomonas maltophilia* SBP-9 augments resistance against biotic and abiotic stress in wheat plants. Front Microbiol 8:1945

[41] Jung, S. (2004). Variation in antioxidant metabolism of young and mature leaves of Arabidopsis thaliana subjected to drought. Plant Sci., 166; 459-466.

[42] Pinheiro, H. A., DaMatta, F. M., Chaves, A. R. M., Fontes, E. P. B., Loureiro, M. E., (2004). Drought tolerance in relation to protection against oxidative stress in clones of *Coffea canephora* subjected to long-term drought. Plant Sci., 167; 1307-1314.

[43] Yıldız, E., Yaman, M., Say, A., (2023). Effects of Rhizobacteria Application on Enzyme Activity of Different Apple Scion–Rootstock Combinations. Current Trends in Natural Sciences, 12(23), 42-48.

[44] Alexieva, V., Ivanov, S., Sergiev, I., Karanov, E., (2003). Interaction between stresses. Bulg. J. Plant Physiol, 29(3- 4), 1-17.

[45] Azarmi, F., Mozafari, V., Abbaszadeh Dahaji, P., Hamidpour, M., (2016). Biochemical, physiological and antioxidant enzymatic activity responses of pistachio seedlings treated with plant growth promoting rhizobacteria and Zn to salinity stress. Acta physiologiae plantarum, 38, 1-16.

[46] Garazhian, M., Gharaghani, A., Eshghi, S., (2020). Genetic diversity and inter-relationships of fruit bio-chemicals and antioxidant activity in Iranian wild blackberry species. Scientific Reports, 10(1), 18983.

e-ISSN: 2149-4584

Erzincan University Journal of Science and Technology

EJSAT 2025, 18 (3) 963-980

Research Article

Synthesis, X-ray Crystallography, Hirshfeld Surface, FT-IR, UV-Vis and DFT Studies of 2,6-Diaminopyridinium Saccharinate

Serkan GÜNEY [1*]

[1*] Ordu University, Ulubey Vocational Higher School, Ordu, Turkey

Received: 25/06/2025, **Revised:** 01/10/2025, **Accepted:** 16/10/2025, **Published:** 31/12/2025

Abstract

In this study, Density Functional Theory (DFT) was employed to explore the molecular geometry, vibrational behavior (FT-IR, UV-Vis spectra), and electronic features (HOMO–LUMO energy levels) of 2,6-diaminopyridinium saccharinate (HDAPYSAC). Computational studies were performed using the B3LYP exchange–correlation functional in conjunction with the 6–311G(d,p) basis set. Structural data obtained from single-crystal X-ray diffraction confirmed that HDAPYSAC, consisting of saccharinate and diaminopyridinium moieties, crystallizes in the orthorhombic crystal system and belongs to the *Fdd2* space group. To further investigate the nature of intermolecular interactions and electron density distribution, Hirshfeld surface mapping and two-dimensional fingerprint plot analyses were carried out. The most significant intermolecular contacts were H···H (32.5%), H···O/O···H (31.7%), H···C/C···H (16.5%), H···N/N···H (7.4%), C···C (5.5%), C···O/O···C (3.0%), and C···N/N···C (2.6%). The calculated HOMO–LUMO energy gap of 3.5661 eV indicates a stable molecular structure. UV–Visible spectroscopy revealed six distinct absorption bands at 276.33, 211.26, 200.10, 173.21, 164.35, and 163.62 nm, corresponding to indirect and direct transition energies of 36188, 47335, 49975, 57733, 60846, and 61117 cm^{-1}, respectively.

Keywords: FT-IR, UV-Vis, Crystal structure, Hirshfeld surface analysis

2,6-Diaminopiridinyum Sakkarinatın Sentezi, X-ışını Kristalografisi, Hirshfeld Yüzey Analizi, FT-IR, UV-Vis ve DFT Çalışmaları

Öz

Bu çalışmada, 2,6-diaminopiridinyum sakkarinat (HDAPYSAC) bileşiğinin moleküler yapısı, titreşimsel özellikleri (FT-IR, UV-Vis) ve elektronik özellikleri (HOMO–LUMO enerji seviyeleri), Yoğunluk Fonksiyonel Teorisi (DFT) kapsamında B3LYP/6–311G(d,p) teorik düzeyinde araştırılmıştır. Sakkarinat ve diaminopiridinyum alt birimlerinden oluşan HDAPYSAC molekülü, ortorombik kristal sisteminde ve *Fdd2* uzay grubunda kristalleşmiştir. Moleküller arası etkileşimler ve elektron yoğunluğu dağılımı, Hirshfeld yüzeyi ve parmak izi analizleriyle değerlendirilmiştir. En belirgin temaslar H···H (%32.5), H···O/O···H (%31.7), H···C/C···H (%16.5), H···N/N···H (%7.4), C···C (%5.5), C···O/O···C (%3.0) ve C···N/N···C (%2.6) olarak hesaplanmıştır. HOMO–LUMO enerji aralığı 3.5661 eV olarak bulunmuş ve bu durum bileşiğin kararlı yapıda olduğunu göstermektedir. UV–görünür bölge spektroskopisi ile yapılan optik analizlerde, bileşiğin 276.33, 211.26, 200.10, 173.21, 164.35 ve 163.62 nm dalga boylarında altı belirgin absorpsiyon bandı gösterdiği ve bu bantlara karşılık gelen dolaylı ve doğrudan geçiş enerji değerlerinin sırasıyla 36188, 47335, 49975, 57733, 60846 ve 61117 cm^{-1} olduğu belirlenmiştir.

Anahtar Kelimeler: FT-IR, UV-Vis., Kristal yapı, Hirshfeld yüzey analizi

*Corresponding Author: serkanguney@odu.edu.tr

Cite this Article: Erzincan University Journal of Science and Technology 2025, 18(3) 963-979.
https://doi.org/10.18185/erzifbed.172743

1. Introduction

Saccharin ($C_7H_5NO_3S$), one of the earliest artificial sweeteners, has garnered significant attention due to its zero-calorie content and remarkable stability under diverse conditions. Its versatility has facilitated its widespread use across various industries, particularly in the food and pharmaceutical sectors, where it is often employed in the form of water-soluble salts, such as sodium saccharin ($Na(sac)\cdot 2H_2O$). The saccharinate anion ($C_7H_4NO_3S^-$), formed through the deprotonation of saccharin, demonstrates exceptional coordination behavior with numerous metal cations, resulting in the formation of ionic saccharinates [1]. Owing to their structural versatility and multifunctional properties, these complexes have been widely investigated for potential roles in catalysis, materials development, and biomedical research [2, 3]. The unique ability of saccharinate to act as a multifunctional ligand is particularly noteworthy. It coordinates through various donor sites, including sulfonyl oxygen and nitrogen atoms, making it an attractive candidate for the design of novel coordination complexes. Structural analyses of various metal saccharinates, such as $Na(sac)\cdot 2/3H_2O$, $K(sac)\cdot 2/3H_2O$, and $Mg(sac)_2\cdot 7H_2O$, have revealed their broad structural adaptability and functional properties [4-6]. In contrast, non-metallic saccharinate salts are relatively rare, with $NH_4(sac)$ [7] and piperazinium disaccharinate, $(H_2ppz)(sac)_2$ [8], being among the few reported examples.

Recently, the focus has shifted towards hybrid organic-inorganic complexes, driven by their unique physicochemical properties and potential applications in crystal engineering and functional materials. Pyridinium-based cations, particularly 2,6-diaminopyridinium, have emerged as promising candidates for the development of innovative coordination compounds. These cations offer additional hydrogen-bonding capabilities, enhancing the stability and dimensionality of saccharinate complexes, and broadening their applicability in supramolecular chemistry [9-11]. Hybrid organic–inorganic complexes have been explored for applications in non-linear optics [12], gas storage and sensing [13], catalysis, and as proton conductors [14], underlining their multifunctionality in advanced material science.

In addition, several recent studies (2022–2024) have reported new saccharin derivatives and their complexes, highlighting their potential roles in supramolecular assemblies, functional materials, and biomedical applications [3, 15].

The synthesis, characterization, and biomedical applications of mixed-ligand metal saccharin complexes represent an intriguing area of study. In this work, we aimed to synthesize a mixed-ligand Zn(II) saccharinate complex containing 2,6-diaminopyridine. However, the 2,6-diaminopyridinium saccharinate compound was obtained instead. A detailed characterization of the compound's molecular and structural properties was accomplished through elemental analysis, FT-IR spectroscopy, and single-crystal X-ray diffraction methods.

The results provide valuable insights into the structural versatility of saccharinate-based systems and their potential for the development of functional materials.

2. Materials and Methods

2.1. Materials

All reagents were sourced from commercial vendors and used directly without undergoing any further purification steps. The precursor complex $[Zn(sac)_2(H_2O)_4]\cdot 2H_2O$ was synthesized following the procedures reported in the literature [16].

2.2. Synthesis

The compound 2,6-diaminopyridinium saccharinate (HDAPYSAC) was unexpectedly obtained as the main product during the reaction between $[Zn(sac)_2(H_2O)_4]\cdot 2H_2O$ and 2,6-diaminopyridine (dapy). Although the original goal of the experiment was to synthesize a zinc-saccharinate complex incorporating the dapy ligand, the reaction led instead to the isolation of HDAPYSAC.

For the synthesis of the target compound, dapy (0.218 g, 2.0 mmol) was first dissolved in 10 cm^3 of a methanol–isopropanol mixture (1:1, v/v). This solution was then gradually introduced into a magnetically stirred solution of tetraaquabis(saccharinato)zinc(II) dihydrate (0.538 g, 1 mmol) in 30 cm^3 of the same solvent mixture at ambient temperature. After mixing, the reaction was allowed to proceed without disturbance under room conditions for 24 hours. Upon completion, colorless crystals of the product were obtained, as illustrated in Figure 1. Elemental analysis for $C_{12}H_{12}N_4O_3S$ (292.32) yielded the following results: calculated C 49.95%, H 4.21%, N 19.23%, S 10.67%; found C 49.31%, H 4.14%, N 19.17%, S 10.97%.

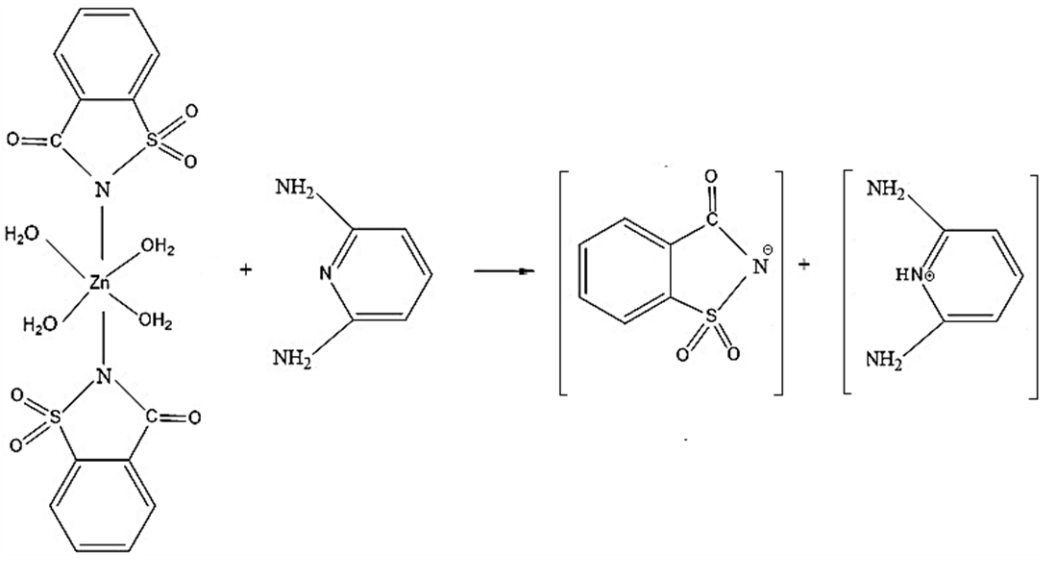

Figure 1. Synthesis scheme of HDAPYSAC

2.3. Physical Measurements

The molecular structure of HDAPYSAC was identified using single-crystal X-ray diffraction. The diffraction data were gathered using a STOE IPDS 2 diffractometer with graphite- X-ray intensity data were collected using monochromatic MoKα radiation (λ = 0.71073 Å) at 296 K [17]. Absorption corrections were carried out using equivalent reflections. Hydrogen atoms were placed in idealized positions and refined using a riding model with bond lengths constrained to 0.93 Å for C—H, 0.82 Å for O—H, and 0.86 Å for N—H. Isotropic displacement parameters were assigned as 1.2Ueq for carbon and nitrogen atoms and 1.5Ueq for oxygen atoms. The structure was solved and refined using the SHELXT-2018/3 program [18]. Molecular graphics were rendered with Mercury for Windows [19], and hydrogen bonding interactions were analyzed using the PLATON software [20]. The crystallographic data were prepared for publication using WinGX [21] and PublCIF [22].

Quantum chemical computations based on DFT were carried out with the Gaussian 09 software package [23], and molecular structures were visualized using GaussView 5.0 [24]. Calculations were performed using the B3LYP method, combining Becke's three-parameter exchange functional [25] and the Lee–Yang–Parr correlation functional [26] with the 6–311G(d,p) basis set.

The intermolecular interactions of the HDAPYSAC molecule were further investigated using Hirshfeld surface (HS) analysis implemented in the CrystalExplorer 17.5 software [27].

Elemental composition (C, H, N, and S) was assessed using a Vario Micro Cube Elemental Analyzer. The FT-IR spectrum was obtained using a Shimadzu IR Affinity-1 spectrophotometer within the range of 4000–300 cm^{-1}.

3. Findings and Discussion

3.1. Crystallography studies, molecular geometry, and structural parameters

Single-crystal X-ray analysis revealed that the compound crystallizes in an orthorhombic system with space group *Fdd2*. Key structural parameters and refinement statistics are provided in Table 1, while the three-dimensional molecular structure is visualized in Figure 2.

Table 1. Crystallographic and refinement data for HDAPYSAC

Crystal data	
Chemical formula	$C_{12}H_{12}N_4O_3S$
Formula weight	292.32
Crystal system, space group	Orthorhombic, *Fdd2*
Temperature (K)	293
a, b, c (Å)	50.121 (4), 14.2546 (8), 7.3490 (4)
V (Å^3)	5250.5 (6)
Z	16
Radiation type	MoKα
μ (mm^{-1})	0.26
Crystal size (mm)	0.35 × 0.29 × 0.21
Data collection	
Diffractometer	STOE IPDS 2
Absorption correction	Integration (X-RED32; Stoe & Cie, 2002)
T_{min}, T_{max}	0.891, 0.971
No. of measured, independent, and observed [I > 2σ(I)] reflections	9081, 2563, 2333
R_{int}	0.069
(sin θ/λ)max (Å^{-1})	0.617
Refinement	
R[F^2 > 2σ(F^2)], wR(F^2), S	0.036, 0.097, 1.06
No. of reflections	2563
No. of parameters	187
No. of restraints	1
H-atom treatment	H atoms treated by a mixture of independent and constrained refinement
$\Delta\rho_{max}$, $\Delta\rho_{min}$ (e Å^{-3})	0.20, −0.16
Absolute structure	Refined as an inversion twin.
Absolute structure parameter	0.03 (11)

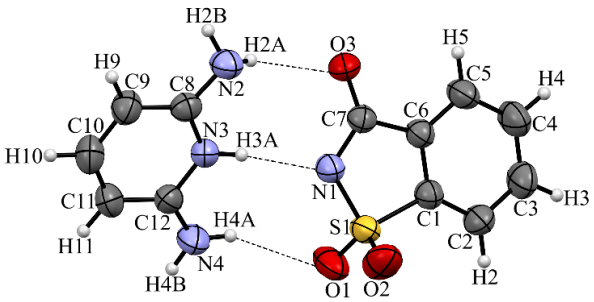

Figure 2. The single crystal structure (ORTEP) of HDAPYSAC

The geometric structure of HDAPYSAC optimized by using DFT at B3LYP/6-311G (d,p) level is shown in Figure 3.

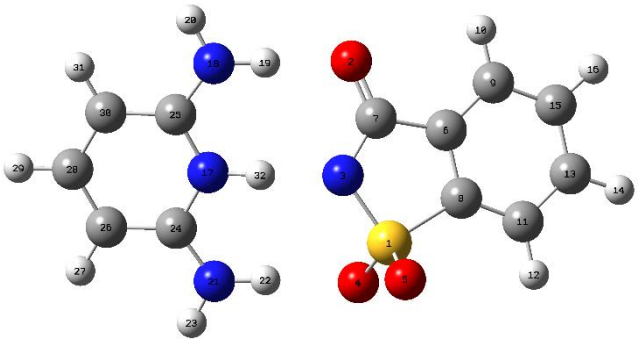

Figure 3. Optimized structure of HDAPYSAC

A comparison of the key geometric parameters obtained from DFT calculations and experimental X-ray data is summarized in Table 2 and Table 3.

Table 2. The optimized and experimental selected bond length of the compound

Bond length (A˚)	XRD	DFT
S1–O1	1.435(3)	1.4351
C2–C3	1.389(5)	1.39
S1–O2	1.441(3)	1.4406
S1–N1	1.613(3)	1.6123
S1–C1	1.770(3)	1.77
C7–C6	1.494(4)	1.4932
N3–C12	1.363(4)	1.3636
N3–C8	1.357(4)	1.3571
C7–O3	1.240(4)	1.2405
N1–C7	1.349(4)	1.3481
N4–C12	1.333(5)	1.3329
N2–C8	1.336(4)	1.3368

Table 3. The optimized and experimental selected bond angles of the compound

Bond angles (°)	XRD	DFT
O1–S1–O2	114.97(18)	114.9686
O1–S1–N1	110.42(17)	110.4346
O2–S1–N1	110.65(17)	110.6535
O1–S1–C1	111.98(17)	111.9581
O2–S1–C1	110.70(18)	110.7134
C12–N3–C8	124.4(3)	124.3672
C7–N1–S1	111.9(2)	111.883
N2–C8–N3	116.9(3)	116.8626
N4–C12–N3	117.2(3)	117.1784
O3–C7–N1	123.2(3)	123.1717
N1–S1–C1	96.66(14)	96.6446

A high level of agreement was observed between the DFT-optimized geometry and the X-ray diffraction results, with only minimal differences attributed to the differing physical states—gas phase for DFT and solid state for XRD. In the saccharin moiety, the S1–O1 and S1–O2 sulfonyl bond lengths were measured as 1.435(3) Å and 1.44(3) Å, respectively, which align closely with those reported for structurally similar sulfonyl compounds [24]. The carbonyl bond (O3–C7) of the benzothiazole group was found to be 1.240(4) Å. A notable deviation was observed in the S1–N1–C7 bond angle (111.9(2)°), which is smaller compared to the 115.0(2)° previously reported [24]. The angles between atoms within conjugated systems, such as N–C–C, N–C–N, O–C–C, and C–N–C, were approximately 120°, a feature typically associated with π-electron delocalization in aromatic systems [21]. Furthermore, the dihedral angle between the benzothiazole ring (C1–C7/N1/S1) and the pyridine ring (C8–C12/N3) was calculated to be 32.810(1)°.

Within the crystalline lattice, intermolecular interactions are established via N4–H4B···O3^{ii} hydrogen bonding, where the pyridinium NH moiety donates a hydrogen bond to the carbonyl oxygen atom. These interactions organize the molecules into C(5) hydrogen-bonded chains aligned along the crystallographic b-axis (Figure 4, Table 4).

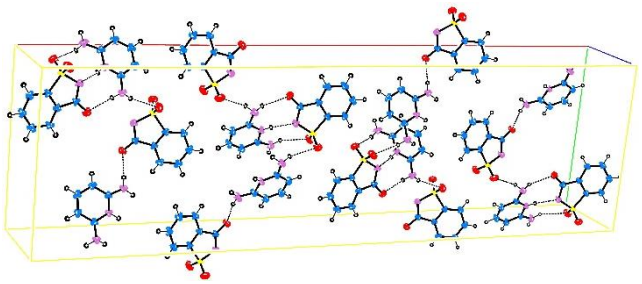

Figure 4. Crystal packing diagram illustrating the intra- and intermolecular hydrogen bonding interactions present in the HDAPYSAC structure

Table 4. Geometric parameters of hydrogen bonds observed in the HDAPYSAC compound

D—H···A	D—H	H···A	D···A	D—H···A
N2—H2A···O3	0.86	2.26	3.032(4)	149.8
N2—H2B···O2^{i}	0.86	2.34	3.151(4)	157.6
N4—H4A···O1	0.86	2.33	3.133(4)	156.5
N4—H4B···O3^{ii}	0.86	2.03	2.879(3)	169.1
N3—H3A···N1	0.82(4)	2.00(4)	2.818(4)	173(4)

Symmetry codes: (i) −x+3/4, y+1/4, z−1/4; (ii) x, y−1/2, z−1/2.

Hydrogen bonding interactions involving N2–H2B ···O2^{i} link the pyridinium NH group to the sulfonyl oxygen of an adjacent molecule, resulting in the formation of C(5) motifs aligned along the crystallographic a-axis. Furthermore, the supramolecular framework is reinforced through additional hydrogen bonds, including N2—H2A···O3 and N3—H3A···N1, which organize the structure into extended chains parallel to the a-axis and give rise to characteristic $R_2^2(8)$ ring patterns. A similar ring motif is also generated by N4—H4A···O1 and N3—H3A···N1 hydrogen bonds, contributing to the overall three-dimensional connectivity.

The HS were generated using a high-resolution setting, with the three-dimensional maps visualized on a fixed color scale ranging from red, indicating shorter-than-expected intermolecular contacts, to blue, indicating longer contacts. This scale spans from –0.5602 to 1.4171 arbitrary units (a.u.). The mapped surface for the HDAPYSAC molecule is shown in Figure 5a. The pale red regions indicate short contacts, primarily associated with N···H···O and N···H···S interactions (Table 2). Figure 5b illustrates the shape index map, generated over the range of –1 to 1 Å. The absence of adjacent red and blue triangle patterns suggests that π–π interactions are not present in the structure. Figure 5c displays the curvedness map in the range of –4.0 to 0.4 Å, where large green areas indicate relatively flat regions on the surface, while blue zones correspond to areas with greater curvature.

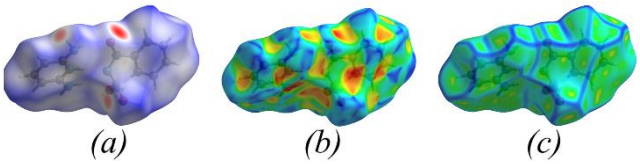

Figure 5. Hirshfeld surface analyses of HDAPYSAC: **(a)** $_{dnorm}$ mapping showing N–H···O and N–H···S short contacts, **(b)** shape index map indicating absence of π–π interactions, and **(c)** curvedness map displaying flat and curved regions.

Figure 6a–g illustrates the Hirshfeld surface mapped with the d_{norm} function, highlighting the intermolecular interactions of H···H, H···O/O···H, H···C/C···H, H···N/N···H, C···C, C···O/O···C, and C···N/N···C, respectively.

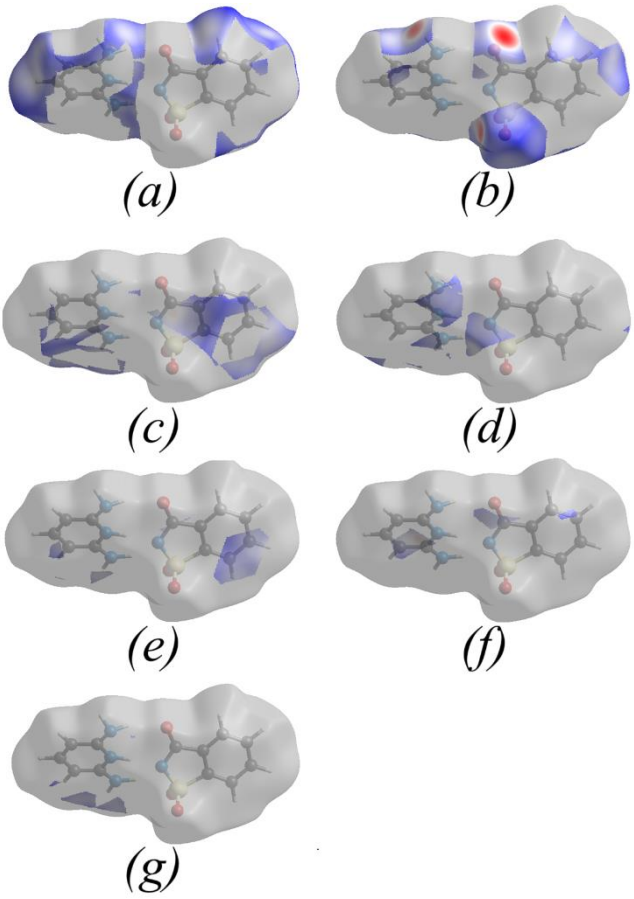

Figure 6. Hirshfeld surface mapped with the d_{norm} function illustrating specific intermolecular interactions: **(a)** H···H, **(b)** H···O/O···H, **(c)** H···C/C···H, **(d)** H···N/N···H, **(e)** C···C, **(f)** C···O/O···C, and **(g)** C···N/N···C contacts.

The comprehensive two-dimensional fingerprint plots, including those segmented by interactions such as H···H, H···O/O···H, H···C/C···H, H···N/N···H, C···C, C···O/O···C, and C···N/N···C, are presented in Figure 7a–h, respectively.

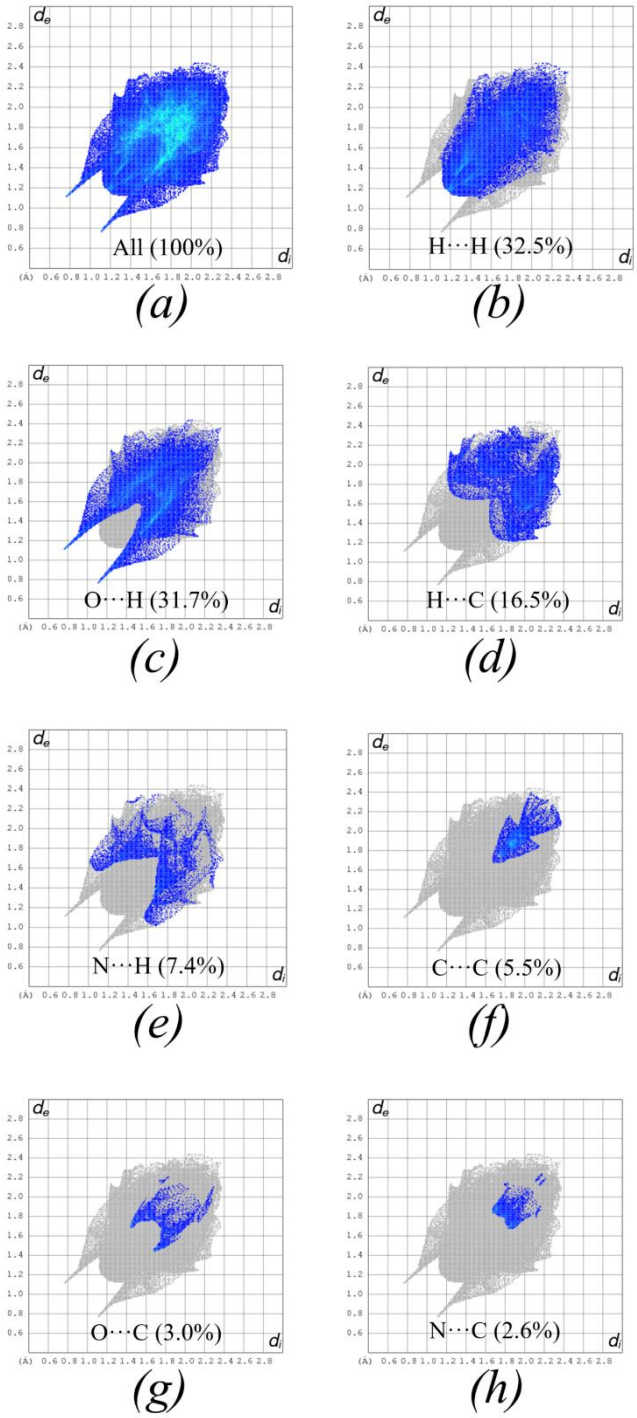

Figure 7. Two-dimensional fingerprint plots of HDAPYSAC: **(a)** overall interactions and breakdown into **(b)** H···H, **(c)** H···O/O···H, **(d)** H···C/C···H, **(e)** H···N/N···H, **(f)** C···C, **(g)** C···O/O···C, and **(h)** C···N/N···C interactions.

The crystal packing is predominantly influenced by H···H interactions, which constitute 32.5% of the Hirshfeld surface area. This is indicated by a central peak at de = di = 1.18 Å in the fingerprint plot. Close behind, H···O/O···H contacts contribute 31.7% and are characterized by a pair of sharp spikes near de + di ≈ 1.85 Å. These interactions primarily result from N—H···O type hydrogen bonds between adjacent molecules (Table 4). Other notable contributions to the

HS analysis indicates that the crystal packing also involves H···C/C···H (16.5%), H···N/N···H (7.4%), C···C (5.5%), C···O/O···C (3.0%), and C···N/N···C (2.6%) intermolecular contacts.

3.2. Frontier Molecular Orbitals (FMOs)

Frontier molecular orbitals, particularly the highest occupied molecular orbital (HOMO) and the lowest unoccupied molecular orbital (LUMO), are essential in defining the optical behavior, electronic characteristics, chemical reactivity, and kinetic stability of molecules. While the HOMO serves as the electron donor, the LUMO acts as the electron acceptor. To deepen the understanding of HDAPYSAC's electronic structure, a frontier molecular orbital analysis was conducted at the B3LYP/6-311G(d,p) theoretical level. Figure 8 presents the graphical depictions of the HOMO and LUMO orbitals.

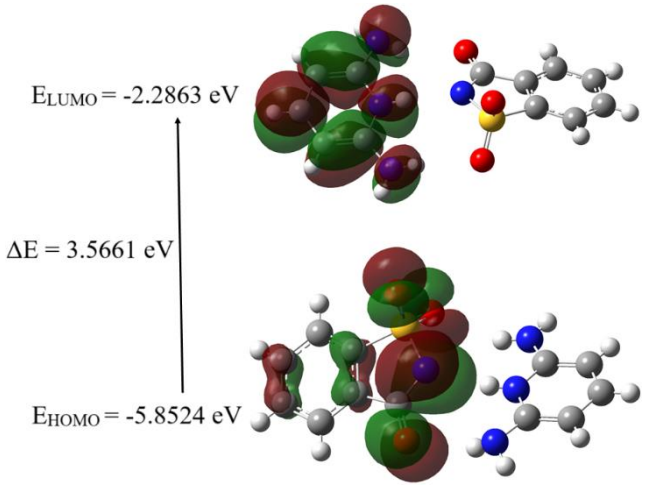

Figure 8. HOMO and LUMO surface plots of the HDAPYSAC molecule obtained from frontier molecular orbital (FMO) analysis

A small energy gap suggests high molecular polarizability and increased chemical reactivity. Table 5 presents a summary of global reactivity descriptors, which include important parameters such as ionization potential (I), electron affinity (A), electronegativity (χ), chemical potential (μ), global hardness (η), global softness (σ), and electrophilicity index (ω). These descriptors are vital for assessing the chemical reactivity of the molecule.

Table 5. The frontier molecular orbitals of HDAPYSAC

FMO	Energy (eV)
E_{HOMO}	-5.8524
E_{LUMO}	-2.2863
Energy difference (ΔE)	3.5661
Ionization Potential (IP)	5.8524
Electron Affinity (EA)	2.2863
Chemical Potential (μ)	-4.0695
Electronegativity (χ)	4.0695
Global Hardness (η)	1.7831
Global Softness (σ)	0.2804
Electrophilicity index (ω)	4.6438

Chemical hardness and softness are indicators of a molecule's stability. These characteristics can be inferred from the HOMO–LUMO energy gap. A large gap suggests that the molecule is hard, while a small gap indicates softness. Soft molecules are generally more polarizable, as they require less energy for electronic excitation. With a HOMO–LUMO gap of 3.5661 eV, the HDAPYSAC molecule can be considered chemically hard.

3.3. Mulliken Atomic Charges

Atomic charges are commonly used to interpret molecular characteristics such as dipole moment, polarizability, electron distribution, and charge transfer behavior. According to the results obtained from DFT diffuse function analysis, atoms H7, H8, H11, H12, H18, H21, H23, H25, and H27 possess positive charges. Hydrogen atoms with positive partial charges may also act as acceptor sites, as indicated in Table 6.

Table 6. Mulliken atomic charges of HDAPYSAC

Atoms	B3LYP/6-311G(d,p)	Atoms	B3LYP/6-311G(d,p)
S1	1.041740	C17	-0.194525
O2	-0.434499	H18	0.096846
N3	-0.413853	C19	-0.199436
N4	-0.670966	C20	0.057445
O5	-0.555582	H21	0.104605
N6	-0.310223	C22	-0.181740
H7	0.206642	H23	0.097620
H8	0.205444	C24	-0.004611
O9	-0.498025	H25	0.083422
N10	-0.413007	C26	0.001095
H11	0.261969	H27	0.095141
H12	0.237757	C28	-0.069659
C13	0.461533	H29	0.088908
C14	0.337072	C30	-0.078576
C15	-0.169324	H31	0.087793
C16	0.435995	H32	0.293000

According to the DFT method and basis set employed for atomic charge analysis, carbon atoms C15, C17, C19, C22, C24, C28, and C30 carry notable negative charges, indicating their role as electron-donating sites. But the charges of C13, C14, C16, C20, and C26 are positive, which are acceptor atoms (Table 6). In addition, positive charges are collected on the S1 atom while negative charges are collected on the O2, N3, N4, O5, N6, O9, and N10 atoms.

3.4. Infrared Spectra

The IR spectrum of the compound shows distinct absorption bands that correspond to the functional groups of its constituent ions. Broad and intense bands observed at 3382 and 3152 cm^{-1} are attributed to the antisymmetric and symmetric N–H stretching vibrations of the 2,6-diaminopyridinium ion, respectively, with some overlap between them. Sharp peaks at 1666 and 1651 cm^{-1} correspond to the carbonyl stretching vibrations of the saccharinate anion. Strong absorption bands around 1261 and 1138 cm^{-1} are assigned to the sulfonyl group vibrations of the saccharinate moiety. Very sharp bands at 1323 and 952 cm^{-1} are related to the symmetric and antisymmetric stretching modes of the CNS group within the saccharinate anion. A summary of the main IR absorption peaks is given in Table 7.

Table 7. Key absorption peaks in the IR spectra of the compound[a] (wavenumber in cm^{-1})

Compound	ν(NH)	ν(CH)	ν(C=O)	$\nu_{asym}(SO_2)$	$\nu_{sym}(SO_2)$	ν_{sym}(CNS)	ν_{asym}(CNS)
(hdapy)(sac)	3382vs 3152vs	3066w 2990w 2851w	1666vs, 1651vs	1261vs	1138vs	1323m	952s

[a] w= weak; vw= very weak; m= medium; s= strong; vs= very strong.

3.5. Ultraviolet Visible Spectral Analysis

The UV-Vis absorption characteristics of the compound were theoretically examined by employing time-dependent density functional theory (TD-DFT) at the B3LYP/6-311G(d,p) computational level, based on the molecule's optimized geometry. The key electronic excitations, along with their corresponding peak wavelengths (λ_{max}), excitation energies, and oscillator strength values, are summarized in Table 8.

Table 8. Summary of excitation energy (cm^{-1}), oscillator strength (f_{os}), and maximum absorption wavelength (λ_{max} in nm) for the HDAPYSAC compound

λ(nm)	E(cm^{-1})	f	Major contributions (>%10)
276.33	36188	0.1592	H-4→LUMO (89%), H-10→L+1 (2%), HOMO→L+2 (4%)
211.26	47335	0.2049	H-4→L+1 (82%), H-12→LUMO (7%), H-10→LUMO (6%)
200.10	49975	0.2188	H-7→L+2 (15%), H-6→L+1 (24%), H-6→L+3 (10%), H3→L+2 (17%), H-2→L+3 (25%), H-5→L+3 (2%)
173.21	57733	0.1679	H-9→L+2 (16%), H-8→L+3 (50%), H-6→L+3 (7%), H-3→L+2 (2%), H-3→L+5 (2%), H-2→L+3 (3%), H-1→L+5 (3%), HOMO→L+4 (6%)
164.35	60846	0.4705	H-12→LUMO (83%), H-11→LUMO (4%), H-4→L+1 (8%)
163.62	61117	0.4882	H-10→L+1 (52%), HOMO→L+5 (19%), HOMO→L+6 (10%), H-9→L+3 (5%)

Two strong absorptions are located at 276.33 and 211.26 nm in the UV-spectrum. The energies of these absorption bands are calculated as 36188, and 473.35 cm^{-1}, respectively. Figure 9 presents a comparison between the experimentally obtained and theoretically predicted UV–vis spectra of the molecule under study.

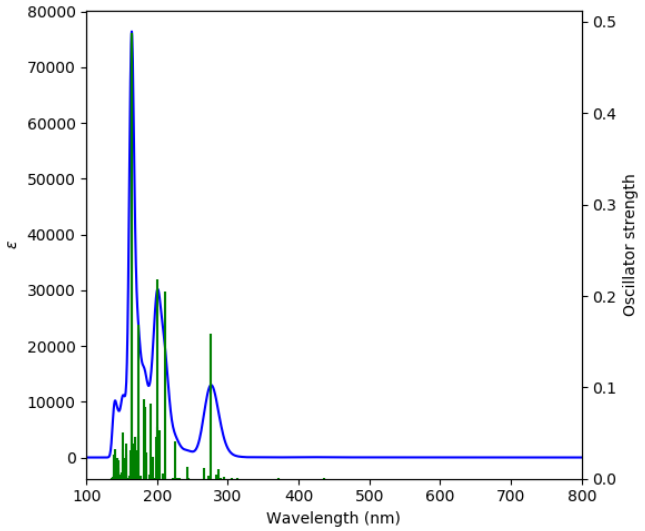

Figure 9. Comparison of calculated and experimental UV–Vis spectra of the HDAPYSAC molecule

The major contributions to the excitation at 276.33 nm originate from the transitions of H-4→LUMO, H-10→L+1, and HOMO→L+2, which correspond to approximately 89%, 2%, and 4%. The excitation at 276.33 nm originates from H-4→L+1, H-12→LUMO, and H-10→LUMO, which correspond approximately 82%, 7% and 6% respectively.

4. Conclusions and Recommendations

In this study, a novel saccharin derivative, 2,6-diaminopyridinium saccharinate ($C_{12}H_{12}N_4O_3S$), was synthesized and its structure was elucidated by FT-IR, UV–vis spectroscopy, and single-crystal X-ray diffraction analysis. The compound was found to crystallize in the orthorhombic system, belonging to the *Fdd2* space group, with unit cell parameters a = 50.121(4) Å, b = 14.2546(8) Å, c = 7.3490(4) Å, and Z = 16. Computational studies on HDAPYSAC were conducted at the DFT/B3LYP/6–311G(d,p) level of theory. Frontier molecular orbital energies were calculated, revealing an energy gap of 3.5661 eV. Mulliken population analysis was employed to determine the atomic charges. Hirshfeld surface analysis and fingerprint plots were utilized to investigate hydrogen bonding and intermolecular interactions in HDAPYSAC. The analysis showed that the crystal packing is mainly governed by H···H (32.5%), H···O/O···H (31.7%), H···C/C···H (16.5%), H···N/N···H (7.4%), C···C (5.5%), C···O/O···C (3.0%), and C···N/N···C (2.6%) contacts. These intermolecular interaction patterns suggest that HDAPYSAC may serve as a promising building block in supramolecular chemistry. Furthermore, the stable molecular framework and hydrogen-bonding features highlight its potential applicability in the design of functional organic–inorganic materials.

Ethics in Publishing

There are no ethical issues regarding the publication of this study.

Acknowledgements

This study has been financed by the Scientific Research Projects Commission of Ordu University (Project number: AR-1650).

References

[1] Baran, E. J., Yılmaz, V. T. (2006). Metal complexes of saccharin. Coord. Chem. Rev., 250(15-16), 1980-1999.

[2] Kaur, K., Srivastava, S. (2020) Artificial sugar saccharin and its derivatives: role as a catalyst. RSC Adv., 10(60), 36571-36608.

[3] İçsel, C., Yılmaz, V. T., Yeşilel, O. Z., Harrison. V. T. A. (2024). Metal complexes of saccharin and thiosaccharin as potential anticancer and antimicrobial agents. Eur. J. Med. Chem. Rep., 12, 100205.

[4] Jovanovski, G., Grupče, O., Šoptrajanov, B. (1990). The O-H and O-D stretching vibrations in the hydrates of sodium and potassium saccharinate: spectra-structure correlations. J. Mol. Struct., 219, 61-66.

[5] Jovanovski, G., Kaitner, B., Grupce, O., Naumov, P. (2004). Crystal structure, infrared and raman spectra of tripotassium trisaccharinate dihydrate, $K_3(C_7H_4NO_3S)_3 \cdot 2H_2O$. Cent. Eur. J. Chem., 2(1), 254-275.

[6] Jovanovski, G., Kamenar, B. (1982). Two ionic saccharinates:(la) sodium saccharinate 2/3 hydrate, $C_7H_4NO_3SNa \cdot 2/3H_2O$;(lb) Magnesium disaccharinate heptahydrate, $(C_7H_4NO_3S)_2Mg \cdot 7H_2O$. Cryst. Struct. Commun., 11, 247–255.

[7] Ng, S. W. (1998). Ammonium saccharin. Acta Crystallogr. Sect. C: Cryst. Struct. Commun., 54(5), 649-651.

[8] Gümüş, S., Güney, S., Yılmaz, V. T., Kazak, C. (2006). A Non-Metallic Ionic Saccharinate. Synthesis, Structure and DFT Calculations of Piperazinium Disaccharinate. Zeitschrift für anorganische und allgemeine Chemie, 632, 1544-1548.

[9] Bouaziz, E., Hassen, C. B., Chniba-Boudjada, N., Daoud, A., Mhiri, T., Boujelbene, M. (2017). Crystal structure, Hirshfeld surface analysis, vibrational, thermal behavior and UV spectroscopy of (2, 6-diaminopyridinium) dihydrogen arsenate. J. Mol. Struct., 1145, 121-131.

[10] Hassen, C. B., Dammak, T., Chniba-Boudjada, N., Mhiri, T., Boujelbene, M. (2017). Chemical synthesis, crystal structure, vibrational spectroscopy, non-linear optical properties and DFT calculation of bis (2, 6-diaminopyridinium) sulfate monohydrate. J. Mol. Struct., 1127, 43-52.

[11] Fredj, D., Hassen, C. B., Elleuch, S., Feki, H., Boudjada, N. C., Mhiri, T., Boujelbene, M. (2017). Structural, vibrational and optical properties of a new organic–inorganic material:$(C_5H_8N_3)_2[BiCl_5]$. Mater. Res. Bull. 85, 23-29.

[12] Li, B., Yu, Y., Xin, M., Xu, J., Zhao, T., Kang, H., Xing, G., Zhao, Zhang, T., Jiang, S. (2023). Second-order nonlinear optical properties of copper-based hybrid organic–inorganic perovskites induced by chiral amines. Nanoscale, 15(4), 1595-1601.

[13] Majhi, S. M., Ali, A., Rai, P., Greish, Y. E., Alzamly, A., Surya, S. G., Qamhieh, N., Mahmoud, S. T. (2022). Metal–organic frameworks for advanced transducer based gas sensors: review and perspectives. Nanoscale Advances, 4(3), 697-732.

14. Sun, P., Wang, Y., Li, Z., Guo, H., Yin, X., Pei, H. (2020). A flexible organic–inorganic hybrid for medium-temperature proton conduction over a wide humidity range. Journal of Materials Science, 55(27), 13075-13084. https://doi.org/10.1007/s10853-020-04984-x

[15] Kanmazalp, S. D., Sagher, M., Dege, N., Içbudak, H. (2023). Synthesis, hirshfeld surface, ftir analysis and single crystal X-ray structure of 2-amino-3-hydroxypyridinium saccharinate. J. Struct. Chem., 64(6), 1137-1146.

[16] Haider, S. Z., Malik, K. M. A., Das, S., & Hursthouse, M. B. (1984). zinc (II) Dihydrate, $[Zn(C_7H_4NO_3S)_2\ (H_2O)_4]\cdot 2H_2O$, and Tetraaquabis (saccharinato-N) cadmium (II) Dihydrate, $[Cd(C_7H_4NO_3S)_2(H_2O)_4]\cdot 2H_2O$. Acta Crystallogr., C, 40, 1147-1150.

[17] Stoe & Cie (2002) X-AREA and X-RED32, Stoe & Cie GmbH, Darmstadt (Germany).

[18] Sheldrick, G. M. (2015). Crystal structure refinement with SHELXL. Acta Cryst., C71, 3–8.

[19] Macrae, C. F., Edgington, P. R., McCabe, P., Pidcock, E., Shields, G. P., Taylor, R., Towler, M., van de Streek, J. (2006). Mercury: visualization and analysis of crystal structures. J. Appl. Crystallogr., 39(3), 453-457.

[20] Spek, A. L. (2003). Single-crystal structure validation with the program PLATON. J. Appl. Crystallogr., 36(1), 7-13.

[21] Farrugia, L.J. (1999). WinGX suite for small-molecule single-crystal crystallography. J. Appl. Crystallogr. 32, 837–838.

[22] Westrip, S. P. (2010). publCIF: software for editing, validating and formatting crystallographic information files. J. Appl. Crystallogr., 43, 920–925.

[23] Frisch, M. J., Trucks, G. W., Schlegel, H. B., Scuseria, G. E., Robb, M. A., Cheeseman, J. R., Scalmani, G., Barone, V., Mennucci, B., Petersson, G. A., Nakatsuji, H., Caricato, M., Li, X., Hratchian, H. P., Izmaylov, A. F., Bloino, J., Zheng, G., Sonnenberg, J. L., Hada, M., Ehara, M., Toyota, K., Fukuda, R., Hasegawa, J., Ishida, M., Nakajima, T., Honda, Y., Kitao, O., Nakai, H., Vreven, T., Montgomery Jr, J. A., Peralta, J. E., Ogliaro, F., Bearpark, M., Heyd, J.

J., Brothers, E., Kudin, K. N., Staroverov, V. N., Keith, T., Kobayashi, R., Normand, J., Raghavachari, K., Rendell, A., Burant, J. C., Iyengar, S. S., Tomasi, J., Cossi, M., Rega, N., Millam, J. M., Klene, M., Knox, J. E., Cross, J. B., Bakken, V., Adamo, C., Jaramillo, J., Gomperts, R., Stratmann, R. E., Yazyev, O., Austin, A. J., Cammi, R., Pomelli, C., Ochterski, J. W., Martin, R. L., Morokuma, K., Zakrzewski, V. G., Voth, G. A., Salvador, P., Dannenberg, J. J., Dapprich, S., Daniels, A. D., Farkas, O., Foresman, J. B., Ortiz, J. V., Cioslowski, J., Fox, D. J. (2010). Gaussian 09, Revision C.01, Gaussian, Inc, Wallingford C.p*ooo-iokı7

[24] Dennington, R., Keith, T., Millam, J. (2010). GaussView, Version 5, Semichem Inc, Shawnee Mission KS.

[25] Becke, A. D. (1988). Density-functional exchange-energy approximation with correct asymptotic behavior. Phys. Rev., A 38, 3098.

[26] Lee, C., Yang, W., Parr, R. G. (1988). Development of the Colle-Salvetti correlation-energy formula into a functional of the electron density. Physical review, B 37, 785.6

[27] Turner, M. J., MacKinnon, J. J., Wolff, S. K., Grimwood, D. J., Spackman, P. R., Jayatilaka, D., Spackman, M. A. (2017). Crystal Explorer Version 17.5, University of Western Australia.

e-ISSN: 2149-4584

Erzincan University Journal of Science and Technology

EJSAT 2025, 18 (3) 713-725

Research Article

Prediction of Shear Thickening Ratio Based on Rheological Parameters Using Machine Learning

Kadir Münir ERCÜMEN[1*]

Department of Aircraft Maintenance and Repair, Erzincan Binali Yıldırım University, Erzincan, Turkey,

Received: 11/08/2025, **Revised:** 13/10/2025, **Accepted:** 14/10/2025, **Published:** 31/10/2025

Abstract

Shear thickening fluids (STFs) show a complex, non-Newtonian rheological behavior in which viscosity increases with shear rate. Accurately estimating the thickening ratio (TR), a summary parameter representing the rheological response, is crucial for optimizing the formulation of these fluids and their effective use in applications. In this study, a machine learning-based approach is proposed to directly predict TR. The modeling process incorporated rheologically relevant input parameters, including particle size, weight-based particle concentration, carrier-fluid concentration, molecular weight of the carrier-fluid, and test temperature. Two advanced ensemble learning algorithms, Extreme Gradient Boosting (XGBOOST) and Random Forest (RF), were used to create the prediction models. The models were trained and validated on various experimental datasets obtained from different independent sources and covering a wide range of STF compositions and experimental conditions. The results showed that XGBOOST achieved 80% and 72% accuracy for RF during the testing phase, with XGBOOST outperforming RF. Furthermore, the calculated feature importance values revealed the main parameters affecting TR. Although the influence values of the parameters on TR were close to each other, the carrier-fluid ratio (OSO) (25.91%) and the silica ratio (SO) (24.32%) stand out as the most influential parameters. This approach offers a simple and effective method for assessing the rheological behavior of STF systems, while also providing significant time and cost advantages by reducing the need for extensive experimental procedures.

Keywords: Shear-thickening fluids, smart materials, thickening ratio, machine learning, rheology,

Reolojik Parametrelere Dayalı Kalınlaşma Oranının Makine Öğrenmesi ile Tahmini

Öz

Kayma kalınlaşması gösteren sıvılar (STF'ler), viskozitenin kayma hızıyla birlikte arttığı karmaşık ve Newtonsal olmayan bir reolojik davranış sergiler. Bu sıvıların formülasyonunun optimize edilmesi ve uygulamalarda etkin kullanımı açısından, reolojik tepkiyi temsil eden özet bir parametre olan kalınlaşma oranının (TR) doğru bir şekilde tahmin edilmesi büyük önem taşımaktadır. Bu çalışmada, TR değerini doğrudan tahmin edebilmek amacıyla makine öğrenmesine dayalı bir yaklaşım önerilmiştir. Modelleme sürecinde, partikül boyutu, ağırlıkça parçacık konsantrasyonu, taşıyıcı sıvı konsantrasyonu, taşıyıcı sıvının moleküler ağırlığı ve test sıcaklığı gibi reolojik açıdan etkili giriş parametreleri kullanılmıştır. Tahmin modellerinin oluşturulmasında iki gelişmiş topluluk öğrenme algoritması olan Gelişmiş Gradyan Artırma (XGBOOST) ve Rastgele Orman (RF) yöntemlerinden yararlanılmıştır. Modeller, farklı ve bağımsız kaynaklardan elde edilen, geniş bir STF bileşimi ile deney koşullarını kapsayan çeşitli deneysel veri setleri kullanılarak eğitilmiş ve doğrulanmıştır. Elde edilen sonuçlar, test aşamasında XGBOOST modelinin %80 RF modelinin ise %72 doğrulukla tahmin yapabildiğini ve XGBOOST'un RF'ye kıyasla daha başarılı olduğunu göstermiştir. Ayrıca hesaplanan öznitelik önemi değerleri TR üzerinde etkili olan temel parametreleri ortaya koymuştur. TR üzerindeki parametrelerin etki değerleri birbirine yakın olduğu görünse de %25,91 ile ortam sıvısı oranı (OSO) ve %24,32 silika oranı (SO) en etkili parametreler olarak öne çıkmaktadır. Bu yaklaşım, STF sistemlerinin reolojik davranışını sade ve etkili bir şekilde değerlendirebilen bir yöntem sunmakta; aynı zamanda kapsamlı deneysel süreçlere duyulan ihtiyacı azaltarak zaman ve maliyet açısından önemli avantajlar sağlamaktadır.

Anahtar Kelimeler: Kayma altında kalınlaşan sıvılar, akıllı malzemeler, kalınlaşma oranı, makine öğrenmesi, reoloji

Corresponding Author: kadir.ercumen@erzincan.edu.tr

Cite this Article: Erzincan University Journal of Science and Technology 2025, 18(3) 981-997. https://doi.org/10.18185/erzifbed.1762456

1. Introduction

Shear Thickening Fluids (STFs) are a special category of non-Newtonian fluids characterized by the property of significantly increasing their viscosity with applied shear stress [1-3]. STFs transition from a liquid-like state to a solid-like state when subjected to stress or impact—a phenomenon called “shear thickening behavior” [4-5]. This unique property makes STFs particularly useful in enhancing the mechanical performance of protective materials such as fabrics and body armor. In addition, these fluids enable them to effectively absorb and dissipate energy during impact events [6-8]. Shear thickening behavior has attracted particular attention in both scientific and technological fields and has found application in improving the ballistic and stab resistance performance of soft body armor [9]. Numerous studies have been conducted on improving the impact resistance performance of textile structures by applying STFs to high-performance fabrics [10-12].At low shear rates, the solid particles in suspension are dispersed in the carrier liquid by Brownian motion. In this case, electrostatic or steric repulsive forces prevent the particles from coming into direct contact with each other, allowing the system to flow at low viscosity. However, as the shear rate increases, hydrodynamic forces overcome the repulsive barriers between the particles. When the critical shear rate is exceeded, the particles briefly come into contact, forming temporary clusters known as ‘hydroclusters’ [13]. These clusters significantly increase resistance to flow, causing a sudden increase in the fluid's viscosity. When the applied stress is removed, the hydrocluster structures disintegrate, and the system returns to its initial low-viscosity state. Thanks to this mechanism, STFs exhibit flexible behaviour under low deformation conditions while demonstrating solid-like strength at high deformation rates, thereby providing superior performance in terms of energy absorption and impact resistance [13-14]. The mechanism of STFs under increasing shear rates is illustrated in Fig. 1. The viscosity of nanofluids and STFs can be experimentally measured at different shear rates using a rheometer [15]. However, this method is time-consuming, expensive, and requires numerous repeated experiments to measure the viscosity of nanofluids at different parameter values, which also increases costs [16,17].

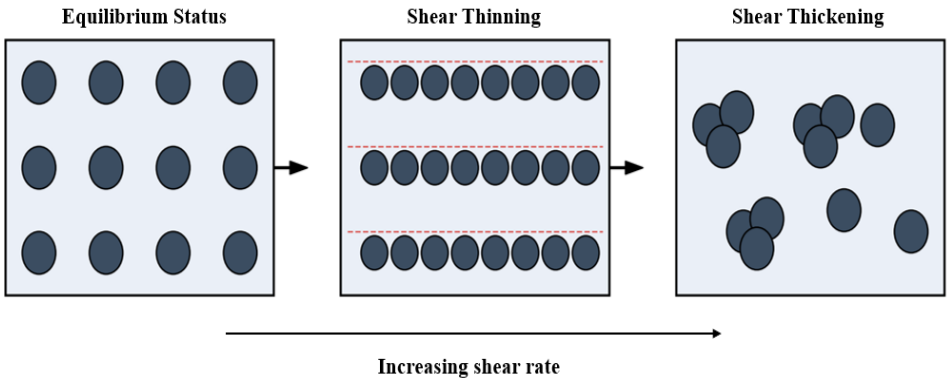

Figure 1. Schematic illustration of the shear thickening mechanism in particle suspensions

Galindo-Rosales et al. [18] propose a new apparent viscosity function for STFs. This function takes into account the three characteristic regions typically exhibited by such materials. Gürgen and et al. [17] adopted a parameter-free artificial intelligence-based approach to model the

complex and non-linear rheological behaviour of multi-phase STF systems and demonstrated that this method can predict viscosity with high accuracy without experimental measurements. Husain et al. [16] used both the Galindo-Rosales-based phenomenological approach and machine learning methods such as SVR and ANN to model the viscosity behaviour of amorphous silica and PEG-based STF systems. As a result, it has been observed that the phenomenological model is prone to learning, whereas machine learning models provide faster, more accurate and generalizable predictions.

A review of the literature reveals various analytical and computational modelling attempts aimed at predicting the entire viscosity curve of STF systems, including not only the shear thickening region but also the shear thinning regions before and after this region. However, the highly complex and variable rheological properties of STFs, such as shear thickening, make it challenging to reliably model the entire viscosity curve. This poses a significant challenge, especially when considering the large number of model parameters and the complex interactions between them.

In this study, instead of modelling the entire viscosity curve, we aim to directly estimate the shear thickening ratio (TR), a summary parameter representing the rheological behaviour of STFs, in order to address the aforementioned literature gaps. In this context, a wide range of parameters was created using independent experimental data sets from different literature sources, and prediction studies were carried out using machine learning-based models. As a result, a simpler and more comparable rheological evaluation method has been developed that enables the comparison of different STF formulations, while also presenting an alternative method that could offer significant time and cost advantages in experimental processes.

2. Material and Methods

2.1. STF Material and Preparation

The basic method used in the production of STFs is to homogenise solid phase particles in a liquid, usually an organic matrix, with the aid of a mechanical mixer. In addition, if the mixture is to be made even more homogeneous, sonochemical techniques are applied to the STFs [19]. Fig. 2 shows a schematic diagram of STF production.

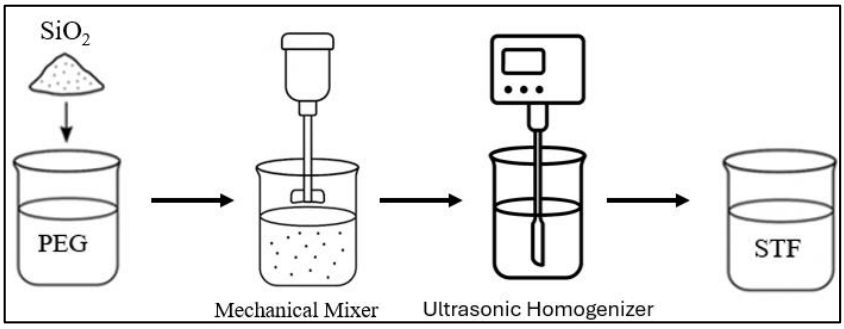

Figure 2. Schematic representation of STF synthesis

STF consists of a carrier fluid and colloidal particles. The particles are typically selected from a range of particle groups containing silica, calcium-carbonate, corn starch, synthetic and naturally occurring minerals, polymers, or a mixture thereof. As a carrier fluid, water, ethylene glycol (EG), glycerine and polyethylene glycol (PEG) are commonly used [20]. Since there are many studies in the literature, in order to limit this situation, studies containing silicon dioxide (SiO_2) as a solid particle and PEG and EG as carrier fluids were taken into consideration in this study.

2.2. Date Sets

The data included in this study were obtained from research articles on STF production by reviewing the literature [21-35]. In the studies reviewed, different types of STFs were experimentally produced and rheologically tested using a rheometer. The common feature of the data selected for data collection is that the two primary components of STF are the solid SiO_2 and the liquid PEG and EG. The main reason for focusing on these materials is that the use of these materials is widely covered in the literature, and this will increase the effect of keeping certain parameters constant on predictability. The model created within the scope of the study includes five independent variables (particle size, molecular weight of the caried fluid, rheological test temperature, carried fluid content by weight, and silica content by weight) and one dependent variable (shear thickening ratio). Descriptions of the six attributes are provided in Table 1.

Table 1. The parameters used in the datasets

Variable Name	Unit	Variable Type	Abbreviation
Particle Size	nm	Independent Variable	SBO
Molecular Weight of The Carrier Fluid	g/mol	Independent Variable	OS
Rheological Test Temperature	°C	Independent Variable	S
Silica Content by Weight	%	Independent Variable	SO
Carrier Fluid Content by Weight	%	Independent Variable	OSO
Shear Thickening Ratio	-	Dependent Variable	TR

Particle size (SBO) refers to the average diameter of solid phase particles, such as SiO_2, used in STF. It has a direct impact on rheological behavior and can vary between submicron and nano-sized ranges [21]. The molecular weight of the carried fluid (OS) indicates the average molecular weight of the carrier fluid constituting the STF. It is an important parameter affecting the viscosity and suspension stability of particles [32]. The rheological test temperature (S) is the temperature at which the test is performed to determine the viscosity-shear rate relationship of STF. Temperature changes can significantly affect flow behavior. As temperature increases, shear thickening phenomena begin to appear at higher shear rates [23,27]. The weight of the carrier fluid content (OSO) refers to the percentage by weight of the fluid used in the STF mixture in the total mixture. The amount of fluid phase determines the fluidity and dispersibility properties of the system [30,31]. Silica content by weight (SO) indicates the percentage by weight of solid phase particles in the total mixture. High ratios can make shear thickening behaviour more pronounced [30,31].

The shear thickening ratio (TR) used as the dependent variable defines the amount of increase in the viscosity of the fluid. It is calculated as the ratio of the maximum viscosity of the suspension to the viscosity at the critical shear rate [28] and is a summary indicator of rheological behaviour. The formula for TR is presented in Equation 1.

$$TR = \frac{\eta\ max}{\eta\ critical\ shear\ rate} \quad (1)$$

2.3. Machine Learning Methods

2.3.1. Extreme Gradient Boosting

Extreme Gradient Boosting (XGBOOST), although developed relatively recently by Chen and Guestrin [36], has rapidly become a popular method in machine learning in recent years. XGBOOST is an algorithm based on gradient boosting trees, which can play a powerful role in gradient boosting. Based on classification and regression tree theory, XGBOOST can be a very effective method for regression and classification problems [37]. The XGBOOST algorithm is widely used due to its high scalability and fast performance. In addition to efficiently handling sparse matrices, it improves model accuracy by assigning weights to examples using the weighted quantile plotting method in tree-based learning. XGBOOST performs cross-validation and automatically handles missing values. It is preferred for large datasets and high-dimensional feature spaces. Additionally, it is resistant to overfitting, and hyperparameter tuning is relatively straightforward. With all these features, it provides a functional algorithm example for users [38].

2.3.2. Random Forest

RF, proposed by Breiman [39], is a non-parametric and tree-based ensemble technique. Unlike traditional statistical methods, RF contains many decision tree models that are easy to interpret

instead of parametric models [39-40]. Thanks to this structure, the generalisation power of individual trees and the correlation between them are evaluated together to minimise the overall error rate of the model. Randomness significantly reduces the risk of overfitting and increases the model's robustness to noise [39,41].

The algorithm achieves high success in classification and regression problems. As the number of features used in node splitting increases, performance metrics such as error, tree strength, and variable interrelationships are evaluated using internal (out-of-bag) predictions made within the model. These internal predictions are also used to determine variable importance levels [41].

2.4. Creating a Rheological Prediction Model with Xgboost and Random Forest

In this study, two different machine learning algorithms were used to model rheological data. XGBOOST and RF algorithms. Both methods stand out with their ability to work effectively with non-linear and multi-variable data structures, provide high prediction success, and ensure model explainability.

In this study, the data set was divided into two parts, 80% training data and 20% test data, for the purpose of evaluating model performance. This ratio is a division strategy that is widely preferred in machine learning literature and has been reported to yield successful results [42-43]. After preparing the training and test data sets, data pre-processing steps were applied in a standard manner and standardisation was performed on all variables. Thus, the data was presented to the model in the same scale range, minimising scale effects that may occur during the learning process of the algorithms. The workflow diagram for the study stages is shown in Fig. 3.

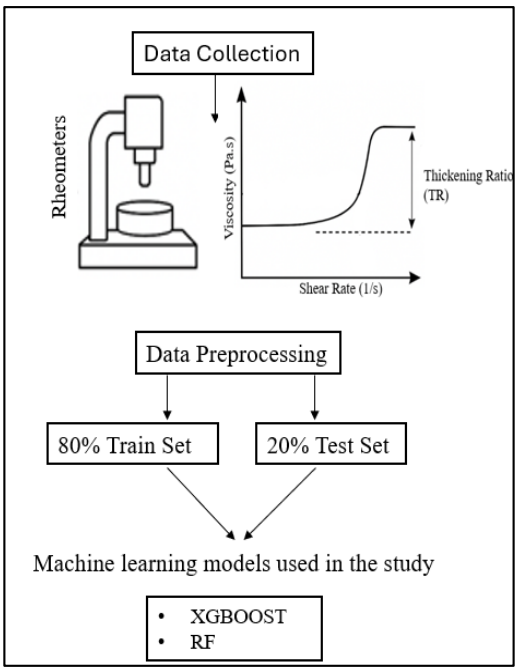

Figure 3. Workflow diagram of the study

In the analyses conducted to evaluate the model's performance, various performance metrics were considered separately and interpreted. To improve these metrics, different data splitting scenarios were tested using the cross-validation method. Cross-validation is a technique commonly used in machine learning and statistical analysis to test the generalisability of a model. The K-fold cross-validation method used in this context divides the data set into equal parts and allows the performance of the model on each subset to be observed [38]. In this study, different K values (between 5 and 10) were tested, and the best performance was obtained when the data set was divided into 5 folds.

In addition, hyperparameter optimisation was performed to further improve the performance of the model. At this stage, various settings of the algorithms used were systematically changed and the parameter combinations at which the model worked most efficiently were determined. Thus, it was aimed to ensure that the model would show a strong prediction ability not only for the existing data but also for new data with a similar structure.

In evaluating model performance, four commonly used statistical metrics were employed. Mean Absolute Error (MAE), Root Mean Square Error (RMSE), Mean Squared Error (MSE), and Determination Coefficient (R^2) [44-45]. The obtained prediction results were compared and analysed using these metrics. The equations for these metrics are presented in Table 2.

Table 2. The equations of performance criteria.

Term	Function	Equation
R^2	Determination Coefficient	$R^2 = 1 - \frac{\sum_{i=1}^{N}(y_i - \hat{y}_i)^2}{\sum_{i=1}^{N}(y_i - \bar{y})^2}$
RMSE	Root Mean Square Error	$RMSE = \sqrt{\frac{1}{N}\sum_{k=1}^{N}(y_k - \hat{y}_k)^2}$
MAE	Mean Absolute Error	$MAE = \frac{1}{N}\sum_{i=1}^{N}\lvert y_i - \hat{y}_i \rvert$
MSE	Mean Squared Error	$MSE = \frac{1}{N}\sum_{i=1}^{N}(y_i - \hat{y}_i)^2$

3. Results and Disscussion

In this study, five basic independent variables were used in the creation of machine learning models. These variables are particle size, molecular weight of the carrier fluid, rheological test temperature, particle weight ratio, and carrier fluid weight ratio, which represent the basic experimental conditions of STF systems. These variables were input into machine learning models designed to predict thickening behaviour.

Two different machine learning algorithms, RF and XGBOOST, were used in the analysis of the rheological data presented in this study. Both algorithms were preferred because of their

good performance in modelling non-linear and multi-variable systems. The performance evaluation metrics of the applied algorithms are presented in Table 3. As seen in Table 3, the XGBOOST model outperformed the RF model in all performance metrics. In particular, the R^2 value was higher at 0.80 in the XGBOOST model, indicating that the model represents the relationship between variables more strongly. The MAE, RMSE, and MSE values, which indicate error rates, were observed as 14.68, 19.85, and 394.05, respectively, in the XGBOOST model. These values are lower than the RF model's values of 15.53, 21.46, and 460.91, respectively, for the same metrics. These results show that the XGBOOST model is more successful in both minimising error rates and making predictions with high explanatory power. Therefore, in the context of this study, the XGBOOST algorithm has demonstrated more effective prediction performance on the data set examined and has emerged as a preferred method.

Table 3. Comparison of machine learning models in terms of effectiveness metrics

Method	**R^2**	**MAE**	**RMSE**	**MSE**
Random Forest (RF)	0.72	15.53	21.46	460.91
Extreme Gradient Boosting (XGBOOST)	0.80	14.68	19.85	394.05

Visual evaluation of the performance of the RF model was performed using the scatter plots of training and test data given in Fig. 4. In the graphs, the actual values are on the horizontal axis and the values predicted by the model are on the vertical axis. The orange dashed line represents the ideal linear relationship ($y = x$).

In the training data graph, it can be observed that the data points are largely close to the ideal line. This shows that the model can make predictions with high accuracy on the training data. However, the presence of some deviations, especially in the high value range, indicates that the model can learn extreme values to a limited extent.

The test data plot shows that the predictions are more scattered around the ideal line. This suggests that the model's generalization capacity on the test data is limited. The increased deviations in high-value examples indicate a decrease in model accuracy in this region. However, it appears that the predicted values vary consistently with the actual values, in line with the general trend, meaning the model is able to capture the underlying pattern.

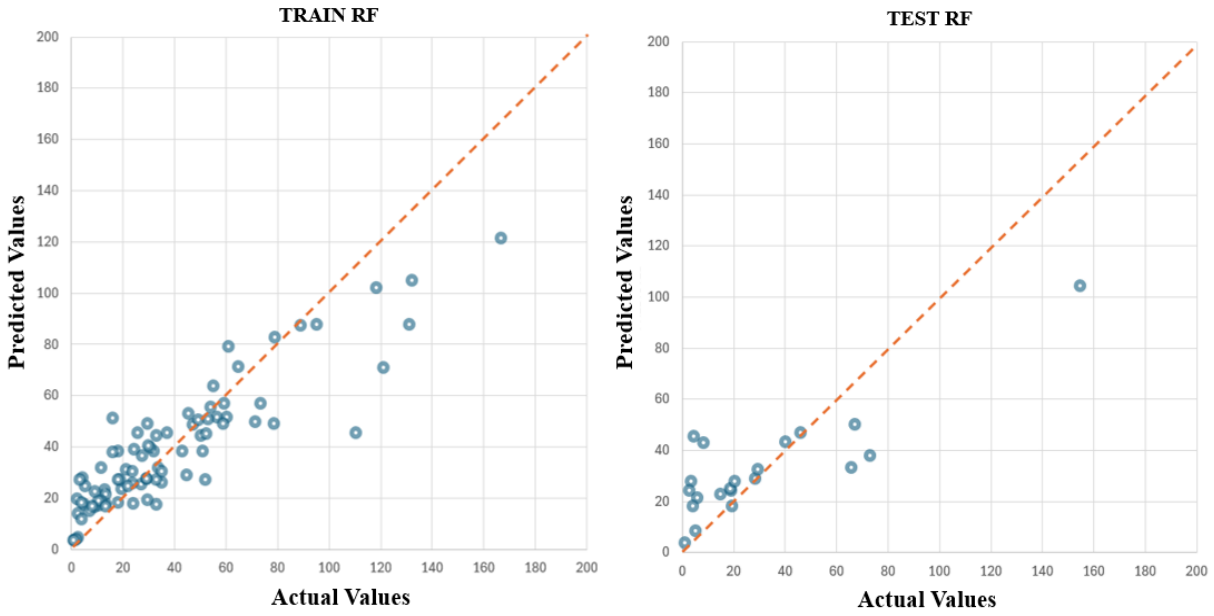

Figure 4. Scatter plot of training and test data of the RF model

The scatter plots of the XGBOOST method are presented in Fig. 5. Through this plot, the relationship between the actual and predicted values of the model can be easily evaluated visually.

In the graph of the training data, it is observed that the predicted values are quite close to the true values across a wide range, and the distribution is densely concentrated around the ideal line. This suggests that the model has adequately learned the data and grasped the general structure without exhibiting a tendency to over-learn. The limited deviations observed in the extreme values indicate that the model is partially challenged in its predictions at the extreme ends.

A similar success is observed in the test data graph. The data points are generally located on or near the ideal line, indicating that the model can generalise with high accuracy on the test data. Although there are a few outlier data points with notable deviations, these are not significant enough to negatively impact the overall model performance.

When compared to Fig. 4 belonging to the RF model, it is noteworthy that the XGBOOST model exhibits a more balanced and line-close distribution. In particular, less dispersion and higher accuracy were obtained in the test set compared to the RF model. This shows that the XGBOOST algorithm has a stronger generalisation ability and prediction performance than RF on the data set used in the study.

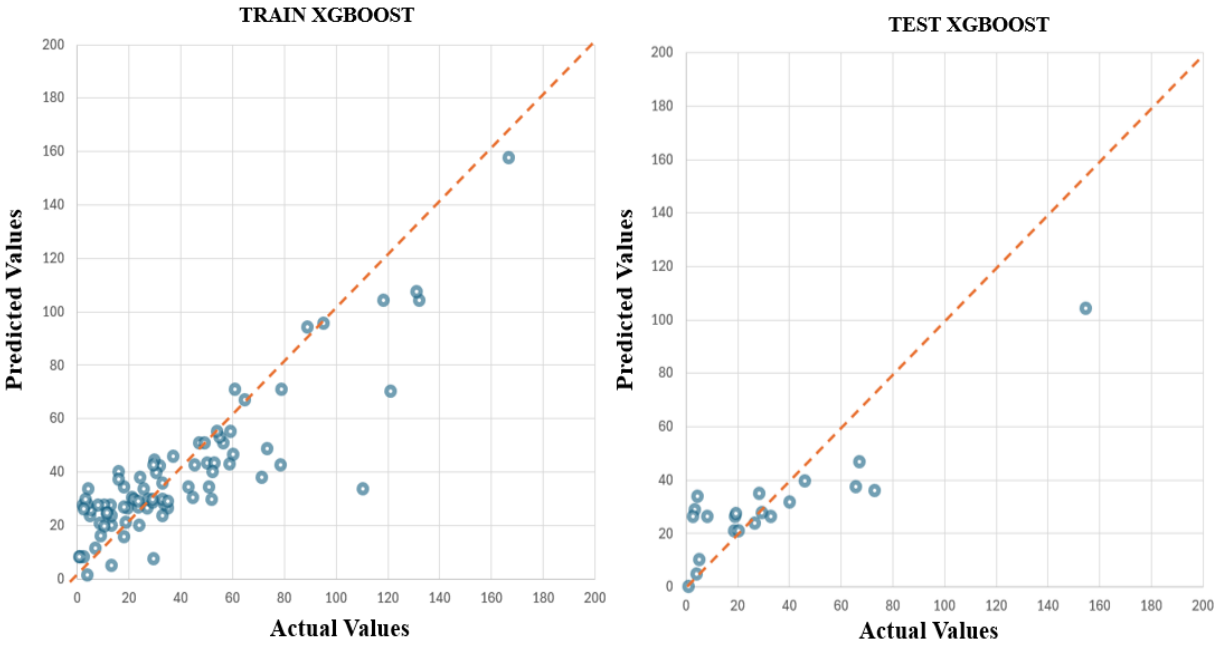

Figure 5. Scatter plot of training and test data of the XGBOOST model

Feature importance is an evaluation method that measures the extent to which independent variables contribute to a machine learning model's prediction process. The aim is to determine which variables are more dominant or effective in the model's decision-making mechanism [46-47]. In the machine learning model used for TR prediction, the percentage feature importance distribution showing the contribution of each feature to the model is presented in Fig. 6. According to the feature importance analysis, the two parameters that contributed the most to the model were OSO (25.91%) and SO (24.31%). These two attributes played a dominant role in the model's TR predictions, accounting for approximately half (50.2%) of the total effects. When reviewing the literature, it can be seen that when the weight ratio of solid particles or fluid medium changes, the rheological properties of dispersion are directly affected. An increase in the solid particle ratio or a decrease in the fluid ratio will cause thickening behaviour to be observed at lower shear rates [25,27,30,31]. This situation reveals the decisive effect of these variables on rheological behaviour. In particular, the highest percentage value of OSO indicates that this variable is referenced more frequently than others in the model's decision-making mechanism. When other attributes are examined, S (18.49%) contributes moderately to the model's accuracy, while OS (15.98%) and SBO (15.30%) have relatively lower contributions. However, the effects of these three variables are similar and support the model's overall prediction performance.

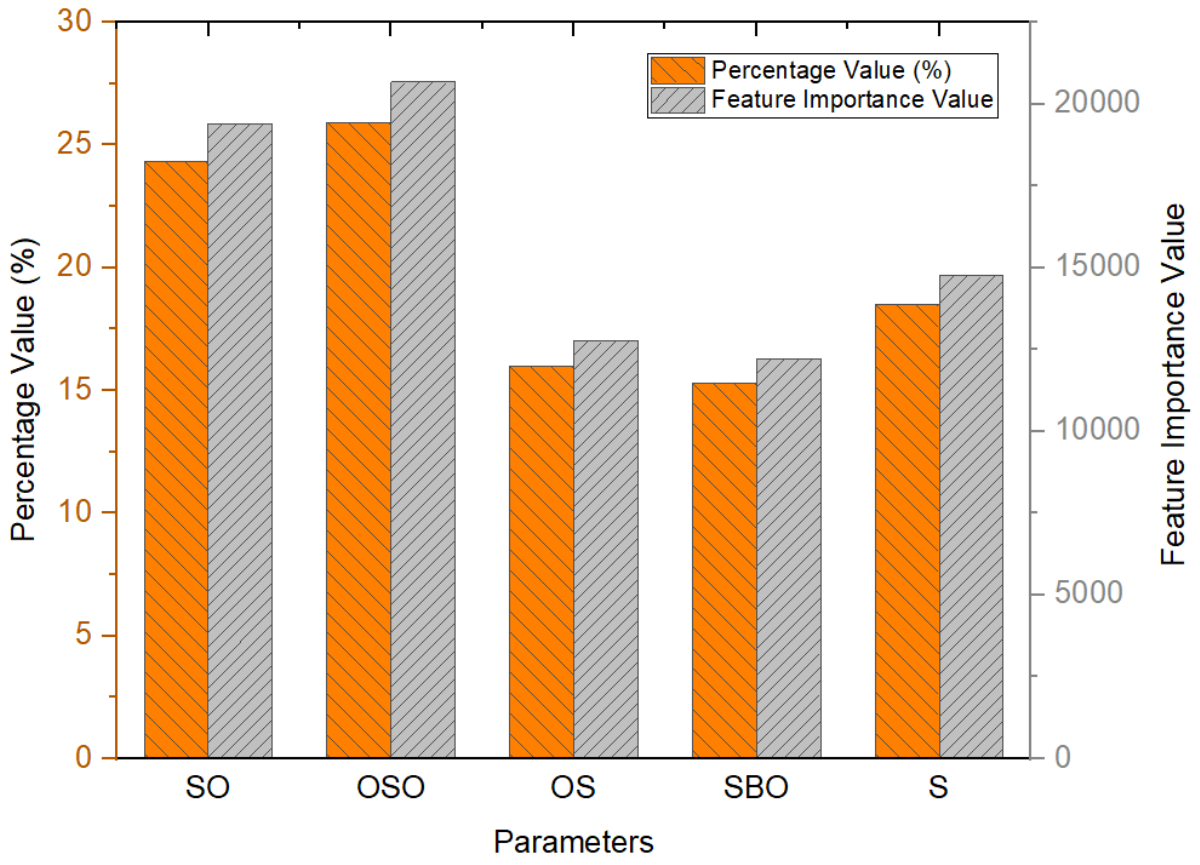

Figure 6. Feature importance values and percentage distributions of the parameters used in TR estimation

These findings demonstrate the machine learning algorithm's ability to distinguish between rheological data attributes and quantitatively evaluate the effect of each variable on the model. Looking at the attribute importance percentages, it can be seen that the variables' contributions to the model exhibit a nearly homogeneous and balanced distribution. This indicates that the model can generalise by considering all features without being overly dependent on any single parameter. The results obtained serve as a reference for both planning experimental processes and making decisions regarding parameter optimisation.

4. Conclusion

In this study, the shear thickening ratio, which characterises the rheological behaviour of STF systems, was estimated using machine learning algorithms instead of classical viscosity curves. The developed models were trained with experimentally obtained multivariate data and their performances were evaluated with statistical indicators.

As a result of the comparative analysis, the XGBOOST algorithm yielded better predictive performance compared to the RF method. The R^2 value of the XGBOOST model on the test data was 0.80, indicating a satisfactory predictive capacity and suggesting potential generalization ability. In contrast, the RF model achieved an R^2 value of 0.72 on the test data,

with performance deviations particularly evident at higher target values. When compared in terms of MAE values, the XGBOOST model reduced the mean absolute error by approximately 5.47% compared to the RF model. Additionally, the XGBOOST model reduced the average squared error by approximately 14.48% compared to RF.

When examining the scatter plots, it was determined that the XGBOOST model showed a distribution close to the ideal prediction line in both training and test data, thus demonstrating consistent performance in terms of both learning and generalisation. In the RF model, a more scattered structure emerged in the test data. However, while the XGBOOST model stands out in terms of statistical metrics and graphical distribution, the difference between the two models is not significantly large in absolute terms.

Furthermore, the calculated feature importance values indicate that the parameter effects on TR are distributed in a balanced manner. The OSO (25.91%) and SO (24.32%) parameters contribute the most, while other features also contribute to a similar extent. This shows that the model performs meaningful learning based on the entire feature set, not just a limited number of variables.

As a result, the data-driven approach proposed in this study stands out as an effective and practical method for predicting the behaviour of STF systems, providing an important contribution that could serve as an alternative to traditional experimental methods.

Ethics in Publishing

There are no ethical issues regarding the publication of this study.

Author Contributions

The research, data collection, evaluation of results, and writing of the article were carried out by Kadir Münir ERCÜMEN.

References

[1] Serra, G. F., Oliveira, L., Gürgen, S., de Sousa, R. A., & Fernandes, F. A. (2024). Shear thickening fluid (STF) in engineering applications and the potential of cork in STF-based composites. Advances in Colloid and Interface Science, 327, 103157. https://doi.org/10.1016/j.cis.2024.103157

[2] Fernandes, T. R., Alves de Sousa, R. J., & Fernandes, F. A. (2025). Multilayered cork-STF composite structures enhanced with laser texturing for impact mitigation. The International Journal of Advanced Manufacturing Technology, 136(1), 97-107. https://doi.org/10.1007/s00170-024-13815-1

[3] Wang, L., Du, Z., Fu, W., & Wang, P. (2021). Study of mechanical property of shear thickening fluid (STF) for soft body-armor. Materials Research Express, 8(4), 045021. DOI 10.1088/2053-1591/abf76a

[4] Park, Y., Baluch, A. H., Kim, Y., & Kim, C. G. (2013). High velocity impact characteristics of shear thickening fluid impregnated Kevlar fabric. International Journal of Aeronautical and Space Sciences, 14(2), 140-145.

[5] Wang, Y., Li, S. K., & Feng, X. Y. (2015). The ballistic performance of multi-layer Kevlar fabrics impregnated with shear thickening fluids. Applied Mechanics and Materials, 782, 153-157. https://doi.org/10.4028/www.scientific.net/AMM.782.153

[6] Khodadadi, A., Liaghat, G., Vahid, S., Sabet, A. R., & Hadavinia, H. (2019). Ballistic performance of Kevlar fabric impregnated with nanosilica/PEG shear thickening fluid. Composites Part B: Engineering, 162, 643-652. https://doi.org/10.1016/j.compositesb.2018.12.121

[7] Zelelew, T. M., Ali, A. N., Kidanemariam, G., Kebede, G. A., & Koricho, E. G. (2025). Effects of shear thickening fluids to enhance the impact resistance of soft body armor composites: a review. Smart Materials and Structures. DOI 10.1088/1361-665X/adbdb2

[8] Ercümen, K. M., & Aydin, M. (2024). Ballistic impact performance of aramid fabrics impregnated with single-phase shear thickening fluids STFs and SiC additive multi-phase shear thickening fluids. Polymer Composites, 45(18), 16850-16865. https://doi.org/10.1002/pc.28936

[9] Hasanzadeh, M., Mottaghitalab, V., Rezaei, M., & Babaei, H. (2017). Numerical and experimental investigations into the response of STF-treated fabric composites undergoing ballistic impact. Thin-Walled Structures, 119, 700-706. https://doi.org/10.1016/j.tws.2017.07.020

[10] Ercümen, K.M., Aydin, M. Experimental Investigation of Ballistic Impact Performance of Composite Structures Prepared by Shear Thickening Fluid Impregnation Into Aramid, Uhmwpe, and Hybrid Fabrics. Exp Tech (2025). https://doi.org/10.1007/s40799-025-00809-1

[11] Fahool, M., & Sabet, A. R. (2016). Parametric study of energy absorption mechanism in Twaron fabric impregnated with a shear thickening fluid. International Journal of Impact Engineering, 90, 61-71. https://doi.org/10.1016/j.ijimpeng.2015.11.016

[12] Aşkan, A., & Aydın, M. (2025). The role of impact energy and silica concentration on dynamic impact and quasi-static puncture resistance of fabrics treated with shear-thickening fluids. Composite Structures, 352, 118689. https://doi.org/10.1016/j.compstruct.2024.118689

[13] Wang, S., Zhang, W., Gao, J., Gao, D., & He, C. (2024). Characteristics of shear thickening fluid and its application in engineering: a state-of-the-art review. The International Journal of

Advanced Manufacturing Technology, 133(5), 1973-2000. https://doi.org/10.1007/s00170-024-13816-0

[14] Zarei, M., & Aalaie, J. (2020). Application of shear thickening fluids in material development. Journal of Materials Research and Technology, 9(5), 10411-10433. https://doi.org/10.1016/j.jmrt.2020.07.049

[15] Astaraki, S., Zamani, E., Moghadam, M., Pol, M. H., & Hasannezhad, H. (2024). Investigating the effect of temperature, angular frequency, and strain on the rheological properties of shear thickening fluid (STF) with different weight fractions of fumed silica. Colloid and Polymer Science, 302(1), 1-11. https://doi.org/10.1007/s00396-023-05173-3

[16] Husain, M., Aftab, R. A., Zaidi, S., & Rizvi, S. J. A. (2025). Shear thickening fluid: A multifaceted rheological modeling integrating phenomenology and machine learning approach. Journal of Molecular Liquids, 425, 127223. https://doi.org/10.1016/j.molliq.2025.127223

[17] Gürgen, S., Sofuoğlu, M. A., & Kuşhan, M. C. (2020). Rheological modeling of multi-phase shear thickening fluid using an intelligent methodology. Journal of the Brazilian Society of Mechanical Sciences and Engineering, 42, 1-7. https://doi.org/10.1007/s40430-020-02681-z

[18] Galindo-Rosales, F. J., Rubio-Hernández, F. J., & Sevilla, A. (2011). An apparent viscosity function for shear thickening fluids. Journal of Non-Newtonian Fluid Mechanics, 166(5-6), 321-325. https://doi.org/10.1016/j.jnnfm.2011.01.001

[19] Chamola, R., Das, S., Ahlawat, D. S., Mishra, Y. K., & Goyat, M. S. (2024). Recent developments in shear thickening fluid-impregnated synthetic and natural fiber-reinforced composites for ballistic applications: a review. Journal of Materials Science, 59(3), 747-793. https://doi.org/10.1007/s10853-023-09201-z

[20] Liu, H., Fu, K., Cui, X., Zhu, H., & Yang, B. (2023). Shear thickening fluid and its application in impact protection: a review. Polymers, 15(10), 2238. https://doi.org/10.3390/polym15102238

[21] Bajya, M., Majumdar, A., Butola, B. S., Verma, S. K., & Bhattacharjee, D. (2020). Design strategy for optimising weight and ballistic performance of soft body armour reinforced with shear thickening fluid. Composites Part B: Engineering, 183, 107721. https://doi.org/10.1016/j.compositesb.2019.107721

[22] Manukonda, B. H., Chatterjee, V. A., Verma, S. K., Bhattacharjee, D., Biswas, I., & Neogi, S. (2020). Rheology based design of shear thickening fluid for soft body armor applications. Periodica Polytechnica Chemical Engineering, 64(1), 75-84. https://doi.org/10.3311/PPch.13626

[23] Das, J., Butola, B. S., & Majumdar, A. (2025). Development of stab resistant armor for different energy levels using shear thickening fluid reinforced multi-layered p-aramid fabrics. Polymer Composites, 46(2), 1843-1856. https://doi.org/10.1002/pc.29077

[24] Chang, C. P., Shih, C. H., You, J. L., Youh, M. J., Liu, Y. M., & Ger, M. D. (2021). Preparation and ballistic performance of a multi-layer armor system composed of kevlar/polyurea composites and shear thickening fluid (Stf)-filled paper honeycomb panels. Polymers, 13(18), 3080. https://doi.org/10.3390/polym13183080

[25] Yeh, S. K., Lin, J. J., Zhuang, H. Y., Chen, Y. C., Chang, H. C., Zheng, J. Y., ... & Rwei, S. P. (2019). Light shear thickening fluid (STF)/Kevlar composites with improved ballistic impact strength. Journal of Polymer Research, 26(6), 155. https://doi.org/10.1007/s10965-019-1811-8

[26] Tian, T., Peng, G., Li, W., Ding, J., & Nakano, M. (2015). Experimental and modelling study of the effect of temperature on shear thickening fluids. Korea-Australia rheology journal, 27(1), 17-24. https://doi.org/10.1007/s13367-015-0003-2

[27] Liu, X. Q., Bao, R. Y., Wu, X. J., Yang, W., Xie, B. H., & Yang, M. B. (2015). Temperature induced gelation transition of a fumed silica/PEG shear thickening fluid. Rsc Advances, 5(24), 18367-18374. https://doi.org/10.1039/C4RA16261G

[28] Gürgen, S., & Kuşhan, M. C. (2017). The ballistic performance of aramid based fabrics impregnated with multi-phase shear thickening fluids. Polymer Testing, 64, 296-306. https://doi.org/10.1016/j.polymertesting.2017.11.003

[29] Baharvandi, H. R., Saeedi Heydari, M., Kordani, N., Alebooyeh, M., Alizadeh, M., & Khaksari, P. (2017). Characterization of the rheological and mechanical properties of shear thickening fluid-coated Twaron® composite. The Journal of The Textile Institute, 108(3), 397-407. https://doi.org/10.1080/00405000.2016.1168091

[30] Liu, L., Yang, Z., Zhao, Z., Liu, X., & Chen, W. (2020). The influences of rheological property on the impact performance of kevlar fabrics impregnated with SiO_2/PEG shear thickening fluid. Thin-Walled Structures, 151, 106717. https://doi.org/10.1016/j.tws.2020.106717

[31] Baharvandi, H. R., Alebooyeh, M., Alizadeh, M., Khaksari, P., & Kordani, N. (2016). Effect of silica weight fraction on rheological and quasi-static puncture characteristics of shear thickening fluid-treated Twaron® composite. Journal of Industrial Textiles, 46(2), 473-494. https://doi.org/10.1177/1528083715589750

[32] Yanen, C. (2021). Hibrit nanopartikül takviyeli kayma altında katılaşan sıvıların balistik uygulamalarında kullanımının araştırılması [Investigation of the use of hybrid nanoparticle-reinforced shear thickening fluids in ballistic applications] (Doctoral dissertation). Elazığ University, Department of Mechanical Engineering.

[33] Li, D., Wang, R., Liu, X., Zhang, S., Fang, S., & Yan, R. (2020). Effect of dispersing media and temperature on inter-yarn frictional properties of Kevlar fabrics impregnated with shear thickening fluid. Composite Structures, 249, 112557. https://doi.org/10.1016/j.compstruct.2020.112557

[34] Mawkhlieng, U., & Majumdar, A. (2019). Deconstructing the role of shear thickening fluid in enhancing the impact resistance of high-performance fabrics. Composites Part B: Engineering, 175, 107167. https://doi.org/10.1016/j.compositesb.2019.107167

[35] Grover, G., Verma, S. K., Thakur, A., Biswas, I., & Bhatacharjee, D. (2020). The effect of particle size and concentration on the ballistic resistance of different shear thickening fluids. Materials Today: Proceedings, 28, 1472-1476. https://doi.org/10.1016/j.matpr.2020.04.823

[36] Chen, T., & Guestrin, C. (2016, August). Xgboost: A scalable tree boosting system. In Proceedings of the 22nd acm sigkdd international conference on knowledge discovery and data mining (pp. 785-794). https://doi.org/10.1145/2939672.2939785.

[37] Qiu, Y., Zhou, J., Khandelwal, M., Yang, H., Yang, P., & Li, C. (2022). Performance evaluation of hybrid WOA-XGBoost, GWO-XGBoost and BO-XGBoost models to predict blast-induced ground vibration. Engineering with Computers, 38(Suppl 5), 4145-4162. https://doi.org/10.1007/s00366-021-01393-9

[38] Aslay, S. E. (2024). Yapım İşlerinde İhale Parametreleri Kullanılarak Makine Öğrenmesi ile Sözleşme Bedeli Tahmini. Karaelmas Fen ve Mühendislik Dergisi, 14(3), 64-73. https://doi.org/10.7212/karaelmasfen.1484595

[39] Breiman, L. (2001). Random forests. Machine learning, 45(1), 5-32. https://doi.org/10.1023/A:1010933404324

[40] Adusumilli, S., Bhatt, D., Wang, H., Bhattacharya, P., & Devabhaktuni, V. (2013). A low-cost INS/GPS integration methodology based on random forest regression. Expert Systems with Applications, 40(11), 4653-4659. https://doi.org/10.1016/j.eswa.2013.02.002

[41] Upreti, K., Verma, M., Agrawal, M., Garg, J., Kaushik, R., Agrawal, C., ... & Narayanasamy, R. (2022). Prediction of mechanical strength by using an artificial neural network and random forest algorithm. Journal of Nanomaterials, 2022(1), 7791582. https://doi.org/10.1155/2022/7791582

[42] Aslan, S., & Yıldız, T. (2022). Makine öğrenmesinde rastgele oran ve sıralı küme örneklemesi yöntemlerinin doğrusal regresyon modellerine etkisi. Dokuz Eylül Üniversitesi Mühendislik Fakültesi Fen ve Mühendislik Dergisi, 24(70), 29-36. https://doi.org/10.21205/deufmd.2022247004

[43] Kilinc, H. C., Haznedar, B., Ozkan, F., & Katipoğlu, O. M. (2024). An evolutionary hybrid method based on particle swarm optimization algorithm and extreme gradient boosting for short-term streamflow forecasting. Acta Geophysica, 72(5), 3661-3681. https://doi.org/10.1007/s11600-024-01307-5

[44] Aslay, S. E. (2025). Building Energy Prediction Model with AI-Based PSO-ANN Approach Integrating Architectural and HVAC Processes. Building and Environment, 113305. https://doi.org/10.1016/j.buildenv.2025.113305

[45] Thodda, G., Madhavan, V. R., & Thangavelu, L. (2023). Predictive modelling and optimization of performance and emissions of acetylene fuelled CI engine using ANN and RSM. Energy Sources, Part A: Recovery, Utilization, and Environmental Effects, 45(2), 3544-3562. https://doi.org/10.1080/15567036.2020.1829191

[46] Brown, M. G., Peterson, M. G., Tezaur, I. K., Peterson, K. J., & Bull, D. L. (2025). Random forest regression feature importance for climate impact pathway detection. Journal of Computational and Applied Mathematics, 464, 116479. https://doi.org/10.1016/j.cam.2024.116479

[47] Aslay, S. E. (2024). Estimating contract value using structural parameters: a machine learning approach with data preprocessing. Dicle Üniversitesi Mühendislik Fakültesi Mühendislik Dergisi, 15(3), 755-765. https://doi.org/10.24012/dumf.1515160